Contaminants Redistribution in Heterogeneous Systems

Dissertation

der Mathematisch-Naturwissenschaftlichen Fakultät

der Eberhard Karls Universität Tübingen

zur Erlangung des Grades eines

Doktors der Naturwissenschaften

(Dr. rer. nat.)

vorgelegt von

Binlong Liu, M.Sc

aus Fujian, China

Tübingen

2024

Gedruckt mit Genehmigung der Mathematisch-Naturwissenschaftlichen Fakultät der Eberhard Karls Universität Tübingen.

Tag der mündlichen Qualifikation:	06.06.2024
Dekan:	Prof. Dr. Thilo Stehle
1. Berichterstatter/-in:	Prof. Dr. Peter Grathwohl
2. Berichterstatter/-in:	Prof. Dr.-Ing. Olaf A. Cirpka

Abstract

Sorption/desorption is important phenomena in various scientific and industrial fields, such as contaminants removal via activated carbon in water treatment, duration of soil remediation, gas separation in chemical engineering, pollutant transport by airborne particles (or suspended particles/sediments in rivers or batch or column tests for biodegradation or contaminant transport), etc. Sorption/desorption kinetics has to be considered for sorbents with large grain sizes (d), distribution coefficients (K_d) or small intraparticle porosities (ε). A coupled model was developed taking both external film diffusion and intraparticle diffusion into account. At early time, external mass transfer resistance dominates mass transfer, while the internal mass transfer resistance takes over at late time. Since no simple analytical solution in real time domain exists for the coupled model even for homogenous sorbent and numerical solutions need intricate discretization in time and space, I derived a semi-Laplace solution for coupled model where the (average) concentrations in each phase (e.g., solid and water) in real time domain can be obtained via a very fast and efficient inverse Laplace transformation. For practical use, a first order approximation solution for coupled model was derived, which can be easily applied for fractional solute uptake in the solid phase ranging from 50 to 91% of equilibrium achieved, representing scenarios typically encountered in batch experiments. The derived solutions showed that mass transfer shifts from external film diffusion to intraparticle diffusion depending on K_d, ε or Sherwood number (Sh).

Secondly, I extended the semi-Laplace solution to redistribution in heterogeneous systems allowing easy adaptation of different kinetics models for different sorbents in terms of their properties (particle size, geometry, intraparticle porosity, organic carbon content, distribution coefficient etc.) by using different transfer functions in Laplace domain; solute concentrations in each phase can be obtained by inverse Laplace transformation. The redistribution model was validated by two batch experiments (Phenanthrene/Anthracene d10 redistribution in mixtures of spherical microplastics of different sizes and a sediment suspension with polyethylene passive samplers). Sherwood numbers fitted to experimental data agree well with Sherwood number relationships for suspended particles based on boundary layer theory and Kolmogorov's turbulence theory. Heterogenous materials (e.g., soils or sediments) with only few percent of strong sorbents might lead to pseudo-equilibration at early times, which rapidly lowers concentration gradients and thus slows down sorption in the remaining part of the mixture tremendously (even slower than in an equivalent homogeneous strong sorbent). The kinetics of this few percent of strong sorbents are super slow and their behaviors cannot be captured in short batch tests, which might explain discrepancies in solute mass recoveries in batch tests (mass release from strong sorbents not captured) and exhaustive solvent extraction methods.

The coupled model application also allows to nicely explain particle/gas distribution kinetics of polycyclic aromatic hydrocarbons (PAHs) in the atmosphere. Mass transfer of low molecular weight PAHs with low distribution coefficients ($K_{pg}s$) is dominated by intraparticle pore diffusion, while external film diffusion is limiting for high molecular weight compounds. The latter results in maximum observed distribution coefficients i.e. apparent bulk distribution coefficients ($K_{pg,b,a}$); appear independent on octanol-air partitioning coefficient (K_{oa}) or subcooled liquid vapor pressure (P_L^o) (slope = 0); for intraparticle pore diffusion they in-/decrease with the square root of K_{oa} or P_L^o. Moderate molecular weight compounds lie in between (slope shifts from 1/2 to 0) and both external and internal mass transfer resistances have to be considered.

Furthermore, I developed a numerical one-dimensional (1D) reactive solute transport model considering different sorption/desorption kinetic mechanisms to investigate the impacts of initial conditions (e.g., pre-equilibrium or after the first flooding of the column) and heterogenous materials on column leaching tests. Through numerical experiments, steep concentration gradients close to the outlet of column have to be expected for compounds with small K_d (< 1 L kg^{-1}). Only for large K_d (> 10 L kg^{-1}), initial conditions can be neglected. Longitudinal dispersion and non-linear sorption smooth the leaching curves and lead to smaller initial concentrations than expected under equilibrium conditions especially for compounds with small K_d values. Sample heterogeneity, including grain size and fractions of sorptive particles, strongly influences leaching curves. A small fraction (< 1%) of strongly sorbing particles with high K_d may cause very slow desorption rates compared to homogeneous sorbent having the same average K_d, especially if mass release is limited by IPPD, leading to non-equilibrium. Mixtures of strongly coarse particles with a small fraction (< 10%) of less sorbing fine material might lead to a stepwise concentration decline in the column effluent.

Finally, I introduced two mesh free methods (semi-Laplace solution and physical informed neural networks (PINNs)) to solve 1D advective-dispersive transport with coupled film-intraparticle pore diffusion (ADE-FIPPD), which can replace the tedious numerical solutions if pre-equilibrium condition (uniform concentration) is initially achieved (e.g., K_d > 10 L kg^{-1}). The semi-Laplace solution shows remarkable performance with deviations of normalized concentrations within the spatial-temporal domain of less than 1% when compared to the numerical solutions. PINNs exhibit slightly higher deviations (< 10%) than the semi-Laplace solution which are still acceptable across most of the spatial-temporal domain excluding the regions with stepwise concentration gradients. Since external mass transfer resistance and dispersion predominate for a very short time period initially, the mass transfer shift in ADE-FIPPD is more likely to be observed for coarse particles with large K_ds (e.g., d >2 cm and K_d > 1000 L kg^{-1}) and intraparticle porosities (ε > 0.2). ADE-FIPPD of fine particles (e.g., d < 400 μm) show almost the same behavior of intraparticle pore diffusion (ADE-IPPD).

This thesis provides various solutions for sorption/desorption kinetics dominated by film diffusion or intraparticle diffusion including coupled models in both homogenous and heterogeneous systems. Those models help us to better understand sorption/desorption behavior in mixtures and the interactions of different sorbents (mass redistribution) within different compartments, which can be easily applied in many fields, such as groundwater remediation, chemical engineering, analytical chemistry, air pollution control, etc.

Zusammenfassung

Sorption/Desorption ist ein wichtiges Phänomen in verschiedenen wissenschaftlichen und industriellen Bereichen, wie z.B. der Entfernung von Schadstoffen mittels Aktivkohle in der Wasseraufbereitung, der Dauer der Bodensanierung, der Verfahrenstechnik, dem partikelgetragenen Schadstofftransport in der Luft (oder auch suspendierte Partikel/Sedimente in Flüssen, Batch - oder Säulentests zur Untersuchung von Bioabbau oder Schadstofftransport). Die Kinetik der Sorption/Desorption muss für Sorbentien mit großen Korngrößen (d), Verteilungskoeffizienten (K_d) oder kleinen intrapartikulären Porositäten (ε) berücksichtigt werden. Ein gekoppeltes Modell wurde entwickelt, das sowohl die äußere Filmdiffusion als auch die intrapartikuläre Diffusion berücksichtigt. Zu Beginn dominiert der Widerstand der Filmdiffusion den die Stoffübertragung, während der innere Stoffübergangswiderstand durch intrapartikuläre Diffusion später limitierend wird. Da für das gekoppelte Modell selbst für homogene Sorptionsmittel keine einfache analytische Lösung im Echtzeitbereich existiert und numerische Lösungen eine komplexe Diskretisierung in Zeit und Raum erfordern, habe ich eine semi-Laplace-Lösung für das gekoppelte Modell abgeleitet, bei der die (durchschnittlichen) Konzentrationen in jeder Phase (z.B. Feststoff und Wasser) mittels einer sehr schnellen und effizienten inversen Laplace-Transformation ermittelt werden können. Für die praktische Anwendung wurde eine Lösung erster Ordnung für das gekoppelte Modell abgeleitet, die gut auf die fraktionierte Aufnahme von Sorbaten in die Festphase im Bereich von 50 bis 91% des erreichten Gleichgewichts angewendet werden kann, was Szenarien repräsentiert, die typischerweise in Batch-Experimenten vorkommen. Die abgeleiteten Lösungen zeigen, dass der Stoffübergang je nach K_d, ε oder Sherwood-Zahl (Sh) vom externen Filmdiffusion zur intrapartikulären Diffusion übergeht.

Zweitens habe ich die semi-Laplace-Lösung auf die Stoffübertragung in heterogenen Systemen erweitert, um eine einfache Anpassung verschiedener Kinetikmodelle für unterschiedliche Sorbentien hinsichtlich ihrer Eigenschaften (Partikelgröße, Geometrie, intrapartikuläre Porosität, organischer Kohlenstoffgehalt, Verteilungskoeffizient usw.) zu ermöglichen. Dies erfolgte durch die Verwendung verschiedener Übertragungsfunktionen im Laplace-Bereich; die Konzentrationen des gelösten Stoffs in jeder Phase können durc h die inverse Laplace-Transformation erhalten werden. Das Umverteilungsmodell wurde durch zwei Batch-Experimente validiert (Phenanthren/Anthracen d10-Umverteilung in Mischungen von sphärischen Mikroplastikpartikeln unterschiedlicher Größe und einer Sediment-Suspension mit Polyethylen-Passivsammlern). Die an die experimentellen Daten angepassten Sherwood-Zahlen stimmen gut mit den Beziehungen für suspendierte Partikel überein, die auf der Grenzschichttheorie und der Turbulenztheorie von Kolmogorov basieren. Heterogene Materialien (z. B. Böden oder Sedimente) mit nur wenigen Prozent stark

sorbierender Anteile können zu einer Pseudo-Gleichgewichtsbildung in den Anfangszeiten führen, was die Konzentrationsgradienten schnell absenkt und somit die Sorption im verbleibenden Teil der Mischung erheblich verlangsamt (sogar langsamer als in einem äquivalenten homogenen stark sorbierenden Stoff). Die Kinetik einer kleinen Fraktion stark sorbierender Anteile ist extrem langsam, und ihr Verhalten kann in kurzen Batch-Tests nicht erfasst werden, was Diskrepanzen zwischen in Batch-Tests und erschöpfenden Extraktionsmethoden erklären könnte (Freisetzung von stark sorbierenden Anteilen wird nicht erfasst).

Die Anwendung des gekoppelten Modells ermöglicht auch eine gute Erklärung der Kinetik der Partikel-/Gasverteilung von polyzyklischen aromatischen Kohlenwasserstoffen (PAK) in der Atmosphäre. Die Stoffübertragung von PAK mit niedrigem Molekulargewicht und niedrigen Verteilungskoeffizienten ($K_{pg}s$) wird von der intrapartikulären Porendiffusion dominiert, während die äußere Filmdiffusion für Verbindungen mit hohem Molekulargewicht begrenzend ist. Letzteres führt zu beobachteten maximalen Verteilungskoeffizienten, d. h. scheinbaren Gesamtverteilungskoeffizienten ($K_{pg,b,a}$); diese scheinen unabhängig vom Octanol-Luft-Partitions-Koeffizienten (K_{oa}) oder dem unterkühlten Dampfdruck (P_L^o) zu sein (Steigung = 0); für die intrapartikuläre Porendiffusion nehmen sie mit der Quadratwurzel von K_{oa} oder P_L^o zu oder ab. Verbindungen mit mittlerem Molekulargewicht liegen dazwischen (die Steigung verschiebt sich von 1/2 auf 0), und sowohl externe als auch interne Stoffübergangswiderstände müssen berücksichtigt werden.

Darüber hinaus habe ich ein numerisches eindimensionales (1D) reaktives tofftransportmodell entwickelt, das verschiedene Sorptions-/Desorptionskinetikmechanismen berücksichtigt, um die Auswirkungen von Anfangsbedingungen (z. B. Vor-Gleichgewicht oder nach dem ersten Durchspülen der Säule) und heterogenen Materialien auf Säulen-Auslaugtests zu untersuchen. Durch numerische Experimente sind steile Konzentrationsgradienten nahe dem Auslass der Säule für Verbindungen mit geringem K_d (< 1 L kg^{-1}) zu erwarten. Nur für große K_d (> 10 L kg^{-1}) können Anfangsbedingungen vernachlässigt werden. Längsdispersion und nichtlineare Sorption glätten die Auslaugkurven und führen zu kleineren Anfangskonzentrationen als unter Gleichgewichtsbedingungen erwartet, besonders für Verbindungen mit geringen K_d-Werten. Die Heterogenität der Proben, einschließlich Korngröße und Anteile sorptiver Partikel, beeinflusst die kurven stark. Eine kleine Fraktion (< 1%) stark sorbierender Partikel mit hohem K_d kann im Vergleich zu einem homogenen Sorptionsmittel mit dem gleichen durchschnittlichen K_d sehr langsame Desorptionsraten verursachen, besonders wenn die Massenfreisetzung durch IPPD begrenzt ist, was zu Nicht-Gleichgewichtszuständen führt. Mischungen aus stark groben Partikeln mit einem kleinen Anteil (< 10%) weniger sorbierendem Feinmaterial können zu einem stufenweisen Konzentrationsabfall im Säulenauslauf führen.

Abschließend habe ich zwei gitterfreie Methoden eingeführt (semi-Laplace-Lösung und physikalisch informierte neuronale Netzwerke (PINNs)), um den 1D advektiv-dispersiven Transport mit gekoppelter Film-Intrapartikel-Porendiffusion (ADE-FIPPD) zu lösen. Diese können die aufwendigen numerischen Lösungen ersetzen, wenn die Gleichgewichtsbedingung (gleichmäßige Konzentration) zu Beginn erreicht ist (z.B. K_d > 10 L kg^{-1}). Die semi-Laplace-Lösung zeigt Abweichungen der normalisierten Konzentrationen von weniger als 1% im Vergleich mit den numerischen Lösungen. PINNs zeigen etwas höhere Abweichungen (< 10%) als die semi-Laplace-Lösung, die jedoch für den Großteil des räumlich-zeitlichen Bereichs akzeptabel sind, ausgenommen in den Bereichen mit stufenweisen Konzentrationsgradienten. Da anfänglich der externe Stoffübergangswiderstand und die Dispersion für einen sehr kurzen Zeitraum vorherrschen, ist der Wechsel im Stoffübergang in ADE-FIPPD wahrscheinlicher bei groben Partikeln mit großen K_ds (z.B. d > 2 cm und K_d > 1000 L kg^{-1}) und intrapartikulären Porositäten (ε > 0,2). ADE-FIPPD von feinen Partikeln (z.B. d < 400 μm) zeigt nahezu dasselbe Verhalten wie die intrapartikuläre Porendiffusion (ADE-IPPD).

Diese Arbeit bietet verschiedene Lösungen zur Beschreibung der Sorptions-/Desorptionskinetik, die von Filmdiffusion oder intrapartikulärer Diffusion dominiert wird, einschließlich gekoppelter Modelle in homogenen und heterogenen Systemen. Diese Modelle helfen uns, das Sorptions-/Desorptionsverhalten in Mischungen und die Interaktionen verschiedener Sorbentien (Massenumverteilung) in verschiedenen Kompartimenten besser zu verstehen und können leicht in vielen Bereichen angewendet werden, wie Grundwassersanierung, Chemietechnik, analytische Chemie, Luftreinhaltung usw.

Acknowledgements

First of all, I would like to thank Prof. Dr. Peter Grathwohl, for providing me the opportunity to work on this dissertation. I learnt a lot of knowledge about sorption isotherms, sorption/desorption kinetics, back diffusion, transverse dispersion in porous media, column leaching test, particle facilitate transport, etc. from his lectures and books. Without this basic knowledge, I would not be able to complete my dissertation. My dissertation was initiated from the inconsistence of fitting Sherwood numbers from lab experiments and empirical relationships for suspended particles in a fluid in my master thesis. The fitting was perfect by using film diffusion model considering multiple grain sizes, while the fitted Sherwood numbers were much smaller than the minimum Sherwood number of 2 (for spherical particles) and violated the classic boundary layer theory and Kolmogorov's turbulence theory which have been proved to be correct by many scientists from physics and chemical engineering. Seldom people realized this problem in many published papers in the field of environmental science and a lot of mass transfer velocities were fitted in different kinds of systems without physical verification. This was the first time Peter taught me to have a critical thinking for scientific works. Thanks to his finding, the coupled model was proposed to solve this problem and this model was also the basis of my dissertation. He also gave me a lot of freedom to do the topics I was interested in and supported me whenever necessary.

I also want to thank my second supervisor (Dr. Michael Finkel) for helping me to improve papers for publication and gave me a lot of useful suggestions and helps for setting up advective-dispersive transport model for column leaching tests. I also learnt many kinds of methods for data calibration from him. Although they are not reflected in my dissertation, it will be of great help to my future works.

I would like to thank Prof. Dr.-Ing. Olaf A. Cirpka for teaching me a lot of knowledge about solving linear partial differential equations (PDEs) with semi-Laplace solutions and numerical methods for solving advective-dispersive transport with different kinds of reactions. Without this knowledge, I cannot successfully complete my dissertation.

I also want to say thank you to Prof. Dr. Christiane Zarfl who provided me the opportunity to be the tutor of "Aquatic environmental chemistry" for many years. During the preparation of tutorial course, I gained a deeper understanding of sorption/desorption kinetics models and facilitate my scientific works.

I am very grateful to Renate Seelig, Hermann Rügner, Jana Meierdierks, Sven Seidensticker, Röhler Klaus, Alexander Haluska, Wenxiao Shi, Qiyue Qin, Jialin Liu and Shuya Xie for their help in the lab and provided me the experimental data for modeling.

I also want to thank my office colleagues (Amirhossein Ershadi and Ran Wei) for sharing the newest information and knowledge about the machine learning and Bayesian inference for

data calibration (Markov Chain Monte Carlo method and simulation-based inference) with me. The fruitful discussions inspired me to obtain new ideas for my scientific works.

I would like to express my gratitude to Philipp Martin for his assistance in translating the abstract of my dissertation into German.

Last but not least, I wanted to thank my family for their support and encouragement.

Notation

The abbreviations shown in brackets represent the dimensionality of the variable being used: M = mass; L = length; L^2 = area; L^3 = volume, T = time, Mol = amount of substance, Pa = pressure.

a = grain radius [L]

a_{ec} = specific surface area of elemental carbon [L^2 M^{-1}]

a_{PE} = half thickness of PE sheets [L]

a_{PE1} = radius of PE1 [L]

a_{PE2} = radius of PE2 [L]

a_{PE3} = radius of PE3 [L]

a_s = half thickness of plane sheets or grain radius of cylindrical particles or grain radius of spherical particles for solid materials [L]; specific surface area of soot particles [L^2 M^{-1}]

a_{sp} = half thickness of plane sheets or grain radius of cylindrical particles or grain radius of spherical particles for porous materials [L]

$a_{sp,1}$ = radius of fine sediment particles [L]

$a_{sp,2}$ = radius of coarse sediment particles [L]

$a_{sphere,equiv.}$= equivalent radius of sphere having the same volume of irregular particle [L]

A_o = empirical constant for calibration of K_{oa} under different temperatures [-]

A_{sp} = total surface area of porous materials [L^2]

A = undetermined coefficient

A^o = specific surface area per unit volume of pore water [L^2]

b = lumped parameter for simplification or intercept of linear regression equation [-] or bias of neural networks [-]

b_L= empirical constant for calibration of P_L^o under different temperatures [-]

B = spatial-temporal differential operator of boundary condition or undetermined coefficient

B_o= empirical constant for calibration of K_{oa} under different temperatures [-]

c = lumped parameter for simplification or intercept of linear regression equation [-]

C = constant term or undetermined coefficient

C_g = pollutant concentration in gaseous phase at time t [M L^{-3}]

$C_{g,0}$, $C_g(0)$ = initial pollutant concentration in gaseous phase [M L^{-3}]

$C_{g,eq}$ = pollutant concentration in gaseous phase under equilibrium condition [M L^{-3}]

$C_{g,p}$ = pollutant concentration in the intraparticle pore gaseous phase [M L^{-3}]

$C_{g,p}(0)$ = initial pollutant concentration in the intraparticle pore gaseous phase [M L^{-3}]

$C_{i,y}$ = concentration of component i at any location, y, within the boundary layer at certain x [M L^{-3}]

C_{max} = maximum concentration [M L^{-3}] or [M M^{-1}]

C_p = pollutant concentration in suspended particles at time t [M L^{-3}]

$C_{p,eq}$ = pollutant concentration in suspended particles under equilibrium condition [M L^{-3}]

C_{PE} = solute concentration in PE sheets [M M^{-1}]

$C_{PE}(0)$ = initial solute concentration in PE sheets [M M^{-1}]

$C_{PE1}(0)$ = initial Phenanthrene concentration in PE1 [M M^{-1}]

$C_{PE2}(0)$ = initial Phenanthrene concentration in PE2 [M M^{-1}]

$C_{PE3}(0)$ = initial Phenanthrene concentration in PE3 [M M^{-1}]

C_w = solute concentrations in bulk water [M L^{-3}]

C'_w = unknown concentration at the particle/water boundary [M L^{-3}]

$C_w(0)$, $C_{w,0}$, $C_{w,ini}$ = initial solute concentration in bulk water [M L^{-3}]

$C_{w,eq}$ = equilibrium solute concentration in the water phase [M L^{-3}]

$C_{w,eq,quasi}$ = equilibrium solute concentration in the aqueous phase under quasi-steady state [M L^{-3}]

$C_{w,in}$ = solute concentration at the inlet of column [M L^{-3}]

$C_{w,p}$ = solute concentration in the intraparticle pore water [M L^{-3}]

$C_{w,p,ini}$ = initial solute concentration in the intraparticle pore water of fines and coarse particles [M L^{-3}]

$C_{w,p}(0)$ = initial solute concentration in the intraparticle pore water of porous materials [M L^{-3}]

$C_{w,p,a_{sp}}$ = solute concentration at the solid/water boundary of porous materials [M L^{-3}]

$C_{w,p,a_{sp}}(0)$ = initial solute concentration at the solid/water boundary of porous materials [M L^{-3}]

$C_{w,peak}$ = peak effluent concentration of solute in the leaching test [M L^{-3}]

$C_{w,PE}$ = solute normalized concentration in PE sheets (= C_{PE}/K_{PE}) [M L^{-3}]

$C_{w,sp,1}$, $C_{w,fines}$ = solute concentration in intraparticle pore water of fine sediment particles [M L^{-3}]

$C_{w,sp,2}$, $C_{w,coarse}$= solute concentration in intraparticle pore water of coarse sediment particles [M L^{-3}]

$C_{w,sp,1}(0)$ = initial solute concentration in intraparticle pore water of fine sediment particles [M L^{-3}]

$C_{w,sp,2}(0)$ = initial solute concentration in intraparticle pore water of coarse sediment

particles [M L^{-3}]

C_s = solute concentration in solid [M M^{-1}]

$C_{s,ini}$ = initial concentration in sediments or solid materials [M M^{-1}]

$C_s(0)$ = initial solute concentration in solid materials [M M^{-1}]

C_{s,a_s} = solute concentration at the solid/water boundary of solid materials [M M^{-1}]

$\Delta C_{w,fines}$ = concentration changes in aqueous phase due to the contribution of fine weak sorbent [M L^{-3}]

$\Delta C_{w,coarse}$ = concentration changes in aqueous phase due to the contribution of coarse strong sorbent [M L^{-3}]

C_w^* = normalized concentration in bulk water in range of 0 to 1 [-]

$C_{w,p}^*$ = normalized concentration in the intraparticle pore water in range of 0 to 1 [-]

$C_{w,PINNs}^*$ = predicted normalized concentration from PINNs in bulk water in range of 0 to 1 [-]

$C_{w,semi-Laplace}^*$ = predicted normalized concentration from semi-Laplace solution in bulk water in range of 0 to 1 [-]

$\tilde{C}_g$ = Laplace transform of solute concentration in gaseous phase [M L^{-3}]

$\tilde{C}_{g,p}$ = Laplace transform of solute concentration in the intraparticle pore gaseous phase [M L^{-3}]

$\tilde{C}_{PE}$ = Laplace transform of solute concentration in microplastics/PE sheets [M M^{-1}]

$\tilde{C}_{PE1}$ = Laplace transform of Phenanthrene concentration in PE1 [M M^{-1}]

$\tilde{C}_{PE2}$ = Laplace transform of Phenanthrene concentration in PE2 [M M^{-1}]

$\tilde{C}_{PE3}$ = Laplace transform of Phenanthrene concentration in PE3 [M M^{-1}]

$\tilde{C}_w$ = Laplace transform of solute concentration in bulk water [M L^{-3}]

$\tilde{C}_{w,in}$ = Laplace transform of solute concentration at the inlet of column [M L^{-3}]

$\tilde{C}_{w,p}$ = Laplace transform of solute concentration in intraparticle pore water of porous materials [M L^{-3}]

$\tilde{C}_{w,p,a}$ = solute concentration at the particle/water boundary in Laplace domain [M L^{-3}]

$\tilde{C}_{w,p,a_{sp}}$ = Laplace transform of solute concentration at the solid/water boundary of porous materials [M L^{-3}]

$\tilde{C}_{w,sp,1}$ = Laplace transform solute concentration in intraparticle pore water of fine sediment particles [M L^{-3}]

$\tilde{C}_{w,sp,2}$ = Laplace transform solute concentration in intraparticle pore water of coarse sediment particles [M L^{-3}]

$\tilde{C}_s$ = Laplace transform of solute concentration in solid materials [M M^{-1}]

$\tilde{C}_{s,*}$= Laplace transform of modified solute concentration in solid materials (= $\tilde{C}_s - C_s(0)/s$)

[M M^{-1}]

$\tilde{C}_s(0)$ = Laplace transform of initial solute concentration in solid materials [M M^{-1}]

d = grain size [L]

d_5 = grain size of 5% sediment particles [L]

d_{10} = grain size of 10% sediment particles [L]

d_{50} = grain size of 50% sediment particles [L]

d_{90} = grain size of 90% sediment particles [L]

d_{95} = grain size of 95% sediment particles [L]

d_{max} = maximum grain size of sediment particles [L]

d_{min} = minimum grain size of sediment particles [L]

$d_{p,coarse}$ = grain size of coarse particles applied in numerical simulation [L]

$d_{p,fine}$ = grain size of fine particles applied in numerical simulation [L]

d_s = thickness of plane sheets or diameter of cylindrical particles or diameter of spherical particles for solid materials [L]

d_{sp} = grain size of sediment particles [L]

$d_{sp,1}$, $d_{sp,fine}$ = grain size of fine sediment particles [L]

$d_{sp,2}$, $d_{sp,coarse}$= grain size of coarse sediment particles [L]

d_{PE} = thickness of PE sheets [L]

dr, Δr = discrete radial distance [L]

dt, Δt = discrete time step [T]

dx, Δx = discrete longitudinal distance [L]

D = molecular diffusion coefficient [L^2 T^{-1}]

D_a = apparent diffusion coefficient [L^2 T^{-1}]

D_{aq} = aqueous diffusion coefficient [L^2 T^{-1}]

D_c = inner column diameter [L]

D_e = effective diffusion coefficient [L^2 T^{-1}]

D_g = gaseous diffusion coefficient of the pollutants [L^2 T^{-1}]

D_p = gaseous diffusion coefficient of the pollutants in the intraparticle pore space (=D_g ε) [L^2 T^{-1}] or pore diffusion coefficient of solute in porous media (=nD_{aq}) [L^2 T^{-1}]

D_L = longitudinal dispersion coefficient [L^2 T^{-1}]

D_{PE} = solute diffusion coefficient in microplastics/PE sheets [L^2 T^{-1}]

D_s = solute diffusion coefficient in the solid materials [L^2 T^{-1}]

E = coefficient of efficiency of model [-] or kinetic energy [M L^2 T^{-2}]

E_k = total kinetic energy [M L^2 T^{-2}]

f = fractional uptake at equilibrium (mass in particle to total mass in the system) [-]

f_{ec} = elemental carbon content of airborne particles [-]

f_{oc} = organic carbon content of airborne particles [-]

f_{om} = organic matter content of airborne particles [-]

F = mass flux density [M L^{-2} T^{-1}]

F_{aq} = mass flux density in the external aqueous boundary layer [M L^{-2} T^{-1}]

F_d = frictional force acting on the interface between the fluid and the particle [M L T^{-2}]

$F_{i,y}$ = mass transfer flux density at any location, y, within the boundary layer (= $v_{x,y}C_{i,y}$) [M L^{-2} T^{-1}]

F_p = mass flux density in the intraparticle pores [M L^{-2} T^{-1}]

F_B = buoyancy force of the spherical particle [M L T^{-2}]

F_G = gravitational force [M L T^{-2}]

$\tilde{F}$ = mass flux density in Laplace domain [M L^{-2} T^{-1}]

g = gravitational acceleration [L T^{-2}]

$\tilde{g}_p$ = transfer functions of airborne particles [L^3 M^{-1}]

$\tilde{g}_s$ = transfer functions of solid materials [L^3 M^{-1}]

$\tilde{g}_{sp}$ = transfer functions of porous materials [L^3 M^{-1}]

$\tilde{g}_{sp,1}$ = transfer function of fine sediment particles [-]

$\tilde{g}_{sp,2}$ = transfer function of coarse sediment particles [-]

$\tilde{g}_{PE}$ = transfer function of PE sheets [L^3 M^{-1}]

$\tilde{g}_{PE1}$ = transfer function of PE1 [L^3 M^{-1}]

$\tilde{g}_{PE2}$ = transfer function of PE2 [L^3 M^{-1}]

$\tilde{g}_{PE3}$ = transfer function of PE3 [L^3 M^{-1}]

I_0 = zero order modified Bessel function of first kind

I_1 = first order modified Bessel function of first kind

k, k_{mt}= mass transfer coefficient [L T^{-1}] or training iteration step of PINNs (k) or wave number (k) [-]

k_s = mass transfer velocity of solid materials [L T^{-1}]

k_{sp} = mass transfer velocity of porous materials [L T^{-1}]

K_d = distribution coefficient [L^3 M^{-1}]

$K_{d,av}$ = average distribution coefficient [L^3 M^{-1}]

$K_{d,b}$ = distribution coefficient between bulk water and porous particle, which also accounts

for mass stored in the intraparticle pore space ($K_{d,b} = K_d + \varepsilon/\rho_p$) [L³ M⁻¹]

$K_{d,b,average}$ = equilibrium average bulk distribution coefficient between mixing sample and water [L³ M⁻¹]

$K_{d,b,fines}$ = bulk distribution coefficient between fine weak sorbent and water [L³ M⁻¹]

$K_{d,b,coarse}$ = bulk distribution coefficient between coarse strong sorbent and water [L³ M⁻¹]

$K^*_{d,b,fines}$ = fitted bulk distribution coefficient of fines based on the initial solute mass obtained from ASE measurement [L³ M⁻¹]

$K_{d,\mathrm{ini}}$ = distribution coefficient at the beginning of the batch experiment [L³ M⁻¹]

$K_{d,50\%}$= distribution coefficient at the end of the batch experiment after 50% sorption [L³ M⁻¹]

$K_{d,91\%}$= distribution coefficient at the end of the batch experiment after 91% sorption [L³ M⁻¹]

$K_{d,mean,50\%}$= mean distribution coefficient for 50% sorption batch experiment [L³ M⁻¹]

$K_{d,mean,91\%}$= mean distribution coefficient for 91% sorption batch experiment [L³ M⁻¹]

K_{fr}, K_{Fr} = Freundlich coefficient [M M⁻¹: (M L⁻³)$^{1/n}$] ($1/n$ is the Freundlich exponent)

K_{oa} = octanol air partitioning coefficient [-]

K_{oc} = organic carbon/water partitioning coefficient [L³ M⁻¹]

K_{pg} = equilibrium gas/particle distribution coefficient [L³ M⁻¹]

$K_{pg,b}$ = equilibrium gas/particle bulk distribution coefficient ($K_{pg,b} = K_{pg} + \varepsilon/\rho_p$) [L³ M⁻¹]

$K_{pg,b,a}$= apparent gas/particle bulk distribution coefficient [L³ M⁻¹]

K_{sa} = surface adsorption coefficients between air and soot particles [L³ M⁻¹]

l_m = mixing length of Prandtl [L]

L, x_L = maximum transport distance [L]

L_c = characteristic length [L]

L_0 = maximum length scale of the vortex and normally can be assumed as the length of paddle in the stirring system or width of a river [L]

$Loss_i$ = loss function that is defined as the mean square error of residuals ($i = total, PDE, IC, BC, data$)

LS = liquid to solid ratio [L³ M⁻¹]

LS_{col} = liquid to solid ratio in column [L³ M⁻¹]

m = slope of linear regression equation [-]

m_{cum} = cumulative leachate concentration based on dry mass of solid materials inside column [M M⁻¹]

$m_{cum,max}$ = maximum cumulative leachate concentration based on dry mass of solid materials inside column [M M⁻¹]

m_d = dry mass of solid phase or suspended particles [M]

m_L= empirical constant for calibration of P_L^o under different temperatures [-]

K_{PE} = partitioning coefficient between polyethylene and water [$L^3\ M^{-1}$]

$m_{d,1}$ = dry mass of fine sediment particles [M]

$m_{d,2}$ = dry mass of coarse sediment particles [M]

$m_{d,fines}$ = dry mass of fine weak sorbent [M]

$m_{d,coarse}$ = dry mass of coarse strong sorbent [M]

m_{PE} = dry mass of PE sheets [M]

m_{PE1} = dry mass of PE1 [M]

m_{PE2} = dry mass of PE2 [M]

m_{PE3} = dry mass of PE3 [M]

m_{tot} = total mass of pollutants in the system [M]

m_w = mass of pollutants in the water phase [M]

$m_{s,i}$ = mass of pollutants in the sorbent *i* [M]

M = mass of solute which has diffused into or out of the particle after a certain time *t* [M]

M_{eq} = mass of solute which has diffused into or out of the particle under equilibrium conditions [M]

$M_{g,eq}$ = mass of solute in the gas phase under equilibrium conditions [M]

$M_{w,eq}$ = mass of solute dissolved in the free aqueous phase under equilibrium conditions [M]

$M_{s,eq}$ = mass of solute in the particles (sorbed and in the intraparticle pore space) under equilibrium conditions [M]

MW_{oct} = molar mass of octanol [M Mol^{-1}]

MW_{om} = molar mass of organic matter [M Mol^{-1}]

n = intergranular porosity [-] or turbulent frequency [T^{-1}]

n_j = total number of different components of solid materials [-]

n_k = total number of different components of porous materials [-]

N = spatial-temporal differential operator of partial differential equations (PDEs)

N_i = number of training data in training PINNs ($i = PDE, IC, BC, data$)

N_p = total number of the spherical particles [-]

P = pressure [Pa]

Pe = Peclet number [-]

P_L^o = subcooled liquid vapor pressure [Pa]

q_n = non-zero roots of transcendental function

q_1^* = first positive solution of transcendental function derived from empirical formula

r = radial coordinate [L]

r_* = dimensionless radial coordinate [-]

r_i^* = normalized radial distance in range of 0 to 1 [-] ($i = PDE, IC, BC, data$)

r_0, r_p = radius of a sphere [L]

r_{mt} = mass transfer rate constant [T^{-1}]

R_d = retardation factor [-]

Re = Reynolds number [-]

R_{ex}= external mass transfer resistance [$T\ L^{-1}$]

R_{in}= internal mass transfer resistance [$T\ L^{-1}$]

Re_K = Reynolds number based on Kolmogorov's scale [-]

Re_{macro} = Reynolds number of macroparticles [-]

Re_{micro} = Reynolds number of microparticles [-]

Re_p = particle Reynolds number [-]

s = complex Laplace coordinate [T^{-1}]

Sh = Sherwood number [-]

$Sh_{sp,1}$ = Sherwood number of fine sediment particles [-]

$Sh_{sp,2}$ = Sherwood number of coarse sediment particles [-]

Sh_{PE1} = Sherwood number of PE1 [-]

Sh_{PE2} = Sherwood number of PE2 [-]

Sh_{PE3} = Sherwood number of PE3 [-]

Sh_x = local Sherwood number [-]

SL = solid to liquid ratio of sediment particles [$M\ L^{-3}$]

Sc = Schmidt number [-]

t = time [T]

t_c = contact time of leaching test [T]

$t_{63.2\%}$ = characteristic time for 63.2% equilibration [T]

t_i^* = normalized time in range of 0 to 1 [-] ($i = PDE, IC, BC, data$)

T = temperature [K] or maximum simulation time [T] or Kolmogorov's time scale [T]

TSP = concentration of total suspended particles [$M\ L^{-3}$]

u = Kolmogorov's velocity scale [$L\ T^{-1}$]

U = time-mean velocity [$L\ T^{-1}$]

U_r = relative velocity between two points [$L\ T^{-1}$]

v = seepage velocity of water [$L\ T^{-1}$]

v_a = relative velocity of water with respect to the particle [L T^{-1}]

v_x = velocity in the flow direction [L T^{-1}]

$v_{x,b}$ = bulk velocity outside the flow boundary layer [L T^{-1}]

$v_{x,y}$ = velocity at location y and x [L T^{-1}]

v_y = velocity in the transverse direction [L T^{-1}]

V_g = volume of ambient air [L^3]

$V_{irregular}$ = total volume of irregular particles [L^3]

V_{sp} = total volume of porous materials [L^3]

V_{sphere} = volume of sphere [L^3]

V_w = volume of water phase [L^3]

V_{tot} = total volume of column [L^3]

w_i = weighting factors of loss terms [-] ($i = PDE, IC, BC, data$)

x = Cartesian coordinate [L] or the length of the column [L] or inputs of neural networks

x_i^* = normalized longitudinal distance in range of 0 to 1 [-] ($i = PDE, IC, BC, data$)

X_{col} = net column length [L]

$X_{s,63.2\%}$ = mass transfer zone length [L]

$X_{s,\mathrm{ADE-FD}}$ = mass transfer zone length for film diffusion [L]

$X_{s,\mathrm{ADE-IPPD}}$ = mass transfer zone length for intraparticle pore diffusion [L]

y = outputs of neural networks

y_x = distance above the surface (y) at any x value [L]

$1/n$ = Freundlich exponent [-]

Z_w = width of the boundary layer in the z direction [L]

Greek symbols

α = lumped parameter for simplification or dispersivity [L]

$\alpha_{1,2}$ = lumped parameter for simplification

β = ratio of the mass of solute dissolved in the bulk aqueous phase to the mass in the particles (sorbed and in the intraparticle pore space) under equilibrium conditions [-] or lumped parameter for simplification

γ = the ratio of particle radius over surface to volme ratio (e.g., $\gamma = 1, 2$ and 3 for plane particles, cylindrical particles and spherical particles, respectively.)

δ = concentration boundary layer thickness [L]

δ_{film} = external film thickness for mass transfer [L]

δ_{aq} = aqueous external film thickness for mass transfer [L]

δ_L = laminar flow boundary layer thickness [L]

δ_p = internal film thickness for mass transfer [L]

δ_{PE} = external film thickness of PE sheets [L]

δ_s = external film thickness of solid materials [L]

δ_{sp} = external film thickness of porous materials [L]

δ_T = thickness of the turbulent flow boundary layer [L]

ε = intraparticle porosity of solid particle [-]

ε_{disp} = energy dissipation rate [L^2 T^{-3}]

ν, ν_k = kinematic viscosity of fluid (e.g., water) [L^2 T^{-1}]

ρ = density [M L^{-3}]

ρ_b = bulk density of the packed bed in the column (= $\rho_s(1\text{-}n)$) [M L^{-3}]

ρ_{ec} = dry density of elemental carbon [M L^{-3}]

ρ_f = mass density of the fluid [M L^{-3}]

ρ_{oct} = density of octanol [M L^{-3}]

ρ_{om} = dry density of organic matter [M L^{-3}]

ρ_p = density of the suspended particle [M L^{-3}] or bulk density of the particle (= $\rho_s(1\text{-}\varepsilon)$) [M L^{-3}]

ρ_{PE} = dry density of polyethylene [M L^{-3}]

ρ_s = dry density of the solid [M L^{-3}]

$\Delta\rho$ = density difference between particle and fluid [M L^{-3}]

τ_{ch} = characteristic time of coupled film and intraparticle diffusion model [T]

τ_{ch}^{in} = characteristic time of intraparticle pore diffusion model [T]

τ_{ch}^{ex} = characteristic time of external film diffusion model [T]

τ_f = tortuosity factor [-]

$\tau_{s,L}$ = shear stress for laminar flow [M T^{-2} L^{-1}]

$\tau_{s,T}$ = shear stress for turbulent flow [M T^{-2} L^{-1}]

φ = undetermined coefficient or lumped parameter for simplification

θ = hyperparameters of the neural networks (weights and bias) or empirical constant to be determined

γ = empirical constant to be determined

γ_{oct} = activity coefficient of octanol [-]

γ_{om} = activity coefficient of organic matter [-]

ϑ = kinematic viscosity of fluid [L^2 T^{-1}]

η = Kolmogorov length scale [L] or learning rate for training the hyperparameters of PINNs

λ_1, λ_2 = lumped parameter for simplification

μ = dynamic viscosity of fluid [M L^{-1} T^{-1}]

ω = lumped parameter for simplification

σ_i = learning rate for training each loss term of PINNs ($i = PDE, IC, BC, data$)

ζ_u = universal turbulence constant, or Karman's constant

Contents

Abstract **2**

Zusammenfassung **5**

Acknowledgements **8**

Notation **10**

Statement of contributions **27**

1 Introduction **29**

1.1 Sorption/desorption kinetics and mass redistribution in heterogeneous systems 29

1.2 Suspended particles in turbulent flow system and Sherwood number relationships 30

1.2.1 Development of mass transfer coefficients from boundary layer theory 30

1.2.2 Development of mass transfer coefficients from Kolmogorov's turbulence theory 39

1.2.3 Summary 45

1.3 The objectives and the structures of the thesis 45

References 48

2 First order approximation for coupled film and intraparticle pore diffusion to model sorption/desorption batch experiments **50**

Abstract 50

2.1 Introduction 50

2.2 Theory 51

2.2.1 Retarded intraparticle pore diffusion 51

2.2.2 Diffusion through an external boundary layer 53

2.3 Methods 56

2.3.1 Coupled film and retarded intraparticle pore diffusion: the first order approximation model (FOAM) 56

2.3.2 Semi-analytical solution with Laplace transform (SALT) 58

2.4 Results 60

2.4.1 Validation of the approximate solution 60

2.4.2 Mass transfer shift analysis 63

2.4.3 Characteristic times 65

2.5 Conclusions 67

References 69

3 Mechanistic modeling of pollutant mass redistribution (sorption/desorption) in heterogeneous systems explaining unexpected slow kinetics **73**

Abstract 73
3.1 Introduction 74
3.2 Materials and methods 75
3.2.1 Phenanthrene redistribution among spherical microplastics of different sizes (tests A-C) 75
3.2.2 Anthracene-d10 and Phenanthrene redistribution in a sediment suspension with polyethylene passive samplers (Test D) 78
3.3 Modeling mass redistribution kinetics in heterogeneous systems 80
3.3.1 Semi-analytical Laplace solutions for coupled intraparticle and external boundary layer diffusion 80
3.3.2 Sherwood number estimation based on Kolmogorov's theory 84
3.4 Results and discussions 85
3.4.1 Phenanthrene redistribution using well defined microplastic particles 85
3.4.2 Anthracene-d10 and Phenanthrene redistribution in a sediment suspension with passive sampling 87
3.4.3 Validation of Sherwood numbers 90
3.4.4 Illustration of heterogeneous sorbents on sorption/desorption kinetics for hypothetical particle mixtures 91
3.5 Implications 94
References 95

4 Modeling of particle/gas distribution kinetics of polycyclic aromatic hydrocarbons (PAHs) in the atmosphere: Relevance of mass transfer resistance shifts 98

Abstract 98
4.1 Introduction 98
4.2 Theory 100
4.2.1 Particle/gas distribution coefficients 100
4.2.1.1 Equilibrium condition 101
4.2.2 Data sources 107
4.3 Results and discussions 109
4.3.1 95% equilibration time scales of PAHs from 3 different kinetics models (FD, IPPD and FIPPD) 109
4.3.2 Log$K_{pg,b,a}$ vs. Log$K_{pg,b}$ of PAHs 111
4.3.3 Model application to data sets 112
4.3.3.1 Case I: PAHs emission from oils combustion in a lab chamber test 112
4.3.3.2 Case II: PAHs concentrations in airborne particles and atmosphere in a northern China city (Yuncheng) by considering the diurnal variation as well as the impact of domestic heating 115
4.3.3.3 Case III: PAHs concentrations in the marine atmosphere monitored in a

research cruise from the Western Pacific to the Southern Ocean ... 117
4.4 Conclusions ... 122
References ... 123

5 Mass transfer principles in column percolation tests: Initial conditions and tailing in heterogeneous materials ... 128

Abstract ... 128
5.1 Introduction ... 129
5.2 Theory and background ... 130
5.2.1 Local equilibrium: the advection-dispersion equation ... 130
5.2.2 Desorption kinetics limited by film diffusion ... 132
5.2.3 Desorption limited by intraparticle pore diffusion ... 134
5.2.4 Set-up of "numerical" column tests ... 136
5.3 Results and discussions ... 137
5.3.1 Impact of initial conditions on leaching ... 137
5.3.2 Initial conditions and leaching with mass transfer limitations ... 141
5.3.3 Nonlinear sorption isotherms ... 143
5.3.4 Impact of heterogeneous sample composition ... 144
5.4 Summary and conclusions ... 151
References ... 154

6 Two mesh free methods for solving non-equilibrium advective-dispersive solute transport with coupled film-intraparticle diffusion ... 158

Abstract ... 158
6.1 Introduction ... 158
6.2 Methodology ... 162
6.2.2 Physical informed neural networks ... 166
6.2.2.1 Self-adaptive PINNs ... 169
6.2.2.2 Training processes of PINNs ... 172
6.2.3 Numerical model ... 175
6.2.4 Simulation parameters ... 175
6.2.4.1 Input parameters for comparison of NM, PINNs and semi-Laplace solution 175
6.2.4.2 Input parameters for investigating mass transfer shift of ADE-FIPPD ... 176
6.3 Results ... 177
6.3.1 Comparison of two mesh free methods (PINNs and semi-Laplace solution) to numerical solution (NM) of ADE-FIPPD ... 177
6.3.2 Sequential training data vs. random training data ... 180
6.3.3 Impact of initial weighting factors of observation data (w_{data}^{1}) on training PINNs ... 182

6.3.4 Mass transfer shifts for ADE-FIPPD 183
6.4 Conclusions 186
References 187

7 Conclusions and outlooks 190

S1 Supplementary information for boundary layer theory and Kolmogorov's turbulence theory 194

S1.1 Derivation of relative velocities of suspended particles in fluid via dimension analysis 194
S1.2 Proof of minimum Sherwood number of 2 for spherical particle 195
S1.3 Mass transfer for particles under gravity (during sedimentation) 197
References 199

S2 Supplementary information for first order approximation for coupled film and intraparticle pore diffusion to model sorption/desorption batch experiments 200

S2.1 Analytical solution of sorption/desorption kinetics limited by external film diffusion in batch experiments 200
S2.2 Analytical solution of batch sorption kinetics limited by intraparticle pore diffusion 203
S2.2.1 First order approximation of intraparticle pore diffusion (IPPD-FOAM) 205
S2.2.2 Comparison the short-term and long-term approximation solutions of IPPD 206
S2.3 First order approximation for coupled film-intraparticle pore diffusion 207
S2.4 Semi-analytical Laplace solution for coupled film-intraparticle pore diffusion 210
S2.4.1 Solution in Laplace domain 210
S2.4.2 Characteristic times of mass transfer 216
S2.5 Empirical relationships to the estimation of Sherwood numbers 218
S2.6 Linearization of nonlinear sorption isotherms 221
References 223

S3 Supplementary information for mechanistic modelling of pollutant mass redistribution (sorption/desorption) in heterogeneous systems explaining unexpected slow kinetics 226

S3.1 Experimental data of batch tests A-D 226
S3.2 Particle size distribution of pulverized sediment and Phenanthrene concentration measurement via accelerated solvent extraction (ASE) 227
S3.3 Semi-analytical Laplace solution for coupled film-intraparticle solid diffusion in a plane sheet (e.g., PE passive sampler) 229
S3.4 Semi-analytical Laplace solution for coupled film-intraparticle solid diffusion in a cylinder 234

S3.5 Semi-analytical Laplace solution for coupled film-intraparticle solid diffusion in a sphere 239
S3.6 Semi-analytical Laplace solution for coupled film-intraparticle pore diffusion in a plane sheet (e.g., porous membrane) 245
S3.7 Semi-analytical Laplace solution for coupled film-intraparticle pore diffusion in a cylinder 249
S3.8 Semi-analytical Laplace solution for coupled film-intraparticle pore diffusion in a sphere 253
S3.9 Model setups for batch experiments 257
S3.9.1 Model setups of Phenanthrene redistribution in spherical microplastics with different sizes 257
S3.9.2 Model setups of Anthracene d10 and Phenanthrene redistribution in a mixed sediment suspension with passive samplers 258
S3.10 Anthracene d10 and Phenanthrene concentration changes in water 260
S3.11 Influence of different geometries of particles on sorption/desorption kinetics 261
S3.12 Solid-to-liquid ratio impact on equilibration time of film diffusion and intraparticle pore diffusion 264
S3.13 Sorption/desorption kinetics in mixed samples of strongly and less sorbing particles 264
S3.14 Sorption/desorption kinetics in mixtures of different grain sizes 266
S3.15 Biased fitting of distribution coefficients in sorptive uptake and desorption experiments with heterogeneous samples containing strong sorbents 268
References 273

S4 Supplementary information for modeling of particle/gas distribution kinetics of polycyclic aromatic hydrocarbons (PAHs) in the atmosphere: Relevance of mass transfer resistance shifts 274

S4.1 Molecular mass, octanol-air partitioning coefficients and supercooled liquid vapor pressures of PAHs 274
S4.2 Apparent distribution coefficients of external film diffusion under non-equilibrium condition 275
S4.3 Apparent distribution coefficients of intraparticle pore diffusion under non-equilibrium condition 278
S4.4 Apparent distribution coefficients derived from semi-Laplace solution for coupled film-intraparticle pore diffusion 281
S4.5 PAHs emission from oils combustion 281
S4.6 Domestic heating impacts on particle/gas partitioning of PAHs in a northern urban city of China 283
S4.7 PAHs sampling in the marine atmosphere from the Western Pacific to the Southern

Ocean 285
References 293

S5 Supplementary information for mass transfer principles in column percolation tests: Initial conditions and tailing in heterogeneous materials 295

S5.1 Empirical relationships for the estimation of Sherwood numbers 295
S5.2 Film diffusion coupled to advective-dispersive transport 296
S5.3 Intraparticle pore diffusion coupled to advective-dispersive transport 299
S5.4 Length of the mass transfer zone (X_s) for the first order analytical solution 305
S5.4.1 Analytical solution based on the film diffusion model 305
S5.4.2 Analytical solution based on the intraparticle pore diffusion model 306
S5.4.3 Comparison of analytical and numerical solution and estimation of mass transfer zone length (X_s) 307
S5.5 Comparison of analytical and numerical solution (code verification) 308
S5.6 Impact of dispersion on leaching curves 310
References 317

S6 Supplementary information for two mesh free methods for solving non-equilibrium advective-dispersive solute transport with coupled film-intraparticle diffusion 319

S6.1 Structure of deep neural networks 319
S6.2 Automatic differentiation 320
S6.3 The half and one quarter of the full training data 322
S6.4 Impacts of various factors on training PINNs 324
S6.4.1 Impact of amount of observation data (N_{data}) 324
S6.4.2 Impact of neuron numbers in each hidden layer of neural networks 324
S6.4.3 Impact of quantities of layers of neural networks 325
S6.4.4 Impact of activation functions of neural networks 326
S6.5 Loss components tracking in training PINNs 328
S6.6 Comparison of NN, PINNs and semi-Laplace solution 329
References 330

Statement of contributions

This thesis is written as a set of (published or yet unpublished) co-authored manuscripts. I was responsible for the model design, data calibration (curve fitting) and analysis. I am the first author on each of the papers. The contributions of all co-authors to the papers are presented in the following tables.

Co-author contributions in % for chapter 2: “First order approximation for coupled film and intraparticle pore diffusion to model sorption/desorption batch experiments”.

Author	Scientific ideas	Data generation	Analysis & interpretation	Paper writing
Binlong Liu	70	100	70	70
Michael Finkel	10	0	15	15
Peter Grathwohl	20	0	15	15
Status in publication process			Published (Liu et al., 2022)	

Co-author contributions in % for chapter 3: “Mechanistic modeling of pollutant mass redistribution (sorption/desorption) in heterogeneous systems explaining unexpected slow kinetics”.

Author	Scientific ideas	Data generation	Analysis & interpretation	Paper writing
Binlong Liu	70	20	70	70
Michael Finkel	10	0	15	15
Qiyue Qin	0	40	0	0
Wenxiao Shi	0	40	0	0
Peter Grathwohl	20	0	15	15
Status in publication process			Unpublished	

Co-author contributions in % for chapter 4: “Modeling of particle/gas distribution kinetics of polycyclic aromatic hydrocarbons (PAHs) in the atmosphere: Relevance of mass transfer resistance shifts”.

Author	Scientific ideas	Data generation	Analysis & interpretation	Paper writing
Binlong Liu	70	100	70	70
Michael Finkel	10	0	15	15

Peter Grathwohl	20	0	15	15
Status in publication process			Unpublished	

Co-author contributions in % for chapter 5: “Mass transfer principles in column percolation tests: Initial conditions and tailing in heterogeneous materials”.

Author	Scientific ideas	Data generation	Analysis & interpretation	Paper writing
Binlong Liu	60	100	70	70
Michael Finkel	20	0	15	15
Peter Grathwohl	20	0	15	15
Status in publication process			Published (Liu et al., 2021)	

Co-author contributions in % for chapter 6: “Two mesh free methods for solving non-equilibrium advective-dispersive solute transport with coupled film-intraparticle diffusion”.

Author	Scientific ideas	Data generation	Analysis & interpretation	Paper writing
Binlong Liu	70	100	70	70
Michael Finkel	15	0	15	15
Peter Grathwohl	15	0	15	15
Status in publication process			Unpublished	

1 Introduction

1.1 Sorption/desorption kinetics and mass redistribution in heterogeneous systems

Sorption/desorption processes play a pivotal role in many fields, such as water purification via activated carbon (Shi et al., 2023), separation of mixtures of chemicals in chromatography (Montes et al., 2017), gas separation or gas storage with selective sorbents (e.g., zeolites) (Qian et al., 2023; Zhang et al., 2023), organic pollutants retarded migration in the mobile phase (e.g., ambient air or water) (Ngueleu et al., 2013), etc. Under non-equilibrium conditions, solute mass redistributes into each compartment via mass transfer until new equilibrium state is reached. Instantaneous sorption/desorption simplifies the mass redistribution problem, allowing for the straightforward calculation of pollutant mass stored in each compartment using the respective distribution coefficients. However, instantaneous sorption/desorption is hard to achieve especially for sorbent with large grain size and high distribution coefficient or with small intraparticle porosity. In such scenarios, sorption/desorption kinetics has to be considered. External film diffusion and intraparticle diffusion models (governing equations and details see Chapter 2) are two widely employed kinetics models in the literatures (Parnis et al., 2020; Wang et al., 2022). The external film diffusion model assumes a concentration boundary layer near the surface of the sorbent with a given thickness and the mass flux density between immobile (solid) and mobile phase (e.g., water or gas phase) is proportional to the mass transfer velocity (k) times the concentration gradient in the boundary layer (Fick's first law). The intraparticle diffusion model considers the mass transfer resistance inside the sorbent. If no intraparticle porosity exists, the mass transfer of sorbents and mobile phase is dominated by solid diffusion while for porous particles, mass transfer is dominated by the concentration gradient inside the intraparticle pores and the instantaneous equilibrium is assumed between pore and solid phase. In contrast to external film diffusion, intraparticle diffusion follows Fick's second law where the diffusion distance increases with the square root of time at early time. For sorption/desorption kinetics, these two mass transfer resistances coexist and single models do not mimic the sorption/desorption kinetics well as proven by many experimental results where the kinetics at early times follow the external film diffusion model, while data at later times obey Fick's second law and thus the intraparticle diffusion model (e.g., Seidensticker et al., 2017). However, there is a lack of research on the shift in mass transfer resistance and the development of corresponding mathematical models, particularly in heterogeneous systems where different compartments interact and sorption and desorption processes occur simultaneously. In addition, redistribution scenarios and their kinetics are relevant for pollutants which enter environmental compartments on particles such as in atmospheric

deposition or suspended solids in rivers. Mathematical models could help us to better understand the mass transfer in those complex systems.

1.2 Suspended particles in turbulent flow system and Sherwood number relationships

1.2.1 Development of mass transfer coefficients from boundary layer theory

Bulk flow in most rivers is turbulent, and thus a high degree of mixing is usually achieved that ensures high rates of mass transfer. The same is true for batch experiments with well stirred or shaken bottles in the laboratory. The movement of a fluid past a solid surface or a fluid/fluid interface results in the development of a boundary layer wherein mass transfer occurs through a combination of molecular diffusion and turbulent flow ("eddy" diffusion). Molecular diffusion occurs close to the surface, where a viscous and laminar sublayer exists, while farther away from the surface, eddies move randomly and transfer solutes by turbulent "eddy" diffusion. Turbulence can be damped at interfaces between the water phase and a second phase by concurrent local movement of the two phases if the second phase travels at essentially the same velocity as the fluid element in which it is suspended (e.g., a particle perfectly suspended in water). This is characteristic of highly dispersed two-phase systems such as clay particles suspended in flowing water or in rapidly stirred but not well-mixed reactors. Thus, although bulk mixing and macroturbulence may be great in such systems, the microturbulence at phase interfaces is low. In the following, flow boundary layers (laminar and turbulent) are discussed and based on that concentration boundary layers are derived which finally leads to mass transfer coefficients.

Flow Boundary Layers

Before discussing engineering approaches to quantification of interphase mass transport, an understanding of the fundamental concept of a boundary layer should be developed. A flow boundary layer occurs whenever a flow pattern is disrupted by a surface. This surface produces shear stress, which causes velocity changes in the vicinity of the boundary. Flow boundary layers affect interphase mass transport processes, and thus both cause and affect the concentration boundary layer. Mathematical relationships to describe flow and concentration boundary layers can be combined to provide a fundamental understanding of the mass transfer coefficient and how it depends on fluid and solute properties.

Partial differential equations allow to describe the thickness and velocity distribution of laminar and turbulent boundary layers. A general sketch of the flow regime near a boundary

is given in Fig. 1.1. The foundation of boundary layer theory can be traced back to the pioneering work of Prandtl in the early twentieth century. Blasius, a student of Prandtl, solved the Navier-Stokes and the continuity equation for laminar flow over a flat plate having a sharp leading edge. The two-dimensional forms of continuity and Navier-Stokes equation to be solved for incompressible laminar steady-state flow are (Weber and DiGiano, 1996):

$$\frac{\partial v_x}{\partial x} + \frac{\partial v_y}{\partial y} = 0$$
$$v_x \frac{\partial v_x}{\partial x} + v_y \frac{\partial v_y}{\partial y} = -\frac{1}{\rho}\frac{\partial P}{\partial x} + \nu_k \left(\frac{\partial^2 v_x}{\partial x^2} + \frac{\partial^2 v_x}{\partial y^2} \right) \quad (1.1)$$
$$v_x \frac{\partial v_x}{\partial x} + v_y \frac{\partial v_y}{\partial y} = -\frac{1}{\rho}\frac{\partial P}{\partial x} + \nu_k \left(\frac{\partial^2 v_y}{\partial x^2} + \frac{\partial^2 v_y}{\partial y^2} \right)$$

ν_k [$L^2\ T^{-1}$] is the kinematic viscosity with $\nu_k = \mu/\rho$ where μ [$M\ L^{-1}\ T^{-1}$] and ρ [$M\ L^{-3}$] denote the dynamic viscosity and the density of the fluid, respectively. The velocity is zero in both x and y direction at the surface of the boundary. For y values exceeding the full thickness of the boundary, the velocity in x direction is constant and the pressure gradient in x direction vanishes ($dP/dx = 0$). Profiles of velocity in the flow direction, $v_x = \varphi(y)$, and transverse velocity $v_y = \varphi(y)$, are obtained at each location, x. The transverse velocity increases with distance from the surface until the bulk flow velocity is reached, which is logical because as the boundary layer increases in thickness with x, flow along the edge of the plate must displace fluid in the y direction. The position y at which v_x becomes equal to the bulk velocity, $v_{x,b}$, represents the total thickness of the boundary layer.

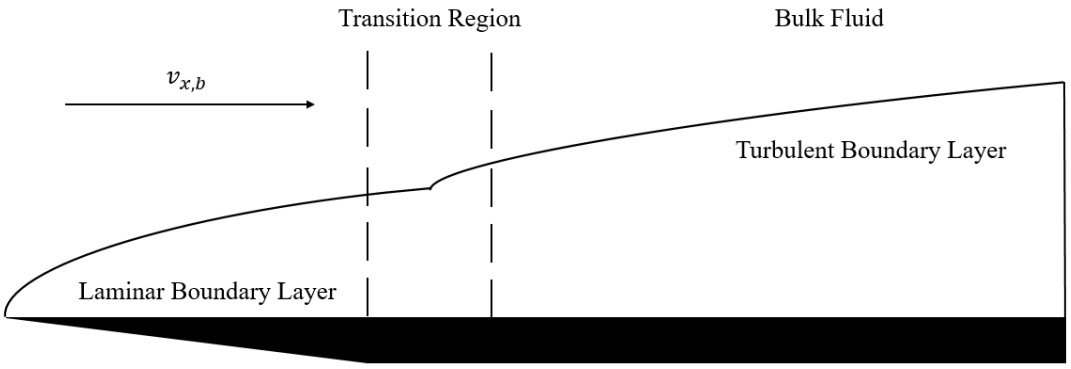

Fig 1.1: Boundary layer development on a sharp-edged flat plate (adapted from Welty et al., 2007).

(a) Laminar flow boundary layer

Blasius (1908) used the Reynolds number in the bulk fluid to derive the laminar boundary layer thickness (δ_L). He showed that the shape of the velocity profile within the boundary layer remains constant regardless of the position along the x direction at which the

boundary layer is examined. Figure 1.2 is the dimensionless plot of the velocity profile. The abscissa is the velocity within the boundary layer (v_x) relative to the velocity in the bulk flow ($v_{x,b}$) and the ordinate is ($y_x Re^{0.5}$)/x, where y_x is the distance above the surface (y) at any x value and the Reynolds number (Re) is calculated from the bulk fluid velocity. It is clear from the Fig. 1.2 that for any x value, the velocity increases linearly with y near the surface, becomes curvilinear farther away, and then asymptotically approaches a terminal velocity. The thickness of the laminar boundary layer (δ_L) can be estimated by evaluating the ordinate when $v_x/v_{x,b} = 0.99$, for which the value of the ordinate is 5 (derivation see Welty et al., 2007).

$$\delta_L = \frac{5x}{Re^{0.5}} \tag{1.2}$$

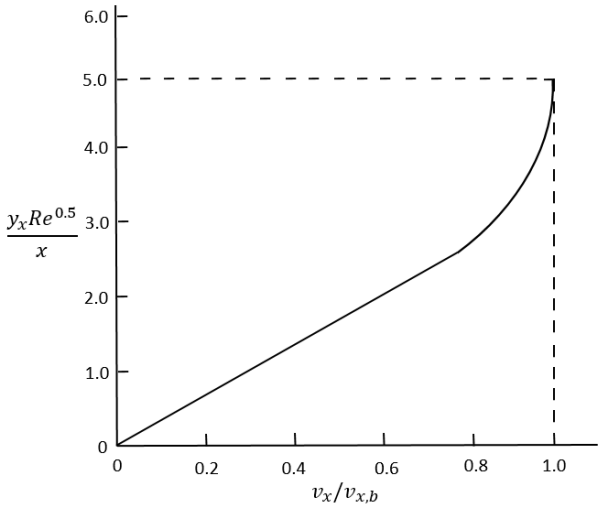

Fig. 1.2: Blasius solution to the Navier-Stokes equation for a laminar boundary layer (adapted from Welty et al., 2007).

Equation 1.2 states that the laminar boundary layer thickness increases with distance along the boundary due to the viscous force and decreases with the square root of the Reynolds number. Similar results can be derived from the von Karman integral, which is derived from the fundamental mass and momentum balance equations.

$$\int_0^{\delta_L} \frac{\partial \rho v_x}{\partial x} dx Z_w dy + \rho v_y Z_w dx = 0 \tag{1.3}$$

for the mass balance and

$$\int_0^{\delta_L} v_x \frac{\partial \rho v_x}{\partial x} dx Z_w dy + \rho v_{x,b} v_y Z_w dx = \tau_{s,L} Z_w dx \tag{1.4}$$

for the momentum balance. Z_w [L] is the width of the boundary layer in the z direction and $\tau_{s,L}$ [M T^{-2} L^{-1}] denotes the shear stress for laminar flow.

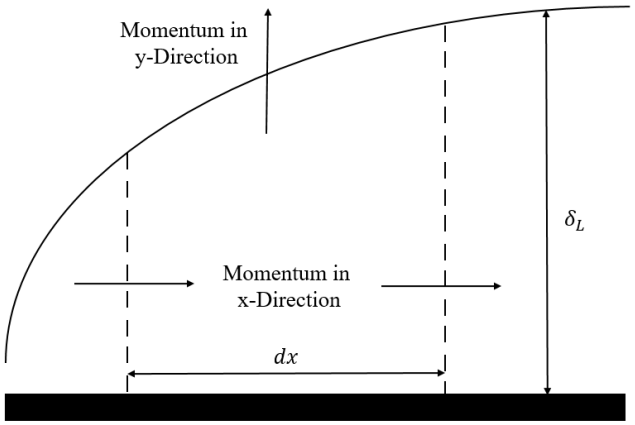

Fig. 1.3: Control volume for analysis of a fluid boundary layer (adapted from Welty et al., 2007).

Dividing Eq. 1.4 by $Z_w dx$ gives:

$$\tau_{s,L} = \frac{d}{dx} \int_0^{\delta_L} \rho v_x^2 dy + \rho v_{x,b} v_y \tag{1.5}$$

and performing the same step on Eq. 1.3, yields:

$$v_y = -\frac{d}{dx} \int_0^{\delta_L} v_x dy \tag{1.6}$$

The von Karman integral is obtained by substitution of Eq. 1.6 for v_y in Eq. 1.5:

$$\tau_{s,L} = -\frac{d}{dx} \int_0^{\delta_L} (v_{x,b} - v_x) \rho v_x dy \tag{1.7}$$

The Blasius solution to the Navier-Stokes equation reveals that the shape of the velocity profile in the boundary layer is independent of x. This shape can thus be approximated by a simple polynomial expression in y (e.g., $v_x = \alpha_0 + \alpha_1 y + \alpha_2 y^2 + \alpha_3 y^3 + \cdots$), which, when forced to conform to four boundary conditions ($y = 0, v_y = 0; y = 0, \frac{\partial^2 v_x}{\partial y^2} = 0; \mathrm{y} = \delta_L, v_x = v_{x,b}; \mathrm{y} = \delta_L, \frac{\partial v_x}{\partial \mathrm{y}} = 0$) gives:

$$\frac{v_x}{v_{x,b}} = \frac{3}{2}\left(\frac{y}{\delta_L}\right) - \frac{1}{2}\left(\frac{y}{\delta_L}\right)^3 \tag{1.8}$$

This expression can be substituted into the right-hand side of Eq. 1.7. The shear stress term on the left-hand side of the von Karman integral given in Eq. 1.7 can be expressed simply as $\tau_{s,L} = \mu(dv_x/dy)|_{y=0}$, and dv_x/dy can now be determined from Eq. 1.8. Performing the same mathematical steps as outlined above, the expression for the thickness of the laminar layer becomes:

$$\delta_L = \frac{4.64x}{Re^{0.5}} \quad \text{for } Re < 10^5 \tag{1.9}$$

The Eq. 1.9 derived from the approximation provided by von Karman integral compares very well to the more exact one derived by Blasius. It is important to remember that the laminar expressions for boundary layer thickness derived herein are applicable strictly only to smooth surfaces.

(b) Turbulent flow boundary layer

The mathematical analysis of a turbulent boundary layer poses greater challenges compared to that for a laminar boundary layer because the velocity in such case becomes a function of time and space. The turbulent boundary layer may be conceptualized as comprising a laminar sublayer and a fully turbulent boundary layer. Assuming a constant shear stress (τ_s) with the sublayer (same as for the laminar boundary layer discussed above), the velocity increases linearly with distance from the surface. The velocity distribution in the remaining portion (fully turbulent layer) is more complex. Mathematical descriptions are based in part on Prandtl's mixing length concept (1925) to describe turbulent shear stress $\tau_{s,T}$, as depicted in Eq. 1.10:

$$\tau_{s,T} = \rho\, l_m^2 \left(\frac{dv_x}{dy}\right)^2 \tag{1.10}$$

where l_m [L] denotes the mixing length.

Prandtl (1925) demonstrated that the mixing length (l_m) is proportional to distance from the surface ($l_m = \zeta_u y$) for regions close to the surface. The coefficient of proportionality ζ_u is the universal turbulence constant, or Karman's constant and must be determined experimentally. A typical value is about 0.4. After taking the square root of both sides of Eq. 1.10 and integration it follows that:

$$\frac{v_x}{v_s} = \frac{1}{\zeta_u} \ln y + C \tag{1.11}$$

where v_s or $(\tau_{s,T}/\rho)^{0.5}$ [L T^{-1}] denote the shear velocity and C is a constant of integration. Eq. 1.11 is not valid in the laminar sublayer, where the velocity profile is linear, and thus is restricted to the domain $y > \delta_{L,s}$, where $\delta_{L,s}$ is the thickness of the laminar sublayer. Equation 1.11 shows that the thickness of the boundary layer increases exponentially with increased velocity.

An empirical power-law equation was suggested by Prandtl to capture the general shape of the velocity distribution given by Eq. 1.11, which is given as:

$$\frac{v_x}{v_{x,b}} = \left(\frac{y}{\delta_T}\right)^{0.143} \tag{1.12}$$

where δ_T [L] denotes the thickness of the turbulent boundary layer. The general shape of the entire velocity profile is shown in Fig. 1.4.

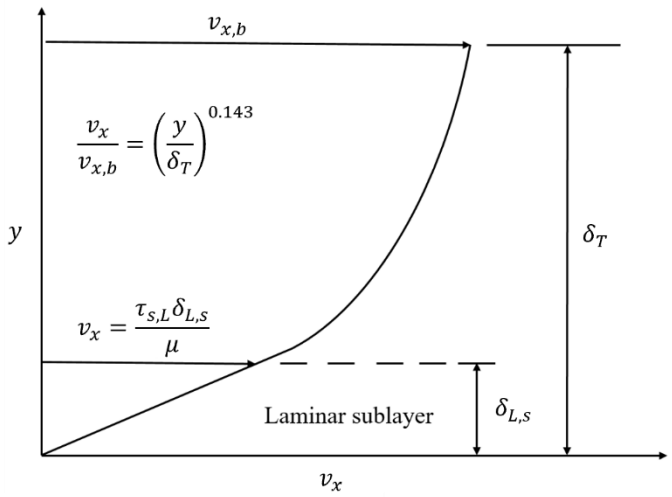

Fig. 1.4: Velocity profile for the laminar sublayer and the turbulent boundary layer (adapted from Welty et al., 2007).

An empirical expression developed by Blasius for shear stress ($\tau_{s,T}$) at the boundary in turbulent flow has the form:

$$\tau_{s,T} = 0.0233\rho v_{x,b}^2 \left(\frac{\nu_k}{v_{x,b}\delta_T}\right)^{0.25} \tag{1.13}$$

Using the von Karman integral equation (Eq. 1.7) and substituting the left-hand side with the Eq. 1.13 and replace v_x at the right-hand side with the Eq. 1.12, the equation becomes:

$$0.0233\rho v_{x,b}^2\left(\frac{\nu_k}{v_{x,b}\delta_T}\right)^{0.25} = \rho v_{x,b}^2\frac{d}{dx}\int_0^{\delta_T}\left[1-\left(\frac{y}{\delta_T}\right)^{0.143}\right]\left(\frac{y}{\delta_T}\right)^{0.143}dy \qquad (1.14)$$

After integrating the right-hand side of Eq. 1.14, we get:

$$0.0233\left(\frac{\nu_k}{v_{x,b}\delta_T}\right)^{0.25} = \frac{d\delta_T}{dx} \qquad (1.15)$$

Finally, after separation the variable and integration (assuming $x = 0, \delta_T = 0$), Eq. 1.15 leads to the following simple expression for the turbulent boundary layer thickness.

$$\delta_T = \frac{0.37x}{Re^{0.2}} \quad \text{for } 5\times10^5 < Re < 10^7 \qquad (1.16)$$

The turbulent boundary layer is thicker than the laminar boundary layer and also has higher mean velocity. Consequently, a turbulent boundary layer involves significantly greater momentum and energy than a laminar layer.

Concentration boundary layer and mass transfer

Turbulent flow is common in the natural systems, such as in rivers especially during floods. Polluted urban particles may be flushed into the rivers and pollutants within river water and native particles are redistributed depending on mass transfer. The concentration of the pollutants in the water phase is of interest in environmental risk assessment. Mass transfer from polluted particles into river water controls the equilibration time scale. In a turbulent flow system, most of suspended particles follow the streamline and show a velocity similar to the fluid. The relative velocity between particles and water is small and thus the laminar boundary layer theory applies in the following discussion.

A mass transfer relationship can be derived by coupling the concept of the flow boundary layer (δ_L) with that of a concentration boundary layer (more details see Weber and DiGiano, 1996). Here, we consider a simple example of mass transport away from a 'soluble' dissolving plate during laminar flow. If the velocity and concentration distribution can be expressed mathematically, the mass transfer flux at any location, y, within the boundary layer can be viewed as the result of advective transport of component $F_{i,y}$ ($= v_{x,y}C_{i,y}$), where $v_{x,y}$ is the velocity at location y and x and $C_{i,y}$ denotes the concentration of component i at this location. For a laminar boundary layer, the thickness of the flow boundary layer is given by Eq. 1.9 and the velocity profile in boundary layer by Eq. 1.8. The concentration boundary layer (δ) is determined by diffusive transport normal to the dissolving plate. Like the velocity profile, the concentration profile can be described by a simple polynomial in y ($C_i = \alpha_0 + \alpha_1 y + \alpha_2 y^2 + \alpha_3 y^3 + \cdots$). After applying the appropriate boundary conditions ($y = 0,\ d^2C_i/\mathrm{d}y^2 = 0;\ \ y = \delta, C_i = 0$ and $\mathrm{d}C_i/dy = 0$), we have:

$$\frac{C_i}{C_{s,i}} = 1 - \frac{3}{2}\left(\frac{y}{\delta}\right) + \frac{1}{2}\left(\frac{y}{\delta}\right)^3 \tag{1.17}$$

where $C_{s,i}$ [M L^{-3}] denotes the solute concentration at surface of the dissolving plate.

The mass balance at steady state in an elemental volume ($Z_w dxdy$) of the fluid in the concentration boundary layer, as shown in Fig. 1.5, is:

$$\int_0^{\delta} \frac{\partial C_i v_x}{\partial x} dx Z_w dy - F_i Z_w dx = 0 \tag{1.18}$$

where F_i [M L^{-2} T^{-1}] denotes the solute mass flux density out of the dissolving plate.

The first term in Eq. 1.18 is the net advective transport in the x direction, while the second term accounts for diffusive transport out of the boundary layer in y direction.

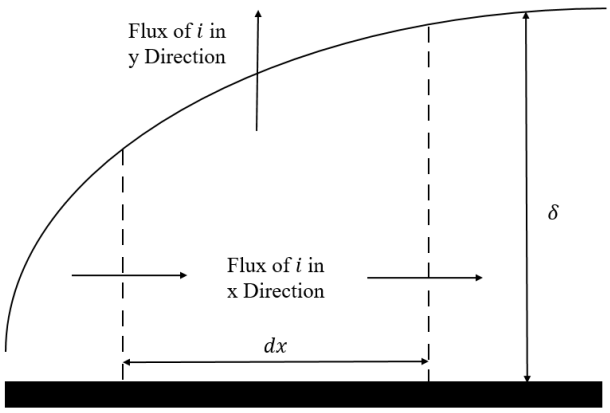

Fig. 1.5: Control volume for analysis of a concentration boundary layer.

Replacing the flux term, F_i, by Fick's law, substituting and dividing by $Z_w dx$ allows to express Eq. 1.18 as:

$$\frac{\partial}{\partial x}\int_0^{\delta} C_i v_x dy = -D_{aq,i}\left.\frac{\partial C_i}{\partial y}\right|_{y=0} \tag{1.19}$$

where $D_{aq,i}$ denotes aqueous diffusion coefficient of compound i.

Assuming that $\delta < \delta_L$, allows to integrate left-hand side of Eq. 1.19 and the right-hand side can be differentiated because both $v_x/v_{x,b}$ and $C_i/C_{s,i}$ are known functions of y/δ_L and y/δ (Eq. 1.8 and Eq. 1.17), respectively. The next step is to differentiate the left-hand side with respect to x. The mathematical derivation is shown below for the left-hand side of Eq. 1.19:

$$\frac{\partial}{\partial x}\int_0^{\delta} C_i v_x dy = \frac{\partial}{\partial x}\int_0^{\delta}\left[1-\frac{3}{2}\left(\frac{y}{\delta}\right)+\frac{1}{2}\left(\frac{y}{\delta}\right)^3\right]\left[\frac{3}{2}\left(\frac{y}{\delta_L}\right)-\frac{1}{2}\left(\frac{y}{\delta_L}\right)^3\right] v_{x,b} C_{s,i}\mathrm{dy}$$
$$= \frac{\partial}{\partial x}\int_0^{\delta}\left[\frac{3}{2}\left(\frac{y}{\delta_L}\right)-\frac{1}{2}\left(\frac{y}{\delta_L}\right)^3-\frac{9}{4}\frac{y^2}{\delta_L\delta}+\frac{3}{4}\frac{y^4}{\delta_L^3\delta}+\frac{3}{4}\frac{y^4}{\delta_L\delta^3}-\frac{1}{4}\frac{y^6}{\delta_L^3\delta^3}\right] v_{x,b} C_{s,i}\mathrm{dy}$$
$$= \frac{\partial}{\partial x}\left[\frac{3}{20}\frac{\delta^2}{\delta_L}-\frac{3}{280}\frac{\delta^4}{\delta_L^3}\right] v_{x,b} C_{s,i} \tag{1.20}$$
$$\approx \left[-\frac{3}{40}\frac{\delta^2 v_{x,b}^{0.5}}{4.64 v^{0.5} x^{1.5}}\right] v_{x,b} C_{s,i} = \left[-\frac{3}{40}\frac{\delta^2 Re^{0.5}}{4.64 x^2}\right] v_{x,b} C_{s,i} = \left[-\frac{3}{40}\frac{\delta^2}{\delta_L x}\right] v_{x,b} C_{s,i}$$
$$= \left[-\frac{3}{40}\left(\frac{\delta}{\delta_L}\right)^2\frac{4.64}{Re^{0.5}}\right] v_{x,b} C_{s,i}$$

and the right-hand side of Eq. 1.19 becomes:

$$-D_{aq,i}\frac{\partial C_i}{\partial y}|_{y=0} = -D_{aq,i}\frac{\partial}{\partial y}\left[1-\frac{3}{2}\left(\frac{y}{\delta}\right)+\frac{1}{2}\left(\frac{y}{\delta}\right)^3\right] C_{s,i}|_{y=0}$$
$$= -D_{aq,i}\left[-\frac{3}{2}\left(\frac{1}{\delta}\right)+\frac{3}{2}\frac{y^2}{\delta^3}\right] C_{s,i}|_{y=0} \tag{1.21}$$
$$\approx \frac{3}{2} D_{aq,i}\frac{1}{\delta} C_{s,i}$$

Coupling Eqs. 1.20 and 1.21 results in:

$$\frac{\delta^3}{\delta_L^2} \sim \frac{D_{aq,i} Re^{0.5}}{v_{x,b}}$$
$$\left(\frac{\delta}{\delta_L}\right)^3 \sim \frac{D_{aq,i} Re^{0.5}}{v_{x,b}}\frac{Re^{0.5}}{x} \sim \frac{D_{aq,i}}{\nu_k} \sim \frac{1}{Sc} \tag{1.22}$$

where Sc [-] denotes the Schmidt number ($\nu_k/D_{aq,i}$). Finally, substitution for δ_L from Eq. 1.9 gives an expression to calculate the thickness of the concentration boundary layer:

$$\delta = \frac{4.64x}{Re^{1/2} Sc^{1/3}} \tag{1.23}$$

Equation 1.23 makes intuitive sense since the thickness of the concentration boundary decreases with increasing Reynolds and Schmidt numbers. Higher Reynolds numbers imply that inertial forces are more important than viscous forces, a fact that is caused by greater momentum transfer in the fluid. The kinematic viscosity (ν_k) represents the proprotionality between shear stress ($\tau_{s,L}$) and the momentum gradient ($\rho\, \partial v_x/\partial y$) - in other words, it is the eddy momentum dispersivity. A high Schmidt number indicates the dominance of macroscale momentum transfer over microscale momentum transfer, the latter produced by molecular diffusion.

Knowing the thickness of the concentration boundary layer allows us to obtain the relationship for mass transfer. The mass transfer flux density is equal to the diffusive flux density given by Fick's law and applied at $y = 0$, namely:

$$F_i = k_{mt,i}\left(C_{s,i} - 0\right) = -D_{aq,i}\left.\frac{\partial C_i}{\partial y}\right|_{y=0} \tag{1.24}$$

where $k_{mt,i}$ [L T^{-1}] denotes the mass transfer coefficient. The diffusional flux is obtained by taking the derivative dC_i/dy of the concentration profile (Eq. 1.17):

$$F_i = \frac{3}{2}\left(\frac{D_{aq,i}C_{s,i}}{\delta}\right) \tag{1.25}$$

Using Eq. 1.23 to substitute the δ and combining with Eq. 1.24, the local Sherwood number (Sh_x) can be expressed as:

$$Sh_x = \frac{k_{mt,i}x}{D_{aq,i}} = 0.323\left(\frac{xv_{x,b}}{\nu_k}\right)^{1/2}\left(\frac{\nu_k}{D_{aq,i}}\right)^{1/3} \tag{1.26}$$

Normally, a characteristic length (L_c) is used instead of x to get an average mass transfer coefficient or an average Sherwood number. Then the Sherwood number correlation derived from laminar boundary layer theory becomes:

$$Sh = \frac{k_{mt,i}\,L_c}{D_{aq,i}} = 0.626\left(\frac{L_c v_{x,b}}{\nu_k}\right)^{1/2}\left(\frac{\nu_k}{D_{aq,i}}\right)^{1/3} = 0.626Re^{1/2}Sc^{1/3} \tag{1.27}$$

It is important to note that the results given in Eq. 1.23, Eq. 1.26 and Eq. 1.27 are obtained through characterization of a realistic physical model (boundary layer theory) by application of fundamental principle of continuity, conservation of momentum and mass transport, which does not include any empirical constant from experiments. Although the application of boundary layer theory to more complex mass transfer situations is limited by our lack of understanding of the physical details, it shows that the mass transfer relationships for different systems can be related to relatively simple dimensionless numbers (e.g., Reynolds number (Re)， Schmidt number (Sc) or Peclet number ($Pe = ReSc$). This leads to a better understanding of empirical correlations for mass transfer.

1.2.2 Development of mass transfer coefficients from Kolmogorov's turbulence theory

Theory of local isotropy of turbulence

Turbulence is always dissipative and requires a continuing supply of energy coming from large scale eddies within the bulk flow to feed it. The mechanical energy associated with bulk flow velocities is dissipated by viscous energy losses in the smaller eddies. In a stirred system, the impeller continually produces primary eddies which are similar in magnitude to

the dimensions of the main flow. When the Reynolds number of the main flow is high, these large primary eddies are unstable due to small disturbances and disintegrate into smaller eddies through inertial interactions. These small eddies, in turn, at high Reynolds number, are also unstable. This process is repeated in the form of a cascade until the Reynolds number of the smallest eddies are too small to permit further degeneration. Clearly nth order sized eddies absorb some of the energy from the (n-1)th order eddies and transfer it on partly to (n+1)th order sized eddies by means of work done against the Reynolds stresses and partly to internal thermal energy. The energy transfer to higher order eddies will be larger compared with the amount of energy dissipated (transform to heat) for the larger eddies. However, the portion of energy which is dissipated by viscosity will increase for very smallest eddies. As the process goes on, the viscous stress will finally dominate the energy dissipation and small eddies are not forming anymore. This situation can be well described in rhyme (Richardson, 1922):

'Big whorls have little whorls, which feed on their velocity;

Little whorls have smaller whorls, and so on unto viscosity. '

As energy transfer from large eddies to small eddies occurs in different directions, the directional information of large eddies is gradually lost. If a volume of fluid is considered whose dimensions are small compared with the scale of main flow, the magnitudes of fluctuating components of the velocity are equal. Thus, isotropic turbulence exists, even though the turbulent motions of the larger eddies maybe far from isotropy.

Kolmogorov (1941) concluded that in fully turbulent flows (large Reynolds number), all eddies which are much smaller than the primary eddies are completely independent of bulk motion and details of the agitation device as well as external condition. The properties of these small eddies are determined solely by the local energy dissipation rate (ε_{disp}), and the kinematic viscosity of the fluid (ν_k). The energy spectrum of turbulent flow has been formulated following a relative difficult mathematical and statistical treatment in the form:

$$E(k) = Ck^4 \exp\left(-2k^2\nu_k t\right) \tag{1.28}$$

where $C = \mathrm{f}(\nu_k, t)$ is a constant, t is time and k (proportional to reciprocal of eddy size) is called the wave number is related to turbulent frequency (n) given by $k = 2\pi n/U$, where U is time-mean velocity. The energy spectrum $E(k)$ as a function of the wave number is shown in Fig. 1.6 and shows that the energy spectrum function $E(k)$ increases rapidly, initially with k^4, then reaches a maximum and finally decreases monotonously as k increases. By integrating over all wave numbers, the total turbulence kinetic energy (E_k [M L^2 T^{-2}]) can be derived:

$$E_k = \int_0^{\infty} E(k)dk \tag{1.29}$$

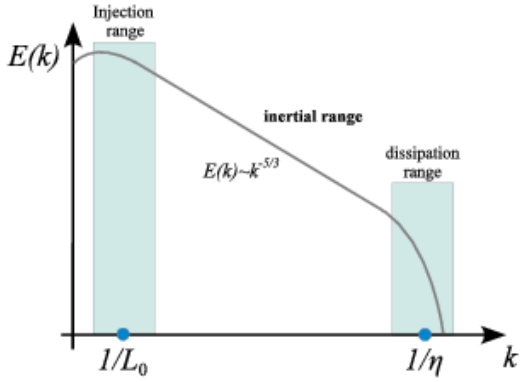

Fig. 1.6: Schematic of turbulent kinetic energy spectrum ($E(k)$) as a function of wave number (k) (L_0 denotes the maximum length scale of the vortex and normally can be assumed as the length of paddle in the stirring system or width of a river. η denotes the Kolmogorov's length scale).

Based on Eq. 1.28 and Eq. 1.29 the rate of change of kinetic energy of turbulent motion (the dissipation rate (ε_{disp}) of turbulence energy) over all wave numbers becomes:

$$\varepsilon_{disp} = \frac{d\int_0^{\infty} E(k)dk}{dt} = -2\nu_k \int_0^{\infty} k^2 E(k)dk \tag{1.30}$$

It is clear from Eq. 1.30 that the energy dissipation is selective towards the high wave number or small eddies. Viscous dissipation reduces the kinetic energy of turbulent flow effectively for a fluid with high viscosity.

Figure 1.6 shows that the energy spectrum of eddies which are much smaller than primary eddies can be divided into two ranges. The first part is the inertial range where the most of kinetic energy of large eddies is transferred to small eddies and the viscous energy lost is negligible. The second part is the dissipation range where the viscous energy lost (thermal energy) is dominant. The boundary between these two ranges is dominated by Kolmogorov's length scale (η). The Kolmogorov's length scale (η), time scale (T) as well as velocity scale (u) are defined as:

$$\eta = \left(\frac{\nu_k^3}{\varepsilon_{disp}}\right)^{\frac{1}{4}}$$
$$T = \left(\frac{\nu_k}{\varepsilon_{disp}}\right)^{\frac{1}{2}} \quad (1.31)$$
$$u = \left(\nu_k \varepsilon_{disp}\right)^{\frac{1}{4}}$$

Calculating the dimensionless Reynolds number (Re_K) based on Kolmogorov's scale gives:

$$Re_K = \frac{\eta u}{\nu_k} = \frac{\left(\frac{\nu_k^3}{\varepsilon_{disp}}\right)^{1/4}\left(\nu_k \varepsilon_{disp}\right)^{\frac{1}{4}}}{\nu_k} = 1 \quad (1.32)$$

When Reynolds numbers of eddies are smaller than 1, the properties of eddies are controlled by the energy dissipation rate (ε_{disp}) as well as the kinematic viscosity (ν_k). However, if the Reynolds numbers of eddies are larger than 1, the properties of eddies are only dominated by the energy dissipation rate (ε_{disp}). The size of the suspended particles (d_p) in water is usually much smaller than the length scale of the primary eddies (L_0). According to the Kolmogorov's length scale, the suspended particles can be divided into two parts (macroparticle ($L_0 \gg d_p > \eta$) and microparticle ($d_p < \eta$).

Relative velocities for suspended particles to the bulk fluid

Kolmogorov assumed that if M_1 and M_2 are two points with distance d in a small volume of turbulent flow, U_1 and U_2 are the velocity components in direction of M_1M_2 at the points of M_1 and M_2, then a relative velocity between two points U_r, can be defined by $\overline{U_r}^2 = \overline{(U_1 - U_2)^2}$, where $\overline{U_r}^2$ denotes the square average relative velocity. $\overline{U_r}^2$ is determined mainly by the small eddies, which are statistically independent of the main flow.

(a) Macroparticle

The square relative fluctuating velocity of macroparticle depends on the energy dissipation rate (ε_{disp}) and the distance (d, here grain size d_p is used). Based on the dimension analysis (see section S1.1), the square relative fluctuating velocity of macroparticle can be expressed as:

$$\overline{U_r}^2 = C_1 \varepsilon_{disp}^{2/3} d_p^{2/3} \quad (1.33)$$

where C_1 is a constant.

(b) Microparticle

The square relative fluctuating velocity of microparticle depends not only on the energy dissipation rate (ε_{disp}) and the grain size (d_p), but also on the kinematic viscosity of fluid (ν_k). The square relative fluctuating velocity of microparticle can be expressed as (derivation see section S1.1):

$$\overline{U_r}^2 = C_2 \frac{\varepsilon_{disp}}{\nu_k} d_p^2 \tag{1.34}$$

where C_2 is a constant.

Sherwood numbers of suspended particles

There are many studies available in the literatures in which solid-liquid mass transfer in agitated and fluidized bed systems was investigated over a wide range of Reynolds numbers. Most of these correlations can be adequately described by the following equation:

$$Sh = A + BRe^{\alpha} Sc^{\beta} \tag{1.35}$$

where A is a constant (spherical particles: $A = 2$; derivation see section S1.2) and B is a constant to be determined using a regression analysis of experimental data. α and β are empirical constants to be determined.

The Schmidt number exponent β of $1/3$ is widely used in many empirical relationships (see Tab. S2.1 in section S2.5) based on the boundary layer theory (see section 1.2.1: $1/3$ comes from the ratio of the thickness of the fluid velocity boundary layer to the thickness of the concentration boundary layer (Eq. 1.22)). The exponent of the Schmidt number might varies slightly in the range of $1/3$ – $1/2$ depending on the hydrodynamic condition (Harriott, 1962; Levins and Glastonbury, 1972). The exponent of the Reynolds number for suspended particles mainly varies in the range of $1/2$ - $3/4$. In the following Sherwood numbers of macroparticle and microparticle are derived based on their relative velocities from Kolmogorov's turbulence theory.

(a) Sherwood number relationship of macroparticle

Substituting the velocity term with Kolmogorov's relative fluctuating velocity of macroparticle (Eq. 1.33), the Reynolds number of macroparticle (Re_{macro}) becomes:

$$Re_{macro} = \frac{\overline{U_r} d_p}{\nu_k} = \frac{\left(\varepsilon_{disp} d_p\right)^{\frac{1}{3}} d_p}{\nu_k} = \left(\frac{d_p}{\eta}\right)^{\frac{4}{3}} \tag{1.36}$$

Harriott (1962) experimentally showed the mass transfer coefficient ($k_{mt} = D_{aq}/\delta = D_{aq} Sh/d_p$) decreases with increasing particle size (d_p) for small particles while the mass transfer coefficient becomes nearly constant for larger particles (equivalent scheme see Fig. S2.6). This finding implies the Sherwood number of macroparticle is proportional to the grain size (d_p), thus the exponent of Reynolds number of macroparticle should be $3/4$. Finally, the Sherwood number relationship of macroparticle is given as:

$$Sh = 2 + BRe_{macro}^{3/4} Sc^{1/3} \tag{1.37}$$

(b) Sherwood number relationship of microparticle

Substituting the velocity term with Kolmogorov's relative fluctuating velocity of microparticle (Eq. 1.34), the Reynolds number of microparticle (Re_{micro}) becomes:

$$Re_{micro} = \frac{\overline{U_r} d_p}{\nu_k} = \frac{\left(\left(\frac{\varepsilon_{disp}}{\nu_k}\right)^{1/2} d_p\right) d_p}{\nu_k} \tag{1.38}$$

Kirwan et al. (1989) produced experimental data to prove the theoretical lower limit of the Sherwood number of 2 for spherical particles and showed that mass transfer of suspended particle in creeping flow (low Reynolds number; microparticles) can be well explained by the Sherwood number relationship proposed by Friedlander (1961), which is given as:

$$Sh = 2 + BPe^{1/3} = 2 + BRe_{micro}^{1/3} Sc^{1/3} \tag{1.39}$$

Pe ($= Re \times Sc$) denotes Peclet number.

Equation 1.39 was derived based on assumption that mass transfer is dominated by the relative velocity between microparticles and microeddies (developing boundary layer model), which originates from continuous formation and disappearance of microeddies that are at the basis of the turbulent energy cascade process. Moreover, the motion of the microeddies, the motion of microparticles in microeddies as well as the motion from one vanishing microeddy all depend on viscous forces (details see Kirwan et al. (1989)).

It is very interesting that many empirical formulas in literatures (for a summary see Kikuchi et al., 1988) are based on Reynolds numbers of macroparticles even if microparticles are applied. Inserting Eq. 1.38 into Eq. 1.39, we obtain:

$$Sh = 2 + BRe_{micro}^{1/3} Sc^{1/3} = 2 + BRe_{macro}^{1/2} Sc^{1/3} \tag{1.40}$$

The correlation of Ranze and Marshall (1952) was based on mass transfer data of microparticles over a wide range of Reynolds numbers and has gained widespread acceptance in the literature; the constant value of *B* is around 0.6:

$$Sh = 2 + 0.6 Re_{macro}^{1/2} Sc^{1/3} \tag{1.41}$$

Different experimental setups and hydrodynamic conditions might obtain slightly different constant values (B). The mass transfer coefficients ($k_{mt} = D_{aq}/\delta = D_{aq} Sh/d_p$) of the suspended macroparticles and microparticles can be calculated by applying corresponding Sherwood number relationships (Eqs. 1.37 and 1.41).

Limitations of Kolmogorov's theory

Kolmogorov's theory assumed that the effect of gravity is small in comparison with that of eddy motion at the particle surface. Harriott (1962) found essentially no effect of density difference (Δρ) over the range 0.005 to 2 g/cm^3 for fully suspended particles. However, if particles have large densities the effect of gravity cannot be neglected, and Kolmogorov's theory doesn't hold any more. For particles under gravity (during sedimentation) according to Stoke's law (1851) reach a terminal velocity which can be used to calculate Sh and thus the mass transfer coefficient (discussed in section S1.3). In addition, Kolmogorov's theory is only able to explain mass transfer for fully suspended particles under the spatially homogeneous energy distribution. In practice, the vertical gradient of particle concentration in suspensions is often visible, which may cause the results departing from the theory.

1.2.3 Summary

In summary, suspended particles can be divided into two parts based on the Kolmogorov's length scale, microparticles and macroparticles. The minimum Sherwood number of spherical particles is 2 (molecular diffusion in an infinite body of stagnant water). The exponents of Reynolds number (based on Re_{macro}) for macroparticles and microparticles are around 3/4 and 1/2, respectively. Based on boundary layer theory, an exponent of 1/3 for Schmidt number is widely used in many Sherwood number relationships (see Tab. S2.1 in section S2.5). The Sherwood number relationships derived from boundary layer theory and Kolmogorov's theory (Eqs. 1.37 and 1.41) provide us a tool to physically determine the mass transfer coefficients of the fully suspended particles and experimentally validation of those theories is described in detail in chapter 3. The energy dissipation rates of different systems (stirrer in the lab, river and ocean) and mass transfer coefficients of different grain sizes as well as the dividing line of suspended particles (the Kolmogorov's length scales) in corresponding systems are discussed in section S2.5.

1.3 The objectives and the structures of the thesis

The objectives of the thesis are:

- to generate analytical and numerical solutions for sorption/desorption kinetics governed by coupled film intraparticle diffusion for both homogeneous (chapters 2 and 4) and heterogeneous systems (multiple sorbents; chapters 3, 5 and 6). The solutions should cover scenarios occurring in batch systems (chapters 2, 3 and 4) as well as cases considering transport process in columns and rivers (chapters 5 and 6).
- to investigate different parameters (e.g., distribution coefficient, intraparticle porosity, grain size, Sherwood number, etc.) impacts on mass transfer shifts in the coupled model

(chapters 2, 3, 4 and 6).

- to figure out solute mass redistribution in heterogenous systems via derived models and understand sorption/desorption behaviors of different sorbents and how they interact with each other (chapters 3 and 5). Moreover, the redistribution model aims to explain some unexpected slow kinetics behaviors of mixed samples.
- to experimentally validate coupled model (chapters 3 and 4) and assess the feasibility of applying Kolmogorov's turbulence theory to elucidate the mass transfer velocity of suspended particles (chapter 3).

The whole thesis is structured as:

Chapter 1 briefly introduces the sorption kinetics models (film diffusion and intraparticle diffusion model) and proposes the questions about the mass transfer shift of coupled film intraparticle diffusion model as well as physical determination of concentration boundary layer of suspended particles. Subsequently, the boundary layer theory and the Kolmogorov's turbulence theory are combined to lead out the dimensionless Sherwood numbers utilized in calculating concentration boundary layer, thus mass transfer velocity.

Chapter 2 theoretically investigates the mass transfer shift of coupled film intraparticle pore diffusion model and a simple first order analytical approximation solution for homogenous sorbent is proposed, which allows to efficiently model coupled model kinetics in batch systems (bath of finite volume) and a semi-analytical Laplace transform solution is derived for validation of this simple analytical approximation solution. Mass transfer shift of coupled model is discussed using mass transfer resistance ratio.

Chapter 3 extends the semi-analytical Laplace transform solutions to heterogeneous systems, which allows to easily apply different sorption/desorption kinetics models for different sorbents in terms of their properties (particle size, geometry, intraparticle porosity, organic carbon content, distribution coefficient etc.) by using different transfer functions in Laplace domain and a computationally very efficient numerical back transformation method. Two batch experiments (Phenanthrene/Anthracene d10 redistribution in mixtures of spherical microplastics of different sizes and a sediment suspension with polyethylene passive samplers) are utilized to verify our redistribution model as well as the Sherwood number relationships based on Kolmogorov's theory.

Chapter 4 presents another application of coupled film intraparticle pore diffusion model in explaining slope discrepancy of particle/gas distribution coefficients (K_{pg}) of polycyclic aromatic hydrocarbons (PAHs) in atmosphere. For model verification, three datasets collected from recently published papers with different contact times between airborne particles and air are utilized.

Chapter 5 presents the application of the kinetics models in leaching tests (based on

German standard). The initial conditions, mass transfer mechanisms as well as sample compositions (heterogeneity) influence on leaching tests are investigated. The traditional leaching tests aim at equilibrium conditions (or uniform concentration distribution) before the leaching starts, but the true concentration distributions inside the column after first flood are seldom discussed. The transport model coupling with external film diffusion and intraparticle diffusion model is utilized to simulate the concentration distribution inside the column and leaching curves by the finite volume method. This chapter shows the complexity of column leaching tests and the generated numerical model can be used to predict the leaching behaviors of the contaminated materials especially when heterogeneity is concerned.

Chapter 6 presents two mesh free methods (semi-analytical Laplace solution and physical informed neural networks (PINNs)) to replace the tedious numerical model for solving non-equilibrium advective-dispersive solute transport with coupled film-intraparticle pore diffusion. The mass transfer shift of coupled model by considering transport process is discussed.

Chapter 7 summarizes the main findings of the thesis and presents the outlooks.

References

Blasius, H., 1908. Grenzschichten in Flüssigkeiten mit kleiner Reibung (The boundary layers in fluids with little friction). In Zeitschrift für Angewandte Mathematik und Physik (Journal of Applied Mathematics and Physics), volume 56, pp. 1–37.

Friedlander, S.K., 1961. A note on transport to spheres in stokes flow. AIChE J. 7, 347–348. https://doi.org/10.1002/aic.690070237.

Harriott, P., 1962. Mass Transfer to Particles: Part I. Suspended in Agitated Tanks. AIChE J. 8, 93–101. https://doi.org/10.1002/aic.690080122.

Kikuchi, K.I., Sugawara, T., Ohashi, H., 1988. Correlation of liquid-side mass transfer coefficient based on the new concept of specific power group. Chem. Eng. Sci. 43, 2533–2540. https://doi.org/10.1016/0009-2509(88)85187-X.

Kirwan, J., Armenante, P.M., 1989. Mass transfer to microparticle systems. Chem. Eng. Sci. 44 (12), 2781–2796. https://doi.org/10.1016/0009-2509(89)85088-2.

Kolmogorov, A.N., 1941. The local structure of turbulence in incompressible viscous fluid for very large Reynolds numbers (English translation by V. Levin, 1991). Process R. Soc. A- Math. Phys. Eng. Sci. 434, 9–13. https://doi.org/10.1098/ rspa.1991.0075.

Levins, D.M., Glastonbury, J.R., 1972. Application of Kolmogorov's theory to particle—liquid mass transfer in agitated vessels. Chem. Eng. Sci. 27, 537–543. https://doi.org/10.1016/0009-2509(72)87009-X.

Montes, R., Aguirre, J., Vidal, X., Rodil, R., Cela, R., Quintana, J.B., 2017. Screening for Polar Chemicals in Water by Trifunctional Mixed-Mode Liquid Chromatography–High Resolution Mass Spectrometry. Environ. Sci. Technol. 51, 6250–6259. https://doi.org/10.1021/acs.est.6b05135.

Ngueleu, S.K., Grathwohl, P., Cirpka, O.A., 2013. Effect of natural particles on the transport of lindane in saturated porous media: Laboratory experiments and model-based analysis. J. Contam. Hydrol. 149, 13–26. https://doi.org/10.1016/j.jconhyd.2013.02.009.

Parnis, J.M., Taskovic, T., Celsie, A.K.D., Mackay, D., 2020. Indoor dust/air partitioning: Evidence for kinetic delay in equilibration for low-volatility SVOCs. Environ. Sci. Technol. 54, 6723–6729. https://doi.org/10.1021/acs.est.0c00632.

Prandtl, L., 1925. Bericht über Untersuchungen zur ausgebildeten Turbulenz. ZAMM - J. Appl. Math. Mech. / Zeitschrift Für Angew. Math. Und Mech. 5, 136–139. https://doi.org/10.1002/zamm.19250050212.

Qian, J., Zhang, W., Yang, X., Yan, K., Shen, M., Pan, H., Zhu, H., Wang, L., 2023. Tailoring zeolite ERI aperture for efficient separation of CO2 from gas mixtures. Sep. Purif. Technol. 309,

123078. https://doi.org/10.1016/j.seppur.2022.123078.

Ranz, W., Marshall, W., 1952. Evaporation from drops. Chem. Eng. Prog. 48, 141–146.

Richardson, Lewis F., 1922. Numerical Prediction by Numerical Process, Cambridge Univ. Press. Second Edition (corrected version of the original with a new Foreward by Peter Lynch), Cambridge University Press 2007: ISBN: 978-0-521-68044-8.

Seidensticker, S., Zarfl, C., Cirpka, O.A., Fellenberg, G., Grathwohl, P., 2017. Shift in Mass Transfer of Wastewater Contaminants from Microplastics in the Presence of Dissolved Substances. Environ. Sci. Technol. 51, 12254–12263. https://doi.org/10.1021/acs.est.7b02664.

Shi, Y., Yang, D., Hu, C., Lyu, L., 2024. Water self-purification via electron donation effect of emerging contaminants arousing oxygen activation over ordered carbon-enhanced CoFe quantum dots. Environ. Sci. Ecotechnology. 20, 100356. https://doi.org/10.1016/j.ese.2023.100356.

Stokes, G.G., 1851. On the effect of the internal friction of fluids on the motion of pendulums. Trans. Camb. Phil. Soc. 9, 8–106.

Wang, J., Guo, X., 2022. Rethinking of the intraparticle diffusion adsorption kinetics model: Interpretation, solving methods and applications. Chemosphere. 309, 136732. https://doi.org/10.1016/j.chemosphere.2022.136732.

Weber, W. J., DiGiano, F. A., 1996. Process dynamics in environmental systems. New York: Wiley.

Welty, J., Wicks, C.E., Wilson, R.E., Rorrer, G.L. (2007) Fundamentals of Momentum, Heat, and Mass Transfer. 5th Edition, John Wiley & Sons Ltd., New York.

Zhang, T., Zhang, S., Gao, J., Li, X., Du, Q., Zhang, Y., Feng, D., Sun, Q., Peng, Y., Tang, Z., Xie, M., Wei, G., 2023. Feasibility assessment of a novel compressed carbon dioxide energy storage system based on 13X zeolite temperature swing adsorption: Thermodynamic and economic analysis. Appl. Energy. 348, 121562. https://doi.org/10.1016/j.apenergy.2023.121562.

2 First order approximation for coupled film and intraparticle pore diffusion to model sorption/desorption batch experiments

Binlong Liu, Michael Finkel, Peter Grathwohl

Abstract

A simple first order approximation was derived to model sorption/desorption kinetics of hazardous compounds in batch experiments based on a coupled film and intraparticle diffusion model. The solution is accurate enough to replace infinite series expansions needed in analytical solution for intraparticle diffusion and it accounts for the mass transfer shift from diffusion in the external aqueous boundary layer to the intraparticle pore space. With increasing distribution coefficient (K_d) and intraparticle particle porosity (ε) or decreasing Sherwood number (Sh) this mass transfer shift from film diffusion to intraparticle pore diffusion is delayed. The simple first order approximation equation allows analyses of mass transfer resistances and calculation of characteristic times which is relevant for the planning of batch experiments. The proposed solution is verified by a semi-analytical solution in Laplace space for fractional mass uptakes in the solid phase at equilibrium ranging from 50 to 91%, representing scenarios typically encountered in batch experiments.

2.1 Introduction

In many experiments on fate and transport of hazardous compounds in the environment the assumption of local equilibrium is questioned, and an analysis of sorption and desorption kinetics is needed (Wang and Guo, 2020). Often, intraparticle diffusion or more specifically intraparticle pore diffusion is limiting mass transfer of sorbates (e.g., organic pollutants) to sorbents like soil aggregates, rock fragments, biochars, etc. (Cooney et al., 1983; Goltz and Roberts, 1986; Hutzler et al., 1986; Roberts et al., 1986; Ball and Roberts, 1991a,b; Sardin et al., 1991; Grathwohl and Reinhard, 1993, Rügner et al., 1999; Kleineidam et al., 1999; Karapanagioti et al., 2000; Allen-King et al., 2002; Sabbah et al., 2005; Finkel and Grathwohl, 2017; Liu et al., 2019; Módenes et al., 2021; Pauletto et al., 2021) but especially at early times (when intraparticle concentration gradients are still very steep), diffusion through the external aqueous boundary layer (film diffusion) may be limiting as for example frequently observed in sorption/desorption experiments of organic or inorganic pollutants with sorbents like volcanic ash-derived soil, activated carbon, peat, microplastics, etc. especially

for sorbates with large distribution coefficients (Ho et al.,1999; Ståhelin et al., 2018; Seidensticker et al., 2017, 2019; Guo et al., 2019; Caceres-Jensen et al., 2020). While sorption/desorption kinetics limited by film diffusion has a simple analytical solution, intraparticle diffusion requires infinite series expansions and attempts to replace it by simplifications has been elusive so far (e.g., Hills et al., 1986); short term and long term approximations only cover small ranges in time or degrees of equilibration. The objective of this work is to develop a simple first order approximation solution for the coupled model which can be easily handled in spreadsheet calculations. The approximation is verified by a semi-analytical solution for mass transfer controlled by retarded intraparticle diffusion and an external aqueous boundary layer using a Laplace transform with numerical inversion. The simple solution allows to analyze how different parameters influence the mass transfer shift from the external boundary layer into the particle (e.g., based on mass transfer resistance ratios); characteristic time scales needed for the design of sorption/desorption batch experiments can be easily assessed.

2.2 Theory

2.2.1 Retarded intraparticle pore diffusion

Spherical intraparticle pore diffusion models are widely used in the design of activated carbon adsorption, ion exchange as well as in chromatography. The governing equation of intraparticle pore diffusion (IPPD) is:

$$\frac{\partial}{\partial t}(\varepsilon C_{w,p} + \rho_p C_s) = D_e\left[\frac{\partial^2 C_{w,p}}{\partial r^2} + \frac{2}{r}\frac{\partial C_{w,p}}{\partial r}\right] \tag{2.1}$$

where r [L] is the radial coordinate and $C_{w,p}$ [M L^{-3}] is the solute concentration in the intraparticle pore water; D_e [L^2 T^{-1}], ε [-] and ρ_p [M L^{-3}] denote the effective diffusion coefficient in the porous particle, the intra-particle porosity, and the bulk density of the particle ($= \rho_s(1-\varepsilon)$; ρ_s [M L^{-3}] is the density of the solid). C_s [M M^{-1}], the solute concentration in the solid phase, is related to the aqueous concentration by the distribution coefficient K_d, i.e. $C_s = K_d\, C_{w,p}$. Eq. 2.1 thus simplifies to:

$$\frac{\partial C_{w,p}}{\partial t} = D_a\left[\frac{\partial^2 C_{w,p}}{\partial r^2} + \frac{2}{r}\frac{\partial C_{w,p}}{\partial r}\right] \tag{2.2}$$

where D_a [L^2 T^{-1}] is the apparent diffusion coefficient:

$$D_a = \frac{D_e}{\varepsilon + K_d\rho_p} = \frac{D_{aq}\varepsilon}{\tau_f(\varepsilon + K_d\rho_p)} \approx \frac{D_{aq}\varepsilon^2}{\varepsilon + K_d\rho_p} \tag{2.3}$$

τ_f [-] is the tortuosity factor and D_{aq} [L^2 T^{-1}] denotes the diffusion coefficient in water. Empirical studies showed that D_e increases approximately with the square of the intraparticle porosity (Boving and Grathwohl, 2001); thus, the tortuosity factor τ_f [-] for diffusion in intra-granular pores may be approximated via the reciprocal of the intra-granular porosity ($\tau_f \approx 1/\varepsilon$). This derivation is based on a linear sorption isotherm. If a non-linear sorption isotherm is available, a linearization is required for the relevant concentration range of the batch experiment (see section S2.6).

Experiments on sorption kinetics are commonly performed in a well-mixed bath of limited volume ("finite bath") and an initial spike of solute in the water (sorption) or contaminated material in initially clean water (desorption). Following Crank (1975) the analytical solution of Eq. 2.2 can be expressed as a series expansion:

$$\frac{M}{M_{eq}} = 1 - \sum_{n=1}^{\infty} \frac{6\beta(\beta+1)}{9 + 9\beta + q_n^2\beta^2} \exp\left[-q_n^2 \frac{D_a}{a^2} t\right] \tag{2.4}$$

M [M] and M_{eq} [M] denote the mass of solute, which has diffused into or out of the particle after a certain time t and after equilibrium was reached, respectively. a [L] denotes the radius of a spherical particle. β represents the ratio of the mass of solute dissolved in the free aqueous phase $M_{w,eq}$ [M] to the mass in the particles (sorbed and in the intraparticle pore space ε) $M_{s,eq}$ [M] under equilibrium conditions:

$$\beta = \frac{M_{w,eq}}{M_{s,eq}} = \frac{V_w}{m_d\left(K_d + \frac{\varepsilon}{\rho_p}\right)} = \frac{1-f}{f} \tag{2.5}$$

V_w [L^3] and m_d [M] denote the volume of water in the batch reactor and the dry mass of the solids; f [-] is the fractional uptake at equilibrium (mass in particle to total mass in the system). Note, M/M_{eq} and thus β and f only refer to the solute mass involved in mass transfer independent on direction (i.e., for sorption and desorption). Very large β values approach infinite bath conditions while small values represent the case where the sorbent "takes it all" (or keeps the solute during desorption). The term $K_d + \varepsilon/\rho_p$ may be interpreted as bulk distribution coefficient between bulk water and porous particles, $K_{d,b}$, which also accounts for the solute mass stored in the intraparticle pore space. q_n denotes the n^{th} non-zero root of $\tan q_n = \frac{3q_n}{3+\beta q_n^2}$.

A large number of terms in the series expansion is needed to obtain an accurate result, which makes the application of short term and long term approximation solutions quite attractive. Barrer (1978) proposed the well-known square root of time solution (Sqrt(t)) as short term approximation of intraparticle diffusion in a batch system:

$$\frac{M}{M_{eq}} = 6\sqrt{\frac{D_a t}{\pi a^2}}\left(1+\frac{1}{\beta}\right) \tag{2.6}$$

which is valid for $M/M_{eq} < 0.1$ when $\beta > 0.1$. Based on Eq. 2.6, the time needed for certain degree of equilibration can be determined for intraparticle pore diffusion:

$$\begin{aligned} t &= \frac{\pi a^2\left(\frac{M}{M_{eq}}\right)^2}{36D_a\left(1+K_{d,b}\frac{m_d}{V_w}\right)^2} \\ &= \frac{\pi a^2\left(\frac{M}{M_{eq}}\right)^2}{36\frac{D_{aq}\varepsilon^2}{\rho_p}\left(\frac{1}{K_{d,b}}+2\frac{m_d}{V_w}+K_{d,b}\left(\frac{m_d}{V_w}\right)^2\right)} \\ &\leq \frac{\pi a^2\left(\frac{M}{M_{eq}}\right)^2}{144\frac{D_{aq}\varepsilon^2}{\rho_p}\frac{m_d}{V_w}} \end{aligned} \tag{2.7}$$

A maximum equilibration time needed exists when liquid to solid ratio equals to distribution coefficient (or $\beta = 1$). For smaller and larger β values mass transfer becomes faster (see Fig. 2.1). Note that this maximum in equilibration time needed only occurs in intraparticle pore diffusion but not in diffusion in solids (without pores) because the diffusion coefficient in solids is independent on distribution coefficient.

A long term approximation solution (LTAM) of intraparticle pore diffusion can be obtained by using the first term of the series expansion solution and the respective transcendental function ($\tan q_n = \frac{3q_n}{3+\beta q_n^2}$) can be easily solved with empirical relationship:

$$\begin{aligned} &\frac{M}{M_{eq}} = 1 - \frac{6\beta(\beta+1)}{9+9\beta+q_1^{*2}\beta^2}\exp\left(-q_1^{*2}\frac{D_a}{a^2}t\right) \\ &\text{with } q_1^*(\beta) = \frac{\pi\beta+3.49}{\beta+0.775} \end{aligned} \tag{2.8}$$

where $q_1^*(\beta)$ represents the first positive solution of transcendental function derived from empirical formula. Equation 2.8 is sufficient to capture more than 90% equilibration of IPPD when β > 0.1 (see Fig. S2.3 in section S2.2).

Equations 2.7 and 2.8 represent just two of many short term or long term approximations of IPPD and more are compared in section S2.2. For small values of β ($\beta < 0.1$), no suitable short term (e.g., square root of time solution) or long term approximation exists. For those cases, the series expansion solution works but may be computationally challenging because a 'infinite' number of terms in the series expansion was needed to capture the short term behavior of IPPD.

2.2.2 Diffusion through an external boundary layer

Mass transfer of contaminants between particles and bulk solution may be limited by diffusion from the particle surface through an aqueous boundary layer. This external film diffusion process (FD) can be well described by the linear driving force equation. The mass flux through the boundary layer ($\partial M/\partial t$ [M T^{-1}], $\partial M/\partial t$ positive in case of desorption) is:

$$\frac{\partial M}{\partial t} = \frac{D_{aq}}{\delta_{aq}} \frac{3 m_d}{\rho_p \, a} (C'_w - C_w) \tag{2.9}$$

The ratio D_{aq}/δ_{aq} represents the mass transfer coefficient k [L T^{-1}] where δ_{aq} [L] is the thickness of the external boundary layer. The term $3m_d/(\rho_p a)$ [L^2] represents the total surface area of the spherical particles. C'_w [M L^{-3}] is the compound's concentration at the particle/water boundary where local equilibrium conditions apply ($C'_w = C_s/K_d$) and C_w [M L^{-3}] denotes the compound's concentration in the bulk water. C'_w can be determined based on mass conservation in the batch system (see section S2.1). For non-linear sorption isotherms, K_d needs to be determined by means of linearization for the relevant concentration range. The solute mass change in the bulk water (due to desorption from or sorption into the solid particles) finally can be expressed as:

$$\frac{\partial M}{\partial t} = k \, \frac{3 m_d}{\rho_p \, a \, V_w} \left(1 + \frac{V_w}{m_d \, K_{d,b}} \right) \left(M_{eq} - M \right) \tag{2.10}$$

Upon integration a simple analytical solution is obtained:

$$\frac{M}{M_{eq}} = 1 - \exp\left(-k \frac{3}{\rho_p \, a} \left(\frac{m_d}{V_w} + \frac{1}{K_{d,b}} \right) t \right) \tag{2.11}$$

For FD, mass transfer becomes independent on $K_{d,b}$ in cases of strong sorption ($1/K_{d,b} \to 0$). Figure 2.1 compares Eq. 2.4 and Eq. 2.11.

The thickness of the external aqueous boundary layer δ_{aq} may be estimated from the empirical Sherwood number (Sh) which relates the mass transfer coefficient k to D_{aq} and thus the particle size d:

$$Sh = \frac{k \, d}{D_{aq}} = \frac{d}{\delta_{aq}} \quad \to \quad \delta_{aq} = \frac{d}{Sh} \tag{2.12}$$

Numerous empirical relationships exist to estimate Sherwood numbers (for a compilation see section S2.5); they typically are based on the particle Reynolds number (Re_p) and the Schmidt number (Sc):

$$Sh = 2 + c \, Re_p^{1/2} Sc^{1/3} = 2 + c \sqrt{d \frac{v_a}{\nu}} \sqrt[3]{\frac{\nu}{D_{aq}}} \tag{2.13}$$

Sc for many solutes is fairly constant with a value in the range of 1000 – 1500 ($Sc^{1/3} \approx 10 -$

11); v [L² T⁻¹] and v_a [L T⁻¹] denote the kinematic viscosity and the relative velocity of water with respect to the particle. In batch tests, particles are usually fully suspended in water (shaken or stirred); here the relative velocity of particles to the fluid may be estimated from Kolmogorov's theory (1941). Sh approaches a minimum value of 2 (a "motionless" particle suspended in stagnant water).

Intraparticle pore diffusion (IPPD) and film diffusion (FD) exhibit quite different characteristics with respect to solute uptake/release kinetics and its dependency on key parameters (Grathwohl, 2014; Liu et al., 2021). To provide a basic analysis, we compare solute uptake/release in a finite bath for β values of 3, 1, 0.3 and 0.1 corresponding to fractional uptakes of 0.25, 0.5, 0.77 and 0.91 (f in Eq. 2.5), which represent typical values for batch experiments on sorption kinetics (Fig. 2.1). At early times, FD is often slower and thus would limit solute uptake. At later times, mass transfer shifts into the particle and becomes limited by IPPD. The exact 'threshold time' when IPPD gets more control on mass transfer than FD depends on β and Sh. Note that FD becomes slower with decreasing values of β while uptake/release limited by IPPD shows a reversed relationship – with fast (de-)sorption kinetics corresponding to high fractional uptakes. A minimum for (de-)sorption kinetics of IPPD is obtained for $\beta = 1$ (see Eq. 2.7) where $K_{d,b}$ equals the liquid to solid ratio. Sorption kinetics with IPPD thus is almost the same for β values of 3 and 0.3 because both cases are exactly (or around) three times higher or lower than $\beta = 1$. Intersections of FD and IPPD shift with increasing sorption (decreasing β) to later times or higher M/M_{eq} indicating longer mass transfer limitation by FD for strongly sorbing compounds. Increasing intraparticle porosity (ε) would facilitate mass transfer by IPPD, and thus FD limits at early times and the mass transfer shift from FD to IPPD occurs later.

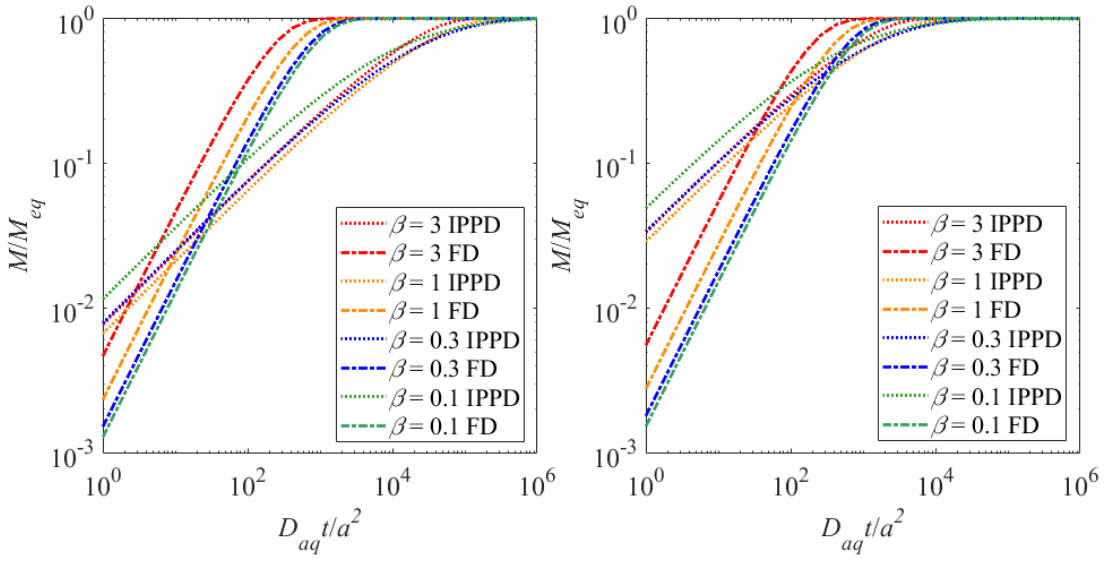

Fig. 2.1: Mass sorbed or desorbed relative to equilibrium conditions (M/M_{eq}) vs.

dimensionless time (Fourier number = $D_{aq}t/a^2$) for film diffusion (FD: dash-dotted lines, Eq. 2.11) and intraparticle pore diffusion (IPPD: dotted lines, Eq. 2.4) in a finite bath with different values for $\beta = \frac{M_{w,eq}}{M_{s,eq}} = \frac{V_w}{K_{d,b}\, m_d}$ (0.1, 0.3, 1 and 3) and for intraparticle porosity $\varepsilon =$ 0.05 (left graph) and $\varepsilon = 0.2$ (right graph); $Sh = 2$.

2.3 Methods

2.3.1 Coupled film and retarded intraparticle pore diffusion: the first order approximation model (FOAM)

In the following, the first order approximation model (FOAM) for intraparticle pore diffusion coupled to external film diffusion is derived based on the dual film diffusion concept describing mass transfer by diffusion through two adjacent films (Fig. 2.2). While the thickness of the external aqueous boundary layer (δ_{aq}) is constant (at given Sh), the internal film in the particle (δ_p) initially follows random walk theory (Stickler and Schachinger, 2016) and grows with the square root of time and apparent diffusion coefficient ($\delta_p = \sqrt{\pi D_a t}$).

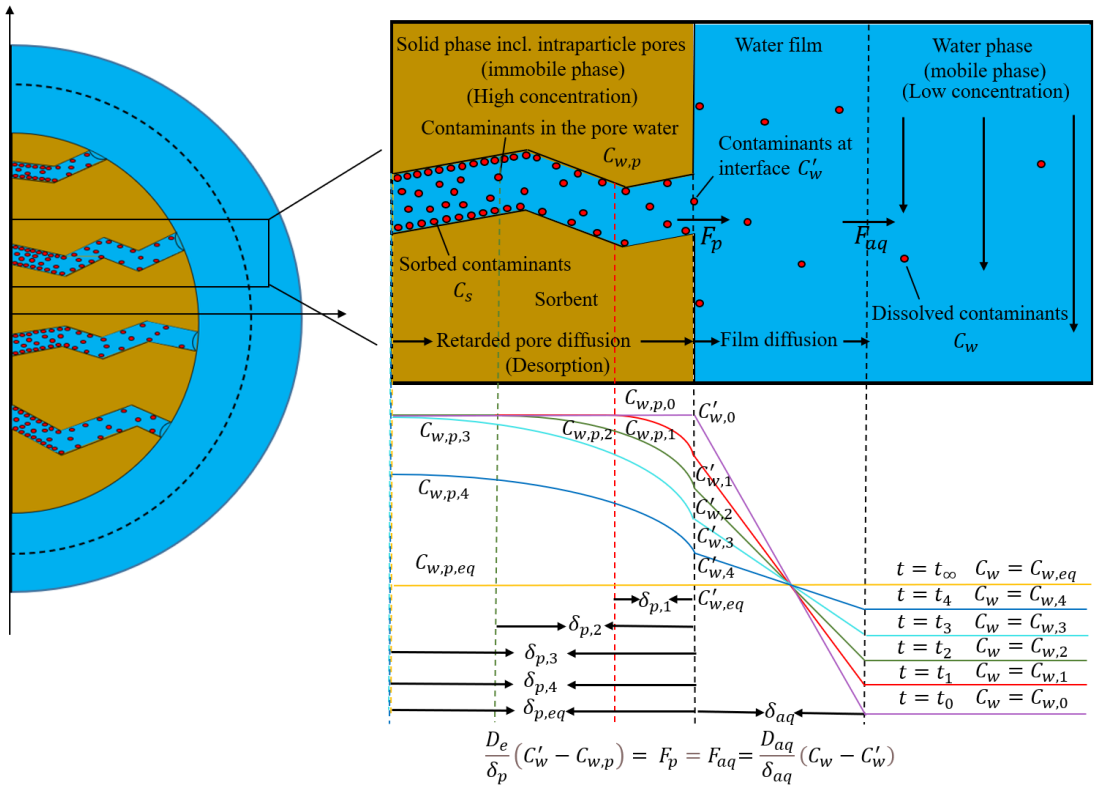

Fig. 2.2: Development of concentration gradients during desorption of a compound from a sphere in a batch experiment limited by diffusion in intraparticle pores (δ_p) and the aqueous boundary layer (δ_{aq}) from time zero (t_0, purple) to equilibrium (t_∞, yellow).

Under steady state conditions the fluxes through the two layers have to be the same:

$$F_{aq} = \frac{D_{aq}}{\delta_{aq}}(C_w - C'_w) = \frac{D_e}{\delta_p}\left(C'_w - C_{w,p}\right) = F_p \tag{2.14}$$

where F_{aq} [M L^{-2} T^{-1}] and F_p [M L^{-2} T^{-1}] denote the mass flux densities in the external aqueous boundary layer and in the intraparticle pores, respectively. D_{aq}/δ_{aq} [L T^{-1}] and D_e/δ_p [L T^{-1}] represent mass transfer coefficients and their inverse may be regarded as mass transfer resistances. As before, Eq. 2.14 can be solved for the compound's concentration at the interface between bulk and pore water (C'_w) which then is inserted into one of the fluxes:

$$F_p = F_{aq} = \frac{1}{\frac{\delta_p}{D_e} + \frac{\delta_{aq}}{D_{aq}}}(C_w - C_{w,p}) \tag{2.15}$$

In a batch experiment, C_w and $C_{w,p}$ change over time but since the total solute mass in the system stays constant (mass conservation) this can be evaluated based on the equilibrium concentrations finally achieved (see section S2.3 for details). The solute mass change in the bulk water (mass which has diffused out (desorption) or into (sorption) the particle) finally can be expressed as:

$$\frac{\partial M}{\partial t} = \frac{1}{\frac{\delta_p}{D_e} + \frac{\delta_{aq}}{D_{aq}}} \frac{m_d\, 3}{\rho_p\, a\, V_w}\left(1 + \frac{V_w}{m_d\, K_{d,b}}\right)\left(M_{eq} - M\right) \tag{2.16}$$

In order to solve that we assume an intra-particle boundary layer initially increasing in thickness with the square root of time. With $D_a = D_e/\left(\varepsilon + K_d\, \rho_p\right) = D_e\, /K_{d,b}\, \rho_p$ the mass transfer resistance depends on time and becomes:

$$\frac{\delta_p}{D_e} = \frac{\sqrt{\pi D_a t}}{D_e} = \sqrt{\frac{\pi\, t}{D_e\, K_{d,b}\, \rho_p}} = \frac{1}{\varepsilon}\sqrt{\frac{\pi\, t}{D_{aq}\, K_{d,b}\, \rho_p}} \tag{2.17}$$

δ_p/D_e decreases with the square root of D_e (or the intraparticle porosity) and increases with decreasing sorption ($K_{d,b}$). Eq. 2.16 then becomes:

$$\frac{\partial M}{\partial t} = \frac{1}{\sqrt{\frac{\pi t}{D_e\, K_{d,b}\, \rho_p}} + \frac{\delta_{aq}}{D_{aq}}} \frac{3}{\rho_p\, a}\left(\frac{m_d}{V_w} + \frac{1}{K_{d,b}}\right)\left(M_{eq} - M\right) \tag{2.18}$$

Upon integration we get (see section S2.3 for details):

$$\frac{M}{M_{eq}} = 1 - \exp\left(-\frac{2}{c^2}\left(b + c\sqrt{t}\right) + \frac{2b}{c^2}\ln\left(b + c\sqrt{t}\right) + \left(\frac{2b}{c^2} - \frac{2b}{c^2}\ln b\right)\right)$$

or simpler:

$$\frac{M}{M_{eq}} = 1 - \exp\left[-\frac{2}{c^2}\left(c\sqrt{t} - b\ln\left(b + c\sqrt{t}\right) + b\ln b\right)\right]$$

with:

$$b = \frac{\delta_{aq}}{D_{aq}\frac{3}{\rho_p\, a}\left(\frac{m_d}{V_w} + \frac{1}{K_{d,b}}\right)} \tag{2.19}$$

and

$$c = \frac{\sqrt{\frac{\pi}{D_e\, K_{d,b}\, \rho_p}}}{\frac{3}{\rho_p\, a}\left(\frac{m_d}{V_w} + \frac{1}{K_{d,b}}\right)}$$

b is the inverse of the rate constant and thus the characteristic time of FD, c is the mass transfer resistance in the particle. If b is close to zero, then intraparticle diffusion dominates in Eq. 2.19. At early times, it approaches the well-known square root of time approximation for intraparticle pore diffusion (Eq. 2.6) in a batch system (Note that $1 - \exp(-x) \approx x$ when $x \to 0$):

$$\begin{aligned}\frac{M}{M_{eq}} &= 1 - \exp\left(-\sqrt{\frac{D_e\, K_{d,b}\, \rho_p t}{\pi}}\frac{6}{\rho_p\, a}\left(\frac{m_d}{V_w} + \frac{1}{K_{d,b}}\right)\right) \\ &\approx \frac{6}{\rho_p a}\left(\frac{m_d}{V_w} + \frac{1}{K_{d,b}}\right)\sqrt{\frac{D_e\, K_{d,b}\, \rho_p t}{\pi}} \\ &= 6\sqrt{\frac{D_a t}{\pi a^2}}\left(1 + \frac{1}{\beta}\right)\end{aligned} \tag{2.20}$$

If c approaches zero, the simple analytical solution for film diffusion (Eq. 2.11) is obtained (because of $\sqrt{\frac{\pi t}{D_e\, K_{d,b}\, \rho_p}} \to 0$ in Eq. 2.18). FOAM can be easily extended for diffusion in nonporous solids (e.g., polymers such as microplastics) by replacing the harmonic mean mass transfer resistance term in Eq. 2.18 ($\frac{1}{\sqrt{\frac{\pi t}{D_e\, K_{d,b}\, \rho_p}} + \frac{\delta_{aq}}{D_{aq}}}$) with $\frac{1}{\frac{1}{K_d}\sqrt{\frac{\pi\, t}{D_s}} + \frac{\delta_{aq}}{D_{aq}}}$ where D_s [$L^2\ T^{-1}$] is the solid diffusion coefficient.

2.3.2 Semi-analytical solution with Laplace transform (SALT)

For the validation of the first order approximation model derived above, we use an analytical expression obtained after Laplace transformation of the governing equations in time.

Seidensticker et al. (2017) used a Laplace solution of film-intraparticle solid diffusion (no pores) to investigate the mass transfer shift of organic contaminants (e.g., phenanthrene, tonalide, and benzophenone) in microplastics. Here, a more general Laplace solution of film-intraparticle pore diffusion is derived where compound mass stored in intra-granular porous water is also considered.

Assuming that the initial concentration within the porous particle is uniform (desorption) or zero (sorptive uptake), $C_{w,p}(r, t = 0) = C_{w,p}(0)$ [M L^{-3}], the governing equation of intraparticle pore diffusion in Laplace domain is:

$$s\tilde{C}_{w,p} - C_{w,p}(0) - D_a\left[\frac{d^2\tilde{C}_{w,p}}{dr^2} + \frac{2}{r}\frac{d\tilde{C}_{w,p}}{dr}\right] = 0$$

with the initial and boundary conditions given by:

$$\tilde{C}_{w,p}(a) = \tilde{C}_{w,p,a} \tag{2.21}$$

$$\left.\frac{d\tilde{C}_{w,p}}{dr}\right|_{r=0} = 0$$

$$\tilde{C}_{w,p}(r) = \tilde{C}_{w,p}(0) \;\; \forall r$$

in which a tilde sign denotes the Laplace transform of the respective variable, and s [T^{-1}] is the complex Laplace coordinate. The solution of Eq. 2.21 in the Laplace domain can be expressed as (see section S2.4 for derivation):

$$\tilde{C}_{w,p}(r,s) = \frac{a}{r}\frac{\sinh\left(r\sqrt{\frac{s}{D_a}}\right)}{\sinh\left(a\sqrt{\frac{s}{D_a}}\right)}\left(\tilde{C}_{w,p,a} - \frac{C_{w,p}(0)}{s}\right) + \frac{C_{w,p}(0)}{s} \tag{2.22}$$

where $\tilde{C}_{w,p,a}$ is the solute concentration at the particle/water boundary in Laplace domain.

The mass transfer through the boundary layer is driven by the concentration difference between the bulk solution and the aqueous concentration at the surface of the spheres. Hence, the continuity of mass fluxes in the Laplace domain requires:

$$\tilde{F} = k\left(\tilde{C}_{w,p,a} - \tilde{C}_w\right) = -D_e\left.\frac{d\tilde{C}_{w,p}}{dr}\right|_{r=a} \tag{2.23}$$

where $\tilde{F}$ and $\tilde{C}_w$ are Laplace transforms of mass flux density and solute concentration in bulk water. Inserting the derivative of Eq. 2.22 at the particle/water boundary ($\left.\frac{\partial\tilde{C}_{w,p}}{\partial r}\right|_{r=a}$) into Eq. 2.23, we obtain:

$$\tilde{C}_{w,p,a} = \frac{D_e\left(\sqrt{\frac{s}{D_a}}\coth\left(a\sqrt{\frac{s}{D_a}}\right) - \frac{1}{a}\right)\frac{C_{w,p}(0)}{s} + k\tilde{C}_w}{k + D_e\left(\sqrt{\frac{s}{D_a}}\coth\left(a\sqrt{\frac{s}{D_a}}\right) - \frac{1}{a}\right)} \tag{2.24}$$

Considering the solute mass transfer in the external boundary, the concentration change in

the bulk water phase can be expressed as:

$$\frac{dC_w}{dt} = (C_{w,p}(a,t) - C_w)k\frac{3}{a}\frac{m_d}{V_w\,\rho_p} \tag{2.25}$$

where $C_{w,p}(a,t)$ [M L^{-3}] is the solute concentration at the particle/water boundary. The Laplace transformation for Eq. 2.25 yields:

$$s\widetilde{C_w} - C_w(0) = (\tilde{C}_{w,p,a} - \tilde{C}_w)k\frac{3}{a}\frac{m_d}{V_w\,\rho_p} \tag{2.26}$$

where $C_w(0)$ [M L^{-3}] denotes the initial solute concentration in the external bulk water phase. Substituting Eq. 2.24 into Eq. 2.26 and rearranging terms finally yields the analytical solution of FIPPD in the Laplace domain, which can be expressed as:

$$\widetilde{C_w} = \frac{\alpha\frac{C_{w,p}(0)}{s} + C_w(0)}{\alpha + s}$$
$$\text{with } \alpha(s) = \frac{D_e\left(\sqrt{\frac{s}{D_a}}\coth\left(a\sqrt{\frac{s}{D_a}}\right) - \frac{1}{a}\right)}{k + D_e\left(\sqrt{\frac{s}{D_a}}\coth\left(a\sqrt{\frac{s}{D_a}}\right) - \frac{1}{a}\right)}\,k\frac{3}{a}\frac{m_d}{V_w\,\rho_p} \tag{2.27}$$

Two limiting cases (the analytical solutions of IPPD and FD in Laplace domain) are also considered (see section S2.4 for details of the derivation). This semi-analytical Laplace transform solutions (SALT) have been compared for the limiting case FD and IPPD to the analytical solution of FD (Eq. 2.11) as well as IPPD with the series expansion (Eq. 2.4), and both cases showed perfect agreement (as is demonstrated in Fig. S2.4 in section S2.4). For back-transformation, we use the numerical inversion method of de Hoog et al. (1982) implemented in Matlab. This semi-analytical Laplace transform solution is computationally very efficient and can replace the series expansion especially for small values of β ($\beta < 0.1$).

2.4 Results

2.4.1 Validation of the approximate solution

In Fig. 2.3 we compare the first order approximation model (FOAM) with FD, IPPD, short and long term approximations of IPPD, and finally the semi-analytical Laplace transform solution (SALT) for two different intraparticle porosities ($\varepsilon = 0.05$ and 0.2) and β values of 0.1 and 1, respectively (corresponding to fractional uptakes of 91% and 50%). At early times, FD limits mass transfer and is well described by the semi-analytical Laplace transform solution (SALT); after the mass transfer resistance shifts into the particle the short (Sqrt(t)) or long term approximations (LTAM) of IPPD do not fit anymore, however the first order approximation

model (FOAM) still matches very well. Increasing intraparticle porosity (ε) or decreasing β values delay the mass transfer shift of FOAM (or SALT) from FD to IPPD. For low β values (e.g., $\beta < 0.1$), the square root of time solution (Sqrt(t)) only works well for $M/M_{eq} < 0.1$, but IPPD at that β range is often not important because FD dominates the mass transfer behavior of strong sorbents (low β) at early times.

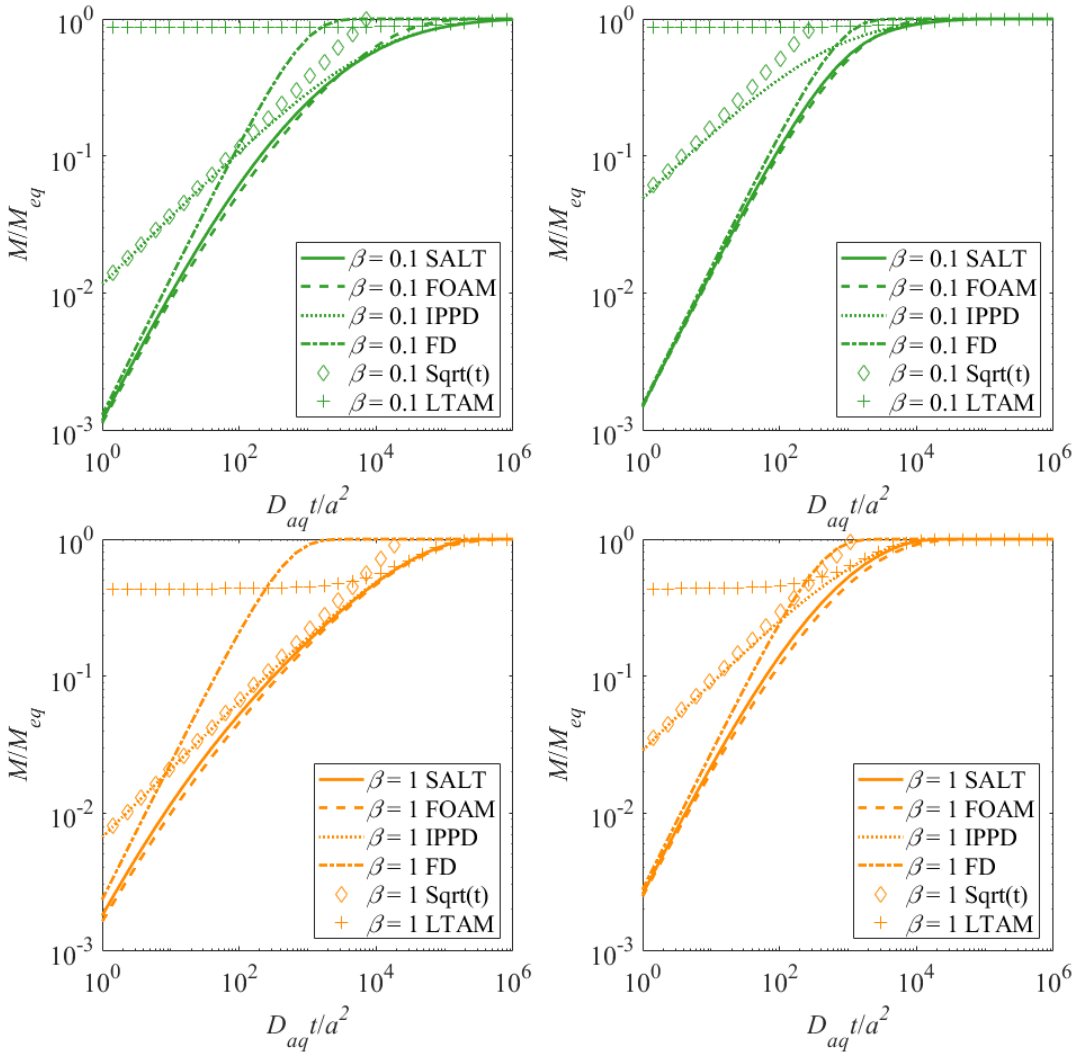

Fig. 2.3: Mass sorbed or desorbed relative to equilibrium conditions (M/M_{eq}) vs. dimensionless time (Fourier number = $D_{aq}t/a^2$) for the semi-analytical Laplace transform solution (SALT: solid lines, Eq. 2.27), the first order approximation model (FOAM: dashed lines, Eq. 2.19), the intraparticle pore diffusion model (IPPD: dotted lines, Eq. 2.4), the film diffusion model (FD: dashed-dotted lines, Eq. 2.11), the square root of time solution (Sqrt(t): diamond symbols, Eq. 2.6) and the long term approximation model (LTAM: cross symbols, Eq. 2.8) in a finite bath with different intraparticle porosities ($\varepsilon = 0.05$ (left) and $\varepsilon = 0.2$ (right)); $Sh = 2$; top: $\beta = \frac{V_w}{K_{d,b}\, m_d} = 0.1$ (fractional uptake = 0.91); bottom: $\beta = 1$ (fractional uptake =

0.50).

The semi-analytical Laplace transform solution (SALT) is used as reference for the validation of the first order approximation model (FOAM). Deviations of FOAM from SALT (Eq. 2.19 vs Eq. 2.27) are shown in Fig. 2.4 for the finite bath with β values of 3, 1, 0.3 and 0.1 with two different intraparticle porosities ($\varepsilon = 0.05$ and 0.2). FOAM agrees reasonably well to SALT. For the small intraparticle porosity case ($\varepsilon = 0.05$), the deviations of FOAM from SALT are less than 15% for β values $0.1 - 3$; at early times FOAM underestimates kinetics slightly while it seems to be too fast for β values 0.1 and 0.3. This also applies to the large intraparticle porosity case ($\varepsilon = 0.2$) where the error becomes maximum (17%) for a β value of 3. Deviations in FOAM especially close to equilibrium may be explained by the assumption of the increase of the internal diffusion distance with the square root of time, but this cannot continue infinitely (it has to stay smaller than the radius of the particle, e.g., limited to 1/5 of the radius, see characteristic times below). In real systems, approaches to equilibrium to more than 90% ($M/M_{eq} > 0.9$) hardly can be accurately followed because the precision of batch experiments is typically less than 10%. The FOAM still is acceptable and can be used as approximation solution for coupled film intraparticle pore diffusion for $M/M_{eq} < 0.9$ if values for ($0.1 < \beta < 1$). Unlike other conventional approximations for intraparticle diffusion (Sqrt(t) and LTAM), FOAM does not produce escalating errors as shown in Fig. S2.3 (bottom) in section S2.2. Close to equilibrium the error almost vanishes (see Fig. 2.4, bottom). Remarkably in the coupled model, sorptive uptake (or desorption) is almost independent on the fractional uptake (or β); all curves are concentrated in narrow ranges (see Fig. 2.4, top). This is because of the distinctly different behaviors of FD and IPPD mass transfer kinetics (see also Fig. 2.1): At early times, when IPPD may be hardly approximated, FD dominates mass transfer and later IPPD takes over.

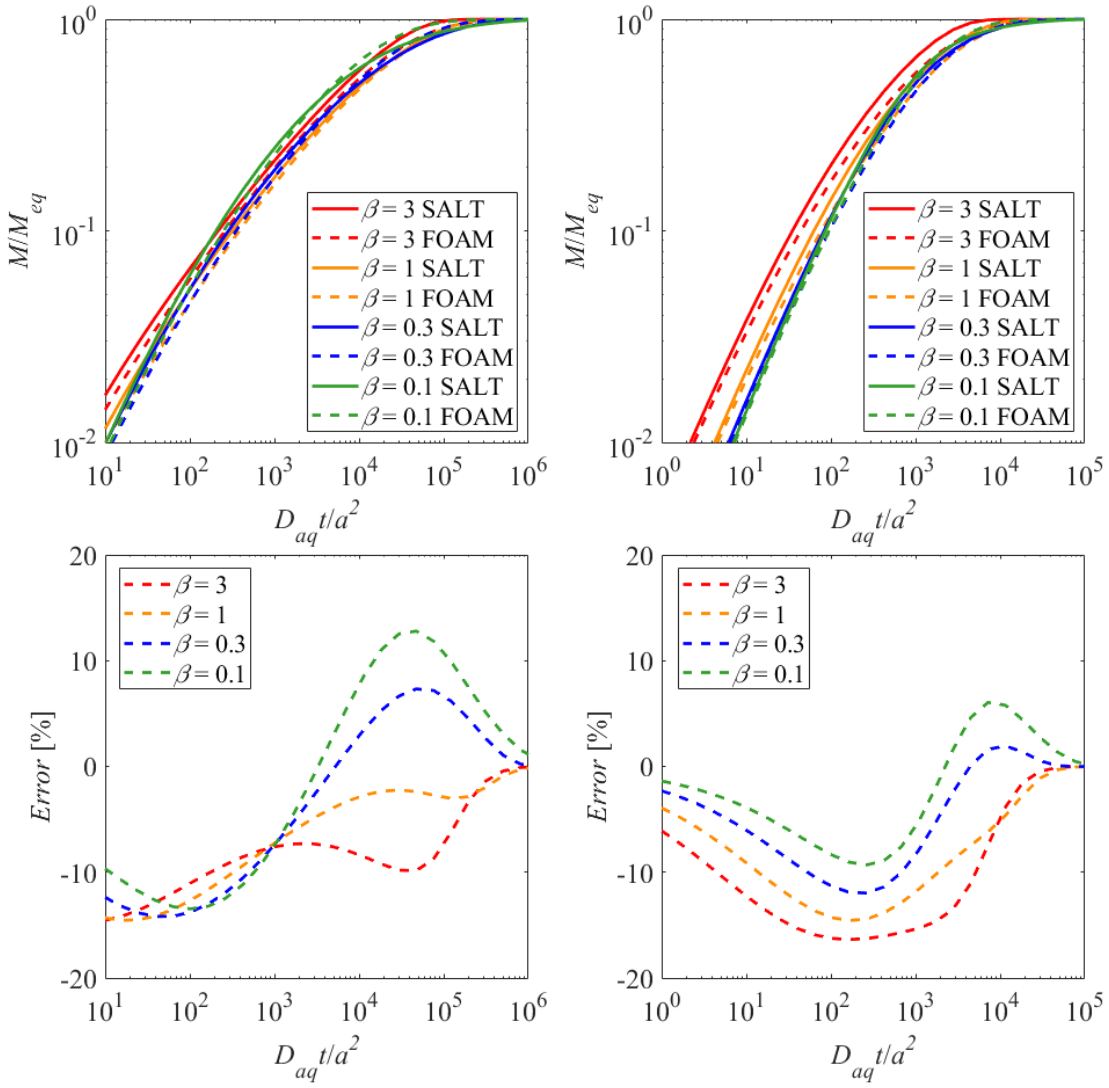

Fig. 2.4: Mass sorbed or desorbed relative to equilibrium conditions (M/M_{eq}) vs. dimensionless time (Fourier number = $D_{aq}t/a^2$) (top) for the semi-analytical Laplace transform solution (SALT: solid lines, Eq. 2.27) and the first order approximation model (FOAM: dashed lines, Eq. 2.19) in a finite bath ($\beta = \frac{V_w}{K_{d,b}\, m_d} = 0.1$, 0.3, 1 and 3, $Sh = 2$) with different intraparticle porosities ($\varepsilon = 0.05$ (left) and $\varepsilon = 0.2$ (right)) and the % deviation of FOAM from SALT (bottom).

2.4.2 Mass transfer shift analysis

The first order approximation model (FOAM) assumes the internal film thickness increases with square root of time while the external film thickness stays constant. Thus, IPPD tends to limit mass transfer at late time periods while at early times FD dominates. In order to elucidate this mass transfer shift, ratios of the external and internal mass transfer

resistances (R_{ex}, R_{in} [T L^{-1}] = inverse mass transfer coefficients) may be used:

$$\frac{R_{ex}}{R_{in}} = \frac{\frac{\delta_{aq}}{D_{aq}}}{\frac{\delta_p}{D_e}} = \frac{\frac{\delta_{aq}}{D_{aq}}}{\frac{\sqrt{\pi D_a t}}{D_{aq}\varepsilon^2}} \approx \frac{\frac{d}{Sh}\varepsilon^2}{\sqrt{\frac{\pi D_{aq}\varepsilon^2}{K_{d,b}\rho_p}t}} = \frac{d\,\varepsilon}{Sh}\sqrt{\frac{K_{d,b}\rho_p}{\pi D_{aq} t}} \tag{2.28}$$

With increasing agitation Sh increases and mass transfer resistance moves into the particle. Using the common empirical Sherwood number relationship of Ranz and Marshall (1952; $Sh = 0.6\, Re_p^{1/2} Sc^{1/3}$), Eq. 2.28 becomes:

$$\frac{R_{ex}}{R_{in}} = \frac{\frac{d}{Sh}\varepsilon^2}{\sqrt{\pi D_a t}} \approx 0.94\,\varepsilon\sqrt{\frac{d}{v_a\, t}\rho_p K_{d,b}}\, Sc^{1/6} \tag{2.29}$$

where d/v_a represents the contact time of particle with water at given velocity. According to Kolmogorov's theory the velocity depends on the energy dissipation rate of the system (ε_{disp}) as well as on the particle size $v_a \sim \left(\varepsilon_{disp} d\right)^{1/3}$ which leads to:

$$\frac{R_{ex}}{R_{in}} \approx 0.94\,\varepsilon\sqrt{\frac{K_{d,b}\,\rho_p}{t}}\, d^{1/3}{\varepsilon_{disp}}^{-1/6}\, Sc^{1/6} \tag{2.30}$$

The energy dissipation rate is quite insensitive in Eq. 2.30 and quite similar for different systems. Chickadel et al. (2011), Fisher et al. (2002) and MacDonald et al. (2007) reported energy dissipation rates in rivers in the range of $10^{-6} - 10^{-5}$ m^2 s^{-3}. In oceans, values are roughly one magnitude lower than in rivers (Moum et al., 1995). As Eq. 2.30 shows, with large distribution coefficients ($K_{d,b}$) and particle sizes (d), mass transfer becomes more limited by the external aqueous boundary layer. With time the ratio drops below one, which indicates the point where intraparticle pore diffusion starts to dominate sorption/desorption kinetics. ε_{disp} and Sc have only minor influence on the ratio of mass transfer resistances.

Alternatively, δ_{aq} may be estimated from the time of the renewal of the aqueous boundary layer, e.g. d/v_a which leads to a definition of Sh as a function of the square root of the Peclet number (e.g., $Sh = 0.1\, Pe^{1/2}$; $Pe = d\,\frac{v_a}{D_{aq}}$; Liu et al. 2014) and eliminates the Schmidt number:

$$\begin{aligned}\frac{R_{ex}}{R_{in}} &= \frac{d\,\varepsilon}{\sqrt{\frac{d\,v_a}{D_{aq}}}}\sqrt{\frac{K_{d,b}\,\rho_p}{\pi D_{aq} t}} = 0.56\,\varepsilon\sqrt{\frac{d\,K_{d,b}\,\rho_p}{v_a\, t}} \\ &\approx 0.56\,\varepsilon\sqrt{\frac{K_{d,b}\,\rho_p}{t}}\, d^{1/3}{\varepsilon_{disp}}^{-1/6}\end{aligned} \tag{2.31}$$

Again, with decreasing intraparticle porosity, mass transfer shifts from the external

boundary layer into the particle and IPPD dominates the sorption kinetics (because D_e becomes very low).

In order to investigate influence of intraparticle porosity (ε), sorption (K_d) or β as well as Sherwood numbers on the mass transfer shift in FIPPD, M/M_{eq} was calculated (Eq. 2.11) at the time point where the external and internal mass transfer resistances are equal ($R_{ex}/R_{in} = 1$) for two different Sherwood numbers ($Sh = 2$ and 20); results are shown in Fig. 2.5. Higher values of M/M_{eq} indicate that the mass transfer shift occur closer to equilibrium (or at later times). For strong sorption (low β), FD controls until M/M_{eq} almost approaches 1 for sorbents with large intraparticle porosity even for small Sherwood numbers approach the minimum of 2, which may be encountered in natural environments (e.g., rivers or oceans). For laboratory experimental conditions (e.g., stirred or shaken in lab) of course higher Sh are expected and mass transfer shifts occur earlier and IPPD becomes more important especially for weak sorbents (high β) or at high liquid to solid ratios. Mass transfer characteristics observed in laboratory experiments thus may not truly reflect natural conditions and mass transfer shifts may be quite different (Seidensticker et al., 2017).

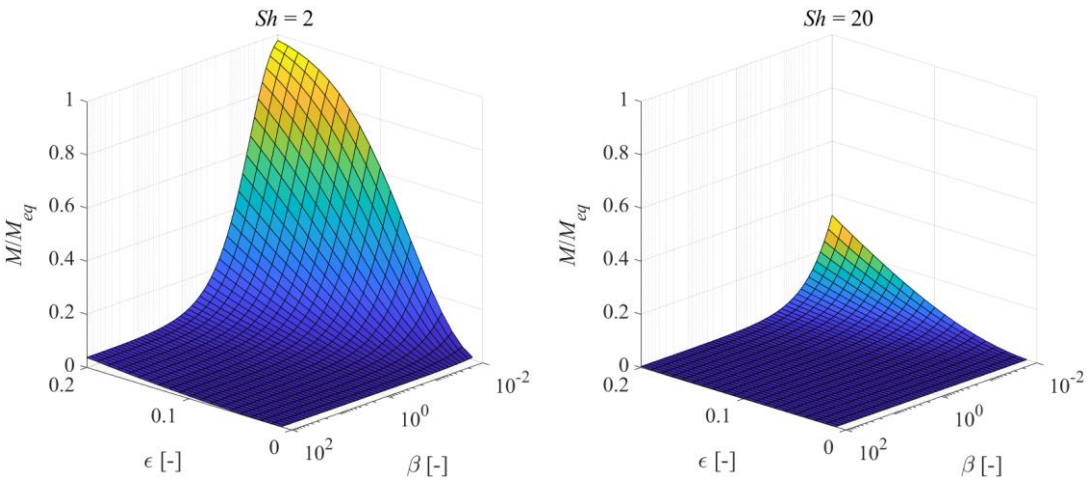

Fig. 2.5: Mass sorbed or desorbed relative to equilibrium conditions (M/M_{eq}) for external film diffusion (FD) at equal external and internal mass transfer resistances ($\frac{R_{ex}}{R_{in}} = 1$) vs. solute ratios in water to solids (β) and intraparticle porosity (ε) for Sherwood numbers (Sh) of 2 (left: rivers, oceans) and 20 (right: laboratory).

2.4.3 Characteristic times

The semi-analytical Laplace solution (SALT) of FIPPD allows to derive characteristic times τ_{ch} for external (film diffusion) and internal mass transfer (intraparticle pore diffusion) (see

section S2.4.2 for derivation):

$$\tau_{ch} = \frac{\int_0^\infty C_w(t) - C_{w,eq}}{C_w(0) - C_{w,eq}} = \frac{\lim_{s\to 0}\left(\widetilde{C_w} - \frac{C_{w,eq}}{s}\right)}{C_w(0) - C_{w,eq}} \tag{2.32}$$

The final result shows that the characteristic time of FIPPD equals:

$$\tau_{ch} = \frac{\rho_p\left(\frac{a}{3k} + \frac{a^2}{15D_e}\right)}{\left(\frac{1}{K_{d,b}} + \frac{m_d}{V_w}\right)} \tag{2.33}$$

which can be interpreted as the sum of two characteristic times τ_{ch}^{ex} and τ_{ch}^{in} for the cases of FD and IPPD, respectively:

$$\begin{aligned}
\tau_{ch}^{ex} &= \frac{1}{\left(\frac{1}{K_{d,b}} + \frac{m_d}{V_w}\right)}\frac{\rho_p a}{3k} = \frac{1}{\left(\frac{1}{K_{d,b}} + \frac{m_d}{V_w}\right)}\frac{2\rho_p a^2}{3D_{aq}Sh} \leq \frac{1}{\left(\frac{1}{K_{d,b}} + \frac{m_d}{V_w}\right)}\frac{\rho_p a^2}{3D_{aq}} \\
\tau_{ch}^{in} &= \frac{1}{\left(\frac{1}{K_{d,b}} + \frac{m_d}{V_w}\right)}\frac{\rho_p a^2}{15D_e} = \frac{1}{\left(\frac{1}{K_{d,b}} + \frac{m_d}{V_w}\right)}\frac{\rho_p a^2}{15D_{aq}\varepsilon^2}
\end{aligned} \tag{2.34}$$

The characteristic time (τ_{ch}) is an important indicator to assess time scales in sorption/desorption experiments. The external characteristic time (τ_{ch}^{ex}) represents an equilibration of 63.2%; a maximum external characteristic time is reached when Sherwood numbers decrease to their minimum of 2. In contrast, the internal characteristic time (τ_{ch}^{in}) does not reflect a constant degree of equilibration (in terms of a fixed M/M_{eq}); for β values ranging from 3 to 0.1, τ_{ch}^{in} denotes equilibration to 68-83%. In the infinite bath, τ_{ch}^{in} is close to the time of ca. 63.2% equilibration (see Glueckauf's solution Eq. S2.14 in section S2.2) and for this case the characteristic time ratio is:

$$\frac{\tau_{ch}^{ex}}{\tau_{ch}^{in}} = \frac{10\varepsilon^2}{Sh} \leq 5\varepsilon^2 \tag{2.35}$$

The characteristic time ratio increases with the square of intraparticle porosity and decreases with the increase of Sherwood number, but it is independent on the distribution coefficient. Note, this conclusion would agree with the mass transfer resistance ratios discussed above (Eq. 2.28) if a fixed internal boundary layer thickness of one-fifth of the particle radius is assumed ($\delta_p = a/5$). Glueckauf (1955) used the same value for a long term approximation of IPPD in the infinite bath ($\beta \to \infty$). This fits for weak sorbents (low $K_{d,b}$) with a large apparent diffusion coefficient and a rapidly increasing internal boundary layer thickness. For strong sorbents (high $K_{d,b}$) the internal diffusion distance is short (and still growing) after the mass transfer resistance shifts from the external boundary layer into the particle ($\delta_p = \sqrt{\pi D_a t} < a/5$). The internal diffusion distance, however, cannot grow infinitely, it has to stay smaller than the radius of the particle (e.g., limited to 1/5 of the radius).

In FOAM 63.2% equilibration is obtained if the argument of the exponential function equals -1 (see Eq. 2.19) and this leads to a different definition of the characteristic time compared to SALT (because δ_p is a function of time). In order to illustrate the differences of the two approaches, M/M_{eq} was calculated for both characteristic times (Eq. 2.19 and 2.33) using the semi-analytical Laplace transform solution (Eq. 2.27) for a range of β values and intraparticle porosities (ε) and for two Sherwood numbers (2 and 20; Fig. 2.6). For strong sorbents (low β), M/M_{eq} obtained in SALT (red surface) amounts to more than 80% while FOAM (green surface) stays around 63%. For weak sorbents (high β), the trend is the opposite where M/M_{eq} obtained in FOAM (green surface) amounts to more than 70% while SALT (red surface) stays around 68%. The deviations of FOAM from SALT are partly due to the overestimation of the internal film thickness ($\delta_p = \sqrt{\pi D_a t} > a/5$). For β values around 1 both methods agree very well with Sherwood numbers (Sh) of 2. The intersection lines shift to higher β values with the increase of Sherwood numbers (better agreement, see Fig. 2.6 right). Figure 2.6 also illustrates the difficulty in defining an unique characteristic time which is valid for a given M/M_{eq}. Nevertheless, in typical batch test conditions ($0.1 < \beta < 1$), the assumption of FOAM ($\delta_p = \sqrt{\pi D_a t}$) seems appropriate and the characteristic times of FOAM correspond to M/M_{eq} in the range of 55% – 70%.

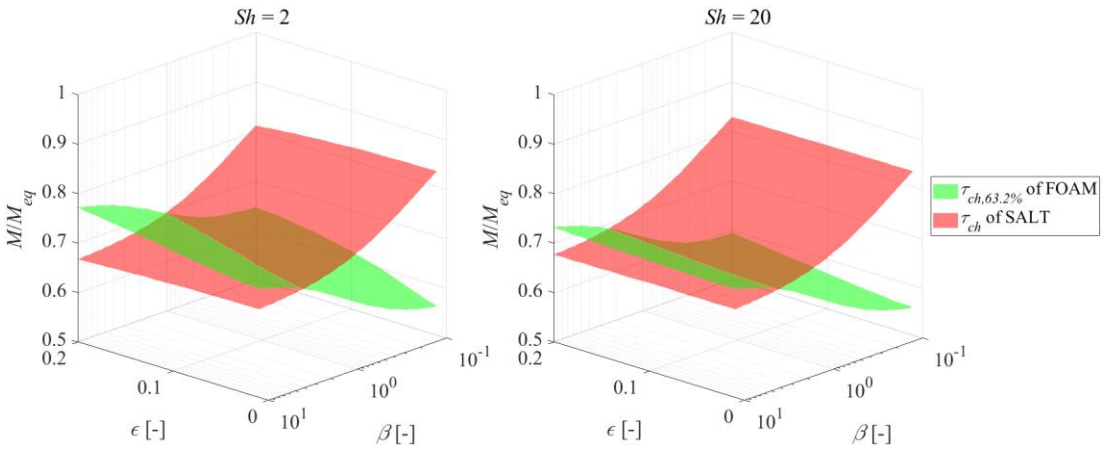

Fig. 2.6: Mass sorbed or desorbed relative to equilibrium conditions (M/M_{eq}) of the coupled film and intraparticle pore diffusion (FIPPD) using characteristic times from the first order approximation solution (FOAM; Eq. 2.19) and the semi-analytical Laplace transform solution (SALT; Eq. 2.33) vs. β and intraparticle porosity (ε) calculated by SALT for Sherwood numbers (Sh) of 2 (left) and 20 (right).

2.5 Conclusions

A fairly simple first order approximation model (FOAM) allows to simulate coupled

intraparticle pore diffusion and mass transfer through an external aqueous boundary (Figs. 2.3 and 2.4) for sorption/desorption batch experiments. In contrast to existing short and long term approximations, FOAM fits the semi-analytical Laplace transform solution (SALT) over the complete time range of a sorption/desorption experiment very well (Fig. 2.4). FOAM may be easily implemented in spreadsheets and deviations to SALT are mostly less than 10% (see Fig. 2.4 bottom). FOAM is applicable to any sorbent and sorbate for typical experimental conditions (ratio of dissolved to sorbed mass, β: $0.1 < \beta < 1$), and it is more friendly and convenient than SALT especially for evaluation of batch experiments if programming experience is limited. In contrast, the semi-analytical Laplace transform solution seems a better choice for modelers with coding experience. FOAM is a simple analytical solution and thus allows for an easy analysis of mass transfer characteristics. For large distribution coefficients ($K_{d,b}$) and intraparticle particle porosities (ε) or small Sherwood numbers (Sh) mass transfer is dominated by the external film diffusion at early time periods (e.g., for strongly sorbing compounds), but on the long term this shifts to intraparticle pore diffusion especially if Sh becomes large like in laboratory experiments (this may be quite different to natural conditions). Due to this mass transfer shift the coupled models become almost independent on sorption and liquid to solids ratios or equilibrium fractional uptake in a batch system (Fig. 2.4). While the characteristic time (τ_{ch}) derived in FOAM applies to M/M_{eq} of 0.63, τ_{ch} in SALT results in M/M_{eq} of 0.6 – 0.8. Despite the good agreement of the first order approximation (FOAM) with the semi-analytical Laplace solution with numerical back transformation (SALT), the latter is the optimal choice for a precise simulation of sorption/desorption kinetics especially if very large or very small β values have to be considered.

References

Allen-King, R.M., Grathwohl, P., Ball, W.P., 2002. New modeling paradigms for the sorption of hydrophobic organic chemicals to heterogeneous carbonaceous matter in soils, sediments, and rocks. Adv. Water Resour. 25, 985–1016. https://doi.org/10.1016/S0309-1708(02)00045-3.

Ball, W.P., Roberts, P. V., 1991. Long-Term Sorption of Halogenated Organic Chemicals by Aquifer Material. 1. Equilibrium. Environ. Sci. Technol. 25, 1223–1237. https://doi.org/10.1021/es00019a002.

Ball, W.P., Roberts, P. V., 1991. Long-Term Sorption of Halogenated Organic Chemicals by Aquifer Material. 2. Intraparticle Diffusion. Environ. Sci. Technol. 25, 1237–1249. https://doi.org/10.1021/es00019a003.

Barrer, R.M., 1978. Zeolites and clay minerals as molecular sieves. Academic Press, London, p. 497.

Boving, T.B., Grathwohl, P., 2001. Tracer diffusion coefficients in sedimentary rocks: Correlation to porosity and hydraulic conductivity. J. Contam. Hydrol. 53, 85–100. https://doi.org/10.1016/S0169-7722(01)00138-3.

Caceres-Jensen, L., Rodriguez-Becerra, J., Escudey, M., Joo-Nagata, J., Villagra, C.A., Dominguez-Vera, V., Neira-Albornoz, A., Cornejo-Huentemilla, M., 2020. Nicosulfuron sorption kinetics and sorption/desorption on volcanic ash-derived soils: proposal of sorption and transport mechanisms. J. Hazard. Mater. 385 (October), 121576 https://doi.org/10.1016/j.jhazmat.2019.121576.

Chickadel, C.C., Talke, S.A., Horner-Devine, A.R., Jessup, A.T., 2011. Infrared-based measurements of velocity, turbulent kinetic energy, and dissipation at the water surface in a tidal river. IEEE Geosci. Remote Sens. Lett. 8, 849–853. https://doi.org/10.1109/LGRS.2011.2125942.

Cooney, D.O., Adesanya, B.A., Hines, A.L., 1983. Effect of particle size distribution on adsorption kinetics in stirred batch systems. Chem. Eng. Sci. 38 (9), 1535–1541. https://doi.org/10.1016/0009-2509(83)80089-X.

Crank, J., 1975. The Mathematics of Diffusion, Second ed. Oxford University Press, London, pp. 69–88.

de Hoog, F.R., Knight, J.H., Stokes, A.N., 1982. An improved method for numerical inversion of Laplace transforms. SIAM J. Sci. Stat. Comput. 3 (3), 357–366. https://doi.org/10.1137/0903022.

Finkel, M., Grathwohl, P., 2017. Impact of pre-equilibration and diffusion limited release

kinetics on effluent concentration in column leaching tests: Insights from numerical simulations. Waste Manag. 63, 58–73. https://doi.org/10.1016/j.wasman.2016.11.031.

Fisher, N.R., Simpson, J.H., Howarth, M.J., 2002. Turbulent dissipation in the Rhine ROFI forced by tidal flow and wind stress. J. Sea Res. 48 (4), 249–258. https://doi.org/10.1016/S1385-1101(02)00194-6.

Glueckauf, E., 1955. Theory of chromatography. Part 10. Formulae for diffusion into spheres and their application to chromatography. Trans. Faraday Soc. 51, 1540–1551. https://doi.org/10.1039/TF9555101540.

Goltz, M.N., Roberts, P.V., 1986. Interpreting organic solute transport data from a field experiment using physical nonequilibrium models. J. Contam. Hydrol. 1 (1–2), 77–93. https://doi.org/10.1016/0169-7722(86)90008-2

Grathwohl, P., Reinhard, M., 1993. Desorption of trichloroethylene in aquifer material: rate limitation at the grain scale. Environ. Sci. Technol. 27 (12), 2360–2366. https://doi.org/10.1021/es00048a008.

Grathwohl, P., 2014. On equilibration of pore water in column leaching tests. Waste Manag. 34 (5), 908–918. https://doi.org/10.1016/j.wasman.2014.02.012.

Guo, X., Liu, Y., Wang, J., 2019. Sorption of sulfamethazine onto different types of microplastics: a combined experimental and molecular dynamics simulation study. Mar. Pollut. Bull. 145 (May), 547–554. https://doi.org/10.1016/j.marpolbul.2019.06.063.

Hills, J.H., 1986. An investigation of the linear driving force approximation to diffusion in spherical particles. Chem. Eng. Sci. 41 (11), 2779–2785. https://doi.org/10.1016/ 0009-2509(86)80009-4.

Ho, Y.S., McKay, G., 1999. The sorption of lead(II) ions on peat. Water Res. 33 (2), 578–584. https://doi.org/10.1016/S0043-1354(98)00207-3.

Hutzler, N.J., Crittenden, J.C., Gierke, J.S., Johnson, A.S., 1986. Transport of organic compounds with saturated groundwater flow: experimental results. Water Resour. Res. 22 (3), 285–295. https://doi.org/10.1029/WR022i003p00285.

Kleineidam, S., Rügner, H., Grathwohl, P., 1999. Impact of grain scale heterogeneity on slow sorption kinetics. Environ. Toxicol. Chem. 18 (8), 1673–1678. https://doi.org/10.1002/etc.5620180810.

Karapanagioti, H., Sabatini, D., Kleineidam, S., Grathwohl, P., 2000. Impacts of heterogeneous organic matter on phenanthrene sorption: equilibrium and kinetic studies with aquifer material. Environ. Sci. Technol. 34 (3), 406–414. https://doi. org/10.1021/es9902219.

Kirwan, J., Armenante, P.M., 1989. Mass transfer to microparticle systems. Chem. Eng. Sci. 44 (12), 2781–2796. https://doi.org/10.1016/0009-2509(89)85088-2.

Kolmogorov, A.N., 1941. The local structure of turbulence in incompressible viscous fluid for very large Reynolds numbers (English translation by V. Levin, 1991). Process R. Soc. A- Math. Phys. Eng. Sci. 434, 9–13. https://doi.org/10.1098/ rspa.1991.0075.

Liu, B., Finkel, M., Grathwohl, P., 2021. Mass transfer principles in column percolation tests: Initial conditions and tailing in heterogeneous materials. Materials 14 (16), 4708. https://doi.org/10.3390/ma14164708.

Liu, C.H., Chuang, Y.H., Li, H., Boyd, S.A., Teppen, B.J., Gonzalez, J.M., Johnston, C.T., Lehmann, J., Zhang, W., 2019. Long-term sorption of lincomycin to biochars: The intertwined roles of pore diffusion and dissolved organic carbon. Water Res. 161, 108 – 118. https://doi.org/10.1016/j.watres.2019.06.006.

Liu, Y., Illangasekare, T.H., Kitanidis, P.K., 2014. Long-term mass transfer and mixing-controlled reactions of a DNAPL plume from persistent residuals. J. Contam. Hydrol. 157, 11–24. https://doi.org/10.1016/j.jconhyd.2013.10.008.

MacDonald, D.G., Goodman, L., Hetland, R.D., 2007. Turbulent dissipation in a near-field river plume: A comparison of control volume and microstructure observations with a numerical model. J. Geophys. Res.: Oceans 112, 1–13. https://doi.org/10.1029/ 2006JC004075.

Moum, J., Gregg, M., Lien, R., Carr, M., 1995. Comparison of turbulence kinetic energy dissipation rate estimates from two ocean microstructure profilers. Atmos. Ocean. Technol. 12, 346–366. https://doi.org/10.1175/1520-0426(1995)012<0346: COTKED>2.0.CO;2.

Módenes, A. N., Bazarin, G., Borba, C. E., Locatelli, P. P. P., Borsato, F. P., Pagno, V., Pedrini, R., Trigueros, D. E. G., Espinoza-Quiñones, F. R., Scheufele, F. B., 2021. Tetracycline adsorption by tilapia fish bone-based biochar: Mass transfer assessment and fixed-bed data prediction by hybrid statistical-phenomenological modeling. J. Clean. Prod. 279, 123775. https://doi.org/10.1016/j.jclepro.2020.123775.

Pauletto, P. S., Moreno-Pérez, J., Hernández -Hernández, L. E., Bonilla -Petriciolet, A., Dotto, G.L., Salau, N.P.G., 2021. Novel biochar and hydrochar for the adsorption of 2-nitrophenol from aqueous solutions: an approach using the PVSDM model. Chemosphere 269, 128748. https://doi.org/10.1016/j.chemosphere.2020.128748.

Ranz, W., Marshall, W., 1952. Evaporation from drops. Chem. Eng. Prog. 48, 141–146.

Roberts, P.V., Goltz, M.N., Mackay, D.M., 1986. A natural gradient experiment on solute transport in a sand aquifer: 3. Retardation estimates and mass balances for organic solutes. Water Resour. Res. 22, 2047–2058. https://doi.org/10.1029/WR022i013p02047.

Rügner, H., Kleineidam, S., Grathwohl, P., 1999. Long-term sorption kinetics of

phenanthrene in aquifer materials. Environ. Sci. Technol. 33 (10), 1645–1651. https://doi.org/10.1021/es980664x.

Sabbah, I., Ball, W.P., Young, D.F., Bouwer, E.J., 2005. Misinterpretations in the modeling of contaminant desorption from environmental solids when equilibrium conditions are not fully understood. Environ. Eng. Sci. 22, 350–366. https://doi.org/ 10.1089/ees.2005.22.350.

Sardin, M., Schweich, D., Leij, F.J., van Genuchten, M.T., 1991. Modeling the nonequilibrium transport of linearly interacting solutes in porous media: a review. Water Resour. Res. 27, 2287–2307. https://doi.org/10.1029/91WR01034.

Seidensticker, S., Zarfl, C., Cirpka, O., Fellenberg, G., Grathwohl, P., 2017. Shift in mass transfer of wastewater contaminants from microplastics in the presence of Dissolved Substances. Environ. Sci. Technol. 51, 12254–12263. https://doi.org/10.1021/acs. est.7b02664.

Seidensticker, S., Zarfl, C., Cirpka, O.A., Grathwohl, P., 2019. Microplastic–contaminant interactions: influence of nonlinearity and coupled mass transfer. Environ. Toxicol. Chem. 38, 1635–1644. https://doi.org/10.1002/etc.4447.

Stähelin, P. M., Valério, A., Guelli Ulson de Souza, S. M. de A., da Silva, A., Borges Valle, J. A., Ulson de Souza, A. A., 2018. Benzene and toluene removal from synthetic automotive gasoline by mono and bicomponent adsorption process. Fuel 231, 45–52. https://doi.org/10.1016/j.fuel.2018.04.169.

Stickler, B.A., Schachinger, E., 2016. The random walk and diffusion theory. Basic Concepts in Computational Physics. Springer, Cham. https://doi.org/10.1007/978- 3-319-27265-8_17.

Wang, J., Guo, X., 2020. Adsorption kinetic models: physical meanings, applications, and solving methods. J. Hazard. Mater. 390 (November), 122156 https://doi.org/ 10.1016/j.jhazmat.2020.122156.

3 Mechanistic modeling of pollutant mass redistribution (sorption/desorption) in heterogeneous systems explaining unexpected slow kinetics

Binlong Liu, Michael Finkel, Qiyue Qin, Wenxiao Shi, Peter Grathwohl

Abstract

Redistribution of pollutants between aqueous and solid phases occurs frequently in field and laboratory settings, but it is rarely considered in data interpretation especially if sorption/desorption kinetics are concerned. Examples are input of polluted particles into soils or rivers or passive sampling in laboratory solid suspensions. Since multiple mass transfer mechanisms are involved and soils and sediments typically are very heterogeneous, modelling of kinetics gets very challenging. Here, we present a semi-analytical model formulated in the Laplace domain to simulate pollutant redistribution kinetics in heterogeneous systems. The model describes the sorption and desorption as a coupled process governed by intraparticle and external boundary layer diffusion. It considers the heterogeneity of various sorbents (e.g., geometric shape, grain size, distribution coefficient, organic carbon content of solid, and intraparticle porosity) as well as mass transfer resistance shifts from an external aqueous boundary layer into the intraparticle space for both solid and porous materials. Pollutant concentration changes in different solid fractions and water are efficiently simulated by numerical inversion of their analytical solutions in the Laplace domain. The model is validated against data of two batch experiments: (i) the redistribution of Phenanthrene in spherical microplastics of different sizes and (ii) redistribution of Anthracene-d10 and Phenanthrene in heterogenous sediment suspension with polyethylene passive samplers. The model allows to explain temporary overshooting of concentrations in the aqueous phase due to different kinetic controls of various particles involved (fast desorption vs. slow sorption) as well as initial fast kinetics followed by surprising long tailing in batch experiments. In heterogeneous particle mixtures, even a small fraction (< 1%) of a strongly sorbing particles may lead to pseudo-equilibration at early times, which rapidly lowers concentration gradients and thus slows down sorption in the remaining part of the mixture tremendously. The mechanistic model allows to elucidate redistribution scenarios and fitted parameters agree with classical mass transfer theories (e.g., Kolmogorov's turbulent theory or Sherwood number relationships).

3.1 Introduction

Pollutant mass redistribution in heterogeneous systems is ubiquitous in the environment such as mixing of polluted urban particles with natural (virtually clean) particles in rivers e.g., during stormwater runoff (Rügner et al., 2013; Schwientek et al., 2013), or deposition of polluted atmospheric particles (e.g., black carbon) in soils. If desorption (e.g., from small particles with high loading) in rivers is faster than uptake of pollutants in natural particles, concentrations in water temporarily peak, which may impact aquatic life (so-called contaminant shock loads) (Meyer et al., 2007 and 2010). Furthermore, laboratory batch tests on pollutant sorption/desorption kinetics or biodegradation with natural soil or sediment samples typically involves mixtures of heterogeneous sorbents, which makes it very difficult to interpret concentration changes in water and solids in terms of simple kinetic models (Kleineidam et al., 1999; Rügner et al., 1999; Karapanagioti et al., 2000; Golikov et al., 2020).

Traditional methods for describing sorption/desorption to/from heterogeneous sorbents are either multiple mass transfer rates e.g., using probability density functions, e.g., lognormal or γ distributions (Culver et al., 1997; Saiers et al., 2000; Shang et al., 2011) or numerical solutions (Golikov et al., 2020; Liu et al., 2021). However, either method leads to fitting parameters sometimes without real physical meaning or is computationally expensive and may involve numerical errors. This gets exaggerated if different mass transfer mechanisms occur in parallel or mass transfer resistances shift from an external boundary layer (film diffusion) into intraparticle space (intraparticle diffusion) as described by Seidensticker et al. (2017) and Liu et al. (2022). Furthermore, classical mass transfer models focus either on sorptive uptake or desorption kinetics, but not on the redistribution where both directions are needed (which for instance applies in passive sampling in sediments suspensions). The objectives of this paper thus are to (i) elucidate redistribution kinetics in heterogeneous systems accounting for external film diffusion, intraparticle diffusion and coupled film-intraparticle diffusion for different geometric shapes (plane, cylinder and sphere) of solid and porous materials, (ii) validate a semi-analytical model formulated in the Laplace domain supported by experimental batch test data (Phenanthrene/Anthracene d10 redistribution in mixtures of spherical microplastics of different sizes and a sediment suspension with polyethylene passive samplers), and (iii) understand how sorbent heterogeneity results in temporarily “overshooting” of aqueous concentrations and unexpected slow sorption/desorption kinetics, and (iv) compare the Sherwood numbers obtained fitting from our experimental data to the values calculated from two different Kolmogorov’s theory length scales. The overarching objective is to demonstrate how mechanistic understanding of mass transfer processes in complicated settings can lead to better insight on pollutant behavior in the environment, e.g., redistribution of pollutants in rivers.

3.2 Materials and methods

Two sets of batch experiments were conducted to study the redistribution of pollutant mass in different materials: a mix of different sized microplastics (see Fig. 3.1) and sediment particles of different sizes in a mix with polyethylene sheets (passive samplers) (see Fig. 3.2). In both cases, pollutants (here PAHs) are transferred from polluted particles to initially clean particles or materials.

3.2.1 Phenanthrene redistribution among spherical microplastics of different sizes (tests A-C)

Batch test setup and sampling: Polyethylene particles (density ρ_{PE} = 0.92 kg L^{-1}) of three sizes were used: PE1 ($d_{PE1} = 145$ µm) and PE2 ($d_{PE2} = 260$ µm) are approximately spherical shaped while PE3 has a cylindrical shape with 4.4 mm diameter and 2.5 mm height (resulting in a sphere equivalent diameter of 4.2 mm based on the equal-volume method = surface to volume ratio). To avoid biodegradation and photo-oxidation of Phenanthrene, 0.05 g L^{-1} NaN_3 were used and bottles were kept in the dark at a temperature of 20 °C. Details on the setup of batch tests A-C are shown in Fig. 3.1. Measured Phenanthrene concentration changes in aqueous phase are presented in Tab. S3.1.

Test A (sorptive uptake in PE1): 0.2 g clean PE1 were added into 200 mL Phenanthrene aqueous solution at a Phenanthrene concentration of 110 µg L^{-1}. Bottles were permanently mixed on a horizontal shaker with a rotational speed of 150 rpm. 1 mL of the supernatant solution was sampled initially and after 5 min, 10 min, 15 min, 20 min, 30 min, 40 min, 60 min, 180 min and 1020 min.

Test B (pre-loaded coarse microplastics PE3 mixed with clean fine microplastics PE2): 0.5 g clean PE2 were added to 450 mL water containing 0.5 g contaminated PE3 leading to an initial equilibrium aqueous Phenanthrene concentration ($C_w(0)$) of 2.94 µg L^{-1}. Bottles were covered with aluminum foil and put on a magnetic stirring system with a rotational speed of 1000 rpm. 1 mL solution was sampled initially and after 10 min, 20 min, 30 min, 40 min, 50 min, 1 h, 2 h, 4 h, 8 h, 12 h, 22 h, 34 h, 45 h, 70 h, 95 h, 150 h, 180 h, 220 h, 300 h and 390 h.

Test C (pre-loaded fine microplastics PE2 mixed with clean coarse microplastics PE3): 400 mL clean water containing 0.5 g clean PE3 were added to 100 mL water containing contaminated 0.5 g PE2 with an initial equilibrium aqueous Phenanthrene concentration of 1.55 µg L^{-1}, which after initial mixing decreases to 0.31 µg L^{-1} ($C_w(0)$) due to dilution. Bottles were shaken as in test A. 1 mL solution was sampled initially and after 10 min, 20 min, 30 min, 40 min, 50 min, 1 h, 2 h, 4 h, 9 h, 23 h, 50 h, 75 h, 150 h, 200 h, 400 h and 600 h.

Chemical analysis: 1 mL water samples were taken using a glass pipet, filtrated by a 20 µm

pore-size glass fiber filter to get rid of potential fine plastic particles (PE1 or PE2) and transferred into a 1 mL glass vial. Particle mass loss was quantified by weighing the microplastics sticking to the glass pipet wall after drying (< 0.005 g, < 1%) at each sampling time. Then, 10 µL of deuterated internal standard solution and 300 µL of cyclohexane (CH) were added into the vials and closed firmly with crimp caps and polytetrafluoroethylene (PTFE) coated silicon septa. After shaking for 40 min, vials were allowed to rest for 5 h and the cyclohexane phase was transferred into 0.3 mL GC-autosampler vials for analysis by GC-MS. For more details on chemicals used and analytical methods see Seidensticker et al. (2017).

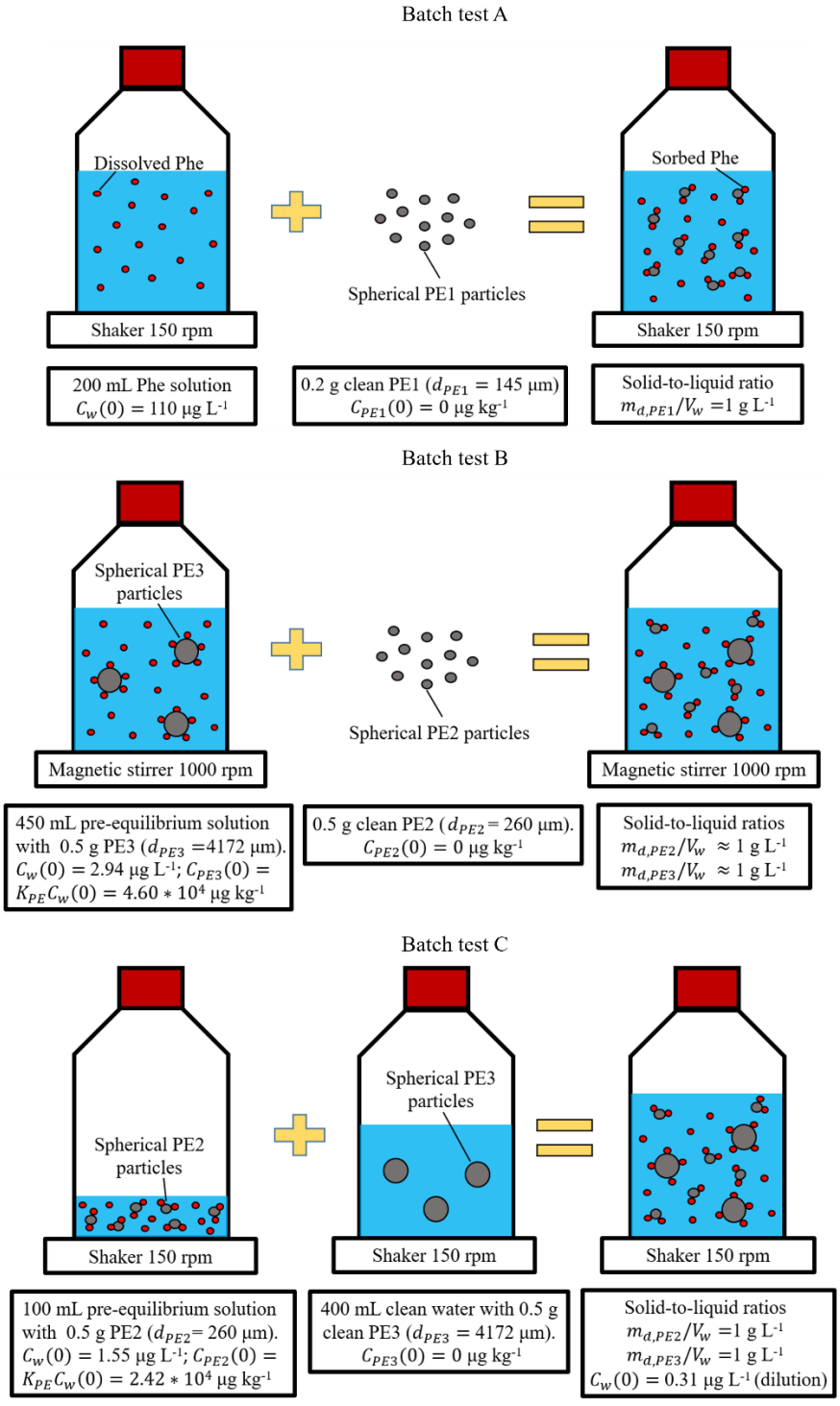

Fig. 3.1: Batch tests of Phenanthrene redistribution between different polyethylene (PE) particles. Batch test A: Sorptive uptake of Phenanthrene in PE1 ($d_{PE1} = 145$ µm); batch test B: Desorption from pre-loaded coarse microplastics (PE3; $d_{PE3} = 4172$ µm) and uptake in initial clean fine microplastics (PE2; $d_{PE2} = 260$ µm); batch test C: Desorption from pre-loaded fine microplastics (PE2) and uptake in clean coarse microplastics (PE3).

3.2.2 Anthracene-d10 and Phenanthrene redistribution in a sediment suspension with polyethylene passive samplers (Test D)

Sediment sample preparation: Urban sediment samples were taken near the inlet of a park pond (so-called 'Anlagensee', a sediment trap) constructed between 1907 and 1908 in the city of Tübingen, Germany. Three samples were taken at 7.5 cm, 15 cm and 30 cm below the surface, well mixed, freeze dried and homogenized in a planet ball mill. Milling reduces particle sizes which is desired to keep experimental times reasonably short, but it does not lead to a uniform particle size (see section S3.2; 50% of the particles were 7 µm and 74 µm in size). Phenanthrene background concentration in sediment was ~ 150 µg kg^{-1} as measured after accelerated solvent extraction (ASE) with acetone/toluene (for details see section S3.2). The grain size distribution of the pulverized sample was measured via laser granulometry (Malvern Mastersizer 2000); 90% of the particle sizes were in the range of 2 - 240 µm (cumulative grain size distribution is shown in Fig. S3.1). For modeling, this grain size distribution was represented by two characteristic equal grain size fractions ($d_{sp,1} = 7$ µm and $d_{sp,2} = 74$ µm, more details are shown in section S3.2). The organic carbon content of the sediment was determined by elemental analysis (TOC = 5%); since most of the particles are in the silt sized fraction, we assumed a homogenous distribution of organic carbon.

Passive samplers preparation: Polyethylene (PE) sheets were used as passive samplers. The sheets were first cut into squares with a mass of ca. 1 g and cleaned with 400 mL cyclohexane (CH) in a 500 mL bottle. After shaking for 24 h on a horizontal shaking bed, PE sheets were transferred to a 500 mL bottle with 400 mL ethyl acetate (EA) and shaken for another 24 h and then purged with Millipore water to remove the remaining organic solvents. PE sheets were then kept in Millipore water on horizontal shaking bed for at least 24 h, before the preloading with Anthracene d10 (Ant-d10) as performance reference compound started. The Ant-d10 stock solution was prepared from a standard solution with a concentration of 1.09 mg mL^{-1} in methanol (500 mL bottle filled with 400 mL Millipore water and 100 mL methanol including 15 µL of Ant-d10 standard solution). Then, 15 pieces cleaned PE sheets (ca. 15 g) were added and all bottles were covered with aluminum foil and kept in the dark. Before batch tests, preloaded bottles were put on the horizontal shaking bed for more than 1 week to ensure equilibration was reached. The initial Ant-d10 concentration in PE sheets ($C_{PE,Ant-d10}(0)$) was 227 µg kg^{-1} (nominal).

Batch test setup and sampling: 24 bottles were prepared for 8 samplings at two solid (sediment)-to-liquid ratios (SL = 0.15 and 0.3 kg L^{-1}); each sampling was performed in triplicate (data are presented in Tab. S3.2). In addition, 6 bottles were prepared for three blanks and the control group. The detailed setup of batch test D is presented in Fig. 3.2. Ant-d10 preloaded PE sheets (1 g in total) were taken out of the stock solution, dried with

lintless tissue, cut into strips (7 cm*4 cm*30 µm) and added to 250 mL sediment containing bottles. Then, bottles were filled with 100 mL Millipore water and put on a horizontal shaker to maintain a well-mixed suspension. At designed sampling times, PE strips were separated from sediment suspension, quickly soaked with Millipore water 4 times until no sediment particles were left on their surface. After cleaning, strips were put in 250 mL brown bottles to avoid photo-oxidation and extracted with 50 mL EA twice; each extraction lasted for 24 h. After extraction, EA extracts of 100 mL in total were collected in round flasks and 10 µL internal standard solution were added for analysis of PAHs. 100 mL solvent were reduced to 10 mL on rotating evaporator and transferred to 1 L brown bottles, then mixed with 800 mL Millipore water and shaken for 30 min; after adding 10 mL CH and shaking for another 30 min PAHs were transferred from the EA/water mixture into CH. Then, all bottles containing extracts and water stood overnight for phase separation of CH from the EA/water mixture. All CH was transferred with a pipette to 10 mL vials and further evaporated to ca. 150 µL under nitrogen and 40 °C on evaporator (Barkey). 150 µL CH were then transferred to autosampler vials and the concentrations of Ant-d10 and Phenanthrene were measured via GC-MS.

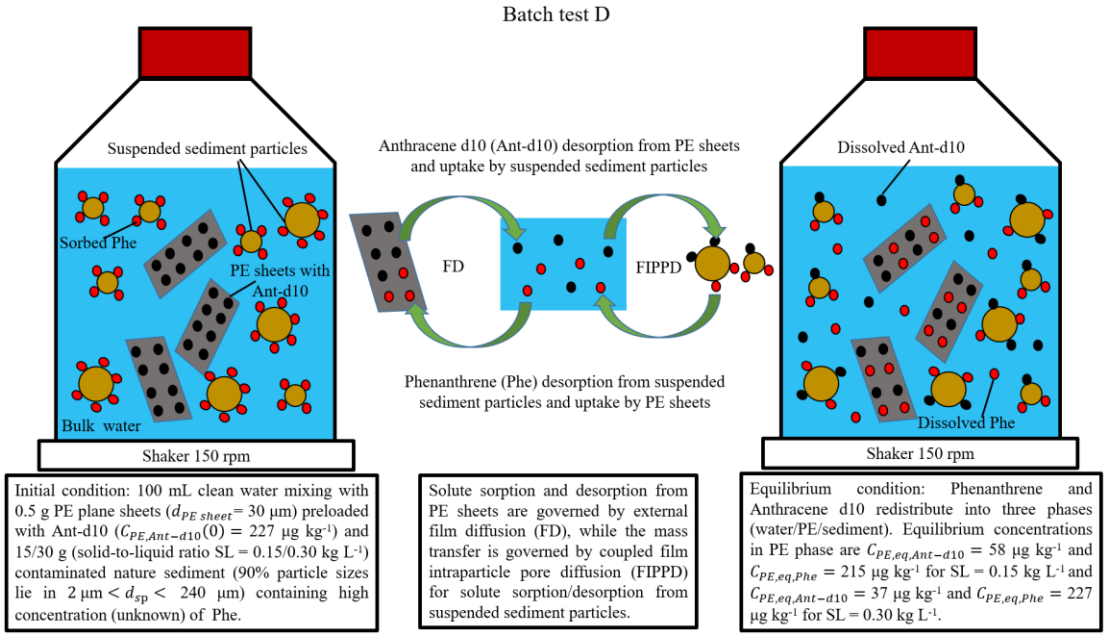

Fig. 3.2: Batch test setup of redistribution of Anthracene-d10 (Ant-d10) and Phenanthrene (Phe) in the sediment suspension with passive samplers (polyethylene (PE) sheets).

3.3 Modeling mass redistribution kinetics in heterogeneous systems

3.3.1 Semi-analytical Laplace solutions for coupled intraparticle and external boundary layer diffusion

Pollutants mass redistribution in heterogeneous materials containing both solid (no intraparticle pores as e.g., in microplastics, minerals.) and porous materials (e.g., soil aggregates, rock fragments, activated carbon, biochars) in a batch system (fixed volume of water: finite bath) can be described assuming mass conservation:

$$\frac{\partial C_w}{\partial t} + \sum_{j=1}^{n_j} \frac{m_{d,j}}{V_w} \frac{\partial C_{s,j}}{\partial t} + \sum_{k=1}^{n_k} \frac{m_{d,k}}{V_w} \left(K_{d,k} + \frac{\varepsilon_k}{\rho_{p,k}} \right) \frac{\partial C_{w,p,k}}{\partial t} = 0 \qquad (3.1)$$

where n_j [-] and n_k [-] denote the total number of different components of solid and porous materials, respectively; variables with subscripts j and k refer to individual components; C_w [M L^{-3}] denotes the pollutant concentration in the bulk water; $C_{s,j}$ [M M^{-1}] denotes the pollutant concentration in solid material components; $C_{w,p,k}$ [M L^{-3}] is the pollutant concentration in the intraparticle porous material's pore water; ε_k [-] and $\rho_{p,k}$ [M L^{-3}] denote the intraparticle porosity and the particle density of the porous material ($= \rho_{s,k}(1 - \varepsilon_k)$ with $\rho_{s,k}$ [M L^{-3}] as dry density of the solid); V_w [L^3] denotes the volume of bulk water; $m_{d,j}$ [M] and $m_{d,k}$ [M] denote the dry mass of the solid and porous material, respectively; $K_{d,k}$ [L^3 M^{-1}] is the distribution coefficient between intraparticle pore water and solid. The term $K_{d,k} + \varepsilon_k/\rho_{p,k}$ may be interpreted as bulk distribution coefficient between bulk water and porous particles, $K_{d,b,k}$, which also considers the pollutant mass stored in the intraparticle pore space. t [T] is the time. The Laplace transformation of the mass balance equation (Eq. 3.1) is given as:

$$s\tilde{C}_w - C_w(0) + \sum_{j=1}^{n_j} \frac{m_{d,j}}{V_w} \left(s\tilde{C}_{s,j} - C_{s,j}(0) \right) + \sum_{k=1}^{n_k} \frac{m_{d,k}}{V_w} K_{d,b,k} \left(s\tilde{C}_{w,p,k} - C_{w,p,k}(0) \right) = 0 \qquad (3.2)$$

where s [T^{-1}] is the complex Laplace coordinate. The tilde sign denotes the Laplace transform of the respective variables. $C_w(0)$, $C_{s,j}(0)$ and $C_{w,p,k}(0)$ denote the initial pollutant concentration in bulk water, solid materials and intraparticle pore water of porous materials, respectively.

The average concentrations in solid materials ($C_{s,j}$) and in intraparticle pore water of porous materials ($C_{w,p,k}$) depend on the solute concentration in bulk water phase (C_w) in form of a convolution with respective transfer functions in real time domain. In Laplace domain, $\tilde{C}_{s,j}$ and $\tilde{C}_{w,p,k}$ are given as:

$$\tilde{C}_{s,j} = \tilde{g}_{s,j}\left(\tilde{C}_w - \frac{C_{s,j}(0)}{K_{d,j}s}\right) + \frac{C_{s,j}(0)}{s}$$
$$\tilde{C}_{w,p,k} = \tilde{g}_{sp,k}\left(\tilde{C}_w - \frac{C_{w,p,k}(0)}{s}\right) + \frac{C_{w,p,k}(0)}{s} \quad (3.3)$$

where $\tilde{g}_{s,j}$ [L^3 M^{-1}] and $\tilde{g}_{sp,k}$ [-] are the transfer functions representing how the average concentration in the solid materials and intraparticle pore water of porous materials would evolve over time when respective sorption/desorption kinetics models are applied. $K_{d,j}$ [L^3 M^{-1}] denotes the distribution coefficient between water and solid materials.

Different sorption/desorption kinetic models can be easily represented in the Laplace solution by using different transfer functions. Mass transfer between sorbents (solid or porous materials) and water may be limited by diffusion from the sorbent surface to bulk water through an aqueous boundary layer (external film diffusion) or diffusion inside the solid materials (or within the intraparticle pore water for porous materials). Depending on distribution coefficients a mass transfer shift from the external boundary layer into intraparticle space may occur and thus a coupled film-intraparticle diffusion has to be used (Seidensticker et al., 2017; Liu et al., 2022). Geometries of sorbents may also influence the sorption/desorption kinetics. Diffusion in three different shapes of particles (plane sheets, cylinders and spheres) is considered here, which covers most of the cases encountered in the environment. Irregular particle shapes may also be considered by means of "equivalent spheres" having the same volume as the irregular particle ($V_{irregular} = V_{sphere} = 4/3\pi a^3_{sphere,equiv.}$with $a_{sphere,equiv.}$ being the equivalent radius of a sphere). Table 3.1 summarizes the transfer functions in Laplace domain for external film diffusion, intraparticle diffusion and coupled film-intraparticle diffusion models for diffusion in solid and porous materials for all three types of particle shapes. Detailed information on the derivation of the transfer functions for plane sheets, cylinders and spheres can be found in sections S3.3-S3.8 (sections S3.3-S3.5 for solid materials and sections S3.6-S3.8 for porous materials).

Inserting Eq 3.3 into Eq 3.2, the pollutant concentration in the bulk water phase in Laplace domain is given as:

$$\tilde{C}_w = \frac{C_w(0) + \sum_{j=1}^{n_j}\frac{m_{d,j}}{V_w}\tilde{g}_{s,j}\frac{C_{s,j}(0)}{K_{d,j}} + \sum_{k=1}^{n_k}\frac{m_{d,k}}{V_w}K_{d,b,k}\tilde{g}_{sp,k}C_{w,p,k}(0)}{\left(1 + \sum_{j=1}^{n_j}\frac{m_{d,j}}{V_w}\tilde{g}_{s,j} + \sum_{k=1}^{n_k}\frac{m_{d,k}}{V_w}K_{d,b,k}\,\tilde{g}_{sp,k}\right)s} \quad (3.4)$$

The pollutant concentrations in solid materials ($\tilde{C}_{s,j}$) and in intraparticle pore water of porous materials ($\tilde{C}_{w,p,k}$) in Laplace domain can be obtained by inserting Eq. 3.4 into Eq. 3.3. For back-transformation, we used the numerical inversion method of de Hoog et al. (1982) implemented in Matlab. The setups of the models for simulating batch tests A to D are explained in more detail in section S3.9. For data calibration, the coefficient of efficiency (E) was used to evaluate the goodness of fitting (Legates et al., 1999).

Tab. 3.1: Transfer functions for external film diffusion, intraparticle diffusion and coupled film-intraparticle diffusion models for diffusion in the plane sheet, cylinder and sphere of solid and porous materials (for derivation of these functions see section S3).

Transfer functions for solid materials: $\tilde{g}_{s,j}$

	Plane sheet	Cylinder	Sphere
Film diffusion (FD)	$\frac{k_{s,j}K_{d,j}}{k_{s,j}+\rho_{s,j}K_{d,j}a_{s,j}s}$	$\frac{k_{s,j}K_{d,j}}{k_{s,j}+\frac{1}{2}\rho_{s,j}K_{d,j}a_{s,j}s}$	$\frac{k_{s,j}K_{d,j}}{k_{s,j}+\frac{1}{3}\rho_{s,j}K_{d,j}a_{s,j}s}$
Intraparticle solid diffusion (IPSD)	$\sqrt{D_{s,j}s}K_{d,j}\tanh\left(a_{s,j}\sqrt{\frac{s}{D_{s,j}}}\right)\frac{1}{a_{s,j}s}$	$\sqrt{D_{s,j}s}K_{d,j}\frac{I_1\left(a_{s,j}\sqrt{\frac{s}{D_{s,j}}}\right)}{I_0\left(a_{s,j}\sqrt{\frac{s}{D_{s,j}}}\right)}\frac{2}{a_{s,j}s}$	$D_{s,j}K_{d,j}\left(\sqrt{\frac{s}{D_{s,j}}}\coth\left(a_{s,j}\sqrt{\frac{s}{D_{s,j}}}\right)-\frac{1}{a_{s,j}}\right)\frac{3}{a_{s,j}s}$
Coupled film-intraparticle solid diffusion (FIPSD)	$\frac{\sqrt{D_{s,j}s}K_{d,j}\tanh\left(a_{s,j}\sqrt{\frac{s}{D_{s,j}}}\right)}{k_{s,j}+\sqrt{D_{s,j}s}\rho_{s,j}K_{d,j}\tanh\left(a_{s,j}\sqrt{\frac{s}{D_{s,j}}}\right)}\frac{k_{s,j}}{a_{s,j}s}$	$\frac{\sqrt{D_{s,j}s}K_{d,j}\frac{I_1\left(a_{s,j}\sqrt{\frac{s}{D_{s,j}}}\right)}{I_0\left(a_{s,j}\sqrt{\frac{s}{D_{s,j}}}\right)}}{k_{s,j}+\sqrt{D_{s,j}s}\rho_{s,j}K_{d,j}\frac{I_1\left(a_{s,j}\sqrt{\frac{s}{D_{s,j}}}\right)}{I_0\left(a_{s,j}\sqrt{\frac{s}{D_{s,j}}}\right)}}\frac{2k_{s,j}}{a_{s,j}s}$	$\frac{D_{s,j}K_{d,j}\left(\sqrt{\frac{s}{D_{s,j}}}\coth\left(a_{s,j}\sqrt{\frac{s}{D_{s,j}}}\right)-\frac{1}{a_{s,j}}\right)}{k_{s,j}+D_{s,j}\rho_{s,j}K_{d,j}\left(\sqrt{\frac{s}{D_{s,j}}}\coth\left(a_{s,j}\sqrt{\frac{s}{D_{s,j}}}\right)-\frac{1}{a_{s,j}}\right)}\frac{3k_{s,j}}{a_{s,j}s}$

Transfer functions for porous materials: $\tilde{g}_{sp,k}$

	Plane sheet	Cylinder	Sphere

Film diffusion (FD)	$\frac{k_{sp,k}}{k_{sp,k}+\rho_{p,k}K_{d,b,k}a_{sp,k}s}$	$\frac{k_{sp,k}}{k_{sp,k}+\frac{1}{2}\rho_{p,k}K_{d,b,k}a_{sp,k}s}$	$\frac{k_{sp,k}}{k_{sp,k}+\frac{1}{3}\rho_{p,k}K_{d,b,k}a_{sp,k}s}$
Intraparticle pore diffusion (IPPD)	$\sqrt{D_{a,k}s}\tanh\left(a_{sp,k}\sqrt{\frac{s}{D_{a,k}}}\right)\frac{1}{a_{sp,k}s}$	$\sqrt{D_{a,k}s}\frac{I_1\left(a_{sp,k}\sqrt{\frac{s}{D_{a,k}}}\right)}{I_0\left(a_{sp,k}\sqrt{\frac{s}{D_{a,k}}}\right)}\frac{2}{a_{sp,k}s}$	$D_{a,k}\left(\sqrt{\frac{s}{D_{a,k}}}\coth\left(a_{sp,k}\sqrt{\frac{s}{D_{a,k}}}\right)-\frac{1}{a_{sp,k}}\right)\frac{3}{a_{sp,k}s}$
Coupled film-intraparticle pore diffusion (FIPPD)	$\frac{\sqrt{D_{a,k}s}\tanh\left(a_{sp,k}\sqrt{\frac{s}{D_{a,k}}}\right)}{k_{sp,k}+\sqrt{D_{a,k}s}\rho_{p,k}K_{d,b,k}\tanh\left(a_{sp,k}\sqrt{\frac{s}{D_{a,k}}}\right)}\frac{k_{sp,k}}{a_{sp,k}s}$	$\frac{\sqrt{D_{a,k}s}\frac{I_1\left(a_{sp,k}\sqrt{\frac{s}{D_{a,k}}}\right)}{I_0\left(a_{sp,k}\sqrt{\frac{s}{D_{a,k}}}\right)}}{k_{sp,k}+\sqrt{D_{a,k}s}\rho_{p,k}K_{d,b,k}\frac{I_1\left(a_{sp,k}\sqrt{\frac{s}{D_{a,k}}}\right)}{I_0\left(a_{sp,k}\sqrt{\frac{s}{D_{a,k}}}\right)}}\frac{2k_{sp,k}}{a_{sp,k}s}$	$\frac{D_{a,k}\left(\sqrt{\frac{s}{D_{a,k}}}\coth\left(a_{sp,k}\sqrt{\frac{s}{D_{a,k}}}\right)-\frac{1}{a_{sp,k}}\right)}{k_{sp,k}+D_{a,k}\rho_{p,k}K_{d,b,k}\left(\sqrt{\frac{s}{D_{a,k}}}\coth\left(a_{sp,k}\sqrt{\frac{s}{D_{a,k}}}\right)-\frac{1}{a_{sp,k}}\right)}\frac{3k_{sp,k}}{a_{sp,k}s}$

Remarks.

$k_{s,j}$ [L T^{-1}] and $k_{sp,k}$ [L T^{-1}] denote the mass transfer velocity for solid materials ($k_{s,j}=D_{aq}/\delta_{s,j}$) and porous materials ($k_{sp,k}=D_{aq}/\delta_{sp,k}$) where D_{aq} [L^2 T^{-1}] is the aqueous diffusion coefficient of the pollutant, $\delta_{s,j}$ [L] and $\delta_{sp,k}$ [L] are the external film thickness of solid particles and porous materials, respectively (both of which can be estimated via dimensionless Sherwood numbers, see section 3.3.2);

$a_{s,j}$ [L] and $a_{sp,k}$ [L] denote the half thickness of plane sheets or grain radius of cylindrical and spherical particles for solid and porous materials, respectively;

$D_{s,j}$ [L^2 T^{-1}] and $D_{a,k}$ [L^2 T^{-1}] denote the solid diffusion coefficient and the apparent diffusion coefficient of pollutant in the intraparticle pore space of porous materials with $D_{a,k}=D_{e,k}/(\rho_{p,k}K_{d,b,k})=D_{aq}\varepsilon_k/(\tau_{f,k}\rho_{p,k}K_{d,b,k})\approx D_{aq}{\varepsilon_k}^2/(\rho_{p,k}K_{d,b,k})$ where $\tau_{f,k}$ [-] is the tortuosity factor; $D_{e,k}$ [L^2 T^{-1}] is the effective diffusion coefficient - empirical studies showed that $D_{e,k}$ increases approximately with the square of the intraparticle porosity (Boving and Grathwohl, 2001), thus, the tortuosity factor $\tau_{f,k}$ [-] can be approximated via the reciprocal of the intraparticle porosity ($\tau_{f,k}\approx 1/\varepsilon_k$);

I_0 and I_1 denote zero order modified Bessel function of first kind and first order modified Bessel function of first kind, respectively; $\rho_{s,j}$ [M L^{-3}] denotes the dry density of the solid materials.

3.3.2 Sherwood number estimation based on Kolmogorov's theory

Mass transfer of strongly sorbing compounds (Seidensticker et al., 2017) in small particles at least initially is limited by the thickness of the external aqueous boundary layer and therefore this so-called "film diffusion" is important. The aqueous boundary layer thickness depends on the relative motion of the particles with respect to bulk water and thus on the surrounding eddies for turbulent conditions as described by Kolmogorov (1941). Following that under fully turbulent flow conditions, all eddies much smaller than the primary eddies (which, e.g., may be represented by the length scale of the paddle in a stirring system or the width of river) are completely independent of the bulk motion of water and thus can be considered as isotropic eddies. In particle suspensions their sizes roughly correspond to grain sizes (of the suspended particles entrapped in the respective eddies). Suspended particles can be classified into two categories via the Kolmogorov's length scale (η) into macroparticles ($\eta < d \ll L_0$) and microparticles ($d < \eta$) where viscous forces dominate the energy dissipation for microparticles:

$$\eta = \left(\frac{\nu^3}{\varepsilon_{disp}}\right)^{1/4} \tag{3.5}$$

ε_{disp} [$L^2\ T^{-3}$] denotes the energy dissipation rate of the system and ν [$L^2\ T^{-1}$] is the kinematic viscosity of the fluid. Based on Kolmogorov's theory, the relative velocities of macroparticles and microparticles to the bulk fluid are proportional to $\left(\varepsilon_{disp} d\right)^{1/3}$ and $\left(\varepsilon_{disp} d^2/\nu\right)^{1/2}$, respectively. Inserting the relative velocities into the definition of the Reynolds number ($Re = v_a d/\nu$ with v_a [$L\ T^{-1}$] as velocity of suspended particles relative to the velocity of water) leads to:

$$\begin{aligned} Re_{macro} &= \frac{\left(\varepsilon_{disp} d\right)^{\frac{1}{3}} d}{\nu} = \frac{{\varepsilon_{disp}}^{\frac{1}{3}} d^{\frac{4}{3}}}{\nu} \\ Re_{micro} &= \frac{\left(\varepsilon_{disp} d^2/\nu\right)^{1/2} d}{\nu} = \frac{{\varepsilon_{disp}}^{\frac{1}{2}} d^2}{\nu^{3/2}} = {Re_{macro}}^{3/2} \end{aligned} \tag{3.6}$$

The Reynolds number of microparticles (Re_{micro}) can be written as the Reynolds number of macroparticles with the power of 3/2. Most of the published empirical relationships of Sherwood numbers (for a summary see Kikuchi et al., 1988) are based on Re_{macro} for both macroparticles and microparticles.

Sherwood numbers are used to calculate the thickness of the external aqueous boundary layer (δ_{aq}; equivalent to $\delta_{s,j}$ and $\delta_{sp,k}$ in Tab. 3.1), which is defined as:

$$Sh = \frac{d}{\delta_{aq}} \rightarrow \delta_{aq} = \frac{d}{Sh} \tag{3.7}$$

Ohashi et al. (1981) compared numerous empirical relationships of Sherwood numbers which typically lead to quite similar results. In this work we use the empirical relationship of Kirwan et al. (1989):

$$Sh = 2 + 0.52\, Re_{macro}^{\alpha} Sc^{1/3} \tag{3.8}$$

where Sc $(= \nu/D_{aq})$ denotes the Schmidt number. Sc is fairly constant for many pollutants and its value is around 1000 – 1500 ($Sc^{1/3} \approx 10 - 11$). α is the exponent of Re_{macro}. Kirwan et al. (1989) focused on mass transfer of microparticles and verified the minimum value of Sherwood number of 2 (a stationary suspended particle in stagnant water) and reported $\alpha = 0.5$ for microparticles, while $\alpha = 0.75$ for macroparticles is supported by many experimental results reported, e.g., by Harriott (1962) or Sano et al. (1974).

3.4 Results and discussions

3.4.1 Phenanthrene redistribution using well defined microplastic particles

In order to simulate the batch tests on Phenanthrene redistribution between microplastic particles of different sizes such that experimental results are reproduced as good as possible, we fitted the partition coefficient (K_{PE}) in batch test A, used that for tests B and C to obtain Sherwood numbers using the Matlab tool "fminsearch" to match measured aqueous concentrations. The semi-analytical model provided a very good fit to experimental data as shown in Fig. 3.3 with a model efficiency coefficient of E = 0.82 (C), 0.98 (B) and 1 (A). Fitted parameter values for partitioning coefficient and Sherwood numbers are listed in Tab. 3.2 (see section 3.4.3 for a detailed discussion). In batch test A (Fig. 3.3a), sorptive uptake of Phenanthrene to PE1 ($d_{PE1} = 145$ µm) can be well described by the coupled film intraparticle solid diffusion model (FIPSD). At very early times, external film diffusion (FD) dominates mass transfer, while at later times the mass transfer resistance shifts into the solid particles. The fitted logarithmic partition coefficient ($\log K_{PE} = \log(C_{PE,eq}/C_{w,eq})$) for Phenanthrene of 4.2 is consistent with $\log K_{PE}$ calculated from empirical relationships of Lohmann (2012) ($\log K_{PE} = 1.22 \log K_{ow,Phe} - 1.22 = 4.23$, using $\log K_{ow,Phe} = 4.47$ from Ma et al. (2010)). Results from batch test B on Phenanthrene desorption from preloaded coarse

microplastics (PE3) followed by uptake onto initially clean fine microplastics (PE2) are shown in Fig. 3.3b. Initially, the concentration of Phenanthrene in aqueous phase (C_w, blue lines) decreases rapidly due to the fast sorptive uptake by fine PE2 and the slow desorption from coarse PE3. At late times, PE2 and water reach a quasi-steady state (green lines and blue lines in Fig. 3.3b overlap) but PE3 still controls overall mass transfer causing a slow increase of Phenanthrene concentration in aqueous phase until final equilibrium is reached. Batch test C (see Fig. 3.3c) illustrates the reverse case where preloaded fine PE2 were mixed with clean coarse PE3. At early times, Phenanthrene concentration in aqueous phase (C_w, blue lines) increases rapidly (within minutes) because of fast release of Phenanthrene from PE2 and slow uptake onto PE3. Then, a relatively high concentration level is maintained for about two days indicating a "pseudo equilibration" controlled by PE2 (green and blue lines in Fig. 3.3c overlap). After that, intraparticle diffusion in PE3 dominates mass transfer, and the concentration of Phenanthrene both in aqueous phase and PE2 decreases rather slowly until an ultimate equilibration is obtained after ~70 days. Test C represents a scenario of polluted urban particles (e.g., from stormwater runoff or snow melts) entering a river leading to a peak aqueous concentration in the river, which is only slowly reduced by redistribution of pollutants to "clean" natural particles suspended in water. In all three test cases, the model captures the redistribution kinetics very well, especially if the loss of fine microplastics (PE1 in test A and PE2 in tests B and C) during sampling is accounted for by the model (using an updated solid-to-liquid ratio at each sampling time; dashed lines in Fig. 3.3).

Tab. 3.2: Partitioning coefficients (K_{PE}), Sherwood numbers (Sh) and coefficient of efficiency (E) for modeling of batch tests on Phenanthrene redistribution in a mix of spherical microplastics (MP) with different sizes and shapes (PE1 – PE3).

Parameters	Batch test A Sorptive uptake on fine MP	Batch test B Desorption from coarse, uptake on fine MP	Batch test C Desorption from fines, uptake on coarse MP
$\log K_{PE}$ [L kg^{-1}]	4.2 [a]	4.2	4.2
Sh_{PE1} [-] 145 µm	13.5	-	-
Sh_{PE2} [-] 260 µm	-	6.6	25
Sh_{PE3} [-] 4172 µm	-	∞[c]	∞[c]
E [b] [-]	1.00	0.98	0.82

[a] fitted value used also for batch tests B and C

[b] coefficient of efficiency of optimal model

[c] mass transfer limited solely by intraparticle solid diffusion

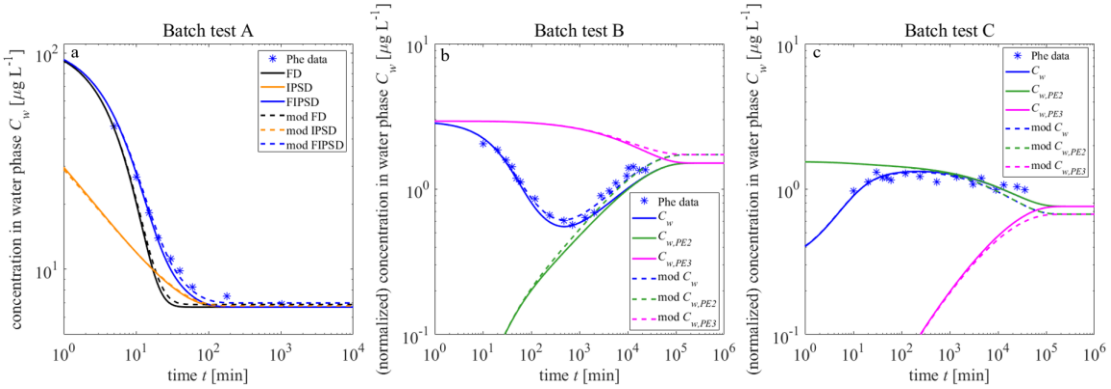

Fig. 3.3: Dynamics of Phenanthrene concentrations in water (blue symbols: measurements; blue lines: coupled model (FIPSD); yellow: intraparticle solid diffusion (IPSD); black: film diffusion (FD)); dashed lines account for loss of PE during sampling (solid lines: mass conservative). (a) Batch test A: Decrease of bulk concentration in water (C_w) because of Phenanthrene uptake in PE1 ($d_{PE1} = 145$ µm); (b) Batch test B: Rapid decrease of initial high Phenanthrene concentration due to uptake by fine microplastics (PE2; $d_{PE2} = 260$ µm) followed by slow release from coarse preloaded microplastics (PE3; $d_{PE3} = 4172$ µm); green and magenta lines indicate "water - equivalent" concentrations in PE2 and PE3 ($C_{w,PE2} = C_{PE2}/K_{PE}$; $C_{w,PE3} = C_{PE3}/K_{PE}$; this has the advantage that at equilibrium lines converge); (c) Batch test C: Rapid initial concentration increase in water (blue lines) caused by Phenanthrene release from preloaded fine microplastics PE2 (green) followed by slow decrease because of slow uptake by coarse microplastics PE3 (magenta).

3.4.2 Anthracene-d10 and Phenanthrene redistribution in a sediment suspension with passive sampling

Anthracene-d10 and Phenanthrene are chemical very similar and were used for fitting following model parameters: intraparticle porosity (ε) and initial concentrations in sediment particles ($C_{s,ini}$), distribution coefficients of Anthracene-d10 and Phenanthrene between fine/coarse sediment particles and water (K_d), between passive samplers and water (K_{PE}), Sherwood numbers of fine/coarse sediment particles ($Sh_{sp,1}, Sh_{sp,2}$) and the film thickness of passive samplers (δ_{PE}). The calibrated model reproduces the observation data very well, with a model efficiency coefficient (E) of 0.96-0.99 (Fig. 3.4 and Tab. 3.3). For polyethylene we used the same partition coefficient fitted in batch test A ($\log K_{PE} = 4.2$, see section 3.4.1). The fitted $\log K_d$ value for the sediment (= 3.2) was 0.2 to 0.3 log units higher than expected

from empirical relationships following the K_{oc}-concept ($K_d = K_{oc} f_{oc}$), either based on K_{ow}(e.g., Karickhoff et al., 1979: $\log K_{oc} = \log K_{ow} - 0.21$, with $\log K_{ow,Ant-d10/Phe} = 4.47$ from Ma et al. (2010)) or on subcooled liquid solubility S_i [kg L^{-1}] (Razzaque et al., 2008: $\log K_{oc} = -0.92 \log S_i - 0.72$ with $\log S_{Ant-d10\ and\ Phe} = -5.36$ from Meierdierks, 2019). High K_{oc} values were also observed by Kleineidam et al. (1999) for carbonaceous materials (coals, charcoals), which may occur in urban sediments. The fitted value of intraparticle porosity (ε) is 0.07, which is in the range of sedimentary rock fragments (Rügner et al., 1999). Finkel et al. (2017) reported similar kinetics with small intraparticle porosities for fine particle sizes ($d_{sp,1} < 7$ µm and $d_{sp,2} < 74$ µm). The fitted initial Phenanthrene concentration in sediment (24-28 µg kg^{-1}) is considerably lower than the concentration obtained from ASE measurement (150 µg kg^{-1}), which may be due to a fast desorbing Phenanthrene fraction (around 20%) with lower concentrations and a slowly desorbing fraction with higher concentrations in strongly sorbing particles (e.g., carbonaceous organic matter particles such as chars), which was not well captured by the model (details see section S3.15). The extraction of the total sample does not allow to distinguish different concentrations in low (small K_d) or strongly sorbing fractions (large K_d). In short term desorption experiments only the release of Phenanthrene from the rapidly desorbing fraction is observed especially at high solid-to-liquid ratios (see exemplary case (iv) in section 3.4.4).

Model results and measurements of Anthracene-d10 and Phenanthrene concentrations in PE sheets, water, fine and coarse sediment particles at two different solid-to-liquid ratios show a very good agreement (Fig. 3.4). Initially, Anthracene-d10 desorbs from PE sheets into the water phase, which leads to an increase of aqueous concentration and consequently to a concentration increase in fine and coarse sediment particles. After 1 h, fine sediment particles control mass transfer and Anthracene-d10 concentration in water starts to decrease, while it still increases in fine and coarse sediment particles until the concentration in fine sediment particles peaks. At this point in time (t = 100 min), a quasi-steady state is achieved for Anthracene-d10 concentration in PE sheets, fine sediment particles and water ($C_{PE} = C_w K_{PE}$ and $C_{s,sp,1} = C_w K_{d,b}$) and their equivalent aqueous concentrations ($C_{w,PE} = C_{PE}/K_{PE}$, $C_{w,sp,1} = C_{s,sp,1}/K_{d,b}$ and C_w) overlap (see Figs. S3.8a-b) indicating a pseudo equilibrium. After 100 min, mass transfer becomes dominated by the coarse sediment particles. Slow uptake of Anthracene-d10 from water into coarse sediment particles results in a concentration decrease in water and desorption of Anthracene-d10 from fine sediment particles as well as in long tailing of Anthracene-d10 concentration in PE sheets at late time until an ultimate equilibrium is achieved. The reverse process is observed for Phenanthrene: initially (within a few seconds) fine sediment particles release Phenanthrene rapidly into water causing an almost simultaneous concentration increase in water and PE passive samplers. After that, PE continues to accumulate Phenanthrene much faster than the total

release rates from fine and coarse particles, which results in a concentration decrease in water. After 1 h, coarse sediment particles control mass transfer and Phenanthrene release into water becomes faster than the uptake into PE, which leads to an increase in aqueous concentration while the concentration in fine sediment particles still decreases slowly until approx. 100 min. After that, a pseudo equilibrium is reached for Phenanthrene in PE sheets, fine sediment particles and water ($C_{PE} = C_w K_{PE}$ and $C_{s,sp,1} = C_w K_{d,b}$) and their equivalent aqueous concentrations ($C_{w,PE} = C_{PE}/K_{PE}$, $C_{w,sp,1} = C_{s,sp,1}/K_{d,b}$ and C_w) overlap (see Figs. S3.8c-d). Finally, Phenanthrene concentration in water continuously increases due to desorption from coarse sediment particles (see Fig. 3.4d) and the concentrations in PE sheets and fine sediment particles adjust accordingly because they are in equilibrium with the aqueous phase (see Figs. S3.8c-d); this leads to a slow concentration increase in fine sediment particles as well as in PE (see Figs. 3.4e and 3.4a). The kinetic behavior of Phenanthrene uptake into PE sheets mirrors (almost) the behavior of Anthracene-d10 (Fig. 3.4b). This is consistent with results of Liu et al. (2021) on monitoring of pyrene uptake into passive samplers and deuterated pyrene release from it. Uptake kinetics do not change significantly if solid-to-liquid ratio is increased. Only at late times, a slightly faster uptake is expected, which may be attributed to the mass transfer shift from PE sheets into sediment particles. The mass conservation plot verifies the semi-analytical model with numerical inversion as shown in Fig. 3.4c.

Tab. 3.3: Fitted parameter values and coefficient of efficiency (E) for Anthracene-d10 and Phenanthrene redistribution in sediment suspension with passive samplers.

Parameters	ε [-]	$\log K_{PE}$ [L kg^{-1}]	$\log K_d$ [L kg^{-1}]	$Sh_{sp,1}$ [-]	$Sh_{sp,2}$ [-]	δ_{PE} [μm]	$C_{s,ini}$ [µg kg^{-1}]	E [-]
Batch test D	0.07	(4.2[a])	3.2	3.4	8.5	5.4	24-28	0.96-0.99[b]

[a] from batch test A

[b] coefficient of efficiency range obtained from Anthracene d10 and Phenanthrene fitting results under two liquid-to-solid ratios (SL = 0.15 kg L^{-1} and SL = 0.30 kg L^{-1}).

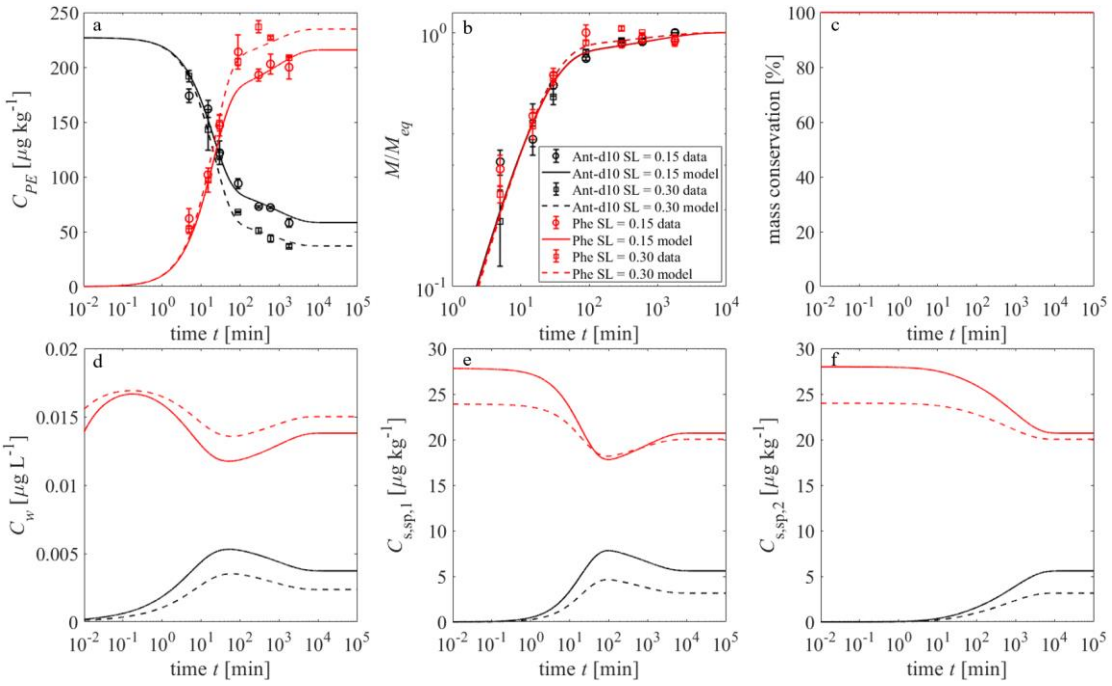

Fig. 3.4: Concentration changes of Anthracene-d10 (black lines and symbols) and Phenanthrene (red lines and symbols) in (a) PE passive samplers (polyethylene sheets $d_{PE} = 30$ µm) for two solid-to-liquid ratios of sediment particles (SL = 0.15 kg L^{-1}: solid lines and SL = 0.30 kg L^{-1}: dashed lines); (b) solute mass sorbed or desorbed by PE relative to equilibrium (M/M_{eq}); (c) mass conservation; (d) to (f) modeled concentrations in water (C_w), and C_w-equivalent concentrations for (e) fine particles ($d_{sp,1} = 7$ µm) and (f) coarse particles ($d_{sp,2} = 74$ µm).

3.4.3 Validation of Sherwood numbers

In order to validate the fitted Sherwood numbers from the microplastic batch tests A-D (shown in Tabs. 3.2-3.3), we compared them with values expected from the empirical relationships of Kirwan et al. (1989), which the energy dissipation rate as relevant parameter. Seidensticker et al. (2019) used a similar magnetic stirring system as employed here and reported an energy dissipation rate of $\varepsilon_{disp,magnetic}$= 10$^{-4.2}$ m^2 s^{-3} corresponding to an empirical Sherwood number of 6.7 for PE2 in batch test B, which is consistent with the fitted Sherwood number of 6.6 (see blue square symbol in Fig. 3.5). For batch tests A, C and D (horizontal shaking), the energy dissipation rate was unknown. The Sherwood number fitted for PE1 (13.5 from batch test A) allowed to back calculate (Eqs. 3.5 and 3.8) two energy dissipation rates ($\varepsilon_{disp,shaker}$= 10$^{-0.82}$ m^2 s^{-3} and 10$^{-1.5}$ m^2 s^{-3}) and two Kolmogorov length scales (η = 50 µm and 75 µm for $\alpha = 0.5$ and 0.75, respectively). PE1 ($d_{PE1} = 145$ µm) is larger than the Kolmogorov length scale (η = 50 µm) and does not belong to "microparticles" and therefore, the energy dissipation rate ($\varepsilon_{disp,shaker}$= 10$^{-1.5}$ m^2 s^{-3}) was used in batch tests C

and D ($\alpha = 0.5$ for $d < \eta$ or 0.75 for $d > \eta$ with η = 75 µm were chosen corresponding to grain sizes of particles). Fitted Sherwood numbers of batch tests C and D (shown in Tabs. 3.2-3.3) are consistent with empirical relationships (see Fig. 3.5) as for microparticles ($d < \eta$), a slope (α) of around 0.5 and for macroparticles ($d > \eta$) a slope of 0.75 is observed. A very large Sherwood number (close to infinity, see Tab. 3.2) had to be set for PE3 in batch test B and C to capture long term data (see Figs. 3.3b-c), which is in-line with sorption/desorption kinetics dominated by intraparticle solid diffusion as expected (see Liu et al., 2022).

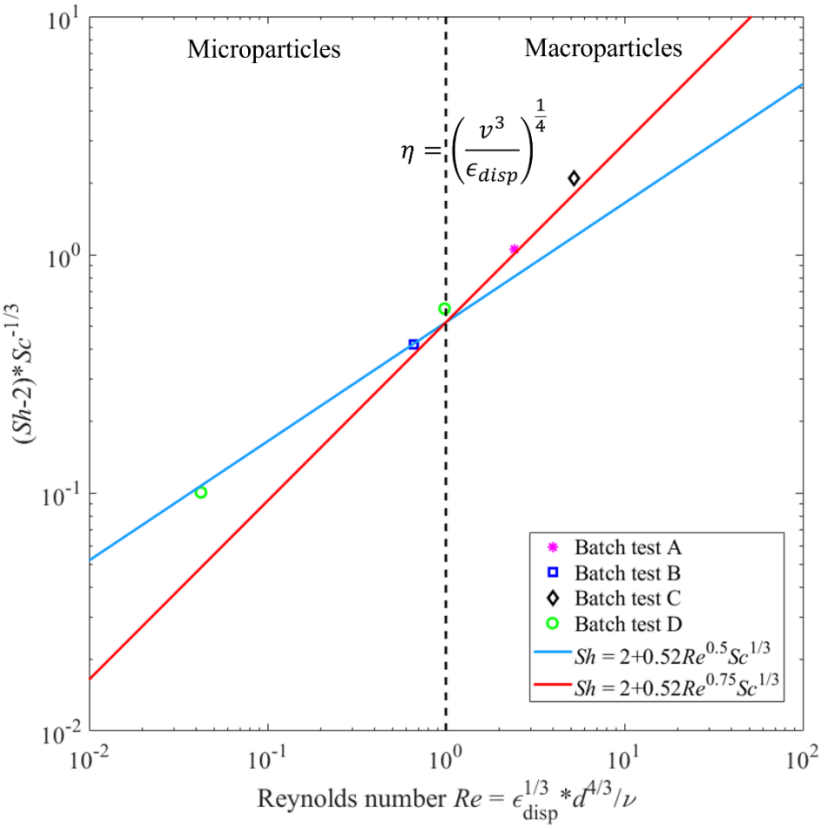

Fig. 3.5: Correlation of fitted Sherwood numbers from batch tests A-D and Reynolds numbers. The black vertical dashed line divides micro- ($d < \eta$) and macroparticles ($d > \eta$) according to the Kolmogorov length scale η. Data are compared to empirical relationships by Kirwan et al. (1989): $Sh = 2 + 0.52Re^{\alpha}Sc^{1/3}$ with $\alpha = 0.5$ for microparticles (blue line) and $\alpha = 0.75$ for macroparticles (red line).

3.4.4 Illustration of heterogeneous sorbents on sorption/desorption kinetics for hypothetical particle mixtures

Natural soils and sediments are typically very heterogeneous especially in terms of particle

sizes and sorption properties which strongly influences sorption/desorption dynamics. The presented coupled model allows to investigate this in great details in different settings (e.g., grain size mixtures, particle shapes and solid-to-liquid ratios). Since possible parameter combinations may get very large in heterogeneous systems, four exemplary, realistic cases were selected to illustrate the impact of sample composition on sorption/desorption kinetics: (i) mixed samples with fine weakly sorbing (fast) and coarse strongly sorbing particles (slow, e.g., particulate organic carbon), (ii) mixtures of fine and coarse particles, (iii) mixed samples of strongly and weakly sorbing particles (same size), and (iv) different particle geometries; (i) is the most relevant case and shown in Fig. 3.6, the other cases are discussed in sections S3.11-3.14 and here summarized as follows: Different particle geometries (iv) may be represented by their surface to volume ratio; (iii) a small fraction of strong sorbents (high distribution coefficients) may result in much slower sorptive uptake rates than expected for an equivalent homogeneous sample (with lower distribution coefficient) and as expected (ii) fine particles dominate sorption/desorption kinetics at early times and coarse particles take over at late times. Figure 3.6 shows kinetics for case (i) which is initially fast but then exhibits extended tailing and final equilibration is even much slower than in the equivalent homogeneous case (100% strongly sorbing coarse particles). This is due to competitive sorption between both particle fractions where initially rapid sorption/desorption is controlled by the fine weakly sorbing particles which leads to a diminished aqueous concentration gradient for the coarse strongly sorbing particles (see Figs. 3.6c-f) leading to slow mass transfer.

At higher solid-to-liquid ratios (e.g., $SL = 0.01$ kg L^{-1}, see Fig. 3.6b), kinetics is mostly dominated by fine particles and the extended tailing caused by the strongly sorbing coarse particles is barely observable experimentally close to M/M_{eq} = 1. If in such experimental setups K_d values obtained by fitting would represent only the fast fraction and thus would be too small (this likely applies to our experimental data of batch test D with a natural sediment sample; see also S3.15 with a detailed mathematical explanation). Even if the mass fraction of strong sorbents is quite low, it may contain a large fraction of pollutant mass (e.g., 1 mass-% of strong sorbent contains 50% of total pollutant mass) and this leads to unexpected slow kinetics in mixtures (i.e. slower than slow fraction alone) and consequently to a misinterpretation of data if the heterogeneity is not considered (see orange symbols and lines in Fig. 3.6).

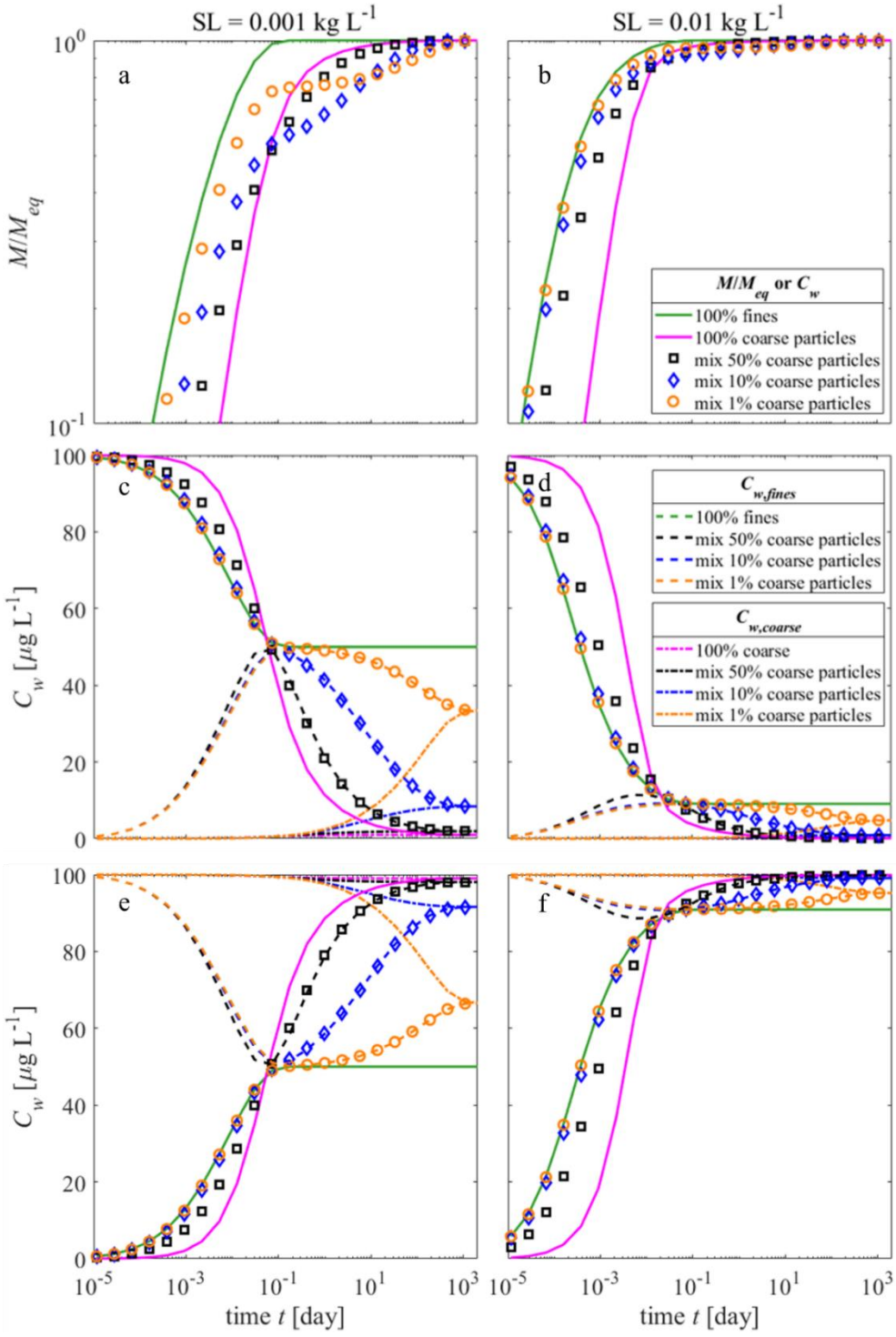

Fig. 3.6: Impact of heterogeneous sorbent compositions on sorption/desorption kinetics of mixtures of fine particles ($d_{sp,fine}$ = 40 µm) with low sorption capacity (K_d = 1000 L kg^{-1}) and coarse particles ($d_{sp,coarse}$ = 400 µm) with high sorption capacity (K_d = 100 000 L kg^{-1}) for two solid-to-liquid ratios (left panel: SL = 0.001 kg L^{-1}, right panel: SL =0.01 kg L^{-1}); top panel (a) and (b): relative mass distribution M/M_{eq} vs. time (t) of pure (solid lines) and bi-modal material compositions of fine and coarse particles with 1 mass-% coarse particles (orange circles), 10 mass-% coarse particles (blue diamonds) and 50 mass-% coarse

particles (black squares) (same curves for both sorption and desorption case); mid panel (c) and (d): concentrations in water during sorptive uptake (symbols and solid lines) and equivalent concentrations for fines (dashed lines: $C_{w,fines} = C_{s,fines}/K_{d,b}$) and coarse particles (dotted-dashed lines: $C_{w,coarse} = C_{s,coarse}/K_{d,b}$) with an initial aqueous concentration of $C_{w,ini}$ = 100 µg L^{-1}; bottom panel (e) and (f): results of the corresponding desorption case; simulation parameter: D_{aq} = 7.6 × 10^{-10} m^2 s^{-1}; ρ_s = 2.7 kg L^{-1}; ε = 0.2; ε_{disp} = $10^{-1.5}$ m^2 s^{-3}; ν = 10^{-6} m^2 s^{-1}; all simulations are based on coupled film-intraparticle pore diffusion model.

3.5 Implications

The two laboratory tests (one on microplastic mixtures and the second with natural sediment and passive samplers) as well as the modeled scenarios with hypothetical particle mixtures show that heterogeneous sorbent compositions may lead to unexpected sorption/desorption kinetics which are hard to interpret. For example, if a small fraction of coarse strong sorbent is mixed with fine weak sorbents (e.g., particulate organic carbon in a sediment or soil) fast initial kinetics are followed by very slow sorption, but this tailing is much longer than for the coarse particle alone. This behavior is not necessarily visible in batch experiments and likely is overlooked especially if solid-to-liquid rations are high (e.g., > 0.01; see Fig. 3.6). Thus, in laboratory batch experiments slow kinetics may be masked and lab observations cannot really be applied to field conditions. Very likely this also complicates biodegradation batch experiments where after a fast initial concentration decline, strongly sorbing particles limit degradation rates.

Proper interpretation of experimental data needs mechanistic models, and as shown here coupled mass transfer (film and intraparticle diffusion) has to be considered. If this is done, data can be interpreted properly and fitting parameters (e.g., K_d, K_{PE}, ε and Sh) are consistent with classical empirical relationships (e.g., Kolmogorov's turbulent theory and empirical relationships as shown in Fig. 3.5 for Sherwood numbers). Mechanistic models also help in optimum experimental design and the selection of right sampling time points. The analytical semi-Laplace solution used here for heterogeneous systems allows to define transfer functions accounting for particle properties (e.g., geometric shape, grain size, distribution coefficient, intraparticle porosity, etc.) as well as different mass transfer mechanisms (e.g., external film diffusion, intraparticle diffusion or coupled film-intraparticle diffusion) as shown in Tab. 3.1. Concentrations in each component can be easily obtained by numerical inversion of its analytical solution in Laplace domain as verified by the two batch experiment results (see Figs. 3.3 and 3.4).

References

Boving, T.B., Grathwohl, P., 2001. Tracer diffusion coefficients in sedimentary rocks: Correlation to porosity and hydraulic conductivity. J. Contam. Hydrol. 53, 85–100. https://doi.org/10.1016/S0169-7722(01)00138-3.

Culver, T.B., Hallisey, S.P., Sahoo, D., Deitsch, J.J., Smith, J.A., 1997. Modeling the desorption of organic contaminants from long-term contaminated soil using distributed mass transfer rates. Environ. Sci. Technol. 31, 1581–1588. https://doi.org/10.1021/es9600946.

de Hoog, F.R., Knight, J.H., Stokes, A.N., 1982. An improved method for numerical inversion of Laplace transforms. SIAM J. Sci. Stat. Comput. 3 (3), 357–366. https://doi.org/10.1137/0903022.

Finkel, M., Grathwohl, P., 2017. Impact of pre-equilibration and diffusion limited release kinetics on effluent concentration in column leaching tests: Insights from numerical simulations. Waste Manag. 63, 58–73. https://doi.org/10.1016/j.wasman.2016.11.031.

Golikov, A., Malakhova, I., Azarova, Y., Eliseikina, M., Privar, Y., Bratskaya, S., 2020. Extended Rate Constant Distribution Model for Sorption in Heterogeneous Systems. 1: Application to Kinetics of Metal Ion Sorption on Polyethyleneimine Cryogels. Ind. Eng. Chem. Res. 59, 1123–1134. https://doi.org/10.1021/acs.iecr.9b06000.

Harriott, P., 1962. Mass Transfer to Particles: Part I. Suspended in Agitated Tanks. AIChE J. 8, 93–101. https://doi.org/10.1002/aic.690080122.

Karapanagioti, H.K., Sabatini, D.A., 2000. Impacts of heterogeneous organic matter on phenanthrene sorption: Different aquifer depths. Environ. Sci. Technol. 34, 2453–2460. https://doi.org/10.1021/es990938w.

Karickhoff, S.W., Brown, D.S., Scott, T.A., 1979. Sorption of hydrophobic pollutants on natural sediments. Water Res. 13, 241–248. https://doi.org/https://doi.org/10.1016/0043-1354(79)90201-X.

Kikuchi, K.I., Sugawara, T., Ohashi, H., 1988. Correlation of liquid-side mass transfer coefficient based on the new concept of specific power group. Chem. Eng. Sci. 43, 2533–2540. https://doi.org/10.1016/0009-2509(88)85187-X.

Kirwan, J., Armenante, P.M., 1989. Mass transfer to microparticle systems. Chem. Eng. Sci. 44 (12), 2781–2796. https://doi.org/10.1016/0009-2509(89)85088-2.

Kleineidam, S., Rügner, H., Grathwohl, P., 1999. Impact of grain scale heterogeneity on slow sorption kinetics. Environ. Toxicol. Chem. 18, 1673–1678. https://doi.org/10.1002/etc.5620180810.

Kolmogorov, A.N., 1941. The local structure of turbulence in incompressible viscous fluid for very large Reynolds numbers (English translation by V. Levin, 1991). Process R. Soc. A- Math. Phys. Eng. Sci. 434, 9–13. https://doi.org/10.1098/ rspa.1991.0075.

Legates, D.R., McCabe Jr., G.J., 1999. Evaluating the use of "goodness-of-fit" Measures in hydrologic and hydroclimatic model validation. Water Resour. Res. 35, 233–241. https://doi.org/https://doi.org/10.1029/1998WR900018.

Liu, B., Finkel, M., Grathwohl, P., 2021. Mass transfer principles in column percolation tests: Initial conditions and tailing in heterogeneous materials. Materials 14 (16), 4708. https://doi.org/10.3390/ma14164708.

Liu, B., Finkel, M., Grathwohl, P., 2022. First order approximation for coupled film and intraparticle pore diffusion to model sorption/desorption batch experiments. J. Hazard. Mater. 429, 128314. https://doi.org/10.1016/j.jhazmat.2022.128314.

Liu, Y., Xie, S., Sun, Y., Ma, L., Lin, Z., Grathwohl, P., Lohmann, R., 2021. In-situ and ex-situ measurement of hydrophobic organic contaminants in soil air based on passive sampling: PAH exchange kinetics, non-equilibrium correction and comparison with traditional estimations. J. Hazard. Mater. 410, 124646. https://doi.org/10.1016/j.jhazmat.2020.124646.

Lohmann, R., 2012. Critical review of low-density polyethylene's partitioning and diffusion coefficients for trace organic contaminants and implications for its use as a passive sampler. Environ. Sci. Technol. 46, 606–618. https://doi.org/10.1021/es202702y.

Ma, Y.G., Lei, Y.D., Xiao, H., Wania, F., Wang, W.H., 2010. Critical review and recommended values for the physical-chemical property data of 15 polycyclic aromatic hydrocarbons at 25 ℃. J. Chem. Eng. Data. 55, 819 –825. https://doi.org/10.1021/je900477x.

Meierdierks, J, 2019. Soil-Atmosphere Exchange of PAHs The Determination of Concentration Gradients with Passive Samplers. PhD thesis, University of Tübingen.

Meyer, T., Wania, F., 2008. Organic contaminant amplification during snowmelt. Water Res. 42, 1847–1865. https://doi.org/10.1016/j.watres.2007.12.016.

Meyer, T., Lei, Y.D., Wania, F., 2011. Transport of polycyclic aromatic hydrocarbons and pesticides during snowmelt within an urban watershed. Water Res. 45, 1147–1156. https://doi.org/10.1016/j.watres.2010.11.004.

Ohashi, H., Sugawara, T., Kikuchi, K. ichi, Konno, H., Konno, H., 1981. Correlation of liquid-side mass transfer coefficient for single particles and fixed beds. J. Chem. Eng. Japan. 14, 433–438. https://doi.org/10.1252/jcej.14.433.

Razzaque, M.M., Grathwohl, P., 2008. Predicting organic carbon-water partitioning of

hydrophobic organic chemicals in soils and sediments based on water solubility. Water Res. 42, 3775–3780. https://doi.org/10.1016/j.watres.2008.07.003.

Rügner, H., Kleineidam, S., Grathwohl, P., 1999. Long term sorption kinetics of phenanthrene in aquifer materials. Environ. Sci. Technol. 33, 1645–1651. https://doi.org/10.1021/es980664x.

Rügner, H., Schwientek, M., Beckingham, B., Kuch, B., Grathwohl, P., 2013. Turbidity as a proxy for total suspended solids (TSS) and particle facilitated pollutant transport in catchments. Environ. Earth Sci. 69, 373–380. https://doi.org/10.1007/s12665-013-2307-1.

Saiers, J.E., Tao, G., 2000. Evaluation of continuous distribution models for rate-limited solute adsorption to geologic media. Water Resour. Res. 36, 1627–1639. https://doi.org/https://doi.org/10.1029/2000WR900050.

Sano, Y., Yamaguchi, N., Adachi, T., 1974. Mass transfer coefficients for suspended particles in agitated vessels and bubble columns. J. Chem. Eng. Japan. 7, 255–261. https://doi.org/10.1252/jcej.7.255.

Schwientek, M., Rügner, H., Beckingham, B., Kuch, B., Grathwohl, P., 2013. Integrated monitoring of particle associated transport of PAHs in contrasting catchments. Environ. Pollut. 172, 155–162. https://doi.org/10.1016/j.envpol.2012.09.004.

Seidensticker, S., Zarfl, C., Cirpka, O.A., Fellenberg, G., Grathwohl, P., 2017. Shift in Mass Transfer of Wastewater Contaminants from Microplastics in the Presence of Dissolved Substances. Environ. Sci. Technol. 51, 12254–12263. https://doi.org/10.1021/acs.est.7b02664.

Seidensticker, S., Zarfl, C., Cirpka, O.A., Grathwohl, P., 2019. Microplastic–Contaminant Interactions: Influence of Nonlinearity and Coupled Mass Transfer. Environ. Toxicol. Chem. 38, 1635–1644. https://doi.org/10.1002/etc.4447.

Shang, J., Liu, C., Wang, Z., Zachara, J.M., 2011. Effect of grain size on uranium(VI) surface complexation kinetics and adsorption additivity. Environ. Sci. Technol. 45, 6025–6031. https://doi.org/10.1021/es200920k.

4 Modeling of particle/gas distribution kinetics of polycyclic aromatic hydrocarbons (PAHs) in the atmosphere: Relevance of mass transfer resistance shifts

Binlong Liu, Michael Finkel, Peter Grathwohl

Abstract

A coupled external film-intraparticle pore diffusion model was derived to compare measured apparent bulk particle/gas distribution coefficients (Log $K_{pg,b,a}$) with equilibrium values (Log$K_{pg,b}$) predicted either from octanol-air distribution coefficients (K_{oa}) or subcooled liquid vapor pressures (P_L^o) of PAHs. The coupled model takes external mass transfer resistance in the bulk air as well as the internal resistance inside the intraparticle pore space into account. For low molecular weight (LMW) compounds (with small Log$K_{pg,b}$), mass transfer is dominated by intraparticle pore diffusion (kinetics follows the square root of time law), while external film diffusion is limiting for high molecular weight (HMW) compounds. The latter results in maximum observed distribution coefficients, i.e., they appear independent on K_{oa} or P_L^o (slope = 0); for intraparticle pore diffusion they in/decrease with the square root of K_{oa} or P_L^o. Moderate molecular weight (MMW) compounds lie in between (slope shifts from $1/2$ to 0) and both external and internal resistances have to be considered. The coupled model is strongly influenced by intraparticle porosity (ε), airborne particle concentration (TSP), grain size (d) as well as the contact time of airborne particle with ambient air. High $K_{pg,b,a}$ are obtained with fast kinetics, i.e., with the increase of intraparticle porosity, TSP, small particle size or long contact time (aged). The coupled model is verified using three data sets with different contact times obtained from recent published papers. Results on $K_{pg,b,a}$ obtained from local sources e.g., oil combustion tests in the lab and urban data can be well explained. However, when analyzing data sets from polar region, a notably higher Log$K_{pg,b}$ (2-3 magnitudes higher than the values predicted from absorption or dual model) is required suggesting different organic particles at remote areas.

4.1 Introduction

Polycyclic aromatic hydrocarbons (PAHs) are a ubiquitous group of semi-volatile organic

compounds in the environment due to their wide variety of sources, chemical stability, and multiple transport pathways (Balmer et al., 2019). Particle/gas distribution coefficients (K_{pg}) are widely used in estimating distribution of PAHs between airborne particles and air and they play a crucial role in determining the transport of PAHs in the atmosphere and their deposition onto soils and the aquatic environment. Subcooled vapor pressures (P_L^o) and octanol air partitioning coefficients (K_{oa}) theoretically are (inverse) proportional to K_{pg} and if plotted in logarithmic form slopes of -1 or 1 are expected under equilibrium conditions. However, many monitoring data show deviations especially for compounds with large molecular weight and thus very large K_{pg} (Mu et al., 2014; Ma et al., 2020; Zhang et al., 2022). Debates still continue and two mainstream perspectives try to explain slope deviations considering chemical properties and kinetic effects. Goss et al. (1998) stated that slope deviations do not necessarily indicate nonequilibrium effects due to the activity coefficients variations of chemical compounds and slopes of 1 or -1 for K_{oa} or P_L^o, respectively are only expected provided that all compounds have the same activity. Since airborne particles sampled in the same location, but from different events show discrepancies, kinetics effects also are important. Chemicals with low volatility need longer times to reach equilibrium and contact times between airborne particles and air likely are too short. Compared to the viewpoints of chemical properties, kinetics effects become more attractive especially for explaining the maximum K_{pg} domain for very low volatile compounds. Parnis et al. (2020) applied a first order sorption kinetics model to explain a plateau domain for K_{pg} in indoor dust/air partitioning for low volatile organic compounds. Zhao et al. (2021) used steady-state multimedia mass balance model based on fugacity theory to explain maximum K_{pg} values of polybrominated diphenyl ethers (PBDEs) by considering the fine and coarse aerosol particles mass transfer with ambient air for seven generic aerosol scenarios (urban, marine, rural, remote, free troposphere, polar and desert); only one scenario data (urban) was well fitted by the model. Fitting results depend on assumption on the mass transfer model: for first order kinetics the slope is either linear (1 or -1) or zero (nonequilibrium). Rounds et al. (1990 and 1993) applied the intraparticle pore diffusion model to describe the particle/gas sorption kinetics accounting for an unexchanged core inside the particles for explaining the overestimation of K_{pg} from the expected values (calculated from empirical equilibration model) for compounds with relatively high values of P_L^o. Theoretically, a shallow slope (= 0.5) would present under non-equilibration condition for intraparticle pore diffusion model, which is consistent to the slopes of monitoring data for PAHs sampling near source zones or polar regions (Mu et al., 2014; Liu et al., 2019; Zhang et al., 2022). However, intraparticle pore diffusion alone cannot explain the maximum K_{pg} domain for very low volatile compounds. Combining the merits of first order kinetics model and intraparticle pore diffusion model, a coupled kinetics model maybe an optimal choice to describe the

mass transfer between air and particles. Mai et al. (2015) used a coupled model but particles without intraparticle pores to investigate the equilibration times needed for airborne particles under infinite bath (gas phase concentration keeps constant.) and finite bath (gas phase concentration would decrease due to the sorption into the particles.). The results indicated mass transfer is controlled by the intraparticle solid diffusion for small K_{pg} compounds while mass transfer is dominated by the gas-phase diffusion (first-order kinetics) for large K_{pg} compounds. This finding demonstrates the feasibility of explaining slope discrepancy of K_{pg} with the coupled model. However, purely descriptive mathematical analysis of different sorption kinetics and their impact on the K_{pg} is still wide-spread (e.g., exponential models or second-order models), despite their lack of allowing any mechanistic understanding of mass transfer processes. Furthermore, to our knowledge all existing models assume more or less heterogeneous mixtures of particles in the atmosphere while heterogeneous particle sizes and properties are likely and complicate mass transfer kinetics even more. Typically numerical models would be used to address heterogeneities, but they are often computationally challenging.

Therefore, this paper introduces a coupled kinetics model, that takes both external and internal mass transfer resistances into account, which is solved in Laplace domain and concentrations in each component are obtained by numerical back transformation. This allows to easily demonstrate the impact of different kinetics models (film diffusion, intraparticle pore diffusion and coupled film intraparticle pore diffusion) on K_{pg} slope deviations. Additionally, the study investigates the effects of various parameters, such as airborne particle concentration, particle size, intraparticle porosity, and contact time on the kinetics models. To validate the kinetics models, three sources of data from recently published papers with different contact times between airborne particles and air are utilized.

4.2 Theory

4.2.1 Particle/gas distribution coefficients

Particle/gas distribution coefficients often are calculated from concentrations monitored in the atmosphere (Pankow, 1994):

$$K_{pg,b,a} = \frac{C_p}{TSP\ C_g} \tag{4.1}$$

where C_p [M L^{-3}] and C_g [M L^{-3}] are the concentrations of pollutants (e.g., PAHs) in atmospheric particles and gas phase, respectively. TSP [M L^{-3}] is concentration of total

suspended particles in gas phase (TSP= m_d/V_g; m_d [M] and V_g [L^3] denote the dry mass of particles and volume of air, respectively.). $K_{pg,b,a}$ (= $K_{pg,a} + \varepsilon/\rho_p$) may be considered as apparent bulk particle/gas distribution coefficient if equilibrium between gas and particulate phase are not reached (it also accounts for pollutants stored within the intraparticle pore space (ε); ρ_p [M L^{-3}] denotes the bulk density of porous particles ($\rho_p = \rho_s(1\text{-}\varepsilon)$); ρ_s [M L^{-3}] is the solid density of particles).

4.2.1.1 Equilibrium condition

During equilibration, apparent bulk particle/gas distribution coefficients approach the equilibrium (bulk) particle/gas distribution coefficients:

$$K_{pg,b} = \frac{C_{p,eq}}{TSP\ C_{g,eq}} \tag{4.2}$$

where $C_{p,eq}$ [M L^{-3}] and $C_{g,eq}$ [M L^{-3}] are the equilibrium concentrations of pollutants (e.g., PAHs) in atmospheric particle and gas phases, respectively. Since $\varepsilon/\rho_p \ll K_{pg}$, $K_{pg,b}$ is approximately equal to K_{pg} for PAHs.

Two types of models, the absorption model according to Harner and Bildeman (1998) and dual sorption model (Lohmann and Lammel, 2004) are widely used to determine the equilibrium particle/gas distribution coefficients. The absorption model is based on Raoult's law and assumes the pollutant sorptive uptake into particles is solely due to partitioning into the organic matter fraction (f_{om}) of the particles (f_{om} may be related to the organic carbon content of particles (f_{oc}) ($f_{om} = 1.5 f_{oc}$).) and thus may be correlated to octanol-air partitioning coefficients (K_{oa}). Harner and Bildeman (1998) assumed similarity of molar mass, density as well as activity coefficients in organic matter and octanol ($\rho_{oct} = 0.82$ kg L^{-1}) and thus derived a simple relationship of K_{oa} and K_{pg}:

$$\mathrm{Log}K_{pg} = \mathrm{Log}K_{oa} + \mathrm{Log}f_{om} - 11.91 \tag{4.3}$$

The dual mode model considers both absorption into organic matter and adsorption onto carbonaceous substances (e.g., soot or black carbon):

$$\mathrm{Log}K_{pg} = \mathrm{Log}\left(\frac{f_{om} MW_{oct} \gamma_{oct}}{MW_{om} \gamma_{om} 10^{12} \rho_{om}} K_{oa} + \frac{f_{ec} a_{ec}}{a_s 10^{12} \rho_{ec}} K_{sa}\right) \tag{4.4}$$

where MW_{oct} [M Mol^{-1}] and MW_{om} [M Mol^{-1}] denote the molar mass of octanol and organic matter, respectively. γ_{oct} [-] and γ_{om} [-] are the activity coefficients of octanol and organic matter, respectively. f_{ec} [-] is the fraction of elemental carbon. a_{ec} [L^2 M^{-1}] and a_s [L^2 M^{-1}] denote the specific surface area of elemental carbon and soot particles, respectively. a_{ec}/a_s is around 1 (Dachs and Eisenreich, 2000). ρ_{om} [M L^{-3}] and ρ_{ec} [M L^{-3}] are the density of organic

matter (assumed to be equal to ρ_{oct}) and elemental carbon (assumed to be equal to 1 kg L^{-1}) respectively. K_{sa} [L^3 M^{-1}] is the surface adsorption coefficients between air and soot particles, which can be estimated from the subcooled liquid vapor pressure (P_L^o) and the specific surface area of elemental carbon (Dach et al., 2004; van Noort, 2003):

$$\mathrm{Log}K_{sa} = -0.85\mathrm{Log}P_L^o + 8.94 - \mathrm{Log}\left(\frac{998}{a_{ec}}\right) \tag{4.5}$$

Both K_{oa} and P_L^o are temperature (T) dependent. Odabashi et al. (2006) presented the following empirical equations for PAHs which can be used to calculate K_{oa} and P_L^o for different temperatures:

$$\begin{aligned} \mathrm{Log}K_{oa} &= A_o + \frac{B_o}{T} \\ \mathrm{Log}P_L^o &= b_L + \frac{m_L}{T} \end{aligned} \tag{4.6}$$

where A_o, B_o, b_L and m_L are constants. Physical and chemical properties and corresponding constant values for PAHs (including naphthalene (Nap), acenaphthylene (Acy), acenaphthene (Ace), fluorene (Fl), phenanthrene (Phe), anthracene (Ant), fluoranthene (Flu), pyrene (Pyr), benzo[*a*]anthracene (BaA), Chrysene (Chr), benzo[*b*]fluoranthene (BbF), benzo[*k*]fluoranthene (BkF), benzo[*a*]pyrene (BaP), indeno [*1,2,3-cd*]pyrene (InP), dibenzo[*a,h*]anthracene (DBA)**,** dibenzo[*a,h*]anthracene (DahA), and benzo[*g,h,i*] perylene (BghiP).) are summarized in Tabs. S4.1 and S4.2, respectively.

4.2.1.2 Equilibration times - kinetics

The equilibrium time between airborne particles and air may cover multiple orders of magnitude due to impacts of the grain sizes, distribution coefficients (K_{pg}), intraparticle porosities (ε), solid to volume ratios (TSP), etc. (see Fig. 4.2). Non-equilibrium conditions often occur for pollutants with large K_{pg} in low TSP atmosphere, as evident from monitoring data in rural areas where $\mathrm{Log}K_{pg,b,a}$ vs. $\mathrm{Log}K_{pg,b}$ shows no correlation (or slope less than 1) in the large $\mathrm{Log}K_{pg,b}$ domain (Zhao et al., 2010; Wang et al., 2011; Qiao et al., 2019). Mass transfer of pollutants between gas and particles may be either governed by an external boundary layer ("gaseous film") or governed by an internal boundary layer where pollutant adsorption occurs inside the intraparticle pore space driven by the concentration gradient in the intraparticle gas phase ($C_{g,p}$) where instantaneous equilibration is assumed between solid (C_p) and $C_{g,p}$ ($C_p = C_{g,p}K_{pg}$).

Film diffusion model (FD): For sorptive uptake scenarios, the analytical solution of external film diffusion is given as (Liu et al., 2022):

$$\frac{C_p}{C_{p,eq}} = 1 - \exp\left(-\frac{k}{K_{pg,b}}\frac{6}{\rho_p\, d}\left(1 + K_{pg,b}\frac{m_d}{V_g}\right)t\right) \tag{4.7}$$

where k [L T^{-1}] is the first order mass transfer velocity ($k = D_g/\delta$; D_g [L^2 T^{-1}] is the gaseous diffusion coefficient of the pollutants and δ [L] is the external film thickness of suspended particles, which can be estimated via dimensionless Sherwood numbers ($Sh = d/\delta$).). d [L] is the grain size of particles. t [T] is the contact time of particles with air.

The relative distribution coefficients ($K_{pg,b,a}/K_{pg,b}$) of external film diffusion can be obtained by combing Eq. 4.7 and mass conservation equation (Eq. S4.3 and derivation details see section S4.2), which is:

$$\frac{K_{pg,b,a}}{K_{pg,b}} = \frac{1 - \exp\left(-\frac{k}{K_{pg,b}}\frac{6}{\rho_p\, d}\left(1 + K_{pg,b}\frac{m_d}{V_g}\right)t\right)}{1 + K_{pg,b}\frac{m_d}{V_g}\exp\left(-\frac{k}{K_{pg,b}}\frac{6}{\rho_p\, d}\left(1 + K_{pg,b}\frac{m_d}{V_g}\right)t\right)} \tag{4.8}$$

For short time approximation (t is small), the numerator of Eq. 4.8 can be replaced by the arguments inside the exponential function (1- exp(-x) ≈ x) and the exponential function in the denominator approaches to 1. Then Eq. 4.8 can be simplified as:

$$\begin{aligned} \frac{K_{pg,b,a}}{K_{pg,b}} &= \frac{\frac{k}{K_{pg,b}}\frac{6}{\rho_p\, d}\left(1 + K_{pg,b}\frac{m_d}{V_g}\right)t}{1 + K_{pg,b}\frac{m_d}{V_g}} = \frac{k}{K_{pg,b}}\frac{6}{\rho_p\, d}t \\ K_{pg,b,a} &= k\frac{6}{\rho_p\, d}t \end{aligned} \tag{4.9}$$

Thus at early times, $K_{pg,b,a}$ is independent on $K_{pg,b}$ which is especially relevant for pollutants with large $K_{pg,b}$ (see Fig. S4.1). This results in a maximum $K_{pg,b,a}$ as observed in many monitoring data of semi-volatile organic compounds (Qiao et al., 2019; Zhu et al., 2021; Li et al., 2022).

Intraparticle pore diffusion model (IPPD): Analytical solution of intraparticle pore diffusion of spherical particles can be expressed as series expansions (Crank, 1975):

$$\frac{C_p}{C_{p,eq}} = 1 - \sum_{n=1}^{\infty}\frac{6\beta(\beta+1)}{9 + 9\beta + q_n^2\beta^2}\exp\left[-q_n^2\frac{D_a}{a^2}t\right] \tag{4.10}$$

a [L] denotes the radius of spherical particles. β represents the ratio of pollutants mass stored in the free gaseous phase $M_{g,eq}$ [M] to the mass in the total suspended particles (sorbed and in the intraparticle pore space) $M_{s,eq}$ [M] under equilibrium condition.

$$\beta = \frac{M_{g,eq}}{M_{s,eq}} = \frac{V_g}{K_{pg,b}m_d} = \frac{1}{K_{pg,b}TSP} \tag{4.11}$$

The $q_n s$ are the n[th] non-zero root of transcendental function $\tan q_n = \frac{3q_n}{3+\beta q_n^2}$. D_a [L^2 T^{-1}] denotes the apparent diffusion coefficients of pollutants in gas phase, which can be estimated via the empirical relationships (Boving and Grathwohl, 2001):

$$D_a = \frac{D_g \varepsilon}{1 + K_{pg}\frac{\rho_p}{\varepsilon}} = \frac{D_p}{R_d} = \frac{D_p \varepsilon}{\rho_p K_{pg,b}} \tag{4.12}$$

D_p [L^2 T^{-1}] denotes the gaseous diffusion coefficient in intraparticle pore space. R_d [-] denotes the retardation factor.

The relative distribution coefficients ($K_{pg,b,a}/K_{pg,b}$) of intraparticle pore diffusion is given as (detail derivation process is presented in section S4.3):

$$\begin{aligned}\frac{K_{pg,b,a}}{K_{pg,b}} &= \frac{\frac{C_p}{C_{p,eq}}}{\left(1+\frac{1}{\beta}\right) - \frac{1}{\beta}\frac{C_p}{C_{p,eq}}} \\ &= \frac{1 - \sum_{n=1}^{\infty} \frac{6\beta(\beta+1)}{9+9\beta+q_n^2\beta^2} \exp\left[-q_n^2 \frac{D_a}{a^2} t\right]}{\left(1+\frac{1}{\beta}\right) - \frac{1}{\beta}\left(1 - \sum_{n=1}^{\infty} \frac{6\beta(\beta+1)}{9+9\beta+q_n^2\beta^2} \exp\left[-q_n^2 \frac{D_a}{a^2} t\right]\right)}\end{aligned} \tag{4.13}$$

For short term approximation, the square root of time solution can be applied:

$$\frac{C_p}{C_{p,eq}} = 6\sqrt{\frac{D_a t}{\pi a^2}}\left(1+\frac{1}{\beta}\right) \tag{4.14}$$

Inserting Eq. 4.14 into Eq. 4.13, $K_{pg,b,a}/K_{pg,b}$ becomes:

$$\begin{aligned}\frac{K_{pg,b,a}}{K_{pg,b}} &= \frac{6\sqrt{\frac{D_a t}{\pi a^2}}\left(1+\frac{1}{\beta}\right)}{\left(1+\frac{1}{\beta}\right) - \frac{6}{\beta}\sqrt{\frac{D_a t}{\pi a^2}}\left(1+\frac{1}{\beta}\right)} \\ &= \frac{6\sqrt{\frac{D_a t}{\pi a^2}}}{1 - \frac{6}{\beta}\sqrt{\frac{D_a t}{\pi a^2}}} \approx 6\sqrt{\frac{D_a t}{\pi a^2}} \quad \text{(when } t \text{ is small)}\end{aligned} \tag{4.15}$$

Since D_a accounts for intraparticle sorption, $K_{pg,b,a}$ increases with the square root of $K_{pg,b}$ (Eq. 4.15 combined with Eq. 4.12):

$$K_{pg,b,a} = 6\sqrt{\frac{D_p \varepsilon t}{\pi a^2 \rho_p K_{pg,b}}} K_{pg,b} = 6\sqrt{\frac{D_p \varepsilon K_{pg,b} t}{\pi a^2 \rho_p}} \tag{4.16}$$

Thus $K_{pg,b,a}$ plotted vs. $K_{pg,b}$ results in a slope of 1/2 (Fig. S4.2). For solid airborne particles (without intraparticle pores), a solid diffusion coefficient (D_s) replaces D_a in Eq. 4.15 and the distribution coefficient stays proportional to K_{pg} even under non-equilibrium conditions (slope = 1 in the plot of Log$K_{pg,a}$ vs. LogK_{pg}).

$$K_{pg,a} = 6\sqrt{\frac{D_s t}{\pi a^2}}K_{pg} \tag{4.17}$$

Coupled film intraparticle pore diffusion (FIPPD): A coupled model is needed to account for the mass transfer resistances outside and inside the particles (see Fig. 4.1). No simple analytical solutions exist so far for the coupled model in real time domain. A first order approximation solution may be alternative, but accuracy is limited only to early time periods (Liu et al., 2022). In order to apply the coupled model under more general conditions, a simple analytical solution in Laplace domain can be used and the results in the real time domain can be obtained by inverse Laplace transformation with numerical methods (de Hoog et al., 1982). The semi-Laplace solution can be also used in systems with heterogeneous composition (e.g., airborne particles with different grain sizes, distribution coefficients (K_{pg}), porosities, etc.). For a detailed derivation of the coupled film-intraparticle diffusion model see Liu et al. (2022). Briefly, mass transfer of pollutants between air and airborne particles (which may be mixtures from different sources, e.g., soot particles, charcoal, dust, etc.) can be expressed assuming mass conservation:

$$\frac{\partial C_g}{\partial t} + \sum_{i=1}^{n_i} \frac{m_{d,i}}{V_g} K_{pg,b,i} \frac{\partial C_{g,p,i}}{\partial t} = 0 \tag{4.18}$$

where n_i [-] denotes the total number of different particle classes. Variables with subscripts i refer to individual components. $C_{g,p,i}$ [M L^{-3}] is the pollutant concentration in the intraparticle pore gaseous phase.

The Laplace transformation of the mass conservation equation becomes:

$$s\tilde{C}_g - C_g(0) + \sum_{i=1}^{n_i} \frac{m_{d,i}}{V_g} K_{pg,b,i} \left(s\tilde{C}_{g,p,i} - C_{g,p,i}(0) \right) = 0 \tag{4.19}$$

where s [T^{-1}] is the complex Laplace coordinate. The tilde sign denotes the Laplace transform of the respective variables. $C_g(0)$ and $C_{g,p,i}(0)$ denote the initial pollutant concentration in gas phase, and intraparticle pore gas phase, respectively.

In real time domain, the average concentration in the intraparticle gas phase ($C_{g,p,i}$) depends on the pollutant concentration in the ambient air (C_g) in form of a convolution with respective transfer functions. In Laplace domain, $\tilde{C}_{g,p,i}$ is:

$$\tilde{C}_{g,p,i} = \tilde{g}_{p,i} \left(\tilde{C}_g - \frac{C_{g,p,i}(0)}{s} \right) + \frac{C_{g,p,i}(0)}{s} \tag{4.20}$$

where $\tilde{g}_{p,i}$ [-] is the transfer function containing the sorption/desorption kinetics information.

For coupled film intraparticle pore diffusion, the transfer function of spherical particles is:

$$\tilde{g}_{p,i} = \frac{D_{a,i}\left(\sqrt{\frac{s}{D_{a,i}}}\coth\left(a_i\sqrt{\frac{s}{D_{a,i}}}\right) - \frac{1}{a_i}\right)}{k_i + D_{a,i}\rho_{p,i}K_{pg,b,i}\left(\sqrt{\frac{s}{D_{a,i}}}\coth\left(a_i\sqrt{\frac{s}{D_{a,i}}}\right) - \frac{1}{a_i}\right)}\frac{3k_i}{a_i s} \tag{4.21}$$

Different geometries of particles, sorption/desorption kinetics models applied as well as internal structures of particles (e.g., with or without intraparticle pores) need slightly different transfer functions as reported by Liu et al. (2023).

Inserting Eq. 4.20 into Eq. 4.19 yields the pollutant concentration in ambient air in Laplace domain ($\tilde{C}_g$) is given as:

$$\tilde{C}_g = \frac{C_g(0) + \sum_{i=1}^{n_i}\frac{m_{d,i}}{V_g}K_{pg,b,i}\tilde{g}_{p,i}C_{g,p,i}(0)}{\left(1 + \sum_{i=1}^{n_i}\frac{m_{d,i}}{V_g}K_{pg,b,i}\,\tilde{g}_{p,i}\right)s} \tag{4.22}$$

The average concentration in particles can be determined via the mass balance:

$$C_p = \left(C_g(0) - C_g\right) \tag{4.23}$$

Combining Eq. 4.22 with Eq. 4.23, $K_{pg,b,a}$ of coupled model can be obtained based on its definition:

$$K_{pg,b,a} = \frac{C_p}{\mathrm{TSP}\;C_g} = \frac{C_g(0) - \mathrm{invlap}\left(\frac{C_g(0) + \sum_{i=1}^{n_i}\frac{m_{d,i}}{V_g}K_{pg,b,i}\tilde{g}_{p,i}C_{g,p,i}(0)}{\left(1 + \sum_{i=1}^{n_i}\frac{m_{d,i}}{V_g}K_{pg,b,i}\,\tilde{g}_{p,i}\right)s}\right)}{\mathrm{TSP}\;\mathrm{invlap}\left(\frac{C_g(0) + \sum_{i=1}^{n_i}\frac{m_{d,i}}{V_g}K_{pg,b,i}\tilde{g}_{p,i}C_{g,p,i}(0)}{\left(1 + \sum_{i=1}^{n_i}\frac{m_{d,i}}{V_g}K_{pg,b,i}\,\tilde{g}_{p,i}\right)s}\right)} \tag{4.24}$$

where invlap denotes the inverse Laplace transformation operator. $K_{pg,b,a}$ is independent on the initial concentration in gas phase ($C_g(0)$, which is often unknown.) and a random positive number can be used in modeling (independent on initial concentration). For sorptive uptake scenarios, $C_{g,p,i}(0)$ is 0.

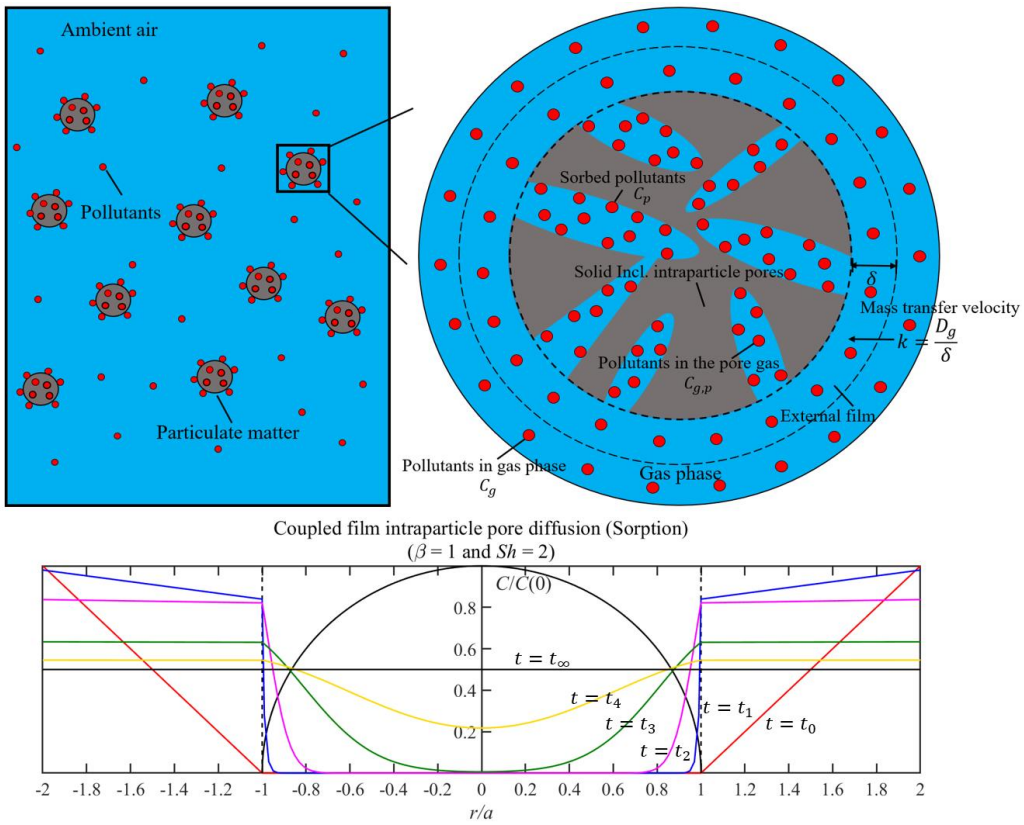

Fig. 4.1: Mass transfer of pollutants from ambient air into airborne particles limited by coupled film-intraparticle pore diffusion (top) and concentration gradients (bottom) in the external boundary layer ($|r/a| \in [1, 2]$) as well as in the intraparticle pore space ($|r/a| \in [0, 1]$) from time zero (t_0, red line) to equilibration (t_∞, black line in the middle) for 50% pollutants uptake in the airborne particles (β =1 or $K_{pg,b} = 1/\text{TSP}$).

4.2.2 Data sources

Three data sets were obtained from recently published papers. These three cases represent short and long contact times of airborne particles with air. The first data set (1) came from Yin et al. (2022) who reported concentrations of 16 EPA PAHs emitted during combustion of different fuels (condensate, diesel and heavy oil) in a test chamber operated in the lab. A second data set (2) was taken from Sun et al. (2022) who measured PAHs concentrations in airborne particles and atmosphere in the city of Yuncheng (a city in Northern China) considering diurnal variations as well as the impact of domestic heating. Finally, a third data set (3) was taken from Zhang et al. (2022) reporting PAHs concentrations in the marine atmosphere monitored during a cruise of a research vessel from the Western Pacific to the Southern Ocean with sampling locations covering the Antarctic regions as well as places remote and close to coasts.

A requirement for the selection of each data set was the availability of sampling temperatures (T), airborne particle concentration (TSP), organic matter content (f_{om}), as well as the specific surface area of elemental carbon (a_{ec}) which is needed for the calculation of the particle/gas distribution coefficient (K_{pg}) either using the empirical relationships of the absorption model (Eq. 4.3) or the dual model (Eq. 4.4). Measured concentrations of PAHs in gaseous and particle phases were utilized to calculate the apparent particle/gas distribution coefficient ($K_{pg,b,a}$) (see Tabs. S4.3, S4.5 and S4.7 for the three data sets). The comparison of the measured $K_{pg,b,a}$ and the equilibrium K_{pg} (calculated from Eqs.4.3 and 4.4) is presented in section S4 (see Tabs. S4.4, S4.6 and S4.8 for three data sets). For sorption kinetics modeling (e.g., FIPPD), inputs include the equilibrium particle/gas distribution coefficient (K_{pg}), TSP, particle size (d), gaseous diffusion coefficient (D_g), intraparticle porosity (ε), dry density of airborne particles (ρ_s), Sherwood numbers (Sh), and contact time between airborne particles and air (t). The gaseous diffusion coefficients of PAHs are similar (e.g., 5 - 9 $\times 10^{-6}$ m^2 s^{-1}), and a value of 6×10^{-6} m^2 s^{-1} is used (Gustafson et. al, 1994). The dry density of airborne particles is assumed to be close to the density of black carbon or soot particles (1.8 kg L^{-1}; Bond et al., 2013). The minimum Sherwood number of 2 for spherical particles is applied in modeling, as the grain size of the airborne particles is in the range of only a few micrometers and the relative velocity between the particles and air is very small. Since calculated K_{pg} from empirical relationships (Eqs. 4.3 or 4.4) may slightly deviate from measured $K_{pg,b,a}$ even for LMW PAHs (assumed to be equilibrium very quickly or $K_{pg} = K_{pg,b,a}$) due to measurement errors or unconsidered potential parameters, the measured $K_{pg,b,a}$ is used as input of $K_{pg,b}$ of kinetics model for LMW PAHs and $K_{pg,b}$ of HMW PAHs is assumed as $K_{pg,b}$ from empirical relationships plus the mean deviations of LMW PAHs. The mean deviations between measured $K_{pg,b,a}$ and empirical relationships (Eqs. 4.3 or 4.4) of LMW PAHs for data sets (1) and (2) are within error ranges (< 0.5 logarithmic unit, see Figs. S4.4 and S4.5), while measured $K_{pg,b,a}$ of LMW PAHs for data set (3) are 2-3 magnitudes higher than empirical relationships (see Fig. S4.6) (explanation see section 4.3.3.3). Intraparticle porosity (which controls the intraparticle pore diffusion coefficient) and contact time are utilized as fitting parameters, and parameter calibration is performed in Matlab via the 'fminsearch' function to minimize errors between the model-estimated and measured apparent particle/gas distribution coefficients. The normalized root mean square error (NRMSE) is determined and it varies from 0 to 1. A low NRMSE value e.g., < 0.2 indicates model's predictions are closer to the measured values.

4.3 Results and discussions

4.3.1 95% equilibration time scales of PAHs from 3 different kinetics models (FD, IPPD and FIPPD)

In Fig. 4.2, we compare the 95% equilibration times of FD, IPPD and FIPPD under two atmospheric particle concentrations (TSP = 20 and 200 μg m^{-3}) and two intraparticle porosities ($\varepsilon = 0.05$ and 0.2) for particle size ranges of 1 to 10 μm and logarithmic bulk distribution coefficient ranges ($\mathrm{Log}K_{pg,b}$) of –5 to 2. The high and low particle concentrations may represent the conditions in urban and remote areas; particle sizes and bulk distribution coefficients are typically observed in environmental monitoring in many countries (e.g., PM1, PM2.5 and PM10) and 16 USEPA priority PAHs, respectively. With the decrease of the grain size (d) or increase of particle concentration (TSP), the 95% equilibration times decrease for all kinetics models. For FD (see Fig. 4.2; blue surfaces), equilibration times firstly increase with increasing $K_{pg,b}$, but then become independent on $K_{pg,b}$ (because for large $K_{pg,b}$ values: $1 + K_{pg,b}\mathrm{TSP} \approx K_{pg,b}\mathrm{TSP}$ and $K_{pg,b}$ is canceled in Eq. 4.7). In contrast to FD, for IPPD (or FIPPD) a maximum equilibration time exists when 1/TSP equals to $K_{pg,b}$ (or $\beta = 1$) as already illustrated by Grathwohl (2014). For higher or lower $K_{pg,b}$, equilibration times would decrease (see Fig. 4.2, red surfaces). Intraparticle porosity (ε) is the most sensitive parameter in IPPD and it controls the retarded pore diffusion coefficient. The 95% equilibration times of IPPD decrease dramatically with the increase of intraparticle porosity (see Figs. 4.2a and b). As to be expected the coupled FIPPD model shows slowest sorption kinetics (or longest equilibration times; magenta surfaces in Fig. 4.2). Liu et al. (2022) adopted the mass transfer resistance ratios to illustrate how mass transfer shifts from FD to IPPD and found that mass transfer is dominated by intraparticle pore diffusion for compounds with small $K_{pg,b}$ (because shift occurs earlier), while the mass transfer shift is delayed with the increase of $K_{pg,b}$ and intraparticle porosity. For PAHs with large $K_{pg,b}$ (or low β), mass transfer is dominated by FD. In the intermediate domain of $K_{pg,b}$, both FD and IPPD play a role. With the increase of TSP and intraparticle porosity, FIPPD follows FD for lower $K_{pg,b}$ values due to a delay in mass transfer shift (see Figs. 4.2b, c, and d).

The 95% equilibration times vary greatly, from few seconds to thousand days. For example, for low molecular weight (LMW) of PAHs (small $K_{pg,b}$), they only take around 10 s to reach the 95% equilibration for 1 μm particles with intraparticle porosity of 0.2 and TSP of 200 μg m^{-3} (see Fig. 4.2d), which is around 10 million times faster than the cases of high molecular weight (HMW) of PAHs (large $K_{pg,b}$) whose maximum equilibration times are more than

1000 days for 10 µm particles with intraparticle porosity of 0.05 and TSP of 20 µg m^{-3} (see Fig. 4.2a). Esmen et al. (1971) showed that the residence times of fine airborne particles (PM2.5 and PM0.1) range from days to weeks, while coarse particles (PM10) have only lifetimes of hours to days. The equilibration times of HMW PAHs are much longer than the residence times of airborne particles and the assumption of equilibration does not hold especially under low TSP conditions (e.g., remote regions) or airborne particles with small intraparticle porosity. On the contrary, LMW PAHs reach equilibration very fast and $K_{pg,b,a}$ values approach equilibrium ($K_{pg,b}$), which can be used in equilibrium models calibration (Eqs. 4.3 and 4.4).

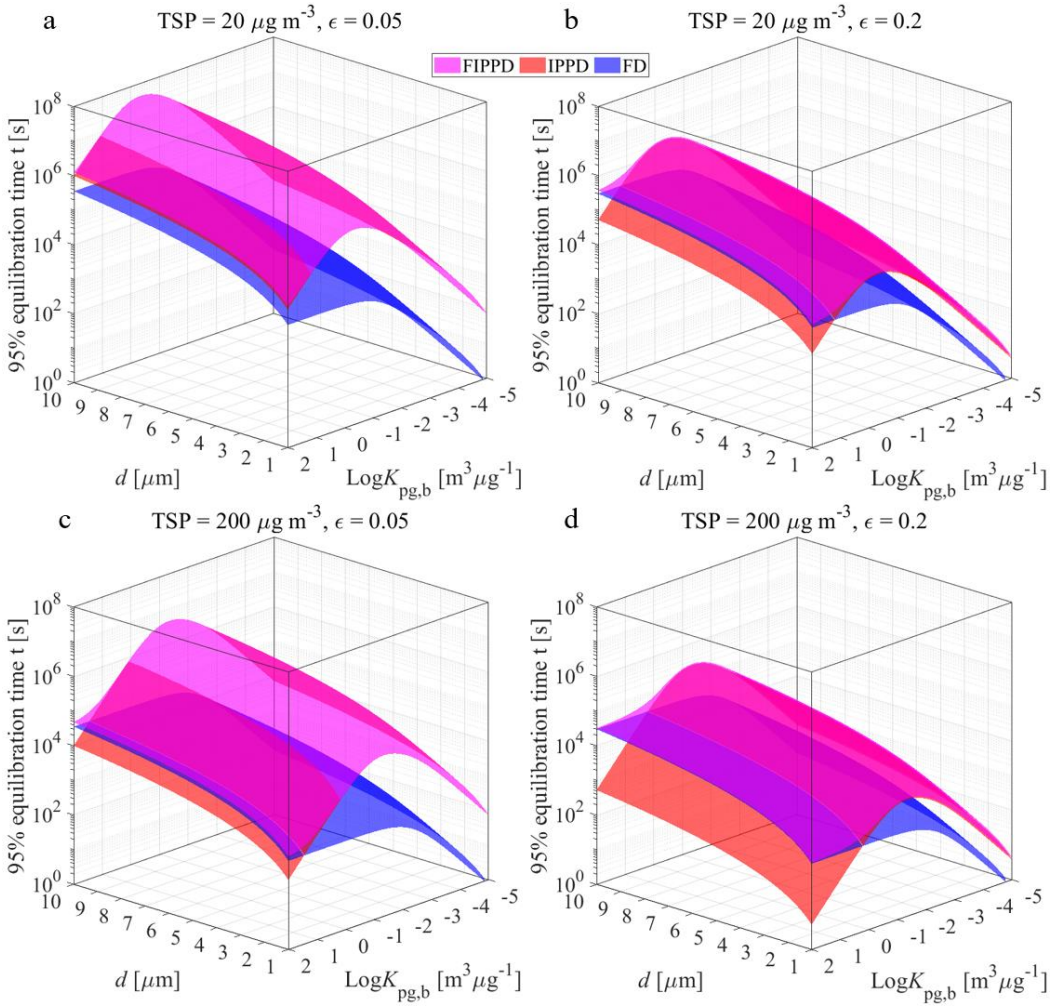

Fig. 4.2: 95% equilibration times for film diffusion (FD), intraparticle pore diffusion (IPPD) and coupled film-intraparticle pore diffusion (FIPPD) vs. grain sizes (d) and particle/gas bulk distribution coefficients (Log$K_{pg,b}$) for spherical particles with two different atmospheric particle contents (TSP = 20 (top) and 200 µg m^{-3} (bottom)) and intraparticle porosities (ε = 0.05 (left) and 0.2 (right)); $D_g = 6\times10^{-6}$ m^2 s^{-1}; $\rho_s = 1.8$ kg L^{-1}; $Sh = 2$ (for small $K_{pg,b}$ values, FIPPD and IPPD overlap completely).

4.3.2 Log$K_{pg,b,a}$ vs. Log$K_{pg,b}$ of PAHs

Three sorption kinetics models (FD, IPPD and FIPPD) are used to calculate the apparent particle/gas bulk distribution coefficients for two TSPs (20 and 200 μg m^{-3}) and two intraparticle porosities (0.05 and 0.2) for contact times of 1×10^3 s and 1×10^6 s. The short and long contact times may represent the cases of sampling near or far away from particle sources. For short contact times (t = 1×10^3 s), FD shows a slope of 1 only for LMW PAHs (Log $K_{pg,b}$< -2.5) indicating equilibrium, while $K_{pg,b,a}$ becomes constant for moderate molecular weight (MMW) PAHs and HMW PAHs (Log$K_{pg,b}$> -2.5); thus $K_{pg,b,a}$ is independent on $K_{pg,b}$ for sorptive uptake of HMW PAHs under nonequilibrium conditions (see Eq. 4.9). For IPPD, sorption kinetics is much slower than in FD for LMW PAHs and equilibrium is only reached for very low Log$K_{pg,b}$ values (e.g., Log$K_{pg,b}$ < -4.8 and -3.5 for ε values of 0.05 and 0.2, respectively.). With the increase of Log$K_{pg,b}$, non-equilibrium conditions show up and a slope of 1/2 is observed for intraparticle pore diffusion (see Eq. 4.16). The coupled model combines FD and IPPD and for low Log$K_{pg,b}$, intraparticle pore diffusion dominates mass transfer and the coupled model follows IPPD, then the slope gradually decreases from 0.5 to 0 until the external boundary layer dominates and Log$K_{pg,a}$ becomes constant (here for 1×10^3 s) like in FD. This corresponds e.g., to data reported by Mu et al. (2014) and Liu et al. (2019) from the emission in coke plants with sampling points close to the sources. Similar results were obtained in PAHs emission tests from the oil combustion in a small chamber directly connected to the sampling devices which have even shorter contact times (Yin et al., 2022). With the increase of the contact time (e.g., t = 1×10^6 s) a higher degree of equilibrium is reached. All PAHs reach equilibrium for FD (slope =1). The curves of FIPPD follow the curves of IPPD. Equilibration conditions are obtained for Log$K_{pg,b}$ < -1.5 and - 0.2 for ε values of 0.05 and 0.2, respectively. For HMW PAHs, mass transfer resistance shifts from the external boundary layer into the particle pore space and the slope becomes 0.5. If the contact time is even longer, all curves would finally follow a slope of 1 indicating equilibration. Zhu et al. (2021) collected data for PAHs in Harbin City from 2014 - 2019 and reported a slope of -0.57 and 0.61 for schemes of Log$K_{pg,b,a}$ vs. LogP_L^o and LogK_{oa}, respectively. Similar slopes (close to 1/2) are also reported from data sets of regular air sampling of different urban cities from Zhao et al. (2010) (-0.58), Yu et al. (2012) (-0.61), Sun et al. (2022) (0.59), etc. IPPD is a plausible explanation for these observations.

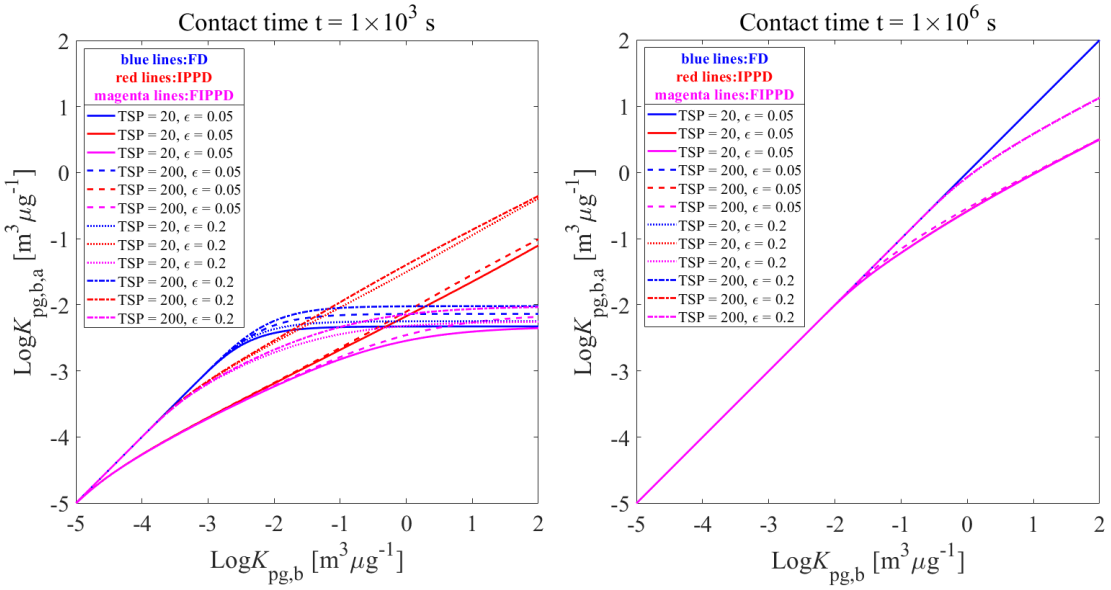

Fig. 4.3: Short term (t = 1×10^3 s; left) and long term (t = 1×10^6 s; right) behaviors of apparent particle/gas bulk distribution coefficients (Log$K_{pg,b,a}$) vs. equilibrium bulk particle/gas distribution coefficients (Log$K_{pg,b}$) of film diffusion, intraparticle pore diffusion and coupled film intraparticle pore diffusion for PAHs sorption into airborne spherical particles under different particle concentrations (TSP = 20 and 200 μg m^{-3}) and intraparticle porosities (ε = 0.05 and 0.2). (D_g = 6×10^{-6} m^2 s^{-1}; ρ_s = 1.8 kg L^{-1}; Sh = 2; d = 2.5 μm)

4.3.3 Model application to data sets

4.3.3.1 Case I: PAHs emission from oils combustion in a lab chamber test

Data of release of sixteen PAHs from combustion of three types of oils (condensate, diesel, heavy oil) was taken from Yin et al. (2022). Sampling temperature, particle contents as well as average PAHs concentrations in gaseous and particle phases are presented in Fig. 4.4a and b, respectively. It can be seen that total PAHs release from combustion of heavy oil is higher than the PAHs emissions of diesel and condensate because heavy oil takes longer heating times resulting in incomplete combustion, while condensate is a light crude oil and more inflammable leading to more complete combustion and diesel oil falls in between (Fingas, 2017). The most abundant PAHs for those three types of oils are the same (Nap, Pyr, Flu and Chr). LMW PAHs (e.g., Nap and Acy) occur mostly in gas phase while HMW PAHs (e.g., BbF, BkF, BaP, InP, DahP and BghiP) are almost completely associated with the particulate phase. The absorption model (Eq. 4.3) describes the equilibrium bulk particle/gas partitioning coefficients (Log$K_{pg,b}$) better than dual model (Eq. 4.4) especially for LMW PAHs (see Fig. S4.4). Therefore, the average Log$K_{pg,b}$ deviations of Nap, Acy and Ace between absorption model and measured Log$K_{pg,b,a}$ are used for correction of equilibrium bulk particle/gas

partitioning coefficients of HMW PAHs ($\text{Log}K_{pg,b,HMW} = \text{Log}K_{pg,b,HMW,absorption}$ + mean deviations of Nap, Acy and Ace) and the results are utilized as the input $\text{Log}K_{pg,b}$ values of kinetics models. The modeling results of three kinetics models (FD, IPPD and FIPPD) are presented in Fig, 4.4c. Since the combustion experiments were run in a chamber (80 cm × 30 cm × 30 cm) in the lab and burning times can be assumed to be similar for all types of oils due to the constant oil volume consumption (30 mL oil for each test) (setups details see Yin et al., 2022). The modeling results show that FIPPD is the best kinetics model for describing $\text{Log}K_{pg,b,a}$ of PAHs from combustion of condensate, while FD is the optimal kinetic model for diesel and heavy oil with the normalized root mean square errors (NRMSE) of 0.13, 0.12 and 0.08, respectively. The intraparticle porosity fitted for the condensate ($\varepsilon = 0.13$) is smaller than the intraparticle porosities of diesel particles ($\varepsilon = 0.51$) and heavy oil particles ($\varepsilon = 0.52$) probably because volatile constituents evaporate during combustion leading to more unburned oil droplets entrapped in the airborne particles which occupy the intraparticle pore space. The intraparticle porosities of airborne particles from combustion of diesel and heavy oil are consistent with the results ($\varepsilon = 0.5$) reported by Strommen et al. (1997 and 1999) who also measured airborne particles (e.g., soot particles) from combustion of diesel. The small intraparticle porosity of condensate increases the internal mass transfer resistance and mass transfer is dominated by IPPD for LMW PAHs (low $\text{Log}K_{pg,b}$), while mass transfer resistance dominated by FD for HMW PAHs (high $\text{Log}K_{pg,b}$). The mass transfer of MMW PAHs is controlled by both external and internal mass transfer resistances (see red solid line in Fig. 4.4c.). With the increase of intraparticle porosity, sorption kinetics facilitates and mass transfer shift from FD to IPPD delays (Liu et al., 2021) and LMW PAHs (Nap, Acy, Ace FI, Phe and Ant) have already reached equilibration and show a slope of 1 for diesel and heavy oils (see blue and black symbols and lines in Fig. 4.4c or Fig. S4.4). For MMW and HMW PAHs, sorption kinetics leads to measured $\text{Log}K_{pg,b,a}$ smaller than the corrected equilibrium $\text{Log}K_{pg,b}$ and both FIPPD (sold lines) and FD (dashed lines) capture the tendency of measurements of diesel and heavy oil, although FD is the optimal model with least NRMSE. The fitted contact time between airborne particles and air is around 10 s based on average particle grain size of 10 μm. A shorter contact time would obtain if a finer grain size was used (e.g., similar fitting results would get for contact time of 1s for grain size of 2.5 μm.). The measured $\text{Log}K_{pg,b,a}$ of LMW PAHs equal to the equilibrium $\text{Log}K_{pg,b}$ even if the contact time is short, because the airborne particle concentration (TSP) is very high (see Fig. 4.4a), which is around three orders of magnitude higher than the airborne particle concentration in ambient air (e.g., ranges from 10-200 μg m^{-3}).

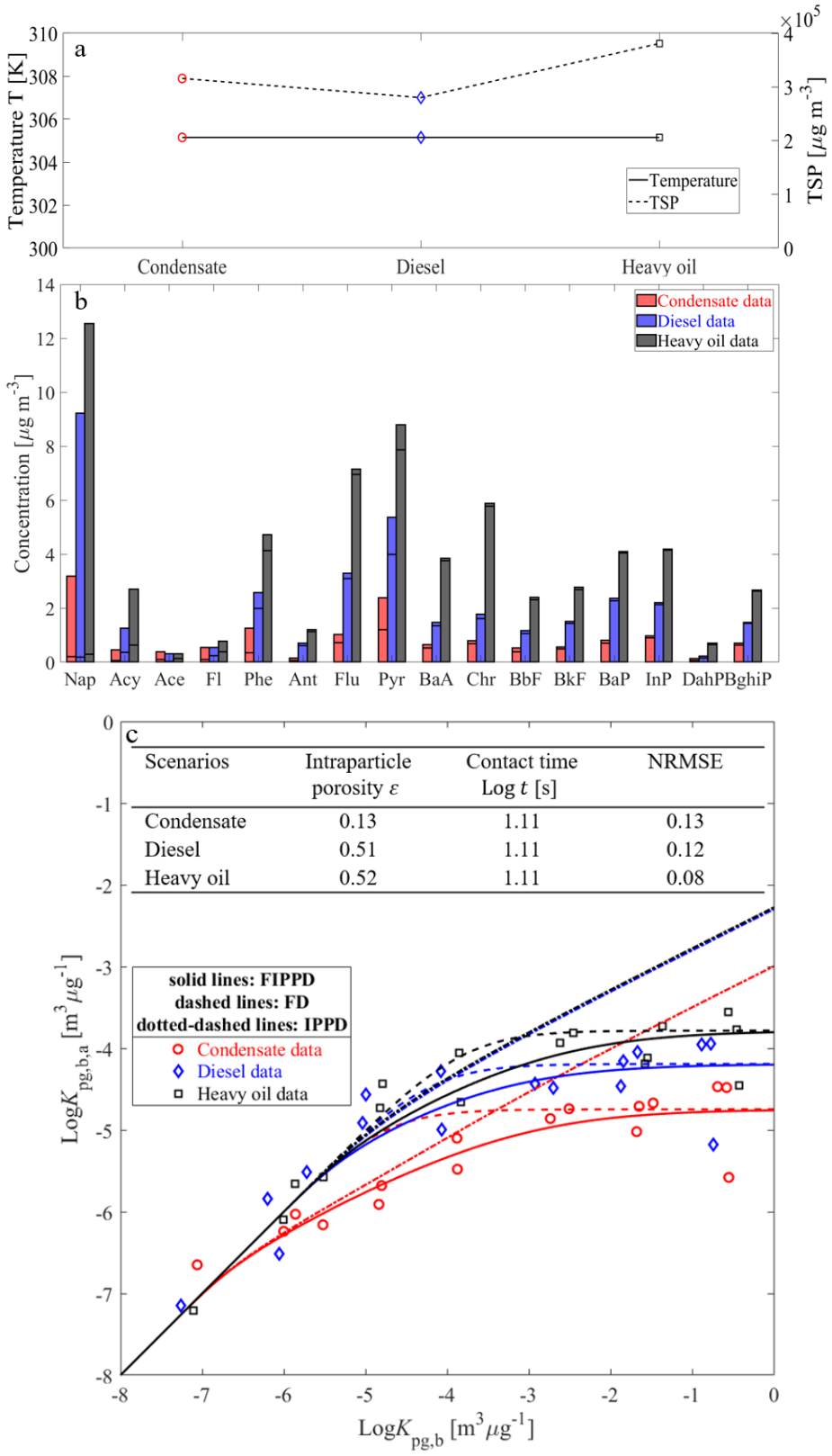

Fig. 4.4: Sixteen EPA targeted PAHs release from emission of oil combustion (condensate (red), diesel (blue), heavy oil (black)) in a lab chamber test. (a) Sampling temperature and total suspended particles concentrations (TSP). (b) Average (in duplicate) PAHs concentrations in the particle (lower part of column) and gas phase (upper part of column).

(c) Apparent particle/gas bulk distribution coefficients (Log$K_{pg,b,a}$) vs. expected equilibrium bulk particle/gas distribution coefficients (Log$K_{pg,b}$) from measurements (symbols) and kinetics modeling of film diffusion (FD), intraparticle pore diffusion (IPPD) and coupled film intraparticle pore diffusion (FIPPD); fitting parameters and normalized root mean square errors (NRMSE) of the optimal kinetics model are presented in table.

4.3.3.2 Case II: PAHs concentrations in airborne particles and atmosphere in a northern China city (Yuncheng) by considering the diurnal variation as well as the impact of domestic heating

For case II, data on PAHs monitoring in an urban northern China city was used (Sun et al., 2022). The airborne particle concentrations and sampling temperatures as well as PAHs concentrations in gaseous and particle phases are presented in Figs. 4.5a and b, respectively. BaA, Flu and Phe are known as typical for coal combustion (Sofowote et al., 2008) and Nap, Pyr, Chr and Flu are confirmed as PAHs produced from petroleum combustion (Yin et al., 2022). The concentrations of those PAHs (Nap, Phe, Flu, Pyr, BaA and Chr) during the heating period (black and magenta bars) are significantly higher than during the non-heating period (red and blue bars) due to the coal and petroleum combustions for domestic heating. Similar to case I, LMW PAHs are mainly occurred in gas phase, while HMW PAHs are primarily stored in particles. Equilibrium bulk particle/gas partitioning coefficients (Log$K_{pg,b}$) calculated from empirical relationships (Eqs. 4.3 and 4.4) are consistent with the measured bulk particle/gas partitioning coefficients (Log$K_{pg,b,a}$) for LMW PAHs (e.g., FI, Phe and Ant) and the dual model performs better than absorption model (see Fig. S4.5). Log$K_{pg,b,a}$ values of Nap, Ace and Acy are larger than predicted Log$K_{pg,b}$ and similar results are reported by Ma et al. (2020) and Li et al. (2022). The underestimation of Log$K_{pg,b}$ of empirical relationships for LMW PAHs (Nap, Ace and Acy) might be attributed to photooxidation reported by Shakya et al. (2010) leading to lower gaseous phase concentrations which result in higher measured Log$K_{pg,b,a}$ values. Similarly, breakthrough of gas phase PAHs in high volume air samplers could lead to losses of 30% or even more (e.g., 50% for Nap; lower C_g leading to higher Log$K_{pg,b}$) especially for compounds with molecular weights less than fluorene (e.g., Nap, Ace and Acy) and measurements are considered as semiquantitative (Fernández et al., 2002). As the LMW PAHs are assumed to reach equilibration very quickly, average deviations of FI, Phe and Ant between measured Log$K_{pg,b,a}$ and Log$K_{pg,b}$ estimated from empirical relationships are used for prediction of equilibrium Log$K_{pg,b}$ of LMW (Nap, Acy and Ace), MMW and HMW PAHs (similar to case I) and results are used as inputs of kinetics models. Modeling results are presented in Fig. 4.5c. Here, FD fits best for data from heating period, while the coupled model (FIPPD) is in line with the data from the non-heating period. The fitted intraparticle

porosities (ε) and contact times are around 0.3 and 2.2 h, respectively. Errors are relatively low (NRMSE < 0.1), which supports the suitability of the kinetics modeled. The fitted intraparticle porosities ($\varepsilon = 0.3$) are slightly lower than the intraparticle porosity of soot particles ($\varepsilon = 0.5$; see case I) probably due to the mixing of multiple sources of urban particles (e.g., dust, minerals, microplastics).

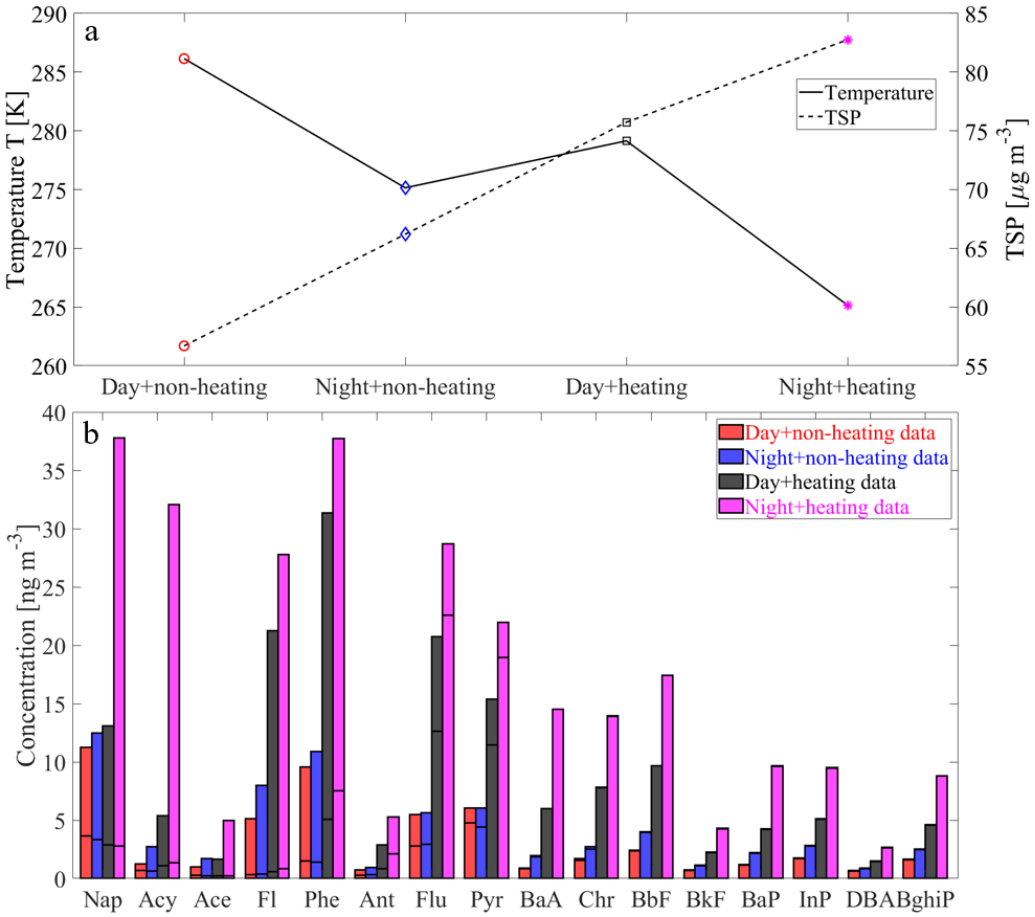

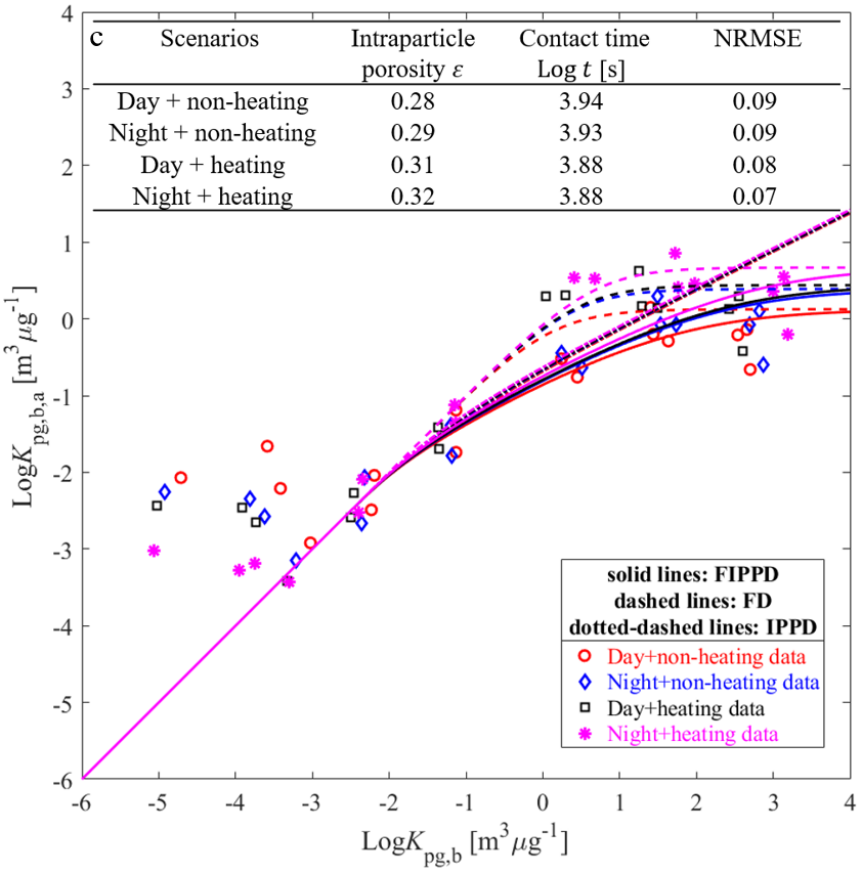

Fig. 4.5: Day/night and heating/non-heating impacts on concentrations of PAHs in atmosphere and airborne particles in a northern China city (Yuncheng). (a) Sampling temperature and total suspended particle concentrations (TSP). (b) Average PAHs concentrations in the particles (bottom part of bars) and gaseous phases (upper part of bars). (c) Apparent particle/gas bulk distribution coefficients (Log$K_{pg,b,a}$) vs. equilibrium bulk particle/gas distribution coefficients (Log$K_{pg,b}$) of measured data (symbols) and kinetic modeling results of film diffusion (FD), intraparticle pore diffusion (IPPD) and coupled film intraparticle pore diffusion (FIPPD). (Fitting parameters and normalized root mean square errors (NRMSE; excluding the data of Nap, Acy and Ace) of the best kinetics model are presented in the table.)

4.3.3.3 Case III: PAHs concentrations in the marine atmosphere monitored in a research cruise from the Western Pacific to the Southern Ocean

PAHs concentrations monitored in the marine atmosphere by Zhang et al. (2022) combined with temperatures (T) and airborne particle concentrations (TSP) of 32 sampling sites are shown in Fig. 4.6a; spatial distribution coefficients between solid and gas phase (data can be found in Tab. S4.8) are presented in Fig. 4.6b. The sites close to coastal cities (e.g., A1-A6 and A33-A36) show much higher total PAHs concentrations than the sampling sites far away

from human activities (e.g., polar regions such as A20-A26) due to predominant local PAHs emissions (e.g., combustion of fossil fuels) or natural sources such as biomass burning and transport from inland to ocean (Zolotov et al., 2000; Cabrerizo et al., 2014; Lima et al., 2005). LMW PAHs dominate total PAHs in remote areas (see Tab. S4.8 and Fig. 4.6b) because particles storing HMW PAHs are hardly transported to remote ocean or polar regions (except for very fine particles) (Kavouras et al., 2002). Phenanthrene (Phe) is the most abundant PAH found in the marine atmosphere, which is in line with sampling results obtained in cities (as shown in case II; see results of Phe). These results provide evidence for gas phase transport of LMW PAHs from terrestrial regions to marine atmosphere. The observed particle/gas partitioning coefficients of PAHs are much higher (2-3 magnitudes) than the predicted values from absorption model or dual model, especially for LMW PAHs (e.g., Acy, Ace, FI, Phe and Ant; see Fig. S4.6), which is consistent with the results reported by Cabrerizo et al. (2014) for PAHs sampling in the Antarctic and Southern Ocean atmosphere. One reason would be "aged" airborne particles (sampling in the remote regions) show higher fractions of strongly sorbing carbonaceous compounds resulting in higher Log$K_{pg,b}$ values (Pankow and Bidleman, 1991; Terzi et al., 2004). Much higher Log$K_{pg,b}$ values may also be expected if nonlinearity of sorption is considered. The underestimation of Log$K_{pg,b}$ of empirical relationships for PAHs might also be attributed to non-exchangeable organic matter stored in the airborne particles, leading to higher concentrations of PAHs in particle phase (Rounds et al., 1993). The organic matter content (f_{om} ranges from 1% to 5%) and elemental carbon fractions (f_{ec} ranges from 0.07% to 0.3%) for all sampling sites are very low in marine atmosphere (see Tab. S4.7) compared to the values obtained in urban space (e.g., f_{om} and f_{ec} range from 36% to 46% and 6% to 9%, respectively in case II.) despite the observed particle/gas partitioning coefficients (Log$K_{pg,b,a}$) in both cases cover similar ranges (roughly from -3.5 to 0.5). The much higher particle/gas partitioning coefficients (Log$K_{pg,b}$) than predicted (from Eqs. 4.3 and 4.4) might also owing to the properties of the organic matters where organic matters in the marine atmosphere particles present higher order of sorption capacity than organic matters containing in airborne particles in the urban city while the empirical relationships (Eqs. 4.3 and 4.4) assume constant sorption capacity for all organic matters. As many factors may result in the discrepancy of Log$K_{pg,b}$, further investigation is needed.

Since the LMW PAHs reach equilibration very fast (see Fig. 4.4) and airborne particles in the marine atmosphere have longer contact times due to long distance transport, the average deviation (2-3 logarithmic units) between measured particle/gas bulk distribution coefficients (Log$K_{pg,b,a}$) of LMW PAHs (FI, Phe and Ant) from equilibration models (e.g., absorption or dual model) is used to fit LogK_{pg} of MMW as well as HMW PAHs (similar in case I) in modelling. A constant grain size ($d = 2.5$ μm) is used and modeling results of 32

locations are presented in Fig. 4.6c. Compared to FD and IPPD, the coupled model (FIPPD) seems the optimal kinetics model for data fitting and the fitted intraparticle porosities (ε) and contact times of 32 locations ranges from 0.03 to 0.18 and 0.4 to 11.6 h, respectively. Errors are reasonably low (NRMSE are mostly less than 0.2), which supports the accuracy of the coupled model. The fitted intraparticle porosities of marine airborne particles are smaller than intraparticle porosities of urban airborne particles (around 0.3; see case II). One possible reason is that the marine airborne particles are composed of other particles besides dust, minerals etc. which have lower intraparticle porosities than urban airborne particles exhibiting slow kinetics for unknown reasons. For Phe and Ant (Acy, Ace and FI reach the equilibration and present a slope of 1.), mass transfer is dominated by IPPD and a shallow slope (close to 0.5) is presented, while FD dominates the mass transfer for HMW PAHs (e.g., InP, DahP and BghiP) and a maximum Log$K_{pg,b,a}$ domain shows up (slope approaches to 0). MMW PAHs are influenced by both FD and IPPD.

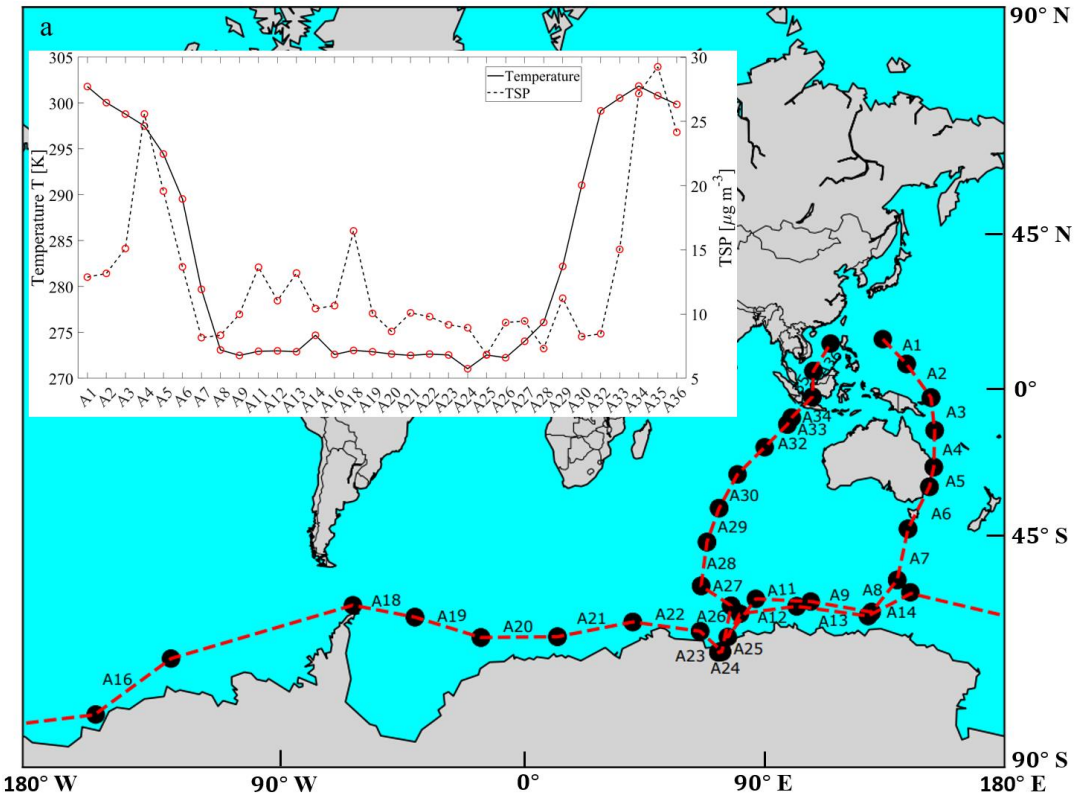

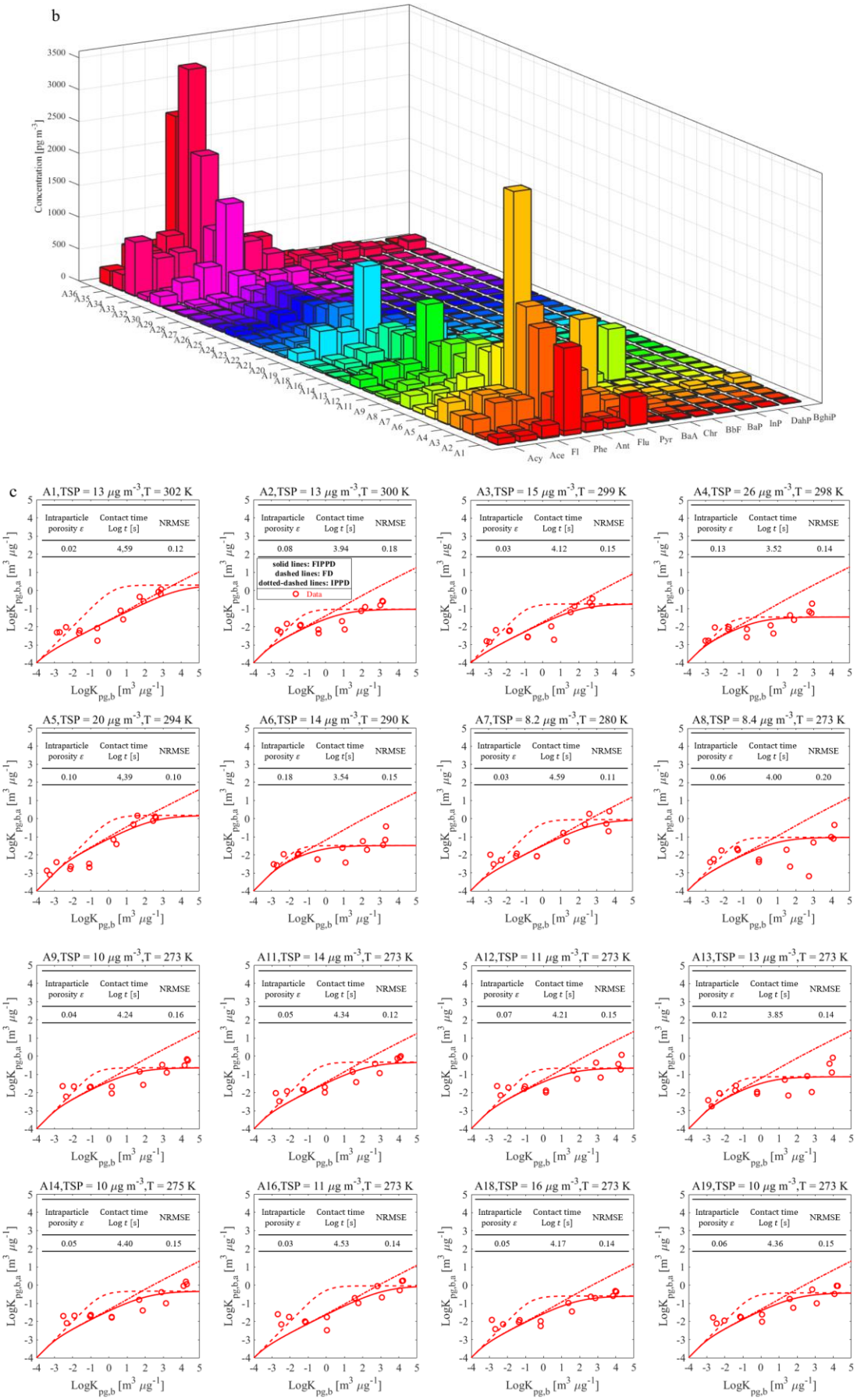
b
Concentration [pg m-3]
3500
3000
2500
2000
1500
1000
500
0
A36 A35 A34 A33 A32 A30 A29 A28 A27 A26 A25 A24 A23 A22 A21 A20 A19 A18 A16 A14 A13 A12 A11 A9 A8 A7 A6 A5 A4 A3 A2 A1
Acy Ace Fl Phe Ant Flu Pyr BaA Chr BbF BaP InP DahP BghiP
c
A1,TSP = 13 μg m-3,T = 302 K
A2,TSP = 13 μg m-3,T = 300 K
A3,TSP = 15 μg m-3,T = 299 K
A4,TSP = 26 μg m-3,T = 298 K
A5,TSP = 20 μg m-3,T = 294 K
A6,TSP = 14 μg m-3,T = 290 K
A7,TSP = 8.2 μg m-3,T = 280 K
A8,TSP = 8.4 μg m-3,T = 273 K
A9,TSP = 10 μg m-3,T = 273 K
A11,TSP = 14 μg m-3,T = 273 K
A12,TSP = 11 μg m-3,T = 273 K
A13,TSP = 13 μg m-3,T = 273 K
A14,TSP = 10 μg m-3,T = 275 K
A16,TSP = 11 μg m-3,T = 273 K
A18,TSP = 16 μg m-3,T = 273 K
A19,TSP = 10 μg m-3,T = 273 K
Intraparticle porosity ε
Contact time Log t [s]
NRMSE
0.02 4.59 0.12
0.08 3.94 0.18
0.03 4.12 0.15
0.13 3.52 0.14
0.10 4.39 0.10
0.18 3.54 0.15
0.03 4.59 0.11
0.06 4.00 0.20
0.04 4.24 0.16
0.05 4.34 0.12
0.07 4.21 0.15
0.12 3.85 0.14
0.05 4.40 0.15
0.03 4.53 0.14
0.05 4.17 0.14
0.06 4.36 0.15
solid lines: FIPPD
dashed lines: FD
dotted-dashed lines: IPPD
Data
LogKpg,b,a [m3 μg-1]
LogKpg,b [m3 μg-1]

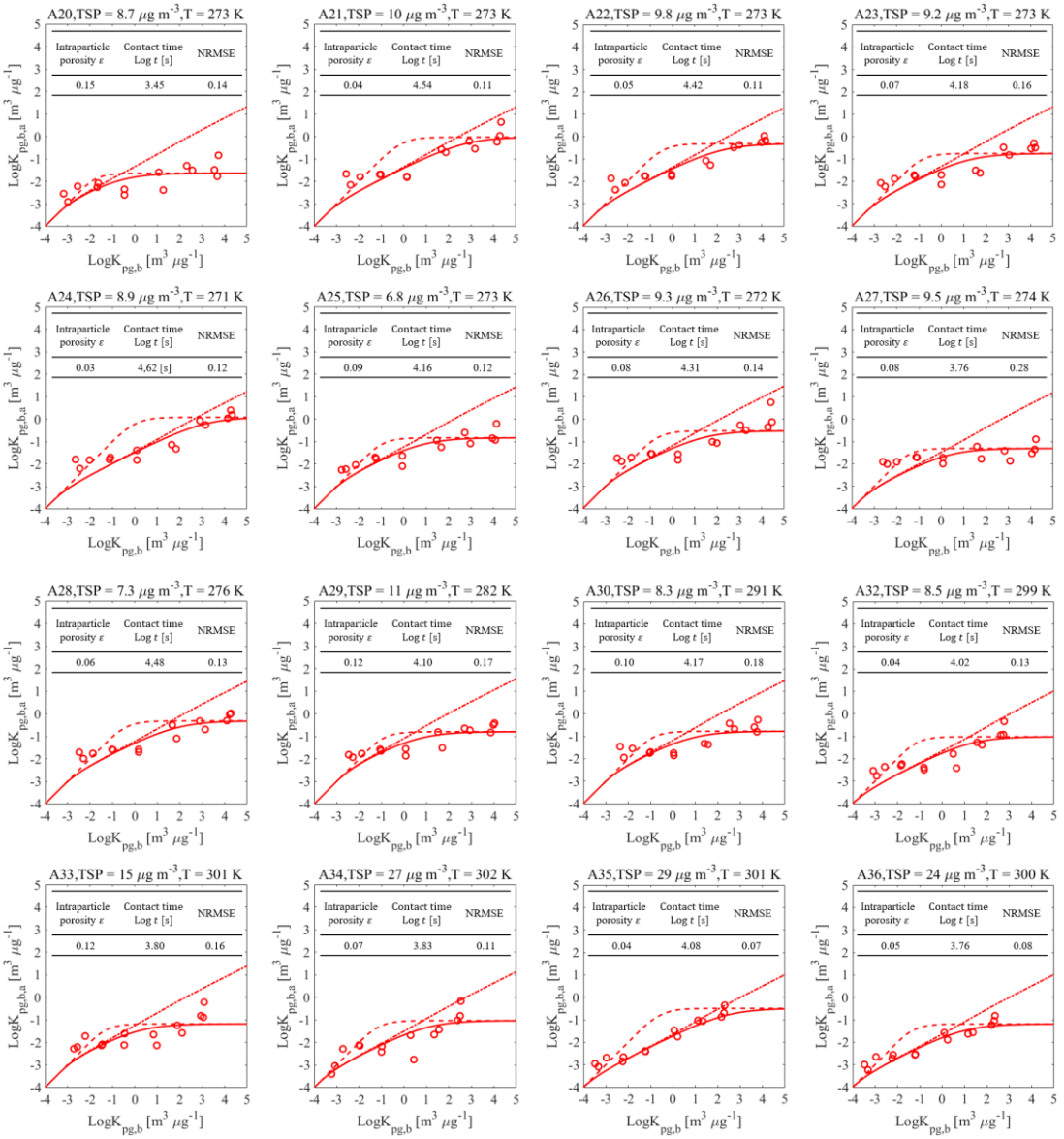

Fig. 4.6: Fourteen PAHs concentrations sampling in marine atmosphere from Western Pacific to Southern Ocean. (a) Track of research vessel and sampling locations (32 in total) as well as the respective information of sampling temperatures and total suspended particles concentrations (TSP). (b) Average PAHs concentrations in particles (bottom part of the histogram) and gaseous phases (upper part of the histogram). (c) Apparent particle/gas bulk distribution coefficients ($\mathrm{Log}K_{pg,b,a}$) vs. equilibrium bulk particle/gas distribution coefficients ($\mathrm{Log}K_{pg,b}$) of measured data (red symbols) and kinetics modeling results of film diffusion (FD), intraparticle pore diffusion (IPPD) and coupled film intraparticle pore diffusion (FIPPD) at 32 sampling locations. (Fitting parameters and normalized root mean square errors (NRMSE) of the best kinetics model are presented in tables.)

4.4 Conclusions

A coupled film intraparticle pore diffusion model is derived and allows to explain the slope deviations of measured particle/gas partitioning coefficients (Log$K_{pg,a}$) and equilibrium particle/gas partitioning coefficients (LogK_{pg}) by considering both external and internal mass transfer resistances. LMW PAHs (low LogK_{pg}) are dominated by intraparticle pore diffusion (IPPD) leading to a slope of 1/2, while HMW PAHs (high LogK_{pg}) are controlled by external film diffusion (FD) resulting in a maximum Log$K_{pg,a}$ (see Eq. 4.10); MMW PAHs are influenced by both FD and IPPD. The measured Log$K_{pg,a}$ of LMW PAHs can be utilized to calibrate equilibrium LogK_{pg} obtained from empirical relationships (Eqs. 4.3 and 4.4) due to short equilibration times. The empirical relationships work well for data sets from well-designed oil combustion experiments (case I) as well as PAHs sampling in the urban city (case II) with deviations less than 0.5 logarithmic unit for LMW PAHs, while the data set from PAHs sampling during a research ocean cruise shows much higher Log$K_{pg,b,a}$ than expected. These deviations observed in the marine atmosphere may be influenced by many factors (e.g., non-exchanged fraction, nonlinearity, contact time (age), photooxidation, breakthrough in air sampler, airborne particle origin, heterogeneity, etc.) and further investigations are needed. The validation of coupled model (FIPPD) is supported by three data sets covering the cases with varying contact times (from short to long) between airborne particles and bulk air. While there are a few subcases where film diffusion performs better, most of the results validate coupled model as the optimal model (NRMSE < 0.2) especially for data from PAHs sampling in the marine atmosphere (Case III, see Fig. 4.6). With the increase of intraparticle porosity, contact time or decrease of grain size of airborne particles, higher Log$K_{pg,a}$ values (much closer to equilibration) would obtain leading to equilibration (slope of 1) for LWM PAHs (see Fig. 4.3). The mass transfer shift from FD to IPPD would delay with the decrease of β ($= 1/(K_{pg,b}\mathrm{TSP})$) or increase of intraparticle porosity (see Fig. 4.2). Figuring out the origins (e.g., coal combustion, vehicle emission, dust, etc.) and properties of airborne particles (e.g., LogK_{pg}, intraparticle porosity, grain size distribution, organic matter content and category, elemental carbon content, etc.) are crucial for choosing suitable kinetics models. The coupled model not only can be used to estimate the mean ages of airborne particles, but also can be easily extended to describe the PAHs redistribution between heterogeneous airborne particles and bulk air (see Eqs. 4.20 and 4.22). Solving coupled model with semi-Laplace solution is fast and flexible compared to tedious numerical methods.

References

Balmer, J.E., Hung, H., Yu, Y., Letcher, R.J., Muir, D.C.G., 2019. Sources and environmental fate of pyrogenic polycyclic aromatic hydrocarbons (PAHs) in the Arctic. Emerg. Contam. 5, 128–142. https://doi.org/10.1016/j.emcon.2019.04.002.

Bond, T.C., Doherty, S.J., Fahey, D.W., Forster, P.M., Berntsen, T., Deangelo, B.J., Flanner, M.G., Ghan, S., Kärcher, B., Koch, D., Kinne, S., Kondo, Y., Quinn, P.K., Sarofim, M.C., Schultz, M.G., Schulz, M., Venkataraman, C., Zhang, H., Zhang, S., Bellouin, N., Guttikunda, S.K., Hopke, P.K., Jacobson, M.Z., Kaiser, J.W., Klimont, Z., Lohmann, U., Schwarz, J.P., Shindell, D., Storelvmo, T., Warren, S.G., Zender, C.S., 2013. Bounding the role of black carbon in the climate system: A scientific assessment. J. Geophys. Res. Atmos. 118, 5380–5552. https://doi.org/10.1002/jgrd.50171.

Boving, T.B., Grathwohl, P., 2001. Tracer diffusion coefficients in sedimentary rocks: Correlation to porosity and hydraulic conductivity. J. Contam. Hydrol. 53, 85–100. https://doi.org/10.1016/S0169-7722(01)00138-3.

Cabrerizo, A., Galbán -Malagón, C., Del Vento, S., Dachs, J., 2014. Sources and fate of polycyclic aromatic hydrocarbons in the Antarctic and Southern Ocean atmosphere. Global Biogeochem. Cycles. 28, 1424–1436. https://doi.org/https://doi.org/10.1002/2014GB004910.

Crank, J., 1975. The Mathematics of Diffusion. Second ed. Oxford University Press, London, pp. 69-88.

de Hoog, F.R., Knight, J.H., Stokes, A.N., 1982. An Improved Method for Numerical Inversion of Laplace Transforms. SIAM J. Sci. Stat. Comput. 3, 357–366. https://doi.org/10.1137/0903022.

Dachs, J., Eisenreich, S.J., 2000. Adsorption onto aerosol soot carbon dominates gas-particle partitioning of polycyclic aromatic hydrocarbons. Environ. Sci. Technol. 34, 3690–3697. https://doi.org/10.1021/es991201+.

Dachs, J., Ribes, S., Van Drooge, B., Grimalt, J., Eisenreich, S.J., Gustafsson, Ø., 2004. Response to the comment on “influence of soot carbon on the soil-air partitioning of polycyclic aromatic hydrocarbons.” Environ. Sci. Technol. 38, 1624–1625. https://doi.org/10.1021/es0307118.

Esmen, N.A., Corn, M., 1971. Residence time of particles in urban air. Atmos. Environ. 5, 571–578. https://doi.org/10.1016/0004-6981(71)90113-2.

Fernández, P., Grimalt, J.O., Vilanova, R.M., 2002. Atmospheric gas-particle partitioning of polycyclic aromatic hydrocarbons in high mountain regions of Europe. Environ. Sci. Technol.

36, 1162–1168. https://doi.org/10.1021/es010190t.

Fingas, M., 2017. Chapter 10 - In situ burning: an update. In: Fingas, M. (Ed.), Oil Spill Science and Technology (Second Edition). Gulf Professional Publishing, Boston, pp. 483–676.

Goss, K.U., Schwarzenbach, R.P., 1998. Gas/solid and gas/liquid partitioning of organic compounds: Critical evaluation of the interpretation of equilibrium constants. Environ. Sci. Technol. 32, 2025–2032. https://doi.org/10.1021/es9710518.

Grathwohl, P., 1990. Influence of organic matter from soils and sediments from various origins on the sorption of some chlorinated aliphatic hydrocarbons: Implications on K_{oc} correlations. Environ. Sci. Technol. 24, 1687–1693. https://doi.org/10.1021/es00081a010.

Grathwohl, P., 2014. On equilibration of pore water in column leaching tests. Waste Manag. 34, 908–918. https://doi.org/10.1016/j.wasman.2014.02.012.

Gustafson, K.E., Dickhut, R.M., 1994. Molecular Diffusivity of Polycyclic Aromatic Hydrocarbons in Air. J. Chem. Eng. Data. 39, 286–289. https://doi.org/10.1021/je00014a020.

Harner, T., Bidleman, T.F., 1998. Octanol-air partition coefficient for describing particle/gas partitioning of aromatic compounds in urban air. Environ. Sci. Technol. 32, 1494–1502. https://doi.org/10.1021/es970890r.

Kavouras, I.G., Stephanou, E.G., 2002. Particle size distribution of organic primary and secondary aerosol constituents in urban, background marine, and forest atmosphere. J. Geophys. Res. Atmos. 107, AAC 7-1-AAC 7-12. https://doi.org/10.1029/2000JD000278.

Li, H.L., Yang, P.F., Liu, L.Y., Gong, B.B., Zhang, Z.F., Ma, W.L., Macdonald, R.W., Nikolaev, A.N., Li, Y.F., 2022. Steady-state based model of airborne particle/gas and settled dust/gas partitioning for semivolatile organic compounds in the indoor environment. Environ. Sci. Technol. 56, 8373–8383. https://doi.org/10.1021/acs.est.1c07819.

Li, P.H., Wang, Y., Li, Y.H., Wai, K.M., Li, H.L., Tong, L., 2016. Gas-particle partitioning and precipitation scavenging of polycyclic aromatic hydrocarbons (PAHs) in the free troposphere in southern China. Atmos. Environ. 128, 165–174. https://doi.org/10.1016/j.atmosenv.2015.12.030.

Lima, A.L.C., Farrington, J.W., Reddy, C.M., 2005. Combustion-derived polycyclic aromatic hydrocarbons in the environment—A Review. Environ. Forensics. 6, 109–131. https://doi.org/10.1080/15275920590952739.

Liu, B., Finkel, M., Grathwohl, P., 2022. First order approximation for coupled film and intraparticle pore diffusion to model sorption/desorption batch experiments. J. Hazard.

Mater. 429, 128314. https://doi.org/10.1016/j.jhazmat.2022.128314.

Liu, B., Finkel, M., Qin, Q., Shi, W., Grathwohl, P., 2023. Mechanistic modelling of pollutant redistribution (sorption/desorption) in heterogeneous systems explaining unexpected slow kinetics (not published yet)

Liu, X., Zhao, D., Peng, L., Bai, H., Zhang, D., Mu, L., 2019. Gas–particle partition and spatial characteristics of polycyclic aromatic hydrocarbons in ambient air of a prototype coking plant. Atmos. Environ. 204, 32–42. https://doi.org/10.1016/j.atmosenv.2019.02.012.

Lohmann, R., Lammel, G., 2004. Adsorptive and absorptive contributions to the gas-particle partitioning of polycyclic aromatic hydrocarbons: State of knowledge and recommended parametrization for modeling. Environ. Sci. Technol. 38, 3793–3803. https://doi.org/10.1021/es035337q.

Ma, W., Zhu, F., Hu, P., Qiao, L., Li, Y., 2020. Gas/particle partitioning of PAHs based on equilibrium-state model and steady-state model. Sci. Total Environ. 706, 136029. https://doi.org/https://doi.org/10.1016/j.scitotenv.2019.136029.

Mai, H., Shiraiwa, M., Flagan, R.C., Seinfeld, J.H., 2015. Under what conditions can equilibrium gas-particle partitioning be expected to hold in the atmosphere? Environ. Sci. Technol. 49, 11485–11491. https://doi.org/10.1021/acs.est.5b02587.

Mu, L., Peng, L., Liu, X., Song, C., Bai, H., Zhang, J., Hu, D., He, Q., Li, F., 2014. Characteristics of polycyclic aromatic hydrocarbons and their gas/particle partitioning from fugitive emissions in coke plants. Atmos. Environ. 83, 202–210. https://doi.org/10.1016/j.atmosenv.2013.09.043.

Odabasi, M., Cetin, E., Sofuoglu, A., 2006. Determination of octanol-air partition coefficients and supercooled liquid vapor pressures of PAHs as a function of temperature: Application to gas-particle partitioning in an urban atmosphere. Atmos. Environ. 40, 6615–6625. https://doi.org/10.1016/j.atmosenv.2006.05.051.

Pankow, J.F., Bidleman, T.F., 1991. Effects of temperature, TSP and per cent non-exchangeable material in determining the gas-particle partitioning of organic compounds. Atmos. Environ. Part A, Gen. Top. 25, 2241–2249. https://doi.org/10.1016/0960-1686(91)90099-S.

Pankow, J.F., 1994. An absorption model of gas/particle partitioning of organic compounds in the atmosphere. Atmos. Environ. 28, 185–188. https://doi.org/10.1016/1352-2310(94)90093-0.

Parnis, J.M., Taskovic, T., Celsie, A.K.D., Mackay, D., 2020. Indoor dust/air partitioning: Evidence for kinetic delay in equilibration for low-volatility SVOCs. Environ. Sci. Technol. 54, 6723–6729. https://doi.org/10.1021/acs.est.0c00632.

Qiao, L. na, Zhang, Z. feng, Liu, L. yan, Song, W. wei, Ma, W. li, Zhu, N. zheng, Li, Y. fan, 2019. Measurement and modeling the gas/particle partitioning of organochlorine pesticides (OCPs) in atmosphere at low temperatures. Sci. Total Environ. 667, 318–324. https://doi.org/10.1016/j.scitotenv.2019.02.347.

Rounds, S.A., Pankow, J.F., 1990. Application of a radial diffusion model to describe gas/particle sorption kinetics. Environ. Sci. Technol. 24, 1378–1386. https://doi.org/10.1021/es00079a012.

Rounds, S.A., Tiffany, B.A., Pankow, J.F., 1993. Description of gas/particle sorption kinetics with an intraparticle diffusion model: desorption experiments. 27, 366–377. https://doi.org/10.1021/es00039a018.

Shakya, K.M., Griffin, R.J., 2010. Secondary organic aerosol from photooxidation of polycyclic aromatic hydrocarbons. Environ. Sci. Technol. 44, 8134–8139. https://doi.org/10.1021/es1019417.

Sofowote, U.M., Mccarry, B.E., Marvin, C.H., 2008. Source apportionment of PAH in Hamilton Harbour suspended sediments: Comparison of two factor analysis methods. Environ. Sci. Technol. 42, 6007–6014. https://doi.org/10.1021/es800219z.

Strommen, M.R., Kamens, R.M., 1997. Development and application of a dual-impedance radial diffusion model to simulate the partitioning of semi-volatile organic compounds in combustion aerosols. Environ. Sci. Technol. 31, 2983–2990. https://doi.org/10.1021/es970079g.

Strommen, M.R., Kamens, R.M., 1999. Simulation of semi-volatile organic compound microtransport at different time scales in airborne diesel soot particles. Environ. Sci. Technol. 33, 1738–1746. https://doi.org/10.1021/es981035q.

Sun, Y., Chen, J., Qin, W., Yu, Q., Xin, K., Ai, J., Huang, H., Liu, X., 2022. Gas-PM2.5 partitioning, health risks, and sources of atmospheric PAHs in a northern China city: Impact of domestic heating. Environ. Pollut. 313, 120156. https://doi.org/10.1016/j.envpol.2022.120156.

Terzi, E., Samara, C., 2004. Gas-particle partitioning of polycyclic aromatic hydrocarbons in urban, adjacent coastal, and continental background sites of western Greece. Environ. Sci. Technol. 38, 4973–4978. https://doi.org/10.1021/es040042d.

van Noort, P.C.M., 2003. A thermodynamics-based estimation model for adsorption of organic compounds by carbonaceous materials in environmental sorbents. Environ. Toxicol. Chem. 22, 1179–1188. https://doi.org/10.1002/etc.5620220601.

Wang, W., Simonich, S., Giri, B., Chang, Y., Zhang, Y., Jia, Y., Tao, S., Wang, R., Wang, B., Li, W., Cao, J., Lu, X., 2011. Atmospheric concentrations and air-soil gas exchange of polycyclic aromatic

hydrocarbons (PAHs) in remote, rural village and urban areas of Beijing-Tianjin region, North China. Sci. Total Environ. 409, 2942–2950. https://doi.org/10.1016/j.scitotenv.2011.04.021.

Yin, F., He, Z., Song, Z., Zhang, W., Li, X., Qin, B., Zhang, L., Su, P., Zhang, J., Kitazawa, D., 2022. Gas-particle partitioning of polycyclic aromatic hydrocarbons from oil combustion involving condensate, diesel and heavy oil. Ecotoxicol. Environ. Saf. 242, 113866. https://doi.org/10.1016/j.ecoenv.2022.113866.

Yu, H., Yu, J.Z., 2012. Polycyclic aromatic hydrocarbons in urban atmosphere of Guangzhou, China: Size distribution characteristics and size-resolved gas-particle partitioning. Atmos. Environ. 54, 194–200. https://doi.org/10.1016/j.atmosenv.2012.02.033.

Zhao, J., Zhang, F., Chen, J., Xu, Y., 2010. Characterization of polycyclic aromatic hydrocarbons and gas/particle partitioning in a coastal city, Xiamen, Southeast China. J. Environ. Sci. 22, 1014–1022. https://doi.org/10.1016/S1001-0742(09)60212-6.

Zhao, F., Riipinen, I., Macleod, M., 2021. Steady-state mass balance model for predicting particle-gas concentration ratios of PBDEs. Environ. Sci. Technol. 55, 9425–9433. https://doi.org/10.1021/acs.est.0c04368.

Zhang, X., Zhang, Z.F., Zhang, X., Zhu, F.J., Li, Y.F., Cai, M., Kallenborn, R., 2022. Polycyclic aromatic hydrocarbons in the marine atmosphere from the Western Pacific to the Southern Ocean: Spatial variability, gas/particle partitioning, and source apportionment. Environ. Sci. Technol. https://doi.org/10.1021/acs.est.1c08429.

Zhu, F.J., Ma, W.L., Liu, L.Y., Zhang, Z.F., Song, W.W., Hu, P.T., Li, W.L., Qiao, L.N., Fan, H.Z., 2021. Temporal trends of atmospheric PAHs: Implications for the gas-particle partition. Atmos. Environ. 261, 118595. https://doi.org/10.1016/j.atmosenv.2021.118595.

Zolotov, M.Y., Shock, E.L., 2000. A thermodynamic assessment of the potential synthesis of condensed hydrocarbons during cooling and dilution of volcanic gases. J. Geophys. Res. Solid Earth. 105, 539–559. https://doi.org/https://doi.org/10.1029/1999JB900369.

5 Mass transfer principles in column percolation tests: Initial conditions and tailing in heterogeneous materials

Binlong Liu, Michael Finkel, Peter Grathwohl

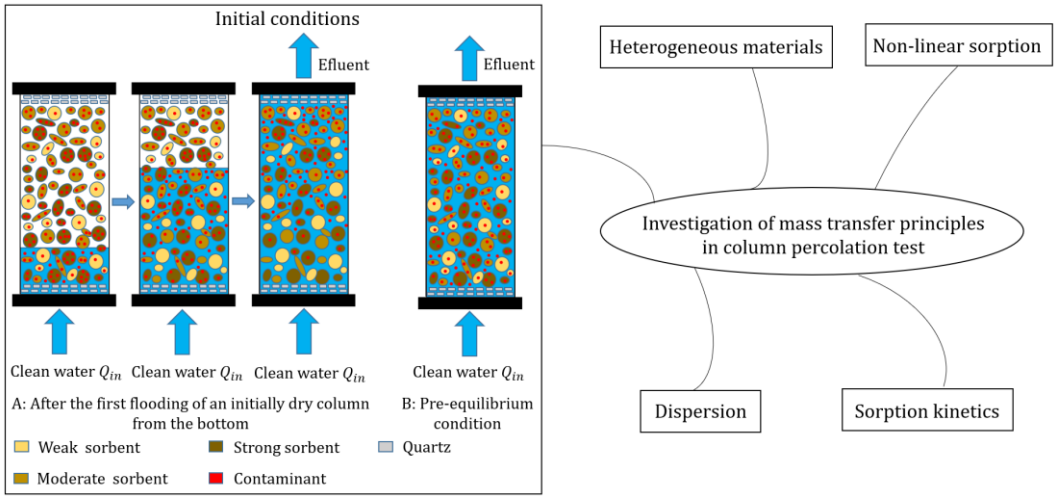

Abstract

Initial conditions (pre-equilibrium or after the first flooding of the column), mass transfer mechanisms and sample composition (heterogeneity) have a strong impact on leaching of less and strongly sorbing compounds in column percolation tests. Mechanistic models as used in this study provide the necessary insight to understand the complexity of column leaching tests especially when heterogeneous samples are concerned. By means of numerical experiments, we illustrate the initial concentration distribution inside the column after the first flooding and how this impacts leaching concentrations. Steep concentration gradients close to the outlet of the column have to be expected for small distribution coefficients ($K_d <$ 1 L kg^{-1}) and longitudinal dispersion leads to smaller initial concentrations than expected under equilibrium conditions. In order to elucidate the impact of different mass transfer mechanisms, film diffusion across an external aqueous boundary layer (first order kinetics, FD) and intraparticle pore diffusion (IPPD) are considered. The results show that IPPD results in slow desorption kinetics due to retarded transport within the tortuous intragranular pores. Non-linear sorption has not much of an effect if compared to K_d values calculated for the appropriate concentration range (e.g., the initial equilibrium

concentration). Sample heterogeneity in terms of grain size and different fractions of sorptive particles in the sample have a strong impact on leaching curves. A small fraction (< 1%) of strongly sorbing particles (high K_d) carrying the contaminant may lead to very slow desorption rates (because of less surface area) - especially if mass release is limited by IPPD – and thus non-equilibrium. In contrast, mixtures of less sorbing fine material ("labile" contamination with low K_d), with a small fraction of coarse particles carrying the contaminant leads to leaching close to or at equilibrium showing a stepwise concentration decline in the column effluent.

5.1 Introduction

Leaching tests are widely used for the determination of contaminant release rates from soils (Kalbe et al., 2014; Löv et al., 2019; Inui et al., 2019; Röhler et al., 2021) , recycling materials (Tsiridis et al., 2015; Di Gianfilippo et al., 2016; Chan et al., 2018; Lange et al., 2019; Kumar et al., 2019; Liu et al., 2020; Zhu et al., 2021), construction products (Schwab et al., 2014; Butera et al., 2015; Bandow et al., 2019; Diotti et al., 2020; Liu et al, 2020), radioactive and other waste materials (Molleda et al., 2020; Chen et al., 2021). Compared to traditional batch shaking tests, column tests are preferred for assessing the risk of release of potential pollutants into groundwater or surface waters because they are closer to natural conditions (Grathwohl et al., 2007; Susset et al., 2011). Different mechanisms controlling desorption kinetics may result in complex leaching behaviors. While initially the observed column effluent concentration often reflects equilibrium conditions between the solid phase (incl. intraparticle pores) and the mobile aqueous phase (Grathwohl et al., 2009; Grathwohl, 2014), the concentrations decrease and often an extended tailing is observed due to slow desorption processes such as intraparticle diffusion (Grathwohl et al., 1993; Rügner et al., 1999; Wang et al., 2007).

Although most leaching test procedures aim at equilibrium conditions in the column before the leaching starts, the true concentration distribution before the start of the percolation depends not only on the test procedure (contact time, pre-equilibration time, flow velocity during first flooding) but also on the properties of both the solid material and the pollutant of interest (Finkel et al., 2017). Equilibration and long-term leaching are further complicated if the test sample consists of a heterogeneous mixture of different material types and grain sizes (Kleineidam et al., 1999; Jäger et al., 2000; Finkel et al., 2017), which is the common case if waste materials such as demolition waste or soils are tested.

Finkel and Grathwohl (2017) evaluated the role of initial conditions for column leaching tests with intraparticle pore diffusion models by comparing the hypothetical scenarios, a

perfectly equilibrated column vs. a column that wasn't equilibrated at all. They could show that in many practical cases, peak and cumulative leachate concentrations are rather independent of the initial conditions. However, if release kinetics are slow due to large grain size or small intragranular porosity, the sensitivity to initial conditions is relevant, in particular for initial peak and early cumulative leachate concentrations.

The shortcoming of all previous studies (Xiao et al., 2015; Finkel et al., 2017; Yin et al., 2020), is that only uniform initial concentrations in the columns were considered in the leaching models. However, due to the specific conditions during the flooding of the column filled with initially dry material, the true initial conditions at the start of the leaching test may considerably deviate from this ideal, i.e., uniform distribution.

Against this background, the objectives of this study are (i) to illustrate the possibly non-uniform initial conditions that may be achieved after the first flooding of the column, (ii) to show the impact of these initial conditions on the temporal development of the effluent concentrations, and (iii) to investigate how heterogeneous mixtures of particles having different properties affect both the initial conditions in the column and the leaching of the solutes. To achieve that, we used numerical solutions for flow and transport in a column coupled to two kinetic models: (i) solute diffusion through an aqueous boundary layer and (ii) intraparticle pore diffusion. The implementation of the numerical models is described in detail in the supplementary information (see section S5).

5.2 Theory and background

5.2.1 Local equilibrium: the advection-dispersion equation

In order to facilitate the understanding of mass transfer-limited cases of contaminant release in a column, we briefly introduce the equilibrium case for which the advection-dispersion model is commonly used:

$$\frac{\partial}{\partial t}(nC_w + \rho_b C_s) + \frac{\partial}{\partial x}\left(nvC_w - nD_L\frac{\partial C_w}{\partial x}\right) = 0 \qquad (5.1)$$

where v [L T^{-1}], n [-] and D_L ($= \alpha v + D_p$) [L^2 T^{-1}] denote the seepage velocity of the water, the intergranular porosity and the longitudinal dispersion coefficient. α [L], D_p ($= nD_{aq}$) [L^2 T^{-1}] and D_{aq} [L^2 T^{-1}] denote the dispersivity, the pore diffusion coefficient and the aqueous diffusion coefficient of the solute. x [L] and t [T] are the length of the column and time. ρ_b ($= (1-n)\rho_s$) [M L^{-3}] is the dry bulk density of the packed bed in the column (porous media; ρ_s is the solids density). For local equilibrium conditions the concentration in the solid phase

(C_s) is in equilibrium with the solute concentration in water (C_w) and the distribution coefficient K_d ($= C_s/C_w$) allowing for the calculation of the respective concentrations. Under these conditions, Eq. 5.1 can be simplified as:

$$\frac{\partial C_w}{\partial t} = \frac{D_L}{R_d}\frac{\partial^2 C_w}{\partial x^2} - \frac{v}{R_d}\frac{\partial C_w}{\partial x} \tag{5.2}$$

where R_d [-] represents the retardation factor, defined as:

$$R_d = 1 + K_d\frac{\rho_b}{n} \tag{5.3}$$

Assuming equilibrium conditions and an initially uniform distribution of the solute in the column, leaching may be described by the analytical solution of Eq. 5.2 (Ogata et al., 1961):

$$\frac{C_w}{C_{w,eq}} = 1 - 0.5\left[\operatorname{erfc}\left(\frac{x - \frac{v}{R_d}t}{2\sqrt{\frac{D_L}{R_d}t}}\right) + \exp\left(\frac{v\,x}{D_L}\right)\operatorname{erfc}\left(\frac{x + \frac{v}{R_d}t}{2\sqrt{\frac{D_L}{R_d}t}}\right)\right] \tag{5.4}$$

where erfc denotes the complementary error function. The aqueous concentration at equilibrium, $C_{w,eq}$, can be calculated from the initial solid concentration ($C_{s,ini}$) accounting for the mass balance when the contaminant mass in the water is equilibrated with the mass in the solid:

$$C_{w,eq} = \frac{C_{s,ini}}{K_d + \frac{n}{\rho_b}} \tag{5.5}$$

The ratio n/ρ_b [$L^3\ M^{-1}$] equals the liquid to solid ratio within the column, which in most cases is much smaller than in a batch leaching test (e.g., 0.25 L kg^{-1} for a column test with a porosity of $n = 0.4$ and a solid density of $\rho_b = 2.65$ g cm^{-3}, compared to e.g., 10 L kg^{-1} in a batch test). Since leaching tests start for practical reasons with material packed more or less dry into the column, a uniform initial concentration is not necessarily achieved during the first flooding of the column. Initial conditions as assumed in Eq. 5.4 (uniform concentration distribution), would only be achieved if the material is first mixed with water, equilibrated and then packed into the column, which is not practical. During the first flooding of the column, especially less sorbing solutes are displaced from the inlet and higher concentrations occur towards the outlet, as illustrated in Fig. 5.1 (see also section S5.5). This may be accounted for by subtracting the distance of the solute displaced initially (x/R_d with $R_d > 1$) in Eq. 5.4:

$$\frac{C_w}{C_{w,eq}} = 1 - 0.5\left[\operatorname{erfc}\left(\frac{\left(x - \frac{x}{R_d}\right) - \frac{v}{R_d}t}{2\sqrt{\frac{D_L}{R_d}t}}\right) + \exp\left(\frac{v\left(x - \frac{x}{R_d}\right)}{D_L}\right)\operatorname{erfc}\left(\frac{\left(x - \frac{x}{R_d}\right) + \frac{v}{R_d}t}{2\sqrt{\frac{D_L}{R_d}t}}\right)\right] \quad (5.6)$$

In this case the initial solute concentration ($C_{w,eq}$) in the column effluent is in equilibrium with the initial concentration in the solids ($C_{w,eq} = C_{s,ini}/K_d$) and higher than calculated in Eq. 5.5 especially if K_d values are low.

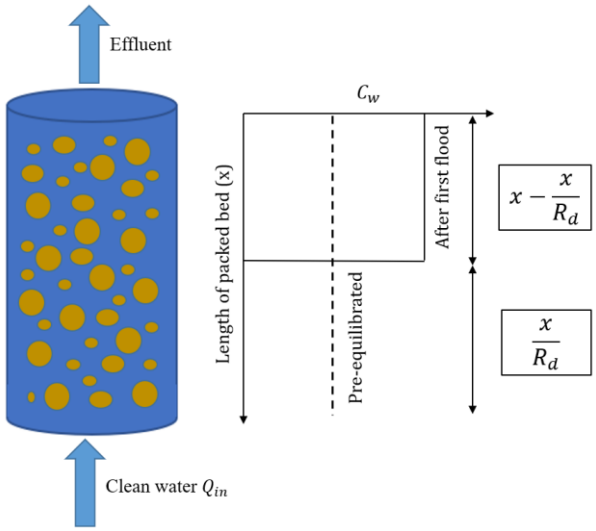

Fig. 5.1: Initial concentration distribution in a column of length x for the "pre-equilibrated" case (dashed line) and after the first flooding of an initially dry column from the bottom (solid line); no dispersion, $R_d = 2$, after Grathwohl and Susset, 2009.

In order to explore the influence of mass transfer limitations on initial and long-term solute concentrations in column tests, two relevant mass transfer mechanisms are compared: (1) film diffusion where diffusion from the solid-water interface occurs through an aqueous boundary layer with a given thickness and (2) intraparticle pore diffusion where diffusion inside the porous particle limits mass transfer.

5.2.2 Desorption kinetics limited by film diffusion

The simplest model for the kinetic release of a solute from solids considers diffusion through an aqueous boundary layer surrounding spherical particles (Fig. 5.2). Such film diffusion

models are also widely used for the dissolution of minerals with high solubilities (e.g., salts). The solute release from the solid surface into the bulk water phase can be described by a linear driving force with constant mass transfer coefficient $k = D_{aq}/\delta_{aq}$:

$$\frac{\partial C_w}{\partial t} = k\, A^o (C'_w - C_w) = \frac{D_{aq}}{\delta_{aq}} \frac{m_d\, 6}{\rho_s\, d\, V_w} (C'_w - C_w) \tag{5.7}$$

where δ_{aq} [L], V_w [L^3], m_d [M] and d [L] denotes the thickness of the external film, the volume of water, the dry mass of the solids in the column and the particle diameter, respectively. A^o $(= 6\, m_d/(V_w\, \rho_s\, d))$ is the specific surface area of the particles per unit volume of water in the column [m^2 m^{-3} = m^{-1}] (the term $6/\rho_s\, d$) represents the specific surface area of spherical particles per dry mass, e.g., in m^2 g^{-1}). C'_w is the concentration at the solid-water interface where local equilibrium conditions apply ($C'_w = C_s/K_d$). The external film thickness (δ_{aq}) can be estimated from empirical Sherwood numbers (Sh) and the particle diameter (d):

$$Sh = \frac{kd}{D_{aq}} = \frac{d}{\delta_{aq}} \quad \rightarrow \quad \delta_f = \frac{d}{Sh} \tag{5.8}$$

For an overview on empirical relationships for the estimation of Sherwood numbers see section S5.1. The mass balance in such two-phase systems expressed by their respective rates is:

$$V_w \frac{\partial C_w}{\partial t} = -\, m_d \frac{\partial C_s}{\partial t} \tag{5.9}$$

Thus, the solute mass gained (or lost) by the water phase equals the solute mass lost (or gained) from the solid phase. If V_w and m_d in a packed bed (porous media) are replaced by n and ρ_b, the density of the solids (ρ_s) in Eq. 5.7 drops out. Film diffusion coupled to the one-dimensional advection-dispersion equation (Eq. 5.1) yields:

$$\frac{\partial C_w}{\partial t} = D_L \frac{\partial^2 C_w}{\partial x^2} - v \frac{\partial C_w}{\partial x} + \frac{D_{aq}}{\delta_{aq}} \frac{6\,(1-n)}{n\, d} \left(\frac{C_s}{K_d} - C_w \right) \tag{5.10}$$

Using the finite volume method, the column is spatially discretized by a number of cells (see Fig. S5.1) and the governing equation (Eq. 5.10) is solved iteratively by employing the Newton–Raphson scheme. Details of the numerical solution of the film diffusion model are presented in section S5.2.

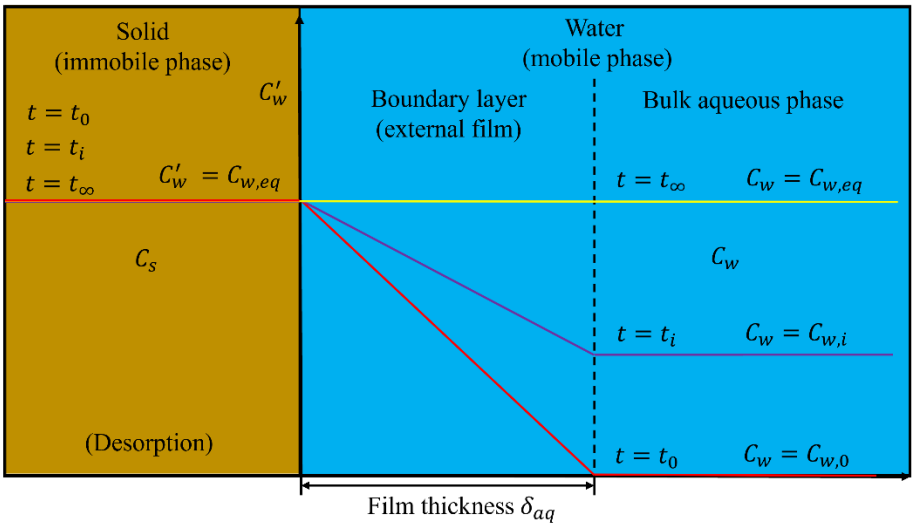

Fig. 5.2: Scheme of mass transfer limited by film diffusion during the first flooding with fixed concentration at the interface (because the infiltrating water is always contacting fresh material as it advances).

5.2.3 Desorption limited by intraparticle pore diffusion

If the release of compounds from the solid phase is governed by intra-granular diffusion, e.g., within a porous grain (Fig. 5.3), then mass transfer is described by Fick's second law in radial coordinates:

$$\frac{\partial}{\partial t}\left(\varepsilon C_{w,p} + \rho_p C_s\right) = D_e\left[\frac{\partial^2 C_{w,p}}{\partial r^2} + \frac{2}{r}\frac{\partial C_{w,p}}{\partial r}\right] \tag{5.11}$$

with the boundary conditions

$$C_{w,p}(r = a, t) = C_w \tag{5.12}$$

$$\frac{\partial C_{w,p}}{\partial r}(r = 0, t) = 0 \tag{5.13}$$

r [L] is the radial coordinate in the sphere and D_e [L^2 T^{-1}] the effective diffusion coefficient. $C_{w,p}$ [M L^{-3}] is the concentration of solute in the intra-granular pore water. ε [-] denotes the intraparticle porosity. a [L] and ρ_p [M L^{-3}] ($= \rho_s(1-\varepsilon)$) denote the radius and bulk density of the particle (sphere).

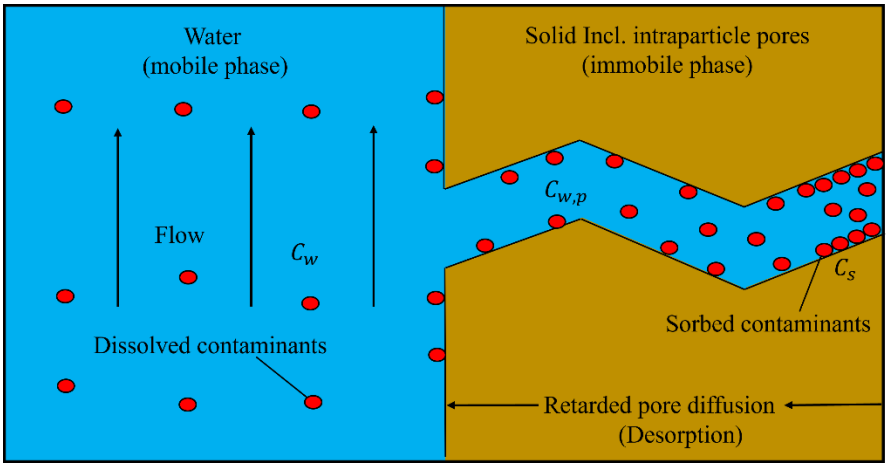

Fig. 5.3: Scheme of mass transfer limited by intraparticle pore diffusion.

For linear sorption with concentration independent distribution coefficients (i.e., $C_s = K_d C_{w,p}$) Eq. 5.11 becomes:

$$\frac{\partial C_{w,p}}{\partial t} = D_a \left[\frac{\partial^2 C_{w,p}}{\partial r^2} + \frac{2}{r} \frac{\partial C_{w,p}}{\partial r} \right] \tag{5.14}$$

where D_a [L² T^{-1}] is the apparent diffusion coefficient, defined as:

$$D_a = \frac{D_e}{\varepsilon + K_d \rho_p} = \frac{D_{aq} \varepsilon}{\tau(\varepsilon + K_d \rho_p)} \approx \frac{D_{aq} \varepsilon^2}{\varepsilon + K_d (1-\varepsilon) \rho_s} \tag{5.15}$$

Empirical studies showed that D_e increases approximately with the square of the porosity (Boving et al., 2001). This corresponds to a tortuosity τ [-] of the intra-granular pores - if expressed as a function of intra-granular porosity - of $\tau \approx 1/\varepsilon$.

Considering intraparticle diffusion, the advection-dispersion model (Eq. 5.1) can be rewritten as:

$$\frac{\partial}{\partial t}\left(nC_w + (1-n)(\varepsilon C_{w,p} + \rho_p C_s)\right) + \frac{\partial}{\partial x}\left(nvC_w - nD_L \frac{\partial C_w}{\partial x}\right) = 0 \tag{5.16}$$

The corresponding equilibrium concentration ($C_{w,eq}$) in water after first flooding can be rewritten as $C_{w,eq} = C_{s,ini}/(\varepsilon/\rho_p + K_d)$, which is slightly lower than for non-porous solids ($C_{w,eq} = C_{s,ini}/K_d$) because the intragranular pore space is assumed to be initially free of water. The deviation becomes insignificant with the increase of K_d ($\varepsilon/\rho_p + K_d \approx K_d$ when $K_d \gg \varepsilon/\rho_p$).

Coupling the intraparticle pore diffusion model (Eq. 5.11) to the one-dimensional advection-dispersion equation (Eq. 5.16) allows for the expression of the change of the solute

concentration in the bulk water:

$$\frac{\partial C_w}{\partial \mathrm{t}} = D_L \frac{\partial^2 C_w}{\partial x^2} - v\frac{\partial C_w}{\partial x} - \frac{(1-n)}{n} D_e \left[\frac{\partial^2 C_{w,p}}{\partial r^2} + \frac{2}{r}\frac{\partial C_{w,p}}{\partial r}\right] \tag{5.17}$$

The intraparticle pore diffusion model (Eqs. 5.11–5.13) was implemented numerically using a finite volume method where the spherical particle was discretized by a number of spherical shells of equal volume (based on the method of Jäger and Liedl (2000)). The column was spatially discretized by a number of cells (see Fig. S5.1) and all the governing equations (Eqs. 5.11–5.13 and Eq. 5.17) were solved iteratively applying the Newton–Raphson scheme. Compared to the 1D film diffusion case, the intraparticle pore diffusion case is more complicated and becomes a 2D problem. Details of the numerical solution of the intraparticle pore diffusion model are given in section S5.3.

5.2.4 Set-up of "numerical" column tests

The boundary conditions of the numerical experiments are based on the set-up of column tests in daily practice in Germany (Kalbe et al., 2007 and 2008; Grathwohl et al., 2009). Table 5.1 lists the relevant material properties and the parameter ranges applied. The saturation time for the first pore volume of the column and the contact time (after the first flooding period) were set to 5 h. Initially, experiments with uniform materials were simulated where the intraparticle porosity, distribution coefficient, aqueous diffusion coefficient and tortuosity were set the same for each grain size fraction. The Sherwood number in packed beds was estimated based on the empirical formula proposed by Liu et al. (2014) (Eq. S5.3). In order to illustrate the influence of longitudinal dispersion on the initial concentration distribution in the column after the first flooding, we used fine particles ($d_{p,fine} = 63$ µm) where kinetics are very fast, and the local equilibrium assumption is valid. The numerical model did not consider dispersion beyond the outlet of the column. Non-linear sorption was simulated using the Freundlich model ($C_s = K_{fr} C_w^{\frac{1}{n}}$ where K_{fr} and $1/n$ denote the Freundlich coefficient and Freundlich exponent, respectively).

Many factors may contribute to sample heterogeneity, such as grain size distribution and particle properties (sorption, porosities, etc.). To highlight the impact of particle size and properties we focused on two grain size classes and different fractions of sorptive/reactive particles in the sample. Distribution coefficients were varied in a range of 0.1-100 L kg^{-1}. Lower K_d values (< 0.1 L kg^{-1}) were not considered here (this would have resulted in very high initial aqueous concentrations). If the K_d values become large (K_d > 100 L kg^{-1}), then the

differences between the pre-equilibrated case and the "first flooding" scenario vanish and effluent concentrations are constant over long time periods. The K_d range chosen covers many frequent environmental contaminants, such as per- and polyfluoroalkyl substances (PFAS), chlorinated solvents, polycyclic aromatic hydrocarbons and some heavy metals.

Tab. 5.1: Summary of parameter values and ranges used to set up the numerical experiments.

Property	**Symbol (Unit)**	**Reference and [Alternative Values]**
Net column length	X_{col} (cm)	30
Inner column diameter	D_c (cm)	5.46
Total volume of column	V_{tot} (L)	0.70
Dry solid density	ρ_s (kg L^{-1})	2.60
Inter-granular porosity	n (-)	0.45
Solid mass in column	m_d (kg)	1
Liquid to solid ratio in column	LS_{col} (L kg^{-1})	0.31
Initial concentration in solid phase	$C_{s,ini}$ (µg kg^{-1})	1000
Contact time	t_c (h)	5
Dispersivity	α (m)	[0, 0.03]
Water flow velocity	v (m s^{-1})	1.67×10^{-5}
Aqueous diffusion coefficient	D_{aq} (m^2 s^{-1})	1×10^{-9}
Particle diameters	d (µm)	[63, 2000]
Distribution coefficients	K_d (L kg^{-1})	[0.1, 1, 10, 100]
Freundlich coefficients	K_{fr} (µg kg^{-1}:(µg L^{-1})$^{1/n}$)	[1.58, 7.94, 39.81]
Freundlich exponent	$1/n$	0.7
Sherwood number	$Sh = 2 + 0.1Pe^{1/2}$ (-)	2.31

5.3 Results and discussions

5.3.1 Impact of initial conditions on leaching

In order to investigate the impact of initial conditions on leaching behavior, we compared two scenarios: (1) a column filled with pre-equilibrated material where the initial concentration distribution in the column was uniform ($C_{w,eq} = C_{s,ini}/(K_d + \frac{n}{\rho_b})$) and (2) columns with non-uniform concentration distributions after first flooding where concentrations increased towards the outlet (to a maximum of $C_{w,eq} = C_{s,ini}/K_d$) while at the inlet the solute was already depleted. To illustrate this, we used the film diffusion model with fine grain sizes, and thus, fast kinetics (local equilibrium conditions). Figure 5.4 shows the initial aqueous concentration distribution in the up-flow column test after the first flooding of the column compared to the pre-equilibrium case. The results show that the differences in the initial concentration profiles became smaller with increasing sorption. At high K_d values,

the deviation of the initial concentration profiles only occurred at the inlet of the column. At low K_d values, very high concentrations are expected at the column outlet; in extreme cases this may lead to a density increase in the leachate and - especially if flow is stopped - to density driven flow within the column. This would cause dilution and lower leachate concentrations when the flow is restarted as was potentially observed by Naka et al. (2016). Density driven mixing may be caused by soluble materials, e.g., sulphate or other salts and not necessarily the target compounds. This phenomenon is quite similar to the case where the dispersion is taken into account (see bottom curves of Fig. 5.4 and also Figs. S5.5-S5.12 in section S5.6), which leads to more "mixing" in the column and thus lower initial concentrations at the outlet, especially for low K_d values.

Figure 5.5 shows how the initial conditions (pre-equilibrated column and column after first flooding) influence the leaching curves. Compared to the pre-equilibrated case, a higher equilibrium concentration appeared at the outlet of the column after the first flooding period and more contaminant mass was released from the column at early times, followed by a rapidly decreasing concentration (see Fig. 5.5, 2nd row). The deviations vanished with increasing K_d and became almost insignificant for $K_d \geq 10$ L kg^{-1}. Dispersion also reduces differences between the pre-equilibrated and the first flooding case. At high K_d values, the maximum concentrations were still achieved but the tailings became smoother. With the decrease of the K_d value, the concentration gradients at the inlet became steeper and the "back" dispersion fluxes towards the outlet increased as well. In extreme cases, the peak concentration at the column outlet was smaller than the maximum concentration expected (e.g., $K_d = 0.1$ L kg^{-1}). The effect of initial conditions on normalized concentrations looks like a phase shift (see Fig. 5.5, 1st row). This would lead to an underestimation of K_d values derived from the pre-equilibrium analytical solution (Eq. 5.4) if the conditions in the column after the first flooding are not appropriately considered. The lower the K_d, the earlier the cumulative leachate concentration reaches its maximum value ($m_{cum,max} = 1000$ µg kg^{-1}). Dispersion shifts this point to later times (see Fig. 5.5, 3rd row)

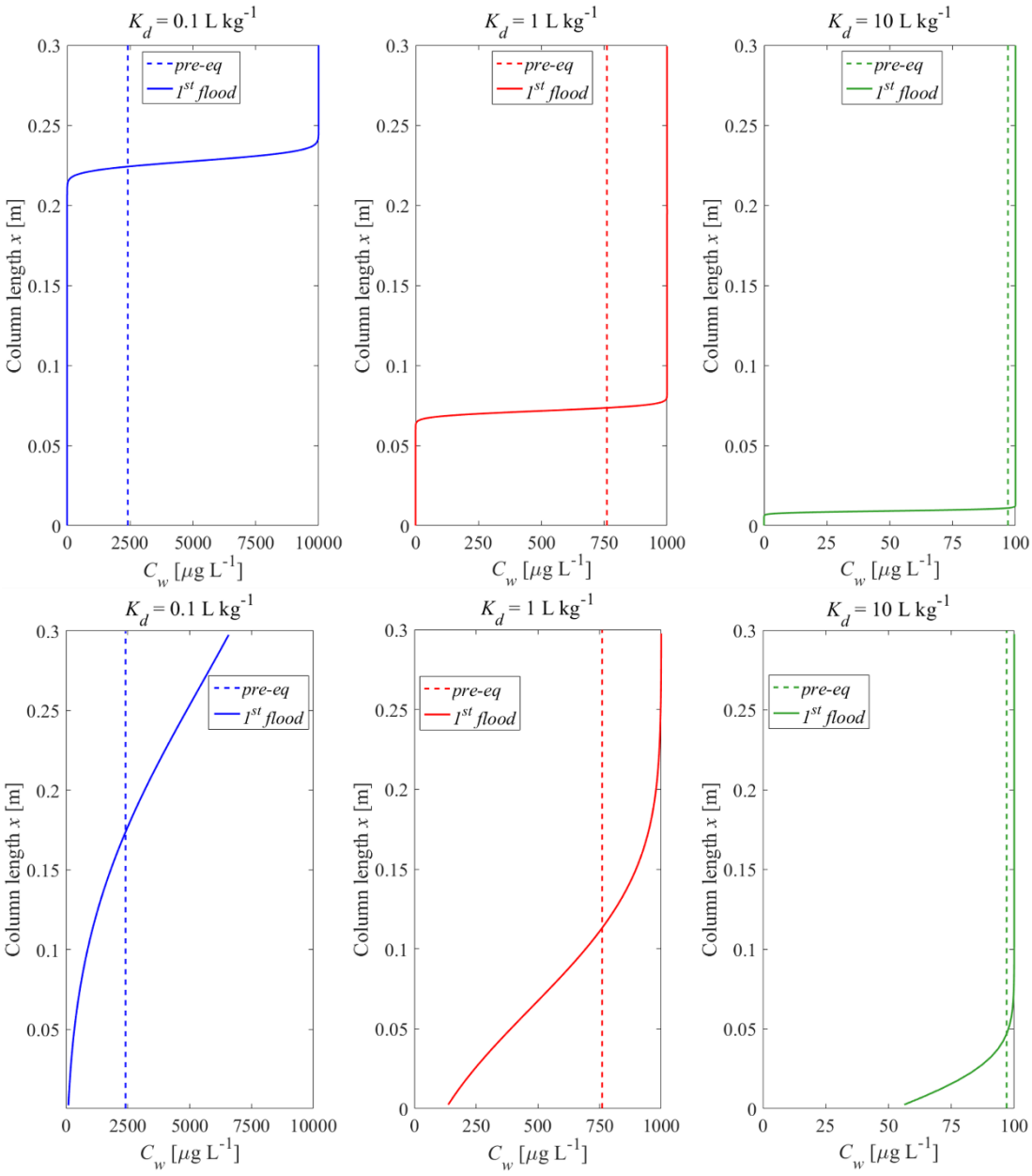

Fig. 5.4: Initial aqueous concentration distributions in the column after the first flooding (solid lines) if mass transfer is controlled by film diffusion for three different distribution coefficients, K_d, compared to the pre-equilibrated case (dashed lines). Top panel: without dispersion; bottom panel: with dispersion; n = 0.45, v = 1.67 × 10^{-5} m s^{-1}, α/x = 0 or 0.1, $C_{s,ini}$ = 1000 µg kg^{-1}, t_c = 5 h, $d_{p,fine}$ = 63 µm.

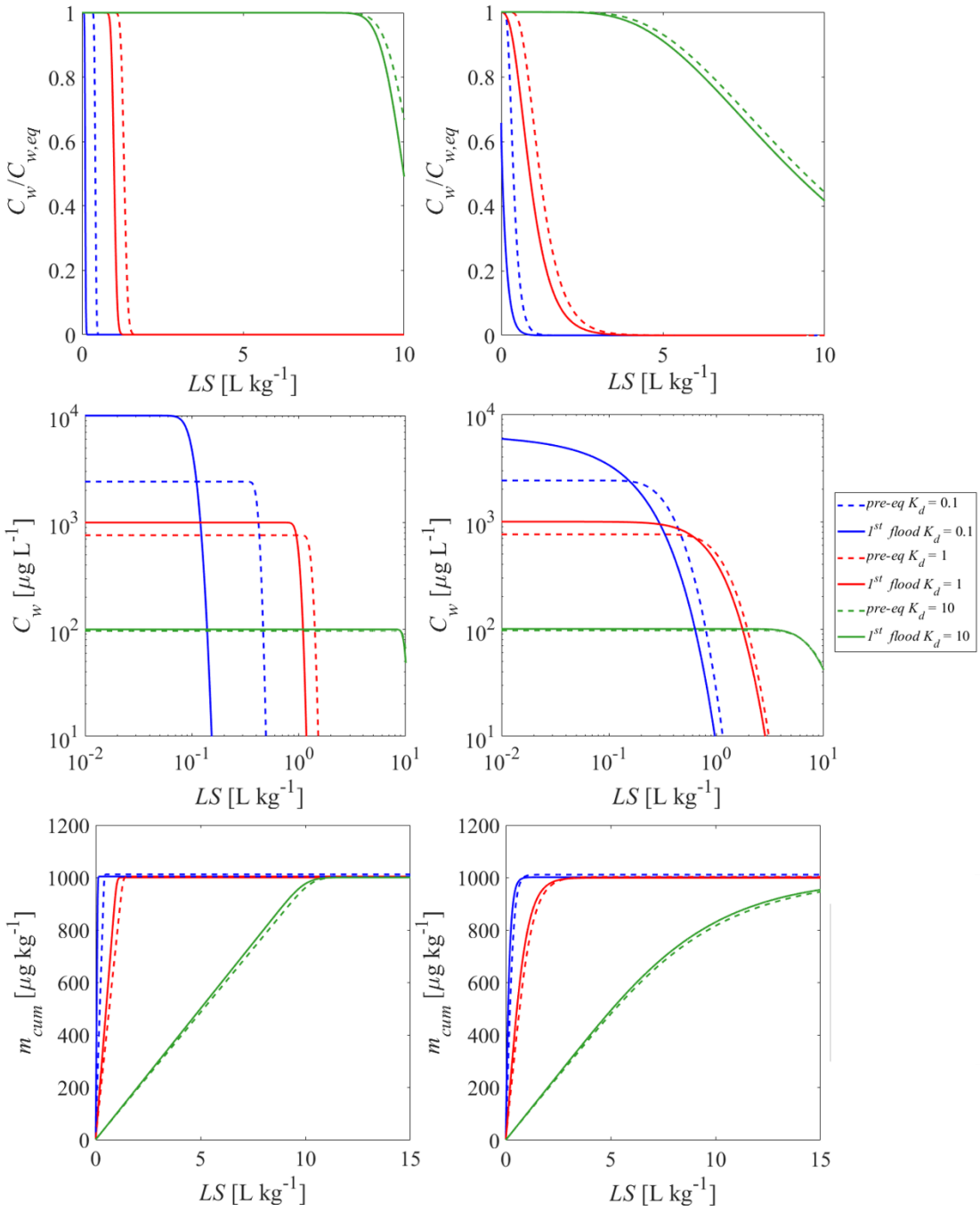

Fig. 5.5: Normalized and absolute concentration ($C_w/C_{w,eq}, C_w$) as well as cumulative concentration (m_{cum}) in the column effluent vs. time (expressed as liquid to solid ratio: *LS*) for the initial conditions (depicted in Fig. 5.4) established after the first flooding of the column (solid lines) compared to the pre-equilibrated case (dashed lines). Left column: without dispersion; right column: with dispersion.

5.3.2 Initial conditions and leaching with mass transfer limitations

Mass transfer limitations may change the picture considerably, with respect to initial conditions and the development of leachate concentrations over time. Figure 5.6 shows the influence of film diffusion (FD) compared to intraparticle pore diffusion (IPPD) limited desorption on the initial concentration distribution in the column after the first flooding period. For large K_d values, equilibration is achieved after shorter distances in the column because of the retardation of the clean water front. The deviations between FD and IPPD are due to different mass transfer zone lengths, $X_{s,63.2\%}$ (see section S5.4 for a discussion of the concept and calculation of this length for FD and IPPD). For FD, the mass transfer zone length is independent of the K_d value and proportional to the particle size (Eq. S5.28). In contrast, for IPPD the length of the mass transfer zone increases with particle size to the power of 3/2 ($d^{3/2}$) and decreases with $\sqrt{K_d}$ (Eq. S5.32) (e.g., $X_{s,63.2\%} = 10$ cm, 3.5 cm, and 1.1 cm for K_d values of 0.1 L kg^{-1}, 1 L kg^{-1} and 10 L kg^{-1} (see Fig. S5.2)). The length of the mass transfer zone for IPPD is much longer than for FD, but differences decrease with increasing K_d values. For K_d values of 1 L kg^{-1} and 10 L kg^{-1}, the mass transfer zone lengths for IPPD are much shorter than the column length (X_{col} = 30 cm), which indicates that the equilibrium concentration is achieved at the outlet of the column after the first flooding. For small K_d values (e.g., $K_d = 0.1$ L kg^{-1}), the equilibrium concentrations are not achieved at the outlet if dispersion is considered (see Fig. 5.6, lower panel) although the mass transfer zone length ($X_{s,63.2\%} = 10\ cm$) is still shorter than the column length. This is because the "clean" water front is close to the column outlet and dispersion "dilutes" the steep concentration gradients ("back dispersion"). The deviations between FD and fast kinetics almost vanish when dispersion is considered, indicating that with film diffusion, equilibrium is almost achieved.

Figure 5.7 shows concentrations in aqueous leachates that correspond to the initial conditions shown in Fig. 5.6. If leaching is limited by IPPD, then the leaching process is slower and concentrations at early times are considerably lower than in the FD or the equilibrium model. This is due to the retarded diffusive transport within the tortuous intragranular pores and the correspondingly small effective diffusion coefficients (D_e). The contaminant release rate becomes lower and lower over time. Leachate concentrations decrease firstly with the square root of time (typical for transient diffusion) and then exponentially (see Fig. 5.7 without dispersion, and section S5.4 for details about the development of the internal mass transfer resistance over time). Note, the cumulative concentration curves confirm the mass conservation of the numerical solutions.

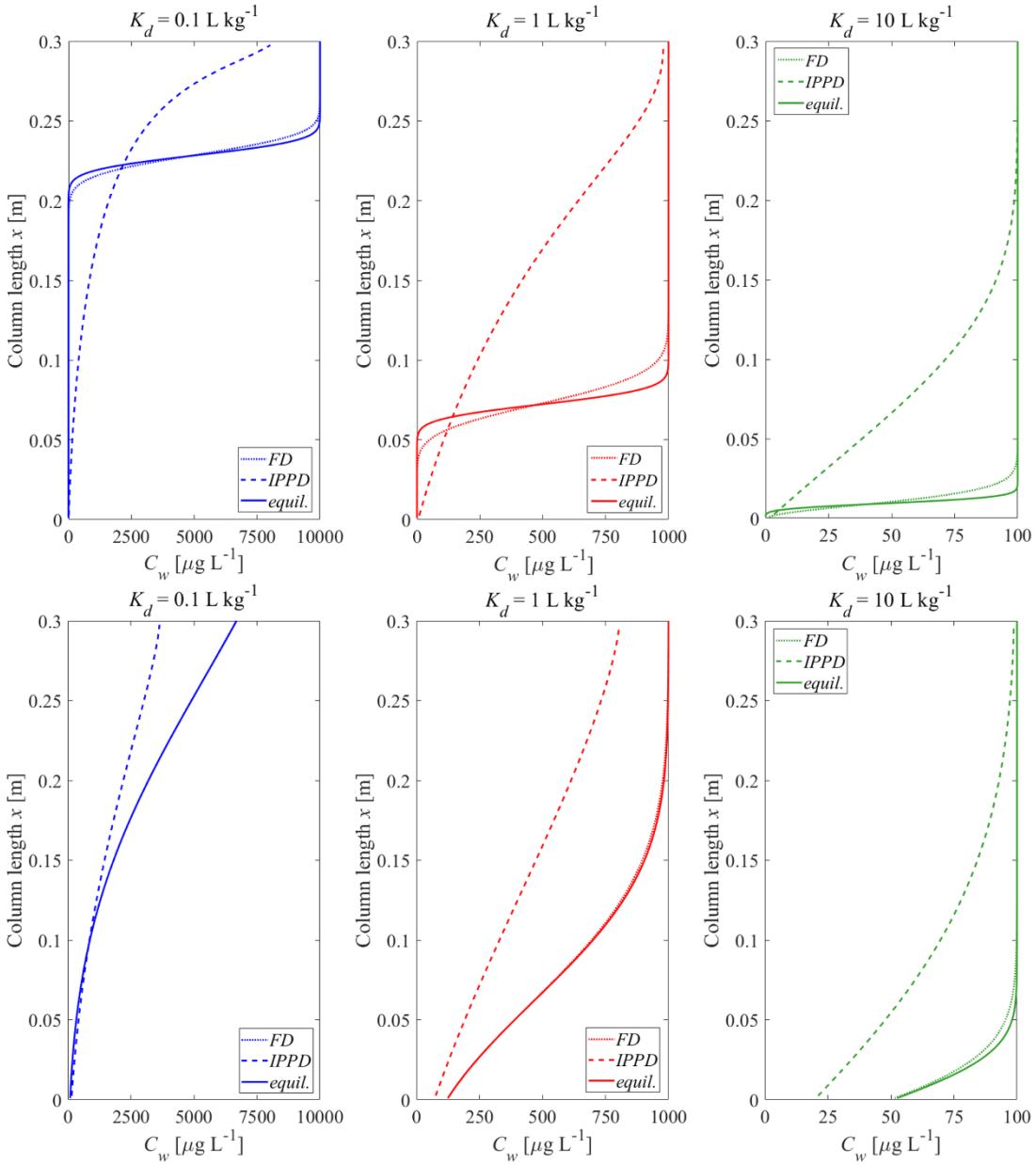

Fig. 5.6: Initial aqueous concentration distributions in the column after the first flooding depending on the mass transfer limitation; dotted lines: film diffusion (FD), dashed lines: intraparticle diffusion (IPPD); solid lines: fast kinetics (equilibrium, fine particles). Top panel: without dispersion; bottom panel: with dispersion; n = 0.45, v = 1.67 × 10^{-5} m s^{-1}, α/x = 0 or 0.1, $C_{s,ini}$ = 1000 µg kg^{-1}, t_c = 5 h, D_{aq} = 1× 10^{-9} m^2 s^{-1}, ε = 0.05, $d_{p,coarse}$ = 2000 µm, $d_{p,fine}$ = 63 µm.

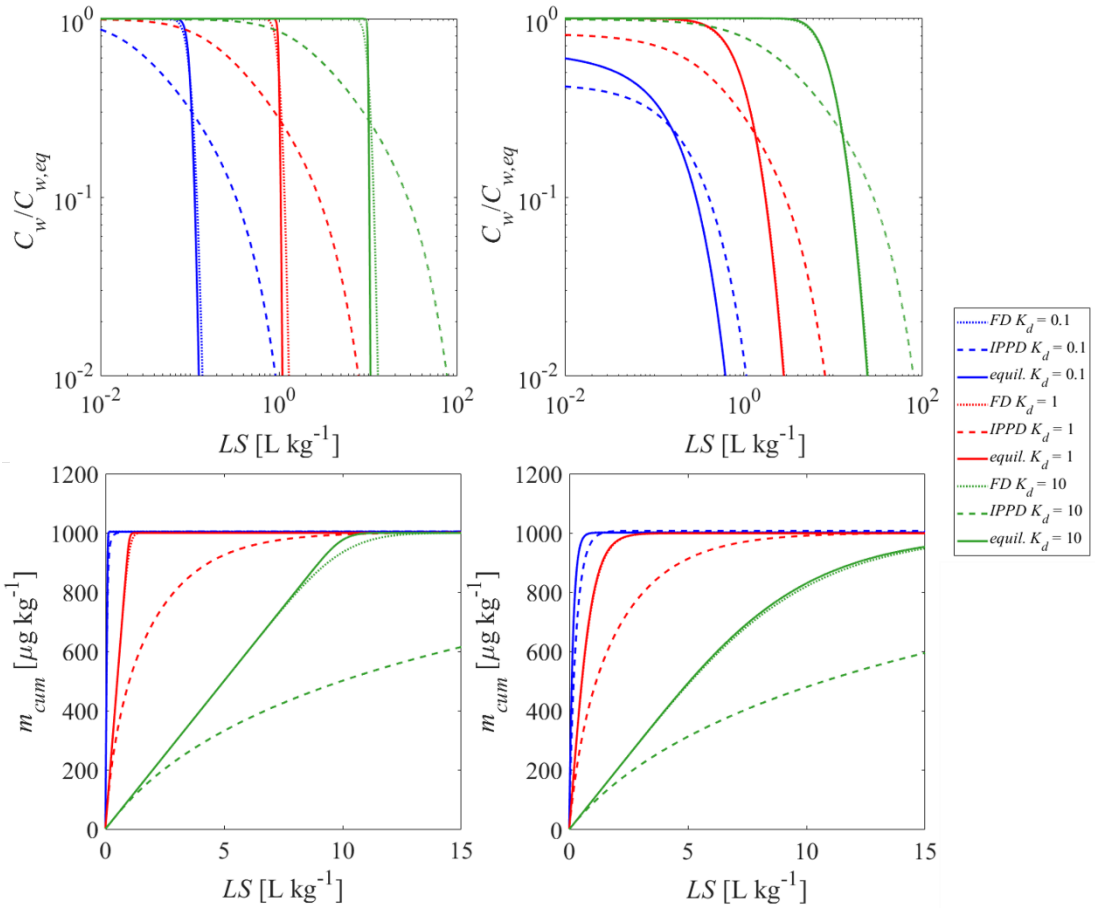

Fig. 5.7: Normalized concentrations ($C_w/C_{w,eq}$) as well as cumulative concentrations (m_{cum}) in the column effluent vs. time (expressed as liquid to solid ratio: *LS*) for different mass-transfer processes, given the initial conditions depicted in Fig. 5.6. Left column: without dispersion; Right column: with dispersion.

5.3.3 Nonlinear sorption isotherms

For many of the environmental contaminants and solid materials that are typically analyzed in column leaching tests, non-linear sorption isotherms describe the distribution of solutes between the aqueous and solid phases. The significance of this non-linearity for the development of the conditions in the column before the leaching starts has been analyzed exemplarily by defining Freundlich isotherms that result in the same "effective" K_d for the aqueous concentration at equilibrium: $K_{fr} = K_d/C_{w,eq}^{\frac{1}{n}-1}$.

Figure 5.8 shows the influence of nonlinear sorption on both the initial concentrations in the column and the leaching curves for the example of K_d = 1 L kg^{-1} when no dispersion is considered. The differences in the concentration distribution before percolation starts are moderate. Concentration profiles tend to be smoother with nonlinear sorption with a slightly

lower maximum concentration at the column outlet for low to mid K_d values if dispersion is considered (see section S5.6, Fig. S5.5). Differences become more obvious in the tailing part of the leaching curves. Freundlich exponents smaller than 1 result in a longer tailing as is expected. The effect of nonlinear sorption looks similar to the dispersion effect, in both cases the leaching curves show more tailing (see section S5.6, Fig. S5.6). Nonlinearity of sorption is notably less significant than kinetic limitations in the mass transfer mechanisms.

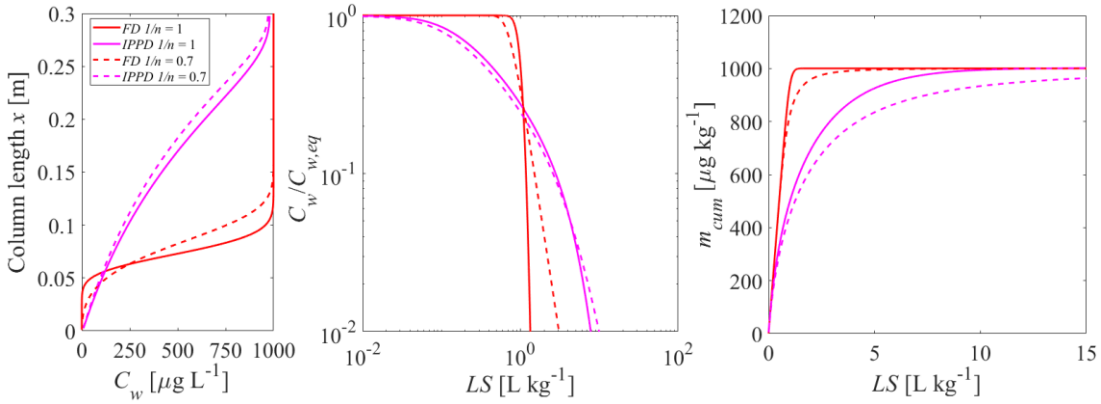

Fig. 5.8: Influence of sorption non-linearity: initial aqueous concentration distribution in the column after the first flooding (left graph) and column effluent concentration (normalized: mid graph, cumulative: right graph) vs. time (expressed as liquid to solid ratio: *LS*); solid lines: linear sorption (K_d = 1 L kg^{-1}); dashed lines: non-linear sorption case (Freundlich coefficient K_{fr} = 7.94, exponent $1/n$ = 0.7); n = 0.45, v = 1.67 × 10^{-5} m s^{-1}, α/x = 0, $C_{s,ini}$ = 1000 µg kg^{-1}, t_c = 5 h, D_{aq} = 1 × 10^{-9} m^2 s^{-1}, ε = 0.05, $d_{p,coarse}$ = 2000 µm.

5.3.4 Impact of heterogeneous sample composition

Real world materials that are typically investigated in leaching tests are not always homogeneous. Although the sample might be addressed as 'one material', its individual grains have different sizes and differ most likely also in other properties such as porosity, tortuosity, sorption capacity, etc., and may contain different amounts of the contaminants of interest. In order to illustrate the impact of material heterogeneity, we have carried out several numerical leaching experiments with hypothetical material compositions.

First, we consider three bi-modal material compositions. Each of these compositions consist of a fraction of contaminated particles (e.g., particulate organic carbon particles with high K_d) and another fraction of particles that neither contain contaminants nor possess any sorption capacity. If equilibrium conditions prevail during the first flooding and leaching, the

heterogeneity of the sample does not matter, it is simply the average K_d ($K_{d,av}$) that rules. The situation changes if mass transfer between the solid and the aqueous phases is limited due to diffusion (FD or IPPD). If only a small fraction of the particles in the sample carries the compounds of interest, the volume of particles released by the compound and thus the surface area available for mass transfer becomes much smaller. This may lead to pronounced non-equilibrium conditions after first flooding (see, e.g., Eqs. S5.26 and S5.30) and during leaching. Figure 5.9 shows a comparison of the initial concentration profiles in the column after the first flooding, as well as the corresponding leaching curves that would develop for the three bi-modal material compositions (100/10/1% of the material is contaminated at a $K_d = 1/10/100$ L kg^{-1}, respectively). A small fraction of strong sorbents showed lower desorption rates compared to a large fraction of the weak sorbents. For this "exotic" case where only 1% of the particles carries all the contamination, initial nonequilibrium and long tailing was observed. This effect was very pronounced for intraparticle pore diffusion; the concentrations initially started on a plateau ("like equilibrium"), but then rapidly declined and showed a pronounced tailing and decrease with the square root of time (or *LS*). It may be noted that longitudinal dispersion becomes less relevant if non-equilibrium conditions prevail at high K_d values (see Figs. S5.7 and S5.8 in section S5.6). If such pronounced initial nonequilibrium is observed, then extended periods of time would be needed to equilibrate the water in the column with the solids (e.g., a manifold of the contact time of 5 h).

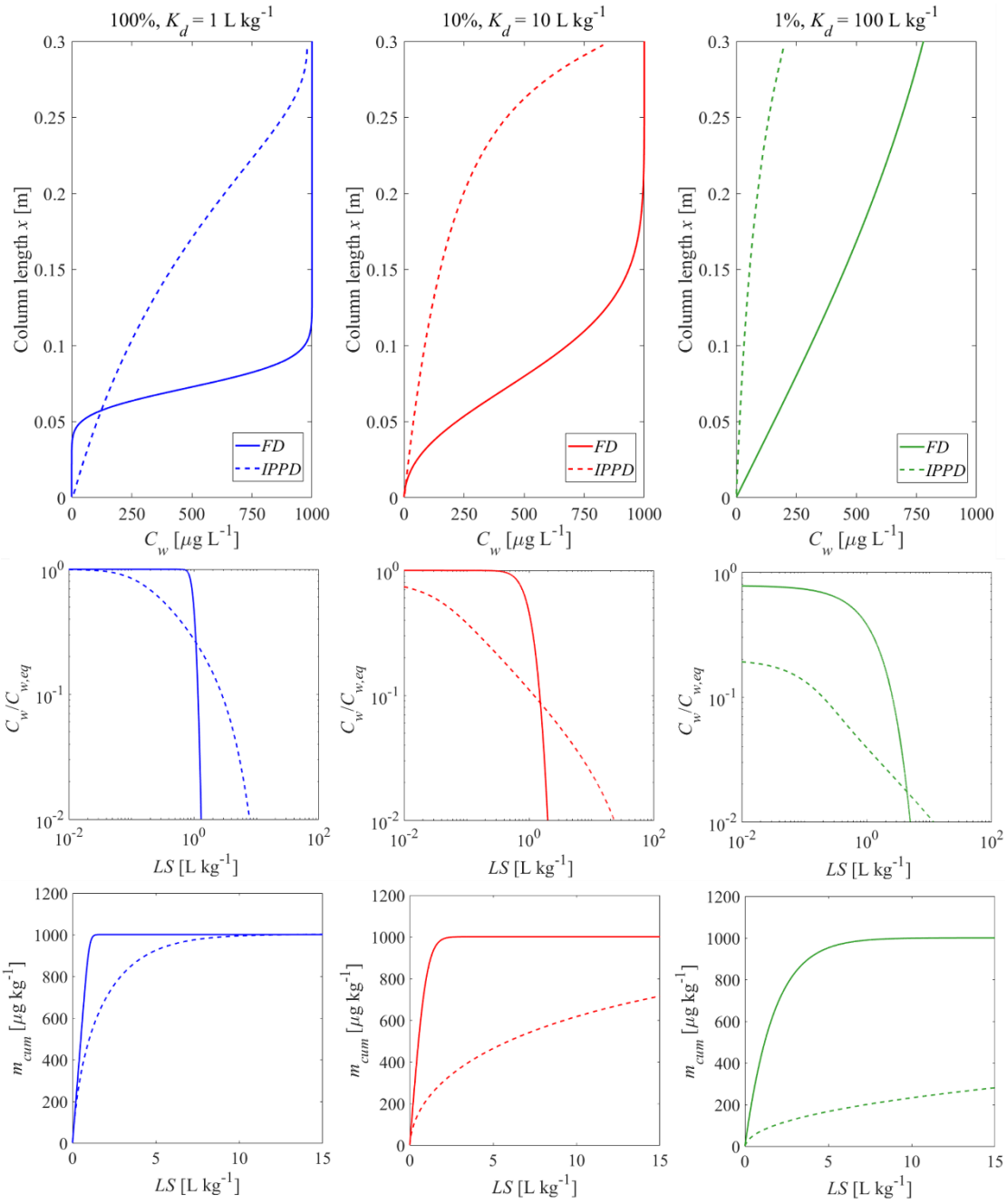

Fig. 5.9: Behavior of bi-modal material compositions of sorbing and non-sorbing particles: initial concentration distribution in the column after the first flooding (top panel) and column effluent concentration (normalized: mid panel, cumulative: bottom panel) vs. time (expressed as liquid to solid ratio: LS). Left column: homogeneous case with average K_d (= $K_{d,av}$ = 1 L kg^{-1}); mid column: only 10% of the particles carry the contaminant at K_d = 10 × $K_{d,av}$; right column: only 1% of the particles carry the contaminant at K_d = 100 × $K_{d,av}$; the average $K_{d,av}$ of the entire material is the same for all compositions; solid lines: film diffusion cases, dashed lines: intraparticle diffusion case; n = 0.45, v = 1.67 × 10^{-5} m s^{-1}, α = 0 (no dispersion), $C_{s,ini}$ = 1000 µg kg^{-1}, t_c = 5 h, D_{aq} = 1×10^{-9} m^2 s^{-1}, ε = 0.05, $d_{p,coarse}$ = 2000 µm.

Samples consisting of mixtures of different particle sizes represent another typical and frequently occurring case of material heterogeneity. To illustrate the impact of such grain size heterogeneity, two bi-modal grain size distributions are considered here, introducing two grain sizes, coarse particles having a diameter of $d_{p,coarse} = 2000$ µm, and fine particles with $d_{p,fine} = 63$ µm. The 1st hypothetical grain size distribution consists of 10% fine particles and 90% coarse particles, the 2nd distribution of 90% fine particles and 10% coarse particles.

If mass transfer is limited by film diffusion, the establishment of the initial conditions as well as leaching (Fig. 5.10) occurs under conditions close to equilibrium for both grain size distributions at all K_d values (0.1, 1, and 10 L kg^{-1}). While the shapes of all leaching curves are very similar, their locations are shifted in time according to the different K_d values by a factor of 10. If intraparticle pore diffusion is considered, tailing is observed if coarse particles predominate. This applies to both, the development of initial conditions in the column and leaching. If fine particles predominate, the leaching is close to equilibrium at early times; at later times, tailing is observed with the typical square root of time behavior. Considering the dispersion effect, non-equilibrium concentrations can be seen at the column effluent after first flooding especially at low K_d values ($K_d = 0.1$ L kg^{-1}). Initial non-equilibrium conditions become more salient for intraparticle pore diffusion if coarse particles predominate (see Figs. S5.9 and S5.10 in section S5.6).

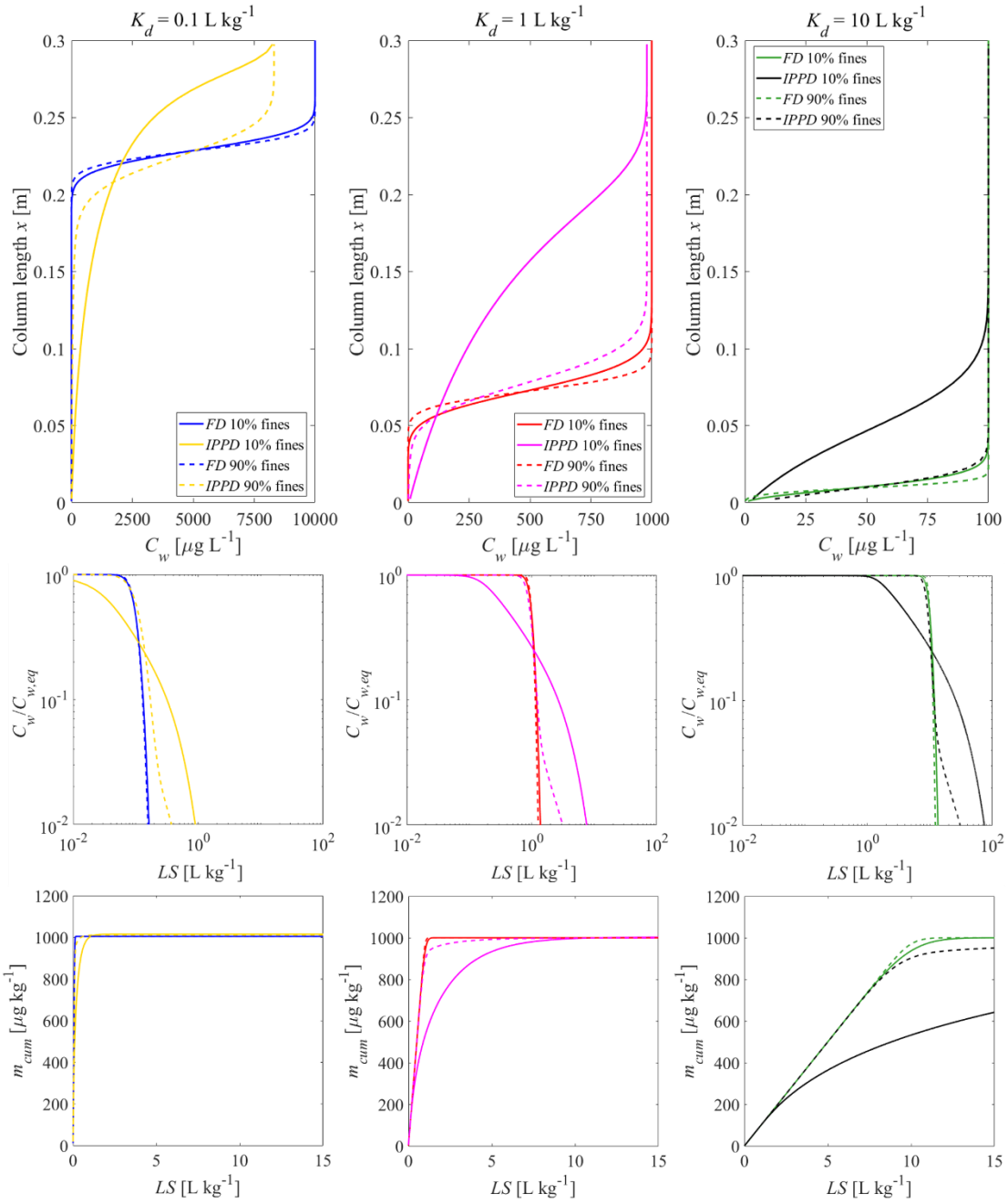

Fig. 5.10: Behavior of the bi-modal material compositions of fine and coarse particles: initial concentration distribution in the column after the first flooding (top panel) and column effluent concentration (normalized: mid panel, cumulative: bottom panel) vs. time (expressed as liquid to solid ratio: *LS*); solid lines: fine particle mass fraction 10%; dashed lines: fine particle mass fraction 90%. (n = 0.45, v = 1.67 × 10^{-5} m s^{-1}, α = 0 (no dispersion), $C_{s,ini}$ = 1000 µg kg^{-1}, t_c = 5 h, D_{aq} = 1 × 10^{-9} m^2 s^{-1}, ε = 0.05, $d_{p,coarse}$ = 2000 µm, $d_{p,fine}$ = 63 µm).

Combining the heterogeneity of particle size (d) and sorption capacity (K_d), we consider three material compositions in the third case, which aims at showing circumstances where

strong non-equilibrium conditions may be expected. For many materials this is probably not very realistic, but it may occur in material mixtures where a small particle fraction carries a "labile" contamination with a low K_d vs. just a few large particles carrying the contaminant with a large K_d. A hypothetical mixture containing 10% of fine particles with low sorption capacity ($K_d = 10$ L kg^{-1}) and 90% of coarse particles with high sorption capacity ($K_d = 100$ L kg^{-1}) is compared with two extreme cases where a hypothetical sample only contains pure fine particles with low sorption capacity and another hypothetical sample contains pure coarse particles with high sorption capacity. Figure 5.11 shows the initial concentration distribution for these three compositions after the first flooding period as well as the corresponding leaching curves. Sorption equilibrium is achieved rapidly if the sample consists of only fine particles with a small K_d or only coarse particles with a high K_d. Pure coarse material with a high K_d shows a low equilibrium concentration ($C_{w,eq} = C_{s,ini}/K_d =$ 1000 µg kg^{-1}/100 L kg^{-1} = 10 µg L^{-1}) while pure fine material with a low K_d presents a much higher equilibrium concentration ($C_{w,eq} = C_{s,ini}/K_d$ = 1000 µg kg^{-1}/10 L kg^{-1} = 100 µg L^{-1}) after a short flow distance. Interestingly, the mixed case where 10% of the column is fine material caused a high concentration which would be sorbed by the coarse materials leading to a slightly higher plateau concentration compared to pure coarse materials. The pollutants were redistributed between fine and coarse materials during the first flooding of the column. The concentration increase towards the outlet of the column in the mixed case is due to fast desorption from the fine material followed by slow sorption by the coarse material. The redistribution is almost complete at the inlet of the column because of the long residence time (t_c = 5 h). Since the fine particles make up only to 10% of the total mass, they are already depleted in contaminant concentrations inside the column and in equilibrium with the coarse particles (reflecting both extreme cases). The front of the high concentration caused by the fine particles is already close to the outlet, while the rest is in equilibrium with the 90% coarse particle fraction.

The leaching curve of the mixed case (red lines) reflects the properties of the two pure (homogeneous) cases with either fine or coarse particles. Ten percent of the fine particles with low sorption capacity led to a peak effluent concentration which was only slightly lower than the equilibrium concentration of the pure fine particles with low sorption capacity. However, because the fine particles made up only 10% of the total mass, this peak concentration leached out rapidly and the eluate concentrations followed the coarse particles with a high sorption capacity for long time periods (blue curves). Although this may appear to indicate non-equilibrium conditions (because of the rapid initial decline of the concentrations followed by a plateau or "tailing"), leaching from fine and coarse particles occurs at, or close to equilibrium. Compared to FD, the IPPD in the mixed sample showed a slower concentration decline because of the desorption kinetics of the IPPD of the coarse

particles was slower than the case of FD and on the long-term control release kinetics. For the cumulative mass release the mixed case is close to the coarse material for both the FD and the IPPD, whereas the fine-grained particles showed a much higher and faster release (see Fig. 5.11: bottom panel).

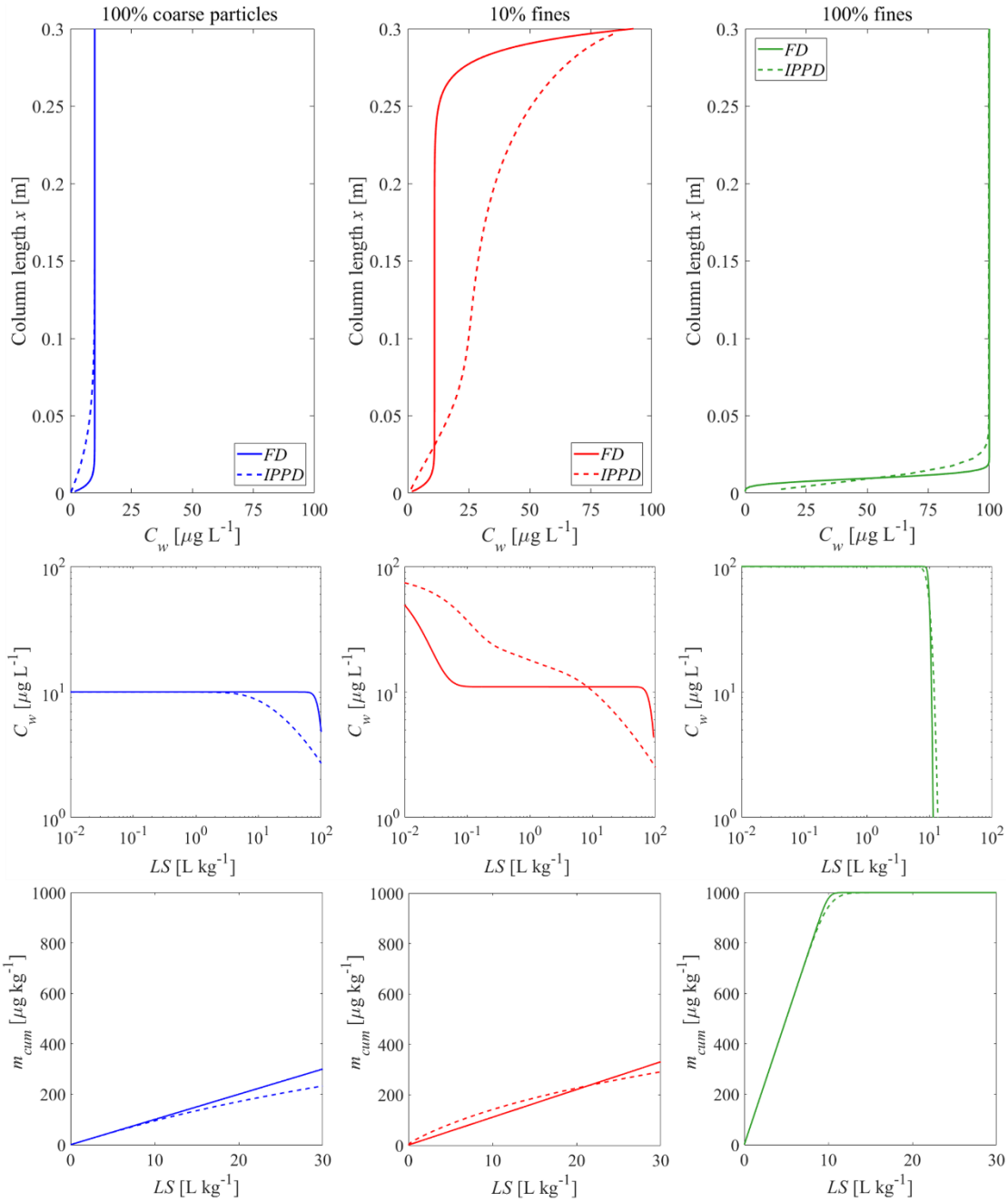

Fig. 5.11: Behavior of bi-modal material compositions of fine particles with low sorption capacity (K_d = 10 L kg^{-1}) and coarse particles with high sorption capacity (K_d = 100 L kg^{-1}): initial concentration distributions in the column after the first flooding (top panel) and the column effluent concentration (normalized: mid panel, cumulative: bottom panel) vs. time

(expressed as liquid to solid ratio: LS). Left column: 100% coarse particles; mid column: mixed sample with 10% fine particles; right column: 100% fine particles; n = 0.45, v = 1.67 × 10^{-5} m s^{-1}, α = 0 (no dispersion), $C_{s,ini}$ = 1000 µg kg^{-1}, t_c = 5 h, D_{aq} = 1 × 10^{-9} m^2 s^{-1}, ε = 0.05, $d_{p,coarse}$ = 2000 µm, $d_{p,fine}$ = 63 µm.

5.4 Summary and conclusions

We conducted numerical simulations to investigate the release characteristics of low to strongly sorbing compounds (K_d = 0.1–100 L kg^{-1}) in column leaching tests. Two different scenarios for the establishment of the initial conditions before the start of the leaching phase were considered: a fully pre-equilibrated column and a more realistic scenario where a column is flooded with water from the bottom. In order to highlight the effect of mass transfer limitations, two mechanisms are compared: film diffusion and intra-particle diffusion. Cases without and with dispersion illustrate how dispersive mixing may mask diffusion limited mass transfer. Furthermore, we looked into the impact of heterogeneous sample compositions in terms of reactive particle fractions and particle sizes. Since possible parameter combinations amount to almost infinite numbers, we have limited our analysis to just a few exemplary cases that illustrate the role of individual material properties. These few cases already show that virtually any leaching behavior can be produced with highly heterogeneous samples (depending on the mixing of different materials). The most important conclusions are:

Initial conditions have a significant impact on leaching at low K_d values (K_d < 1 L kg^{-1}). With increasing K_d, the differences between pre-equilibrium and non-equilibrium conditions gradually vanish for K_d > 10 L kg^{-1} (see Fig. 5.5). Compounds with very low K_d ("salts") would reach extremely high concentrations (K_d << 1 L kg^{-1}) at the column outlet (see Fig. 5.4) potentially leading to enhanced dispersion due to density fingering. The K_d values derived from retardation factors (R_d in Eq. 5.4) would be underestimated if the conditions in the column after the first flooding are not appropriately considered, due to a "phase shift" in normalized concentrations curves ($C_w/C_{w,eq}$ vs. LS).

Dispersion generally causes "smoothing" of concentrations gradients in the column and tends to "mask" film and intraparticle diffusion characteristics due to enhanced "mixing" of the solute within the column. It may lead to smaller initial concentrations at the column outlet after the first flooding period than expected for equilibrium; this is pronounced especially at low K_d values (see Fig. 5.7 and Fig. S5.6), which may be interpreted as non-equilibrium, but is just a consequence of dilution by dispersive mixing.

Intraparticle pore diffusion (IPPD) generally shows slower desorption kinetics than **film diffusion** (FD) through an aqueous boundary layer. This is due to the much smaller effective diffusion coefficient in the intraparticle pores and the large diffusion distance that develops inside the particle over time, resulting in the typical square root of time decrease of concentrations (a slope of $1/2$ is observed in log-log plots of leaching curves, see Figs. 5.7, 5.9 and 5.10). IPPD is more sensitive to the variation of particle sizes than FD (see Fig. 5.10). Mass transfer limitations in an aqueous boundary layer commonly exists for surface adsorbed compounds and easily soluble solids ("salts"). Elements such as heavy metals, which are slowly released from the solid phase, would require much lower solid state diffusion coefficients; if reaction fronts propagate into the particle releasing metals, intraparticle (solid) diffusion models apply again (shrinking core), which are very similar to the IPPD approach used here.

Non-linear sorption has little influence on the leaching test results if the "right" effective K_d value is calculated for the proper concentration range (since for the nonlinear sorption the K_d depends on the concentration, large deviations may occur if just the K_{fr} is determined far away of the sample's concentration is used as "K_d"); nevertheless, as concentrations decrease nonlinear sorption causes more tailing (see Fig. 5.8).

Heterogeneous samples with only a small fraction of strongly sorbing particles lead to much slower desorption rates (because of less surface area), especially if mass release is limited by intraparticle pore diffusion (see Fig. 5.9). In extreme cases (just 1% of the material is contaminated at $K_d = 100 \times K_{d,av}$), leaching may start at a plateau (suggesting equilibrium), but far below equilibrium concentrations ($C_{w,peak} \ll C_{w,eq}$) and concentrations later decrease further; The K_d values derived from the initial aqueous concentration ($K_d = C_{s,ini}/C_{w,peak}$) would be overestimated while the K_d values calculated from retardation factors would be underestimated.

In contrast to that, already relatively small amounts of fine particles lead to initial equilibrium, but long-term tailing occurs and is dominated by the coarse particle fraction, especially for intraparticle pore diffusion. Since our FD simulations are close to equilibrium, results are not very affected by grain size heterogeneity (see Fig. 5.10). Material mixtures of small amounts of fine particles (10%) with low sorption capacity ($K_d = 10$ L kg^{-1}) and large amounts of coarse particles with high sorption capacity ($K_d = 100$ L kg^{-1}), exhibit the respective characteristics of each of the individual components in different time periods (see Fig. 5.11). Small amounts of fine particles with low sorption capacity dominate short term behavior of the mixtures and lead to a peak effluent concentration ($C_{w,peak}$) which approaches the equilibrium concentration expected for fine particles (see Fig. 5.11). Since the mass fraction of fine particles is small (10%), the leachate concentrations drop rapidly and

reach slightly higher equilibrium levels of 100% pure coarse particles due to the redistribution of pollutants between fine and coarse particles. Ten percent of fine particles with low sorption capacity causes a high equilibrium concentration which are sorbed by the coarse particles with high sorption capacity. K_d values derived from the initial aqueous concentration ($K_d = C_{s,ini}/C_{w,peak}$) would be underestimated, while K_d values derived from the following plateau concentration would be overestimated. Cumulative mass release, however, is often quite insensitive to mass transfer mechanisms (FD or IPPD) especially for $LS < 5$ (see Fig. 5.11).

References

Bandow, N., Finkel, M., Grathwohl, P., Kalbe, U., 2019. Influence of flow rate and particle size on local equilibrium in column percolation tests using crushed masonry. J. Mater. Cycles Waste Manag. 21, 642–651. https://doi.org/10.1007/s10163-019-00827-3.

Boving, T.B., Grathwohl, P., 2001. Tracer diffusion coefficients in sedimentary rocks: Correlation to porosity and hydraulic conductivity. J. Contam. Hydrol. 53, 85–100. https://doi.org/10.1016/S0169-7722(01)00138-3.

Butera, S., Hyks, J., Christensen, T.H., Astrup, T.F., 2015. Construction and demolition waste: Comparison of standard up-flow column and down-flow lysimeter leaching tests. Waste Manag. 43, 386–397. https://doi.org/https://doi.org/10.1016/j.wasman.2015.04.032.

Chan, W.P., Ren, F., Dou, X., Yin, K., Chang, V.W.C., 2018. A large-scale field trial experiment to derive effective release of heavy metals from incineration bottom ashes during construction in land reclamation. Sci. Total Environ. 637–638, 182–190. https://doi.org/10.1016/J.SCITOTENV.2018.05.026.

Chen, Z., Zhang, P., Brown, K.G., Branch, J.L., van der Sloot, H.A., Meeussen, J.C.L., Delapp, R.C., Um, W., Kosson, D.S., 2021. Development of a Geochemical Speciation Model for Use in Evaluating Leaching from a Cementitious Radioactive Waste Form. Environ. Sci. Technol. 55, 8642–8653. https://doi.org/10.1021/acs.est.0c06227.

Di Gianfilippo, M., Costa, G., Verginelli, I., Gavasci, R., Lombardi, F., 2016. Analysis and interpretation of the leaching behaviour of waste thermal treatment bottom ash by batch and column tests. Waste Manag. 56, 216–228. https://doi.org/10.1016/j.wasman.2016.07.034.

Diotti, A., Perèz Galvin, A., Piccinali, A., Plizzari, G., Sorlini, S., 2020. Chemical and Leaching Behavior of Construction and Demolition Wastes and Recycled Aggregates. Sustainability. 12. https://doi.org/10.3390/su122410326.

Finkel, M., Grathwohl, P., 2017. Impact of pre-equilibration and diffusion limited release kinetics on effluent concentration in column leaching tests: Insights from numerical simulations. Waste Manag. 63, 58–73. https://doi.org/10.1016/j.wasman.2016.11.031.

Grathwohl, P., Reinhard, M., 1993. Desorption of trichloroethylene in aquifer material: rate limitation at the grain scale. Environ. Sci. Technol. 27, 2360–2366. https://doi.org/10.1021/es00048a008.

Grathwohl, P., van der Sloot, H., 2007. Groundwater risk assessment at contaminated sites (GRACOS): Test methods and modelling approaches. In Groundwater Science and Policy;

Quevauviller, P., Ed.; RSC Publishing: Cambridge, UK.

Grathwohl, P., Susset, B., 2009. Comparison of percolation to batch and sequential leaching tests: Theory and data. Waste Manag. 29, 2681–2688. https://doi.org/10.1016/j.wasman.2009.05.016.

Grathwohl, P., 2014. On equilibration of pore water in column leaching tests. Waste Manag. 34, 908–918. https://doi.org/10.1016/j.wasman.2014.02.012.

Inui, T., Hori, M., Takai, A., Katsumi, T., 2019. Column percolation tests for evaluating the leaching behavior of marine sediment containing non-anthropogenic arsenic. In: Zhan, L., Chen, Y., Bouazza, A. (eds) Proceedings of the 8th International Congress on Environmental Geotechnics Volume 1. ICEG 2018. Environmental Science and Engineering. Springer, Singapore. https://doi.org/10.1007/978-981-13-2221-1_50.

Jaeger, R., Liedl, R., 2000. Prognose der Sorptionskinetik organischer Schadstoffe in heterogenem Aquifermaterial. Grundwasser. 5, 57–66. https://doi.org/10.1007/s767-000-8348-2.

Kalbe, U., Berger, W., Simon, F.-G., Eckardt, J., Christoph, G., 2007. Results of interlaboratory comparisons of column percolation tests. J. Hazard. Mater. 148, 714–720. https://doi.org/10.1016/j.jhazmat.2007.03.039.

Kalbe, U., Berger, W., Eckardt, J., Simon, F.-G., 2008. Evaluation of leaching and extraction procedures for soil and waste. Waste Manag. 28, 1027–1038. https://doi.org/10.1016/j.wasman.2007.03.008.

Kalbe, U., Bandow, N., Bredow, A., Mathies, H., Piechotta, C., 2014. Column leaching tests on soils containing less investigated organic pollutants. J. Geochemical Explor. 147, 291–297. https://doi.org/10.1016/j.gexplo.2014.06.014.

Kleineidam, S., Rügner, H., Grathwohl, P., 1999. Impact of grain scale heterogeneity on slow sorption kinetics. Environ. Toxicol. Chem. 18, 1673–1678. https://doi.org/10.1002/etc.5620180810.

Kumar, A., Samadder, S.R., Kumar, V., 2019. Assessment of groundwater contamination risk due to fly ash leaching using column study. Environ. Earth Sci. 78, 18. https://doi.org/10.1007/s12665-018-8009-y.

Lange, C.N., Flues, M., Hiromoto, G., Boscov, M.E.G., Camargo, I.M.C., 2019. Long-term leaching of As, Cd, Mo, Pb, and Zn from coal fly ash in column test. Environ. Monit. Assess. 191, 602. https://doi.org/10.1007/s10661-019-7798-0.

Liu, Y., Illangasekare, T.H., Kitanidis, P.K., 2014. Long-term mass transfer and mixing-

controlled reactions of a DNAPL plume from persistent residuals. J. Contam. Hydrol. 157, 11–24. https://doi.org/10.1016/j.jconhyd.2013.10.008.

Liu, B., Li, J., Wang, Z., Zeng, Y., Ren, Q., 2020. Long-term leaching characterization and geochemical modeling of chromium released from AOD slag. Environ. Sci. Pollut. Res. 27, 921–929. https://doi.org/10.1007/s11356-019-07008-7.

Liu, H., Zhang, J., Li, B., Zhou, N., Xiao, X., Li, M., Zhu, C., 2020. Environmental behavior of construction and demolition waste as recycled aggregates for backfilling in mines: Leaching toxicity and surface subsidence studies. J. Hazard. Mater. 389, 121870. https://doi.org/10.1016/j.jhazmat.2019.121870.

Löv, Å., Larsbo, M., Sjöstedt, C., Cornelis, G., Gustafsson, J.P., Kleja, D.B., 2019. Evaluating the ability of standardised leaching tests to predict metal(loid) leaching from intact soil columns using size-based elemental fractionation. Chemosphere. 222, 453–460. https://doi.org/10.1016/j.chemosphere.2019.01.148.

Molleda, A., López, A., Cuartas, M., Lobo, A., 2020. Release of pollutants in MBT landfills: Laboratory versus field. Chemosphere. 249, 126145. https://doi.org/10.1016/J.CHEMOSPHERE.2020.126145.

Naka, A., Yasutaka, T., Sakanakura, H., Kalbe, U., Watanabe, Y., Inoba, S., Takeo, M., Inui, T., Katsumi, T., Fujikawa, T., Sato, K., Higashino, K., Someya, M., 2016. Column percolation test for contaminated soils: Key factors for standardization. J. Hazard. Mater. 320, 326–340. https://doi.org/10.1016/j.jhazmat.2016.08.046.

Ogata, A., Banks, R.B., 1961. A solution of the differential equation of longitudinal dispersion in porous media. In Professional Paper; Geological Survey (U.S.); pp. A1–A7, Available online: http://pubs.er.usgs.gov/publication/pp411A (accessed on).

Röhler, K., Haluska, A.A., Susset, B., Liu, B., Grathwohl, P., 2021. Long-term behavior of PFAS in contaminated agricultural soils in Germany. J. Contam. Hydrol. 241, 103812. https://doi.org/10.1016/J.JCONHYD.2021.103812.

Rügner, H., Kleineidam, S., Grathwohl, P., 1999. Long term sorption kinetics of phenanthrene in aquifer materials. Environ. Sci. Technol. 33, 1645–1651. https://doi.org/10.1021/es980664x.

Schwab, O., Bayer, P., Juraske, R., Verones, F., Hellweg, S., 2014. Beyond the material grave: Life Cycle Impact Assessment of leaching from secondary materials in road and earth constructions. Waste Manag. 34, 1884–1896. https://doi.org/10.1016/j.wasman.2014.04.022.

Susset, B., Grathwohl, P., 2011. Leaching standards for mineral recycling materials – A

harmonized regulatory concept for the upcoming German Recycling Decree. Waste Manag. 31, 201–214. https://doi.org/10.1016/j.wasman.2010.08.017.

Tsiridis, V., Petala, M., Samaras, P., Sakellaropoulos, G.P., 2015. Evaluation of interactions between soil and coal fly ash leachates using column percolation tests. Waste Manag. 43, 255–263. https://doi.org/10.1016/j.wasman.2015.05.031.

Wang, G., Kleineidam, S., Grathwohl, P., 2007. Sorption/desorption reversibility of phenanthrene in soils and carbonaceous materials. Environ. Sci. Technol. 41, 1186–1193. https://doi.org/10.1021/es060805s.

Xiao, Y., Feng, Z., Huang, X., Huang, L., Chen, Y., Wang, L., Long, Z., 2015. Recovery of rare earths from weathered crust elution-deposited rare earth ore without ammonia-nitrogen pollution: I. leaching with magnesium sulfate. Hydrometallurgy. 153, 58–65. https://doi.org/10.1016/j.hydromet.2015.02.011.

Yin, K., Chan, W.-P., Dou, X., Lisak, G., Chang, V.W.-C., 2020. Kinetics and modeling of trace metal leaching from bottom ashes dominated by diffusion or advection. Sci. Total Environ. 719, 137203. https://doi.org/10.1016/j.scitotenv.2020.137203.

Zhu, Y., Hu, Y., Guo, Q., Zhao, L., Li, L., Wang, Y., Hu, G., Wibowo, H., Di Maio, F., 2021. The effect of wet treatment on the distribution and leaching of heavy metals and salts of bottom ash from municipal solid waste incineration. Environ. Eng. Sci. 39, 409–417. https://doi.org/10.1089/ees.2021.0065.

6 Two mesh free methods for solving non-equilibrium advective-dispersive solute transport with coupled film-intraparticle diffusion

Binlong Liu, Michael Finkel, Peter Grathwohl

Abstract

Two mesh free methods (semi-Laplace solution and physical informed neural networks (PINNs)) are introduced to solve 1D advective-dispersive transport with coupled film-intraparticle pore diffusion (ADE-FIPPD), taking into account both external (FD) and internal (IPPD) mass transfer resistances. The semi-Laplace solution shows remarkable performance with deviations of normalized concentrations within the spatial-temporal domain of less than 1% when compared to the numerical model (NM). PINNs are a promising alternative to NM in practical applications; they exhibit slightly higher deviations (< 10%) than the semi-Laplace solution which are still acceptable across most of the spatial-temporal domain excluding the regions with stepwise concentration gradients. To enhance total loss function convergence during PINNs training, a self-adaptive loss weighting factor is applied to each training data point. This study investigates the influence of various factors on training PINNs, including the structures of neural networks (such as the number of layers and neurons, activation functions), types and quantities of training data, and parameters (initial loss weighing factors and learning and decay rates). External resistance and dispersion predominate during very short times initially, then mass transfer resistance shifts from ADE-FD to ADE-IPPD which is observed especially for coarse particles. Mass transfer shift is delayed with increasing distribution coefficient (K_d) and intraparticle porosity (ε).

6.1 Introduction

1-D advective-dispersive transport equation has been widely used in simulating transport of organic pollutants in porous media and sorption/desorption of pollutants from an immobile phase (e.g., solids) leading to the retardation of the concentration front and tailing during leaching is often observed especially for persistent compounds (e.g., polycyclic aromatic hydrocarbons (PAHs), polychlorinated biphenyls (PCBs), per- and polyfluoroalkyl substances (PFAS), dioxin, etc.) (Ngueleu et al., 2013; Guo et al., 2020). Many simple analytical solutions exist when equilibrium sorption/desorption is assumed and transport or reaction related

parameters (e.g., velocity (v), dispersion coefficient (D_L), mass transfer rate constant (r_{mt})) can be easily modified by a retardation factor (R_d) (van Genuchten and Alves, 1982). However, the equilibrium sorption/desorption is often questioned especially for sorbents with large grain sizes or pollutants present large distribution coefficients (K_d), thus sorption/desorption kinetics must be considered in solute transport. Furthermore, depending on grain size, relative velocity, intraparticle porosity and distribution coefficient may lead to the mass transfer resistance shift from the external boundary layer (external film) into the solid sorbents (intraparticle solid/pore space), which has been observed recently in batch tests on PAHs sorption/desorption into/from microplastics (Seidensticker et al., 2017) and soil suspension with passive samplers (Liu et al., 2023). Using coupled film intraparticle solid/pore diffusion models in solid/porous materials becomes necessary for capturing both short-term (dominated by film diffusion) and long-term (dominated by intraparticle diffusion) behaviors of sorption/desorption kinetics of the pollutants.

While 1-D advective-dispersive transport with coupled film intraparticle diffusion (ADE-FIPPD) can be solved via numerical methods (e.g., finite volume method and finite element method), those methods are computationally demanding and time-consuming especially when diffusion inside the intraparticle solid/pore space is considered where spatial discretization is needed in both flow (e.g., water) and radial direction of the solid (see Fig. 6.1). The numerical iteration method applied to update the solute concentrations in each node at each discrete time step slows down the model further if a fully implicit method is utilized. In addition, selecting appropriate discrete time steps (Δt), longitudinal (dx) and radial (dr) distances is challenging, and improper discretization often leads to the instability of the numerical model or non-conservation of total mass. This issue becomes more severe when dealing with heterogeneous sorbents, particularly in cases where sorption/desorption kinetics of the sorbents exhibits distinct behaviors (e.g., fast sorbing particles mixed with slow sorbing particles). To avoid the shortcomings of numerical models, two mesh free methods (semi-Laplace solution and physical informed neural networks) are tested and compared in this study. Instead of simulating the concentration gradient inside the intraparticle solid/pore space, the semi-Laplace solution uses an average concentration that yields the same total mass as the numerical method through integration of the entire sphere's volume. Mathematically, the average concentration can be expressed as the convolution of concentration in bulk water phase (C_w) and a transfer function and different sorption/desorption kinetics models can be easily replaced by just changing their corresponding transfer functions (Liu et al., 2023). Thanks to the convenience of computing convolution in the Laplace domain, it becomes feasible to derive the analytical solutions of ADE-FIPPD. The (average) concentration changes in each phase can be obtained by inverse Laplace transformation using a very efficient numerical method. Due to the simplification of

addressing concentration gradient inside the intraparticle space, semi-Laplace solutions emerges as a favorable alternative replacing numerical approaches.

With the advent of the big data era, the ability to collect and generate observation data far surpasses our capacity to sensibly absorb, let alone understand and explain it. Many machine learning (ML) models are entirely data-driven and can fit observations exceptionally well, but their predictions may exhibit physical inconsistencies or implausibilities due to extrapolation or observational biases, which can result in subpar generalization performance. Therefore, integrating fundamental physical laws and domain knowledge (e.g., initial and boundary conditions) to train ML models about governing physical rules (called physical learning) becomes necessary. This, in turn, can provide "information priors" - that is strong theoretical constraints and inductive biases of our observations (Karniadakis et al., 2021). Physical informed neural networks (PINNs) are one of the most widely used deep learning methods reflecting this new learning philosophy. PINNs are not just a pure surrogate of numerical models when observation data is used in training process, but they account for data uncertainty and capture latent physical principles or processes that may elude our prior knowledge. Neural networks within PINNs can learn and incorporate these hidden processes from data, leading to superior fits compared to numerical models (or semi-Laplace solutions) and exhibit better performance in prediction when dealing with the real measured datasets.

The objectives of this study are to (i) verify the feasibility of two-mesh methods in solving ADE-FIPPD, (ii) compare their performances and respective errors, and (iii) and elucidate parameter sensitivity (e.g., distribution coefficient, grain size, intraparticle porosity, etc.).

Figure 6.1 illustrates advective-dispersive transport with coupled film intraparticle pore diffusion (ADE-FIPPD). In step 1: the domain is discretized into N parts and each part contains both solid and water phase. The solid phase is represented as a composition of grains having different sizes and properties and each grain is discretized into certain shells. The mass transfer is limited by coupled film intraparticle pore diffusion in spheres. In step 2: solute concentrations in both water (C_w) and intraparticle pore water phase ($C_{w,p,k}$) of each node are solved simultaneously for each discrete time step (Δt) with numerical iteration method. In step 3: a 2-D map of solute concentrations in the intraparticle pore water phase in both longitudinal (x) and radial (r) directions is presented at each discrete time point.

Step 1: Discretization of domain and defining the governing equations of each node

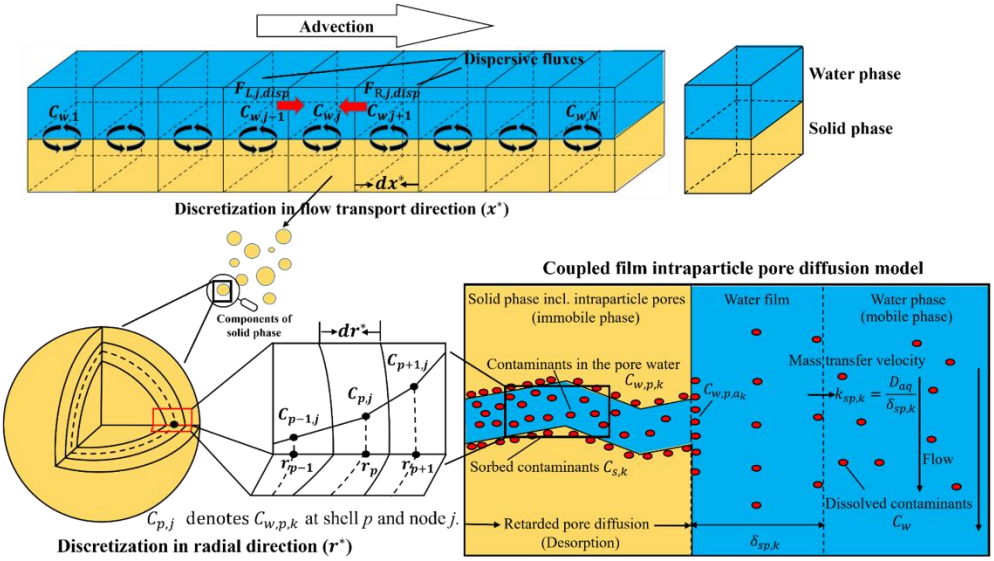

Governing equations:

$$\frac{\partial C_w}{\partial t} = -\sum_{k=1}^{n_k} \frac{3 f_k (1-n) D_{e,k}}{n a_k} \frac{\partial C_{w,p,k}}{\partial r}\bigg|_{r=a_k} - v\frac{\partial C_w}{\partial x} + D_L \frac{\partial^2 C_w}{\partial x^2}$$

$$\frac{\partial C_{w,p,k}}{\partial t} = D_{a,k}\left[\frac{\partial^2 C_{w,p,k}}{\partial r^2} + \frac{2}{r}\frac{\partial C_{w,p,k}}{\partial r}\right]$$

With initial and boundary condiions:

$$C_{w,p,k}(r = a_k) = C_{w,p,a_k} \quad \forall t$$

$$\frac{\partial C_{w,p,k}}{\partial r}\bigg|_{r=0} = 0 \quad \forall t$$

$$-D_L \frac{\partial C_w}{\partial x}\bigg|_{x=L} = 0 \quad \forall t$$

$$C_w(x=0) - \frac{D_L}{v}\frac{\partial C_w}{\partial x}\bigg|_{x=0} = C_{w,in} = 0 \quad \forall t$$

$$k_{sp,k}\left(C_{w,p,a_k} - C_w\right) = -D_{e,k}\frac{\partial C_{w,p,k}}{\partial r}\bigg|_{r=a_k} \quad \forall t$$

$$C_w(t=0) = 0 \quad \forall x$$

$$C_{w,p,k}(t=0) = C_{w,p,k}(0) \quad \forall r$$

a_k: radius of k-th spherical particles [L]
C_w: solute concentration in bulk water phase [M L^{-3}]
$C_{w,p,k}$: solute concentration in the intraparticle pore water phase of k-th porous materials [M L^{-3}]
$C_{w,in}$: inlet solute concentration [M L^{-3}]
$D_{e,k}$: effective diffusion coefficient inside k-th spherical particles [L^2 T^{-1}]
$D_{a,k}$: apparent diffusion coefficient inside k-th spherical particles [L^2 T^{-1}]
D_L: longitudinal dispersion coefficient [L^2 T^{-1}]
f_k: mass fraction of k-th porous materials (assuming dry density of all porous materials are the same) [-]
$k_{sp,k}$: mass transfer velocity for k-th porous materials [L T^{-1}]
L: maximum transport distance [L]
n: interparticle porosity [-]
r: radial coordinate [L]
r^*: normalized radial coordinate [-]
t: time [T]
t^*: normalized time [-]
v: seepage velocity [L T^{-1}]
x: longitudinal coordinate [L]
x^*: normalized longitudinal coordinate [-]

Step 2: Updating concentrations of each node with tedious numerical iteration method (e.g., Newtown Raphson scheme)

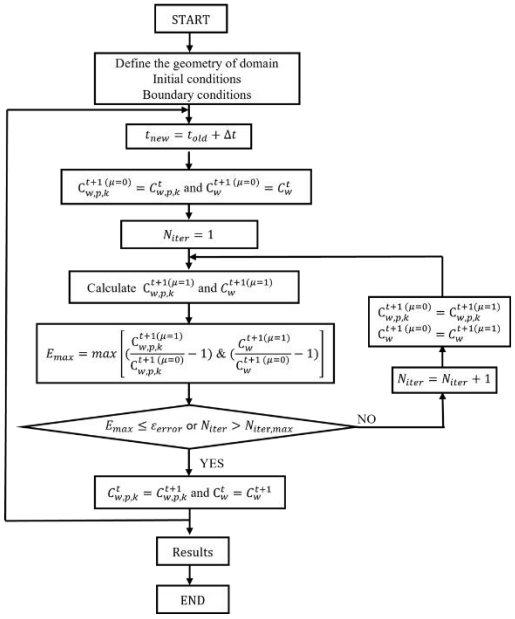

Step 3: Plotting the 2-D solute concentration profile along the flow transport direction (x^*) as well as the radial direction (r^*) where the concentration gradient inside the intraparticle pore water phase is monitored

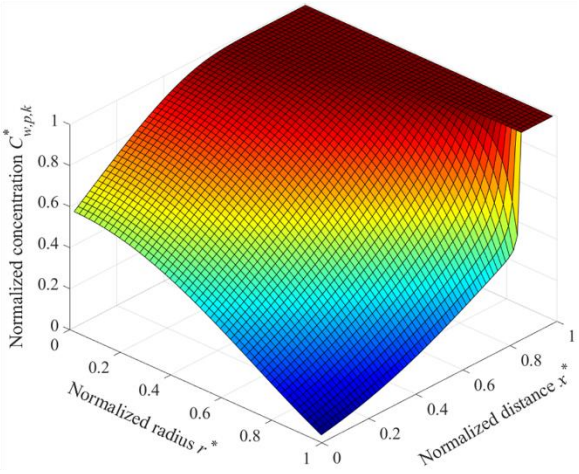

Fig. 6.1: Scheme of numerical method (here: finite volume method) for solving 1-D non-

equilibrium advective-dispersive solute transport with coupled film-intraparticle pore diffusion.

6.2 Methodology

Considering 1-D contaminant transport in heterogeneous materials (e.g., soil samples containing mixtures of porous (e.g., charcoal, soil aggregates, etc.) and non-porous materials (e.g., microplastics, tyre wear particles, etc.) with different grain sizes and sorption coefficients (K_d)), the governing equation reads as:

$$\frac{\partial C_w}{\partial t} + \sum_{j=1}^{n_j} \frac{m_{d,j}}{V_w} \frac{\partial C_{s,j}}{\partial t} + \sum_{k=1}^{n_k} \frac{m_{d,k}}{V_w} K_{d,b,k} \frac{\partial C_{w,p,k}}{\partial t} + v \frac{\partial C_w}{\partial x} - D_L \frac{\partial^2 C_w}{\partial x^2} = 0 \tag{6.1}$$

$$C_w(x, t = 0) = C_w(0) \tag{6.2}$$

$$C_w - \frac{D_L}{v} \frac{\partial C_w}{\partial x} = C_{w,in}(t) \; @x = 0 \tag{6.3}$$

$$\lim_{x \to x_L} \frac{\partial C_w}{\partial x} = 0 \;\; \forall t \tag{6.4}$$

where n_j [-] and n_k [-] denote the total number of solid materials and porous materials, respectively; variables with subscripts *j* and *k* refer to individual components of solid and porous materials, respectively. C_w [M L^{-3}], $C_{s,j}$ [M M^{-1}] and $C_{w,p,k}$ [M L^{-3}] denote the pollutant concentration in the bulk water, in the solid materials and in the intraparticle pore water of porous materials, respectively; $C_{w,in}$ [M L^{-3}] represents pollutant concentration at the inlet of the domain. $m_{d,j}$ [M], $m_{d,k}$ [M] and V_w [L^3] are the dry mass of solid materials and porous materials and volume of water, respectively; ε_k [-] and $\rho_{p,k}$ [M L^{-3}] denote the intraparticle porosity and the bulk density of porous materials ($= \rho_{s,k}(1 - \varepsilon_k)$; $\rho_{s,k}$ [M L^{-3}] is the dry density of the solid); $K_{d,b,k}$ [L^3 M^{-1}] is the bulk distribution coefficient between bulk water and porous materials ($= K_{d,k} + \varepsilon_k/\rho_{p,k}$; $K_{d,k}$ [L^3 M^{-1}] is the distribution coefficient between bulk water and solid) where the pollutant mass stored in the intraparticle pore water phase is considered. v [L T^{-1}] and D_L [L^2 T^{-1}] denote the seepage velocity and longitudinal dispersion coefficient, respectively. x [L] represents the longitudinal coordinate. t [T] is the time. The Laplace transformation of Eqs. 6.1-6.4 are given as:

$$s\tilde{C}_w - C_w(0) + \sum_{j=1}^{n_j} \frac{m_{d,j}}{V_w}\left(s\tilde{C}_{s,j} - C_{s,j}(0)\right) + \sum_{k=1}^{n_k} \frac{m_{d,k}}{V_w} K_{d,b,k}\left(s\tilde{C}_{w,p,k} - C_{w,p,k}(0)\right) + v\frac{d\tilde{C}_w}{\partial x} - D_L\frac{d^2\tilde{C}_w}{\partial x^2} = 0 \quad (6.5)$$

$$\lim_{s\to\infty} \tilde{C}_w(x) = \tilde{C}_w(0) \quad (6.6)$$

$$\tilde{C}_w - \frac{D_L}{v}\frac{d\tilde{C}_w}{dx} = \tilde{C}_{w,in}(s)\ @x = 0 \quad (6.7)$$

$$\lim_{x\to x_L} \frac{d\tilde{C}_w}{dx} = 0\ \forall s \quad (6.8)$$

where s [T^{-1}] is the complex Laplace coordinate. The tilde sign denotes the Laplace transform of the respective variables.

Finkel et al. (2016) used the semi-Laplace solution to solve the 1-D advective-dispersive transport by considering intraparticle pore diffusion (ADE-IPPD) for heterogeneous systems and showed that the average concentration of pore water inside the porous materials ($C_{w,p,k}$) can be expressed as a function of bulk water (C_w) in form of convolution with respective transfer function in real time domain. Liu et al. (2023) extended the semi-Laplace solution to more general form by considering coupled film intraparticle diffusion for different geometries of particles (e.g., plane sheet, cylinder and sphere) and used it in solving PAHs redistribution in microplastics and soil suspension with passive samplers in batch systems and corresponding transfer functions for coupled film intraparticle diffusion; here only transfer functions of coupled film intraparticle diffusion of spherical porous ($\tilde{g}_{sp,k}$) and solid materials ($\tilde{g}_{s,j}$) are presented:

$$\begin{aligned}
\tilde{C}_{s,j} &= \tilde{g}_{s,j}\left(\tilde{C}_w - \frac{C_{s,j}(0)}{K_{d,j}s}\right) + \frac{C_{s,j}(0)}{s} \\
\tilde{C}_{w,p,k} &= \tilde{g}_{sp,k}\left(\tilde{C}_w - \frac{C_{w,p,k}(0)}{s}\right) + \frac{C_{w,p,k}(0)}{s} \\
\tilde{g}_{s,j} &= \frac{D_{s,j}K_{d,j}\left(\sqrt{\frac{s}{D_{s,j}}}\coth\left(a_{s,j}\sqrt{\frac{s}{D_{s,j}}}\right) - \frac{1}{a_{s,j}}\right)}{k_{s,j} + D_{s,j}\rho_{s,j}K_{d,j}\left(\sqrt{\frac{s}{D_{s,j}}}\coth\left(a_{s,j}\sqrt{\frac{s}{D_{s,j}}}\right) - \frac{1}{a_{s,j}}\right)}\frac{3k_{s,j}}{a_{s,j}s} \\
\tilde{g}_{sp,k} &= \frac{D_{a,k}\left(\sqrt{\frac{s}{D_{a,k}}}\coth\left(a_{sp,k}\sqrt{\frac{s}{D_{a,k}}}\right) - \frac{1}{a_{sp,k}}\right)}{k_{sp,k} + D_{a,k}\rho_{p,k}K_{d,b,k}\left(\sqrt{\frac{s}{D_{a,k}}}\coth\left(a_{sp,k}\sqrt{\frac{s}{D_{a,k}}}\right) - \frac{1}{a_{sp,k}}\right)}\frac{3k_{sp,k}}{a_{sp,k}s}
\end{aligned} \quad (6.9)$$

where $K_{d,j}$ [L^3 M^{-1}] denotes the distribution coefficient between water and solid materials.

$a_{s,j}$ [L] and $a_{sp,k}$ [L] denote grain radius spherical particles for solid materials and porous materials, respectively; $k_{s,j}$ [L T^{-1}] and $k_{sp,k}$ [L T^{-1}] are the mass transfer velocity for solid materials ($k_{s,j} = D_{aq}/\delta_{s,j}$; D_{aq} [L^2 T^{-1}] is the aqueous diffusion coefficient of the compound and $\delta_{s,j}$ [L] is the external film thickness of solid particles, which can be estimated via dimensionless Sherwood numbers ($Sh = 2a_{s,j}/\delta_{s,j}$).) and porous materials ($k_{sp,k} = D_{aq}/\delta_{sp,k}$; $\delta_{sp,k}$ [L] is the external film thickness of the porous materials), respectively; $D_{s,j}$ [L^2 T^{-1}] and $D_{a,k}$ [L^2 T^{-1}] denote the solid diffusion coefficient and the apparent diffusion coefficient of compound in the intraparticle pore space of porous materials ($D_{a,k} = D_{e,k}/(\rho_{p,k}K_{d,b,k}) = D_{aq}\varepsilon_k/(\tau_{f,k}\rho_{p,k}K_{d,b,k}) \approx D_{aq}{\varepsilon_k}^2/(\rho_{p,k}K_{d,b,k})$; $\tau_{f,k}$ [-] is the tortuosity factor; $D_{e,k}$ [L^2 T^{-1}] is the effective diffusion coefficient and empirical studies showed that $D_{e,k}$ increases approximately with the square of the intraparticle porosity (Boving et al., 2001), thus, the tortuosity factor $\tau_{f,k}$ [-] can be approximated via the reciprocal of the intraparticle porosity ($\tau_{f,k} \approx 1/\varepsilon_k$)); $\rho_{s,j}$ [M L^{-3}] denotes the dry density of the solid materials. Inserting Eq. 6.9 into Eq. 6.5, the mass conservation equation in Laplace domain can be simplified as a function of $\tilde{C}_w$:

$$\begin{aligned}
&\omega(s)\tilde{C}_w + v\frac{d\tilde{C}_w}{\partial x} - D_L\frac{d^2\tilde{C}_w}{\partial x^2} = \varphi(s)\\
&\omega(s) = \left(1 + \sum_{j=1}^{n_j}\frac{m_{d,j}}{V_w}\tilde{g}_{s,j} + \sum_{k=1}^{n_k}\frac{m_{d,k}}{V_w}K_{d,b,k}\,\tilde{g}_{sp,k}\right)s\\
&\varphi(s) = C_w(0) + \sum_{j=1}^{n_j}\frac{m_{d,j}}{V_w}\tilde{g}_{s,j}\frac{C_{s,j}(0)}{K_{d,j}} + \sum_{k=1}^{n_k}\frac{m_{d,k}}{V_w}K_{d,b,k}\tilde{g}_{sp,k}C_{w,p,k}(0)
\end{aligned} \tag{6.10}$$

Equation 6.10 can be solved with the following guess solution:

$$\tilde{C}_w(x,s) = \left(\tilde{C}_w(x=0,s) - \beta\right)\exp(-\alpha x) + \beta \tag{6.11}$$

Then the first order and second order derivative of the $\tilde{C}_w(x,s)$ can be expressed as:

$$\begin{aligned}
&\frac{d\tilde{C}_w(x,s)}{dx} = -\alpha\left(\tilde{C}_w(x=0,s) - \beta\right)\exp(-\alpha x)\\
&\frac{d^2\tilde{C}_w(x,s)}{dx^2} = \alpha^2\left(\tilde{C}_w(x=0,s) - \beta\right)\exp(-\alpha x)
\end{aligned} \tag{6.12}$$

Substitute into Eq. 6.10 yields:

$$\begin{aligned}
&(\omega(s) - \alpha v - \alpha^2 D)\left(\tilde{C}_w(x=0,s) - \beta\right)\exp(-\alpha x) + \omega(s)\beta - \varphi(s) = 0\\
&\begin{cases} D_L\alpha^2 + v\alpha - \omega(s) = 0 \\ \omega(s)\beta - \varphi(s) = 0 \end{cases} \Rightarrow \begin{cases} \alpha_{1,2} = \dfrac{-v \pm \sqrt{v^2 + 4D_L\omega(s)}}{2D} \\ \beta = \dfrac{\varphi(s)}{\omega(s)} \end{cases}
\end{aligned} \tag{6.13}$$

Thus $\tilde{C}_w(x,s)$ can be expressed as:

$$\tilde{C}_w(x,s) = \lambda_1\left[\left(\tilde{C}_w(x=0,s)-\beta\right)\exp(-\alpha_1 x)+\beta\right] + \lambda_2\left[\left(\tilde{C}_w(x=0,s)-\beta\right)\exp(-\alpha_2 x)+\beta\right] \tag{6.14}$$

where λ_1 and λ_2 are the constants determined by the boundary conditions (Eqs. 6.7 and 6.8).

The first order derivative of $\tilde{C}_w(x,s)$ is given as:

$$\frac{d\tilde{C}_w(x,s)}{dx} = -\lambda_1\left[\alpha_1\left(\tilde{C}_w(x=0,s)-\beta\right)\exp(-\alpha_1 x)\right] - \lambda_2\left[\alpha_2\left(\tilde{C}_w(x=0,s)-\beta\right)\exp(-\alpha_2 x)\right] \tag{6.15}$$

By inserting Eqs. 6.14 and 6.15 into Eqs. 6.7 and 6.8, λ_1 and λ_2 can be determined.

$$\lambda_1 = \frac{-\frac{v}{D_L}\left(\tilde{C}_{w,in}(s)-\tilde{C}_w(x=0,s)\right)\exp(-\alpha_2 x_L)}{\alpha_1\left(\tilde{C}_w(x=0,s)-\beta\right)(\exp(-\alpha_1 x_L)-\exp(-\alpha_2 x_L))}$$
$$\lambda_2 = \frac{\frac{v}{D_L}\left(\tilde{C}_{w,in}(s)-\tilde{C}_w(x=0,s)\right)\exp(-\alpha_1 x_L)}{\alpha_2\left(\tilde{C}_w(x=0,s)-\beta\right)(\exp(-\alpha_1 x_L)-\exp(-\alpha_2 x_L))} \tag{6.16}$$

For satisfying Eq. 6.11 at $x=0$, the summation of λ_1 and λ_2 should be 1, thus $\tilde{C}_w(x=0,s)$ can be calculated.

$$\tilde{C}_w(x=0,s) = \frac{\frac{v}{D_L}(\alpha_1\exp(-\alpha_1 x_L)-\alpha_2\exp(-\alpha_2 x_L))\tilde{C}_{w,in}(s)+\alpha_1\alpha_2\beta(\exp(-\alpha_1 x_L)-\exp(-\alpha_2 x_L))}{\frac{v}{D_L}(\alpha_1\exp(-\alpha_1 x_L)-\alpha_2\exp(-\alpha_2 x_L))+\alpha_1\alpha_2(\exp(-\alpha_1 x_L)-\exp(-\alpha_2 x_L))} \tag{6.17}$$

In summary, the final solution of $\tilde{C}_w$ can be expressed as:

$$\tilde{C}_w(x,s) = \lambda_1\left[\left(\tilde{C}_w(x=0,s)-\beta\right)\exp(-\alpha_1 x)+\beta\right] + \lambda_2\left[\left(\tilde{C}_w(x=0,s)-\beta\right)\exp(-\alpha_2 x)+\beta\right]$$

$$\lambda_1 = \frac{-\frac{v}{D_L}\left(\tilde{C}_{w,in}(s)-\tilde{C}_w(x=0,s)\right)\exp(-\alpha_2 x_L)}{\alpha_1\left(\tilde{C}_w(x=0,s)-\beta\right)(\exp(-\alpha_1 x_L)-\exp(-\alpha_2 x_L))}$$

$$\lambda_2 = \frac{\frac{v}{D_L}\left(\tilde{C}_{w,in}(s)-\tilde{C}_w(x=0,s)\right)\exp(-\alpha_1 x_L)}{\alpha_2\left(\tilde{C}_w(x=0,s)-\beta\right)(\exp(-\alpha_1 x_L)-\exp(-\alpha_2 x_L))}$$

$$\tilde{C}_w(x=0,s) = \frac{\frac{v}{D_L}(\alpha_1\exp(-\alpha_1 x_L)-\alpha_2\exp(-\alpha_2 x_L))\tilde{C}_{w,in}(s)+\alpha_1\alpha_2\beta(\exp(-\alpha_1 x_L)-\exp(-\alpha_2 x_L))}{\frac{v}{D_L}(\alpha_1\exp(-\alpha_1 x_L)-\alpha_2\exp(-\alpha_2 x_L))+\alpha_1\alpha_2(\exp(-\alpha_1 x_L)-\exp(-\alpha_2 x_L))} \quad (6.18)$$

$$\alpha_{1,2} = \frac{-v \pm \sqrt{v^2+4D_L\omega(s)}}{2D_L}$$

$$\beta = \frac{\varphi(s)}{\omega(s)}$$

$$\omega(s) = \left(1+\sum_{j=1}^{n_j}\frac{m_{d,j}}{V_w}\tilde{g}_{s,j}+\sum_{k=1}^{n_k}\frac{m_{d,k}}{V_w}K_{d,b,k}\,\tilde{g}_{sp,k}\right)s$$

$$\varphi(s) = C_w(0)+\sum_{j=1}^{n_j}\frac{m_{d,j}}{V_w}\tilde{g}_{s,j}\frac{C_{s,j}(0)}{K_{d,j}}+\sum_{k=1}^{n_k}\frac{m_{d,k}}{V_w}K_{d,b,k}\tilde{g}_{sp,k}C_{w,p,k}(0)$$

The pollutant concentration in bulk water in real time domain ($C_w(x,t)$) can be obtained by numerical back transformation of $\tilde{C}_w(x,s)$ with the numerical method of de Hoog et al. (1982) implemented in Matlab. The temporal and spatial average pollutant concentrations in solid materials ($C_{s,j}$) and in the intraparticle pore water of porous materials ($C_{w,p,k}$) can be calculated by inserting Eq. 6.18 into Eq. 6.9 and do the back transformation as mentioned before. For simplification, only the simulations of ADE-FIPPD (only porous materials are considered) are presented in the rest of the study.

6.2.2 Physical informed neural networks

Physical informed neural networks (PINNs) have been used as an alternative to traditional numerical methods (e.g., finite volume method (FVM) and finite element method (FEM)) for solving partial differential equations (PDEs) (Raissi, 2018; Raissi et al., 2019). Unlike the traditional time stepping PDE solvers obtaining a discrete solution on a grid, PINNs solution defines functions over the entire spatial-temporal domain at once and the functions (or networks) are trained by using training points distributed across the domain. This approach eliminates the requirements to create computationally expensive grids and takes into account the physical understanding of the targeted problem and constrains the output of neural networks by means of a system of PDEs. For simplification, only 1-D ADE-FIPPD by considering homogeneous sorbent is presented here and two neural networks (see Fig. 6.2)

are utilized as approximators for pollutant concentrations in bulk water phase (C_w) and in the intraparticle pore water phase inside the sorbent ($C_{w,p}$). This method can be easily extended to heterogenous systems by using more neural networks to represent multi-sorbents. The normalized form of ADE-FIPPD is used where the concentrations (C_w and $C_{w,p}$), time (t), distance (x) and radial distance (r) are normalized by their corresponding maximum values (C_{max}, T, L and a), which could significantly reduce the PINNs approximation error reported by Zong et al. (2023). The normalized PDEs, initial & boundary conditions (IC & BC) of ADE-FIPPD are presented in Fig. 6.2. The observation data used in training PINNs is generated from semi-Laplace solution. All normalized equations can be abbreviated as:

$$\begin{aligned}
&N\left(C_w^*({t^*}_{PDE}, {x^*}_{PDE}, \theta_1), C_{w,p}^*({t^*}_{PDE}, {x^*}_{PDE}, {r^*}_{PDE}, \theta_2)\right) \\
&\qquad = f({t^*}_{PDE}, {x^*}_{PDE}, {r^*}_{PDE}), \quad {t^*}_{PDE}, {x^*}_{PDE}, {r^*}_{PDE} \in [0,1] \\
&B\left(C_w^*({t^*}_{BC}, {x^*}_{BC}, \theta_1), C_{w,p}^*({t^*}_{BC}, {x^*}_{BC}, {r^*}_{BC}, \theta_2)\right) \\
&\qquad = h({t^*}_{BC}, {x^*}_{BC}, {r^*}_{BC}), \ \ {t^*}_{BC}, {x^*}_{BC}, {r^*}_{BC} \in [0,1] \\
&C_i^*({t^*}_{IC} = 0, {x^*}_{IC}, ({r^*}_{IC}), \theta_1 \text{ or } \theta_2) = q\left({t^*}_{IC} = 0, {x^*}_{IC}, ({r^*}_{IC})\right), \ \ {x^*}_{IC}, {r^*}_{IC} \in [0,1] \\
&C_i^*({t^*}_{data}, {x^*}_{data}, ({r^*}_{data}), \theta_1 \text{ or } \theta_2) \\
&\qquad = C_{i,ob}^*\left({t^*}_{data}, {x^*}_{data}, ({r^*}_{data})\right), \ \ {t^*}_{data}, {x^*}_{data}, ({r^*}_{data}) \in [0,1]
\end{aligned} \tag{6.19}$$

where N and B are spatial-temporal differential operators of PDEs and boundary conditions. $C_i^*({t^*}_{IC} = 0, {x^*}_{IC}, ({r^*}_{IC}), \theta_1 \text{ or } \theta_2)$ is the prediction of initial normalized concentration in bulk water (C_w^*; θ_1 is used) or in the intraparticle pore water ($C_{w,p}^*$; θ_2 is used) from neural networks. θ_1 and θ_2 denote the hyperparameters (weights and biases; details see section S6.1) of neural network 1 (used for prediction of C_w^*) and 2 (used for prediction of $C_{w,p}^*$), respectively. $C_i^*({t^*}_{data}, {x^*}_{data}, ({r^*}_{data}), \theta_1 \text{ or } \theta_2)$ denotes the prediction of observation data of C_w^* (θ_1 is used) or $C_{w,p}^*$ (θ_2 is used) from neural networks. The problem data (includes observation and simulation data) is provided by forcing the PDE functions $f({t^*}_{PDE}, {x^*}_{PDE}, {r^*}_{PDE})$, the boundary condition functions $h({t^*}_{BC}, {x^*}_{BC}, {r^*}_{BC})$, the initial condition functions $q\left({t^*}_{IC} = 0, {x^*}_{IC}, ({r^*}_{IC})\right)$ and the observation data $C_{i,ob}^*\left({t^*}_{data}, {x^*}_{data}, ({r^*}_{data})\right)$.

Thanks to the reverse mode of auto differentiation (details see section S6.2), the derivatives of neural network outputs respective to the neural network inputs can be quickly and accurately calculated ($\frac{\partial C_w^*}{\partial t^*}$, $\frac{\partial C_w^*}{\partial x^*}$, $\frac{\partial^2 C_w^*}{\partial {x^*}^2}$, $\frac{\partial C_{w,p}^*}{\partial t^*}$, $\frac{\partial C_{w,p}^*}{\partial r^*}$ and $\frac{\partial^2 C_{w,p}^*}{\partial {r^*}^2}$) and thus the values of $N\left(C_w^*({t^*}_{PDE}, {x^*}_{PDE}, \theta_1), C_{w,p}^*({t^*}_{PDE}, {x^*}_{PDE}, {r^*}_{PDE}, \theta_2)\right)$ and $B\left(C_w^*({t^*}_{BC}, {x^*}_{BC}, \theta_1), C_{w,p}^*({t^*}_{BC}, {x^*}_{BC}, {r^*}_{BC}, \theta_2)\right)$ can be determined.

The total loss function is defined as the weighted summation of the mean square errors of

residuals for the PDEs ($Loss_{PDE}$), the initial and boundary conditions ($Loss_{IC}$ & $Loss_{BC}$), and the observation data ($Loss_{data}$):

$$\begin{aligned} Loss_{total}(\theta) = \; & w_{PDE}Loss_{PDE}(\theta) + w_{IC}Loss_{IC}(\theta) + w_{BC}Loss_{BC}(\theta) \\ & + w_{data}Loss_{data}(\theta) \quad \text{where } \theta = \{\theta_1, \theta_2\} \end{aligned} \tag{6.20}$$

where w_{PDE}, w_{IC}, w_{BC} and w_{data} are weighting factors of loss terms of PDEs, initial conditions, boundary conditions and observation data. θ denotes the hyperparameters of all neural networks (here we used 2 neural networks).

The reason of introducing those weights is to magnify the differences of loss components to make sure the larger loss components would be punished more during training and the total loss function would decrease more efficiently. The loss functions without weights ('baseline PINNs algorithm') may somehow works for some non-stiff PDEs, but its performance on stiff PDEs (e.g., ADE) is very bad and produce inaccurate approximations (Wight and Zhao, 2021; Wang et al., 2021). This occurs due to the nature of gradient descent method as a greedy process. It has the tendency to prioritize certain loss components over others, creating an imbalance in the descent rates among these components. This imbalance hinders convergence to the accurate solution (McClenny and Braga-Neto, 2023). The loss components can be expressed by:

$$\begin{aligned} Loss_{PDE}(\theta) &= \frac{1}{N_{PDE}} \sum_{j}^{N_{PDE}} \Big| N\left(C_w^*\left(t^{*j}_{PDE}, x^{*j}_{PDE}, \theta_1\right), C_{w,p}^*\left(t^{*j}_{PDE}, x^{*j}_{PDE}, r^{*j}_{PDE}, \theta_2\right)\right) \\ &\quad - f\left(t^{*j}_{PDE}, x^{*j}_{PDE}, r^{*j}_{PDE}\right)\Big|^2 \\ Loss_{IC}(\theta) &= \frac{1}{N_{IC}} \sum_{j}^{N_{IC}} \left| C_i^*\left(t^{*j}_{IC} = 0, x^{*j}_{IC}, \left(r^{*j}_{IC}\right), \theta_1 \text{ or } \theta_2\right) - q\left(t^{*j}_{IC} = 0, x^{*j}_{IC}, \left(r^{*j}_{IC}\right)\right)\right|^2 \\ Loss_{BC}(\theta) &= \frac{1}{N_{BC}} \sum_{j}^{N_{BC}} \Big| B\left(C_w^*\left(t^{*j}_{BC}, x^{*j}_{BC}, \theta_1\right), C_{w,p}^*\left(t^{*j}_{BC}, x^{*j}_{BC}, r^{*j}_{BC}, \theta_2\right)\right) \\ &\quad - h\left(t^{*j}_{BC}, x^{*j}_{BC}, r^{*j}_{BC}\right)\Big|^2 \\ Loss_{data}(\theta) &= \frac{1}{N_{data}} \sum_{j}^{N_{data}} \Big| C_i^*\left(t^{*j}_{data}, x^{*j}_{data}, \left(r^{*j}_{data}\right), \theta_1 \text{ or } \theta_2\right) \\ &\quad - C_{i,ob}^*\left(t^{*j}_{data}, x^{*j}_{data}, \left(r^{*j}_{data}\right)\right)\Big|^2 \end{aligned} \tag{6.21}$$

$\left\{t^{*j}_{PDE}, x^{*j}_{PDE}, r^{*j}_{PDE}\right\}_{j=1}^{N_{PDE}}$ are training (or collocation) points used in forcing the PDEs for neural networks; $\left\{t^{*j}_{IC} = 0, x^{*j}_{IC}, r^{*j}_{IC}\right\}_{j=1}^{N_{IC}}$ and $\left\{t^{*j}_{BC}, x^{*j}_{BC}, r^{*j}_{BC}\right\}_{j=1}^{N_{BC}}$ are training points used in forcing the initial and boundary conditions for neural networks, respectively; $\left\{t^{*j}_{data}, x^{*j}_{data}, r^{*j}_{data}\right\}_{j=1}^{N_{data}}$ are training points used in forcing the observation data for neural

networks. N_{PDE}, N_{IC}, N_{BC} and N_{data} denote the total number of the collocation points, the initial and boundary condition points and observation data points, respectively.

6.2.2.1 Self-adaptive PINNs

Now the question arises for choosing the weighting factors for loss terms. A simple way is to give a constant weighting factor for each loss term. While it could improve the stability and accuracy compared to baseline PINNs, the approximation error is still large especially for step boundary conditions. To overcome that problem, this paper employed the self-adaptive PINNs algorithm, as proposed by McClenny and Braga-Neto (2023), in which the weights of the loss function are updated via gradient descent concurrently with network hyperparameters. Thus, the total loss function (Eq. 6.20) can be modified as:

$$\begin{aligned} Loss_{total}(\theta, w_{PDE}, w_{IC}, w_{BC}, w_{data}) \\ = \; Loss_{PDE}(\theta, w_{PDE}) + Loss_{IC}(\theta, w_{IC}) + Loss_{BC}(\theta, w_{BC}) \\ + Loss_{data}(\theta, w_{data}) \end{aligned} \tag{6.22}$$

where $w_{PDE} = \{w_{PDE}^1, \dots, w_{PDE}^{N_{PDE}}\}$, $w_{IC} = \{w_{IC}^1, \dots, w_{IC}^{N_{IC}}\}$, $w_{BC} = \{w_{BC}^1, \dots, w_{IC}^{N_{BC}}\}$ and $w_{data} = \{w_{data}^1, \dots, w_{data}^{N_{data}}\}$ are trainable, nonnegative self-adaptative weights for training points of PDEs, initial, boundary and observation data, respectively.

The loss components can be modified as:

$$\begin{aligned} &Loss_{PDE}(\theta, w_{PDE}) \\ &= \frac{1}{N_{PDE}} \sum_{j}^{N_{PDE}} m(w_{PDE}^j) \left| N\left(C_w^*({t^*}_{PDE}^j, {x^*}_{PDE}^j, \theta_1), C_{w,p}^*({t^*}_{PDE}^j, {x^*}_{PDE}^j, {r^*}_{PDE}^j, \theta_2)\right)\right. \\ &\left. - f({t^*}_{PDE}^j, {x^*}_{PDE}^j, {r^*}_{PDE}^j)\right|^2 \\ &Loss_{IC}(\theta) = \frac{1}{N_{IC}} \sum_{j}^{N_{IC}} m(w_{IC}^j) \left| C_i^*({t^*}_{IC}^j = 0, {x^*}_{IC}^j, ({r^*}_{IC}^j), \theta_1 \text{ or } \theta_2)\right. \\ &\left. - q\left({t^*}_{IC}^j = 0, {x^*}_{IC}^j, ({r^*}_{IC}^j)\right)\right|^2 \\ &Loss_{BC}(\theta) = \frac{1}{N_{BC}} \sum_{j}^{N_{BC}} m(w_{BC}^j) \left| B\left(C_w^*({t^*}_{BC}^j, {x^*}_{BC}^j, \theta_1), C_{w,p}^*({t^*}_{BC}^j, {x^*}_{BC}^j, {r^*}_{BC}^j, \theta_2)\right)\right. \\ &\left. - h({t^*}_{BC}^j, {x^*}_{BC}^j, {r^*}_{BC}^j)\right|^2 \\ &Loss_{data}(\theta) = \frac{1}{N_{data}} \sum_{j}^{N_{data}} m(w_{data}^j) \left| C_i^*({t^*}_{data}^j, {x^*}_{data}^j, ({r^*}_{data}^j), \theta_1 \text{ or } \theta_2)\right. \\ &\left. - C_{i,ob}^*\left({t^*}_{data}^j, {x^*}_{data}^j, ({r^*}_{data}^j)\right)\right|^2 \end{aligned} \tag{6.23}$$

where a non-negative, differentiable, strictly increasing self-adaptation function $m(w_i^j)$ is defined, for i = *PDE, IC, BC, data*. The self-adaptation function used in this paper is a simple

quadratic function where $m(w_i^j) = (w_i^j)^2$. A lot of polynomial functions with higher power (e.g., >2) or sigmoidal functions also can be used as candidates, but excessively sharp functions should be avoided in practice in case numerical overflow and more details of choosing suitable self-adaptation function see McClenny and Braga-Neto (2023).

The main idea of self-adaptive PINNs is that the total loss function ($Loss_{total}(\theta, w_{PDE}, w_{IC}, w_{BC}, w_{data})$) is minimized with the updated of the hyperparameters of the neural networks (θ), as usual, but is maximized with respect to the self-adaptation weights ($w_{PDE}, w_{IC}, w_{BC}, w_{data}$), which can be expressed by:

$$\min_{\theta} \max_{w_{PDE}, w_{IC}, w_{BC}, w_{data}} Loss_{total}(\theta, w_{PDE}, w_{IC}, w_{BC}, w_{data}) \tag{6.24}$$

By using the gradient descent/ascent method (e.g., Adam), the updated training parameters in each iteration process are given as:

$$\begin{aligned}
\theta^{k+1} &= \theta^k - \eta^k \nabla_\theta Loss_{total}(\theta^k, w_{PDE}^k, w_{IC}^k, w_{BC}^k, w_{data}^k) \\
w_{PDE}^{k+1} &= w_{PDE}^k + \sigma_{PDE}^k \nabla_{w_{PDE}} Loss_{total}(\theta^k, w_{PDE}^k, w_{IC}^k, w_{BC}^k, w_{data}^k) \\
w_{IC}^{k+1} &= w_{IC}^k + \sigma_{IC}^k \nabla_{w_{IC}} Loss_{total}(\theta^k, w_{PDE}^k, w_{IC}^k, w_{BC}^k, w_{data}^k) \\
w_{BC}^{k+1} &= w_{BC}^k + \sigma_{BC}^k \nabla_{w_{BC}} Loss_{total}(\theta^k, w_{PDE}^k, w_{IC}^k, w_{BC}^k, w_{data}^k) \\
w_{data}^{k+1} &= w_{data}^k + \sigma_{data}^k \nabla_{w_{data}} Loss_{total}(\theta^k, w_{PDE}^k, w_{IC}^k, w_{BC}^k, w_{data}^k)
\end{aligned} \tag{6.25}$$

where $\eta^k (> 0)$ is the learning rate for the hyperparameters of neural networks at training iteration step k; σ_{PDE}^k, σ_{IC}^k, σ_{BC}^k and σ_{data}^k (> 0) are separate learning rates for updating weights of loss terms of PDEs, initial and boundary conditions and observation data, respectively.

A large learning rate makes the training process faster but might cause the training parameters oscillate or even diverging away from the optimal values, while a smaller learning rate can slow down training but may lead to a more precise convergence. A decay rate (λ_{decay}) is defined to reduce the learning rate during each training iteration step. The purpose of decay is to fine-tune the learning rate as the optimization process progresses. Initially, a larger learning rate might be suitable for faster convergence, and as training continues, a smaller learning rate might be helpful for the model to fine-tune and converge more accurately towards the optimal parameters. The adaptive learning rates can be expressed as:

$$
\begin{aligned}
\mathfrak{y}^k &= \frac{\mathfrak{y}^1}{1+\lambda_{decay}*k} \\
\sigma_{PDE}^k &= \frac{\sigma_{PDE}^1}{1+\lambda_{decay}*k} \\
\sigma_{IC}^k &= \frac{\sigma_{IC}^1}{1+\lambda_{decay}*k} \\
\sigma_{BC}^k &= \frac{\sigma_{BC}^1}{1+\lambda_{decay}*k} \\
\sigma_{data}^k &= \frac{\sigma_{data}^1}{1+\lambda_{decay}*k}
\end{aligned}
\tag{6.26}
$$

where $\mathfrak{y}^1$, σ_{PDE}^1, σ_{IC}^1, σ_{BC}^1 and σ_{data}^1 denotes the initial learning rates for training the hyperparameters, PDEs, initial and boundary conditions and observation data, respectively. k denotes the training iteration step.

The gradient term with respect to the neural network hyperparameter (θ) is computed through the backpropagation algorithm (Rumelhart et al., 1986). The gradient terms with respect to the weighting factors in Eq. 6.25 are given as:

$$
\begin{aligned}
&\nabla_{w_{PDE}} Loss_{total}(\theta^k, w_{PDE}^k, w_{IC}^k, w_{BC}^k, w_{data}^k) \\
&= \begin{bmatrix} m'\left(w_{PDE}^{k,1}\right)\left|N\left(C_w^*\left(t^{*1}_{PDE}, x^{*1}_{PDE}, \theta_1^k\right), C_{w,p}^*\left(t^{*1}_{PDE}, x^{*1}_{PDE}, r^{*1}_{PDE}, \theta_2^k\right)\right) - f\left(t^{*1}_{PDE}, x^{*1}_{PDE}, r^{*1}_{PDE}\right)\right|^2 \\ \vdots \\ m'\left(w_{PDE}^{k,N_{PDE}}\right)\left|N\left(C_w^*\left(t^{*N_{PDE}}_{PDE}, x^{*N_{PDE}}_{PDE}, \theta_1^k\right), C_{w,p}^*\left(t^{*N_{PDE}}_{PDE}, x^{*N_{PDE}}_{PDE}, r^{*N_{PDE}}_{PDE}, \theta_2^k\right)\right) - f\left(t^{*N_{PDE}}_{PDE}, x^{*N_{PDE}}_{PDE}, r^{*N_{PDE}}_{PDE}\right)\right|^2 \end{bmatrix} \\
&\nabla_{w_{IC}} Loss_{total}(\theta^k, w_{PDE}^k, w_{IC}^k, w_{BC}^k, w_{data}^k) \\
&= \begin{bmatrix} m'\left(w_{IC}^{k,1}\right)\left|C_i^*\left(t^{*1}_{IC} = 0, x^{*1}_{IC}, \left(r^{*1}_{IC}\right), \theta_1^k \text{ or } \theta_2^k\right) - q\left(t^{*1}_{IC} = 0, x^{*1}_{IC}, \left(r^{*1}_{IC}\right)\right)\right|^2 \\ \vdots \\ m'\left(w_{IC}^{k,N_{IC}}\right)\left|C_i^*\left(t^{*N_{IC}}_{IC} = 0, x^{*N_{IC}}_{IC}, \left(r^{*N_{IC}}_{IC}\right), \theta_1^k \text{ or } \theta_2^k\right) - q\left(t^{*N_{IC}}_{IC} = 0, x^{*N_{IC}}_{IC}, \left(r^{*N_{IC}}_{IC}\right)\right)\right|^2 \end{bmatrix} \\
&\nabla_{w_{BC}} Loss_{total}(\theta^k, w_{PDE}^k, w_{IC}^k, w_{BC}^k, w_{data}^k) \\
&= \begin{bmatrix} m'\left(w_{BC}^{k,1}\right)\left|B\left(C_w^*\left(t^{*1}_{BC}, x^{*1}_{BC}, \theta_1^k\right), C_{w,p}^*\left(t^{*1}_{BC}, x^{*1}_{BC}, r^{*1}_{BC}, \theta_2^k\right)\right) - h\left(t^{*1}_{BC}, x^{*1}_{BC}, r^{*1}_{BC}\right)\right|^2 \\ \vdots \\ m'\left(w_{BC}^{k,N_{BC}}\right)\left|B\left(C_w^*\left(t^{*N_{BC}}_{BC}, x^{*N_{BC}}_{BC}, \theta_1^k\right), C_{w,p}^*\left(t^{*N_{BC}}_{BC}, x^{*N_{BC}}_{BC}, r^{*N_{BC}}_{BC}, \theta_2^k\right)\right) - h\left(t^{*N_{BC}}_{BC}, x^{*N_{BC}}_{BC}, r^{*N_{BC}}_{BC}\right)\right|^2 \end{bmatrix} \\
&\nabla_{w_{data}} Loss_{total}(\theta^k, w_{PDE}^k, w_{IC}^k, w_{BC}^k, w_{data}^k) \\
&= \begin{bmatrix} m'\left(w_{data}^{k,1}\right)\left|C_i^*\left(t^{*1}_{data}, x^{*1}_{data}, \left(r^{*1}_{data}\right), \theta_1^k \text{ or } \theta_2^k\right) - C_{i,ob}^*\left(t^{*1}_{data}, x^{*1}_{data}, \left(r^{*1}_{data}\right)\right)\right|^2 \\ \vdots \\ m'\left(w_{data}^{k,N_{data}}\right)\left|C_i^*\left(t^{*N_{data}}_{data}, x^{*N_{data}}_{data}, \left(r^{*N_{data}}_{data}\right), \theta_1^k \text{ or } \theta_2^k\right) - C_{i,ob}^*\left(t^{*N_{data}}_{data}, x^{*N_{data}}_{data}, \left(r^{*N_{data}}_{data}\right)\right)\right|^2 \end{bmatrix}
\end{aligned}
\tag{6.27}
$$

Since $m'\left(w_i^j\right) = 2w_i^j > 0$, $\nabla_{w_{PDE}} Loss_{total}$, $\nabla_{w_{IC}} Loss_{total}$, $\nabla_{w_{BC}} Loss_{total}$, $\nabla_{w_{data}} Loss_{total} \geq 0$, which indicates that the sequence of the loss weighting factors increase monotonically ($w_i^{1,j} < w_i^{2,j} < \cdots < w_i^{k,j} < \cdots$) if unmasked losses (terms inside the absolute sign) are nonzero. According to Eq. 6.27, the loss weighting factors get larger with the increase of the unmasked losses, which leads to stronger penalty of training neural networks and improve the prediction at those domains. As loss weighting factor of each training point becomes training parameter in SA-PINNs, the given initial values become crucial, depending on the problem. Since different unmasked loss terms might exhibit different magnitudes at the

beginning of training, the initial weighting factor is designed to magnify these magnitudes, ensuring that the higher unmasked loss terms obtain a larger weighting factor and much stronger penalty would be imposed initially to reduce the total loss more effectively.

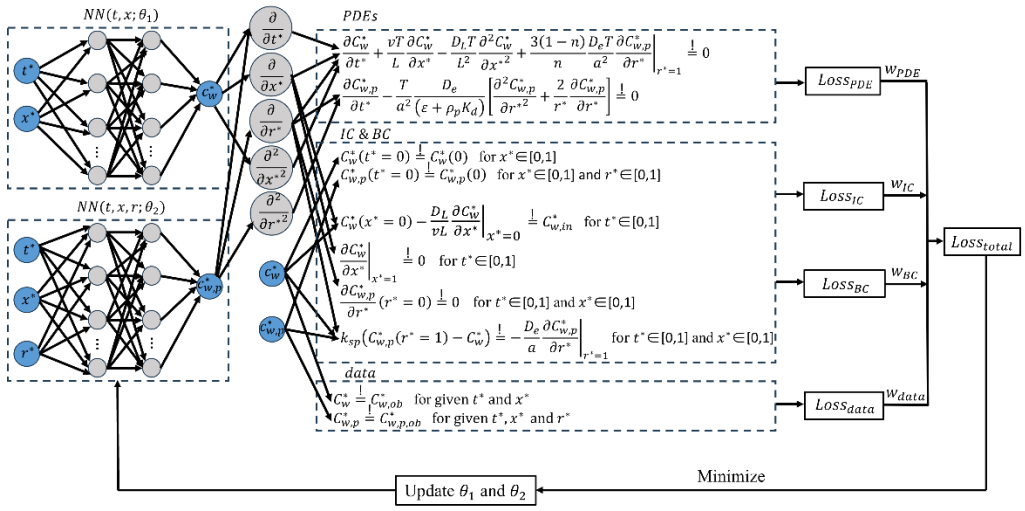

Fig. 6.2: Scheme of physical informed neural networks for solving 1-D advective dispersive transport with coupled film intraparticle pore diffusion (ADE-FIPPD).

6.2.2.2 Training processes of PINNs

Some parts of the training processes have been alluded in previous section, but several crucial details remain unexplored. In this section, we illustrate the details of training processes step by step.

The first step is to generate training data. 2500 and 50000 collocation points (black symbols in Fig. 6.3) are employed as training points to enforce two PDEs individually (see Fig. 6.2). 100 (50*2) and 5000 (2500*2) points (blue symbols in Fig. 6.3) are utilized to impose four boundary conditions ($x^* = 0$ and 1; $r^* = 0$ and 1). Furthermore, 50 and 2500 points (red symbols in Fig. 6.3) are applied in forcing the initial conditions of C_w^* and $C_{w,p}^*$, respectively. Lastly, 2500 points (green symbols in Fig. 6.3) are used in training to enforce the observation data at corresponding coordinates. The collective set of all forementioned training points is referred to as the full training data set in the text. To investigate the impacts of total number of training data on training PINNs, two cases (using half of the full training data or one quarter of full training data; details see Fig. S6.2) are compared to the case using the full training data (see Fig. 6.5). Additionally, two types of training data (sequential or random) are tested (excluding observation data) in training PINNs (see Fig. 6.5), with random training data sampled from a uniform distribution ranging from 0 to 1. Unless otherwise specified,

the training results of the main text are based on sequential training data. Since left boundary concentration of C_w^* $(x = 0)$ provides us the prior information that the concentration gradient is steep at the inlet of the transport at early time, dense sampling observation data at early time may obtain better training results. Moreover, limited observation data are frequently encountered in practice due to measurement challenges or cost constraints. To test the performance of PINNs, a scenario utilizing the full training dataset but with significantly fewer observation points (130 points) is compared to a case involving the full training dataset (2500 points) (see Fig. S6.3).

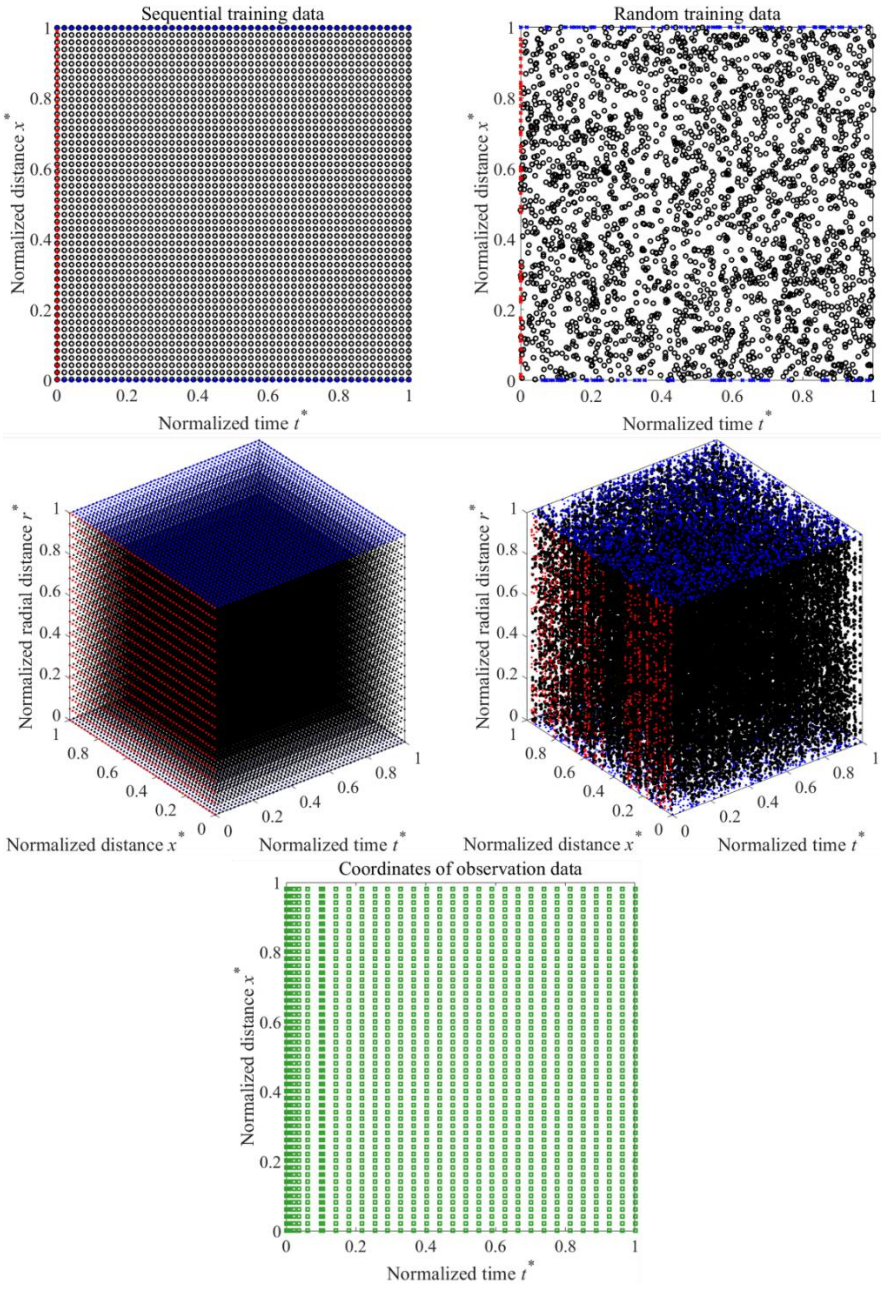

Fig. 6.3: Training data of physical informed neural networks (PINNs). The first row and

second row represent the training points of PDEs (black symbols), initial conditions (red symbols) and boundary conditions (blue symbols) of the first (output of C_w^*) and the second (output of $C_{w,p}^*$) neural network by using sequential (left column) or random (right column) training points, respectively. The third row depicts the spatial temporal coordinates of observation data applied in semi-Laplace solution to generate virtual true concentrations (here only C_w^*) as training data of PINNs.

The second step is to construct the neural networks. Two neural networks are used and both neural networks architecture with 9 fully connect operations (1 input layer + 8 hidden layers + 1 output layer) with 20 hidden neurons each (details of neutral networks see section S6.1) and the complexity of neural networks has been proved to be able to solve second order partial differential equations (e.g., Burgers' equation) by Raissi et al. (2019). Since no standard criterion for choosing the optimal neural network structures, we explored the impacts of the neural numbers in each hidden layer (see Fig. S6.4) and hidden layer numbers (see Fig. S6.5) on training PINNs. Selecting suitable activation function (e.g., sigmoid, tanh and leakyReLU (Rectified Linear Unit)) for neural networks is also crucial. The weakness of the sigmoid (or tanh) activation function lies in its vulnerability to the vanishing gradient problem, notably during backpropagation in deep networks. This hinders the neural networks' capacity to learn and adapt to intricate data patterns. Additionally, sigmoid or tanh functions tends to squash extreme values, causing saturated neurons and slower convergence in training. Alternative activation functions like leakyReLU are often preferred in training neural networks. However, selecting an activation function lacks a one-size-fits-all solution. It must be discerned based on training outcomes. Various problems may necessitate distinct activation functions, each yielding diverse effects. In our study, the leakyReLU activation function does not work well compared to sigmoid and tanh functions (see Fig. S6.6). Finally, the sigmoid function (y ∈ [0,1]) was chosen because the normalized concentrations (C_w^* and $C_{w,p}^*$) ensure neural networks outputs also fall within the range from 0 to 1 and the total loss function begins with a relatively low value, potentially leading to more efficient loss convergence initially.

The third step is defining the total loss function (Eqs. 6.22 and 6.23). The initial weighting factors for PDEs (w_{PDE}^1), initial and boundary conditions (w_{BC}^1 and w_{IC}^1) as well as observation data (w_{data}^1) are set to 1, 100, 100 and 1000, respectively. The given values are based on initial magnitudes of each loss term, higher loss terms would be punished more by giving larger initial weighting factors. Since PDEs might have infinite solutions without the constrains of initial and boundary conditions, higher initial weighting factors for w_{BC}^1 and w_{IC}^1 are better for training. Moreover, a relatively high w_{data}^1 might improve training results.

However, it's crucial to strike a balance, as excessively small or large values for w_{data}^1 may respectively result in neural networks driven solely by physical laws or purely data-driven models. As no specific criterion existed so far for giving optimal w_{data}^1, the influence of w_{data}^1 on training PINNs for ADE-FIPPD was investigated (see Fig. 6.6).

The last step is using gradient descent methods (e.g., Adam or Limited memory Broyden–Fletcher–Goldfarb–Shanno algorithm (L-BFGs)) to minimize the total loss function and find the optimal hyperparameters (θ) of neural networks. The initial learning rates (η^1, σ_{PDE}^1, σ_{IC}^1, σ_{BC}^1 and σ_{data}^1) and the decay rate (λ_{decay}) are set to 0.01. Training PINNs on the entire dataset at once can be computationally expensive and memory-intensive, especially when dealing with large datasets. Therefore, PINNs are trained with 10000 epochs by Adam and 10 mini batches are used in each epoch. The loss components of PDEs ($Loss_{PDE}$), initial and boundary conditions ($Loss_{ICBC}$), observation data ($Loss_{data}$) as well as total loss ($Loss_{total}$) are tracked in each epoch (see example in Fig. S6.7). The code is executed in 'Matlab' by using its deep learning toolbox to facilitate the training processes. After training of PINNs, trained neural networks are utilized to evaluate their performances in the test dataset.

6.2.3 Numerical model

Numerical model (NM) solved by using finite volume method has been presented in Fig. 6.1 and the details of discretization process as well as numerical iteration method (e.g., Newtown Raphson scheme) to update the solute concentration of each node at each discrete time has been explained in Liu et al. (2021).

6.2.4 Simulation parameters

Column leaching tests are widely employed to determine the capacity of pollutants release from various sources, such as soils (Kalbe et al., 2014; Röhler et al., 2021), construction and demolition wastes (Bandow et al., 2019; Prieto-Espinoza et al., 2022), and radioactive materials (Chen et al., 2021). Existing German column leaching standard (Finkel and Grathwohl, 2017) are used as input parameters for testing our models.

6.2.4.1 Input parameters for comparison of NM, PINNs and semi-Laplace solution

The summary of input parameters used in comparing of NM, PINNs and semi-Laplace solution are presented in Tab. 6.1. The contact time of mobile water with contaminated solids (here porous materials) inside the column is set to 5 h and if expressed as liquid to

solid ratio in the column (LS_{col}) we get around 0.26 L kg^{-1}. For normalizing the simulation time (t), the maximum liquid to solid ratio (LS_{end}) applied is 200 L kg^{-1}, resulting in a maximum time (T) of 3845 h. This maximum liquid to solid ratio has been tested to be able to capture the concentration descent of the breakthrough curve of reference K_d value (100 L kg^{-1}). To validate three methods' (NN, PINNs and semi-Laplace solution) performances under different K_d values, two additional K_d values (10 L kg^{-1} and 1000 kg^{-1}) are examined (see Fig. 6.4). The intraparticle porosity (ε) is set at 0.05, a value approximating sedimentary rock or concrete fragments (Rügner et al., 1999). The inter-granular porosity (n) of 0.4 is close the values applied in real experiments (e.g., 0.38-0.48 in Grathwohl and Susset, 2009). Since the aqueous diffusion coefficient (D_{aq}) of of organic compounds are similar, D_{aq} is designated as 7×10^{-10} m^2 s^{-1}, closely resembling the values for polycyclic aromatic hydrocarbons (PAHs) (Gustafson and Dickhut, 1994). The empirical Sherwood number relationship for packed beds proposed by Liu et al. (2014) is used (see Tab. 6.1).

Tab. 6.1: Input physical parameters for model comparison (NM, PINNs and semi-Laplace solutions)

Property	Symbol (Unit)	Reference and [Alternative Values]
Net column length	L (m)	0.30
Dry solid density	ρ_s (kg L^{-1})	2.70
Inter-granular porosity	n (-)	0.40
Intraparticle porosity	ε (-)	0.05
Bulk density of particles	$\rho_p = \rho_s \times (1-\varepsilon)$ (kg L^{-1})	2.57
Liquid to solid ratio in column	$LS_{col} = \frac{n}{\rho_p \times (1-n)}$ (L kg^{-1})	0.26
Liquid to solid ratio at the end	LS_{end} (L kg^{-1})	200
Contact time	t_c (h)	5
Maximum simulation time	$T = \frac{LS_{end}}{LS_{col}} \times t_c$ (h)	3846
Water flow velocity	$v = L/t_c$ (m s^{-1})	1.67×10^{-5}
Dispersivity	$\alpha = 0.1 \times L$ (m)	0.03
Aqueous diffusion coefficient	D_{aq} (m^2 s^{-1})	7.00×10^{-10}
Pore diffusion coefficient	$D_p = D_{aq} \times n$ (m^2 s^{-1})	2.80×10^{-10}
Longitudinal dispersion coefficient	$D_L = D_p + \alpha \times v$ (m^2 s^{-1})	5.00×10^{-7}
Particle diameter	d (µm)	400
Distribution coefficients	K_d (L kg^{-1})	[10,100,1000]
Kinematic viscosity of water	ϑ (m^2 s^{-1})	1.00×10^{-6}
Reynolds number	$Re = d \times v/\vartheta$ (-)	6.67×10^{-3}
Schmidt number	$Sc = \vartheta/D_{aq}$ (-)	1.43×10^{3}
Sherwood number	$Sh = 2 + 0.1Pe^{1/2}$ (-)	2.31

6.2.4.2 Input parameters for investigating mass transfer shift of ADE-FIPPD

Liu et al. (2022) used the ratios of external film diffusion (FD) and intraparticle pore

diffusion (IPPD) mass transfer resistances (R_{ex}, R_{in} = inverse mass transfer coefficients) to elucidate mass transfer shift of FIPPD, which is given as:

$$\frac{R_{ex}}{R_{in}} = \frac{d\varepsilon}{Sh}\sqrt{\frac{K_{d,b}\rho_p}{\pi D_{aq} t}} \tag{6.28}$$

The time duration dominated by film diffusion is approximated by setting R_{ex}/R_{in} to 1 (e.g., $t = \frac{K_{d,b}\rho_p}{\pi D_{aq}}\left(\frac{d\varepsilon}{Sh}\right)^2 = 0.88, 8.8$, and 88 s for K_d values of 10, 100 and 1000 L kg^{-1}, respectively; parameters used see Tab. 6.1.). Compared to maximum simulation time ($T = 3846$ h), the detection time for observing mass transfer shift of ADE-FIPPD via the breakthrough curve (BTC) is too short and condition gets worse if concentration profile is smoothed by dispersion during transport at early time. With the increase of time ($R_{ex}/R_{in} \ll 1$), mass transfer resistance shifts to intraparticle pore diffusion and the tailing of the BTC of ADE-FIPPD reflects only IPPD behavior. It is quite common to see the BTC of ADE-FIPPD to overlap with curve of ADE-IPPD when using fine-grained material with small K_d and intraparticle porosity (ε). To better elucidate the mass transfer shift behavior of ADE-FIPPD, a larger grain size of material (d = 2 cm) is compared to fine-grained material (d = 400 µm). Moreover, impacts of K_d and ε on mass transfer shift of ADE-FIPPD for both fine and coarse materials are investigated (see Fig. 6.7). Table 6.2 summarizes only the distinct physical parameters compared to Tab. 6.1; for any other required but unmentioned parameters, refer to Tab. 6.1.

Tab. 6.2: The distinct physical parameters used in simulation compared to Tab. 6.1.

Property	**Symbol (Unit)**	**Reference and [Alternative Values]**
Intraparticle porosity	ε (-)	0.05 [0.01, 0.20]
Bulk density of particles	$\rho_p = \rho_s \times (1-\varepsilon)$ (kg L^{-1})	2.57 [2.67, 2.16]
Liquid to solid ratio in column	$LS_{col} = \frac{n}{\rho_p \times (1-n)}$ (L kg^{-1})	0.26 [0.25, 0.31]
Maximum simulation time	$T = \frac{LS_{end}}{LS_{col}} \times t_c$ (h)	3846 [4010, 3226]
Particle diameter	d (µm)	400 [20000]
Reynolds number	$Re = d \times v / \vartheta$ (-)	6.67 × 10^{-3} [0.33]
Sherwood number	$Sh = 2 + 0.1Pe^{1/2}$ (-)	2.31 [4.18]

6.3 Results

6.3.1 Comparison of two mesh free methods (PINNs and semi-Laplace solution) to numerical solution (NM) of ADE-FIPPD

This section evaluates the performances of NM, PINNs as well as semi-Laplace solution in solving the ADE-FIPPD under three distribution coefficients ($K_d = 10, 100, 1000$ L kg^{-1}). Two mesh free methods almost present the same spatial-temporal normalized solute aqueous concentrations (C_w^*) profiles as NM, in particular semi-Laplace solution gives a surprising good result with absolute error ($|C_{w,PINNs}^* - C_{w,semi-Laplace}^*|$) less than 0.01 for K_d values of 10 and 1000 L kg^{-1}. In case of $K_d = 100$ L kg^{-1}, the slightly higher absolute error (< 0.05) shows up at the locations with steep concentration gradients (see Fig. 6.4; bottom panel of case 2). This deviation might not come from semi-Laplace solution, but numerical error produced by NM resulting from insufficient spatial-temporal discretization or error accumulation at each iteration or discrete time step. PINNs also perform well for all three cases and absolute error ($|C_{w,PINNs}^* - C_{w,semi-Laplace}^*|$) is less than 0.1 for most of the locations inside the spatial-temporal domain except the locations close to the inlet of the column ($x^* \to 0$) at early time ($t^* \to 0$). This is the domain with the steepest concentration gradient and thus the absolute error increases, but it is still less than 0.2. The BTC of column leaching test is crucial and most of standards are based on cumulative concentration of recycling materials at certain liquid to solid ratio (LS) (or time) (e.g., $LS = 2$ in German standard; see Bundesgesetzblatt, 2021), which can be easily obtained by integration of the BTC over time. Moreover, distribution coefficients (K_d) of porous material also can be roughly approximated by finding the corresponding LS (or time) of the BTC when eluate concentration decreases to half of its initial concentration (e.g., when $C_w^* = 0.5$ in case 2 ($K_d = 100$ L kg^{-1}), t^* is around 0.5, which is equivalent to $LS = 0.5\ LS_{end} = 100$ L kg^{-1}; Grathwohl and Susset, 2009). The comparison of the BTCs of ADE-FIPPD by using two mesh free methods and NM are presented as well in Fig. 6.4. The BTCs of semi-Laplace solution overlap the curves of NM for all three K_d cases, while PINNs slightly underestimate the BTCs for K_d values of 100 and 1000 L kg^{-1}, but the errors stay below 10%, which is lower than the measurement error and can be used in practice. The underestimation of the BTCs is due to sigmoid activation function of PINNs and in some cases a better performance might be obtained by using the tanh activation function (see case 2 in Fig. S6.6). The performance of the sigmoid seems better than the tanh function if the observation data points decrease to 130 points especially at the inlet of the column at early times (see case 1 in Fig. S6.6). Initial total loss ($Loss_{total}$) in training PINNs sometimes is larger by using the tanh function compared to sigmoid function. Training PINNs using the tanh function might get worse training result if training times decrease. Balancing training accuracy and training times of PINNs is always an open question.

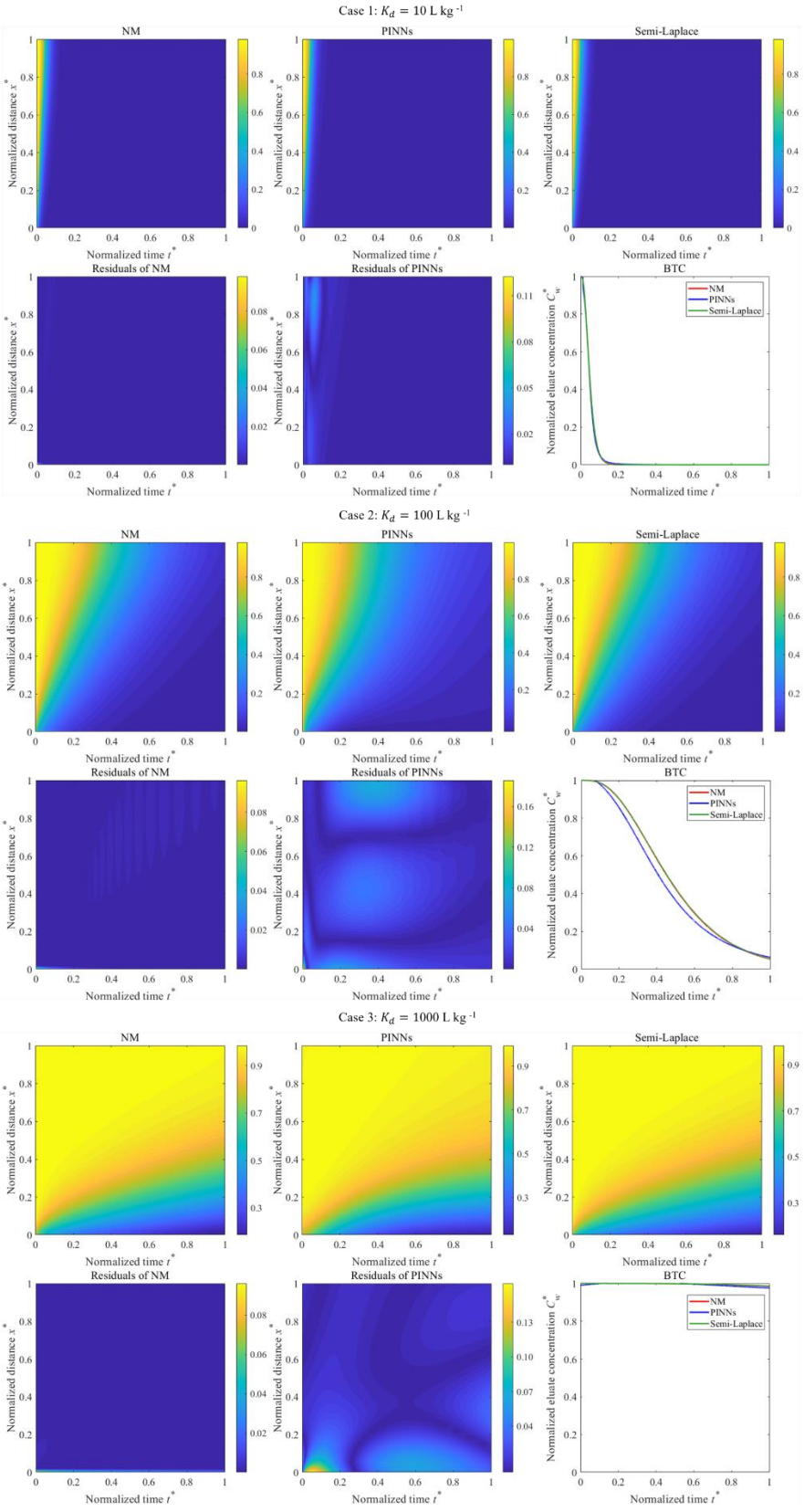

Fig. 6.4: Comparison of numerical solution (using finite volume method) and PINNs solution with semi-Laplace solution of advective-dispersive transport with coupled film intraparticle pore diffusion (ADE-FIPPD) for three K_d cases (K_d = 10, 100, 1000 L kg^{-1}). In each case, spatial-temporal normalized solute aqueous concentrations (C_w^*) of three methods are

presented in the top panel. The absolute errors of numerical solution ($|C^*_{w,NM} - C^*_{w,semi-Laplace}|$) and PINNs ($|C^*_{w,PINNs} - C^*_{w,semi-Laplace}|$) as well as breakthrough curves (BTCs) at the outlet ($x^* = 1$) of the transport are depicted in the bottom panel. (Parameters used in simulation are described in section 6.2.4.1.)

6.3.2 Sequential training data vs. random training data

The training data for PINNs is crucial as it plays a significant role in how well the networks can learn and they represent the underlying physical of the problem. In this section, the performances of PINNs by using different amounts of sequential training data or random training data are compared. With the increase of the total amounts of sequential training data, there is no significant improvement in training results (see first column of Fig. 6.5). The BTCs for all three cases (full training data, half and one quarter of the full training data) result in similarly good results (see red lines in the last column of Fig. 6.5). Surprisingly, PINNs trained with half of the full training data exhibit poorer performance than those trained with one-quarter of the full training data (see second column of Fig. 6.5). Merely increasing the random training data might not always improve the training results of PINNs. The efficiency of training PINNs with random data is strongly influenced by the distribution of training data in spatial-temporal domain. In comparison to the BTCs of three cases obtained using sequential training data, those derived from random training data cannot be replicated and the stepwise BTCs occur for PINNs trained with half of the full training data and one quarter of training data (see blue lines in the last column of Fig. 6.5). PINNs trained with full training data, whether sequential or random, consistently yield good results. This indicates that type of training data is not important for PINNs when the total amount of training data possesses sufficient spatial and temporal resolution to capture the intricacies of the underlying physics. However, sequential training data seems a better choice in training PINNs when training data is too sparse.

The good performance of PINNs might be suspected to be due to abundant observation data (2500 observation data) with the relatively larger initial weighting factor ($w^1_{data} = 1000$, discussed in next section), potentially rendering PINNs as predominantly data-driven model. To rule out this hypothesis, we conducted an analysis by training PINNs using the full training data but with limited observation data (130 points). Surprisingly, the training result demonstrates comparable performance to the case using the full 2500 observation data (see Fig. S6.3). This adaptability to limited observation data makes PINNs a valuable tool in situations where acquiring extensive datasets may be challenging or costly.

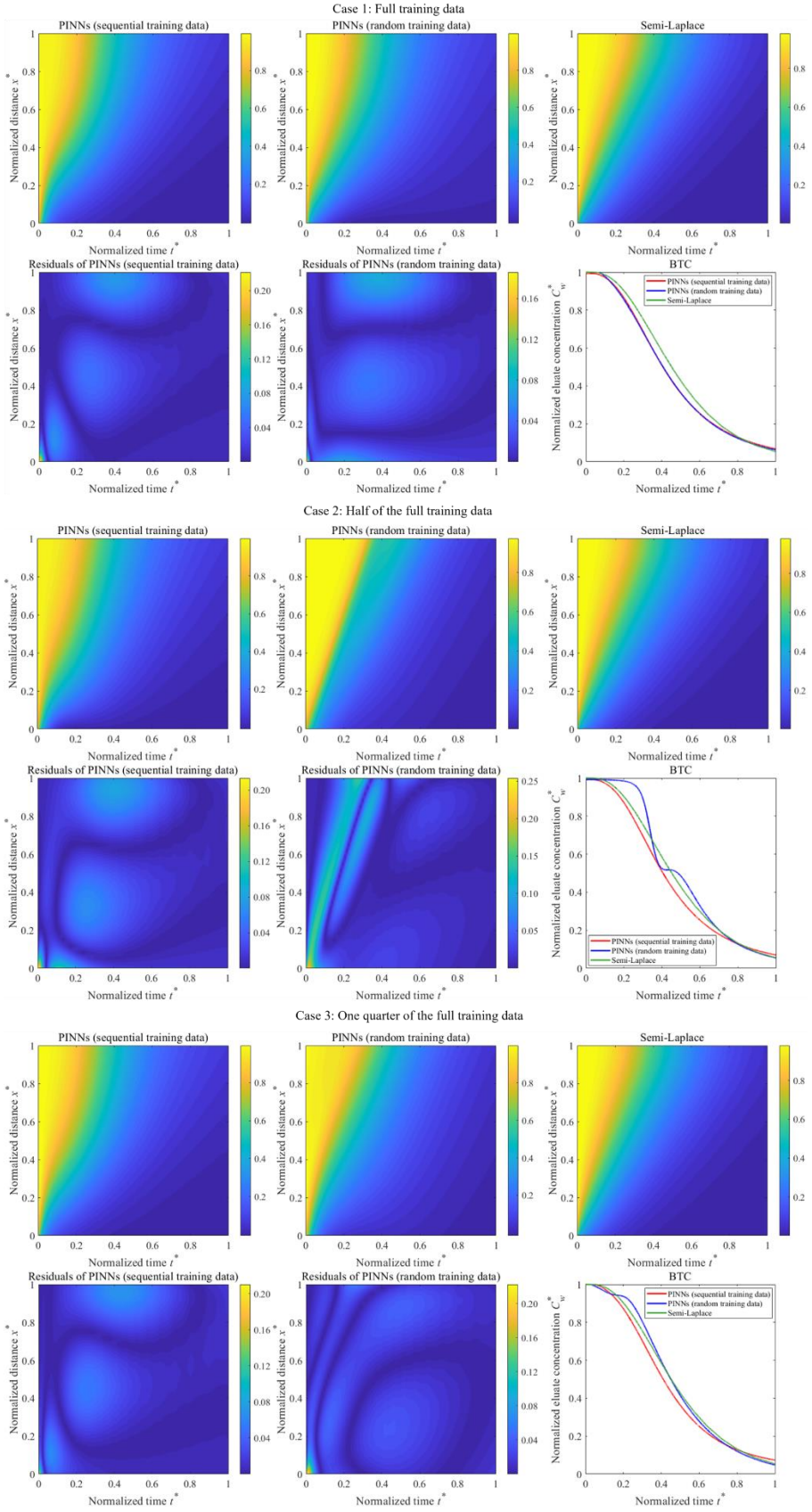

Fig. 6.5: Comparison of PINNs solutions by using different amounts of sequential training data and random training data (case 1: Full training data; case 2: Half of the full training data; case 3: One quarter of the full training data) with semi-Laplace solution (as reference) of

advective-dispersive transport with coupled film intraparticle pore diffusion (ADE-FIPPD). In each case, spatial-temporal normalized solute aqueous concentrations (C_w^*) of PINNs solutions and semi-Laplace solution are presented in the top panel. The absolute errors of PINNs solutions ($|C_{w,PINNs}^* - C_{w,semi-Laplace}^*|$) as well as the breakthrough curves (BTCs) at the outlet ($x^* = 1$) of the transport are showed in the bottom panel. (Parameters used in simulation are described in section 6.2.4.1; here only case of $K_d = 100$ L kg^{-1} is displayed.)

6.3.3 Impact of initial weighting factors of observation data (w_{data}^1) on training PINNs

Initial weighting factors of observation data (w_{data}^1) are used as regulator between purely data driven models and purely physics driven models. In our case, training PINNs with the higher w_{data}^1 (1000) performs better than PINNs trained with small w_{data}^1 (= 100) for both spatial-temporal concentrations as well as BTCs (see Fig. 6.6). w_{data}^1 of 100 is the same as the weighting factors of initial and boundary conditions (w_{BC}^1 and w_{IC}^1), which might lead to an equivalently punishment in gradient descent. However, the weakness of the PINNs in simulating steep gradients (initial and boundary conditions) may interfere the training of observation data and results in bad training results. The deviations might be reduced with the increase of training epochs or learning rates but of course time-consuming.

The comparison of the pure data-driven model and PINNs is presented in Fig. S6.8. The pure data-driven model, implemented as a neural network (NN), exhibits good performance as expected across the entire spatial-temporal domain when large amounts of training data is used (2500 points), especially in regions with very steep concentration gradients. In contrast, PINNs, which integrate both physical laws and observation data, perform slightly poorer, particularly in areas with sharp gradients (see Fig. S6.8 case 2). Despite the observation data being generated from a semi-Laplace solution that adheres to the same physical laws, PINNs struggle to accurately capture very steep gradient regions. The opposite scenario occurs when the overall quantity of observation data decrease to 130 points (see Fig. S6.8, case 1). In this context, predictions of NN deteriorate compared to PINNs, particularly in regions where training data is sparse. PINNs demonstrate superior performance by adhering to physical laws, whereas the NN struggles to grasp these principles, resulting in unrealistic predictions. Moreover, observation data in practice result from the complex interplay of certain physical laws, which not always adequately explain the observed phenomena. In scenarios where physical laws alone fall short, PINNs may outperform single (or few) physical-law-based numerical models by assigning higher weights (w_{data}^1) during training.

Essentially, PINNs serve as a conduit between the truth (observation data) and our understanding of the truth based on physical laws.

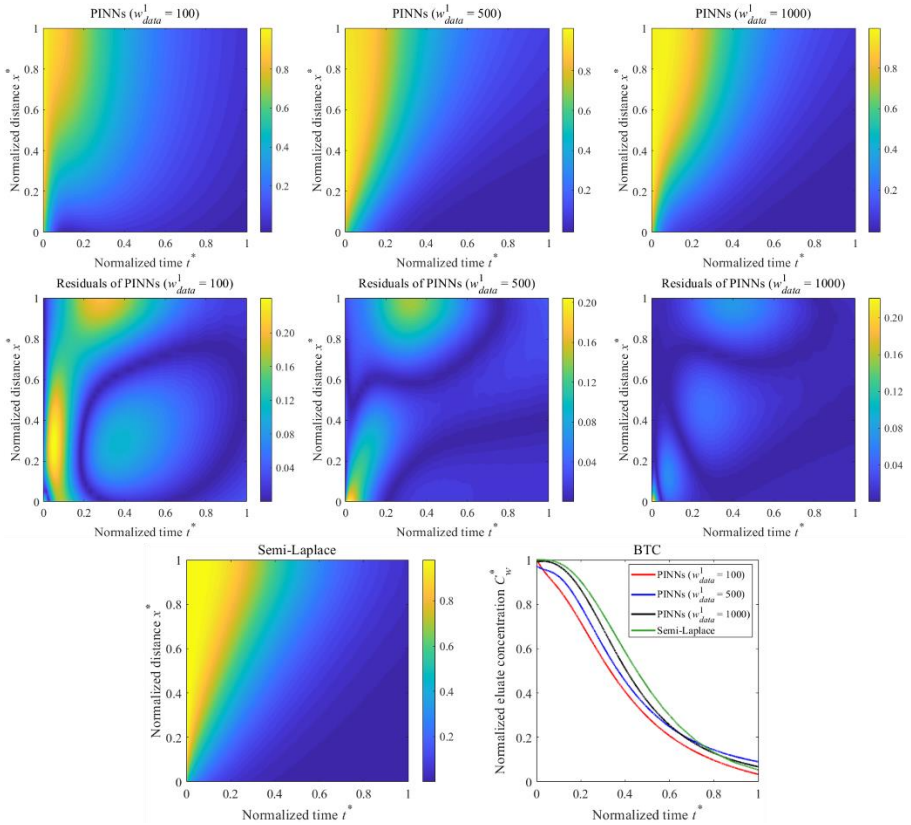

Fig. 6.6: Comparison of PINN solutions by using different initial loss weighting factors of observation data (w^1_{data} = 100, 500, 1000) with the semi-Laplace solution (as reference) of advective-dispersive transport with coupled film intraparticle pore diffusion (ADE-FIPPD). In each case, spatial-temporal normalized solute aqueous concentrations (C^*_w) of PINNs solutions are presented in the top panel. The absolute errors of PINN solutions ($|C^*_{w,PINNs} - C^*_{w,semi-Laplace}|$) and semi-Laplace solutions as well as the breakthrough curves (BTCs) at the outlet ($x^* = 1$) of the transport are shown in the mid and bottom panel, respectively. (Parameters used in simulation are described in section 6.2.4.1; here only cases of $K_d = 100$ L kg^{-1} are displayed.)

6.3.4 Mass transfer shifts for ADE-FIPPD

Grathwohl (2014) defined the mass transfer zone lengths for both film diffusion ($X_{s,\mathrm{ADE-FD}}$) and intraparticle pore diffusion ($X_{s,\mathrm{ADE-IPPD}}$) to present the distance traveled after 63.2% of equilibrium is reached after the first pore volume of water inside the column (initial pre-equilibrium water (see Eq. 6.2)) is displaced.

$$X_{s,\mathrm{ADE-FD}} = \frac{v\,n\,d}{6\,(1-n)\,k_{sp}} = \frac{v\,n\,d^2}{6\,(1-n)D_{aq}\,Sh}$$
$$X_{s,\mathrm{ADE-IPPD}} = \frac{v\,n\,d}{6(1-n)}\frac{\sqrt{\pi D_a \frac{d}{v}}}{D_e} = \frac{n}{6(1-n)}\sqrt{\frac{\pi d^3 v}{D_e\left(\varepsilon + K_d\rho_p\right)}} \quad (6.29)$$

$X_{s,\mathrm{ADE-FD}}$ is independent on K_d, while $X_{s,\mathrm{ADE-IPPD}}$ decreases with the increase of $\sqrt{K_d}$. Longer mass transfer zone lengths mean slower desorption kinetics and the equilibration concentration is not reached if the transport distance is shorter. The relative mass transfer zone length ratio ($X_{s,\mathrm{ADE-FD}}$ /$X_{s,\mathrm{ADE-IPPD}}$) equals to mass transfer resistance ratio (R_{ex}/R_{in}, Eq. 6.28) by setting contact time t to d/v.

$$\frac{X_{s,\mathrm{ADE-FD}}}{X_{s,\mathrm{ADE-IPPD}}} = \frac{d\varepsilon}{Sh}\sqrt{\frac{K_{d,b}\rho_p}{\pi D_{aq}\frac{d}{v}}} = \frac{\varepsilon}{Sh}\sqrt{\frac{K_{d,b}\rho_p d v}{\pi D_{aq}}} \quad (6.30)$$

In case 1, $X_{s,\mathrm{ADE-FD}}$ for all K_d values are 1.84×10^{-4} m for fines ($d = 400$ μm) and 0.25 m for coarse particles ($d = 2$ cm), respectively. $X_{s,\mathrm{ADE-IPPD}}$ for K_d values of 10, 100 and 1000 L kg^{-1} are 9.60×10^{-4} m, 3.01×10^{-4} m, and 9.61×10^{-5} m for fines ($d = 400$ μm) and 0.34 m, 0.11 m and 0.03 m for coarse particles ($d = 2$ cm), respectively. $X_{s,\mathrm{ADE-FD}}$ of fines for K_d values of 10 and 100 L kg^{-1} are shorter than $X_{s,\mathrm{ADE-IPPD}}$, which leads to the first drop of the BTCs of ADE-IPPD (open circle symbols in the upper left of Fig. 6.7) compared to the curves of ADE-FD (cross symbols). $X_{s,\mathrm{ADE-FD}}$ and $X_{s,\mathrm{ADE-IPPD}}$ of fines are much shorter than column length ($L = 0.30$ m) and equilibration concentration ($C_w^* = 1$) holds for longer times compared to the coarse particles. The retardation factor (R_d) increases with the increase of K_d and concentration drop profiles come later for larger K_d values (blue lines and symbols drop lastly). The BTCs of ADE-FIPPD (lines in the upper left of Fig. 6.7) almost overlap the curves of ADE-IPPD for fines due to too short duration times dominated by ADE-FD (discussed in section 6.2.4.2). The reverse behaviors show up with the increase of grain size, and $X_{s,\mathrm{ADE-IPPD}}$ of the coarse particles for K_d values of 10 and 100 L kg^{-1} (0.11 m and 0.03 m) becomes shorter than $X_{s,\mathrm{ADE-FD}}$ (0.25 m), which leads to the first drop of the BTCs of ADE-FD (cross symbols in the upper right of Fig. 6.7) instead of curves of ADE-IPPD (open circle symbols). $X_{s,\mathrm{ADE-FD}}$ of the coarse particles (0.25 m) is close to the total length of the column (0.3 m) and equilibrium concentration cannot reach after displacing the first pore volume of water, but a second step peak controlled by slow desorption of film diffusion shows up for a while and decrease finally until all solutes are washed out from column. For large K_d (= 1000 L kg^{-1}), the BTCs of ADE-FIPPD (blue lines in the upper right of Fig. 6.7) follow the curve of ADE-FD at early time and shift to ADE-IPPD at late time. With the decrease of K_d, mass transfer shift from ADE-FD to ADE-IPPD occurs earlier and ADE-FIPPD only shows the behavior of ADE-IPPD (see red lines in the upper right of Fig. 6.7). In case 2, impact of

intraparticle porosity ($\varepsilon = 0.01, 0.05$ and 0.20) on mass transfer shift of ADE-FIPPD was investigated. Like in batch tests (Liu et al., 2022), mass transfer shifts in ADE-FIPPD from ADE-FD to ADE-IPPD is delayed with the increase of intraparticle porosity (see lines and symbols in the bottom right of Fig. 6.7). The BTCs of coarse particle with large intraparticle porosity (orange lines) shift to ADE-IPPD (orange open circle symbols) later compared to the particle with small intraparticle porosity (see red lines and symbols). The BTCs of ADE-FIPPD using PINNs (solid lines in Fig. 6.7) and semi-Laplace solution (dashed lines in Fig. 6.7) almost overlap under different K_ds and intraparticle porosities, which validates the feasibility of PINNs in investigating mass transfer shift of coupled model. In summary, mass transfer shift of ADE-FIPPD might only be detected at early times for the coarse particles with large $K_d s$ and intraparticle porosities. Fines particles merely present the behavior of ADE-IPPD.

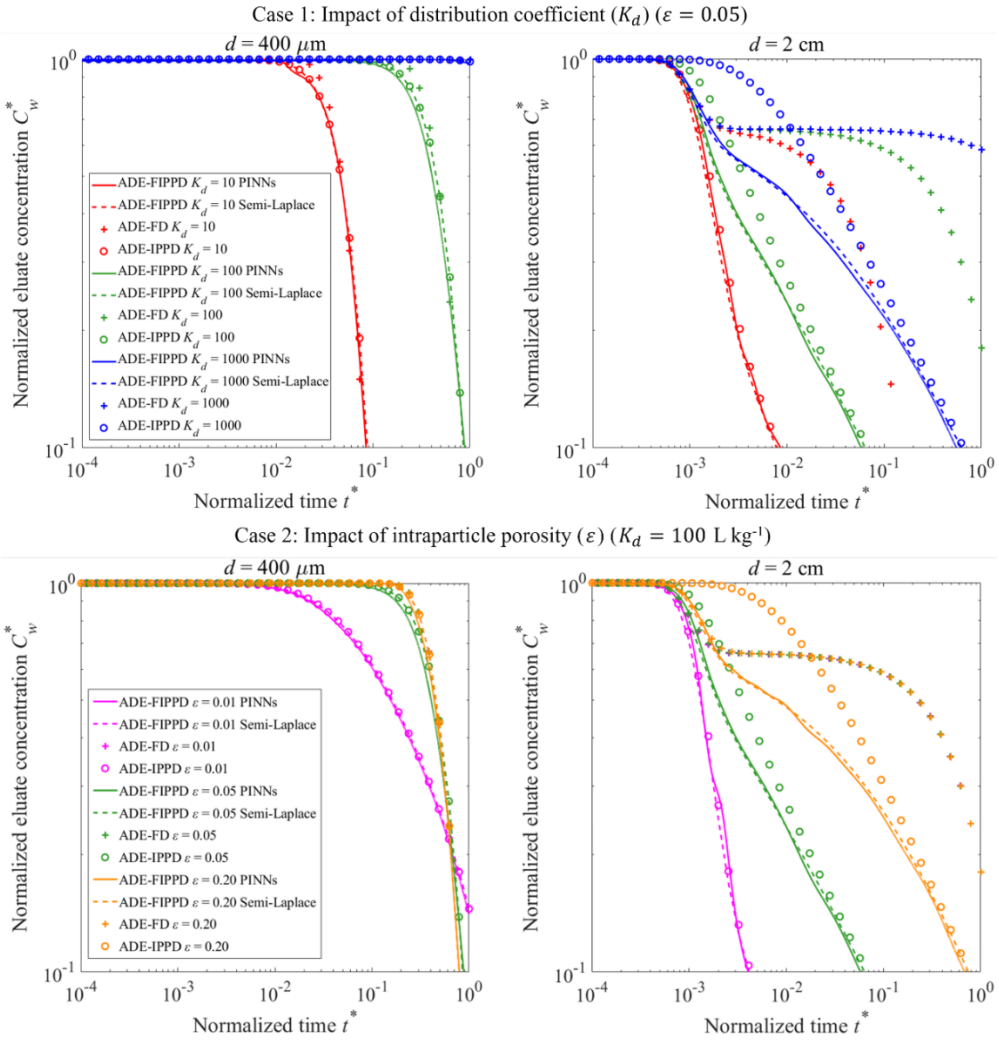

Fig. 6.7: Impact of distribution coefficient (K_d) (case 1; top panel) and intraparticle porosity (ε) (case 2; bottom panel) on mass transfer shift of advective-dispersive transport with

coupled film intraparticle pore diffusion for homogeneous fines ($d = 400$ μm; left column) and coarse particles ($d = 2$ cm; right column). Normalized eluate concentrations (C_w^*) vs. normalized time (t^*) curves of coupled model (ADE-FIPPD) using PINNs (solid lines) and semi-Laplace solution (dashed lines), film diffusion model (ADE-FD; cross symbols) and intraparticle pore diffusion model (ADE-IPPD; circle symbols) are compared. (FD and IPPD simulation results are based on semi-Laplace solution.)

6.4 Conclusions

Both semi-Laplace solution and PINNs can be used as alternatives of numerical models (NM) for solving ADE-FIPPD. Semi-Laplace solution performs best with deviations of normalized concentration being less than 1% compared to NM (see Fig. 6.4); moreover, the numerical inverse Laplace transformation is very efficient and precise. However, we must note that the semi-Laplace solution only works for linear sorption (or non-linear sorption approximated by linear sorption) and should not be viewed as a fully replacement of classical NM (works also for non-linear sorption). The results of PINNs are slightly worse than semi-Laplace solution but the accuracy is sufficient for practical purposes (deviations <10%; less than typical analytical measurement errors) in most of the spatial-temporal domain excluding the prediction at the inlet of the domain (locations with the steepest concentration gradient, deviations <20%). While setting up PINNs is an easy process, the task of selecting the optimal neural network structures (including number of layers and neurons, activation functions, neural network initialization methods, etc.), training data (such as the type and quantity of training data) and parameters (initial loss weighting factors, training epochs, learning rate, decay rate and loss optimization method, etc.) are time-consuming and tricky. Although the total training time of PINNs may take longer than NM in the 1D case, PINNs offer us with a new idea to solve partial differential equations, and it might be more effective than NM in higher dimension cases where computational demand increases tremendously. The mass transfer shift of ADE-FIPPD is more likely to be observed for the coarse particles with large K_ds and intraparticle porosities. ADE-FIPPD of fines almost presents the same behavior of ADE-IPPD due to short duration dominated by ADE-FD at early time as well as kinetics diluted by dispersion especially at high concentration gradient domain.

References

Bandow, N., Finkel, M., Grathwohl, P., Kalbe, U., 2019. Influence of flow rate and particle size on local equilibrium in column percolation tests using crushed masonry. J. Mater. Cycles Waste Manag. 21, 642–651. https://doi.org/10.1007/s10163-019-00827-3.

Bundesgesetzblatt, 2021. Verordnung zur Einführung einer Ersatzbaustoffverordnung, zur Neufassung der Bundes-Bodenschutz- und Altlastenverordnung und zur Anderung ¨der Deponieverordnung und der Gewerbeabfallverordnung. Bundesgesetzblatt Teil I Nr. 43, Bonn, 16. Juli 2021.

Chen, Z., Zhang, P., Brown, K.G., Branch, J.L., van der Sloot, H.A., Meeussen, J.C.L., Delapp, R.C., Um, W., Kosson, D.S., 2021. Development of a geochemical speciation model for use in evaluating leaching from a cementitious radioactive waste form. Environ. Sci. Technol. 55, 8642–8653. https://doi.org/10.1021/acs.est.0c06227.

de Hoog, F.R., Knight, J.H., Stokes, A.N., 1982. An improved method for numerical inversion of Laplace transforms. SIAM J. Sci. Stat. Comput. 3, 357–366. https://doi.org/10.1137/0903022.

Finkel, M., Grathwohl, P., Cirpka, O.A., 2016. A travel time-based approach to model kinetic sorption in highly heterogeneous porous media via reactive hydrofacies. Water Resour. Res. 52, 9390–9411. https://doi.org/https://doi.org/10.1002/2016WR019147.

Finkel, M., Grathwohl, P., 2017. Impact of pre-equilibration and diffusion limited release kinetics on effluent concentration in column leaching tests: Insights from numerical simulations. Waste Manag. 63, 58–73. https://doi.org/10.1016/j.wasman.2016.11.031.

Guo, B., Zeng, J., Brusseau, M.L., 2020. A mathematical model for the release, transport, and retention of per- and polyfluoroalkyl substances (PFAS) in the vadose zone. Water Resour. Res. 56, e2019WR026667. https://doi.org/https://doi.org/10.1029/2019WR026667.

Gustafson, K.E., Dickhut, R.M., 1994. Molecular diffusivity of polycyclic aromatic hydrocarbons in aqueous solution. J. Chem. Eng. Data. 39, 281–285. https://doi.org/10.1021/je00014a019.

Grathwohl, P., Susset, B., 2009. Comparison of percolation to batch and sequential leaching tests: Theory and data. Waste Manag. 29, 2681–2688. https://doi.org/https://doi.org/10.1016/j.wasman.2009.05.016.

Kalbe, U., Bandow, N., Bredow, A., Mathies, H., Piechotta, C., 2014. Column leaching tests on soils containing less investigated organic pollutants. J. Geochemical Explor. 147, 291–297. https://doi.org/10.1016/j.gexplo.2014.06.014.

Karniadakis, G.E., Kevrekidis, I.G., Lu, L., Perdikaris, P., Wang, S., Yang, L., 2021. Physics-

informed machine learning. Nat. Rev. Phys. 3, 422–440. https://doi.org/10.1038/s42254-021-00314-5.

L. Wight, C., Zhao, J., 2021. Solving Allen-Cahn and Cahn-Hilliard Equations Using the Adaptive Physics Informed Neural Networks. Commun. Comput. Phys. 3, 930–954. https://doi.org/http://doi.org/10.4208/cicp.OA-2020-0086.

Liu, B., Finkel, M., Grathwohl, P., 2021. Mass transfer principles in column percolation tests: Initial conditions and tailing in heterogeneous materials. Materials (Basel). 14, 4708. https://doi.org/10.3390/ma14164708.

Liu, B., Finkel, M., Grathwohl, P., 2022. First order approximation for coupled film and intraparticle pore diffusion to model sorption/desorption batch experiments. J. Hazard. Mater. 429, 128314. https://doi.org/10.1016/j.jhazmat.2022.128314.

Liu, B., Finkel, M., Qin, Q., Shi, W., Grathwohl, P., 2023. Mechanistic modelling of pollutant redistribution in heterogeneous systems. (not published yet)

Liu, Y., Illangasekare, T.H., Kitanidis, P.K., 2014. Long-term mass transfer and mixing-controlled reactions of a DNAPL plume from persistent residuals. J. Contam. Hydrol. 157, 11–24. https://doi.org/https://doi.org/10.1016/j.jconhyd.2013.10.008.

McClenny, L.D., Braga-Neto, U.M., 2023. Self-adaptive physics-informed neural networks. J. Comput. Phys. 474, 111722. https://doi.org/https://doi.org/10.1016/j.jcp.2022.111722.

Ngueleu, S.K., Grathwohl, P., Cirpka, O.A., 2013. Effect of natural particles on the transport of lindane in saturated porous media: Laboratory experiments and model-based analysis. J. Contam. Hydrol. 149, 13–26. https://doi.org/https://doi.org/10.1016/j.jconhyd.2013.02.009.

Prieto-Espinoza, M., Susset, B., Grathwohl, P., 2022. Long-term leaching behavior of organic and inorganic pollutants after wet processing of solid waste materials. Materials 15, 858. https://doi.org/10.3390/ma15030858.

Raissi, M., 2018. Forward-backward stochastic neural networks: Deep learning of high-dimensional partial differential equations. arXiv preprint arXiv:1804.07010. https://doi.org/10.48550/arXiv.1804.07010

Raissi, M., Perdikaris, P., Karniadakis, G.E., 2019. Physics-informed neural networks: A deep learning framework for solving forward and inverse problems involving nonlinear partial differential equations. J. Comput. Phys. 378, 686–707. https://doi.org/https://doi.org/10.1016/j.jcp.2018.10.045.

Rumelhart, D.E., Hinton, G.E., Williams, R.J., 1986. Learning representations by back-

propagating errors. Nature. 323, 533–536. https://doi.org/10.1038/323533a0.

Rügner, H., Kleineidam, S., Grathwohl, P., 1999. Long term sorption kinetics of phenanthrene in aquifer materials. Environ. Sci. Technol. 33, 1645–1651. https://doi.org/10.1021/es980664x.

Röhler, K., Haluska, A.A., Susset, B., Liu, B., Grathwohl, P., 2021. Long-term behavior of PFAS in contaminated agricultural soils in Germany. J. Contam. Hydrol. 241, 103812. https://doi.org/10.1016/J.JCONHYD.2021.103812.

Seidensticker, S., Zarfl, C., Cirpka, O.A., Fellenberg, G., Grathwohl, P., 2017. Shift in Mass Transfer of Wastewater Contaminants from Microplastics in the Presence of Dissolved Substances. Environ. Sci. Technol. 51, 12254–12263. https://doi.org/10.1021/acs.est.7b02664.

van Genuchten, M.Th., Alves W. J., 1982. "Analytical Solutions of the One–Dimensional Convective–Dispersive Solute Transport Equation," Technical Bulletin (United States Department of Agriculture), No. 1661.

Wang, S., Teng, Y., Perdikaris, P., 2021. Understanding and Mitigating Gradient Flow Pathologies in Physics-Informed Neural Networks. SIAM J. Sci. Comput. 43, A3055–A3081. https://doi.org/10.1137/20M1318043.

Zong, Y., He, Q., Tartakovsky, A.M., 2023. Improved training of physics-informed neural networks for parabolic differential equations with sharply perturbed initial conditions. Comput. Methods Appl. Mech. Eng. 414, 116-125. https://doi.org/https://doi.org/10.1016/j.cma.2023.116125.

7 Conclusions and outlooks

To theoretically investigate the mass transfer governed by coupled film-intraparticle diffusion, semi-Laplace and numerical solutions are proposed in both, batch systems as well as advective transport cases. For linear sorption (or where linearization of non-linear sorption is possible), the semi-Laplace solution can be easily applied in heterogeneous systems (mixing samples) and different kinetics models can be flexibly changed by using different transfer functions. The average concentration in each sorbent can be obtained efficiently by doing inverse Laplace transformation. The numerical solution has to be used for strongly non-linear sorption cases. For practical use, a first order approximation solution is derived, which can be easily applied for fractional mass uptakes in the homogenous sorbent at equilibrium ranging from 50 to 91%, representing scenarios typically encountered in batch experiments. As an alternative of numerical solution, the physical informed neural networks (PINNs) are utilized in solving advective dispersive transport with coupled model. The accurate and approximate solutions (or surrogate models) mentioned above provide us the tools to investigate the mass transfer shift of the coupled model. The mass transfer shift of the coupled model from external film diffusion into intraparticle diffusion is delayed with the increase of distribution coefficient (K_d), intraparticle porosity (ε), and the decrease of Sherwood number. The threshold time point of mass transfer shift can be approximated by setting the mass transfer resistance ratio (R_{ex}/R_{in}) to 1. The mass transfer shift can be easily observed for large grain size of strong sorbents (e.g., microplastic, tire wear, etc.) with large intraparticle porosity (e.g., activated carbon, biochar, etc.) at early times in batch tests. For advective-dispersive transport with coupled model (ADE-FIPPD), the mass transfer shift behavior is very difficult to be observed via breakthrough curves (BTCs) due to the dilution effect of dispersion at early times as well as the relatively short duration time of mass transfer shift compared to the total running time of transport. The tailing of BTCs of ADE-FIPPD only presents the kinetics behavior of intraparticle diffusion.

In a real case application, the coupled model is used to explain the particle/gas distribution kinetics of polycyclic aromatic hydrocarbons (PAHs) in the atmosphere. Low molecular weight PAHs (low LogK_{pg}) are dominated by intraparticle pore diffusion (IPPD) leading to a slope of 1/2, while high molecular weight PAHs (high LogK_{pg}) are controlled by external film diffusion (FD) resulting in a maximum Log$K_{pg,a}$ (slope of 0). Intermediate PAHs are influenced by both FD and IPPD (transition zone). The semi-Laplace solution in heterogenous systems is validated against data of two batch experiments: (i) the redistribution of Phenanthrene in spherical microplastics of different sizes and (ii) redistribution of Anthracene-d10 and Phenanthrene in heterogenous sediment suspension with polyethylene passive samplers. The fitted Sherwood numbers (or mass transfer

coefficients) are consistent to the values obtained based on Kolmogorov's turbulence theory. The discrepancy of fitting K_d values from sorption and desorption kinetics data in batch test (ii) implies the sediments might contain small fraction of strong sorbents (e.g., soot or charcoal particles). The sorption/desorption kinetics of those strong sorbents are super slow (few months to years) but carry large amount of pollutants, which can not be detected via batch tests conducted only for few weeks. The inert strong sorbents might be part of reason why the concentrations of the PAHs in soils or sediments are quite stable especially for HMW PAHs (large K_d).

Numerical simulations are run to investigate leaching behavior of compounds for a K_d range of 0.1 – 100 L kg^{-1}, covering most of the targeted compounds (e.g., heavy metals, sulfate, PAHs, etc.) listed in German standards. Two scenarios for initial conditions are considered: a fully pre-equilibrated column and a more realistic scenario with bottom-flooded water through dry sample (first flooding case)). The study explores the impacts of dispersion, mass transfer models (FD and IPPD), non-linear sorption and heterogenous sample compositions on leaching behaviors of compounds. The simulation results reveal that a pronounced influence of the initial conditions on leaching, particularly evident at low K_d values (K_d < 1 L kg^{-1}). As the K_d value increases, distinctions between pre-equilibrium and first flooding conditions progressively diminish, becoming negligible for K_d > 10 L kg^{-1}. Dispersion smoothens concentration gradients in the column in particular at low K_d values (K_d < 1 L kg^{-1}), leading to a lower initial concentrations at the column outlet after first flooding period and thus non-equilibrium. Intraparticle pore diffusion (IPPD) generally shows slower desorption kinetics than film diffusion (FD) and a slope of $1/2$ is observed at tailing parts in log-log plots of leaching curves. Compared to linear sorption case, non-linear sorption exhibits much longer tailing due to the decrease of concentration (increase of K_d or retardation factor). Heterogeneous samples with only a small fraction of strongly sorbing particles present much slower desorption rates due to less surface area for mass transfer compared to the homogenous samples having the same average distribution coefficient ($K_{d,av}$). Fine particle fraction (harmonic mean of grain sizes) dominates the leaching behaviors at early times, while long-term tailing is dominated by the coarse particle fraction (geometric mean of grain sizes). Material mixtures of small amounts of fine particles (10%) with low sorption capacity (K_d = 10 L kg^{-1}) and large amounts of coarse particles with high sorption capacity (K_d =100 L kg^{-1}), exhibit the respective characteristics of each of the individual components in different time periods. A peak effluent concentration ($C_{w,peak}$) shows up initially, which approaches the equilibrium concentration expected for homogenous fine particles. With the small mass fraction of fine particles, leachate concentrations decline rapidly and ultimately reach slightly elevated equilibrium levels of 100% pure coarse particles due to the redistribution of pollutants between the fine and coarse particles. The cumulative mass release of leaching

tests is relatively insensitive to mass transfer mechanisms especially for liquid to solid ratio (LS) less than 5.

In summary, contaminant redistribution in heterogenous systems is complicated when the mass transfer resistance shift of coupled model is considered. The proposed models of this thesis provide us the tools to better understand the sorption/desorption kinetics of mixtures, which can be easily applied in many fields, such as groundwater remediation, chemical engineering, analytical chemistry, etc. The models also allow to investigate the complexity of mass transfer in heterogenous systems.

Research directions elucidated in this thesis point to further developments, encompassing:

Semi-Laplace solution extension: The primary focus of the thesis revolves around sorption/desorption kinetics, although it is crucial to acknowledge the multitude of reactions concurrently transpiring in the real world, such as photooxidation, biodegradation, and biotransformation. If the governing equations of these reactions readily lend themselves to Laplace transformations, these diverse processes can be coupled with semi-Laplace solutions. The semi-Laplace solutions articulated in the thesis extend their applicability to a broader range of fields.

Existence of strongly sorbing compounds verification in soil: Chapter 3 assumes that in soils and sediments some strongly sorbents may exist which contains a lot of pollutant mass but might not be detected in sorption/desorption experiments in the lab especially if a high solid to liquid ratios are used. Identifying the constituents of these strongly sorbents become crucial for a more comprehensive understanding of pollutant mass distribution in the environment. This task can be accomplished through methods such as density separation or microscope methods.

Particle/gas distribution coefficients of PAHs in the atmosphere: Chapter 4 shows that particle/gas distribution coefficients (K_{pg}) of LMW and MMW PAHs in marine atmosphere is much higher (>2-3 orders of magnitudes) than the predictions from empirical relationships of dual model. More investigations are needed to find out the reasons.
Surrogate models generation: Chapter 5 demonstrates that developing numerical models for heterogeneous systems is a laborious and time-consuming task, especially when incorporating non-linear sorption. To streamline this process, leveraging deep learning methods, such as physical informed neural networks (PINNs), to construct surrogate models using training data from numerical models proves advantageous. Employing the surrogate models in subsequent analyses would significantly reduce time consumption, particularly in tasks like inverse modeling, such as Markov Chain and Monte Carlo simulation (MCMC).

Analysis of leaching standards: Chapter 5 exclusively presents simulation results based on

the German standard. An intriguing avenue for further investigation involves conducting analogous experiments with the same materials and comparing results across multiple standards, such as the European standard, Japanese standard, US standard, and Dutch standard. These standards, characterized by a stop-flow period after initial saturation, warrant examination to determine the consistency or divergence of conclusions drawn for specific recycling materials when assessed against different international standards.

Training optimization of PINNs: Chapter 6 applies the PINNs to solve advective-dispersive solute transport with coupled film-intraparticle diffusion (ADE-FIPPD). However, the prediction of PINNs at very steep concentration domain is not very good even the self-adaptative weighting factors are utilized. A novel and concise method of training PINNs for stiff partial differential equations (PDEs) might be helpful to increase the accuracy of predictions of PINNs. If possible, tedious numerical methods can be avoided especially for high dimension scenarios where numerical simulation is computationally very demanding.

S1 Supplementary information for boundary layer theory and Kolmogorov's turbulence theory

S1.1 Derivation of relative velocities of suspended particles in fluid via dimension analysis

(a) Macroparticle

The square relative fluctuating velocity of macroparticle ($\overline{U_r}^2$ [L^2 T^{-2}]) depends on the energy dissipation rate (ε_{disp} [L^2 T^{-3}]) and the grain size (d_p [L]). The unit balance equation is given as:

$$\left[\frac{L^2}{T^2}\right] = \left[\frac{L^2}{T^3}\right]^{\alpha} [L]^{\beta}$$

$$\begin{cases} 2 = 2\alpha + \beta \\ 2 = 3\alpha \end{cases} \Rightarrow \begin{cases} \alpha = \frac{2}{3} \\ \beta = \frac{2}{3} \end{cases} \tag{S1.1}$$

In order to determine the relative fluctuating velocity of macroparticle based on Eq. 1.33, an appropriate distance (d) value must be given. It is intuitive to use the particle size (d_p), which is justified by theory as follows: When laminar flow encounters a fixed particle, it proceeds against a drag force and results in a reduction in kinetic energy. The reduced kinetic energy per unit mass of fluid, which is changed to heat as local dissipation of energy per unit mass around the particle (ε_{disp}) can be determined as:

$$\varepsilon_{disp} = -\frac{1}{2}\frac{dU_r^2}{dt} \tag{S1.2}$$

where U_r [L T^{-1}] denotes the real relative velocity between fixed particle and fluid, which is different from the $\overline{U_r}$ based on statistical considerations. Assuming an encounter time $t = d_p/U_r$ yields:

$$\varepsilon_{disp} = -\frac{1}{2}\frac{dU_r^2}{dt} \sim \frac{U_r^2}{t} \sim \frac{U_r^3}{d_p} \quad or \quad U_r^2 \sim \left(\varepsilon_{disp} d_p\right)^{2/3} \tag{S1.3}$$

Since small particles in a highly turbulent flow encounter small eddies with low Reynolds number, laminar flow may exist around the particles. The equation above has a similar form as derived by Kolmogorov and by dimension analysis before. Therefore, d may be replaced by the particle size (d_p) to estimate the relative velocity between the suspended particle and fluid. Therefore, the square average velocity can be finally expressed as:

$$\overline{U_r}^2 = C_1 \varepsilon_{disp}^{2/3} d_p^{2/3} \tag{S1.4}$$

(b) Microparticle

The square relative fluctuating velocity of microparticle depends on the energy dissipation rate (ε_{disp}), the grain size (d_p) and the kinematic viscosity (ν_k [L^2 T^{-1}]). The unit balance equation is given as:

$$\left[\frac{L^2}{T^2}\right] = \left[\frac{L^2}{T^3}\right]^{\alpha} [L]^{\beta} \left[\frac{L^2}{T}\right]^{\gamma}$$
$$\begin{cases} 2 = 2\alpha + \beta + 2\gamma \\ 2 = 3\alpha + \gamma \end{cases} \Rightarrow \begin{cases} \alpha = 1 \\ \beta = 2 \\ \gamma = -1 \end{cases} \tag{S1.5}$$

Thus, the square average velocity of microparticles can be expressed by:

$$\overline{U_r}^2 = C_2 \frac{\varepsilon_{disp}}{\nu_k} {d_p}^2 \tag{S1.6}$$

S1.2 Proof of minimum Sherwood number of 2 for spherical particle

If the fluid is stagnant, mass transfer occurs only by molecular diffusion. If the fluid medium is infinite in extent, it is theoretically possible to reach steady state of solute fluxes from or to spherical particles. Let r be the radial distance from the center of the sphere and r_0 the sphere radius (shown in Fig. S1.1). The molar flux density (F) through the spherical shell at radius r (r>r_0) is given by:

$$F(4\pi r_0^2) = -D(4\pi r^2)\frac{dC}{dr} \tag{S1.7}$$

where r_0 [L] denotes radius and $4\pi r_0^2$ is the surface area of the sphere. D [L^2 T^{-1}] is the molecular diffusion coefficient. r [L] denotes the radial distance from the center of sphere and $4\pi r^2$ is the surface area at distance r. dC/dr [M L^{-4}] denotes concentration gradient. A flux through a "shell" in distance r has to be the same as at the surface of the sphere.

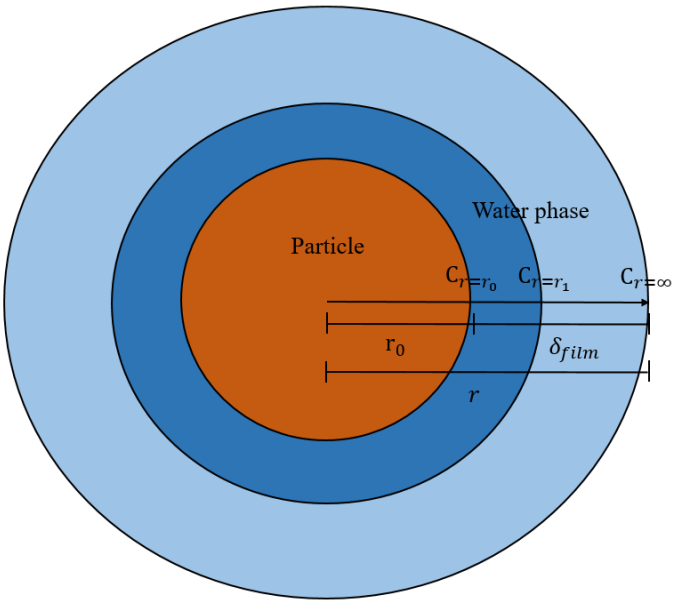

Fig. S1.1: Molecular diffusion from a spherical particle (different blue colors represent concentration gradients; δ_{film} denotes the external film thickness)

Integration between the limits $C = C_{r=r_0}$ at $r = r_0$ and $C = C_{r=\infty}$ at $r = \infty$ leads to:

$$\int_{r_0}^{\infty} r_0^2 \frac{1}{r^2} dr = -\int_{C_{r=r_0}}^{C_{r=\infty}} \frac{D}{F} dC \tag{S1.8}$$

After integration, Eq. S1.8 becomes:

$$\frac{F}{\left(C_{r=r_0} - C_{r=\infty}\right)} = \frac{D}{r_0} = k_{mt} \tag{S1.9}$$

Based on external film diffusion theory, the left-hand side of Eq. S1.9 denotes the molecular diffusion mass transfer rate coefficient ($k_{mt} = D/\delta$). The Sherwood number for molecular diffusion for a spherical particle thus becomes:

$$Sh = \frac{k_{mt} d_p}{D} = \frac{\frac{D}{r_0}(2r_0)}{D} = 2 \tag{S1.10}$$

Equation S1.10 shows that if the suspended particles have the same velocity as the fluid, the relative velocity becomes zero and the molecular diffusion dominates the mass transfer rate. It also implies that the smallest Sherwood number for spherical particles is 2. This is why many empirical and theoretical relationships to calculate Sh start at 2 (see section S2.5).

S1.3 Mass transfer for particles under gravity (during sedimentation)

In this section, mass transfer for suspended particles which are free to move under the action of gravity will be discussed. In 1851, George Gabriel Stokes derived an expression for the frictional force (drag force) exerted on spherical objects with very small Reynolds number in a viscous fluid. The force of viscosity on a small sphere moving through a viscous fluid is given by:

$$F_d = 6\pi\mu r_p U_r \tag{S1.11}$$

where: F_d [M L T^{-2}] is the frictional force acting on the interface between the fluid and the particle. r_p [L] is the radius of the spherical particle. U_r [L T^{-1}] is flow velocity relative to the particle.

If the suspended particles reach the steady state in the fluid, the total net force becomes zero and thus the drag force (F_d) equals to the difference between the weight (F_G) and buoyancy of the sphere (F_B). The force balance equation can be expressed as:

$$F_d = F_G - F_B = \left(\rho_p - \rho_f\right) g \frac{4}{3}\pi\, r_p^3 \tag{S1.12}$$

where ρ_p [M L^{-3}] and ρ_f [M L^{-3}] denote the mass densities of the spherical particle and fluid, respectively. g [L T^{-2}] denotes the gravitational acceleration. Combining Eq. S1.11 and Eq. S1.12, the terminal velocity of sphere falling in a fluid can be determined:

$$U_r = \frac{2}{9}\frac{\Delta\rho g r_p^2}{\mu} = \frac{1}{18}\frac{\Delta\rho g d_p^2}{\mu} \tag{S1.13}$$

where $\Delta\rho$ denotes density difference between particle and fluid.

The flow field in laminar 'creeping flow' around a sphere has been successfully treated analytically and most of previous results are combined with diffusion theory to obtain the mass transfer coefficients. The results are summarized in Fig. S1.2. The curve represents the results of theoretical analysis of mass transfer in creeping flow by Brian et al. (1969), which is perhaps the best of the several theoretical studies of the problem. Sherwood number for Peclet number (Pe) less than 10000 can be well explained by following correlation:

$$Sh = \left(4 + 1.21 Pe^{2/3}\right)^{1/2} \tag{S1.14}$$

For Peclet numbers (Pe) larger than 10000, the Sherwood number correlation becomes:

$$Sh = 2 + 1\,Pe^{1/3} \tag{S1.15}$$

Equation S1.15 was obtained by Levich (1962) and Friedlander (1961) with a constant of 1.01 and 0.991, respectively.

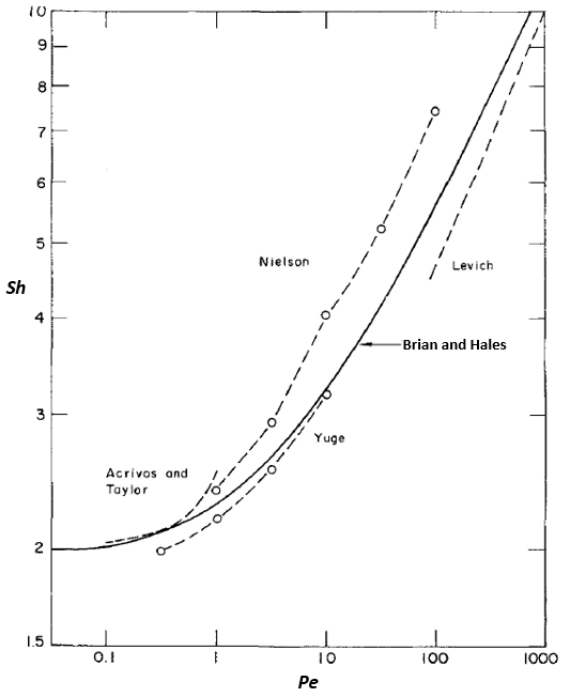

Fig. S1.2: Mass transfer correlations at low relative velocities from Brian et al. (1969).

Use the Eq. S1.13 to calculate the Peclet number and the mass transfer rate of particles under the action of gravity can be expressed:

$$\begin{aligned} Pe &= \frac{d_p U_r}{D} = \frac{g d_p^3 \Delta\rho}{18\mu D} = \left(\frac{k_{mt} d_p}{D}\right)^3 \\ k_{mt} &= 0.38 \left(\frac{g\mu\Delta\rho}{\rho_f^2}\right)^{1/3} Sc^{-2/3} \end{aligned} \tag{S1.16}$$

Thus, mass transfer coefficients for freely falling particles are independent on the particle size. Calderbank and Moo-Young (1961) reported experimental results for mass transfer in stirred tank reactors combined with published data for heat and mass transfer in liquid-liquid and solid-gas dispersions as well as on transfer by free convection from spheres. These data suggest following correlation:

$$k_{mt} = 0.31\left(\frac{\Delta\rho\mu g}{\rho_f^2}\right)^{1/3} Sc^{-2/3} \quad \text{(S1.17)}$$

Equation S1.17 is very similar to the Eq. S1.16 derived from theory. The slight difference might be due to the effect of turbulent eddy motions around the particles which is not considered in theory.

References

Brian, P.L.T., Hales, H.B., Sherwood, T.K., 1969. Transport of heat and mass between liquids and spherical particles in an agitated tank. AIChE J. 15, 727–733. https://doi.org/10.1002/aic.690150518.

Calderbank, P.H., Moo-Young, M.B., 1961. The continuous phase heat and mass-transfer properties of dispersions. Chem. Eng. Sci. 16, 39–54. https://doi.org/10.1016/0009-2509(61)87005-X.

Friedlander, S.K., 1961. A note on transport to spheres in stokes flow. AIChE J. 7, 347–348. https://doi.org/10.1002/aic.690070237.

Levich, V.G., 1962. Physicochemical hydrodynamics. Prentice-hall, Englewood Cliffs, NJ.

Stokes, G.G., 1851. On the effect of the internal friction of fluids on the motion of pendulums. Trans. Camb. Phil. Soc. 9, 8–106.

S2 Supplementary information for first order approximation for coupled film and intraparticle pore diffusion to model sorption/desorption batch experiments

S2.1 Analytical solution of sorption/desorption kinetics limited by external film diffusion in batch experiments

Batch experiments are often used to quantify the dynamics of sorptive uptake and desorption of solutes by soils and sediment particles. These experiments are commonly performed in a well-mixed bath of a limited volume of water. The first order external film diffusion model (Fig. S2.1) is widely used in simulating dissolution of minerals, (de-)sorption of contaminants from soil matrix, etc. The governing equation of external film diffusion (FD) is:

$$\frac{\partial C_w}{\partial t} = \frac{D_{aq}}{\delta_{aq}} \frac{m_d\, 3}{\rho_p\, a\, V_w} (C_w' - C_w) = k\, A^o (C_w' - C_w) \tag{S2.1}$$

The total mass of the solute in the system is the sum of the solute mass in bulk water ($C_w V_w$) and the solute mass in the porous particle ($C_s m_d + C_w' \frac{m_d \varepsilon}{\rho_p}$), which also applies for equilibrium conditions (C_{weq}):

$$C_w V_w + C_s m_d + C_w' \frac{m_d \varepsilon}{\rho_p} = C_{w,eq} V_w + K_d C_{w,eq} m_d + C_{w,eq} \frac{m_d \varepsilon}{\rho_p} \tag{S2.2}$$

Thus, the unknown concentration C_w' can be calculated via the concentration in the solid (C_s) which is in equilibrium with C_w'. C_s is obtained from the total mass in the system $\left(\text{at equilibrium: } C_{w,eq} V_w + K_d C_{w,eq} m_d + C_{w,eq} \frac{m_d \varepsilon}{\rho_p}\right)$ minus the solute mass in water ($C_w V_w$) and the mass stored in intragranular pores $\left(C_w' \frac{m_d \varepsilon}{\rho_p}\right)$.

$$\begin{aligned} C_w' &= \frac{C_s}{K_d} = \frac{\left(C_{w,eq} V_w + K_d C_{w,eq} m_d + C_{w,eq} \frac{m_d \varepsilon}{\rho_p} - C_w V_w - C_w' \frac{m_d \varepsilon}{\rho_p}\right)}{K_d\, m_d} \\ C_w' &= C_{w,eq} \left(\frac{V_w}{\left(K_d + \frac{\varepsilon}{\rho_p}\right) m_d} + 1 \right) - \frac{C_w V_w}{\left(K_d + \frac{\varepsilon}{\rho_p}\right) m_d} \end{aligned} \tag{S2.3}$$

The concentration difference in Eq. S2.1 then becomes:

$$\begin{aligned} C_w' - C_w &= C_{w,eq}\left(\frac{V_w}{\left(K_d + \frac{\varepsilon}{\rho_p}\right) m_d} + 1\right) - \frac{C_w V_w}{\left(K_d + \frac{\varepsilon}{\rho_p}\right) m_d} - C_w \\ &= \left(\frac{V_w}{\left(K_d + \frac{\varepsilon}{\rho_p}\right) m_d} + 1\right)\left(C_{w,eq} - C_w\right) \\ &= \left(\frac{V_w}{K_{d,b}\, m_d} + 1\right)\left(C_{w,eq} - C_w\right) \end{aligned} \tag{S2.4}$$

The term ($= K_d + \varepsilon/\rho_p$) may be interpreted as distribution coefficient between bulk water and porous particle, which also accounts for mass stored in the intraparticle pore space ($K_{d,b} = K_d + \varepsilon/\rho_p$). Inserting Eq. S2.4 into Eq. S2.1 yields:

$$\frac{\partial C_w}{\partial t} = k\, A^o \left(\frac{V_w}{K_{d,b}\, m_d} + 1\right)\left(C_{w,eq} - C_w\right) \tag{S2.5}$$

which upon integration yields the analytical solution for the initial condition $C_{w(t=0)} = 0$ (desorption):

$$\begin{aligned} \int_0^{C_w} \frac{\partial C_w}{C_{w,eq} - C_w} &= \int_0^t k\, A^o \left(\frac{V_w}{K_{d.b}\, m_d} + 1\right) \partial t \\ -\ln\left(C_{w,eq} - C_w\right) + \ln\left(C_{w,eq}\right) &= -\ln\left(1 - \frac{C_w}{C_{w,eq}}\right) = k\, A^o \left(\frac{V_w}{K_{d.b}\, m_d} + 1\right) t \\ \frac{C_w}{C_{w,eq}} &= 1 - \exp\left(-k\, A^o \left(\frac{V_w}{K_{d,b}\, m_d} + 1\right) t\right) \\ \text{with } A^\circ &= \frac{m_d\, 6}{\rho_p\, d\, V_w} \\ \frac{C_w}{C_{w,eq}} &= 1 - \exp\left(-\frac{k}{K_{d,b}} \frac{6}{\rho_p\, d}\left(1 + K_{d,b}\frac{m_d}{V_w}\right) t\right) \end{aligned} \tag{S2.6}$$

In sorptive uptake experiments the initial condition commonly is $C_{w\,(t=0)} = C_{w,0}$ and following solution is obtained (sorption):

$$\int_{C_{w,0}}^{C_w} \frac{\partial C_w}{C_{w,eq} - C_w} = \int_0^t k\, A^o \left(\frac{V_w}{K_{d,b}\, m_d} + 1\right) \partial t$$

$$-\ln\left(C_{w,eq} - C_w\right) + \ln\left(C_{w,eq} - C_{w,0}\right) = k\, A^o \left(\frac{V_w}{K_{d,b}\, m_d} + 1\right) t$$

$$\frac{C_w - C_{w,eq}}{C_{w,0} - C_{w,eq}} = \exp\left(-k\, A^o \left(\frac{V_w}{K_{d,b}\, m_d} + 1\right) t\right) \tag{S2.7}$$

$$\text{with } A° = \frac{m_d\, 6}{\rho_p\, d\, V_w}$$

$$C_w = C_{w,eq} - \exp\left(-\frac{k}{K_d}\frac{6}{\rho_p\, d}\left(1 + K_d \frac{m_d}{V_w}\right) t\right)\left(C_{w,eq} - C_{w,0}\right)$$

Realizing that $(C_{w,0} - C_{w,eq})V_w$ represents the mass adsorbed under equilibrium conditions $C_{s,eq} m_d \left(1 + \frac{\varepsilon}{\rho_p K_d}\right)$ and $(C_w - C_{w,eq})V_w$ (the mass in the water to be sorbed) equals $\left(C_{s,eq} - C_s\right) m_d \left(1 + \frac{\varepsilon}{\rho_p K_d}\right)$, leads to the relative change of the concentration in the solids:

$$\frac{C_s}{C_{s,eq}} = 1 - \exp\left(-\frac{k}{K_{d,b}}\frac{6}{\rho_p\, d}\left(1 + K_{d,b} \frac{m_d}{V_w}\right) t\right) \tag{S2.8}$$

Using the definition of the mass (M) which has diffused into or out of the solid (sorbed or desorbed) after time t relative to the mass at equilibrium (M_{eq}), Equations S2.6 and Eq. S2.8 become:

$$\frac{M}{M_{eq}} = 1 - \exp\left(-\frac{k}{K_{d,b}}\frac{6}{\rho_p\, d}\left(1 + K_{d,b} \frac{m_d}{V_w}\right) t\right) \tag{S2.9}$$

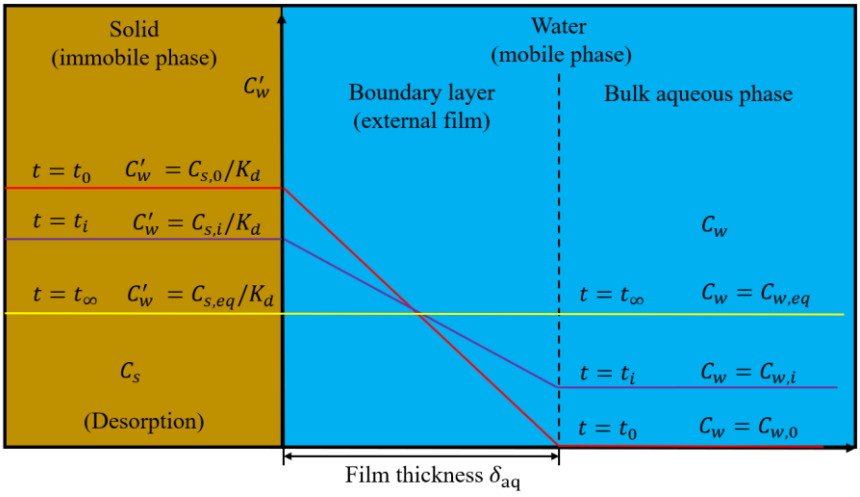

Fig. S2.1: Scheme of mass transfer limited by film diffusion during desorption in a finite bath

(batch experiment)

S2.2 Analytical solution of batch sorption kinetics limited by intraparticle pore diffusion

The spherical intraparticle pore diffusion (Fig. S2.2) model is widely used to describe sorption/desorption kinetics of organic contaminants in porous materials, such as activated carbon, zeolites and many other technical and natural materials. The governing equation of intraparticle pore diffusion (IPPD) follows Fick's second law in radial coordinates:

$$\frac{\partial C_{w,p}}{\partial t} = D_a \left[\frac{\partial^2 C_{w,p}}{\partial r^2} + \frac{2}{r} \frac{\partial C_{w,p}}{\partial r} \right] \tag{S2.10}$$

Boundary conditions are:

$$C_{w,p}(r = a, t) = C_w \tag{S2.11}$$

$$\frac{\partial C_{w,p}}{\partial r}(r = 0, t) = 0 \tag{S2.12}$$

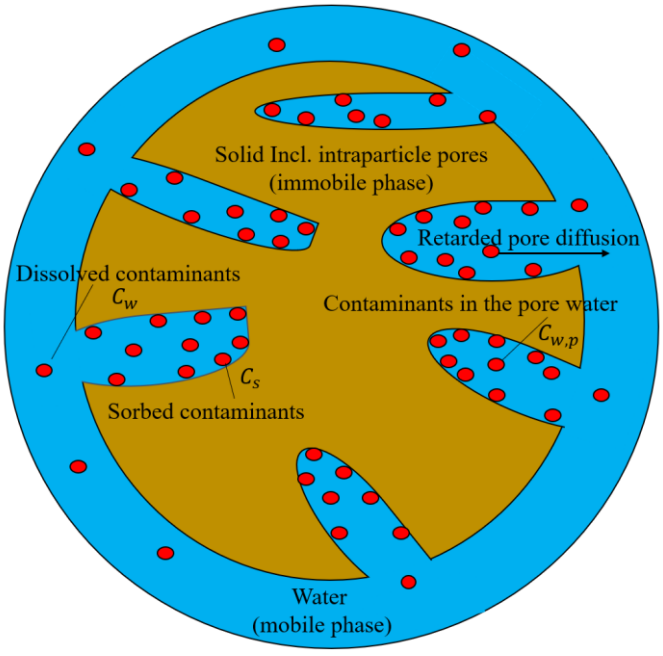

Fig. S2.2: Scheme of mass transfer limited by intraparticle pore diffusion (desorption)

The analytical solution of IPPD (Eq. 2.4 in main text) is given by a series expansion which at early times needs a large number of terms and is quite tedious to solve. For this reason, simple first order approximation based on linear driving force models are often employed. Here, the rate of sorption is written as the product of mass transfer coefficient *k,* surface area of sphere and a concentration difference between the intragranular bulk concentration ($C_{w,p}$) and the surface concentration (C_w).

$$\text{Rate} = \frac{4}{3}\pi a^3(\varepsilon + \rho_p K_d)\frac{\partial C_{w,p}}{\partial t} = k4\pi a^2\left(C_w - C_{w,p}\right) \text{ or}$$
$$\frac{\partial C_{w,p}}{\partial t} = \frac{3k}{a(\varepsilon + \rho_p K_d)}\left(C_w - C_{w,p}\right) \tag{S2.13}$$

Glueckauf (1955) derived the linear driving force equation for chromatographic columns and showed that the mass transfer coefficient k corresponds to $5D_e/a$ leading to:

$$\frac{M}{M_{eq}} = 1 - \exp\left(-15\frac{D_a}{a^2}\left(1 + \frac{1}{\beta}\right)t\right) \tag{S2.14}$$

Glueckauf's solution (Eq. S2.14) may be used as long-term approximation of IPPD especially for large β values ($\beta \to \infty$); according to Crank (1975) the precise approximation solution in infinite bath ($\beta \to \infty$) consists of the first term of the series expansion (Eq. 2.4 in the main text):

$$\frac{M}{M_{eq}} = 1 - \frac{6}{\pi^2}\exp\left[-\pi^2\frac{D_a}{a^2}t\right] \tag{S2.15}$$

For small values of β Hills (1986) discussed a long-term approximation with a more complicated rate constant:

$$\frac{M}{M_{eq}} = 1 - \exp\left(-\frac{\pi^2(1+\beta)}{1 + \beta - \pi^2/15}\frac{D_a}{a^2}t\right) \tag{S2.16}$$

A more precise long-term approximation solution in the finite bath can be obtained by using the first term of the series expansion solution and the transcendental function ($\tan q_n = \frac{3q_n}{3+\beta q_n^2}$) which can be easily solved with an empirical relationship:

$$\frac{M}{M_{eq}} = 1 - \frac{6\beta(\beta+1)}{9 + 9\beta + q_1^{*2}\beta^2}\exp\left(-q_1^{*2}\frac{D_a}{a^2}t\right)$$
$$\text{with } q_1^*(\beta) = \frac{\pi\beta + 3.49}{\beta + 0.775} \tag{S2.17}$$

where $q_1^*(\beta)$ represents the first positive solution of the transcendental function.

All these approximations (Eqs. S2.14, S2.15, S2.16 and S2.17) assume fixed rate constants and thus fail to capture the short-term behavior of IPPD (Hills, 1986).

S2.2.1 First order approximation of intraparticle pore diffusion (IPPD-FOAM)

In order to capture the short-term behavior of IPPD, a first-order approximation solution may be used based on the assumption of an internal diffusion distance δ_p, which grows initially with the square root of time ($\delta_p = \sqrt{\pi D_a\, t}$) and thus leads to a decreasing mass transfer coefficient ($k = D_e/\delta_p$):

$$\frac{\partial C_w}{\partial t} = \frac{D_e}{\delta_p} A^o \left(C_{w,p} - C_w\right) = \frac{D_e}{\sqrt{\pi D_a\, t}} \frac{m_d\, 3}{\rho_p\, a\, V_w} \left(C_{w,p} - C_w\right) \tag{S2.18}$$

Considering mass conservation, the intragranular bulk concentration $\left(C_{w,p}\right)$ can be calculated:

$$C_{w,p} = \frac{C_s}{K_d} = \frac{\left(C_{w,eq}\left(V_w + \left(K_d + \frac{\varepsilon}{\rho_p}\right) m_d\right) - C_w V_w - C_{w,p}\frac{m_d \varepsilon}{\rho_p}\right)}{K_d m_d} \tag{S2.19}$$

the concentration difference in S2.18 then becomes

$$C_{w,p} - C_w = \left(1 + \frac{V_w}{K_{d,b}\, m_d}\right)\left(C_{w,eq} - C_w\right)$$

Inserting Eq. S2.19 into Eq. S2.18 gives:

$$\begin{aligned} \frac{\partial C_w}{\partial t} &= \frac{D_e}{\sqrt{\pi D_a\, t}} \frac{m_d\, 3}{\rho_p\, a\, V_w} \left(1 + \frac{V_w}{K_{d,b}\, m_d}\right)\left(C_{w,eq} - C_w\right) \\ &= 3\sqrt{\frac{D_a}{\pi a^2}}\,(1 + \frac{1}{\beta})\left(C_{w,eq} - C_w\right)\frac{1}{\sqrt{t}} \end{aligned} \tag{S2.20}$$

which upon integration yields the following analytical solution for the initial condition $C_{w\,(t=0)} = 0$ (desorption):

$$\int_0^{C_w} \frac{\partial C_w}{C_{w,eq} - C_w} = \int_0^t 3\sqrt{\frac{D_a}{\pi a^2}}\,(1 + \frac{1}{\beta})\frac{1}{\sqrt{t}}\partial t$$

$$-\ln\left(C_{w,eq} - C_w\right) + \ln\left(C_{w,eq}\right) = -\ln\left(1 - \frac{C_w}{C_{w,eq}}\right) = 6\sqrt{\frac{D_a}{\pi a^2}}\,(1 + \frac{1}{\beta})\sqrt{t} \tag{S2.21}$$

$$\frac{C_w}{C_{w,eq}} = 1 - \exp\left(-6\sqrt{\frac{D_a}{\pi a^2}}\,(1 + \frac{1}{\beta})\sqrt{t}\right)$$

The same results are obtained for sorptive uptake ($C_s/C_{s,eq}$). Using the definition of the mass which has diffused into or out of the spherical particle (sorbed or desorbed) after time t (M) relative to the mass at equilibrium (M_{eq}), Eq. S2.21 can be generally expressed as:

$$\frac{M}{M_{eq}} = 1 - \exp\left(-6\sqrt{\frac{D_a t}{\pi a^2}}(1+\frac{1}{\beta})\right) \quad \text{(S2.22)}$$

which corresponds to the square root of time solution (Sqrt(t)) for small arguments (short times) in the exponential function:

$$\frac{M}{M_{eq}} = 6\sqrt{\frac{D_a t}{\pi a^2}}(1+\frac{1}{\beta}) \quad \text{(S2.23)}$$

S2.2.2 Comparison the short-term and long-term approximation solutions of IPPD

For better understanding of the performance of different approximation solutions, Fig. S2.3 compares M/M_{eq} vs. time (Fourier numbers) of the series expansion model (Eq. 2.4 in main text), the first order approximation model (Eq. S2.22), the square root of time solution (Eq. S2.23) and long-term approximation solution (Eq. S2.17) of IPPD for finite bath conditions ($0.1 < \beta < 3$) with different intraparticle porosities. The square root of time solution (Sqrt(t)) only fits the series expansion model (SEM) at early times ($M/M_{eq} < 0.1$), while the first order approximation model (FOAM) fits SEM for longer time periods up to $M/M_{eq} < 0.5$ especially for large β values (low sorption). For $\beta = 1$, FOAM fits SEM almost perfectly until 90% equilibration. The deviations of Sqrt(t) from SEM increase rapidly with time, whereas deviations in FOAM stay less than 15% for $0.1 < \beta < 3$. Compared to Sqrt(t), FOAM is a much better choice to approximate SEM. Increasing intraparticle porosity facilitates internal mass transfer. Long-term approximations (LTAM) follow SEM well only at very late time periods ($M/M_{eq} > 0.9$) and only for large values of β. In contrast, FOAM not only works well at early time periods, but also at the long term for $0.1 < \beta < 3$ (maximum deviation stays less than 15%). At larger β values (e.g., $\beta = 3$), FOAM slightly underestimates SEM and due to the overestimation of the internal film thickness ($\delta_p = \sqrt{\pi D_a\, t} > a/5$) at late times. As shown in Fig. S2.3 (bottom, left) errors in Sqrt(t) and LTAM escalate at around $D_{aq}t/a^2$ = 1x10^4 while FOAM stays within a deviation of less than 15%. Compared to Sqrt(t) and LTAM, FOAM still the best choice as a simple approximate solution of IPPD for batch tests. At low β values ($\beta \leq$ 0.1 or high $K_{d,b}$) and early times mass transfer is dominated by the external boundary layer and IPPD, which in early is hard to fit, is not relevant.

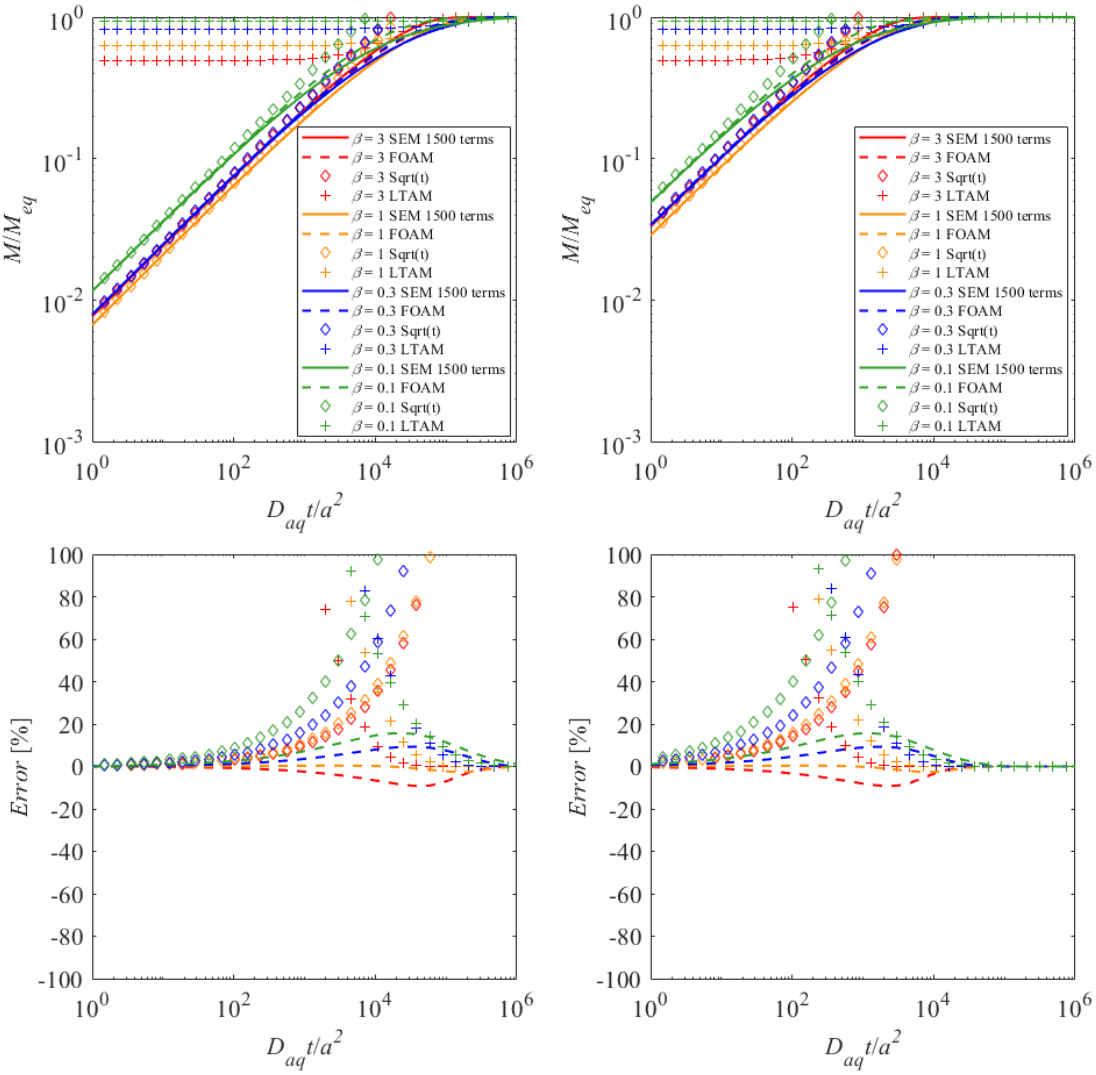

Fig. S2.3: Mass sorbed or desorbed relative to equilibrium conditions (M/M_{eq}) vs. dimensionless time or Fourier number (= $D_{aq}t/a^2$) (top) of intraparticle pore diffusion (IPPD) calculated with the analytical series expansion solution (SEM: solid lines, 1500 terms in Eq. 2.4), the first order approximation (FOAM: dashed lines, Eq. S2.22), the square root of time solution (Sqrt(t): diamonds, Eq. S2.23) and the long-term approximation (LTAM: crosses, Eq. S2.17) under finite bath conditions ($\beta = \frac{V_w}{m_d K_{d,b}}$ = 0.1, 0.3, 1 and 3, $Sh = 2$) with intraparticle porosities (ε) of 0.05 (left) and 0.2 (right); bottom: % deviations of FOAM, Sqrt(t) and LTAM from SEM.

S2.3 First order approximation for coupled film-intraparticle pore diffusion

In the following, an analytical solution for coupled film-intraparticle pore diffusion is derived.

The model is inspired by the double film diffusion model with constant film thicknesses. At early times (see section S2.2) intraparticle pore diffusion can be well described by a first-order approximation with an internal film thickness increasing with the square root of time ($\delta_p = \sqrt{\pi D_a t}$). This is coupled to diffusion through the external boundary layer (δ_{aq}) with constant film thickness. If these two films (δ_p, δ_{aq}) are combined, the mass flux densities through the respective diffusion layer can be expressed as:

$$F_{aq} = \frac{D_{aq}}{\delta_{aq}} (C_w - C'_w) \tag{S2.24}$$

$$F_p = \frac{D_e}{\delta_p} \left(C'_w - C_{w,p}\right) \tag{S2.25}$$

where F_{aq} [M L^{-2} T^{-1}] and F_p [M L^{-2} T^{-1}] denote the mass flux densities in the external aqueous boundary layer and in the particle, respectively. D_{aq}/δ_{aq} and D_e/δ_p are mass transfer coefficients [L T^{-1}] and their inverse may be regarded as mass transfer resistances. Rearranging Eq. S2.24, C'_w becomes:

$$C'_w = C_w - \frac{F_{aq}\, \delta_{aq}}{D_{aq}} \tag{S2.26}$$

Inserting Eq. S2.26 into Eq. S2.25, leads to the double (or dual) film diffusion model:

$$\frac{F_p\, \delta_p}{D_e} + \frac{F_{aq}\, \delta_{aq}}{D_{aq}} = C_w - C_{w,p} \tag{S2.27}$$

Using the steady state assumption that all flux densities are equal ($F_{aq} = F_p = F$), allows rearranging Eq. S2.27 as:

$$F = \frac{1}{\frac{\delta_p}{D_e} + \frac{\delta_{aq}}{D_{aq}}} (C_w - C_{w,p}) \tag{S2.28}$$

The total mass of the solute in the system is the sum of the solute mass in the water phase ($C_w V_w$) and the solute mass in the porous solid sphere ($C_s m_d + C_{w,p} \frac{m_d \varepsilon}{\rho_p}$). The mass balance is given as:

$$C_w V_w + C_s m_d + C_{w,p} \frac{m_d \varepsilon}{\rho_p} = C_{w,eq} V_w + K_d C_{w,eq} m_d + C_{w,eq} \frac{m_d \varepsilon}{\rho_p} \tag{S2.29}$$

$C_{w,p}$ is always equilibrium with the compound's concentration in the solid phase (C_s). Rearranging Eq. S2.29 and substituting $C_{w,p}$ in Eq. S2.28 with C_s/K_d leads to:

$$F = -\frac{1}{\frac{\delta_p}{D_e} + \frac{\delta_{aq}}{D_{aq}}}\left(1 + \frac{V_w}{m_d K_{d,b}}\right)(C_{w,eq} - C_w) \tag{S2.30}$$

The change of the solute concentration in bulk water is obtained by introducing the specific area (total surface area of spheres per volume of water):

$$\frac{\partial C_w}{\partial t} = FA^o = \frac{1}{\frac{\delta_p}{D_e} + \frac{\delta_{aq}}{D_{aq}}}\frac{m_d\, 3}{\rho_p\, a\, V_w}\left(1 + \frac{V_w}{m_d K_{d,b}}\right)(C_{w,eq} - C_w) \tag{S2.31}$$

In sorptive uptake experiments the initial condition commonly is $C_{w(t=0)} = C_{w,0}$ leading to following solution:

$$\int_{C_{w,0}}^{C_w} \frac{C_w}{(C_{w,eq} - C_w)} = \int_0^t \frac{1}{\frac{\sqrt{\pi D_a t}}{D_e} + \frac{\delta_{aq}}{D_{aq}}}\frac{m_d\, 3}{\rho_p\, a\, V_w}\left(1 + \frac{V_w}{m_d K_{d,b}}\right)\partial t \tag{S2.32}$$

The integration of the right side can be simplified as:

$$\int \frac{1}{\frac{\sqrt{\pi D_a t}}{D_e} + \frac{\delta_{aq}}{D_{aq}}}\frac{m_d\, 3}{\rho_p\, a\, V_w}\left(1 + \frac{V_w}{m_d K_{d,b}}\right)\partial t = \int \frac{1}{b + c\sqrt{t}}\partial t \tag{S2.33}$$

where: $b = \frac{\delta_{aq}}{D_{aq}\frac{3}{\rho_p\, a}\left(\frac{m_d}{V_w} + \frac{1}{K_{d,b}}\right)}$; $c = \frac{\sqrt{\frac{\pi}{D_e K_{d,b}\rho_p}}}{\frac{3}{\rho_p\, a}\left(\frac{m_d}{V_w} + \frac{1}{K_{d,b}}\right)}$.

$\int \frac{1}{b+c\sqrt{t}}\partial t$ can be solved by the element changing method. If we assume $b + c\sqrt{t} = x$, Eq. S2.33 can be rearranged as:

$$\int \frac{1}{b + c\sqrt{t}}\partial t = \int \frac{1}{x}\partial\left(\frac{x-b}{c}\right)^2 = \int \frac{2(x-b)}{c^2 x}\partial x \tag{S2.34}$$

Integration of Eq. S2.34 yields:

$$\int \frac{2(x-b)}{c^2 x}\partial x = \frac{2}{c^2}x - \frac{2b}{c^2}\ln x + C \tag{S2.35}$$

where C is a constant. Re-substitution of x with $b + c\sqrt{t}$ leads to:

$$\int_0^t \frac{1}{b + c\sqrt{t}}\partial t = \frac{2}{c^2}\left(b + c\sqrt{t}\right) - \frac{2b}{c^2}\ln\left(b + c\sqrt{t}\right) - \left(\frac{2b}{c^2} - \frac{2b}{c^2}\ln b\right) \tag{S2.36}$$

Then the final solution of Eq. S2.32 can be expressed as:

$$\frac{C_w - C_{w,eq}}{C_{w,0} - C_{w,eq}} = \exp\left(-\frac{2}{c^2}\left(b + c\sqrt{t}\right) + \frac{2b}{c^2}\ln\left(b + c\sqrt{t}\right) + \left(\frac{2b}{c^2} - \frac{2b}{c^2}\ln b\right)\right) \tag{S2.37}$$

Realizing that $(C_{w,0} - C_{w,eq})V_w$ represents the mass adsorbed under equilibrium condition $\left(C_{s,eq} m_d (1 + \frac{\varepsilon}{\rho_p K_d})\right)$ and $(C_w - C_{w,eq})V_w$ (the mass in the water to be sorbed) equals $\left((C_{s,eq} - C_s) m_d (1 + \frac{\varepsilon}{\rho_p K_d})\right)$ allows to calculate the relative change of the concentration in the solids. Using the definition of the mass which has diffused into or out of the solid (sorbed or desorbed) after time t (M) relative to the mass at equilibrium (M_{eq}), Eq. S2.37 generally can be rewritten as:

$$\frac{M}{M_{eq}} = 1 - \exp\left(-\frac{2}{c^2}\left(b + c\sqrt{t}\right) + \frac{2b}{c^2}\ln\left(b + c\sqrt{t}\right) + \left(\frac{2b}{c^2} - \frac{2b}{c^2}\ln b\right)\right) \tag{S2.38}$$

S2.4 Semi-analytical Laplace solution for coupled film-intraparticle pore diffusion

S2.4.1 Solution in Laplace domain

Section S2.2 shows the governing equations of intraparticle pore diffusion in a spherical particle (Eqs. S2.10-S2.12). If we assume that the initial concentration within the porous particle is uniform, $C_{w,p}(0)$ [M L^{-3}], the Laplace transformation of governing equations and initial conditions (Eqs. S2.10-S2.12) can be expressed as:

$$s\tilde{C}_{w,p} - C_{w,p}(0) - D_a\left[\frac{d^2\tilde{C}_{w,p}}{dr^2} + \frac{2}{r}\frac{d\tilde{C}_{w,p}}{dr}\right] = 0 \tag{S2.39}$$

$$\tilde{C}_{w,p}(a) = \tilde{C}_{w,p,a} \tag{S2.40}$$

$$\left.\frac{\partial\tilde{C}_{w,p}}{\partial r}\right|_{r=0} = 0 \tag{S2.41}$$

$$\tilde{C}_{w,p}(r) = \tilde{C}_{w,p}(0) \;\; \forall r \tag{S2.42}$$

in which variable with a tilde represent Laplace transforms, and s [T^{-1}] is the complex Laplace coordinate. Equation S2.39 can be solved starting from:

$$\tilde{C}_{w,p}(r,s) \propto \frac{1}{r}\exp(r\varphi) + C \tag{S2.43}$$

where φ and C are undetermined coefficients.

$$\frac{d\tilde{C}_{w,p}}{dr} \propto -\frac{1}{r^2}\exp(r\varphi) + \frac{\varphi}{r}\exp(r\varphi) = (-\frac{1}{r} + \varphi)\frac{1}{r}\exp(r\varphi) \tag{S2.44}$$

$$\frac{d^2\tilde{C}_{w,p}}{dr^2} \propto (\frac{2}{r^2} - \frac{2\varphi}{r} + \varphi^2)\frac{1}{r}\exp(r\varphi) \tag{S2.45}$$

Inserting Eqs. S2.44, S2.45 into Eq. S2.39 yields:

$$\begin{aligned} & s\frac{1}{r}\exp(r\varphi) + sC - C_{w,p}(0) - D_a\left[\frac{2}{r^2} - \frac{2\varphi}{r} + \varphi^2 + \frac{2}{r}\left(-\frac{1}{r} + \varphi\right)\right]\frac{1}{r}\exp(r\varphi) \\ & \qquad = 0 \\ & (\mathrm{s} - \varphi^2 D_a)\frac{1}{r}\exp(r\varphi) + sC - C_{w,p}(0) = 0 \\ & \longrightarrow \begin{cases} \mathrm{s} - \varphi^2 D_a = 0 \\ sC - C_{w,p}(0) = 0 \end{cases} \longrightarrow \begin{cases} \varphi = \pm\sqrt{\dfrac{s}{D_a}} \\ C = \dfrac{C_{w,p}(0)}{s} \end{cases} \end{aligned} \tag{S2.46}$$

Then the solution of Eq. S2.39 can finally be expressed as:

$$\tilde{C}_{w,p}(r,s) = \frac{A}{r}\exp\left(r\sqrt{\frac{s}{D_a}}\right) + \frac{B}{r}\exp\left(-r\sqrt{\frac{s}{D_a}}\right) + \frac{C_{w,p}(0)}{s} \tag{S2.47}$$

where A and B are undetermined coefficients, which can be determined via the boundary conditions of the governing equation (Eq. S2.40 and Eq. S2.41).

$$\begin{aligned} \frac{d\tilde{C}_{w,p}}{dr} &= A\left[-\frac{1}{r^2}\exp\left(r\sqrt{\frac{s}{D_a}}\right) + \frac{1}{r}\sqrt{\frac{s}{D_a}}\exp\left(r\sqrt{\frac{s}{D_a}}\right)\right] \\ &\quad + B\left[-\frac{1}{r^2}\exp\left(-r\sqrt{\frac{s}{D_a}}\right) - \frac{1}{r}\sqrt{\frac{s}{D_a}}\exp\left(-r\sqrt{\frac{s}{D_a}}\right)\right] \\ &= A\left(-\frac{1}{r^2} + \frac{1}{r}\sqrt{\frac{s}{D_a}}\right)\exp\left(r\sqrt{\frac{s}{D_a}}\right) \\ &\quad + B\left(-\frac{1}{r^2} - \frac{1}{r}\sqrt{\frac{s}{D_a}}\right)\exp\left(-r\sqrt{\frac{s}{D_a}}\right) \end{aligned} \tag{S2.48}$$

The exponential function can be approximated by using an infinite number of terms of its Taylor series:

$$e^x = \exp(x) = \sum_{n=0}^{\infty}\frac{x^n}{n!} = 1 + x + \frac{x^2}{2!} + \frac{x^3}{3!} + \cdots \tag{S2.49}$$

$\exp\left(r\sqrt{\frac{s}{D_a}}\right)$ and $\exp\left(-r\sqrt{\frac{s}{D_a}}\right)$ in Eq. S2.48 can be approximated as:

$$\exp\left(r\sqrt{\frac{s}{D_a}}\right) \approx 1 + r\sqrt{\frac{s}{D_a}}$$
$$\exp\left(-r\sqrt{\frac{s}{D_a}}\right) \approx 1 - r\sqrt{\frac{s}{D_a}} \tag{S2.50}$$

Inserting Eq. S2.50 into Eq. S2.48 gives:

$$\begin{aligned}\frac{d\tilde{C}_{w,p}}{dr} &= A\left(-\frac{1}{r^2}+\frac{1}{r}\sqrt{\frac{s}{D_a}}\right)\left(1+r\sqrt{\frac{s}{D_a}}\right)+B\left(-\frac{1}{r^2}-\frac{1}{r}\sqrt{\frac{s}{D_a}}\right)\left(1-r\sqrt{\frac{s}{D_a}}\right) \\ &= (A+B)\left(-\frac{1}{r^2}+\frac{s}{D_a}\right)\end{aligned} \tag{S2.51}$$

The internal boundary condition (Eq. S2.41) shows that the $d\tilde{C}_{w,p}/dr$ approaches 0 when r approaches 0:

$$\left.\frac{\partial\tilde{C}_{w,p}}{\partial r}\right|_{r=0} = \lim_{r\to 0}(A+B)\left(-\frac{1}{r^2}+\frac{s}{D_a}\right) = 0$$
$$\Longrightarrow \quad A = -B \tag{S2.52}$$

Then Eq. S2.47 can be rearranged as:

$$\begin{aligned}\tilde{C}_{w,p}(r,s) &= \frac{A}{r}\exp\left(r\sqrt{\frac{s}{D_a}}\right)-\frac{A}{r}\exp\left(-r\sqrt{\frac{s}{D_a}}\right)+\frac{C_{w,p}(0)}{s} \\ \tilde{C}_{w,p}(r,s) &= \frac{2A}{r}\left[\frac{1}{2}\exp\left(r\sqrt{\frac{s}{D_a}}\right)-\frac{1}{2}\exp\left(-r\sqrt{\frac{s}{D_a}}\right)\right]+\frac{C_{w,p}(0)}{s} \\ \tilde{C}_{w,p}(r,s) &= \frac{2A}{r}\sinh\left(r\sqrt{\frac{s}{D_a}}\right)+\frac{C_{w,p}(0)}{s}\end{aligned} \tag{S2.53}$$

Based on the external boundary condition (Eq. S2.40), the unknown coefficient $2A$ can be determined.

$$\tilde{C}_{w,p}(a,s) = \frac{2A}{a}\sinh\left(a\sqrt{\frac{s}{D_a}}\right)+\frac{C_{w,p}(0)}{s} = \tilde{C}_{w,p,a}$$
$$\Longrightarrow \quad 2A = \frac{\left(\tilde{C}_{w,p,a}-\frac{C_{w,p}(0)}{s}\right)a}{\sinh\left(a\sqrt{\frac{s}{D_a}}\right)} \tag{S2.54}$$

Thus, the analytical solution of Eq. S2.39 in Laplace domain can be expressed as:

$$\tilde{C}_{w,p}(r,s) = \frac{a}{r}\frac{\sinh\left(r\sqrt{\frac{s}{D_a}}\right)}{\sinh\left(a\sqrt{\frac{s}{D_a}}\right)}\left(\tilde{C}_{w,p,a}-\frac{C_{w,p}(0)}{s}\right)+\frac{C_{w,p}(0)}{s} \tag{S2.55}$$

If we assume the solute mass release (or uptake) from the surface of the porous spherical

particles into the bulk solution is driven by diffusion through the external boundary layer (δ_{aq}) which does not store any solute mass, the continuity of the mass flux density (F [M L^{-2} T^{-1}]) requires:

$$F = k\big(C_{w,p}(a,t) - C_w(t)\big) = -D_e \frac{\partial \tilde{C}_{w,p}}{\partial r}\bigg|_{r=a} \tag{S2.56}$$

The solute concentration change in bulk water is given by:

$$\frac{dC_w}{dt} = F\,A^o = k\frac{3}{a}\frac{m_d}{V_w\,\rho_p}(C_{w,p}(a,t) - C_w) \tag{S2.57}$$

Next, the Laplace transformation of Eq. S2.56 is used.

$$\tilde{F} = k\big(\tilde{C}_{w,p,a} - \tilde{C}_w\big) = -D_e \frac{\partial \tilde{C}_{w,p}}{\partial r}\bigg|_{r=a} \tag{S2.58}$$

$\frac{\partial \tilde{C}_{w,p}}{\partial r}\Big|_{r=a}$ in Eq. S2.58 can be calculated via Eq. S2.55:

$$\begin{aligned}\frac{\partial \tilde{C}_{w,p}}{\partial r}\bigg|_{r=a} &= \left(\frac{a}{r}\sqrt{\frac{s}{D_a}}\frac{\cosh\left(r\sqrt{\frac{s}{D_a}}\right)}{\sinh\left(a\sqrt{\frac{s}{D_a}}\right)} - \frac{a}{r^2}\frac{\sinh\left(r\sqrt{\frac{s}{D_a}}\right)}{\sinh\left(a\sqrt{\frac{s}{D_a}}\right)}\right)\left(\tilde{C}_{w,p,a} - \frac{C_{w,p}(0)}{s}\right)\bigg|_{r=a} \\ &= \left(\sqrt{\frac{s}{D_a}}\coth\left(a\sqrt{\frac{s}{D_a}}\right) - \frac{1}{a}\right)\left(\tilde{C}_{w,p,a} - \frac{C_{w,p}(0)}{s}\right)\end{aligned} \tag{S2.59}$$

Rearranging Eq. S2.58 with Eq. S2.59 gives the expression of $\tilde{C}_{w,p,a}$:

$$\begin{aligned} k\big(\tilde{C}_{w,p,a} - \tilde{C}_w\big) &= -D_e\left(\sqrt{\frac{s}{D_a}}\coth\left(a\sqrt{\frac{s}{D_a}}\right) - \frac{1}{a}\right)\left(\tilde{C}_{w,p,a} - \frac{C_{w,p}(0)}{s}\right) \\ \left[k + D_e\left(\sqrt{\frac{s}{D_a}}\coth\left(a\sqrt{\frac{s}{D_a}}\right) - \frac{1}{a}\right)\right]\tilde{C}_{w,p,a} &= D_e\left(\sqrt{\frac{s}{D_a}}\coth\left(a\sqrt{\frac{s}{D_a}}\right) - \frac{1}{a}\right)\frac{C_{w,p}(0)}{s} + k\tilde{C}_w \\ \tilde{C}_{w,p,a} &= \frac{D_e\left(\sqrt{\frac{s}{D_a}}\coth\left(a\sqrt{\frac{s}{D_a}}\right) - \frac{1}{a}\right)\frac{C_{w,p}(0)}{s} + k\tilde{C}_w}{k + D_e\left(\sqrt{\frac{s}{D_a}}\coth\left(a\sqrt{\frac{s}{D_a}}\right) - \frac{1}{a}\right)} \end{aligned} \tag{S2.60}$$

The Laplace transformation of Eq. S2.57 yields:

$$s\widetilde{C_w} - C_w(0) = k\frac{3}{a}\frac{m_d}{V_w\,\rho_p}(\tilde{C}_{w,p,a} - \tilde{C}_w) \tag{S2.61}$$

where $C_w(0)$ [M L^{-3}] denotes the initial solute concentration in the bulk water. Inserting Eq.

S2.60 into Eq. S2.61 and rearranging terms finally yields the Laplace transform solution for FIPPD:

$$\widetilde{C_w} = \frac{\alpha \frac{C_{w,p}(0)}{s} + C_w(0)}{\alpha + s}$$
$$\text{with } \alpha(s) = \frac{D_e \left(\sqrt{\frac{s}{D_a}} \coth\left(a \sqrt{\frac{s}{D_a}} \right) - \frac{1}{a} \right)}{k + D_e \left(\sqrt{\frac{s}{D_a}} \coth\left(a \sqrt{\frac{s}{D_a}} \right) - \frac{1}{a} \right)} \, k \frac{3}{a} \frac{m_d}{V_w \, \rho_p} \tag{S2.62}$$

Two limiting cases may be considered:

1. $\lim\ k \to \infty$: This describes the case where external mass transfer resistance vanishes. The denominator in Eq. S2.62 in this case simplifies to $\lim_{k\to\infty} \left(k + D_e \left(\sqrt{\frac{s}{D_a}} \coth\left(a \sqrt{\frac{s}{D_a}} \right) - \frac{1}{a} \right) \right) = k$, which leads to:

$$\widetilde{C_w} = \frac{\alpha \frac{C_{w,p}(0)}{s} + C_w(0)}{\alpha + s}$$
$$\text{with } \alpha(s) = \left(D_e \left(\sqrt{\frac{s}{D_a}} \coth\left(a \sqrt{\frac{s}{D_a}} \right) - \frac{1}{a} \right) \right) \frac{3}{a} \frac{m_d}{V_w \, \rho_p} \tag{S2.63}$$

2. $\lim D_a \to \infty$: This describes the case of a sphere with a uniform concentration distribution (well mixed interior), where only the external boundary layer controls mass transfer. To obtain the solution for this case, we need to consider the limit of coth(x) for arguments approaching 0. The Taylor series expansion shows that coth(x) can be approximated with:

$$\lim_{x\to 0} \coth(x) \approx \frac{1}{x} + \frac{x}{3} \tag{S2.64}$$

Using Eq. S2.64 to determine the limit of $\lim_{D_a\to\infty} \left(D_e \left(\sqrt{\frac{s}{D_a}} \coth\left(a \sqrt{\frac{s}{D_a}} \right) - \frac{1}{a} \right) \right)$ yields:

$$\lim_{D_a\to\infty} \coth\left(a\sqrt{\frac{s}{D_a}}\right) \approx \frac{1}{a\sqrt{\frac{s}{D_a}}} + \frac{a\sqrt{\frac{s}{D_a}}}{3}$$

$$\lim_{D_a\to\infty} D_e\left(\sqrt{\frac{s}{D_a}}\coth\left(a\sqrt{\frac{s}{D_a}}\right) - \frac{1}{a}\right)$$

$$= \lim_{D_a\to\infty}\left(\left(\varepsilon+\rho_p K_d\right)\left(\sqrt{D_a s}\coth\left(a\sqrt{\frac{s}{D_a}}\right) - \frac{D_a}{a}\right)\right) \tag{S2.65}$$

$$= \lim_{D_a\to\infty}\left(\left(\varepsilon+\rho_p K_d\right)\left(\sqrt{D_a s}\left(\frac{1}{a\sqrt{\frac{s}{D_a}}} + \frac{a\sqrt{\frac{s}{D_a}}}{3}\right) - \frac{D_a}{a}\right)\right)$$

$$= \frac{1}{3}as\left(\varepsilon+\rho_p K_d\right)$$

This finally leads to:

$$\widetilde{C_w} = \frac{\alpha\frac{C_{w,p}(0)}{s} + C_w(0)}{\alpha + s}$$
$$\lim_{D_a\to\infty} \alpha(s) = \frac{\left(\varepsilon+\rho_p K_d\right)s}{\left(\varepsilon+\rho_p K_d\right)\frac{1}{3}as + k}\,k\frac{m_d}{\rho_p V_w} \tag{S2.66}$$

Back-transformation of the solution in the Laplace domain is done numerically using the method of de Hoog et al. (1982) implemented in Matlab. In order to validate the semi-analytical Laplace transform solutions of FD and IPPD, the analytical solutions of FD (Eq. S2.9) and IPPD (Eq. 2.4 in main text) were used as references (see Fig. S2.4). As to be expected, the agreement with the analytical solution of FD (Eq. S2.9) is perfect and comparison to the analytical solution of IPPD (Eq. 2.4 in main text) shows only slight deviation at very early times due to the finite series expansion terms (1500 terms). Thus, the semi-Laplace transform solution of IPPD (Eq. S2.63) improves the computational efficiency a lot especially at low β values ($\beta < 0.1$) where a large number of terms (>1500) are needed in the series expansion in order to avoid overestimation of M/M_{eq} at early times.

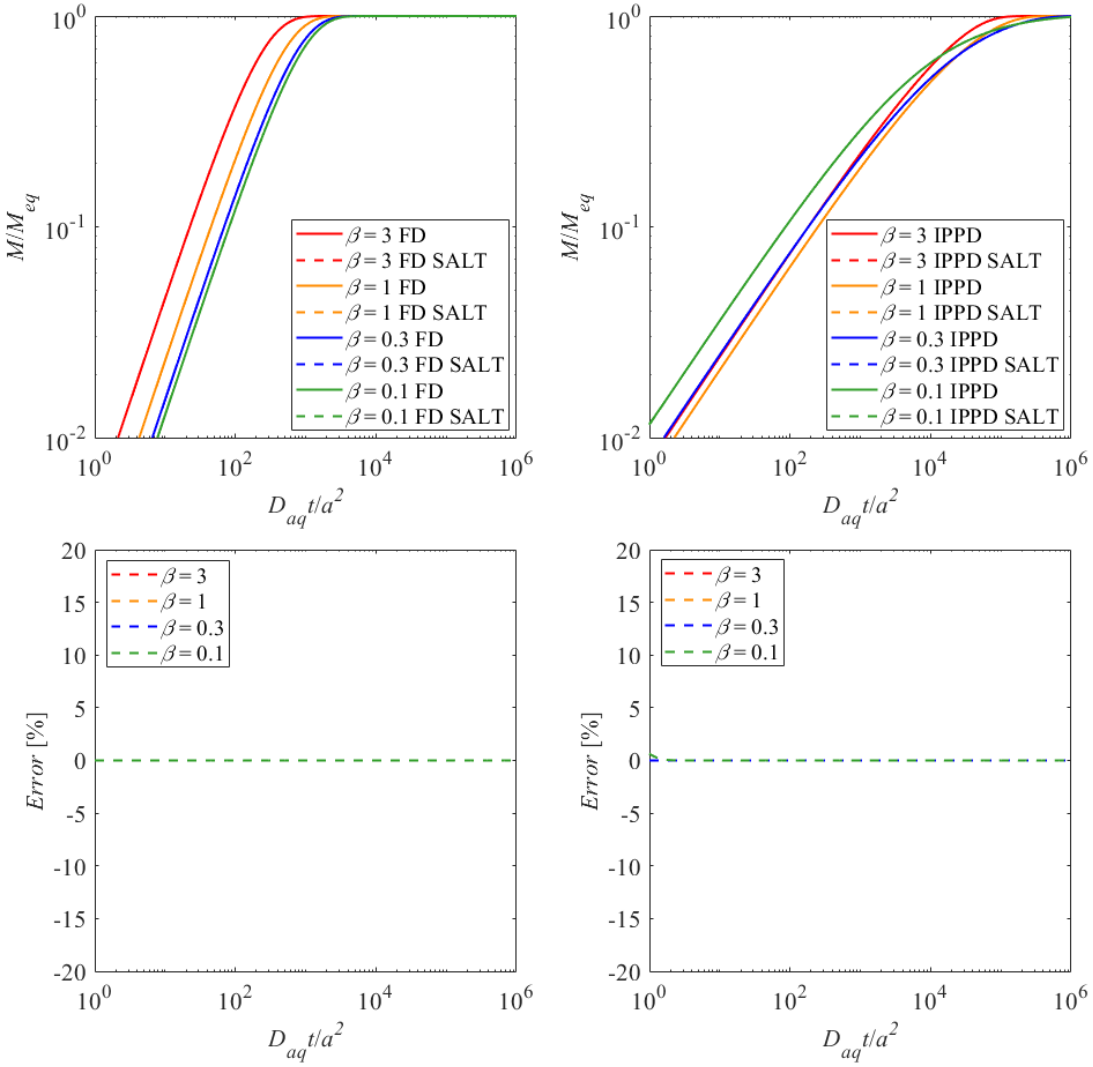

Fig. S2.4: Mass sorbed or desorbed relative to equilibrium conditions (M/M_{eq}) vs. dimensionless time (Fourier number = $D_{aq}t/a^2$) for FD (left) and IPPD (right) calculated with the analytical solutions (FD: Eq. S2.9; IPPD: Eq. 2.4 in main text with 1500 terms) compared to the semi-analytical Laplace transform solution (FD SALT: Eq. S2.66; IPPD SALT: Eq. S2.63); finite bath with $\beta(=\frac{V_w}{m_d K_{d,b}})$ = 0.1, 0.3, 1 and 3 ($Sh = 2, \varepsilon = 0.05$). Bottom: % deviation of SALT from the analytical solutions.

S2.4.2 Characteristic times of mass transfer

Based on mass conservation (Eq. S2.29), the equilibrium concentration ($C_{w,eq}$) in bulk water can be determined:

$$C_{w,eq} = \frac{C_w(0) + C_{w,p}(0) K_{d,b} \frac{m_d}{V_w}}{1 + K_{d,b} \frac{m_d}{V_w}} \tag{S2.67}$$

The deviation from the equilibrium concentration (ΔC_w) is:

$$\Delta C_w(t) = C_w(t) - C_{w,eq} \tag{S2.68}$$

A characteristic time τ_{ch} may be defined as the integral of the concentration signal, i.e., the integral of ΔC_w over time divided by its initial value (for sorption illustrated in Fig. S2.5):

$$\tau_{ch} = \int_0^\infty (1 - \frac{M}{M_{eq}})\, dt = \frac{\int_0^\infty \Delta C_w(t)\, dt}{\Delta C_w(0)} = \frac{\lim_{s \to 0} \left(\widetilde{C_w} - \frac{C_{w,eq}}{s} \right)}{C_w(0) - C_{w,eq}} \tag{S2.69}$$

The initial deviation $\Delta C_w(0)$ is:

$$\Delta C_w(0) = \frac{\left(C_w(0) - C_{w,p}(0) \right) K_{d,b} \frac{m_d}{V_w}}{1 + K_{d,b} \frac{m_d}{V_w}} \tag{S2.70}$$

Inserting Eq. S2.62, Eq. S2.67 and Eq. S2.70 into Eq. S2.69, the result shows that the characteristic time of film-intraparticle pore diffusion (FIPPD) is:

$$\tau_{ch} = \frac{\rho_p \left(\frac{a}{3k} + \frac{a^2}{15 D_e} \right)}{\left(\frac{1}{K_{d,b}} + \frac{m_d}{V_w} \right)} \tag{S2.71}$$

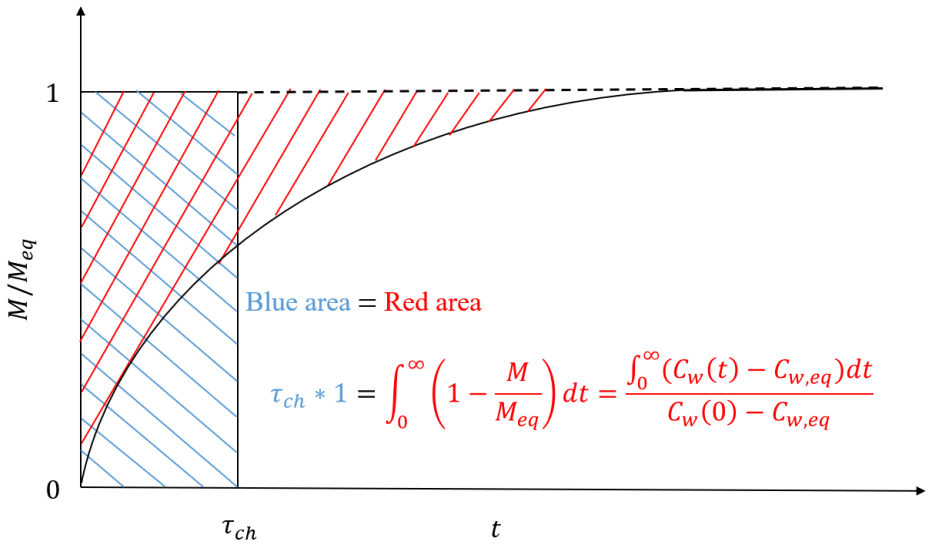

Fig. S2.5: Exponential curve: Mass sorbed or desorbed relative to equilibrium conditions (M/M_{eq}) vs. time (t). The characteristic time τ_{ch} is defined when the area above the exponential curve (red lines) equals to the area of the vertical rectangle (blue lines). Note:

$\frac{M}{M_{eq}} = 1 - \frac{C_w(t) - C_{w,eq}}{C_w(0) - C_{w,eq}}$ for the sorptive uptake case.

S2.5 Empirical relationships to the estimation of Sherwood numbers

Many empirical relationships are reported in literature on solid-liquid mass transfer in agitated and fluidized bed systems over a wide range of Reynolds numbers. Most of these correlations can be generally described by the following equation:

$$Sh = A + BRe^{\theta}Sc^{\gamma} \tag{S2.72}$$

where Sh [-] is the Sherwood number. A and B are constants (for spherical particles $A = 2$; B is a fitting parameter obtained from experimental data). Re and Sc denote the Reynolds and Schmidt number. θ and γ are empirical constants to be determined. Schmidt and Reynolds numbers are defined as:

$$Sc = \frac{\nu}{D_{aq}} \qquad Re = \frac{d\, v_a}{\nu} \tag{S2.73}$$

ν [$L^2\ T^{-1}$] and v_a [$L\ T^{-1}$] denote the kinematic viscosity and the relative velocity of water with respect to the particle. The Blasius (1908) solved the Navier-Stokes equation and continuity equation for laminar flow over a sharp leading edge and found that the ratio of fluid velocity boundary layer thickness to concentration boundary layer thickness is proportional to the Schmidt number with a power of 1/3; thus γ of 1/3 is widely used in many studies (see Tab. S2.1). Liu et al. (2014) showed a higher empirical exponent γ of 1/2 by using penetration theory (Sherwood et al. 1975).

Kolmogorov (1941) showed that the kinetic energy supplied by the system is dissipated primarily by viscous interaction of smallest eddies, whose turbulent motion is isotropic. This theory was widely used in investigating the mass transfer of solid particles suspended in agitated vessels showing that the relative velocity of water with respect to the particle is proportional to the product of energy dissipation rate (ε_{disp}) and particle size (d) with the power of 1/3 ($v_a \sim \left(\varepsilon_{disp} d\right)^{1/3}$). The Reynolds number of suspended particles thus can be expressed as:

$$Re = \frac{{\varepsilon_{disp}}^{1/3} d^{4/3}}{\nu} \quad \text{(S2.74)}$$

Values for θ in Eq. S2.72 from empirical relationships are in a range of 0.5-0.75 which is expected from the Kolmogorov length scale ($\eta = \left(\nu^3/\varepsilon_{disp}\right)^{1/4}$). Microparticles by definition are smaller than the Kolmogorov length scale ($d < \eta$) while macroparticles are smaller than the dimension of the vessel ($\eta < d \ll L_0$). Kirwan et al. (1989) focused on the mass transfer to microparticles in agitated systems and the experimental results resulted in θ of 0.52, which is consistent with the theoretical study of Batchelor (1980) who assumes that the particle dimension is small compared with the smallest eddy size (= η) in turbulent flow where θ is 0.5. Empirical relationships found for macroparticles (Levins and Glastonbury, 1972b) show higher θ values of 0.62 or ¾ (Calderbank and Moo-Young, 1961). For θ = 3/4, the Sherwood number becomes proportional to particle size (d) and the corresponding mass transfer velocity ($k = D_{aq}Sh/d$) gets independent on particle size. Sherwood number relationships for solid-liquid mass transfer depend on experimental setup in different flow systems but are quite similar as compiled in Tab. S2.1 and shown in Fig. S2.6.

Tab. S2.1: Sherwood number relationships for solid–liquid mass transfer in different systems

Reference	Correlation	System
Friedlander (1961)	$Sh = 2 + 0.991Pe^{1/3}$	Stokes Flow (Re < 1), $Pe = Re\,Sc$
Calderbank and Moo-Young (1961)	$Sh = 2 + 0.13Re^{3/4}Sc^{1/3}$	Stirred tank
Levins and Glastonbury (1972b)	$Sh = 2 + 0.47Re^{0.62}Sc^{0.36}(D_s/T)^{0.17}$	Stirred tank (D_s: stirrer diameter T: tank diameter)
Sano et al. (1974)	$Sh = 2 + 0.4Re^{3/4}Sc^{1/3}$	Bubble column and stirred tank
Ohashi et al. (1981)	$Sh = \left(2 + 0.695Re^{0.60}Sc^{1/3}\right)\varphi$	Fixed bed (φ: surface factor)
Ohashi et al. (1982)	$Sh = 2 + 0.44Re^{0.63}Sc^{1/3}$	Two phase pipe flow
Kirwan et al. (1989)	$Sh = 2 + 0.52Re^{0.52}Sc^{1/3}$	Stirred tank
Arters and Fan (1990)	$Sh = 2 + 0.4Re^{3/4}Sc^{1/3}$	Fluidized bed
Mao et al. (1992)	$Sh = 2 + 0.48Re^{0.72}Sc^{1/3}$	External loop airlift reactor
Liu et al. (2014)	$Sh = 2 + 0.1Pe^{1/2}$	Fixed bed

The energy dissipation rate (ε_{disp}) in Eq. S2.74 represents the power input per mass of water (W/kg = J s^{-1} kg^{-1} = kg m^2 s^{-3} kg^{-1} = m^2 s^{-3}) which in contrast to natural systems can be easily

determined in laboratory settings. Chickadel et al. (2011), Fisher et al. (2002) and MacDonald et al. (2007) reported energy dissipation rate in rivers in the range of 10^{-6} - 10^{-5} m^2 s^{-3}. In oceans, values are roughly one magnitude lower than in rivers (Moum et al., 1995). Seidensticker et al. (2019) used a magnetic stirrer system in (de-)sorption batch tests with microplastics and reported a higher energy dissipation rate of $10^{-4.2}$ m^2 s^{-3}. In Fig S2.6, we illustrate the influence of particle size on Sherwood numbers as well as on the mass transfer coefficients under different flow regimes (magnetic stirrer batch systems, rivers, oceans). The Sherwood number relationships for microparticles and macroparticles are based on the results of Kirwan et al. (1989) and Sano et al. (1974), respectively. Figure S2.6 shows that Sherwood numbers increase with the increase of particle size. Particle smaller than 600 µm and 1000 µm can be regarded as the microparticles in rivers and oceans. Glaser et al. (2020) showed suspended particles of the Ammer river (South-western Germany) lie in the size range of 10-30 µm, which is much less than 600 µm. Thus θ = 0.5 is appropriate in estimating mass transfer coefficients for suspended particles in rivers. In addition, mass transfer coefficients are not very sensitive to particle sizes less than 10 µm because the lower limit of Sh of 2 is approached. In this range mass transfer coefficients increase linearly with decreasing particle sizes.

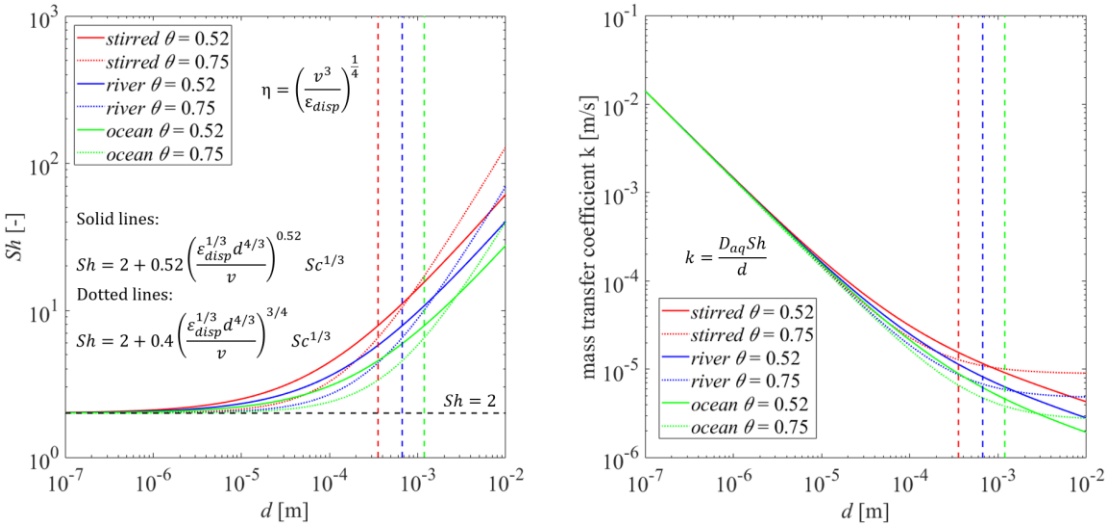

Fig. S2.6: Influence of particle size (d) on Sherwood numbers (left) and mass transfer coefficients (right) in different flow systems (stirred, rivers, ocean with energy dissipation rates (ε_{disp}) of $10^{-4.2}$ m^2 s^{-3}, 5×10^{-6} m^2 s^{-3}, and 5×10^{-7} m^2 s^{-3}). The horizontal and vertical dashed lines denote minimum values of the Sherwood number ($Sh = 2$) and Kolmogorov length scales $\left(\eta = \nu^3/\varepsilon_{disp}\right)^{1/4}$, repectively.

S2.6 Linearization of nonlinear sorption isotherms

Non-linear sorption isotherms are frequently observed for pesticides and many other organic compounds in soils and sediments, while the proposed models (FOAM and SALT) are based on linear sorption isotherms. In order to apply the proposed models, linearization of the sorption isotherms in the concentration range relevant to the batch experiment may be considered. Figure S2.7 illustrates how average K_d values increase from an initially high concentration of 100 µg L^{-1} to intermediate and finally equilibrium concentrations (50 µg L^{-1} and 10 µg L^{-1}). Linearization may be done based on average K_ds or by calculating K_d at an intermediate concentration; e.g., for a Freundlich coefficient of 2000 µg kg^{-1}: (µg L^{-1})$^{0.8}$ and a Freundlich exponent of 0.8 we get:

$$K_{d,50\%} = K_{Fr} * C_{w,eq}^{1/n-1} = 2000 \frac{\mu g\ kg^{-1}}{(\mu g\ L^{-1})^{0.8}} * (50\ \mu g\ L^{-1})^{-0.2} = 915\ L\ kg^{-1} \quad (S2.75)$$

A mean value may be calculated as follows:

$$K_{d,mean,91\%} = \frac{K_{d,ini} + K_{d,91\%}}{2} = \frac{800\ L\ kg^{-1} + 1262\ L\ kg^{-1}}{2} = 1031\ L\ kg^{-1} \quad (S2.76)$$

The difference between both is around 10% and thus below analytical and experimental errors. In Fig. S2.8 we compare M/M_{eq} simulated with a numerical model for linearized K_d values and the non-linear Freundlich sorption isotherms in the finite bath (β = 0.1 and 1). Deviations are just minor (impossible to quantify within the experimental error), confirming that constant K_d values (linear sorption) can be applied for non-linear sorption if the relevant concentration ranges are considered.

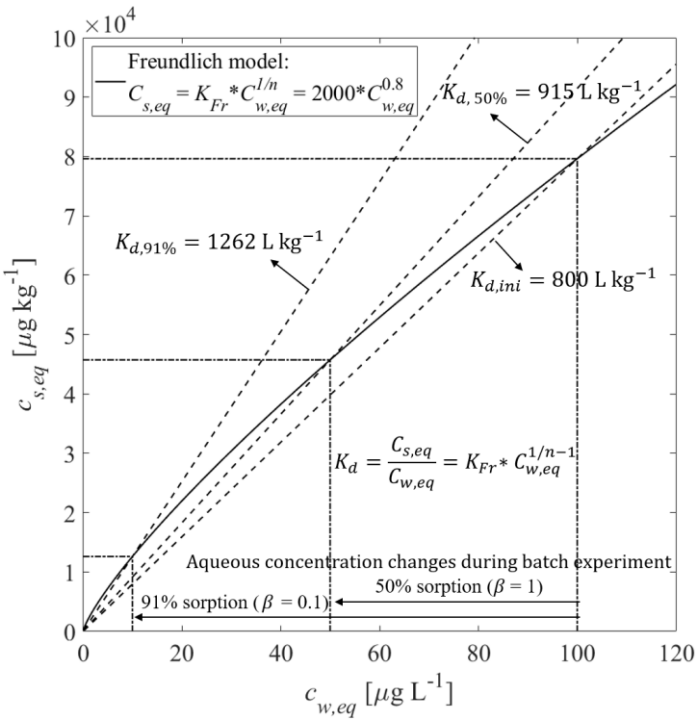

Fig. S2.7: Scheme for linearization of the Freundlich sorption model

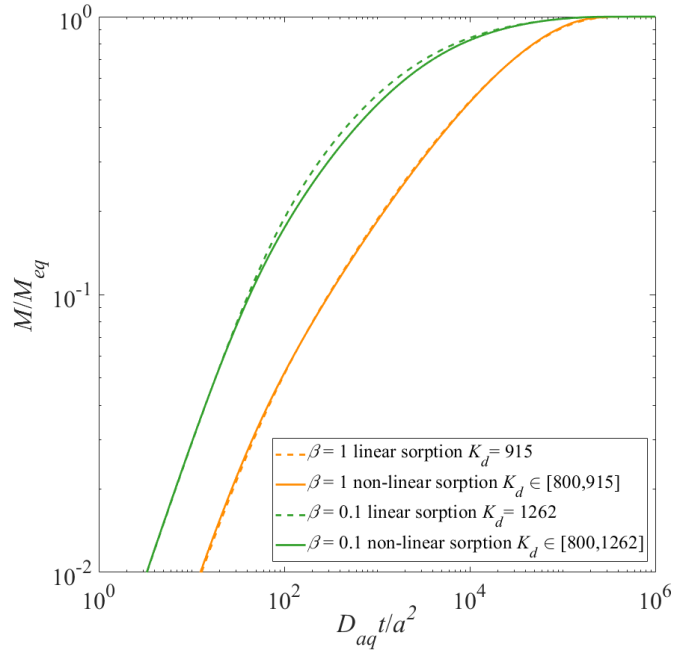

Fig. S2.8: Mass sorbed relative to equilibrium conditions (M/M_{eq}) vs. dimensionless time (Fourier number = $D_{aq}t/a^2$) calculated with a numerical solution for a nonlinear Freundlich sorption isotherm (Fig. S2.7, $1/n$ = 0.8) and linearized distribution coefficients (K_d) as shown in Fig. S2.7; finite bath conditions with $\beta(=\frac{V_w}{m_d K_{d,b}})$ = 0.1 and 1 ($Sh = 2$, $\varepsilon = 0.05$).

References

Arters, D.C., Fan, L.S., 1990. Experimental methods and correlation of solid—liquid mass transfer in fluidized beds. Chem. Eng. Sci. 45, 965–975. https://doi.org/10.1016/0009-2509(90)85019-A.

Batchelor, G.K., 1980. Mass transfer from small particles suspended in turbulent fluid. J. Fluid Mech. 98, 609–623. https://doi.org/doi: 10.1017/S0022112080000304.

Blasius, H., 1908. Grenzschichten in Flüssigkeiten mit kleiner Reibung (The boundary layers in fluids with little friction). In Zeitschrift für Angewandte Mathematik und Physik (Journal of Applied Mathematics and Physics), volume 56, pp. 1–37.

Calderbank, P.H., Moo-Young, M.B., 1961. The continuous phase heat and mass-transfer properties of dispersions. Chem. Eng. Sci. 16, 39–54. https://doi.org/10.1016/0009-2509(61)87005-X.

Chickadel, C.C., Talke, S.A., Horner-Devine, A.R., Jessup, A.T., 2011. Infrared-based measurements of velocity, turbulent kinetic energy, and dissipation at the water surface in a tidal river. IEEE Geosci. Remote Sens. Lett. 8, 849–853. https://doi.org/10.1109/LGRS.2011.2125942.

Crank, J., 1975. The Mathematics of Diffusion, Second ed. Oxford University Press, London, pp. 69–88.

de Hoog, F.R., Knight, J.H., Stokes, A.N., 1982. An improved method for numerical inversion of Laplace transforms. SIAM J. Sci. Stat. Comput. 3 (3), 357–366. https://doi.org/10.1137/0903022.

Fisher, N.R., Simpson, J.H., Howarth, M.J., 2002. Turbulent dissipation in the Rhine ROFI forced by tidal flow and wind stress. J. Sea Res. 48 (4), 249–258. https://doi.org/10.1016/S1385-1101(02)00194-6.

Friedlander, S. K., 1961. A note on transport to spheres in stokes flow. AIChE Journal, 7, 347–348. https://doi.org/10.1002/aic.690070237.

Glaser, C., Zarfl, C., Rügner, H., Lewis, A., Schwientek, M., 2020. Analyzingparticle-associated pollutant transport to identify in-stream sediment processes during a high flow event. Water. 12(6). https://doi.org/10.3390/w12061794.

Glueckauf, E., 1955. Theory of chromatography: Part 10. - Formula for diffusion into spheres and their application to chromatography. Trans. Faraday Soc. 51, 1540–1551. https://doi.org/10.1039/TF9555101540.

Hills, J.H., 1986. An investigation of the linear driving force approximation to diffusion in spherical particles. Chem. Eng. Sci. 41, 2779–2785. https://doi.org/10.1016/0009-2509(86)80009-4.

Kirwan, J., Armenante, P.M., 1989. Mass transfer to microparticle systems. Chem. Eng. Sci. 44 (12), 2781–2796. https://doi.org/10.1016/0009-2509(89)85088-2.

Kolmogorov, A.N., 1941. The local structure of turbulence in incompressible viscous fluid for very large Reynolds numbers (English translation by V. Levin, 1991). Process R. Soc. A- Math. Phys. Eng. Sci. 434, 9–13. https://doi.org/10.1098/ rspa.1991.0075.

Liu, Y., Illangasekare, T.H., Kitanidis, P.K., 2014. Long-term mass transfer and mixing-controlled reactions of a DNAPL plume from persistent residuals. J. Contam. Hydrol. 157, 11–24. https://doi.org/10.1016/j.jconhyd.2013.10.008.

Levins, D.M., Glastonbury, J.R., 1972. Application of Kolmogorov's theory to particle—liquid mass transfer in agitated vessels. Chem. Eng. Sci. 27, 537–543. https://doi.org/10.1016/0009-2509(72)87009-X.

Mao, H.H., Chisti, Y., Moo-Young, M., 1992. Multiphase hydrodynamics and solid-liquid mass transfer in an external-loop airlift reactor–a comparative study. Chem. Eng. Commun. 113, 1–13. https://doi.org/10.1080/00986449208936000.

MacDonald, D.G., Goodman, L., Hetland, R.D., 2007. Turbulent dissipation in a near-field river plume: A comparison of control volume and microstructure observations with a numerical model. J. Geophys. Res. Ocean. 112, 1–13. https://doi.org/https://doi.org/10.1029/2006JC004075.

Moum, J.N., Gregg, M.C., Lien, R.C., Carr, M.E., 1995. Comparison of Turbulence Kinetic Energy Dissipation Rate Estimates from Two Ocean Microstructure Profilers. J. Atmos. Ocean. Technol. 12, 346–366. https://doi.org/10.1175/1520-0426(1995)012<0346:COTKED>2.0.CO;2.

Ohashi, H., Sugawara, T., Kikuchi, K.I., 1981. Mass transfer between particles and liquid in solid-liquid two-phase flow through vertical tubes. J. Chem. Eng. Japan. 14, 489–491. https://doi.org/10.1252/jcej.14.489.

Ohashi, H., Sugawara, T., Kikuchi, K.I., Takeda, M., 1982. Mass transfer between particles and liquid in solid-liquid two-phase flow through horizontal tubes. J. Chem. Eng. Japan. 15, 311–313. https://doi.org/10.1252/jcej.15.311.

Sano, Y., Yamaguchi, N., Adachi, T., 1974. Mass transfer coefficients for suspended particles in agitated vessels and bubble columns. J. Chem. Eng. Japan. 7, 255–261. https://doi.org/10.1252/jcej.7.255.

Sherwood, T.K., Pigford, R.L., Wilke, R.L., 1975. “Mass Transfer”, McGraw-Hill: New York, NY, USA.

Seidensticker, S., Zarfl, C., Cirpka, O.A., Grathwohl, P., 2019. Microplastic–contaminant interactions: Influence of nonlinearity and coupled mass transfer. Environ. Toxicol. Chem. 38, 1635–1644. https://doi.org/10.1002/etc.4447.

S3 Supplementary information for mechanistic modelling of pollutant mass redistribution (sorption/desorption) in heterogeneous systems explaining unexpected slow kinetics

S3.1 Experimental data of batch tests A-D

Tab. S3.1: Sampling time points and Phenanthrene concentrations in aqueous phase of batch tests A-C.

Batch test A		Batch test B		Batch test C	
time [min]	C_w [µg L^{-1}]	time [min]	C_w [µg L^{-1}]	time [min]	C_w [µg L^{-1}]
0	104.32	0	2.94	0	0.31
5	45.74	10	2.05	10	0.97
10	26.60	20	1.86	20	1.12
15	18.21	30	1.59	30	1.31
20	13.92	40	1.42	40	1.20
30	11.20	50	1.19	50	1.20
40	9.83	60	1.12	60	1.16
60	8.26	120	0.86	120	1.28
180	7.52	240	0.66	240	1.22
1020	6.89	480	0.61	540	1.12
		720	0.57	1380	1.21
		1320	0.64	3000	1.08
		2040	0.69	4500	1.19
		2760	0.90	9120	0.99
		4200	0.97	13320	1.07
		5700	1.10	24600	1.04
		9540	1.24	36000	0.99
		10560	1.40		
		13140	1.42		
		17760	1.34		

		23400	1.36		

Tab. S3.2: Sampling time points and Anthracene d10 and Phenanthrene concentrations in PE sheets of batch test D.

Batch test D								
	SL = 0.15 kg L^{-1}				SL = 0.30 kg L^{-1}			
time [min]	Anthracene d10		Phenanthrene		Anthracene d10		Phenanthrene	
	C_{PE} [µg kg^{-1}]	std [µg kg^{-1}]	C_{PE} [µg kg^{-1}]	std [µg kg^{-1}]	C_{PE} [µg kg^{-1}]	std [µg kg^{-1}]	C_{PE} [µg kg^{-1}]	std [µg kg^{-1}]
0	227	7.8	0	0.0	227	8.0	6	7.1
5	174	6.1	62	8.8	192	5.3	52	3.8
15	162	7.8	102	6.2	143	18.5	97	10.8
30	122	10.8	147	9.9	120	4.2	149	7.3
90	94	4.7	214	15.8	68	0.8	205	3.3
300	73	1.0	193	5.7	51	2.4	237	5.7
600	72	1.2	203	9.0	44	3.1	227	1.2
1800	58	3.7	200	10.5	37	1.7	209	0.5

where: std denotes the standard deviations of data.

S3.2 Particle size distribution of pulverized sediment and Phenanthrene concentration measurement via accelerated solvent extraction (ASE)

Figure S3.1 shows cumulative grain size distribution curves obtained from laser particle analysis after planet ball milling of the sample. Assuming that densities of various particle classes in the sample are the same, the volumetric fractions are equivalent to mass fractions. The size of particles varies from 0.4 µm to ca. 724 µm, but around 90% of particles are in the range from 2 µm to 240 µm. Half of sediment particles are smaller than 23 µm. For model simulation, particles are divided into two parts with equal mass fraction (50%) and two characteristic grain sizes are used to represent the fine particles ($d_{sp,1} = 7$ µm) and coarse particles ($d_{sp,2} = 74$ µm). Characteristic grain sizes of fine and coarse particles are based on the geometric mean diameters of particle size ranges of $d_5 - d_{50}$ ($d_{sp,1} = \sqrt{d_5 d_{50}}$) and $d_{50} - d_{95}$ ($d_{sp,2} = \sqrt{d_{50} d_{95}}$), respectively.

Tab. S3.3: Particle size distribution measured in laser diffraction.

Particle size class	Particle diameter [µm]	Volumetric fraction [%]
d_{min}	0.4	0
d_5	2	5
d_{10}	3	10
d_{50}	23	50
d_{90}	138	90
d_{95}	240	95
d_{max}	724	100

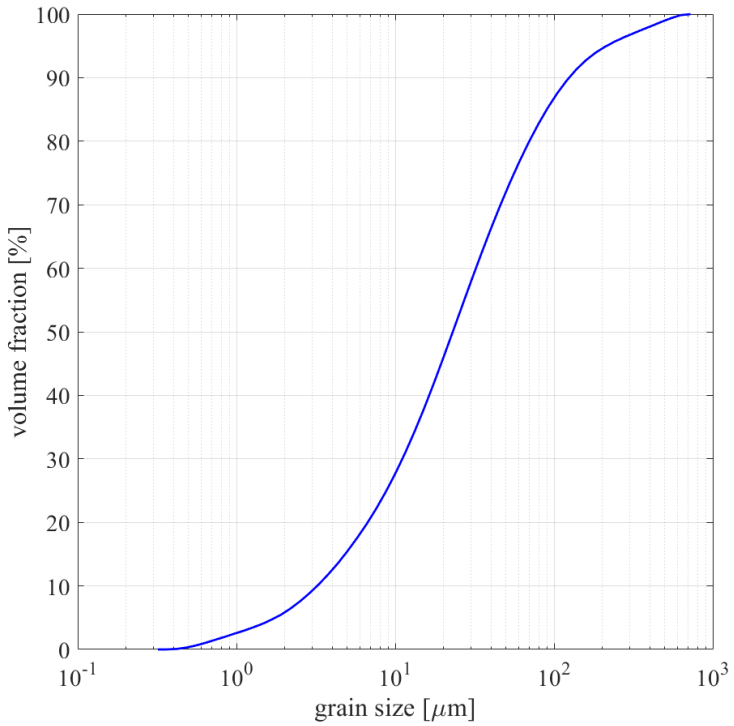

Fig. S3.1: Cumulative particle size distribution of the sediment sample after planet ball milling.

PAHs were extracted from pulverized bulk sediment in a two-step procedure using ASE with acetone and toluene as solvents. 21 g of sediment were mixed manually with 21 g of quartz sand and filled into 30 mL cells. Pressure used in ASE was 100 bars and temperatures were 100 ℃ for extraction with acetone and 150 ℃ for toluene. Two consequent extraction cycles were performed for each solvent to guarantee a complete extraction of target compound. Toluene extracts were then reduced to about 1.5 mL on a rotating evaporator and measured at the GC/MS. Acetone extracts were transferred into 2L bottles and mixed with 1600 mL

Millipore water and extracted again with cyclohexane, then reduced to about 150 µL under stream of nitrogen with heating to 40 ℃ before the measurement at the GC/MS.

S3.3 Semi-analytical Laplace solution for coupled film-intraparticle solid diffusion in a plane sheet (e.g., PE passive sampler)

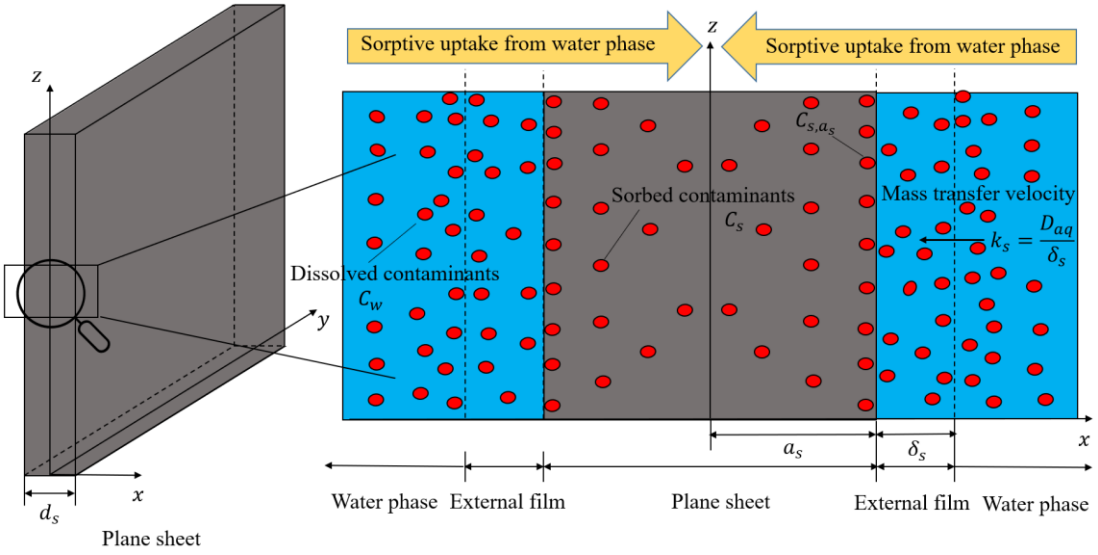

Fig. S3.2: Scheme of mass transfer limited by coupled film intraparticle solid diffusion in plane sheets.

Solid diffusion. Considering the case of diffusion into a plane sheet (e.g., PE sheets, see Fig. S3.2) whose thickness (d_s) is so thin that effectively all the diffusing substance enters through the plane faces (diffusion through the edges is negligible), may be described by Fick's second law:

$$\frac{\partial C_s}{\partial t} = D_s \frac{\partial^2 C_s}{\partial x^2} \tag{S3.1}$$

Boundary and initial conditions are:

$$C_s(x = a_s, t) = C_{s,a_s} \tag{S3.2}$$

$$\frac{\partial C_s}{\partial x}(x = 0, t) = 0 \tag{S3.3}$$

$$C_s(x, t = 0) = C_s(0) \ \forall x \tag{S3.4}$$

where x [L] is the Cartesian coordinate; a_s [L] is half thickness and C_s [M M^{-1}] is the solute concentration in the solid; C_{s,a_s} [M M^{-1}] is the solute concentration at the solid/water boundary; $C_s(0)$ [M M^{-1}] is the initial solute concentration in solid materials; D_s [L^2 T^{-1}] is the solutes solid diffusion coefficient and t [T] denotes time.

The Laplace transformation of governing equations and corresponding initial and boundary conditions can be expressed as:

$$s\tilde{C}_s - C_s(0) - D_s\frac{d^2\tilde{C}_s}{dx^2} = 0 \tag{S3.5}$$

$$\tilde{C}_s(a_s) = \tilde{C}_{s,a_s} \tag{S3.6}$$

$$\left.\frac{d\tilde{C}_s}{dx}\right|_{x=0} = 0 \tag{S3.7}$$

$$\tilde{C}_s(x) = \tilde{C}_s(0) \ \forall x \tag{S3.8}$$

in which the variables with a tilde represent Laplace transforms, and s [T^{-1}] is the complex Laplace coordinate. Equation S3.5 can be solved starting from:

$$\tilde{C}_s(x, s) \propto \exp(x\varphi) + C \tag{S3.9}$$

where φ and C are undetermined coefficients.

$$\frac{d\tilde{C}_s}{dx} \propto \varphi \exp(x\varphi) \tag{S3.10}$$

$$\frac{d^2\tilde{C}_s}{dx^2} \propto \varphi^2 \exp(x\varphi) \tag{S3.11}$$

Inserting Eqs. S3.10, S3.11 into Eq. S3.5 yields:

$$s\exp(x\varphi) + sC - C_s(0) - D_s\varphi^2\exp(x\varphi) = 0$$
$$(\mathrm{s} - \varphi^2 D_s)\exp(x\varphi) + sC - C_s(0) = 0$$
$$\Longrightarrow \begin{cases} \mathrm{s} - \varphi^2 D_s = 0 \\ sC - C_s(0) = 0 \end{cases} \Longrightarrow \begin{cases} \varphi = \pm\sqrt{\dfrac{s}{D_s}} \\ C = \dfrac{C_s(0)}{s} \end{cases} \tag{S3.12}$$

The solution of Eq. S3.5 can finally be expressed as:

$$\tilde{C}_s(x,s) = A\exp\left(x\sqrt{\frac{s}{D_s}}\right) + B\exp\left(-x\sqrt{\frac{s}{D_s}}\right) + \frac{C_s(0)}{s} \tag{S3.13}$$

where A and B are undetermined coefficients, which can be determined via the boundary conditions of the governing equation (Eq. S3.6 and Eq. S3.7).

$$\frac{d\tilde{C}_s}{dx} = A\sqrt{\frac{s}{D_s}}\exp\left(x\sqrt{\frac{s}{D_s}}\right) - B\sqrt{\frac{s}{D_s}}\exp\left(-x\sqrt{\frac{s}{D_s}}\right) \tag{S3.14}$$

The internal boundary condition (Eq. S3.7) shows that the $d\tilde{C}_s/dx$ approaches 0 when x approaches 0:

$$\left.\frac{d\tilde{C}_s}{dx}\right|_{x=0} = \lim_{x\to 0}(A-B)\sqrt{\frac{s}{D_s}} = 0 \tag{S3.15}$$
$$\Longrightarrow A = B$$

Then Eq. S3.13 can be rearranged as:

$$\tilde{C}_s(x,s) = A\exp\left(x\sqrt{\frac{s}{D_s}}\right) + A\exp\left(-x\sqrt{\frac{s}{D_s}}\right) + \frac{C_s(0)}{s}$$
$$\tilde{C}_s(x,s) = 2A\left[\frac{1}{2}\exp\left(x\sqrt{\frac{s}{D_s}}\right) + \frac{1}{2}\exp\left(-x\sqrt{\frac{s}{D_s}}\right)\right] + \frac{C_s(0)}{s} \tag{S3.16}$$
$$\tilde{C}_s(x,s) = 2A\cosh\left(x\sqrt{\frac{s}{D_s}}\right) + \frac{C_s(0)}{s}$$

Based on the external boundary condition (Eq. S3.6), the unknown coefficient $2A$ can be determined.

$$\tilde{C}_s(a_s,s) = 2A\cosh\left(a_s\sqrt{\frac{s}{D_s}}\right) + \frac{C_s(0)}{s} = \tilde{C}_{s,a_s}$$
$$2A = \frac{\left(\tilde{C}_{s,a_s} - \dfrac{C_s(0)}{s}\right)}{\cosh\left(a_s\sqrt{\dfrac{s}{D_s}}\right)} \tag{S3.17}$$

Thus, the analytical solution of Eq. S3.5 in Laplace domain can be expressed as:

$$\tilde{C}_s(x,s) = \frac{\cosh\left(x\sqrt{\frac{s}{D_s}}\right)}{\cosh\left(a_s\sqrt{\frac{s}{D_s}}\right)}\left(\tilde{C}_{s,a_s} - \frac{C_s(0)}{s}\right) + \frac{C_s(0)}{s} \tag{S3.18}$$

Film diffusion. Assuming the solute mass release (or uptake) from the surface of the plane sheet into the bulk solution is additionally limited by diffusion through the external boundary layer (δ_s) which does not store any solute mass, the continuity of the mass flux density (F [M L^{-2} T^{-1}]) requires:

$$F = k_s\left(\frac{C_s(x=a_s,t)}{K_d} - C_w(t)\right) = -D_s\rho_s\left.\frac{\partial C_s}{\partial x}\right|_{x=a_s} \tag{S3.19}$$

where k_s [L T^{-1}] denotes the mass transfer velocity and ρ_s [M L^{-3}] denotes the density of the plane sheets. K_d [L^3 M^{-1}] denotes the distribution coefficient between solid plane sheets and water.

The Laplace transformation of mass flux density can be expressed as:

$$\tilde{F} = k_s\left(\frac{\tilde{C}_{s,a_s}}{K_d} - \tilde{C}_w\right) = -D_s\rho_s\left.\frac{d\tilde{C}_s}{dx}\right|_{x=a_s} \tag{S3.20}$$

$\left.\frac{d\tilde{C}_s}{dx}\right|_{x=a_s}$ in Eq. S3.20 can be calculated via Eq. S3.18:

$$\begin{aligned}\left.\frac{d\tilde{C}_s}{dx}\right|_{x=a_s} &= \left.\frac{\sqrt{\frac{s}{D_s}}\sinh\left(x\sqrt{\frac{s}{D_s}}\right)}{\cosh\left(a_s\sqrt{\frac{s}{D_s}}\right)}\left(\tilde{C}_{s,a_s} - \frac{C_s(0)}{s}\right)\right|_{x=a_s} \\ &= \sqrt{\frac{s}{D_s}}\tanh\left(a_s\sqrt{\frac{s}{D_s}}\right)\left(\tilde{C}_{s,a_s} - \frac{C_s(0)}{s}\right)\end{aligned} \tag{S3.21}$$

Rearranging Eq. S3.20 with Eq. S3.21 gives the expression of $\tilde{C}_{s,a_s}$:

$$\begin{aligned}&k_s\left(\frac{\tilde{C}_{s,a_s}}{K_d} - \tilde{C}_w\right) = -D_s\rho_s\sqrt{\frac{s}{D_s}}\tanh\left(a_s\sqrt{\frac{s}{D_s}}\right)\left(\tilde{C}_{s,a_s} - \frac{C_s(0)}{s}\right) \\ &\left[\frac{k_s}{K_d} + \sqrt{D_s s}\rho_s\tanh\left(a_s\sqrt{\frac{s}{D_s}}\right)\right]\tilde{C}_{s,a_s} = \sqrt{D_s s}\rho_s\tanh\left(a_s\sqrt{\frac{s}{D_s}}\right)\frac{C_s(0)}{s} + k_s\tilde{C}_w \\ &\tilde{C}_{s,a_s} = \frac{\sqrt{D_s s}\rho_s\tanh\left(a_s\sqrt{\frac{s}{D_s}}\right)\frac{C_s(0)}{s} + k_s\tilde{C}_w}{\left[\frac{k_s}{K_d} + \sqrt{D_s s}\rho_s\tanh\left(a_s\sqrt{\frac{s}{D_s}}\right)\right]}\end{aligned} \tag{S3.22}$$

The solute concentration change in solid materials is given by:

$$\frac{\partial C_s}{\partial t} = -F\,A^o = k_s \frac{1}{a_s \rho_s}\left(C_w(t) - \frac{C_s(x = a_s, t)}{K_d}\right) \tag{S3.23}$$

where A^o [L^{-1}] denotes specific surface area of solid materials per unit volume of water in a batch system. Next, the Laplace transformation of Eq. S3.23 is used.

$$s\tilde{C}_s - C_s(0) = k_s \frac{1}{a_s \rho_s}\left(\tilde{C}_w - \frac{\tilde{C}_{s,a_s}}{K_d}\right) \tag{S3.24}$$

Inserting Eq. S3.22 into Eq. S3.24 and rearranging terms finally yields the Laplace transform solution for coupled film-intraparticle solid diffusion of plane sheets:

$$\begin{aligned} \tilde{C}_s &= \tilde{g}_s\left(\tilde{C}_w - \frac{C_s(0)}{K_d s}\right) + \frac{C_s(0)}{s} \\ \text{with } \tilde{g}_s &= \frac{\sqrt{D_s s}K_d \tanh\left(a_s\sqrt{\frac{s}{D_s}}\right)}{k_s + \sqrt{D_s s}\rho_s K_d \tanh\left(a_s\sqrt{\frac{s}{D_s}}\right)} \frac{k_s}{a_s s} \end{aligned} \tag{S3.25}$$

where $\tilde{g}_s$ [$L^3\,M^{-1}$] denotes the transfer function of coupled film-intraparticle solid diffusion of plane solid materials.

Two limiting cases may be considered:

1. $\lim\ k_s \to \infty$: This describes the case where external mass transfer resistance vanishes. The denominator in Eq. S3.25 in this case simplifies to $\lim_{k_s\to\infty}\left(k_s + \sqrt{D_s s}\rho_s K_d \tanh\left(a_s\sqrt{\frac{s}{D_s}}\right)\right) = k_s$, which leads to:

$$\begin{aligned} \tilde{C}_s &= \tilde{g}_s\left(\tilde{C}_w - \frac{C_s(0)}{K_d s}\right) + \frac{C_s(0)}{s} \\ \text{with } \tilde{g}_s &= \sqrt{D_s s}K_d \tanh\left(a_s\sqrt{\frac{s}{D_s}}\right)\frac{1}{a_s s} \end{aligned} \tag{S3.26}$$

2. $\lim D_s \to \infty$: This describes the case of a plane sheet with a uniform concentration distribution (well mixed interior), where only the external boundary layer controls mass transfer. To obtain the solution for this case, we need to consider the limit of tanh(x) for arguments approaching 0. The Taylor series expansion shows that tanh(x) can be approximated with:

$$\lim_{x\to 0} \tanh(x)\ \approx x \tag{S3.27}$$

Using Eq. S3.27 to determine the limit of $\lim_{D_s\to\infty}\left(\sqrt{D_s s}K_d \tanh\left(a_s\sqrt{\frac{s}{D_s}}\right)\right)$ yields:

$$\lim_{D_s \to \infty} \tanh\left(a_s \sqrt{\frac{s}{D_s}}\right) \approx a_s \sqrt{\frac{s}{D_s}}$$

$$\lim_{D_s \to \infty} \sqrt{D_s s} K_d \tanh\left(a_s \sqrt{\frac{s}{D_s}}\right) \tag{S3.28}$$

$$= \lim_{D_s \to \infty} \sqrt{D_s s} K_d a_s \sqrt{\frac{s}{D_s}}$$

$$= K_d a_s s$$

This finally leads to:

$$\tilde{C}_s = \tilde{g}_s \left(\tilde{C}_w - \frac{C_s(0)}{K_d s}\right) + \frac{C_s(0)}{s}$$

$$\lim_{D_s \to \infty} \tilde{g}_s = \frac{K_d a_s s}{k_s + \rho_s K_d a_s s} \frac{k_s}{a_s s} \tag{S3.29}$$

$$= \frac{k_s K_d}{k_s + \rho_s K_d a_s s}$$

S3.4 Semi-analytical Laplace solution for coupled film-intraparticle solid diffusion in a cylinder

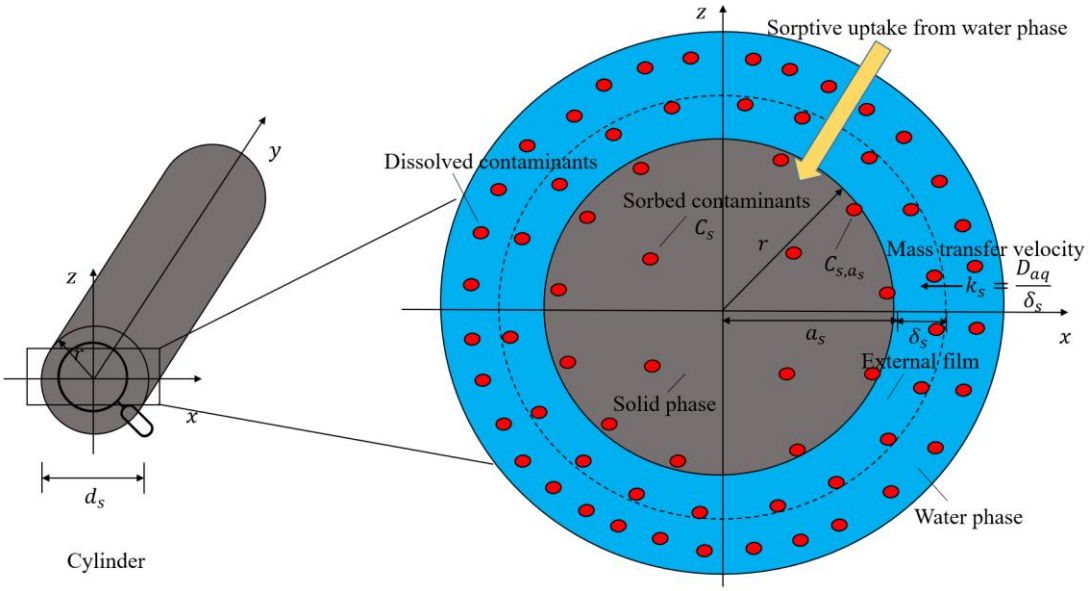

Fig. S3.3: Scheme of mass transfer limited by coupled film intraparticle solid diffusion in cylinders.

Solid diffusion. Considering the diffusion in a long circular cylinder in which diffusion only occurs in radial direction (see Fig. S3.3). According to Crank (1975), the governing equation

of the intraparticle solid diffusion of cylindrical particle follows Fick's second law:

$$\frac{\partial C_s}{\partial t} = D_s \left[\frac{\partial^2 C_s}{\partial r^2} + \frac{1}{r} \frac{\partial C_s}{\partial r} \right] \tag{S3.30}$$

Boundary and initial conditions are:

$$C_s(r = a_s, t) = C_{s,a_s} \tag{S3.31}$$

$$\frac{\partial C_s}{\partial r}(r = 0, t) = 0 \tag{S3.32}$$

$$C_s(r, t = 0) = C_s(0) \ \ \forall r \tag{S3.33}$$

where r [L] is the radial coordinate and a_s [L] is the radius of cylindrical particles.

The Laplace transformation of governing equations and corresponding initial and boundary conditions can be expressed as:

$$s\tilde{C}_s - C_s(0) - D_s \left[\frac{d^2 \tilde{C}_s}{dr^2} + \frac{1}{r} \frac{d\tilde{C}_s}{dr} \right] = 0 \tag{S3.34}$$

$$\tilde{C}_s(a_s) = \tilde{C}_{s,a_s} \tag{S3.35}$$

$$\left. \frac{d\tilde{C}_s}{dr} \right|_{r=0} = 0 \tag{S3.36}$$

$$\tilde{C}_s(r) = \tilde{C}_s(0) \ \ \forall r \tag{S3.37}$$

Introducing the dimensionless radial coordinate r_*:

$$r_* = r \sqrt{\frac{s}{D_s}} \tag{S3.38}$$

The governing equation (Eq. S3.34) can be rearranged as:

$$r_*^2 \frac{d^2 \tilde{C}_s}{dr_*^2} + r_* \frac{d\tilde{C}_s}{dr_*} - r_*^2 \left(\tilde{C}_s - \frac{C_s(0)}{s} \right) = 0 \tag{S3.39}$$

With the modified $\tilde{C}_{s,*} = \tilde{C}_s - \frac{C_s(0)}{s}$, Eq. S3.39 becomes:

$$r_*^2 \frac{d^2\tilde{C}_{s,*}}{dr_*^2} + r_* \frac{d\tilde{C}_{s,*}}{dr_*} - r_*^2 \tilde{C}_{s,*} = 0 \tag{S3.40}$$

which is the modified Bessel differential equation of zero order. Considering the internal boundary condition (Eq. S3.36) which has a derivative of zero at r = 0, the solution of Eq. S3.40 is the zero-order modified Bessel function of the first type $I_0(r_*)$.

$$\tilde{C}_{s,*}(r,s) = AI_0\left(r\sqrt{\frac{s}{D_s}}\right) \tag{S3.41}$$

Considering the initial condition ($\tilde{C}_{s,*}(r) = \tilde{C}_s(r) - \frac{C_s(0)}{s} = 0$), the solution of Eq. S3.34 can be described as:

$$\tilde{C}_s(r,s) = AI_0\left(r\sqrt{\frac{s}{D_s}}\right) + \frac{C_s(0)}{s} \tag{S3.42}$$

Based on the external boundary condition (Eq. S3.35), the unknown coefficient A can be determined.

$$A = \frac{\tilde{C}_{s,a_s} - \frac{C_s(0)}{s}}{I_0\left(a_s\sqrt{\frac{s}{D_s}}\right)} \tag{S3.43}$$

Inserting Eq. S3.43 into Eq. S3.42, the final solution of Eq. S3.34 can be expressed as:

$$\tilde{C}_s(r,s) = \frac{I_0\left(r\sqrt{\frac{s}{D_s}}\right)}{I_0\left(a_s\sqrt{\frac{s}{D_s}}\right)}\left(\tilde{C}_{s,a_s} - \frac{C_s(0)}{s}\right) + \frac{C_s(0)}{s} \tag{S3.44}$$

Film diffusion. If we assume the solute mass release (or uptake) from the surface of the cylinders into the bulk solution is additionally driven by diffusion through the external boundary layer (δ_s), the continuity of the mass flux density (F [M L^{-2} T^{-1}]) requires:

$$F = k_s\left(\frac{C_s(r=a_s,t)}{K_d} - C_w(t)\right) = -D_s\rho_s\left.\frac{\partial C_s}{\partial r}\right|_{r=a_s} \tag{S3.45}$$

Laplace transformation of mass flux density can be expressed as:

$$\tilde{F} = k_s\left(\frac{\tilde{C}_{s,a_s}}{K_d} - \tilde{C}_w\right) = -D_s\rho_s\left.\frac{d\tilde{C}_s}{dr}\right|_{r=a_s} \tag{S3.46}$$

$\left.\frac{d\tilde{C}_s}{dr}\right|_{r=a_s}$ in Eq. S3.46 can be calculated via Eq. S3.44:

$$\left.\frac{d\tilde{C}_s}{dr}\right|_{r=a_s} = \left.\frac{\sqrt{\frac{s}{D_s}}I_1\left(r\sqrt{\frac{s}{D_s}}\right)}{I_0\left(a_s\sqrt{\frac{s}{D_s}}\right)}\left(\tilde{C}_{s,a_s}-\frac{C_s(0)}{s}\right)\right|_{r=a_s}$$
$$= \sqrt{\frac{s}{D_s}}\frac{I_1\left(a_s\sqrt{\frac{s}{D_s}}\right)}{I_0\left(a_s\sqrt{\frac{s}{D_s}}\right)}\left(\tilde{C}_{s,a_s}-\frac{C_s(0)}{s}\right) \quad \text{(S3.47)}$$

where $I_1\left(a_s\sqrt{\frac{s}{D_s}}\right)$ is the first order modified Bessel function of the first type at the corresponding argument ($a_s\sqrt{\frac{s}{D_s}}$).

Rearranging Eq. S3.46 with Eq. S3.47 gives the expression of $\tilde{C}_{s,a_s}$:

$$k_s\left(\frac{\tilde{C}_{s,a_s}}{K_d}-\tilde{C}_w\right) = -D_s\rho_s\sqrt{\frac{s}{D_s}}\frac{I_1\left(a_s\sqrt{\frac{s}{D_s}}\right)}{I_0\left(a_s\sqrt{\frac{s}{D_s}}\right)}\left(\tilde{C}_{s,a_s}-\frac{C_s(0)}{s}\right)$$
$$\left[\frac{k_s}{K_d}+\sqrt{D_s s}\rho_s\frac{I_1\left(a_s\sqrt{\frac{s}{D_s}}\right)}{I_0\left(a_s\sqrt{\frac{s}{D_s}}\right)}\right]\tilde{C}_{s,a_s} = \sqrt{D_s s}\rho_s\frac{I_1\left(a_s\sqrt{\frac{s}{D_s}}\right)}{I_0\left(a_s\sqrt{\frac{s}{D_s}}\right)}\frac{C_s(0)}{s}+k_s\tilde{C}_w \quad \text{(S3.48)}$$
$$\tilde{C}_{s,a_s} = \frac{\sqrt{D_s s}\rho_s\frac{I_1\left(a_s\sqrt{\frac{s}{D_s}}\right)}{I_0\left(a_s\sqrt{\frac{s}{D_s}}\right)}\frac{C_s(0)}{s}+k_s\tilde{C}_w}{\left[\frac{k_s}{K_d}+\sqrt{D_s s}\rho_s\frac{I_1\left(a_s\sqrt{\frac{s}{D_s}}\right)}{I_0\left(a_s\sqrt{\frac{s}{D_s}}\right)}\right]}$$

The solute concentration change in solid materials is given by:

$$\frac{\partial C_s}{\partial t} = -F\,A^o = k_s\frac{2}{a_s\rho_s}\left(C_w(t)-\frac{C_s(r=a_s,t)}{K_d}\right) \quad \text{(S3.49)}$$

Next, the Laplace transformation of Eq. S3.49 is used:

$$s\tilde{C}_s - C_s(0) = k_s\frac{2}{a_s\rho_s}\left(\tilde{C}_w-\frac{\tilde{C}_{s,a_s}}{K_d}\right) \quad \text{(S3.50)}$$

Inserting Eq. S3.48 into Eq. S3.50 and rearranging terms finally yields the Laplace transform solution for coupled film-intraparticle solid diffusion of cylindrical particles:

$$\tilde{C}_s = \tilde{g}_s\left(\tilde{C}_w - \frac{C_s(0)}{K_d s}\right) + \frac{C_s(0)}{s}$$

$$\text{with } \tilde{g}_s = \frac{\sqrt{D_s s}K_d \dfrac{I_1\left(a_s\sqrt{\dfrac{s}{D_s}}\right)}{I_0\left(a_s\sqrt{\dfrac{s}{D_s}}\right)}\dfrac{2k_s}{a_s s}}{k_s + \sqrt{D_s s}\rho_s K_d \dfrac{I_1\left(a_s\sqrt{\dfrac{s}{D_s}}\right)}{I_0\left(a_s\sqrt{\dfrac{s}{D_s}}\right)}} \tag{S3.51}$$

Two limiting cases may be considered:

1. $\lim\ k_s \to \infty$: This describes the case where the external mass transfer resistance vanishes. The denominator in Eq. S3.51 in this case simplifies to $\lim_{k_s\to\infty}\left(k_s + \sqrt{D_s s}\rho_s K_d \frac{I_1\left(a_s\sqrt{\frac{s}{D_s}}\right)}{I_0\left(a_s\sqrt{\frac{s}{D_s}}\right)}\right) = k_s$, which leads to:

$$\tilde{C}_s = \tilde{g}_s\left(\tilde{C}_w - \frac{C_s(0)}{K_d s}\right) + \frac{C_s(0)}{s}$$

$$\text{with } \tilde{g}_s = \sqrt{D_s s}K_d \frac{I_1\left(a_s\sqrt{\dfrac{s}{D_s}}\right)}{I_0\left(a_s\sqrt{\dfrac{s}{D_s}}\right)}\frac{2}{a_s s} \tag{S3.52}$$

2. $\lim D_s \to \infty$: This describes the case of a cylindrical particle with a uniform concentration distribution (well mixed interior), where only the external boundary layer controls mass transfer. To obtain the solution for this case, the limit of $\frac{I_1(x)}{I_0(x)}$ for arguments approaching 0 has to be considered. The Taylor series expansion shows that $\frac{I_1(x)}{I_0(x)}$ can be approximated with:

$$\lim_{x\to 0}\frac{I_1(x)}{I_0(x)} \approx \frac{1}{2}x \tag{S3.53}$$

Using Eq. S3.53 to determine the limit of $\lim_{D_s\to\infty}\left(\sqrt{D_s s}K_d \frac{I_1\left(a_s\sqrt{\frac{s}{D_s}}\right)}{I_0\left(a_s\sqrt{\frac{s}{D_s}}\right)}\right)$ yields:

$$\lim_{D_s \to \infty} \frac{I_1\left(a_s\sqrt{\frac{s}{D_s}}\right)}{I_0\left(a_s\sqrt{\frac{s}{D_s}}\right)} \approx \frac{1}{2}a_s\sqrt{\frac{s}{D_s}}$$

$$\lim_{D_s \to \infty} \sqrt{D_s s}K_d \frac{I_1\left(a_s\sqrt{\frac{s}{D_s}}\right)}{I_0\left(a_s\sqrt{\frac{s}{D_s}}\right)} \tag{S3.54}$$

$$= \lim_{D_s \to \infty} \sqrt{D_s s}K_d \frac{1}{2}a_s\sqrt{\frac{s}{D_s}}$$

$$= \frac{1}{2}K_d a_s s$$

This finally leads to:

$$\tilde{C}_s = \tilde{g}_s\left(\tilde{C}_w - \frac{C_s(0)}{K_d s}\right) + \frac{C_s(0)}{s}$$

$$\lim_{D_s \to \infty} \tilde{g}_s = \frac{\frac{1}{2}K_d a_s s}{k_s + \frac{1}{2}\rho_s K_d a_s s}\frac{2k_s}{a_s s} \tag{S3.55}$$

$$= \frac{k_s K_d}{k_s + \frac{1}{2}\rho_s K_d a_s s}$$

S3.5 Semi-analytical Laplace solution for coupled film-intraparticle solid diffusion in a sphere

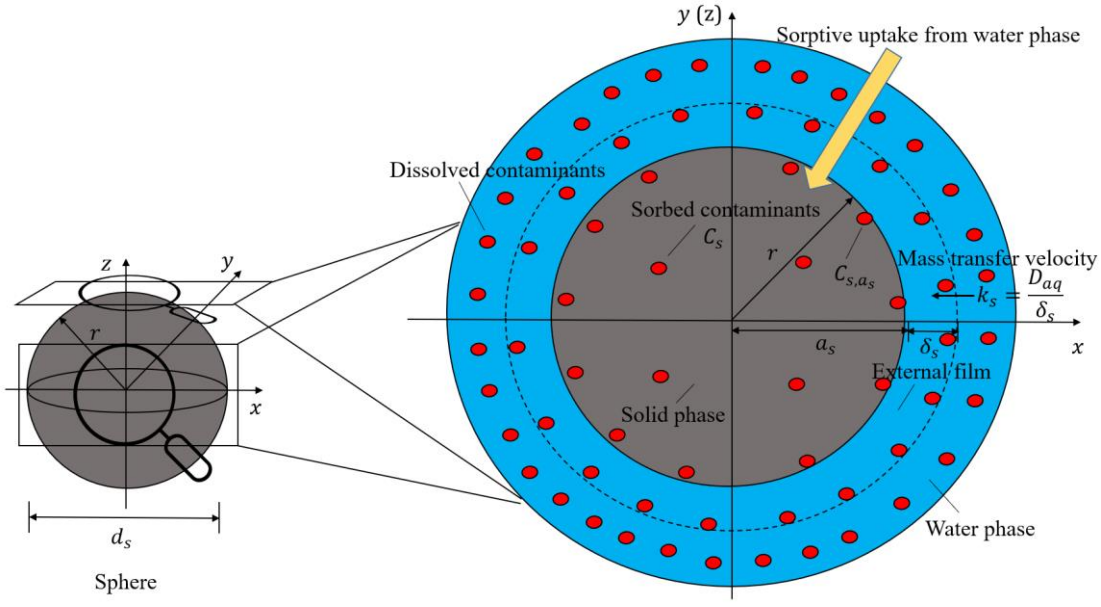

Fig. S3.4: Scheme of mass transfer limited by coupled film intraparticle solid diffusion in spheres.

Intraparticle solid diffusion. Spherical diffusion models (see. Fig. S3.4) are widely used in simulating mass transfer of sorbates (e.g., organic pollutants) to sorbents like microplastics, tire wear particles, etc. The governing equation of intraparticle solid diffusion of spherical particle is:

$$\frac{\partial C_s}{\partial t} = D_s\left[\frac{\partial^2 C_s}{\partial r^2} + \frac{2}{r}\frac{\partial C_s}{\partial r}\right] \tag{S3.56}$$

Boundary and initial conditions are:

$$C_s(r = a_s, t) = C_{s,a_s} \tag{S3.57}$$

$$\frac{\partial C_s}{\partial r}(r = 0, t) = 0 \tag{S3.58}$$

$$C_s(r, t = 0) = C_s(0) \ \forall r \tag{S3.59}$$

where a_s [L] is the radius of solid spherical particle.

The Laplace transformation of governing equations and corresponding initial and boundary conditions can be expressed as:

$$s\tilde{C}_s - C_s(0) - D_s\left[\frac{d^2\tilde{C}_s}{dr^2} + \frac{2}{r}\frac{d\tilde{C}_s}{dr}\right] = 0 \tag{S3.60}$$

$$\tilde{C}_s(a_s) = \tilde{C}_{s,a_s} \tag{S3.61}$$

$$\left.\frac{d\tilde{C}_s}{dr}\right|_{r=0} = 0 \tag{S3.62}$$

$$\tilde{C}_s(r) = \tilde{C}_s(0) \ \forall r \tag{S3.63}$$

Equation S3.60 can be solved starting from:

$$\tilde{C}_s(r, s) \propto \frac{1}{r}\exp(r\varphi) + C \tag{S3.64}$$

where φ and C are undetermined coefficients.

$$\frac{d\tilde{C}_s}{dr} \propto -\frac{1}{r^2}\exp(r\varphi) + \frac{\varphi}{r}\exp(r\varphi) = (-\frac{1}{r} + \varphi)\frac{1}{r}\exp(r\varphi) \tag{S3.65}$$

$$\frac{d^2\tilde{C}_s}{dr^2} \propto (\frac{2}{r^2} - \frac{2\varphi}{r} + \varphi^2)\frac{1}{r}\exp(r\varphi) \tag{S3.66}$$

Inserting Eqs. S3.65, S3.66 into Eq. S3.60 yields:

$$\begin{aligned} & s\frac{1}{r}\exp(r\varphi) + sC - C_s(0) - D_s\left[\frac{2}{r^2} - \frac{2\varphi}{r} + \varphi^2 + \frac{2}{r}\left(-\frac{1}{r} + \varphi\right)\right]\frac{1}{r}\exp(r\varphi) = 0 \\ & (\mathrm{s} - \varphi^2 D_s)\frac{1}{r}\exp(r\varphi) + sC - C_s(0) = 0 \\ & \longrightarrow \begin{cases} \mathrm{s} - \varphi^2 D_s = 0 \\ sC - C_s(0) = 0 \end{cases} \longrightarrow \begin{cases} \varphi = \pm\sqrt{\dfrac{s}{D_s}} \\ C = \dfrac{C_s(0)}{s} \end{cases} \end{aligned} \tag{S3.67}$$

Then the solution of Eq. S3.60 can finally be expressed as:

$$\tilde{C}_s(r,s) = \frac{A}{r}\exp\left(r\sqrt{\frac{s}{D_s}}\right) + \frac{B}{r}\exp\left(-r\sqrt{\frac{s}{D_s}}\right) + \frac{C_s(0)}{s} \tag{S3.68}$$

where A and B are undetermined coefficients, which can be determined via the boundary conditions of the governing equation (Eq. S3.61 and Eq. S3.62):

$$\begin{aligned} \frac{d\tilde{C}_s}{dr} = {} & A\left[-\frac{1}{r^2}\exp\left(r\sqrt{\frac{s}{D_s}}\right) + \frac{1}{r}\sqrt{\frac{s}{D_s}}\exp\left(r\sqrt{\frac{s}{D_s}}\right)\right] \\ & + B\left[-\frac{1}{r^2}\exp\left(-r\sqrt{\frac{s}{D_s}}\right) - \frac{1}{r}\sqrt{\frac{s}{D_s}}\exp\left(-r\sqrt{\frac{s}{D_s}}\right)\right] \\ = {} & A\left(-\frac{1}{r^2} + \frac{1}{r}\sqrt{\frac{s}{D_s}}\right)\exp\left(r\sqrt{\frac{s}{D_s}}\right) \\ & + B\left(-\frac{1}{r^2} - \frac{1}{r}\sqrt{\frac{s}{D_s}}\right)\exp\left(-r\sqrt{\frac{s}{D_s}}\right) \end{aligned} \tag{S3.69}$$

The exponential function can be approximated by using an infinite number of terms of its Taylor series:

$$e^x = \exp(x) = \sum_{n=0}^{\infty}\frac{x^n}{n!} = 1 + x + \frac{x^2}{2!} + \frac{x^3}{3!} + \cdots \tag{S3.70}$$

$\exp\left(r\sqrt{\frac{s}{D_s}}\right)$ and $\exp\left(-r\sqrt{\frac{s}{D_s}}\right)$ in Eq. S3.69 can be approximated as:

$$\exp\left(r\sqrt{\frac{s}{D_s}}\right) \approx 1 + r\sqrt{\frac{s}{D_s}}$$
$$\exp\left(-r\sqrt{\frac{s}{D_s}}\right) \approx 1 - r\sqrt{\frac{s}{D_s}} \tag{S3.71}$$

Inserting Eq. S3.71 into Eq. S3.69 gives:

$$\begin{aligned}\frac{d\tilde{C}_s}{dr} &= A\left(-\frac{1}{r^2}+\frac{1}{r}\sqrt{\frac{s}{D_s}}\right)\left(1+r\sqrt{\frac{s}{D_s}}\right)+B\left(-\frac{1}{r^2}-\frac{1}{r}\sqrt{\frac{s}{D_s}}\right)\left(1-r\sqrt{\frac{s}{D_s}}\right)\\ &= (A+B)\left(-\frac{1}{r^2}+\frac{s}{D_s}\right)\end{aligned} \tag{S3.72}$$

The internal boundary condition (Eq. S3.62) shows that the $d\tilde{C}_s/dr$ approaches 0 when r approaches 0:

$$\left.\frac{d\tilde{C}_s}{dr}\right|_{r=0} = \lim_{r\to 0}(A+B)\left(-\frac{1}{r^2}+\frac{s}{D_s}\right) = 0 \tag{S3.73}$$
$$\Longrightarrow \quad A = -B$$

Then Eq. S3.68 can be rearranged as:

$$\begin{aligned}\tilde{C}_s(r,s) &= \frac{A}{r}\exp\left(r\sqrt{\frac{s}{D_s}}\right)-\frac{A}{r}\exp\left(-r\sqrt{\frac{s}{D_s}}\right)+\frac{C_s(0)}{s}\\ \tilde{C}_s(r,s) &= \frac{2A}{r}\left[\frac{1}{2}\exp\left(r\sqrt{\frac{s}{D_s}}\right)-\frac{1}{2}\exp\left(-r\sqrt{\frac{s}{D_s}}\right)\right]+\frac{C_s(0)}{s}\\ \tilde{C}_s(r,s) &= \frac{2A}{r}\sinh\left(r\sqrt{\frac{s}{D_s}}\right)+\frac{C_s(0)}{s}\end{aligned} \tag{S3.74}$$

Based on the external boundary condition (Eq. S3.61), the unknown coefficient $2A$ can be determined:

$$\begin{aligned}\tilde{C}_s(a_s,s) &= \frac{2A}{a_s}\sinh\left(a_s\sqrt{\frac{s}{D_s}}\right)+\frac{C_s(0)}{s} = \tilde{C}_{s,a_s}\\ 2A &= \frac{\left(\tilde{C}_{s,a_s}-\frac{C_s(0)}{s}\right)a_s}{\sinh\left(a_s\sqrt{\frac{s}{D_s}}\right)}\end{aligned} \tag{S3.75}$$

Thus, the analytical solution of Eq. S3.60 in Laplace domain can be expressed as:

$$\tilde{C}_s(r,s) = \frac{a_s}{r}\frac{\sinh\left(r\sqrt{\frac{s}{D_s}}\right)}{\sinh\left(a_s\sqrt{\frac{s}{D_s}}\right)}\left(\tilde{C}_{s,a_s}-\frac{C_s(0)}{s}\right)+\frac{C_s(0)}{s} \tag{S3.76}$$

Film diffusion. If we assume the solute mass release (or uptake) from the surface of the

solid spherical particles into the bulk solution is additionally driven by diffusion through the external boundary layer (δ_s), the continuity of the mass flux density (F [M L^{-2} T^{-1}]) also can be expressed by Eq. S3.45.

$\left.\frac{d\tilde{C}_s}{dr}\right|_{r=a_s}$ in Eq. S3.46 can be calculated via Eq. S3.76:

$$\begin{aligned}\left.\frac{d\tilde{C}_s}{dr}\right|_{r=a_s} &= \left(\frac{a_s}{r}\sqrt{\frac{s}{D_s}}\frac{\cosh\left(r\sqrt{\frac{s}{D_s}}\right)}{\sinh\left(a_s\sqrt{\frac{s}{D_s}}\right)} - \frac{a_s}{r^2}\frac{\sinh\left(r\sqrt{\frac{s}{D_s}}\right)}{\sinh\left(a_s\sqrt{\frac{s}{D_s}}\right)}\right)\left(\tilde{C}_{s,a_s} - \frac{C_s(0)}{s}\right)\Bigg|_{r=a_s} \\ &= \left(\sqrt{\frac{s}{D_s}}\coth\left(a_s\sqrt{\frac{s}{D_s}}\right) - \frac{1}{a_s}\right)\left(\tilde{C}_{s,a_s} - \frac{C_s(0)}{s}\right)\end{aligned} \tag{S3.77}$$

Rearranging Eq. S3.46 with Eq. S3.77 gives the expression of $\tilde{C}_{s,a_s}$:

$$\begin{aligned}k_s\left(\frac{\tilde{C}_{s,a_s}}{K_d} - \tilde{C}_w\right) &= -D_s\rho_s\left(\sqrt{\frac{s}{D_s}}\coth\left(a_s\sqrt{\frac{s}{D_s}}\right) - \frac{1}{a_s}\right)\left(\tilde{C}_{s,a_s} - \frac{C_s(0)}{s}\right) \\ \left[\frac{k_s}{K_d} + D_s\rho_s\left(\sqrt{\frac{s}{D_s}}\coth\left(a_s\sqrt{\frac{s}{D_s}}\right) - \frac{1}{a_s}\right)\right]\tilde{C}_{s,a_s} &= D_s\rho_s\left(\sqrt{\frac{s}{D_s}}\coth\left(a_s\sqrt{\frac{s}{D_s}}\right) - \frac{1}{a_s}\right)\frac{C_s(0)}{s} + k_s\tilde{C}_w \\ \tilde{C}_{s,a_s} &= \frac{D_s\rho_s\left(\sqrt{\frac{s}{D_s}}\coth\left(a_s\sqrt{\frac{s}{D_s}}\right) - \frac{1}{a_s}\right)\frac{C_s(0)}{s} + k_s\tilde{C}_w}{\frac{k_s}{K_d} + D_s\rho_s\left(\sqrt{\frac{s}{D_s}}\coth\left(a_s\sqrt{\frac{s}{D_s}}\right) - \frac{1}{a_s}\right)}\end{aligned} \tag{S3.78}$$

The solute concentration change in solid spherical particles is given by:

$$\frac{\partial C_s}{\partial t} = -F\,A^o = k_s\frac{3}{a_s\rho_s}\left(C_w(t) - \frac{C_s(r=a_s,t)}{K_d}\right) \tag{S3.79}$$

Next, the Laplace transformation of Eq. S3.79 is used:

$$s\tilde{C}_s - C_s(0) = k_s\frac{3}{a_s\rho_s}\left(\tilde{C}_w - \frac{\tilde{C}_{s,a_s}}{K_d}\right) \tag{S3.80}$$

Inserting Eq. S3.78 into Eq. S3.80 and rearranging terms finally yields the Laplace transform solution for coupled film-intraparticle solid diffusion of spherical particle:

$$\begin{aligned}\tilde{C}_s &= \tilde{g}_s\left(\tilde{C}_w - \frac{C_s(0)}{K_d s}\right) + \frac{C_s(0)}{s} \\ \text{with } \tilde{g}_s &= \frac{D_s K_d\left(\sqrt{\frac{s}{D_s}}\coth\left(a_s\sqrt{\frac{s}{D_s}}\right) - \frac{1}{a_s}\right)}{k_s + D_s\rho_s K_d\left(\sqrt{\frac{s}{D_s}}\coth\left(a_s\sqrt{\frac{s}{D_s}}\right) - \frac{1}{a_s}\right)}\frac{3k_s}{a_s s}\end{aligned} \tag{S3.81}$$

Two limiting cases may be considered:

1. $\lim\ k_s \to \infty$: This describes the case where the external mass transfer resistance vanishes. The denominator in Eq. S3.81 in this case simplifies to $\lim_{k_s\to\infty}\left(k_s + D_s\rho_s K_d\left(\sqrt{\frac{s}{D_s}}\coth\left(a_s\sqrt{\frac{s}{D_s}}\right)-\frac{1}{a_s}\right)\right) = k_s$, which leads to:

$$\begin{aligned}\tilde{C}_s &= \tilde{g}_s\left(\tilde{C}_w - \frac{C_s(0)}{K_d s}\right) + \frac{C_s(0)}{s}\\ \text{with}\ \ \tilde{g}_s &= D_s K_d\left(\sqrt{\frac{s}{D_s}}\coth\left(a_s\sqrt{\frac{s}{D_s}}\right)-\frac{1}{a_s}\right)\frac{3}{a_s s}\end{aligned} \tag{S3.82}$$

2. $\lim D_s \to \infty$: This describes the case of a sphere with a uniform concentration distribution (well mixed interior), where only the external boundary layer controls mass transfer. To obtain the solution for this case, we need to consider the limit of coth(x) for arguments approaching 0. The Taylor series expansion shows that coth(x) can be approximated with:

$$\lim_{x\to 0}\coth(x)\ \approx \frac{1}{x}+\frac{x}{3} \tag{S3.83}$$

Using Eq. S3.83 to determine the limit of $\lim_{D_s\to\infty}\left(D_s K_d\left(\sqrt{\frac{s}{D_s}}\coth\left(a_s\sqrt{\frac{s}{D_s}}\right)-\frac{1}{a_s}\right)\right)$ yields:

$$\begin{aligned}&\lim_{D_s\to\infty}\coth\left(a_s\sqrt{\frac{s}{D_s}}\right) \approx \frac{1}{a_s\sqrt{\frac{s}{D_s}}}+\frac{a_s\sqrt{\frac{s}{D_s}}}{3}\\ &\lim_{D_s\to\infty} D_s K_d\left(\sqrt{\frac{s}{D_s}}\coth\left(a_s\sqrt{\frac{s}{D_s}}\right)-\frac{1}{a_s}\right)\\ &= \lim_{D_s\to\infty}\left(K_d\left(\sqrt{D_s s}\left(\frac{1}{a_s\sqrt{\frac{s}{D_s}}}+\frac{a_s\sqrt{\frac{s}{D_s}}}{3}\right)-\frac{D_s}{a_s}\right)\right)\\ &= \frac{1}{3}K_d a_s s\end{aligned} \tag{S3.84}$$

This finally leads to:

$$\begin{aligned}\tilde{C}_s &= \tilde{g}_s\left(\tilde{C}_w - \frac{C_s(0)}{K_d s}\right) + \frac{C_s(0)}{s}\\ \lim_{D_s\to\infty}\tilde{g}_s &= \frac{k_s K_d}{k_s + \frac{1}{3}\rho_s K_d a_s s}\end{aligned} \tag{S3.85}$$

S3.6 Semi-analytical Laplace solution for coupled film-intraparticle pore diffusion in a plane sheet (e.g., porous membrane)

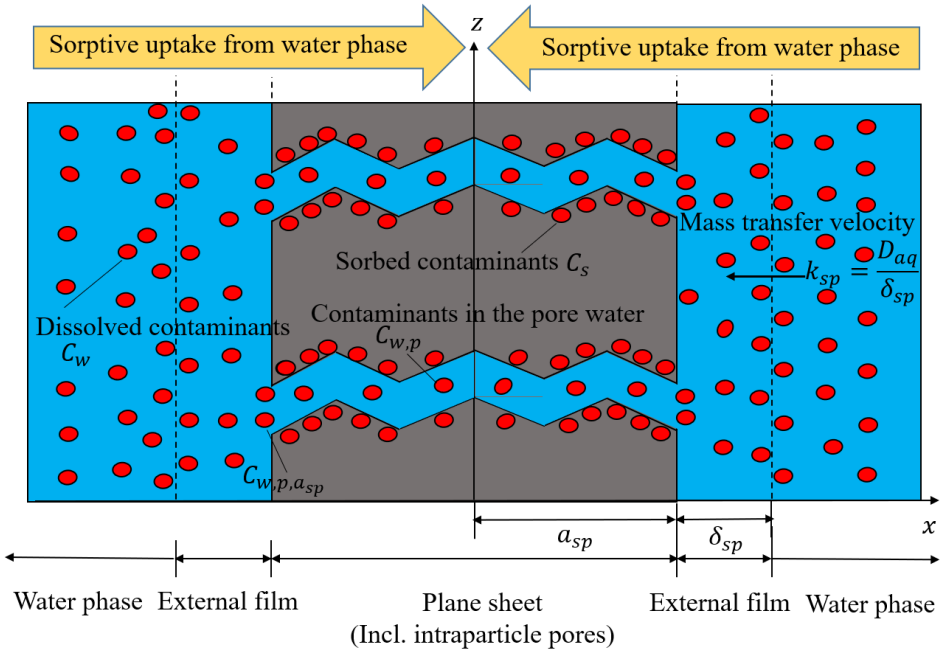

Fig. S3.5: Scheme of mass transfer limited by coupled film intraparticle pore diffusion in a plane sheet geometry.

Pore diffusion. Considering the solute mass stored inside the intraparticle pore space of plane sheet (see Fig. S3.5), the governing equation of intraparticle pore diffusion can be denoted as:

$$\frac{\partial}{\partial t}(\varepsilon\, C_{w,p} + \rho_p C_s) = D_e \frac{\partial^2 C_s}{\partial x^2} \tag{S3.86}$$

Boundary and initial conditions are:

$$C_{w,p}(x = a_{sp}, t) = C_{w,p,a_{sp}} \tag{S3.87}$$

$$\frac{\partial C_{w,p}}{\partial x}(x = 0, t) = 0 \tag{S3.88}$$

$$C_{w,p}(x, t = 0) = C_{w,p}(0) \ \forall x \tag{S3.89}$$

where a_{sp} [L] is the half of the thickness of porous plane sheet; $C_{w,p}$ [M L^{-3}] is the solute concentration in the intraparticle pore water; $C_{w,p,a_{sp}}$ [M L^{-3}] is the solute concentration at the solid/water boundary; $C_{w,p}(0)$ [M L^{-3}] is the initial solute concentration in the intraparticle pore water; D_e [L^2 T^{-1}], ε [-] and ρ_p [M L^{-3}] denote the effective diffusion coefficient in the porous particle, the intra-particle porosity, and the bulk density of the particle ($= \rho_s(1 - \varepsilon)$). C_s [M M^{-1}], the solute concentration in the solid phase, is related to the aqueous concentration by the distribution coefficient K_d, i.e. $C_s = K_d\, C_{w,p}$. Eq. S3.86 thus simplifies to:

$$\frac{\partial C_{w,p}}{\partial t} = D_a \frac{\partial^2 C_{w.p}}{\partial x^2} \tag{S3.90}$$

where D_a [L^2 T^{-1}] is the apparent diffusion coefficient:

$$D_a = \frac{D_e}{\varepsilon + K_d \rho_p} = \frac{D_{aq}\varepsilon}{\tau_f(\varepsilon + K_d \rho_p)} \approx \frac{D_{aq}\varepsilon^2}{\varepsilon + K_d \rho_p} \tag{S3.91}$$

τ_f [-] is the tortuosity factor and D_{aq} [L^2 T^{-1}] denotes the solute diffusion coefficient in water. Previous research showed that D_e increases approximately with the square of the intraparticle porosity (Boving and Grathwohl, 2001); thus, the tortuosity factor τ_f [-] for diffusion in intra-granular pores may be approximated via the reciprocal of the intra-granular porosity ($\tau_f \approx 1/\varepsilon$).

The Laplace transformation of governing equations and corresponding initial and boundary conditions can be expressed as:

$$s\tilde{C}_{w,p} - C_{w,p}(0) - D_a \frac{d^2 \tilde{C}_{w,p}}{dx^2} = 0 \tag{S3.92}$$

$$\tilde{C}_{w,p}(a_{sp}) = \tilde{C}_{w,p,a_{sp}} \tag{S3.93}$$

$$\left.\frac{d\tilde{C}_{w,p}}{dx}\right|_{x=0} = 0 \tag{S3.94}$$

$$\tilde{C}_{w,p}(x) = \tilde{C}_{w,p}(0) \ \forall x \tag{S3.95}$$

Similar to solid diffusion in plane sheet (see section S3.3) this can be applied for pore diffusion, thus, the analytical solution of Eq. S3.92 in Laplace domain can be expressed as:

$$\tilde{C}_{w,p}(x,s) = \frac{\cosh\left(x\sqrt{\frac{s}{D_a}}\right)}{\cosh\left(a_{sp}\sqrt{\frac{s}{D_a}}\right)}\left(\tilde{C}_{w,p,a_{sp}} - \frac{C_{w,p}(0)}{s}\right) + \frac{C_{w,p}(0)}{s} \tag{S3.96}$$

Film diffusion. Assuming the solute mass release (or uptake) from the surface of the porous plane sheet into the bulk solution is additionally driven by diffusion through the external boundary layer (δ_{sp}) which does not store any solute mass, the continuity of the mass flux density (F [M L^{-2} T^{-1}]) requires:

$$F = k_{sp}\left(C_{w,p}(x = a_{sp}, t) - C_w(t)\right) = -D_e \frac{\partial C_{w,p}}{\partial x}\bigg|_{x=a_{sp}} \tag{S3.97}$$

where k_{sp} [L T^{-1}] denotes the mass transfer velocity of porous materials.

The Laplace transformation of the mass flux density can be expressed as:

$$\tilde{F} = k_{sp}\left(\tilde{C}_{w,p,a_{sp}} - \tilde{C}_w\right) = -D_e \frac{d\tilde{C}_{w,p}}{dx}\bigg|_{x=a_{sp}} \tag{S3.98}$$

$\frac{d\tilde{C}_{w,p}}{dx}\Big|_{x=a_{sp}}$ in Eq. S3.98 can be calculated via Eq. S3.96 and is:

$$\begin{aligned}\frac{d\tilde{C}_{w,p}}{dx}\bigg|_{x=a_{sp}} &= \frac{\sqrt{\frac{s}{D_a}}\sinh\left(x\sqrt{\frac{s}{D_a}}\right)}{\cosh\left(a_{sp}\sqrt{\frac{s}{D_a}}\right)}\left(\tilde{C}_{w,p,a_{sp}} - \frac{C_{w,p}(0)}{s}\right)\bigg|_{x=a_{sp}} \\ &= \sqrt{\frac{s}{D_a}}\tanh\left(a_{sp}\sqrt{\frac{s}{D_a}}\right)\left(\tilde{C}_{w,p,a_{sp}} - \frac{C_{w,p}(0)}{s}\right)\end{aligned} \tag{S3.99}$$

Rearranging Eq. S3.98 with Eq. S3.99 allows to express $\tilde{C}_{w,p,a_{sp}}$:

$$\begin{aligned}&k_{sp}\left(\tilde{C}_{w,p,a_{sp}} - \tilde{C}_w\right) = -D_e\sqrt{\frac{s}{D_a}}\tanh\left(a_{sp}\sqrt{\frac{s}{D_a}}\right)\left(\tilde{C}_{w,p,a_{sp}} - \frac{C_{w,p}(0)}{s}\right) \\ &\left[k_{sp} + D_e\sqrt{\frac{s}{D_a}}\tanh\left(a_{sp}\sqrt{\frac{s}{D_a}}\right)\right]\tilde{C}_{w,p,a_{sp}} \\ &\qquad = D_e\sqrt{\frac{s}{D_a}}\tanh\left(a_{sp}\sqrt{\frac{s}{D_a}}\right)\frac{C_{w,p}(0)}{s} + k_{sp}\tilde{C}_w \\ &\tilde{C}_{w,p,a_{sp}} = \frac{D_e\sqrt{\frac{s}{D_a}}\tanh\left(a_{sp}\sqrt{\frac{s}{D_a}}\right)\frac{C_{w,p}(0)}{s} + k_{sp}\tilde{C}_w}{\left[k_{sp} + D_e\sqrt{\frac{s}{D_a}}\tanh\left(a_{sp}\sqrt{\frac{s}{D_a}}\right)\right]}\end{aligned} \tag{S3.100}$$

The solute concentration change in porous materials is given by:

$$\begin{aligned}\left(\varepsilon+\rho_p K_d\right)\frac{\partial C_{w,p}}{\partial t} &= -F\,A^o = k_{sp}\frac{1}{a_{sp}}\left(C_w(t)-C_{w,p}\left(x=a_{sp},t\right)\right)\\ \frac{\partial C_{w,p}}{\partial t} &= k_{sp}\frac{1}{a_{sp}\left(\varepsilon+\rho_p K_d\right)}\left(C_w(t)-C_{w,p}\left(x=a_{sp},t\right)\right)\end{aligned} \tag{S3.101}$$

Next, the Laplace transformation of Eq. S3.101 is used.

$$s\tilde{C}_{w,p}-C_{w,p}(0)=k_{sp}\frac{1}{a_{sp}\left(\varepsilon+\rho_p K_d\right)}\left(\tilde{C}_w-\tilde{C}_{w,p,a_{sp}}\right) \tag{S3.102}$$

Inserting Eq. S3.100 into Eq. S3.102 and rearranging terms finally yields the Laplace transform solution for coupled film-intraparticle pore diffusion of plane sheet:

$$\begin{aligned}\tilde{C}_{w,p} &= \tilde{g}_{sp}\left(\tilde{C}_w-\frac{C_{w,p}(0)}{s}\right)+\frac{C_{w,p}(0)}{s}\\ \text{with }\ \tilde{g}_{sp} &= \frac{\sqrt{D_a s}\tanh\left(a_{sp}\sqrt{\frac{s}{D_a}}\right)}{k_{sp}+\sqrt{D_a s}\rho_p K_{d,b}\tanh\left(a_{sp}\sqrt{\frac{s}{D_a}}\right)}\frac{k_{sp}}{a_{sp}s}\end{aligned} \tag{S3.103}$$

The term $K_{d,b}$ denotes the bulk distribution coefficient between bulk water and porous materials ($= K_d + \varepsilon/\rho_p$), which also accounts for the solute mass stored in the intraparticle pore space.

Two limiting cases may be considered:

1. $\lim\ k_{sp}\to\infty$: This describes the case where external mass transfer resistance vanishes. The denominator in Eq. S3.103 in this case simplifies to $\lim_{k_{sp}\to\infty}\left(k_{sp}+\sqrt{D_a s}\rho_p K_{d,b}\tanh\left(a_{sp}\sqrt{\frac{s}{D_a}}\right)\right)=k_{sp}$, which leads to:

$$\begin{aligned}\tilde{C}_{w,p} &= \tilde{g}_{sp}\left(\tilde{C}_w-\frac{C_{w,p}(0)}{s}\right)+\frac{C_{w,p}(0)}{s}\\ \text{with }\ \tilde{g}_{sp} &= \sqrt{D_a s}\tanh\left(a_{sp}\sqrt{\frac{s}{D_a}}\right)\frac{1}{a_{sp}s}\end{aligned} \tag{S3.104}$$

2. $\lim D_a\to\infty$: This describes the case of a plane sheet with a uniform concentration distribution (well mixed interior), where only the external boundary layer controls mass transfer. To obtain the solution for this case, we need to consider the limit of tanh(x) for arguments approaching 0. Using Eq. S3.27 to determine the limit of $\lim_{D_a\to\infty}\left(\sqrt{D_a s}\tanh\left(a_{sp}\sqrt{\frac{s}{D_a}}\right)\right)$ yields:

$$\lim_{D_a\to\infty} \tanh\left(a_{sp}\sqrt{\frac{s}{D_a}}\right) \approx a_{sp}\sqrt{\frac{s}{D_a}}$$

$$\lim_{D_a\to\infty} \sqrt{D_a s}\tanh\left(a_{sp}\sqrt{\frac{s}{D_a}}\right) \tag{S3.105}$$

$$= \lim_{D_a\to\infty} \sqrt{D_a s}\, a_{sp}\sqrt{\frac{s}{D_a}}$$

$$= a_{sp}s$$

This finally leads to:

$$\tilde{C}_{w,p} = \tilde{g}_{sp}\left(\tilde{C}_w - \frac{C_{w,p}(0)}{s}\right) + \frac{C_{w,p}(0)}{s}$$

$$\lim_{D_a\to\infty} \tilde{g}_{sp} = \frac{a_{sp}s}{k_{sp} + \rho_p K_{d,b} a_{sp} s}\frac{k_{sp}}{a_{sp}s} \tag{S3.106}$$

$$= \frac{k_{sp}}{k_{sp} + \rho_p K_{d,b} a_{sp} s}$$

S3.7 Semi-analytical Laplace solution for coupled film-intraparticle pore diffusion in a cylinder

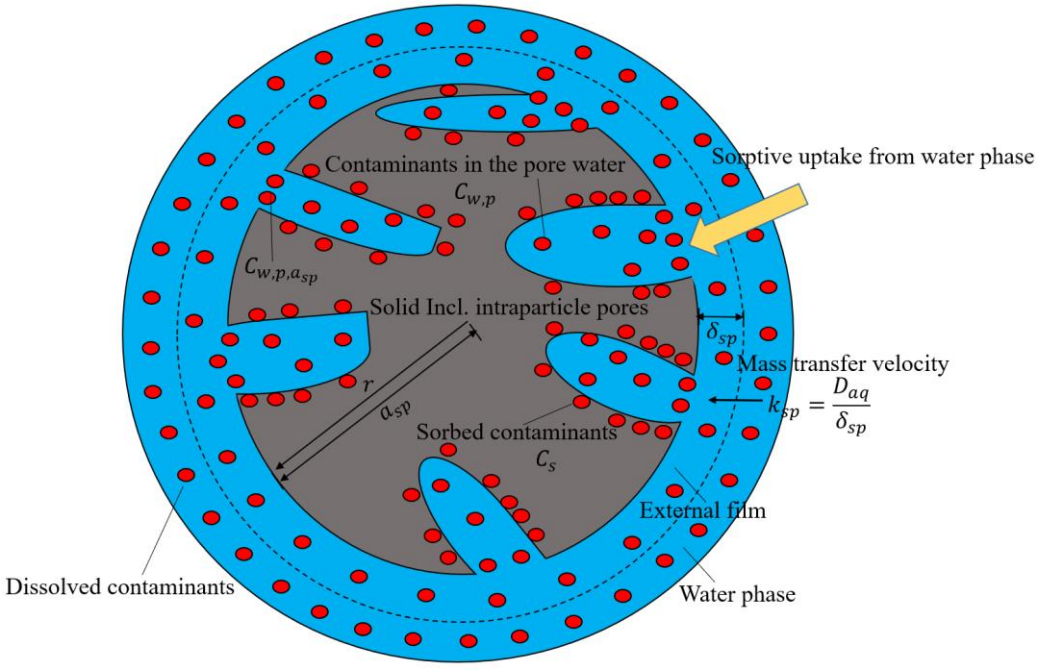

Fig. S3.6: Scheme of mass transfer limited by coupled film intraparticle pore diffusion in cylinders.

Intraparticle pore diffusion. Considering the diffusion in a long circular cylinder with

intraparticle pores in which diffusion only occurs in radial direction (see Fig. S3.6). According to Crank (1975), the governing equation of the intraparticle pore diffusion follows Fick's second law:

$$\frac{\partial C_{w,p}}{\partial t} = D_a \left[\frac{\partial^2 C_{w,p}}{\partial r^2} + \frac{1}{r} \frac{\partial C_{w,p}}{\partial r} \right] \tag{S3.107}$$

Boundary and initial conditions are:

$$C_{w,p}(r = a_{sp}, t) = C_{w,p,a_{sp}} \tag{S3.108}$$

$$\frac{\partial C_{w,p}}{\partial r}(r = 0, t) = 0 \tag{S3.109}$$

$$C_{w,p}(r, t = 0) = C_{w,p}(0) \ \forall r \tag{S3.110}$$

where a_{sp} [L] denotes the radius of porous cylindrical particle.

The Laplace transformation of governing equations and initial conditions (Eqs. S3.107-S3.110) can be expressed as:

$$s\tilde{C}_{w,p} - C_{w,p}(0) - D_a \left[\frac{d^2 \tilde{C}_{w,p}}{dr^2} + \frac{1}{r} \frac{d\tilde{C}_{w,p}}{dr} \right] = 0 \tag{S3.111}$$

$$\tilde{C}_{w,p}(a_{sp}) = \tilde{C}_{w,p,a_{sp}} \tag{S3.112}$$

$$\left. \frac{d\tilde{C}_{w,p}}{dr} \right|_{r=0} = 0 \tag{S3.113}$$

$$\tilde{C}_{w,p}(r) = \tilde{C}_{w,p}(0) \ \forall r \tag{S3.114}$$

Analytical solution of Eq. S3.111 can be expressed as (the derivation process can refer to the case of intraparticle solid diffusion present in section S3.4):

$$\tilde{C}_{w,p}(r, s) = \frac{I_0 \left(r \sqrt{\frac{s}{D_a}} \right)}{I_0 \left(a_{sp} \sqrt{\frac{s}{D_a}} \right)} \left(\tilde{C}_{w,p,a_{sp}} - \frac{C_{w,p}(0)}{s} \right) + \frac{C_{w,p}(0)}{s} \tag{S3.115}$$

Film diffusion. Considering the solute mass release (or uptake) from the surface of the porous cylindrical particle into the bulk water phase is additionally driven by diffusion through the external boundary layer (δ_{sp}) which does not store any solute mass, the

continuity of the mass flux density (F [M L^{-2} T^{-1}]) requires:

$$F = k_{sp}\left(C_{w,p}\left(r = a_{sp}, t\right) - C_w(t)\right) = -D_e \left.\frac{\partial C_{w,p}}{\partial r}\right|_{r=a_{sp}} \tag{S3.116}$$

Laplace transformation of mass flux density can be expressed as:

$$\tilde{F} = k_{sp}\left(\tilde{C}_{w,p,a_{sp}} - \tilde{C}_w\right) = -D_e \left.\frac{d\tilde{C}_{w,p}}{dr}\right|_{r=a_{sp}} \tag{S3.117}$$

$\left.\frac{d\tilde{C}_{w,p}}{dr}\right|_{r=a_{sp}}$ in Eq. S3.117 can be calculated via Eq. S3.115:

$$\begin{aligned}\left.\frac{d\tilde{C}_{w,p}}{dr}\right|_{r=a_{sp}} &= \left.\frac{\sqrt{\frac{s}{D_a}} I_1\left(r\sqrt{\frac{s}{D_a}}\right)}{I_0\left(a_{sp}\sqrt{\frac{s}{D_a}}\right)}\left(\tilde{C}_{w,p,a_{sp}} - \frac{C_{w,p}(0)}{s}\right)\right|_{r=a_{sp}} \\ &= \sqrt{\frac{s}{D_a}}\frac{I_1\left(a_{sp}\sqrt{\frac{s}{D_a}}\right)}{I_0\left(a_{sp}\sqrt{\frac{s}{D_a}}\right)}\left(\tilde{C}_{w,p,a_{sp}} - \frac{C_{w,p}(0)}{s}\right)\end{aligned} \tag{S3.118}$$

Rearranging Eq. S3.117 with Eq. S3.118 gives the expression of $\tilde{C}_{w,p,a_{sp}}$:

$$\begin{aligned}&k_{sp}\left(\tilde{C}_{w,p,a_{sp}} - \tilde{C}_w\right) = -D_e\sqrt{\frac{s}{D_a}}\frac{I_1\left(a_{sp}\sqrt{\frac{s}{D_a}}\right)}{I_0\left(a_{sp}\sqrt{\frac{s}{D_a}}\right)}\left(\tilde{C}_{w,p,a_{sp}} - \frac{C_{w,p}(0)}{s}\right) \\ &\left[k_{sp} + D_e\sqrt{\frac{s}{D_a}}\frac{I_1\left(a_{sp}\sqrt{\frac{s}{D_a}}\right)}{I_0\left(a_{sp}\sqrt{\frac{s}{D_a}}\right)}\right]\tilde{C}_{w,p,a_{sp}} = D_e\sqrt{\frac{s}{D_a}}\frac{I_1\left(a_{sp}\sqrt{\frac{s}{D_a}}\right)}{I_0\left(a_{sp}\sqrt{\frac{s}{D_a}}\right)}\frac{C_{w,p}(0)}{s} + k_{sp}\tilde{C}_w \\ &\tilde{C}_{w,p,a_{sp}} = \frac{D_e\sqrt{\frac{s}{D_a}}\frac{I_1\left(a_{sp}\sqrt{\frac{s}{D_a}}\right)}{I_0\left(a_{sp}\sqrt{\frac{s}{D_a}}\right)}\frac{C_{w,p}(0)}{s} + k_{sp}\tilde{C}_w}{\left[k_{sp} + D_e\sqrt{\frac{s}{D_a}}\frac{I_1\left(a_{sp}\sqrt{\frac{s}{D_a}}\right)}{I_0\left(a_{sp}\sqrt{\frac{s}{D_a}}\right)}\right]}\end{aligned} \tag{S3.119}$$

The surface to volume ratio of a cylinder is twice as much as the case of plane sheet and the solute concentration change in cylindrical porous materials is given by:

$$\begin{aligned}\left(\varepsilon + \rho_p K_d\right)\frac{\partial C_{w,p}}{\partial t} &= -F\,A^o = k_{sp}\frac{2}{a_{sp}}\left(C_w(t) - C_{w,p}\left(r = a_{sp}, t\right)\right) \\ \frac{\partial C_{w,p}}{\partial t} &= k_{sp}\frac{2}{a_{sp}\left(\varepsilon + \rho_p K_d\right)}\left(C_w(t) - C_{w,p}\left(r = a_{sp}, t\right)\right)\end{aligned} \tag{S3.120}$$

Next, the Laplace transformation of Eq. S3.120 is used:

$$s\tilde{C}_{w,p} - C_{w,p}(0) = k_{sp}\frac{2}{a_{sp}(\varepsilon + \rho_p K_d)}\left(\tilde{C}_w - \tilde{C}_{w,p,a_{sp}}\right) \tag{S3.121}$$

Inserting Eq. S3.119 into Eq. S3.121 and rearranging terms finally yields the Laplace transform solution for coupled film-intraparticle pore diffusion of cylinder:

$$\begin{aligned} \tilde{C}_{w,p} &= \tilde{g}_{sp}\left(\tilde{C}_w - \frac{C_{w,p}(0)}{s}\right) + \frac{C_{w,p}(0)}{s} \\ \text{with } \tilde{g}_{sp} &= \frac{\sqrt{D_a s}\dfrac{I_1\left(a_{sp}\sqrt{\dfrac{s}{D_a}}\right)}{I_0\left(a_{sp}\sqrt{\dfrac{s}{D_a}}\right)}}{k_{sp} + \sqrt{D_a s}\rho_p K_{d,b}\dfrac{I_1\left(a_{sp}\sqrt{\dfrac{s}{D_a}}\right)}{I_0\left(a_{sp}\sqrt{\dfrac{s}{D_a}}\right)}}\frac{2k_{sp}}{a_{sp}s} \end{aligned} \tag{S3.122}$$

Two limiting cases may be considered:

1. $\lim\ k_{sp} \to \infty$: This describes the case where external mass transfer resistance vanishes. The denominator in Eq. S3.122 in this case simplifies to $\lim_{k_{sp}\to\infty}\left(k_{sp} + \sqrt{D_a s}\rho_p K_{d,b}\frac{I_1\left(a_{sp}\sqrt{\frac{s}{D_a}}\right)}{I_0\left(a_{sp}\sqrt{\frac{s}{D_a}}\right)}\right) = k_{sp}$, which leads to:

$$\begin{aligned} \tilde{C}_{w,p} &= \tilde{g}_{sp}\left(\tilde{C}_w - \frac{C_{w,p}(0)}{s}\right) + \frac{C_{w,p}(0)}{s} \\ \text{with } \tilde{g}_{sp} &= \sqrt{D_a s}\frac{I_1\left(a_{sp}\sqrt{\dfrac{s}{D_a}}\right)}{I_0\left(a_{sp}\sqrt{\dfrac{s}{D_a}}\right)}\frac{2}{a_{sp}s} \end{aligned} \tag{S3.123}$$

2. $\lim\ D_a \to \infty$: This describes the case of a cylindrical particle with a uniform concentration distribution (well mixed interior), where only the external boundary layer controls mass transfer. Using Eq. S3.53 to determine the limit of $\lim_{D_a\to\infty}\left(\sqrt{D_a s}\frac{I_1\left(a_{sp}\sqrt{\frac{s}{D_a}}\right)}{I_0\left(a_{sp}\sqrt{\frac{s}{D_a}}\right)}\right)$ yields:

$$\lim_{D_a\to\infty}\frac{I_1\left(a_{sp}\sqrt{\frac{s}{D_a}}\right)}{I_0\left(a_{sp}\sqrt{\frac{s}{D_a}}\right)}\approx\frac{1}{2}a_{sp}\sqrt{\frac{s}{D_a}}$$

$$\lim_{D_a\to\infty}\sqrt{D_a s}\frac{I_1\left(a_{sp}\sqrt{\frac{s}{D_a}}\right)}{I_0\left(a_{sp}\sqrt{\frac{s}{D_a}}\right)} \tag{S3.124}$$

$$=\lim_{D_a\to\infty}\sqrt{D_a s}\frac{1}{2}a_{sp}\sqrt{\frac{s}{D_a}}$$

$$=\frac{1}{2}a_{sp}s$$

This finally leads to:

$$\tilde{C}_{w,p}=\tilde{g}_{sp}\left(\tilde{C}_w-\frac{C_{w,p}(0)}{s}\right)+\frac{C_{w,p}(0)}{s}$$

$$\lim_{D_a\to\infty}\tilde{g}_{sp}=\frac{\frac{1}{2}a_{sp}s}{k_{sp}+\frac{1}{2}\rho_p K_{d,b}a_{sp}s}\frac{2k_{sp}}{a_{sp}s} \tag{S3.125}$$

$$=\frac{k_{sp}}{k_{sp}+\frac{1}{2}\rho_p K_{d,b}a_{sp}s}$$

S3.8 Semi-analytical Laplace solution for coupled film-intraparticle pore diffusion in a sphere

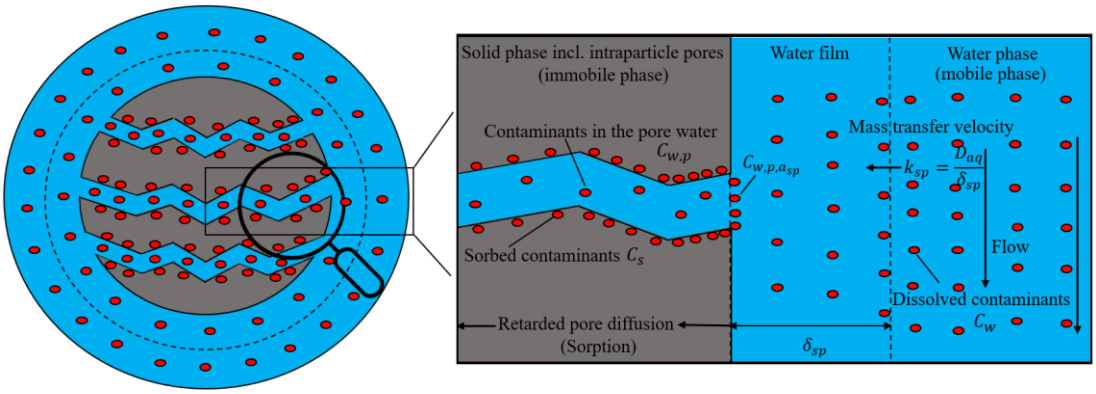

Fig. S3.7: Scheme of mass transfer limited by coupled film intraparticle pore diffusion in spheres.

Intraparticle pore diffusion. The governing equation of intraparticle pore diffusion of sphere (see Fig. S3.7) is:

$$\frac{\partial C_{w,p}}{\partial t} = D_a \left[\frac{\partial^2 C_{w,p}}{\partial r^2} + \frac{2}{r} \frac{\partial C_{w,p}}{\partial r} \right] \tag{S3.126}$$

Boundary and initial conditions are:

$$C_{w,p}(r = a_{sp}, t) = C_{w,p,a_{sp}} \tag{S3.127}$$

$$\frac{\partial C_{w,p}}{\partial r}(r = 0, t) = 0 \tag{S3.128}$$

$$C_{w,p}(r, t = 0) = C_{w,p}(0) \ \forall r \tag{S3.129}$$

where a_{sp} [L] denotes the radius of porous spherical particles.

The Laplace transformation of governing equations and initial conditions (Eqs. S3.126-S3.129) can be expressed as (more detail information of derivation was present in Liu et al. (2022)):

$$s\tilde{C}_{w,p} - C_{w,p}(0) - D_a \left[\frac{d^2 \tilde{C}_{w,p}}{dr^2} + \frac{2}{r} \frac{d\tilde{C}_{w,p}}{dr} \right] = 0 \tag{S3.130}$$

$$\tilde{C}_{w,p}(a_{sp}) = \tilde{C}_{w,p,a_{sp}} \tag{S3.131}$$

$$\left. \frac{d\tilde{C}_{w,p}}{dr} \right|_{r=0} = 0 \tag{S3.132}$$

$$\tilde{C}_{w,p}(r) = \tilde{C}_{w,p}(0) \ \forall r \tag{S3.133}$$

Analytical solution of Eq. S3.130 can be expressed as (the derivation process can refer to the case of intraparticle solid diffusion present in section S3.5):

$$\tilde{C}_{w,p}(r, s) = \frac{a_{sp}}{r} \frac{\sinh\left(r\sqrt{\frac{s}{D_a}}\right)}{\sinh\left(a_{sp}\sqrt{\frac{s}{D_a}}\right)} \left(\tilde{C}_{w,p,a_{sp}} - \frac{C_{w,p}(0)}{s} \right) + \frac{C_{w,p}(0)}{s} \tag{S3.134}$$

Film diffusion. Assuming the solute mass release (or uptake) from the surface of the porous spherical particle into the bulk water phase is additionally driven by diffusion through the external boundary layer (δ_{sp}) which does not store any solute mass, the continuity of the mass flux density ($\tilde{F}$ [M L^{-2} T^{-1}]) in Laplace domain also can be described with Eq. S3.117.

$\left.\frac{d\tilde{C}_{w,p}}{dr}\right|_{r=a_{sp}}$ in Eq. S3.117 can be calculated via Eq. S3.134, which yields:

$$\left.\frac{d\tilde{C}_{w,p}}{dr}\right|_{r=a_{sp}} = \left(\frac{a_{sp}}{r}\sqrt{\frac{s}{D_a}}\frac{\cosh\left(r\sqrt{\frac{s}{D_a}}\right)}{\sinh\left(a_{sp}\sqrt{\frac{s}{D_a}}\right)} - \frac{a_{sp}}{r^2}\frac{\sinh\left(r\sqrt{\frac{s}{D_a}}\right)}{\sinh\left(a_{sp}\sqrt{\frac{s}{D_a}}\right)}\right)\left(\tilde{C}_{w,p,a_{sp}} - \frac{C_{w,p}(0)}{s}\right)\Bigg|_{r=a_{sp}}$$
$$= \left(\sqrt{\frac{s}{D_a}}\coth\left(a_{sp}\sqrt{\frac{s}{D_a}}\right) - \frac{1}{a_{sp}}\right)\left(\tilde{C}_{w,p,a_{sp}} - \frac{C_{w,p}(0)}{s}\right) \quad \text{(S3.135)}$$

Rearranging Eq. S3.117 with Eq. S3.135 gives the expression of $\tilde{C}_{w,p,a_{sp}}$:

$$k_{sp}\left(\tilde{C}_{w,p,a_{sp}} - \tilde{C}_w\right) = -D_e\left(\sqrt{\frac{s}{D_a}}\coth\left(a_{sp}\sqrt{\frac{s}{D_a}}\right) - \frac{1}{a_{sp}}\right)\left(\tilde{C}_{w,p,a_{sp}} - \frac{C_{w,p}(0)}{s}\right)$$
$$\left[k_{sp} + D_e\left(\sqrt{\frac{s}{D_a}}\coth\left(a_{sp}\sqrt{\frac{s}{D_a}}\right) - \frac{1}{a_{sp}}\right)\right]\tilde{C}_{w,p,a_{sp}}$$
$$= D_e\left(\sqrt{\frac{s}{D_a}}\coth\left(a_{sp}\sqrt{\frac{s}{D_a}}\right) - \frac{1}{a_{sp}}\right)\frac{C_{w,p}(0)}{s} + k_{sp}\tilde{C}_w \quad \text{(S3.136)}$$
$$\tilde{C}_{w,p,a_{sp}} = \frac{D_e\left(\sqrt{\frac{s}{D_a}}\coth\left(a_{sp}\sqrt{\frac{s}{D_a}}\right) - \frac{1}{a_{sp}}\right)\frac{C_{w,p}(0)}{s} + k_{sp}\tilde{C}_w}{k_{sp} + D_e\left(\sqrt{\frac{s}{D_a}}\coth\left(a_{sp}\sqrt{\frac{s}{D_a}}\right) - \frac{1}{a_{sp}}\right)}$$

The surface to volume ratio of sphere is three times as much as the case of plane sheet and the solute concentration change in spherical porous materials is given by:

$$\left(\varepsilon + \rho_p K_d\right)\frac{\partial C_{w,p}}{\partial t} = -F\,A^o = k_{sp}\frac{3}{a_{sp}}\left(C_w(t) - C_{w,p}\left(r = a_{sp}, t\right)\right)$$
$$\frac{\partial C_{w,p}}{\partial t} = k_{sp}\frac{3}{a_{sp}\left(\varepsilon + \rho_p K_d\right)}\left(C_w(t) - C_{w,p}\left(r = a_{sp}, t\right)\right) \quad \text{(S3.137)}$$

Next, the Laplace transformation of Eq. S3.137 is used:

$$s\tilde{C}_{w,p} - C_{w,p}(0) = k_{sp}\frac{3}{a_{sp}\left(\varepsilon + \rho_p K_d\right)}\left(\tilde{C}_w - \tilde{C}_{w,p,a_{sp}}\right) \quad \text{(S3.138)}$$

Inserting Eq. S3.136 into Eq. S3.138 and rearranging terms finally yields the Laplace transform solution for coupled film-intraparticle pore diffusion of spherical particle:

$$\tilde{C}_{w,p} = \tilde{g}_{sp}\left(\tilde{C}_w - \frac{C_{w,p}(0)}{s}\right) + \frac{C_{w,p}(0)}{s}$$
$$\text{with } \tilde{g}_{sp} = \frac{D_a\left(\sqrt{\frac{s}{D_a}}\coth\left(a_{sp}\sqrt{\frac{s}{D_a}}\right) - \frac{1}{a_{sp}}\right)}{k_{sp} + D_a\rho_p K_{d,b}\left(\sqrt{\frac{s}{D_a}}\coth\left(a_{sp}\sqrt{\frac{s}{D_a}}\right) - \frac{1}{a_{sp}}\right)}\frac{3k_{sp}}{a_{sp}s} \tag{S3.139}$$

Two limiting cases may be considered:

1. $\lim\ k_{sp} \to \infty$: This describes the case where the external mass transfer resistance vanishes. The denominator in Eq. S3.139 in this case simplifies to $\lim_{k_{sp}\to\infty}\left(k_{sp} + D_a\rho_p K_{d,b}\left(\sqrt{\frac{s}{D_a}}\coth\left(a_{sp}\sqrt{\frac{s}{D_a}}\right) - \frac{1}{a_{sp}}\right)\right) = k_{sp}$, which leads to:

$$\tilde{C}_{w,p} = \tilde{g}_{sp}\left(\tilde{C}_w - \frac{C_{w,p}(0)}{s}\right) + \frac{C_{w,p}(0)}{s}$$
$$\text{with } \tilde{g}_{sp} = D_a\left(\sqrt{\frac{s}{D_a}}\coth\left(a_{sp}\sqrt{\frac{s}{D_a}}\right) - \frac{1}{a_{sp}}\right)\frac{3}{a_{sp}s} \tag{S3.140}$$

2. $\lim D_a \to \infty$: This describes the case of a sphere with a uniform concentration distribution (well mixed interior), where only the external boundary layer controls mass transfer. Using Eq. S3.85 to determine the limit of $\lim_{D_a\to\infty}\left(D_a\left(\sqrt{\frac{s}{D_a}}\coth\left(a_{sp}\sqrt{\frac{s}{D_a}}\right) - \frac{1}{a_{sp}}\right)\right)$ yields:

$$\lim_{D_a\to\infty}\coth\left(a_{sp}\sqrt{\frac{s}{D_a}}\right) \approx \frac{1}{a_{sp}\sqrt{\frac{s}{D_a}}} + \frac{a_{sp}\sqrt{\frac{s}{D_a}}}{3}$$
$$\lim_{D_a\to\infty} D_a\left(\sqrt{\frac{s}{D_a}}\coth\left(a_{sp}\sqrt{\frac{s}{D_a}}\right) - \frac{1}{a_{sp}}\right)$$
$$= \lim_{D_a\to\infty}\left(\sqrt{D_a s}\left(\frac{1}{a_{sp}\sqrt{\frac{s}{D_a}}} + \frac{a_{sp}\sqrt{\frac{s}{D_a}}}{3}\right) - \frac{D_a}{a_{sp}}\right) \tag{S3.141}$$
$$= \frac{1}{3}a_{sp}s$$

This finally leads to:

$$\tilde{C}_{w,p} = \tilde{g}_{sp}\left(\tilde{C}_w - \frac{C_{w,p}(0)}{s}\right) + \frac{C_{w,p}(0)}{s}$$
$$\lim_{D_a\to\infty}\tilde{g}_{sp} = \frac{\frac{1}{3}a_{sp}s}{k_{sp} + \frac{1}{3}\rho_p K_{d,b}a_{sp}s}\frac{3k_{sp}}{a_{sp}s} \tag{S3.142}$$
$$= \frac{k_{sp}}{k_{sp} + \frac{1}{3}\rho_p K_{d,b}a_{sp}s}$$

S3.9 Model setups for batch experiments

S3.9.1 Model setups of Phenanthrene redistribution in spherical microplastics with different sizes

In this example solid spherical microplastics (no intraparticle porosity) are modeled with the coupled film-intraparticle solid diffusion model (FIPSD) in Laplace domain. Based on the transfer function of FIPSD presented in Tab. 3.1 (main text), Phenanthrene concentrations in bulk water phase ($\tilde{C}_w$) and in microplastics ($\tilde{C}_{PE1}$, $\tilde{C}_{PE2}$ and $\tilde{C}_{PE3}$) in Laplace domain of the three batch tests A-C are for

batch test A:

$$\begin{aligned}
\tilde{g}_{PE1} &= \frac{D_{PE}K_{PE}\left(\sqrt{\frac{s}{D_{PE}}}\coth\left(a_{PE1}\sqrt{\frac{s}{D_{PE}}}\right)-\frac{1}{a_{PE1}}\right)}{\frac{D_{aq}Sh_{PE1}}{2a_{PE1}}+D_{PE}\rho_{PE}K_{PE}\left(\sqrt{\frac{s}{D_{PE}}}\coth\left(a_{PE1}\sqrt{\frac{s}{D_{PE}}}\right)-\frac{1}{a_{PE1}}\right)}\frac{3D_{aq}Sh_{PE1}}{2a_{PE1}^2 s} \\
\tilde{C}_w &= \frac{C_w(0)+\frac{m_{PE1}}{V_w}\tilde{g}_{PE1}\frac{C_{PE1}(0)}{K_{PE}}}{\left(1+\frac{m_{PE1}}{V_w}\tilde{g}_{PE1}\right)s} \\
\tilde{C}_{PE1} &= \tilde{g}_{PE1}\left(\tilde{C}_w-\frac{C_{PE1}(0)}{K_{PE}\,s}\right)+\frac{C_{PE1}(0)}{s}
\end{aligned} \tag{S3.143}$$

and for batch tests B-C:

$$\begin{aligned}
\tilde{g}_{PE2} &= \frac{D_{PE}K_{PE}\left(\sqrt{\frac{s}{D_{PE}}}\coth\left(a_{PE2}\sqrt{\frac{s}{D_{PE}}}\right)-\frac{1}{a_{PE2}}\right)}{\frac{D_{aq}Sh_{PE2}}{2a_{PE2}}+D_{PE}\rho_{PE}K_{PE}\left(\sqrt{\frac{s}{D_{PE}}}\coth\left(a_{PE2}\sqrt{\frac{s}{D_{PE}}}\right)-\frac{1}{a_{PE2}}\right)}\frac{3D_{aq}Sh_{PE2}}{2a_{PE2}^2 s} \\
\tilde{g}_{PE3} &= \frac{D_{PE}K_{PE}\left(\sqrt{\frac{s}{D_{PE}}}\coth\left(a_{PE3}\sqrt{\frac{s}{D_{PE}}}\right)-\frac{1}{a_{PE3}}\right)}{\frac{D_{aq}Sh_{PE3}}{2a_{PE3}}+D_{PE}\rho_{PE}K_{PE}\left(\sqrt{\frac{s}{D_{PE}}}\coth\left(a_{PE3}\sqrt{\frac{s}{D_{PE}}}\right)-\frac{1}{a_{PE3}}\right)}\frac{3D_{aq}Sh_{PE3}}{2a_{PE3}^2 s} \\
\tilde{C}_w &= \frac{C_w(0)+\frac{m_{PE2}}{V_w}\tilde{g}_{PE2}\frac{C_{PE2}(0)}{K_{PE}}+\frac{m_{PE3}}{V_w}\tilde{g}_{PE3}\frac{C_{PE3}(0)}{K_{PE}}}{\left(1+\frac{m_{PE2}}{V_w}\tilde{g}_{PE2}+\frac{m_{PE3}}{V_w}\tilde{g}_{PE3}\right)s} \\
\tilde{C}_{PE2} &= \tilde{g}_{PE2}\left(\tilde{C}_w-\frac{C_{PE2}(0)}{K_{PE}\,s}\right)+\frac{C_{PE2}(0)}{s} \\
\tilde{C}_{PE3} &= \tilde{g}_{PE3}\left(\tilde{C}_w-\frac{C_{PE3}(0)}{K_{PE}\,s}\right)+\frac{C_{PE3}(0)}{s}
\end{aligned} \tag{S3.144}$$

D_{PE} [$L^2\,T^{-1}$] denotes the Phenanthrene diffusion coefficient in polyethylene. K_{PE} [$L^3\,M^{-1}$] is the partition coefficient between polyethylene and water. a_{PE1} [L], a_{PE2} [L] and a_{PE3} [L] are the radii of PE1, PE2 and PE3, respectively. m_{PE1}/V_w [$M\,L^{-3}$], m_{PE2}/V_w [$M\,L^{-3}$] and m_{PE3}/V_w [$M\,L^{-3}$] denote the solid-to-liquid ratios of PE1, PE2 and PE3, respectively. $\tilde{g}_{PE1}$, $\tilde{g}_{PE2}$ and $\tilde{g}_{PE3}$

are the transfer functions of FIPSD in Laplace domain of PE1, PE2 and PE3, respectively. Sh_{PE1}, Sh_{PE2} and Sh_{PE3} are Sherwood numbers of PE1, PE2 and PE3, respectively. $C_{PE1}(0)$, $C_{PE2}(0)$ and $C_{PE3}(0)$ denote the initial Phenanthrene concentrations in PE1, PE2 and PE3, respectively.

The input parameters of the semi-Laplace solution for batch tests A-C are compiled in Tab. S3.4. Based on Eqs. S3.143 and S3.144, the unknown parameters are the partition coefficients (K_{PE}) and Sherwood numbers (Sh_{PE1}, Sh_{PE2} and Sh_{PE3}), which are obtained by fitting experimental observation data (here aqueous concentration measurements).

Tab. S3.4: Summary of input parameters for modelling of batch tests A-C.

Global parameters							
Parameters	D_{aq} [a] [m² s⁻¹]	D_{PE} [a] [m² s⁻¹]	ρ_{PE} [kg L⁻¹]				
Values	7.60E-10	1.60E-13	0.92				
Batch specific input parameters							
Parameters	a_{PE1} [µm]	m_{PE1}/V_w [kg L⁻¹]	$C_w(0)$ [µg L⁻¹]	$C_{PE1}(0)$ [µg kg⁻¹]			
Batch test A	73	1.00E-3	110	0			
Parameters	a_{PE2} [µm]	a_{PE3} [µm]	m_{PE2}/V_w [kg L⁻¹]	m_{PE3}/V_w [kg L⁻¹]	$C_w(0)$ [µg L⁻¹]	$C_{PE2}(0)$ [µg kg⁻¹]	$C_{PE3}(0)$ [µg kg⁻¹]
Batch test B	130	2086	1.11E-3	1.11E-3	2.94	0	4.60E4
Batch test C	130	2086	1.00E-3	1.00E-3	0.31	2.42E4	0

[a] data from Seidensticker et al. (2017), at 25℃.

S3.9.2 Model setups of Anthracene d10 and Phenanthrene redistribution in a mixed sediment suspension with passive samplers

Here the sediment particles are assumed as porous spherical particles and the coupled film-intraparticle pore diffusion (FIPPD) is used while only the external film diffusion is applied to plane passive samplers (PE sheets) due to its large distribution coefficient (K_{PE}) and thin thickness ($d_{PE} = 30$ µm). The Anthracene d10/Phenanthrene concentrations in bulk water ($\tilde{C}_w$), PE sheets ($\tilde{C}_{PE}$), fine sediment particles ($\tilde{C}_{w,sp,1}$) and coarse sediment particles ($\tilde{C}_{w,sp,2}$) in Laplace domain of batch test D can be expressed as:

$$\tilde{g}_{PE} = \frac{\frac{D_{aq}}{\delta_{PE}} K_{PE}}{\frac{D_{aq}}{\delta_{PE}} + \rho_{PE} K_{PE} a_{PE} s}$$

$$\tilde{g}_{sp,1} = \frac{D_a \left(\sqrt{\frac{s}{D_a}} \coth\left(a_{sp,1} \sqrt{\frac{s}{D_a}} \right) - \frac{1}{a_{sp,1}} \right)}{\frac{D_{aq} Sh_{sp,1}}{2 a_{sp,1}} + D_a \rho_p K_{d,b} \left(\sqrt{\frac{s}{D_a}} \coth\left(a_{sp,1} \sqrt{\frac{s}{D_a}} \right) - \frac{1}{a_{sp,1}} \right)} \frac{3 D_{aq} Sh_{sp,1}}{2 a_{sp,1}^2 s}$$

$$\tilde{g}_{sp,2} = \frac{D_a \left(\sqrt{\frac{s}{D_a}} \coth\left(a_{sp,2} \sqrt{\frac{s}{D_a}} \right) - \frac{1}{a_{sp,2}} \right)}{\frac{D_{aq} Sh_{sp,2}}{2 a_{sp,2}} + D_a \rho_p K_{d,b} \left(\sqrt{\frac{s}{D_a}} \coth\left(a_{sp,2} \sqrt{\frac{s}{D_a}} \right) - \frac{1}{a_{sp,2}} \right)} \frac{3 D_{aq} Sh_{sp,2}}{2 a_{sp,2}^2 s} \quad \text{(S3.145)}$$

$$\tilde{C}_w = \frac{C_w(0) + \frac{m_{PE}}{V_w} \tilde{g}_{PE} \frac{C_{PE}(0)}{K_{PE}} + \frac{m_{d,1}}{V_w} K_{d,b} \tilde{g}_{sp,1} C_{w,sp,1}(0) + \frac{m_{d,2}}{V_w} K_{d,b} \tilde{g}_{sp,2} C_{w,sp,2}(0)}{\left(1 + \frac{m_{PE}}{V_w} \tilde{g}_{PE} + \frac{m_{d,1}}{V_w} K_{d,b} \tilde{g}_{sp,1} + \frac{m_{d,2}}{V_w} K_{d,b} \tilde{g}_{sp,2} \right) s}$$

$$\tilde{C}_{PE} = \tilde{g}_{PE} \left(\tilde{C}_w - \frac{C_{PE}(0)}{K_{PE}\, s} \right) + \frac{C_{PE}(0)}{s}$$

$$\tilde{C}_{w,sp,1} = \tilde{g}_{sp,1} \left(\tilde{C}_w - \frac{C_{w,sp,1}(0)}{s} \right) + \frac{C_{w,sp,1}(0)}{s}$$

$$\tilde{C}_{w,sp,2} = \tilde{g}_{sp,2} \left(\tilde{C}_w - \frac{C_{w,sp,2}(0)}{s} \right) + \frac{C_{w,sp,2}(0)}{s}$$

where a_{PE} [L], $a_{sp,1}$ [L] and $a_{sp,2}$ [L] denote the half thickness of PE sheets, radius of fine and coarse sediment particles, respectively. m_{PE}/V_w [M L^{-3}], $m_{d,1}/V_w$ [M L^{-3}] and $m_{d,2}/V_w$ [M L^{-3}] denote the solid-to-liquid ratios of PE sheets, fine and coarse sediment particles, respectively. $\tilde{g}_{PE}$ denotes the transfer function of FD in Laplace domain for PE sheets. $\tilde{g}_{sp,1}$ and $\tilde{g}_{sp,2}$ are the transfer functions of FIPPD in Laplace domain for fine and coarse sediment particles, respectively. δ_{PE}, $Sh_{sp,1}$ and $Sh_{sp,2}$ are film thickness of PE sheets and Sherwood numbers of fine and coarse sediment particles, respectively. $C_{PE}(0)$, $C_{w,sp,1}(0)$ and $C_{w,sp,2}(0)$ are the initial Anthracene d10/Phenanthrene concentrations in PE sheets, intraparticle pore water of fine and coarse sediment particles, respectively.

The input parameters of the semi-Laplace solution of batch test D are listed in Tab. S3.5. Based on Eq. S3.145, the unknown parameters are the partition and distribution coefficients (K_{PE}, K_d), intraparticle porosity (ε), film thickness of PE sheets (δ_{PE}), Sherwood numbers ($Sh_{sp,1}$ and $Sh_{sp,2}$) and the initial Phenanthrene concentration in sediment solids ($C_{s,ini}$), which may be obtained by fitting the model to the observation data (here measurement of concentrations in PE).

Tab. S3.5: Summary of input parameters of semi-Laplace solution of batch tests D.

Global input parameters							
Parameters	D_{aq}[a] [m^2 s^{-1}]	D_{PE}[a] [m^2 s^{-1}]	ρ_{PE} [kg L^{-1}]	ρ_s [kg L^{-1}]	a_{PE} [µm]	$a_{sp,1}$ [µm]	$a_{sp,2}$ [µm]

Values	7.60E-10	1.60E-13	0.92	2.7	15	3.5	37
Batch specific input parameters (solid/liquid ratios: SL = 0.15 and 0.30)							
Parameters	m_{PE}/V_w [kg L^{-1}]	$m_{d,1}/V_w$ [kg L^{-1}]	$m_{d,2}/V_w$ [kg L^{-1}]	$C_w(0)$ [µg L^{-1}]	$C_{PE}(0)$ [µg kg^{-1}]	$C_{w,sp,1}(0)$ [µg L^{-1}]	$C_{w,sp,2}(0)$ [µg L^{-1}]
Ant-d10 SL = 0.15	5.00E-3	0.075	0.075	0	227	0	0
Ant-d10 SL = 0.30	5.00E-3	0.15	0.15	0	227	0	0
Phe SL = 0.15	5.00E-3	0.075	0.075	0	0	unknown[b]	unknown[b]
Phe SL = 0.30	5.00E-3	0.15	0.15	0	0	unknown[b]	unknown[b]

[a] data from Seidensticker et al. (2017), at 25℃.

[b] unknown initial Phenanthrene concentrations in the intraparticle pore water of fine and coarse sediment particles can be calculated from initial Phenanthrene concentration in sediments ($C_{w,sp,1}(0) = C_{s,ini}/K_{d,b}$; $C_{w,sp,2}(0) = C_{s,ini}/K_{d,b}$).

S3.10 Anthracene d10 and Phenanthrene concentration changes in water

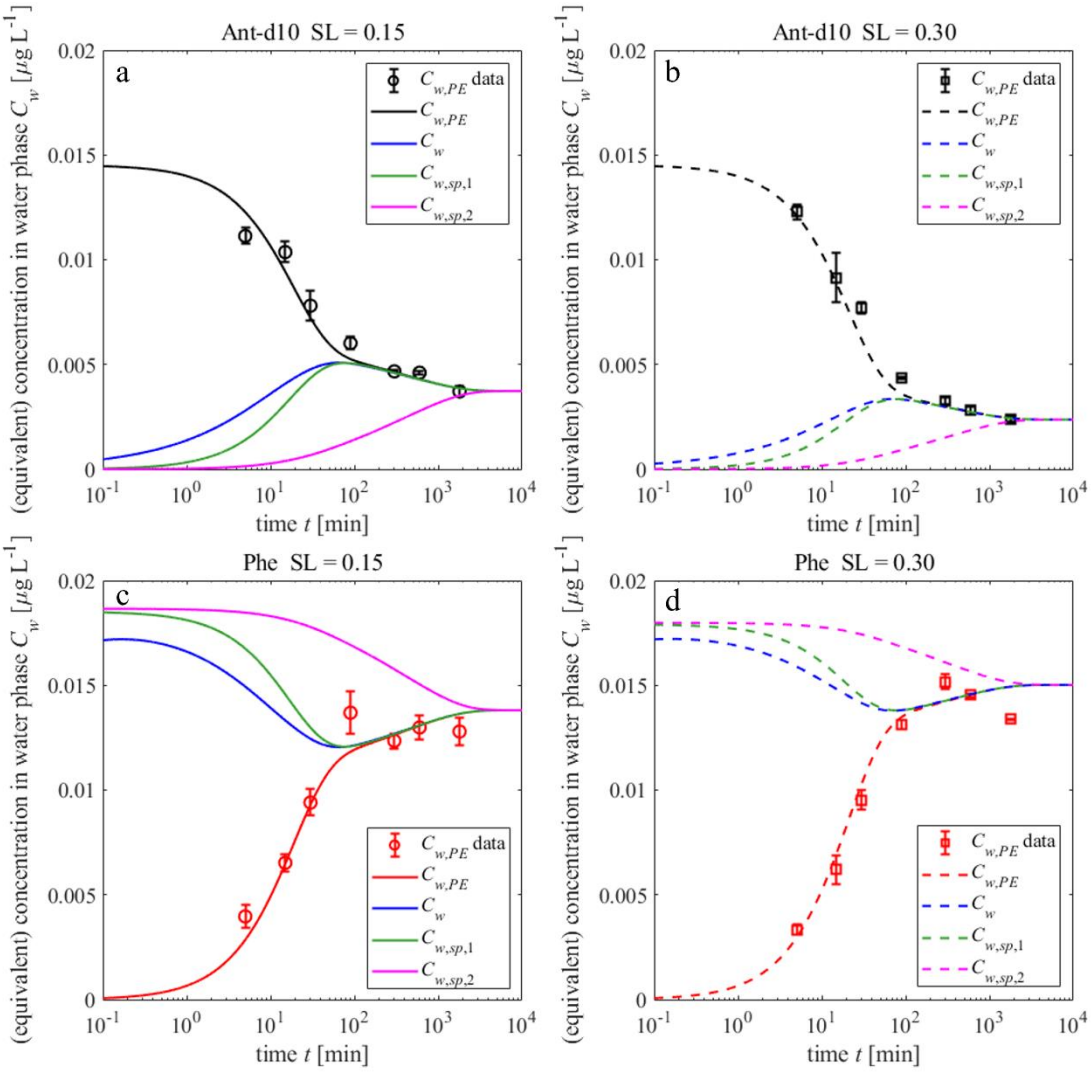

Fig. S3.8: Anthracene d10 and Phenanthrene concentration changes over time in water (blue lines) and PE passive samplers (polyethylene sheets $d_{PE} = 30$ µm; Anthracene d10: black lines, symbols; Phenanthrene: red lines, symbols), fine particles ($d_{sp,1} = 7$ µm; green lines) and coarse particles ($d_{sp,2} = 74$ µm; magenta lines) for two solid-to-liquid ratios (SL = 0.15 kg L^{-1} (solid lines, left panel) and SL = 0.30 kg L^{-1} (dashed lines, right panel)); for the solids, concentrations are reported by their equivalent aqueous concentrations ($C_{w,PE} = C_{PE}/K_{PE}$; $C_{w,sp,1} = C_{s,\mathrm{sp},1}/K_{d,b}$; $C_{w,sp,2} = C_{s,\mathrm{sp},2}/K_{d,b}$ for PE passive samplers, fine and coarse particles), which has the advantage that at equilibrium between all phases all lines converge.

S3.11 Influence of different geometries of particles on sorption/desorption kinetics

Different geometric shapes of particles have different surface to volume ratios (A_{sp}/V_{sp}) leading to different sorption/desorption behaviors. For better illustrating the impact of surface to volume ratio on coupled film intraparticle pore diffusion model (FIPPD), short term approximations of analytical solutions of external film diffusion (FD) and intraparticle pore diffusion (IPPD) versus Fourier numbers ($D_{aq}t/\left(V_{sp}/A_{sp}\right)^2$) can be used:

$$\begin{aligned}\frac{M}{M_{eq}} &= \frac{1}{2}\frac{D_{aq}\,Sh\,A_{sp}}{\rho_p K_{d,b} a_{sp} V_{sp}}\left(1 + K_{d,b}\mathrm{SL}\right)t \\ &= \frac{1}{2\gamma}\frac{Sh}{\rho_p K_{d,b}}\left(1 + K_{d,b}\mathrm{SL}\right)\frac{D_{aq}t}{\left(V_{sp}/A_{sp}\right)^2} \quad \text{for FD} \\ \frac{M}{M_{eq}} &= 2\sqrt{\frac{\varepsilon^2}{\pi\rho_p K_{d,b}}}\left(1 + K_{d,b}\mathrm{SL}\right)\sqrt{\frac{D_{aq}t}{\left(V_{sp}/A_{sp}\right)^2}} \text{ for IPPD}\end{aligned} \tag{S3.146}$$

where M [M] and M_{eq} [M] denote the mass of solute, which has diffused into or out of the particle after a certain time t and after equilibrium was reached, respectively. Sh [-] denotes the Sherwood number. SL [M L^{-3}] is the solid-to-liquid ratio. γ denotes the ratio of particle radius over surface to volume ratio (e.g., $\gamma = 1, 2$ and 3 for plane particles, cylindrical particles and spherical particles, respectively.).

In Fig. S3.9, sorption/desorption kinetics for pure spherical particles are fastest, followed by cylindrical particles and slowest for plane particles, because of the higher surface to volume ratio ($A_{sp}/V_{sp} = 3/a_{sp}$) of spherical particles compared to cylindrical particles ($2/a_{sp}$) and the plane sheets ($1/a_{sp}$). At early times sorptive uptake/desorption rates are independent on particle geometry and solely depend on the surface to volume ratio of a particle (Grathwohl, 1998, see Fig. S3.9b) and this also applies to mixtures. The slightly different

slopes of fines and coarse particles at early time are due to different mass transfer shifts in the coupled film-intraparticle pore diffusion model (details see discussion for Fig. S3.10). If instead of A_{sp}/V_{sp} the radii or thicknesses are used to calculate dimensionless time (Fig. S3.9a) differences in geometries become more obvious also for mixtures (e.g., faster for cylinders: spheres = 1: 1 or slower for mixed plane sheets: cylinders = 1: 1), but differences are still within one order of magnitude in time.

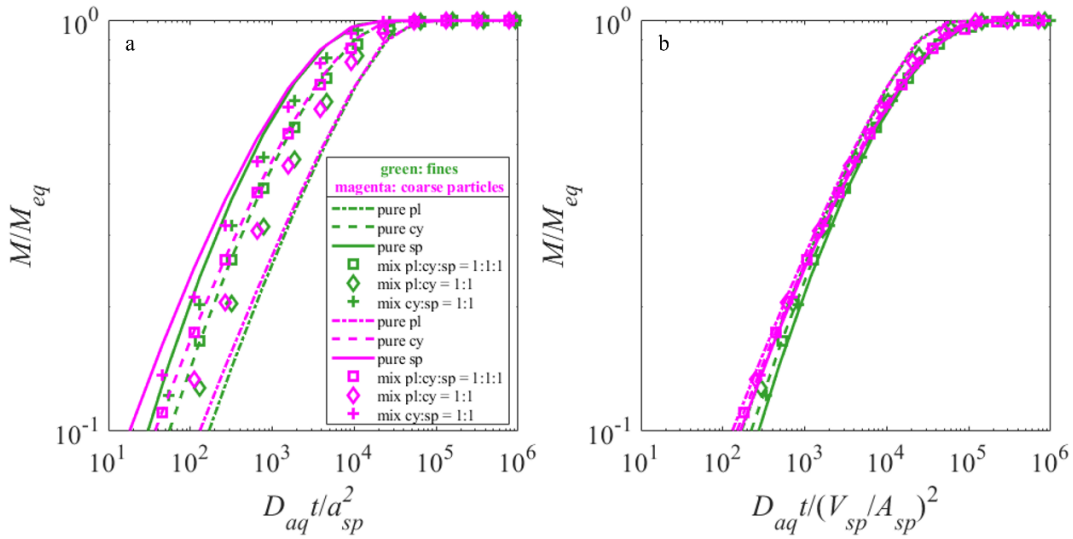

Fig. S3.9: Impact of geometry of particles on sorption/desorption kinetics of mixtures of fines ($d_{sp,fine}$ = 40 µm) and coarse particles ($d_{sp,coarse}$ = 400 µm) for solid-to-liquid ratio (SL) of 0.001 kg L^{-1}. (a): Mass sorbed or desorbed relative to equilibrium conditions (M/M_{eq}) vs. dimensionless time based on the radius (or half thickness of plane sheets; Fourier number = $D_{aq}t/a_{sp}^2$) for different geometries and mixtures of plane sheets (pl), cylinders (cy) and spheres (sp). (b): M/M_{eq} vs. time normalized to surface to volume ratio (A_{sp}/V_{sp}) of different geometries. D_{aq} = 7.6 × 10^{-10} m^2 s^{-1}; ρ_s = 2.7 kg L^{-1}; ε = 0.2; ε_{disp} = 10$^{-1.5}$ m^2 s^{-3}; ν = 10^{-6} m^2 s^{-1}; K_d = 1000 L kg^{-1} (reference value). All simulations are based on coupled film-intraparticle pore diffusion model.

Liu et al. (2022) showed how mass transfer shift of FIPPD from FD to IPPD gets delayed with increasing distribution coefficient and intraparticle porosity and decreasing Sherwood number (Eqs. 2.28-2.31). While external mass transfer resistance dominates for longer time (t) with the increase of grain size (seems like "delay"), mass transfer shift of FIPPD for coarse particles presents reverse results ("acceleration") in figure of M/M_{eq} vs. dimensionless time (see green and magenta lines in Fig. S3.10) because the time dominated by FD is normalized by the total equilibration time of FIPPD where coarse particles take much longer time

compared to fines and mass transfer shift occurs quite early for coarse particles (at very low M/M_{eq}). Thus, for coarse particles mass transfer shifts earlier to IPPD and IPPD is independent on the ratio of particle radius or surface to volume ratio (γ) (see Eq. S3.146); plane sheets, cylindrical and spherical particles show almost the same kinetics at early times (magenta lines almost overlap); for fine particles, however, FD dominates at early time and since FD is dependent on γ this leads to deviations between various green lines seen in Fig. S3.10 (see SL = 0.001 kg L^{-1}). Although kinetics for both FD and IPPD in the finite bath accelerates with the increase of the solid-to-liquid ratio (see Eq. S3.146), this is more significant for the latter (IPPD) (discussed in section S3.12). Equilibration times reduce by a factor of 25 times for fines and around 50 times for coarse particles at early time if SL increases only by a factor of 10 (see Fig. S3.10 (right panel; deviations between green lines and magenta lines become larger).

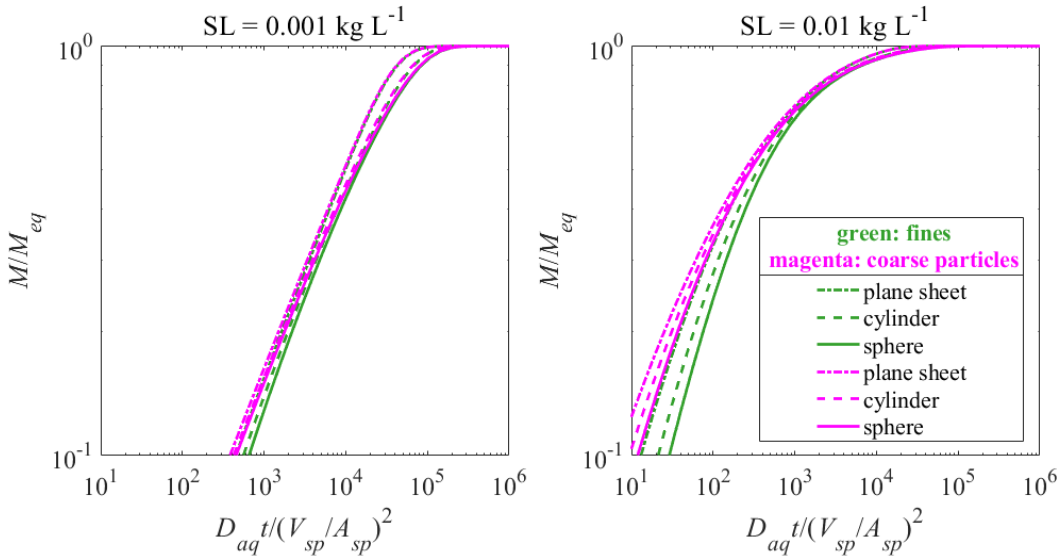

Fig. S3.10: Mass sorbed or desorbed relative to equilibrium conditions (M/M_{eq}) vs. dimensionless time (Fourier number = $D_{aq}t/(V_{sp}/A_{sp})^2$) of homogeneous samples of plane sheet particles (dashed-dotted lines), cylindrical particles (dashed lines) and spherical particles (solid lines) for two solid-to-liquid ratios (SL = 0.001 kg L^{-1}, left and SL = 0.01 kg L^{-1}, right) for fine ($d_{sp,fine}$ = 40 µm, green lines) and coarse particles ($d_{sp,coarse}$ = 400 µm, magenta lines), respectively. D_{aq} = 7.6 × 10^{-10} m^2 s^{-1}; ρ_s = 2.7 kg L^{-1}; ε = 0.2; ε_{disp} = $10^{-1.5}$ m^2 s^{-3}; ν = 10^{-6} m^2 s^{-1}; K_d = 1000 L kg^{-1}. All simulations are based on the coupled film-intraparticle pore diffusion model (FIPPD).

S3.12 Solid-to-liquid ratio impact on equilibration time of film diffusion and intraparticle pore diffusion

Solid-to-liquid ratio (SL) impacts on external film diffusion or intraparticle pore diffusion are different, which can be mathematically illustrated by using their analytical solutions. The analytical solutions of external film diffusion (FD) and intraparticle pore diffusion (IPPD) (e.g., short term approximation) for spherical particles are given as:

$$\begin{aligned} \frac{M}{M_{eq}} &= \frac{3}{2}\frac{Sh}{\rho_p K_{d,b}}\left(1 + K_{d,b}\mathrm{SL}\right)\frac{D_{aq}t}{a_{sp}^2} \quad \text{for FD} \\ \frac{M}{M_{eq}} &= 6\sqrt{\frac{\varepsilon^2}{\pi\rho_p K_{d,b}}}\left(1 + K_{d,b}\mathrm{SL}\right)\sqrt{\frac{D_{aq}t}{a_{sp}^2}} \quad \text{for IPPD} \end{aligned} \tag{S3.147}$$

For very strong sorbents ($K_{d,b}\mathrm{SL} \gg 1$), the equilibrium time decreases 10 times for one magnitude increase of solid-to-liquid ratio for film diffusion ($K_{d,b}$ actually drops out), while the equilibrium time decreases 100 times for intraparticle pore diffusion (t here appears under the square root and a maximum equilibration time occurs when $K_{d,b} = 1/\mathrm{SL}$ (see Liu et al., 2022), thus large $K_{d,b}$ values would accelerate equilibration further). For moderate sorbents ($K_{d,b}\mathrm{SL}$ is close to 1), the solid-to-liquid ratio impact on mass transfer becomes weaker and equilibrium time decrease is dependent on the variation of the "acceleration" term ($1 + K_{d,b}\mathrm{SL}$). For weak sorbents ($K_{d,b}\mathrm{SL} \ll 1$), the solid-to-liquid ratio influence on mass transfer can be neglected and the equilibrium time is independent on the solid-to-liquid ratio (because $1 + K_{d,b}\mathrm{SL} \approx 1$).

S3.13 Sorption/desorption kinetics in mixed samples of strongly and less sorbing particles

Figure S3.11 illustrates sorption/desorption kinetics of three mixed samples where 100%, 10%, and 1% of the particles have distribution coefficients (K_d) of 1000, 10000 and 100000, respectively (keeping the overall K_d constant = same average K_d). If the fraction of sorbing particles decreases to only 10% or 1%, then only these particle fractions carry the contaminant leading to increased concentrations (Figs. S3.11a and b: dashed or dotted-dashed lines); in this case sorption/desorption kinetics slows down at each step as expected (Figs. S3.11a and b: dashed or dotted-dashed lines). This may be illustrated for film diffusion (kinetics at early times: $\frac{M}{M_{eq}} = \frac{3}{2}\frac{Sh}{\rho_p}\left(\frac{1}{K_{d,b}} + \mathrm{SL}\right)\frac{D_{aq}t}{a_{sp}^2}$) where at each step $1/K_{d,b}$ and SL decrease by one order of magnitude (both are the same in Fig. S3.11a). If SL > $1/K_{d,b}$ (Fig. S3.11b) the

faster kinetics are due to increasing SL. Generally increasing solid-to-liquid ratios accelerate equilibration in batch systems as demonstrated by Fig. S3.11a (left panel: $\frac{1}{K_{d,b}} + \mathrm{SL} = 2/1000$) compared to Fig. S3.11b (right panel: $\frac{1}{K_{d,b}} + \mathrm{SL} = 1.1/100$). Fine particles (green) seem slower at early times than coarse particles (magenta) despite dimensionless time is used; this is because mass transfer resistance dominated by film diffusion is more important for fine particles than for coarse particles because of the grain size dependence of the Sherwood number. We also note that this difference is more pronounced at large SL ratios (Fig. S3.11b) although mass transfer shifts in principle should be independent on SL (Liu et al., 2022); this is because the ratios of characteristic times or ratios of mass transfer resistances are approximations at finite bath conditions (do not apply to the same M/M_{eq}) and thus SL does not cancel out completely and this results in slight differences between fines and coarse particles at early times for SL = 0.01 kg L^{-1} (see Fig. S3.11b).

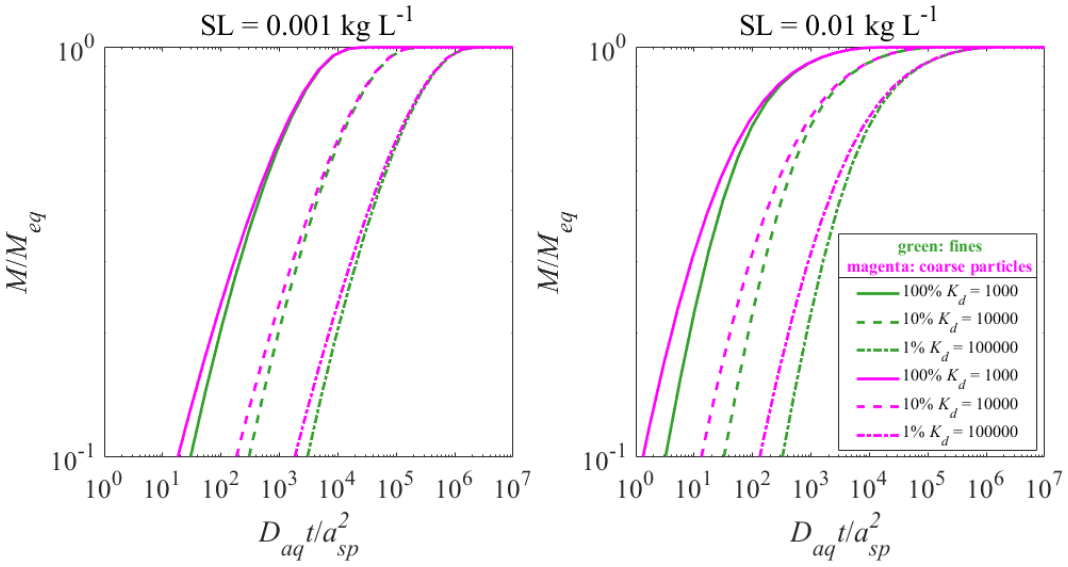

Fig. S3.11: Impact of the fraction of sorbing particles on sorption/desorption kinetics of mixtures of fines ($d_{sp,fine}$ = 40 µm) and coarse spherical particles ($d_{sp,coarse}$ = 400 µm) for two solid-to-liquid ratios (SL= 0.001 kg L^{-1} (left) and 0.01 kg L^{-1} (right panel)) for pure (100%) and bi-modal mixtures of sorbing and non-sorbing particles with the same average K_d (= $K_{d,av}$ = 1000 L kg^{-1}; solid lines); dashed lines: 10% of the particles carry the contaminant (K_d = 10 × $K_{d,av}$); dashed-dotted lines: only 1% of the particles carry the contaminant (K_d = 100 × $K_{d,av}$); M/M_{eq}: Mass sorbed or desorbed relative to equilibrium conditions vs. dimensionless time; D_{aq} = 7.6 × 10^{-10} m^2 s^{-1}; ρ_s = 2.7 kg L^{-1}; ε = 0.2; ε_{disp} = 10$^{-1.5}$ m^2 s^{-3}; ν = 10^{-6} m^2 s^{-1}; K_d = 1000 L kg^{-1} (reference value). All simulations are based on the coupled film-intraparticle pore diffusion model (more film diffusion limitation for fines slow

down kinetics at early time).

S3.14 Sorption/desorption kinetics in mixtures of different grain sizes

In Fig. S3.12, sorption/desorption kinetics in mixtures of two grain sizes ($d_{sp,fine} = 40$ μm; $d_{sp,coarse} = 400$ μm) with three mass fractions (10%, 50%, 90% fines) are compared to the homogeneous cases containing either 100% fines or 100% coarse particles. Materials with 90% fines (Figs. S3.12a and b: blue diamonds) show similar kinetics as the sample containing just fines (Figs. S3.12a and b: green solid lines). Fines dominate sorption kinetics at early times and a quasi-steady state is reached between fines and water and equivalent aqueous concentrations overlap indicating equilibrium ($C_{w,fines} = C_w$; see Figs. S3.12c and d). An important feature is an "overshooting" i.e., a rapid solute uptake by fines which gradually decreases when coarse particles (Figs. S3.12c and d: dotted-dashed lines) slowly take up the compound at late times leading to solute desorption from fines. The 50% mixture at early times shows the typical increase in M/M_{eq} but shifts to much slower kinetics dominated by coarse particles. Materials with only 10% fines follow closely the homogenous coarse sample (Figs. S3.12a and b: magenta solid lines) at late time. Sorption/desorption kinetics are quite sensitive to grain size distributions and as expected equilibration times increase a hundredfold for one order of magnitude increase in grain size.

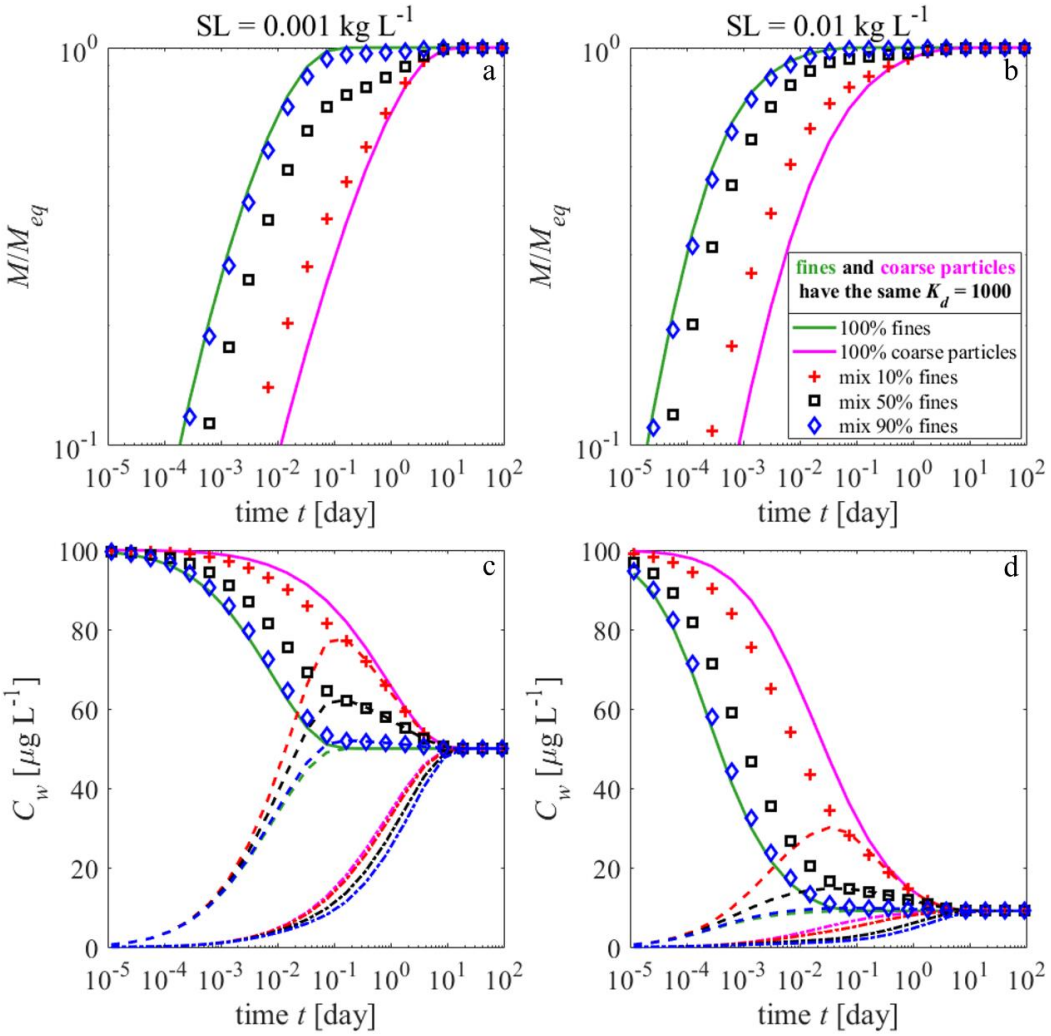

Fig. S3.12: Impact of heterogeneous sorbent compositions on sorption/desorption kinetics of mixtures of fines ($d_{sp,fine}$ = 40 µm) and coarse particles ($d_{sp,coarse}$ = 400 µm) for two solid-to-liquid ratios (SL = 0.001 and 0.01 kg L^{-1}); (a) and (b): M/M_{eq} vs. time (t) of bi-modal material compositions of fine and coarse particles with 10% fines (red cross symbols), 50% fines (black square symbols) and 90% fines (blue diamond symbols) as well as homogeneous samples of pure fines (green solid lines) and pure coarse particles (magenta solid lines); (c) and (d): changes in aqueous concentrations (symbols or solid lines) and equivalent equilibrium concentrations in water for fines ($C_{w,fines} = C_{s,fines}/K_{d,b}$, dashed lines) and coarse particles ($C_{w,coarse} = C_{s,coarse}/K_{d,b}$, dotted-dashed lines) for the sorptive uptake case (equilibrium if lines overlap); initial aqueous concentration $C_{w,ini}$ = 100 µg L^{-1}; D_{aq} = 7.6 × 10^{-10} m^2 s^{-1}; ρ_s = 2.7 kg L^{-1}; ε = 0.2; ε_{disp} = 10$^{-1.5}$ m^2 s^{-3}; ν = 10^{-6} m^2 s^{-1}, K_d = 1000 L kg^{-1} (reference value). All simulations are based on coupled film-intraparticle pore diffusion model.

S3.15 Biased fitting of distribution coefficients in sorptive uptake and desorption experiments with heterogeneous samples containing strong sorbents

Considering the pollutant redistribution in two phases (water and solids) system where the solid phase is a mixture of different sorbents the mass conservation equation is given as:

$$m_{tot} = m_w + \sum_{i=1}^{n} m_{s,i} \tag{S3.148}$$

where m_{tot} [M] denotes the total mass of pollutants in the system. m_w [M] and $m_{s,i}$ [M] are pollutant mass stored in the water phase and in the sorbent i, respectively.

Under equilibrium conditions, the "retardation" factor (R_d) can be expressed as:

$$R_d = \frac{m_{tot}}{m_w} = 1 + \sum_{i=1}^{n} K_{d,i} \frac{m_{d,i}}{V_w} \tag{S3.149}$$

The final equilibrium concentration in aqueous phase is:

$$C_{w,eq} = \frac{m_{tot}}{V_w + \sum_{i=1}^{n} K_{d,i} m_{d,i}} \tag{S3.150}$$

In the following, we use the case of a mixed sample with fine weakly sorbing and coarse strongly sorbing particles (case (i) in section 3.4.4 of the main text; the analysis also applies to redistribution of PAHs in sediments and passive samplers) as an example to illustrate why the K_d values obtained by fitting in sorptive uptake and desorption experiments may differ. This example aims to demonstrate that kinetics of strong sorbents (particulate organic carbon, char, coal, tire wear, microplastics etc.) in sorption/desorption batch experiments may be masked if they are mixed with a fast sorbing fraction.

If in a sorptive uptake experiment (results shown in Figs. 3.6a-d of main text), initially all solute mass is in water, then the mass balance equation is given as:

$$\begin{aligned} m_{tot} &= C_{w,ini} V_w \\ &= C_{w,eq} (V_w + K_{d,b,fines} m_{d,fines} + K_{d,b,coarse} m_{d,coarse}) \end{aligned} \tag{S3.151}$$

where $C_{w,ini}$ [M L^{-3}] is the initial solute concentration ($C_{w,ini} = 100$ µg L^{-1}). $K_{d,b,fines}$ [L^3 M^{-1}] and $K_{d,b,coarse}$ [L^3 M^{-1}] denote the bulk distribution of fine weak sorbent and coarse strong sorbent, respectively. $m_{d,fines}$ [M] and $m_{d,coarse}$ denote the mass of fine weak sorbent and coarse strong sorbent, respectively.

The final equilibrium concentration ($C_{w,eq}$) can be denoted as:

$$C_{w,eq} = \frac{C_{w,ini}}{1 + K_{d,b,fines}\frac{m_{d,fines}}{V_w} + K_{d,b,coarse}\frac{m_{d,coarse}}{V_w}} \quad \text{(S3.152)}$$

The apparent average bulk distribution of the mixing sample ($K_{d,b,a}$) (applied in both sorption and desorption cases) can be calculated as:

$$K_{d,b,a} = \frac{m_{tot} - C_w(t)V_w}{(m_{d,fines} + m_{d,coarse})C_w(t)} \quad \text{(S3.153)}$$

The equilibrium average bulk distribution of the mixing sample ($K_{d,b,average}$) can be obtained by replacing $C_w(t)$ with $C_{w,eq}$ in Eq. S3.153.

Owing to much slower sorption kinetics of coarse strong sorbent, the fine weak sorbent dominates the mass transfer at early times and a quasi-steady state may be observed, where the solute concentration in aqueous phase becomes:

$$C_{w,eq,quasi} = \frac{C_{w,ini}}{1 + K_{d,b,fines}\frac{m_{d,fines}}{V_w}} \quad \text{(S3.154)}$$

The ratio of the equilibrium concentrations in aqueous phase due to the contributions of fine and coarse sorbents ($\Delta C_{w,fines}/\Delta C_{w,coarse}$) can be determined (e.g., taking a mixture of fine particles (K_d =1000 L kg^{-1}) containing 1% coarse particles (K_d =100 000 L kg^{-1}) (orange symbols and lines in Figs. 3.6a-d in main text)):

$$\frac{\Delta C_{w,fines}}{\Delta C_{w,coarse}} = \frac{C_{w,ini} - \frac{C_{w,ini}}{1 + K_{d,b,fines}\frac{m_{d,fines}}{V_w}}}{\frac{C_{w,ini}}{1 + K_{d,b,fines}\frac{m_{d,fines}}{V_w}} - \frac{C_{w,ini}}{1 + K_{d,b,fines}\frac{m_{d,fines}}{V_w} + K_{d,b,coarse}\frac{m_{d,coarse}}{V_w}}}$$

$$= \frac{100\ \frac{\mu g}{L} - \frac{100\ \frac{\mu g}{L}}{1 + 1000\frac{L}{kg} * 10^{-3}\frac{kg}{L} * 99\%}}{\frac{100\ \frac{\mu g}{L}}{1 + 1000\frac{L}{kg} * 10^{-3}\frac{kg}{L} * 99\%} - \frac{100\ \frac{\mu g}{L}}{1 + 1000\frac{L}{kg} * 10^{-3}\frac{kg}{L} * 99\% + 100000\frac{L}{kg} * 10^{-3}\frac{kg}{L} * 1\%}} \quad \text{(S3.155)}$$

$$= 3$$

Thus, the aqueous concentration decrease caused by fines is three times larger than concentration decrease caused by coarse particles (see Fig. 3.6c in main text) for a solid-to-liquid ratio of 0.001 kg L^{-1}. This increases with solid-to-liquid ratio and for SL = 0.01 kg L^{-1} (see Fig. 3.6d in main text) the ratio ($\Delta C_{w,fines}/\Delta C_{w,coarse}$) becomes already 21; here the mixed sample with 1% coarse particles shows almost the same sorptive uptake kinetics as the sample containing only fines (see Fig. 3.6b in main text). In such cases, the short term behavior mainly reflects the distribution coefficient of the fine weak sorbent ($K_{d,b,fines}$)

while kinetics of the coarse strong sorbent ($K_{d,b,coarse}$) would be masked especially at large solid-to-liquid ratios (see Figs. S3.13c and d, sorption case).

In a desorption experiment (results shown in Figs. 3.6e and f in main text), the initial solute mass is stored in fines and coarse sorbents (in equilibrium with each other). The mass balance equation is given as:

$$\begin{aligned} m_{tot} &= C_{w,p,ini}(K_{d,b,fines}m_{d,fines} + K_{d,b,coarse}m_{d,coarse}) \\ &= C_{w,eq}(V_w + K_{d,b,fines}m_{d,fines} + K_{d,b,coarse}m_{d,coarse}) \end{aligned} \quad \text{(S3.156)}$$

where $C_{w,p,ini}$ [M L^{-3}] is the initial solute concentration in the intraparticle pore water ($C_{w,p,ini} = 100$ µg L^{-1}).

The final equilibrium concentration of desorption experiment can be expressed as:

$$C_{w,eq} = \frac{C_{w,p,ini}(K_{d,b,fines}\frac{m_{d,fines}}{V_w} + K_{d,b,coarse}\frac{m_{d,coarse}}{V_w})}{1 + K_{d,b,fines}\frac{m_{d,fines}}{V_w} + K_{d,b,coarse}\frac{m_{d,coarse}}{V_w}} \quad \text{(S3.157)}$$

For the fines, the quasi-steady state aqueous concentration becomes:

$$C_{w,eq,quasi} = \frac{C_{w,p,ini}K_{d,b,fines}\frac{m_{d,fines}}{V_w}}{1 + K_{d,b,fines}\frac{m_{d,fines}}{V_w}} \quad \text{(S3.158)}$$

The ratio of the concentration changes in aqueous phase due to the contributions of fines and coarse particles ($\Delta C_{w,fines}/\Delta C_{w,coarse}$) also can be determined (taking the mixture containing 1% coarse particles as an example (orange symbols and lines in Figs. 3.6e and f in main text)):

$$\begin{aligned} \frac{\Delta C_{w,fines}}{\Delta C_{w,coarse}} &= \frac{\frac{C_{w,p,ini}K_{d,b,fines}\frac{m_{d,fines}}{V_w}}{1 + K_{d,b,fines}\frac{m_{d,fines}}{V_w}}}{\frac{C_{w,p,ini}(K_{d,b,fines}\frac{m_{d,fines}}{V_w} + K_{d,b,coarse}\frac{m_{d,coarse}}{V_w})}{1 + K_{d,b,fines}\frac{m_{d,fines}}{V_w} + K_{d,b,coarse}\frac{m_{d,coarse}}{V_w}} - \frac{C_{w,p,ini}K_{d,b,fines}\frac{m_{d,fines}}{V_w}}{1 + K_{d,b,fines}\frac{m_{d,fines}}{V_w}}} \\ &= \frac{\frac{100\ \frac{\mu g}{L} * 1000\frac{L}{kg} * 10^{-3}\frac{kg}{L} * 99\%}{1 + 1000\frac{L}{kg} * 10^{-3}\frac{kg}{L} * 99\%}}{\frac{100\ \frac{\mu g}{L} * (1000\frac{L}{kg} * 10^{-3}\frac{kg}{L} * 99\% + 100000\frac{L}{kg} * 10^{-3}\frac{kg}{L} * 1\%)}{1 + 1000\frac{L}{kg} * 10^{-3}\frac{kg}{L} * 99\% + 100000\frac{L}{kg} * 10^{-3}\frac{kg}{L} * 1\%} - \frac{100\ \frac{\mu g}{L} * 1000\frac{L}{kg} * 10^{-3}\frac{kg}{L} * 99\%}{1 + 1000\frac{L}{kg} * 10^{-3}\frac{kg}{L} * 99\%}} \\ &= 3 \end{aligned} \quad \text{(S3.159)}$$

For higher solid-to-liquid ratios (e.g., SL = 0.01 kg L^{-1}, see Fig. 3.6f in main text), $\Delta C_{w,fines}/\Delta C_{w,coarse}$ would again amount to 21. Unlike in sorptive uptake experiments, the initial concentration in the solids usually is measured in total (e.g., by accelerated solvent extraction). If the initial concentration is fitted from experiment data (as in test D see section 3.4.2 of main text), it again reflects only the less sorbing fine fraction and the concentration

in coarse particle is underestimated (much less than value obtained from ASE). This also applies to fitted concentration in intraparticle pore water ($C_{w,p,ini}$) and finally K_d values, which would be too low. The distribution coefficient based on extraction of the total sample is given as:

$$\begin{aligned} C_{w,p,ini}\left(K_{d,b,fines}m_{d,fines} + K_{d,b,coarse}m_{d,coarse}\right) \\ = C_{w,eq,quasi}\left(V_w + K^*_{d,b,fines}m_{d,fines}\right) \\ K^*_{d,b,fines} = \frac{C_{w,p,ini}\left(K_{d,b,fines}m_{d,fines} + K_{d,b,coarse}m_{d,coarse}\right)}{C_{w,eq,quasi}m_{d,fines}} - \frac{V_w}{m_{d,fines}} \end{aligned} \quad \text{(S3.160)}$$

where $K^*_{d,b,fines}$ [L³ M⁻¹] denotes the fitted distribution coefficient of fines based on the initial solute mass obtained from extraction. If only the solute mass stored in fines is considered, the solid-to-liquid ratio of fines is:

$$\begin{aligned} C_{w,p,ini}K_{d,b,fines}m_{d,fines} = C_{w,eq,quasi}\left(V_w + K_{d,b,fines}m_{d,fines}\right) \\ \frac{V_w}{m_{d,fines}} = K_{d,b,fines}\frac{\left(C_{w,p,ini} - C_{w,eq,quasi}\right)}{C_{w,eq,quasi}} \end{aligned} \quad \text{(S3.161)}$$

Inserting Eq. S3.161 into Eq. S3.160, the distribution coefficient of fines based on extraction can be simplified as:

$$\begin{aligned} K^*_{d,b,fines} &= K_{d,b,fines} + \frac{C_{w,p,ini}}{C_{w,eq,quasi}}\frac{m_{d,coarse}}{m_{d,fines}}K_{d,b,coarse} \\ &= 1000\frac{\text{L}}{\text{kg}} + \frac{100\ \frac{\mu\text{g}}{\text{L}}}{50\ \frac{\mu\text{g}}{\text{L}}} * \frac{1\%}{99\%} * 100000\frac{\text{L}}{\text{kg}} \\ &= 3000\ \frac{\text{L}}{\text{kg}} \end{aligned} \quad \text{(S3.162)}$$

$K^*_{d,b,fines}$ is three times of $K_{d,b,fines}$ for SL = 0.001 kg L^{-1} ($K^*_{d,b,fines} = 2110$ L kg^{-1} for SL = 0.01 kg L^{-1}) if 1% of coarse strong sorbent is considered.

The deviations of distribution coefficient between sorptive uptake experiment ($K_{d,b,fines}$) and desorption experiment ($K^*_{d,b,fines}$) are:

$$\Delta K_{d,b,fines} = \frac{C_{w,p,ini}}{C_{w,eq,quasi}}\frac{m_{d,coarse}}{m_{d,fines}}K_{d,b,coarse} \quad \text{(S3.163)}$$

$K_{d,b,coarse}$ can only be determined if the mass of coarse strong sorbents is known (e.g., using density separation method to determine the strong sorbents).

The biased distribution coefficient ($\Delta K_{d,b,fines}$) between sorption ($K_{d,b,fines}$) and desorption ($K^*_{d,b,fines}$) for short time (e.g., few days) batch experiments are confirmed by our modeling results (see Figs. S3.13c and d) for time scales of days to weeks. Equilibrium conditions are achieved after long time periods of a few years (see Figs. S3.13e and f) which usually never is covered in batch tests in the lab. These modelling results show how fitted parameters (e.g.,

initial compound mass (m_{tot}) and K_d values) from desorption experiments could be underestimated compared to independent measurements if majority of solute mass is stored in coarse strongly sorbing particles (see Phenanthrene redistribution in sediment suspension with passive sampler results in section 3.4.2 of main text).

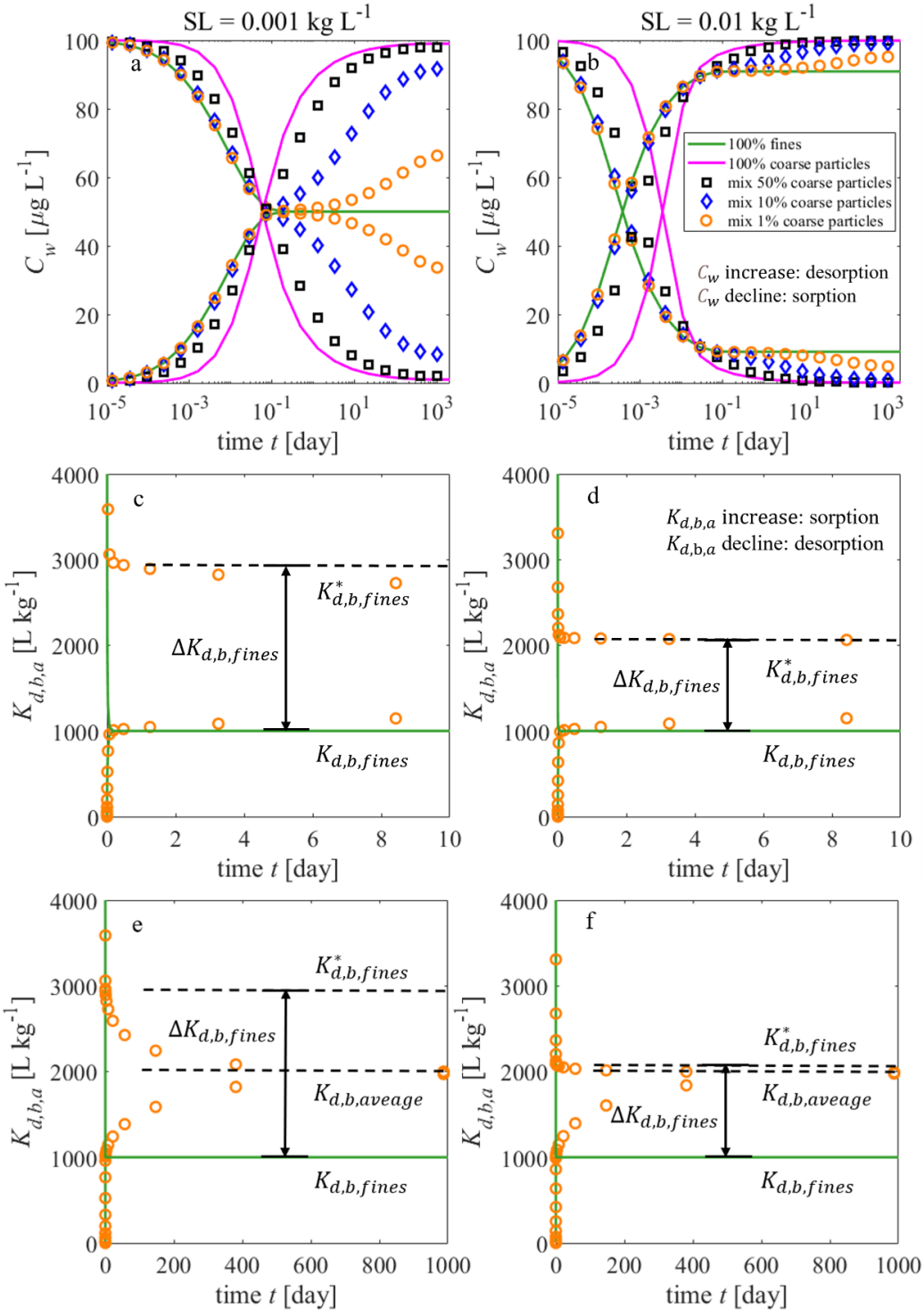

Fig. S3.13: Impact of heterogeneous sample composition on sorption/desorption kinetics

for a mixture of fines particles ($d_{sp,fine} = 40$ µm) with low sorption capacity ($K_d = 1000$ L kg^{-1}) and coarse particles ($d_{sp,coarse} = 400$ µm) with high sorption capacity ($K_d = 100\,000$ L kg^{-1}) for two solid-to-liquid ratios (SL = 0.001 and 0.01 kg L^{-1}); solid green and magenta lines represent fine and coarse pure particles (homogeneous sample) while symbols represent the mixtures, which are slower than the coarse particles alone. (a) and (b): Aqueous concentration (C_w) vs. time (t) of pure (solid lines) and bi-modal material compositions of fine and coarse particles with 1% coarse particles (orange circles), 10% coarse particles (blue diamonds) and 50% coarse particles (black squares); (c) and (d): Short term behavior of apparent distribution coefficient ($K_{d,b,a}$) vs. time (t) for the cases of fines (green lines) containing 1% coarse particles (orange circles); (e) and (f): Long term behavior of apparent distribution coefficient ($K_{d,b,a}$) vs. time (t). Fitted distribution coefficients differ between sorptive uptake ($K_{d,b,fines}$) and desorption experiments ($K^*_{d,b,fines}$) at short to intermediate time scales (c and d) and very long time periods are needed until they converge to the final equilibrium average distribution coefficient ($K_{d,b,average}$); D_{aq} = 7.6 × 10^{-10} m^2 s^{-1}; ρ_s = 2.7 kg L^{-1}; ε = 0.2; ε_{disp} = 10$^{-1.5}$ m^2 s^{-3}; ν = 10^{-6} m^2 s^{-1}; all simulations are based on coupled film-intraparticle pore diffusion model.

References

Boving, T.B., Grathwohl, P., 2001. Tracer diffusion coefficients in sedimentary rocks: correlation to porosity and hydraulic conductivity. J. Contam. Hydrol. 53, 85–100. https://doi.org/10.1016/S0169-7722(01)00138-3.

Crank, J., 1975. The Mathematics of Diffusion. 2nd Ed. Oxford University Press, London.

Grathwohl, P., 1998. Diffusion in Natural Porous Media: Contaminant Transport, Sorption/Desorption and Dissolution Kinetics. Kluwer Academic Publishers: Norwell, MA.

Liu, B., Finkel, M., Grathwohl, P., 2022. First order approximation for coupled film and intraparticle pore diffusion to model sorption/desorption batch experiments. J. Hazard. Mater. 429, 128314. https://doi.org/10.1016/j.jhazmat.2022.128314.

Seidensticker, S., Zarfl, C., Cirpka, O.A., Fellenberg, G., Grathwohl, P., 2017. Shift in mass transfer of wastewater contaminants from microplastics in the presence of dissolved substances. Environ. Sci. Technol. 51, 12254–12263. https://doi.org/10.1021/acs.est.7b02664.

S4 Supplementary information for modeling of particle/gas distribution kinetics of polycyclic aromatic hydrocarbons (PAHs) in the atmosphere: Relevance of mass transfer resistance shifts

S4.1 Molecular mass, octanol-air partitioning coefficients and supercooled liquid vapor pressures of PAHs

Tab. S4.1: Physical and chemical properties of PAHs (from Lei et al., 2002; Odabasi et al., 2006)

PAHs	Structure (# of rings)	Molar mass [g mol^{-1}]	LogK_{oa} at 25°C	LogP_L^o at 25°C [Pa]
Naphthalene (Nap)	2	128.17	4.81	1.56
Acenaphthylene (Acy)	3	152.20	6.33	0.35
Acenaphthene (Ace)	3	154.21	6.51	0.18
Fluorene (FI)	3	166.22	6.89	-0.23
Phenanthrene (Phe)	3	178.23	7.67	-1.07
Anthracene (Ant)	3	178.23	7.71	-1.11
Fluoranthene (Flu)	4	202.26	8.75	-2.23
Pyrene (Pyr)	4	202.26	8.81	-2.21
Benz[*a*]anthracene (BaA)	4	228.29	10.28	-3.45
Chrysene (Chr)	4	228.29	10.29	-3.89
Benzo[*b*]fluoranthene (BbF)	5	252.32	11.33	-4.79
Benzo[*k*]fluoranthene (BkF)	5	252.32	11.36	-4.82
Benzo[*a*]pyrene (BaP)	5	252.32	11.55	-5.03
Indeno[*1,2,3-cd*]pyrene (InP)	6	276.34	12.42	-5.96
Dibenzo[*a,h*]anthracene (DBA)	5	278.35	12.58	-6.12
Dibenzo[*a,h*]pyrene (DahP)	6	302.37	12.58	-6.12
Benzo[*g,h,i*]perylene (BghiP)	6	276.33	12.54	-6.09

Tab. S4.2: Parameters A_o, B_o, b_L and m_L for temperature correction. (from Lei et al., 2002; Odabasi et al., 2006)

PAHs	A_o	B_o	b_L	m_L
Nap	1.57	965	11.39	-2930
Acy	-1.97	2476	9.93	-2855
Ace	-2.20	2597	10.17	-2979
FI	-2.61	2833	10.61	-3233
Phe	-3.37	3293	11.43	-3726
Ant	-3.41	3316	11.47	-3750
Flu	-4.34	3904	12.47	-4382
Pyr	-4.56	3985	11.70	-4146

BaA	-5.64	4746	10.87	-4269
Chr	-5.65	4754	13.87	-5294
BbF	-6.40	5285	12.48	-5148
BkF	-6.42	5301	12.50	-5165
BaP	-6.50	5382	12.59	-5252
InP	-7.00	5791	13.13	-5691
DBA	-7.17	5887	13.31	-5794
DahP	-7.17	5887	13.31	-5794
BghiP	-7.03	5834	13.15	-5737

S4.2 Apparent distribution coefficients of external film diffusion under non-equilibrium condition

Apparent bulk distribution coefficients ($K_{pg,b,a}$) are quite often used in comparison of sorption kinetics data from different scenarios, because the sorptive uptake data to some extent is independent on solid to volume ratios (m_d/V_g, which is equivalent to the concentration of total suspended particles (TSP) in gas phase). Many research papers show inconsistencies between measured bulk distribution coefficients ($K_{pg,b,a}$) and equilibrium bulk distribution coefficients ($K_{pg,b}$) derived either from octanol-air distribution coefficients (K_{oa}) or subcooled liquid vapor pressures (P_L^o) of targeted compounds. This indicates non-equilibrium condition and sorption kinetics may play a role (Mu et al., 2014; Ma et al., 2020; Parnis et al., 2020; Zhao et al., 2021). Often deviations in slopes (much less than 1; slope (m =1) in empirical relationships (e.g., $\log K_{pg,b,a} = m^*\log K_{oa} + b$ or $\log K_{pg,b,a} = -m^*\log P_L^o + c$ where b and c are constants.) are observed and finally a maximum distribution coefficients obtained (= constant $K_{pg,b,a}$) independent on the compounds' K_{oa} or P_L^o. Such a plateau is well explained by the external film diffusion model (FD) whose analytical solution for porous spherical particles (see Liu et al., 2022) is given as (for sorptive uptake):

$$\frac{C_p}{C_{p,eq}} = 1 - \exp\left(-\frac{k}{K_{pg,b}}\frac{6}{\rho_p\, d}\left(1 + K_{pg,b}\frac{m_d}{V_g}\right)t\right) \qquad \text{(S4.1)}$$

where C_p [M L^{-3}] and $C_{p,eq}$ [M L^{-3}] denote the pollutant concentration in suspended particles at time t and at equilibration, respectively. d [L] is the grain size of the particles. k [L T^{-1}] is the first order mass transfer velocity ($k = D_g/\delta$; D_g [L^2 T^{-1}] is the gaseous diffusion coefficient of the pollutants and δ [L] is the external film thickness of suspended particles, which can be estimated via dimensionless Sherwood numbers ($Sh = d/\delta$; for spherical particles $Sh \geq 2$). ρ_p (= $\rho_s(1-\varepsilon)$) [M L^{-3}] is the bulk density of the suspended particles where ρ_s [M L^{-3}] and ε [-] denote the dry density and intraparticle porosity of suspended particles, respectively. $K_{pg,b}$ (= $K_{pg} + \varepsilon/\rho_p$) [L^3 M^{-1}] is the distribution coefficient between

gas and porous suspended particles, which also considers the pollutant mass stored in the intraparticle pore space.

The relative distribution coefficients are defined as ratio of apparent distribution coefficients $K_{pg,b,a}$ to the equilibrium distribution coefficients:

$$\frac{K_{pg,b,a}}{K_{pg,b}} = \frac{C_p/C_g}{C_{p,eq}/C_{g,eq}} = \frac{C_p/C_{p,eq}}{C_g/C_{g,eq}} \tag{S4.2}$$

where C_g [M L^{-3}] and $C_{g,eq}$ [M L^{-3}] denote the pollutant concentration in gas phase at time t and at equilibration, respectively.

The numerator of Eq. S4.2 can be expressed by Eq. S4.1 and the denominator of Eq. S4.2 can be determined by considering mass conservation where all pollutant mass initially is stored in gas phase.

$$\begin{aligned} C_{g,0}V_g &= C_{g,eq}\left(V_g + K_{pg,b}m_d\right) \\ C_{g,0} &= C_{g,eq}\left(1 + K_{pg,b}\frac{m_d}{V_g}\right) \end{aligned} \tag{S4.3}$$

Realizing that $(C_{g,0} - C_{g,eq})\,V_g$ represents the mass sorbed under equilibrium condition $(C_{p,eq}V_g)$ and $(C_{g,0} - C_g)\,V_g$ equals to (C_pV_g) leads to:

$$\frac{C_{g,0} - C_g}{C_{g,0} - C_{g,eq}} = 1 - \exp\left(-\frac{k}{K_{pg,b}}\frac{6}{\rho_p\, d}\left(1 + K_{pg,b}\frac{m_d}{V_g}\right)t\right) \tag{S4.4}$$

Inserting Eq. S4.3 into Eq. S4.4, $C_g/C_{g,eq}$ becomes:

$$\frac{C_g}{C_{g,eq}} = 1 + K_{pg,b}\frac{m_d}{V_g}\exp\left(-\frac{k}{K_{pg,b}}\frac{6}{\rho_p\, d}\left(1 + K_{pg,b}\frac{m_d}{V_g}\right)t\right) \tag{S4.5}$$

Putting Eq. S4.1 and Eq. S4.5 into Eq. S4.2 leads to relative distribution coefficients:

$$\frac{K_{pg,b,a}}{K_{pg,b}} = \frac{1 - \exp\left(-\frac{k}{K_{pg,b}}\frac{6}{\rho_p\, d}\left(1 + K_{pg,b}\frac{m_d}{V_g}\right)t\right)}{1 + K_{pg,b}\frac{m_d}{V_g}\exp\left(-\frac{k}{K_{pg,b}}\frac{6}{\rho_p\, d}\left(1 + K_{pg,b}\frac{m_d}{V_g}\right)t\right)} \tag{S4.6}$$

In the infinite bath ($K_{pg,b}\frac{m_d}{V_g} \ll 1$ or $\beta(=\frac{V_g}{K_{pg,b}m_d}) \gg 1$), $1 + K_{pg,b}\frac{m_d}{V_g}$ approaches to 1 and the term $\left(K_{pg,b}\frac{m_d}{V_g}\exp\left(-\frac{k}{K_{pg,b}}\frac{6}{\rho_p\, d}\left(1 + K_{pg,b}\frac{m_d}{V_g}\right)t\right)\right)$ can be neglected, which leads to:

$$\frac{K_{pg,b,a}}{K_{pg,b}} = 1 - \exp\left(-\frac{k}{K_{pg,b}}\frac{6}{\rho_p\, d}t\right) \tag{S4.7}$$

Note that 1-exp(-x)≈x when x is small. $K_{pg,b,a}$ at early time in infinite bath can be expressed by:

$$K_{pg,b,a} = k\frac{6}{\rho_p\, d}t \tag{S4.8}$$

In this case $K_{pg,b,a}$ becomes independent on compound properties (besides D_g) and TSP.

In case the sorbent takes it all ("infinite sorption") ($K_{pg,b}\frac{m_d}{V_g} \gg 1$ or $\beta \ll 1$), $1 + K_{pg,b}\frac{m_d}{V_g}$ approaches to $K_{pg,b}\frac{m_d}{V_g}$ and the term $\left(K_{pg,b}\frac{m_d}{V_g}\exp\left(-\frac{k}{K_{pg,b}}\frac{6}{\rho_p\, d}\left(1 + K_{pg,b}\frac{m_d}{V_g}\right)t\right)\right)$ is much larger than 1, which leads to:

$$\frac{K_{pg,b,a}}{K_{pg,b}} = \frac{1 - \exp\left(-k\frac{6}{\rho_p\, d}\frac{m_d}{V_g}t\right)}{K_{pg,b}\frac{m_d}{V_g}\exp\left(-k\frac{6}{\rho_p\, d}\frac{m_d}{V_g}t\right)} \tag{S4.9}$$

At early times, $K_{pg,b,a}$ in the infinite sorption case can be expressed by:

$$K_{pg,b,a} = \frac{k\frac{6}{\rho_p\, d}t}{\exp\left(-k\frac{6}{\rho_p\, d}\frac{m_d}{V_g}t\right)} \tag{S4.10}$$

In this case, $K_{pg,b,a}$ depends on the airborne particle concentration (TSP or m_d/V_g) in contrast to the infinite bath (Eq. S4.8).

Log$K_{pg,b,a}$ vs. Log$K_{pg,b}$ curves of external film diffusion under different particle concentrations (TSP = 20 or 200 μg m^{-3}) with different contact times (t = 1e2, 1e3, 1e4 and 1e5 s) are presented in Fig. S4.1. At early times (t = 100 s), particle concentrations (TSP) have not much influence on FD (see red lines in Fig. S4.1), while with increasing TSP higher Log$K_{pg,b,a}$ values are obtained at late times (t = 1e3 and 1e4; see green and blue lines in Fig. S4.1) especially for compounds with large Log$K_{pg,b}$. FD shows a slope of 1 for compounds with small Log$K_{pg,b}$ as well as a maximum Log$K_{pg,b,a}$ domain for compounds with large Log$K_{pg,b}$ at early times. With the increase of contact times, higher degree of equilibration is reached, and the slope gradually shifts to 1 even for compounds with large Log$K_{pg,b}$ at late times.

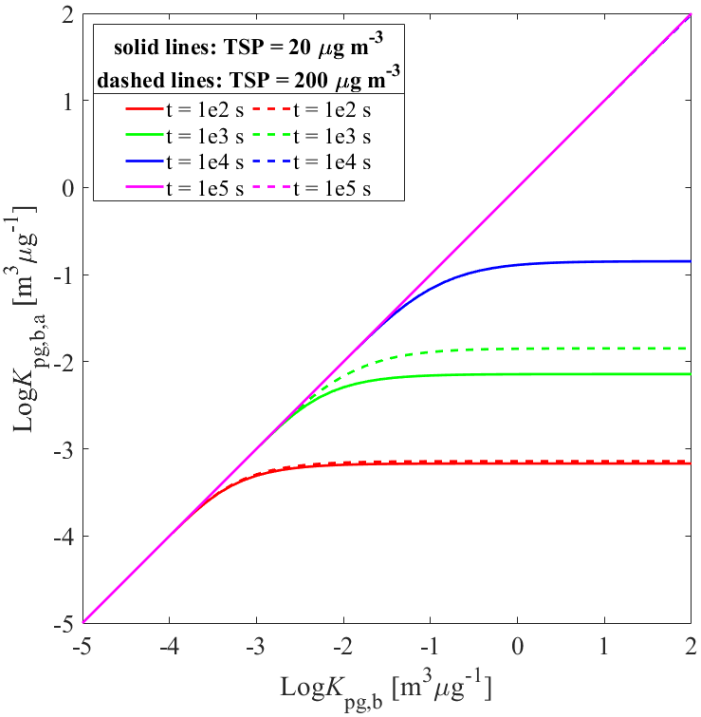

Fig. S4.1: Log$K_{pg,b,a}$ vs. Log$K_{pg,b}$ of external film diffusion at different times (increasing from bottom to top). (D_g = 6e-6 m^2 s^{-1}; $Sh = 2$; d = 2.5 μm; $k = D_g Sh/d$ = 4.8 m s^{-1}; TSP = m_d/V_g = 20 or 200 μg m^{-3}; ρ_s = 1.8 kg L^{-1}; $\varepsilon = 0.05$)

S4.3 Apparent distribution coefficients of intraparticle pore diffusion under non-equilibrium condition

The analytical solution of intraparticle pore diffusion in finite bath for spherical particles is given as (Crank, 1975):

$$\frac{M}{M_{eq}} = 1 - \sum_{n=1}^{\infty} \frac{6\beta(\beta+1)}{9+9\beta+q_n^2\beta^2} \exp\left[-q_n^2 \frac{D_a}{a^2} t\right] \tag{S4.11}$$

where M [M] and M_{eq} [M] denote the mass of pollutants, which has diffused into or out of suspended particles after time t and after equilibrium is reached, respectively.

For sorptive uptake scenarios, $C_p/C_{p,eq}$ can be expressed by Eq. S4.11 and $C_g/C_{g,eq}$ also can be determined by accounting for the mass conservation (Eq. S4.3):

$$\frac{C_g}{C_{g,eq}} = \left(1+\frac{1}{\beta}\right) - \frac{1}{\beta}\frac{C_p}{C_{p,eq}} \tag{S4.12}$$

Thus, the relative distribution coefficients of intraparticle pore diffusion become:

$$\frac{K_{pg,b,a}}{K_{pg,b}} = \frac{\frac{C_p}{C_{p,eq}}}{\frac{C_g}{C_{g,eq}}} = \frac{\frac{C_p}{C_{p,eq}}}{\left(1+\frac{1}{\beta}\right) - \frac{1}{\beta}\frac{C_p}{C_{p,eq}}} = \frac{1 - \sum_{n=1}^{\infty} \frac{6\beta(\beta+1)}{9+9\beta+q_n^2\beta^2} \exp\left[-q_n^2 \frac{D_a}{a^2} t\right]}{\left(1+\frac{1}{\beta}\right) - \frac{1}{\beta}\left(1 - \sum_{n=1}^{\infty} \frac{6\beta(\beta+1)}{9+9\beta+q_n^2\beta^2} \exp\left[-q_n^2 \frac{D_a}{a^2} t\right]\right)} \tag{S4.13}$$

In the infinite bath condition ($\beta \gg 1$), series expansion solution (Eq. S4.11) can be simplified as:

$$\frac{M}{M_{eq}} = 1 - \frac{6}{\pi^2} \sum_{n=1}^{\infty} \frac{1}{n^2} \exp\left[-n^2 \frac{D_a}{a^2} t\right] \tag{S4.14}$$

For short term approximation, square root of time solution can be used.

$$\frac{M}{M_{eq}} = 6\sqrt{\frac{D_a t}{\pi a^2}} \tag{S4.15}$$

Inserting Eq. S4.15 into Eq. S4.13 and D_a is estimated via Eq. 4.12 in the main text. $K_{pg,b,a}$ becomes:

$$K_{pg,b,a} = 6\sqrt{\frac{D_p K_{pg,b} t}{\pi a^2}} \tag{S4.16}$$

For long term approximation, first term of series expansion can be utilized. Similar to short term case, $K_{pg,b,a}$ can be expressed by:

$$K_{pg,b,a} = \left(1 - \frac{6}{\pi^2} \exp\left[-\frac{D_p}{K_{pg,b}\, a^2} t\right]\right) K_{pg,b} \tag{S4.17}$$

In the infinite sorption case ($\beta \ll 1$), we could modify the square root of time in finite bath (Eq. 4.14 in main text) as:

$$\frac{M}{M_{eq}} = \frac{6}{\beta}\sqrt{\frac{D_a t}{\pi a^2}} \tag{S4.18}$$

Inserting Eq. S4.18 into Eq. S4.13, short term approximation of $K_{pg,b,a}$ in the infinite sorption case can be expressed by:

$$\frac{K_{pg,b,a}}{K_{pg,b}} = \frac{\frac{C_p}{C_{p,eq}}}{\frac{1}{\beta} - \frac{1}{\beta}\frac{C_p}{C_{p,eq}}} = \frac{6\sqrt{\frac{D_a t}{\pi a^2}}}{\left(1 - \frac{6}{\beta}\sqrt{\frac{D_a t}{\pi a^2}}\right)} \approx 6\sqrt{\frac{D_a t}{\pi a^2}} \text{ (when } t \text{ is small)}$$
$$K_{pg,b,a} \approx 6\sqrt{\frac{D_p K_{pg,b} t}{\pi a^2}} \tag{S4.19}$$

For long term approximation of infinite sorption, first term of series expansion solution (Eq. S4.11) can be simplified as:

$$\frac{M}{M_{eq}} = 1 - \frac{2}{3}\beta \exp\left[-\pi^2 \frac{D_a}{a^2} t\right] \tag{S4.20}$$

Thus, $K_{pg,b,a}$ is given as:

$$\frac{K_{pg,b,a}}{K_{pg,b}} = \frac{\frac{C_p}{C_{p,eq}}}{\frac{1}{\beta} - \frac{1}{\beta}\frac{C_p}{C_{p,eq}}} = \frac{1 - \frac{2}{3}\beta \exp\left[-\pi^2 \frac{D_a}{a^2} t\right]}{\frac{2}{3}\exp\left[-\pi^2 \frac{D_a}{a^2} t\right]}$$
$$K_{pg,b,a} = \frac{K_{pg,b} - \frac{2}{3}\frac{V_g}{m_d}\exp\left[-\pi^2 \frac{D_a}{a^2} t\right]}{\frac{2}{3}\exp\left[-\pi^2 \frac{D_a}{a^2} t\right]} \tag{S4.21}$$

In summary, for infinite bath condition ($\beta \gg 1$) of IPPD, $K_{pg,b,a}$ is independent on particle concentration (TSP); this also applies for the infinite sorption case ($\beta \ll 1$) at early times. Only at late times the particle concentration (TSP) shows a minor effect.

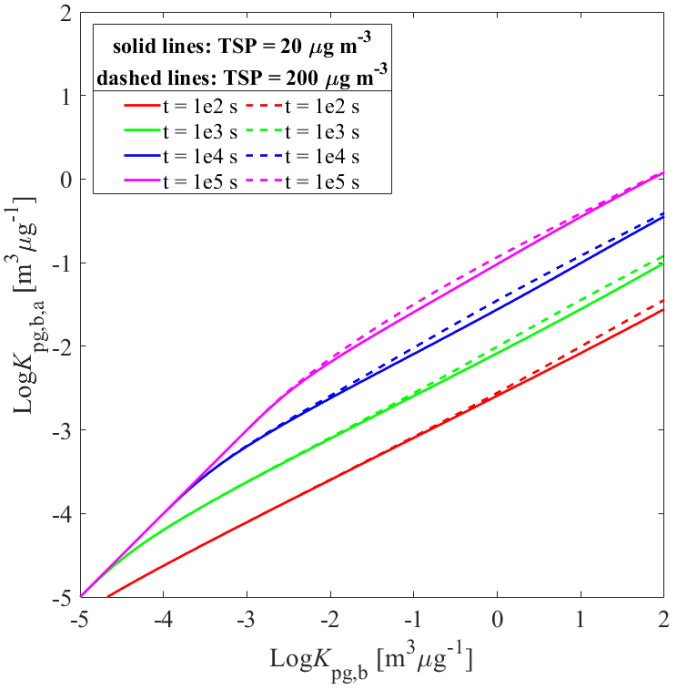

Fig. S4.2: Log$K_{pg,b,a}$ vs. Log$K_{pg,b}$ of intraparticle pore diffusion at different times (time increase from bottom to top). (D_g = 6e-6 m^2 s^{-1}; d = 2.5 μm; TSP = m_d/V_g = 20 or 200 μg m^{-3}; ρ_s = 1.8 kg L^{-1}; ε = 0.05; n = 5000 in Eq. S4.13)

S4.4 Apparent distribution coefficients derived from semi-Laplace solution for coupled film-intraparticle pore diffusion

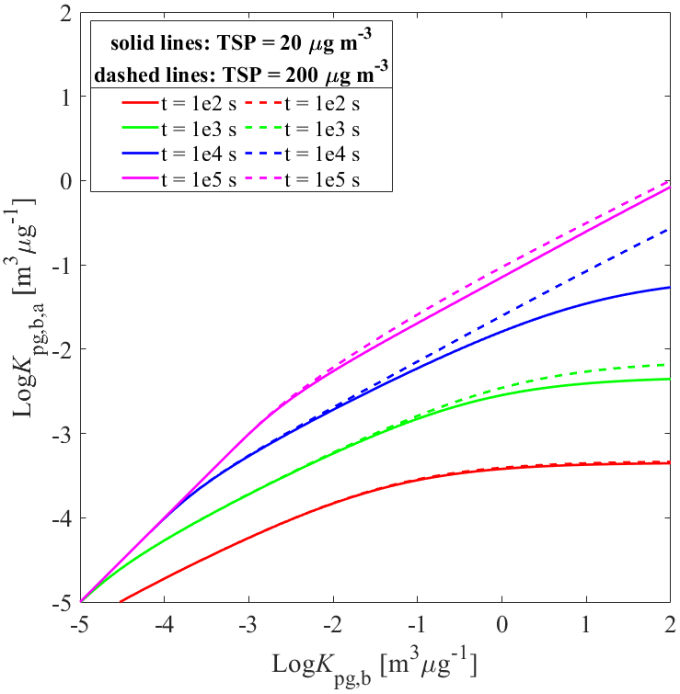

Fig. S4.3: Log$K_{pg,b,a}$ vs. Log$K_{pg,b}$ of coupled film-intraparticle pore diffusion at different times (time increase from bottom to top). (D_g = 6e-6 m^2 s^{-1}; d = 2.5 μm; TSP = m_d/V_g = 20 or 200 μg m^{-3}; ρ_s = 1.8 kg L^{-1}; ε = 0.05)

S4.5 PAHs emission from oils combustion

Tab. S4.3: PAH concentrations (in μg m^{-3}) in gaseous and particle phases from fuel combustion (condensate, diesel and heavy oil) as well as information of sampling temperature (T; in unit of K), airborne particle concentration (TSP; in unit of μg m^{-3}), organic carbon content (f_{om}), elemental carbon content (f_{ec}) and specific surface area of elemental carbon (a_{ec}; in unit of m^2 g^{-1}). (Data from Yin et al., 2022)

PAHs	Condensate		Diesel		Heavy oil	
	Gas phase	Particle phase	Gas phase	Particle phase	Gas phase	Particle phase
Nap	2.98±0.27	0.21±0.05	9.04±1.53	0.18±0.05	12.26±0.25	0.29±0.03
Acy	0.39±0.07	0.07±0.02	0.90±0.01	0.36±0.01	2.08±0.29	0.63±0.16
Ace	0.29±0.07	0.09±0.02	0.29±0.03	0.02±0.00	0.17±0.03	0.14±0.04
Fl	0.44±0.03	0.10±0.03	0.29±0.12	0.25±0.05	0.39±0.05	0.39±0.00

Phe	0.91±0.06	0.35±0.04	0.58±0.11	2.00±0.24	0.59±0.01	4.14±1.19
Ant	0.09±0.00	0.06±0.01	0.08±0.00	0.62±0.07	0.08±0.02	1.13±0.31
Flu	0.29±0.04	0.73±0.02	0.21±0.05	3.09±0.89	0.21±0.00	6.95±0.05
Pyr	1.17±0.46	1.21±0.27	1.38±0.07	3.99±0.98	0.93±0.10	7.86±0.92
BaA	0.12±0.02	0.53±0.11	0.13±0.01	1.35±0.41	0.08±0.02	3.76±0.48
Chr	0.12±0.03	0.68±0.09	0.17±0.04	1.61±0.37	0.10±0.00	5.78±0.24
BbF	0.13±0.01	0.39±0.05	0.11±0.00	1.06±0.06	0.09±0.03	2.32±0.74
BkF	0.08±0.00	0.49±0.04	0.07±0.00	1.44±0.04	0.09±0.05	2.69±0.63
BaP	0.11±0.01	0.71±0.18	0.09±0.00	2.28±0.02	0.06±0.00	4.04±0.75
InP	0.08±0.01	0.90±0.01	0.07±0.01	2.13±0.18	0.04±0.01	4.15±1.30
DahP	0.08±0.00	0.06±0.01	0.08±0.02	0.15±0.00	0.05±0.01	0.65±0.05
BghiP	0.06±0.01	0.64±0.15	0.04±0.01	1.44±0.18	0.04±0.01	2.63±0.54
Total	7.34±1.05	7.22±1.10	13.56±2.01	22.00±3.55	17.26±0.88	47.53±7.43
TSP	315750		280147		380817	
T	305.15		305.15		305.15	
f_{om}	0.30		0.50		0.65	
f_{ec}	0.41		0.65		0.32	
a_{ec}	38.1		38.1		38.1	

Tab. S4.4: LogK_{pg} (in unit of m^3 μg^{-1}) values of 16 EPA PAHs based on the absorption and dual mode models.

PAHs	Condensate			Diesel			Heavy oil		
	Measured	Absorption model	Dual model	Measured	Absorption model	Dual model	Measured	Absorption model	Dual model
Nap	-6.65±0.07	-7.70	-6.37	-7.15±0.05	-7.48	-6.16	-7.21±0.04	-7.36	-6.44
Acy	-6.24±0.05	-6.29	-5.31	-5.84±0.01	-6.07	-5.10	-6.10±0.05	-5.95	-5.34
Ace	-6.03±0.05	-6.12	-5.16	-6.52±0.05	-5.90	-4.96	-5.66±0.05	-5.79	-5.19
FI	-6.16±0.10	-5.76	-4.83	-5.52±0.10	-5.54	-4.62	-5.58±0.06	-5.42	-4.85
Phe	-5.91±0.02	-5.01	-4.14	-4.91±0.03	-4.79	-3.94	-4.73±0.12	-4.68	-4.16
Ant	-5.68±0.07	-4.98	-4.11	-4.57±0.05	-4.75	-3.90	-4.43±0.01	-4.64	-4.12
Flu	-5.10±0.05	-3.98	-3.18	-4.28±0.02	-3.76	-2.98	-4.06±0.00	-3.64	-3.18
Pyr	-5.48±0.08	-3.93	-3.18	-4.99±0.09	-3.71	-2.97	-4.66±0.00	-3.60	-3.17
BaA	-4.86±0.02	-2.52	-2.04	-4.43±0.10	-2.30	-1.83	-3.93±0.06	-2.18	-1.95
Chr	-4.74±0.05	-2.50	-1.81	-4.48±0.00	-2.28	-1.61	-3.81±0.02	-2.17	-1.79
BbF	-5.02±0.02	-1.51	-0.98	-4.46±0.02	-1.29	-0.78	-4.19±0.01	-1.18	-0.91
BkF	-4.71±0.04	-1.48	-0.95	-4.16±0.01	-1.26	-0.75	-4.12±0.17	-1.15	-0.88
BaP	-4.67±0.07	-1.30	-0.78	-4.05±0.00	-1.07	-0.57	-3.73±0.08	-0.96	-0.70
InP	-4.47±0.05	-0.46	0.01	-3.95±0.03	-0.23	0.21	-3.56±0.03	-0.12	0.11
DahP	-5.58±0.07	-0.31	0.15	-5.18±0.11	-0.09	0.35	-4.45±0.05	0.03	0.25
BghiP	-4.48±0.03	-0.34	0.12	-3.94±0.06	-0.12	0.33	-3.77±0.02	-0.01	0.22

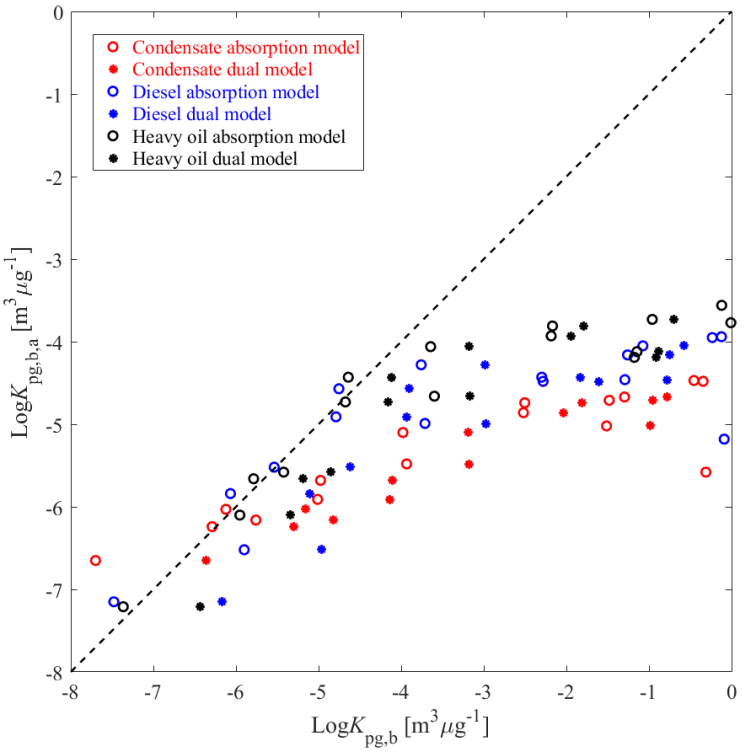

Fig. S4.4: Measured apparent gas/particle bulk distribution coefficients (Log$K_{pg,b,a}$) vs. equilibrium bulk gas/particle distribution coefficients (Log$K_{pg,b}$) based on absorption model (open circle symbols) and dual model (solid circle symbols) for PAHs emissions from three fuels (condensate (red), diesel (blue) and heavy oil (black).). The dashed black line denotes a 1:1 relationship.

S4.6 Domestic heating impacts on particle/gas partitioning of PAHs in a northern urban city of China

Tab. S4.5: PAHs concentrations (in unit of ng m^{-3}) in gaseous and particle phases sampling in a northern city of China (Yuncheng) as well as information on sampling temperature (T in K), particle concentration (TSP in μg m^{-3}), organic carbon content (f_{om}), elemental carbon content (f_{ec}) and specific surface area of elemental carbon (a_{ec}; in unit of m^2 g^{-1}) by considering the diurnal variation as well as the impact of domestic heating (Data from Sun et al., 2022).

PAHs	Non-heating				Heating			
	Day		Night		Day		Night	
	Gas phase	Particle phase	Gas phase	Particle phase	Gas phase	Particle phase	Gas phase	Particle phase
Nap	7.57	3.66	9.13	3.33	10.18	2.89	34.99	2.77
Acy	0.56	0.69	2.11	0.64	4.28	1.12	30.74	1.33

Ace	0.75	0.26	1.44	0.25	1.42	0.24	4.71	0.25
FI	4.80	0.33	7.64	0.36	20.65	0.60	26.97	0.83
Phe	8.07	1.48	9.49	1.39	26.24	5.10	30.21	7.53
Ant	0.50	0.26	0.60	0.34	2.04	0.83	3.16	2.12
Flu	2.70	2.80	2.71	2.95	8.15	12.61	6.14	22.57
Pyr	1.30	4.76	1.62	4.41	3.93	11.43	3.01	18.93
BaA	0.05	0.86	0.08	1.87	0.04	5.98	0.05	14.49
Chr	0.16	1.57	0.17	2.55	0.05	7.77	0.05	13.88
BbF	0.03	2.39	0.03	3.97	0.03	9.65	0.03	17.40
BkF	0.02	0.71	0.02	1.11	0.02	2.24	0.02	4.27
BaP	0.04	1.16	0.04	2.18	0.04	4.22	0.04	9.62
InP	0.05	1.73	0.05	2.76	0.05	5.08	0.05	9.48
DBA	0.05	0.62	0.05	0.83	0.05	1.44	0.05	2.61
BghiP	0.04	1.63	0.03	2.49	0.03	4.58	0.03	8.79
Total	26.69	24.91	35.21	31.43	77.20	75.78	140.25	136.87
TSP	56.69		66.19		75.73		82.76	
T	286.15		275.15		279.15		265.15	
f_{om}	0.36		0.33		0.37		0.46	
f_{ec}	0.06		0.07		0.08		0.09	
a_{ec}	100		100		100		100	

Tab. S4.6: LogK_{pg} (in unit of $m^3\ \mu g^{-1}$) values of 16 EPA targeted PAHs based on absorption model and dual model.

PAHs	Non-heating						Heating					
	Day			Night			Day			Night		
	Measured	Absorption model	Dual model	Measured	Absorption model	Dual model	Measured	Absorption model	Dual model	Measured	Absorption model	Dual model
Nap	-2.07	-7.41	-6.23	-2.26	-7.31	-5.83	-2.43	-7.31	-5.90	-3.02	-7.04	-5.38
Acy	-1.66	-5.67	-5.10	-2.34	-5.36	-4.72	-2.46	-5.44	-4.79	-3.28	-4.88	-4.27
Ace	-2.21	-5.48	-4.93	-2.58	-5.15	-4.54	-2.65	-5.24	-4.61	-3.19	-4.65	-4.07
FI	-2.92	-5.06	-4.54	-3.15	-4.71	-4.12	-3.42	-4.80	-4.21	-3.43	-4.17	-3.62
Phe	-2.49	-4.22	-3.75	-2.66	-3.79	-3.27	-2.59	-3.92	-3.38	-2.52	-3.20	-2.71
Ant	-2.04	-4.18	-3.71	-2.07	-3.75	-3.23	-2.27	-3.87	-3.34	-2.09	-3.15	-2.66
Flu	-1.74	-3.05	-2.65	-1.78	-2.54	-2.09	-1.69	-2.70	-2.23	-1.35	-1.86	-1.45
Pyr	-1.19	-2.99	-2.65	-1.39	-2.47	-2.11	-1.42	-2.63	-2.25	-1.12	-1.78	-1.47
BaA	-0.52	-1.41	-1.27	-0.45	-0.78	-0.66	0.30	-0.98	-0.84	0.54	0.01	0.09
Chr	-0.76	-1.39	-1.07	-0.64	-0.76	-0.40	0.31	-0.96	-0.59	0.53	0.03	0.35
BbF	0.15	-0.28	-0.11	0.30	0.42	0.58	0.63	0.19	0.37	0.85	1.28	1.40
BkF	-0.20	-0.25	-0.08	-0.08	0.45	0.62	0.17	0.23	0.41	0.41	1.33	1.44
BaP	-0.29	-0.05	0.12	-0.08	0.67	0.82	0.14	0.44	0.61	0.46	1.55	1.66
InP	-0.21	0.88	1.02	-0.08	1.66	1.78	0.13	1.40	1.55	0.36	2.59	2.68
DBA	-0.66	1.05	1.18	-0.60	1.83	1.96	-0.42	1.58	1.72	-0.20	2.79	2.87
BghiP	-0.14	1.00	1.14	0.10	1.78	1.91	0.30	1.53	1.67	0.55	2.73	2.82

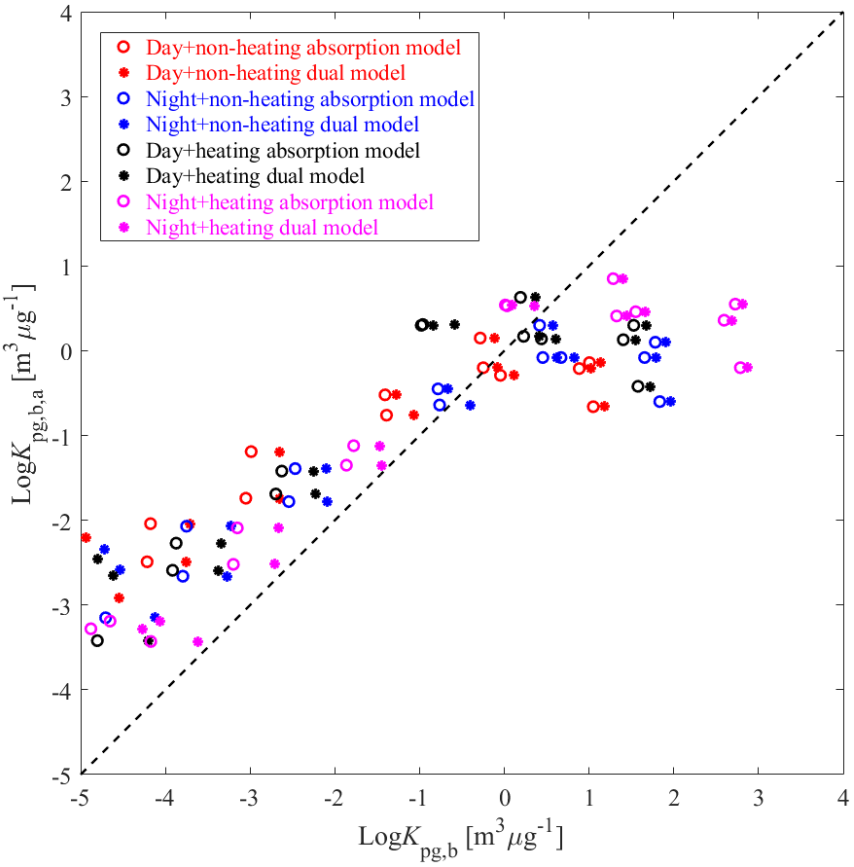

Fig. S4.5: Measured apparent bulk gas/particle distribution coefficients (Log$K_{pg,b,a}$) vs. equilibrium bulk gas/particle distribution coefficients (Log$K_{pg,b}$) based on the absorption model (open circle symbols) and dual model (solid circle symbols) for PAHs sampling in a northern China city (Yuncheng) by considering the diurnal variation as well as the impact of domestic heating. The dashed black line denotes a 1:1 relationship.

S4.7 PAHs sampling in the marine atmosphere from the Western Pacific to the Southern Ocean

Tab. S4.7: PAH concentrations (in pg m^{-3}) in gaseous and particle phases sampled in the marine atmosphere from the Western Pacific to the Southern Ocean (32 locations) as well as information on sampling temperature (T in K), airborne particle concentration (TSP in μg m^{-3}), organic carbon content (f_{om}), elemental carbon content (f_{ec}) and specific surface area of elemental carbon (a_{ec} in m^2 g^{-1}) (Data from Zhang et al., 2022).

PAHs	A1		A2		A3		A4	
	Gas phase	Particle phase	Gas phase	Particle phase	Gas phase	Particle phase	Gas phase	Particle phase
Acy	96	6.0	41	3.6	230	5.4	210	8.8
Ace	84	5.4	87	6.1	440	9.4	470	20

FI	180	22	120	23	400	39	370	85
Phe	1300	75	460	70	1400	120	1500	280
Ant	150	12	57	9.5	170	16	160	39
Flu	91	9.8	100	9.2	360	14	620	41
Pyr	440	9.6	140	8.1	240	10	240	44
BaA	12	12	9.8	2.6	23	3.6	30	9.0
Chr	19	6.2	32	3.0	84	2.4	88	9.4
BbF	1.9	11	5.4	5.3	4.3	4.1	8.5	9.3
BaP	1.1	3.6	3.2	5.2	0.46	0.93	11	6.6
InP	1.0	11	4.2	8.5	0.65	2.1	4.9	8.6
DahP	0.27	4.1	0.37	1.2	0.14	0.73	0.44	2.1
BghiP	1.1	9.2	2.0	7.0	0.92	2.0	4.8	6.9
Total	2377	197	1062	162	3353	230	3718	570
TSP	12.88		13.17		15.11		25.58	
T	301.80		300.05		298.80		297.50	
f_{om}	0.024		0.024		0.021		0.012	
f_{ec}	0.0016		0.0015		0.0013		0.0008	
a_{ec}	200		200		200		200	
PAHs	A5		A6		A7		A8	
	Gas phase	Particle phase	Gas phase	Particle phase	Gas phase	Particle phase	Gas phase	Particle phase
Acy	330	8.7	120	5.0	69	5.7	200	6.5
Ace	410	6.4	300	11	200	4.9	230	11
FI	400	31	280	42	460	19	270	39
Phe	3400	110	860	120	780	54	730	130
Ant	470	21	93	15	92	8.8	100	15
Flu	330	21	140	11	110	7.3	360	12
Pyr	1300	52	96	7.4	98	6.7	200	9.0
BaA	35	48	7.2	2.4	4.3	5.7	24	3.8
Chr	68	52	37	1.9	13	5.9	130	2.4
BbF	5.4	51	3.6	2.8	1.9	7.4	806	4.4
BaP	0.91	26	3.2	0.84	0.47	7.1	2.5	1.0
InP	4.1	61	3.1	1.5	2.1	9.0	3.1	2.5
DahP	0.64	14	0.14	0.71	0.13	2.7	0.23	0.86
BghiP	3.3	84	1.4	1.3	4.4	7.2	2.9	1.9
Total	6757	586	1945	223	1835	151	3059	239
TSP	19.58		13.68		8.17		8.36	
T	294.45		289.55		279.70		273.10	
f_{om}	0.016		0.023		0.038		0.037	
f_{ec}	0.0010		0.0015		0.0024		0.0024	
a_{ec}	200		200		200		200	
PAHs	A9		A11		A12		A13	
	Gas phase	Particle phase	Gas phase	Particle phase	Gas phase	Particle phase	Gas phase	Particle phase
Acy	27	6.1	47	6.0	27	6.7	130	6.4
Ace	110	6.6	160	7.3	95	7.3	280	6.4
FI	130	28	210	34	150	31	250	30

Phe	480	93	590	120	510	89	1000	170
Ant	62	13	81	16	63	15	130	41
Flu	51	11	52	14	68	9.6	170	24
Pyr	100	9.1	87	12	75	8.4	160	18
BaA	5.5	7.9	4.5	8.6	4.1	7.2	12	7.9
Chr	12	3.2	7	3.6	7.7	4.8	58	5.2
BbF	1.9	6.4	1.1	5.7	1.4	6.8	4.0	4.2
BaP	1.1	1.4	1.0	1.6	1.9	1.4	4.1	0.57
InP	1.4	4.4	0.51	5.3	1.4	5.7	0.63	3.2
DahP	0.22	1.3	0.11	1.5	0.13	1.7	0.11	1.2
BghiP	0.53	3.6	0.33	3.8	2.6	5.3	1.2	2.0
Total	983	195	1242	239	1007	200	2200	320
TSP	9.99		13.65		11.05		13.2	
T	272.50		272.95		273.00		272.90	
f_{om}	0.031		0.023		0.028		0.024	
f_{ec}	0.0020		0.0015		0.0018		0.0015	
a_{ec}	200		200		200		200	
PAHs	A14		A16		A18		A19	
	Gas phase	Particle phase	Gas phase	Particle phase	Gas phase	Particle phase	Gas phase	Particle phase
Acy	31	6.5	16	4.3	29	5.8	33	5.4
Ace	94	8.0	43	3.2	92	5.7	67	5.2
FI	160	35	73	14	200	23	180	20
Phe	480	100	480	52	490	75	340	62
Ant	66	16	78	7.5	62	12	56	9.4
Flu	64	12	52	9.7	57	9.7	32	7.7
Pyr	55	9.5	310	11	80	7.3	66	6.4
BaA	4.4	7.2	5.3	11	3.8	6.5	3.4	5.9
Chr	7.1	3.0	7.7	8.5	5.0	2.9	4.6	2.6
BbF	1.1	4.7	1.9	18	0.97	3.7	0.92	5.3
BaP	0.77	0.81	2.6	5.9	0.75	2.4	1.1	1.1
InP	0.58	5.5	3.4	19	0.76	3.2	1.0	3.3
DahP	0.11	1.3	0.27	5.1	0.14	1.0	0.12	1.1
BghiP	0.24	3.9	1.0	18	0.28	2.2	0.27	2.5
Total	964	213	1074	187	1022	160	785	138
TSP	10.43		10.66		16.48		10.06	
T	274.70		272.60		273.05		272.90	
f_{om}	0.030		0.029		0.019		0.031	
f_{ec}	0.0019		0.0019		0.0012		0.0020	
a_{ec}	200		200		200		200	
PAHs	A20		A21		A22		A23	
	Gas phase	Particle phase	Gas phase	Particle phase	Gas phase	Particle phase	Gas phase	Particle phase
Acy	150	3.7	31	6.8	44	5.8	50	3.9
Ace	440	4.7	94	6.7	110	4.5	91	4.9
FI	360	19	160	26	250	21	160	19
Phe	1300	62	380	79	480	81	390	68
Ant	130	9.5	67	14	78	13	65	9.8

Flu	230	8.9	59	10	61	12	62	11
Pyr	310	6.7	59	9.2	53	8.8	130	8.6
BaA	10	2.2	5.2	14	3.2	2.6	6.4	1.8
Chr	56	2.0	6.0	12	5.6	2.9	12	2.6
BbF	7.9	3.4	1.5	9.3	1.1	3.5	1.6	4.8
BaP	7.8	2.1	1.7	4.9	0.63	2.6	2.2	3.0
InP	9.6	2.7	1.7	10	0.58	3.1	1.8	4.8
DahP	0.39	0.49	0.098	4.4	0.14	0.92	0.22	0.64
BghiP	17	2.5	0.68	7.4	0.21	2.2	0.83	3.8
Total	3029	130	867	214	1087	164	973	147
TSP	8.65		10.1		9.8		9.17	
T	272.65		272.50		272.65		272.55	
f_{om}	0.036		0.031		0.032		0.034	
f_{ec}	0.0023		0.0020		0.0020		0.0022	
a_{ec}	200		200		200		200	
PAHs	A24		A25		A26		A27	
	Gas phase	Particle phase	Gas phase	Particle phase	Gas phase	Particle phase	Gas phase	Particle phase
Acy	28	4.0	91	3.4	39	6.5	36	4.2
Ace	66	3.7	79	3.2	73	8.8	55	5.1
FI	120	16	240	15	180	32	180	21
Phe	370	53	370	50	340	90	410	78
Ant	52	9.1	65	7.7	54	14	60	11
Flu	62	8.3	45	7.1	44	11	62	11
Pyr	33	12	100	5.5	68	9.5	88	8.5
BaA	3.1	2.0	5.2	4.0	4.1	3.7	13	7.3
Chr	6.2	2.6	6.0	2.3	4.3	3.4	14	2.2
BbF	0.58	4.4	2.1	3.6	1.2	6.0	9.1	3.3
BaP	0.47	2.3	3.4	1.9	1.3	3.8	8.6	1.1
InP	0.36	3.5	2.7	2.6	1.2	4.9	12	3.3
DahP	0.07	0.97	0.19	0.81	0.11	0.76	0.68	0.81
BghiP	0.099	2.2	2.1	1.7	0.078	4.1	7.0	2.9
Total	742	124	1012	109	810	198	955	160
TSP	8.94		6.85		9.34		9.47	
T	271.05		272.55		272.25		274.05	
f_{om}	0.035		0.045		0.033		0.033	
f_{ec}	0.0022		0.0029		0.0021		0.0021	
a_{ec}	200		200		200		200	
PAHs	A28		A29		A30		A32	
	Gas phase	Particle phase	Gas phase	Particle phase	Gas phase	Particle phase	Gas phase	Particle phase
Acy	25	3.6	24	4.1	13	3.7	151	3.7
Ace	40	3.0	35	4.6	50	4.6	320	4.6
FI	110	14	99	19	77	18	490	18
Phe	240	46	200	60	360	53	1400	59
Ant	41	7.5	37	9.4	48	7.8	190	9.3
Flu	36	6.9	26	8.2	48	7.1	240	8.2

Pyr	39	5.7	41	6.3	47	5.4	240	6.5
BaA	3.1	7.2	3.9	6.8	3.6	1.4	21	2.9
Chr	4.9	2.9	5.2	1.8	5.7	2.0	72	2.3
BbF	1.0	3.5	1.5	3.8	1.0	3.1	7.3	3.3
BaP	0.81	1.2	1.0	2.1	0.87	1.5	4.6	1.6
InP	0.85	3.1	1.5	2.5	1.0	2.1	2.8	2.7
DahP	0.13	1.0	0.21	0.91	0.15	0.67	0.23	0.9
BghiP	0.26	1.8	0.66	2.4	1.3	1.7	1.9	1.9
Total	542	107	476	132	657	112	3141	125
TSP	7.32		11.24		8.25		8.47	
T	276.10		282.20		291.05		299.15	
f_{om}	0.042		0.028		0.038		0.037	
f_{ec}	0.0027		0.0018		0.0024		0.0024	
a_{ec}	200		200		200		200	
PAHs	A33		A34		A35		A36	
	Gas phase	Particle phase	Gas phase	Particle phase	Gas phase	Particle phase	Gas phase	Particle phase
Acy	69	5.4	840	9.0	250	8.1	230	5.6
Ace	82	7.7	530	13	550	13	540	7.6
FI	98	28	510	71	720	43	520	28
Phe	870	96	1700	350	3200	130	2400	110
Ant	130	16	260	50	440	28	270	18
Flu	140	16	550	56	490	58	360	24
Pyr	95	35	310	56	490	56	330	23
BaA	12	4.0	32	18	67	66	42	27
Chr	49	5.4	150	7.0	110	57	58	18
BbF	6.8	5.8	10	6.0	36	99	23	13
BaP	8.4	3.3	2.3	2.3	53	136	32	21
InP	2.4	5.5	2.9	7.5	28	110	24	34
DahP	0.12	1.1	0.092	1.7	4.0	52	2.5	9.1
BghiP	2.6	5.1	2.1	8.6	22	130	12	26
Total	1565	234	4899	656	6460	986	4843	364
TSP	15.04		27.17		29.25		24.16	
T	300.55		301.85		300.80		299.85	
f_{om}	0.021		0.011		0.011		0.013	
f_{ec}	0.0013		0.0007		0.0007		0.0008	
a_{ec}	200		200		200		200	

Tab. S4.8: LogK_{pg} (in unit of $m^3\ \mu g^{-1}$) values of 14 EPA targeted PAHs based on absorption model and dual model.

PAHs	A1			A2			A3			A4		
	Measured	Absorption model	Dual model	Measured	Absorption model	Dual model	Measured	Absorption model	Dual model	Measured	Absorption model	Dual model
Acy	-2.31	-7.29	-6.80	-2.18	-7.26	-6.76	-2.81	-7.28	-6.79	-2.79	-7.47	-6.98
Ace	-2.30	-7.12	-6.65	-2.27	-7.08	-6.61	-2.85	-7.11	-6.63	-2.78	-7.30	-6.82
FI	-2.02	-6.75	-6.30	-1.84	-6.71	-6.25	-2.19	-6.73	-6.27	-2.05	-6.91	-6.46

Phe	-2.35	-5.99	-5.58	-1.94	-5.93	-5.52	-2.25	-5.95	-5.54	-2.14	-6.13	-5.72
Ant	-2.21	-5.95	-5.54	-1.90	-5.90	-5.49	-2.21	-5.91	-5.50	-2.02	-6.09	-5.69
Flu	-2.08	-4.93	-4.58	-2.16	-4.87	-4.51	-2.59	-4.87	-4.52	-2.59	-5.04	-4.69
Pyr	-2.77	-4.88	-4.56	-2.36	-4.82	-4.50	-2.56	-4.82	-4.50	-2.14	-4.99	-4.68
BaA	-1.11	-3.44	-3.28	-1.70	-3.36	-3.21	-1.98	-3.35	-3.20	-1.93	-3.51	-3.37
Chr	-1.60	-3.43	-3.14	-2.15	-3.34	-3.06	-2.72	-3.34	-3.05	-2.38	-3.50	-3.21
BbF	-0.35	-2.42	-2.23	-1.13	-2.32	-2.14	-1.20	-2.31	-2.13	-1.37	-2.46	-2.29
BaP	-0.60	-2.20	-2.02	-0.91	-2.10	-1.93	-0.87	-2.09	-1.92	-1.63	-2.24	-2.07
InP	-0.07	-1.34	-1.19	-0.81	-1.24	-1.09	-0.67	-1.22	-1.07	-1.16	-1.36	-1.22
DahP	0.07	-1.19	-1.04	-0.61	-1.09	-0.94	-0.46	-1.07	-0.92	-0.73	-1.21	-1.07
BghiP	-0.19	-1.23	-1.07	-0.58	-1.12	-0.98	-0.84	-1.10	-0.96	-1.25	-1.25	-1.10

PAHs	A5			A6			A7			A8		
	Measured	Absorption model	Dual model	Measured	Absorption model	Dual model	Measured	Absorption model	Dual model	Measured	Absorption model	Dual model
Acy	-2.87	-7.27	-6.78	-2.52	-6.97	-6.48	-2.00	-6.45	-5.96	-2.41	-6.24	-5.76
Ace	-3.10	-7.09	-6.62	-2.57	-6.79	-6.32	-2.52	-6.25	-5.78	-2.24	-6.03	-5.57
FI	-2.40	-6.70	-6.25	-1.96	-6.38	-5.93	-2.30	-5.81	-5.37	-1.76	-5.58	-5.14
Phe	-2.78	-5.90	-5.49	-1.99	-5.55	-5.15	-2.07	-4.93	-4.54	-1.67	-4.65	-4.27
Ant	-2.64	-5.86	-5.46	-1.93	-5.51	-5.11	-1.93	-4.89	-4.50	-1.75	-4.61	-4.23
Flu	-2.49	-4.79	-4.44	-2.24	-4.41	-4.07	-2.09	-3.71	-3.38	-2.40	-3.39	-3.06
Pyr	-2.69	-4.74	-4.43	-2.25	-4.35	-4.06	-2.08	-3.64	-3.38	-2.27	-3.31	-3.06
BaA	-1.15	-3.23	-3.10	-1.61	-2.80	-2.69	-0.79	-2.00	-1.91	-1.72	-1.60	-1.53
Chr	-1.41	-3.22	-2.94	-2.43	-2.79	-2.51	-1.26	-1.98	-1.73	-2.66	-1.58	-1.34
BbF	-0.32	-2.16	-2.00	-1.25	-1.70	-1.56	-0.32	-0.84	-0.72	-3.19	-0.39	-0.29
BaP	0.16	-1.93	-1.78	-1.72	-1.47	-1.33	0.27	-0.59	-0.48	-1.32	-0.13	-0.04
InP	-0.12	-1.04	-0.91	-1.45	-0.55	-0.44	-0.28	0.37	0.47	-1.02	0.86	0.94
DahP	0.05	-0.89	-0.76	-0.43	-0.39	-0.28	0.41	0.55	0.64	-0.35	1.05	1.12
BghiP	0.11	-0.93	-0.79	-1.17	-0.44	-0.32	-0.70	0.50	0.59	-1.11	0.99	1.07

PAHs	A9			A11			A12			A13		
	Measured	Absorption model	Dual model	Measured	Absorption model	Dual model	Measured	Absorption model	Dual model	Measured	Absorption model	Dual model
Acy	-1.65	-6.30	-5.82	-2.03	-6.45	-5.97	-1.65	-6.36	-5.88	-2.43	-6.44	-5.95
Ace	-2.22	-6.09	-5.63	-2.48	-6.24	-5.78	-2.16	-6.15	-5.69	-2.76	-6.22	-5.76
FI	-1.67	-5.63	-5.20	-1.93	-5.78	-5.35	-1.73	-5.69	-5.26	-2.04	-5.77	-5.33
Phe	-1.71	-4.70	-4.32	-1.83	-4.86	-4.48	-1.80	-4.77	-4.39	-1.89	-4.84	-4.46
Ant	-1.68	-4.66	-4.28	-1.84	-4.82	-4.43	-1.67	-4.73	-4.34	-1.62	-4.80	-4.42
Flu	-1.67	-3.43	-3.11	-1.71	-3.59	-3.27	-1.89	-3.50	-3.18	-1.97	-3.57	-3.25
Pyr	-2.04	-3.35	-3.11	-2.00	-3.51	-3.27	-1.99	-3.42	-3.18	-2.07	-3.50	-3.25
BaA	-0.84	-1.64	-1.57	-0.85	-1.81	-1.74	-0.80	-1.72	-1.65	-1.30	-1.79	-1.72
Chr	-1.57	-1.62	-1.38	-1.42	-1.79	-1.54	-1.25	-1.70	-1.45	-2.17	-1.77	-1.52
BbF	-0.47	-0.42	-0.33	-0.42	-0.59	-0.49	-0.36	-0.50	-0.40	-1.10	-0.57	-0.47
BaP	-0.89	-0.17	-0.08	-0.93	-0.34	-0.24	-1.18	-0.25	-0.15	-1.98	-0.32	-0.22
InP	-0.50	0.83	0.91	-0.12	0.66	0.74	-0.43	0.75	0.83	-0.41	0.68	0.76
DahP	-0.23	1.02	1.09	0.00	0.84	0.92	0.07	0.93	1.01	-0.08	0.86	0.94
BghiP	-0.17	0.96	1.04	-0.07	0.79	0.87	-0.73	0.88	0.95	-0.90	0.81	0.89

PAHs	A14			A16			A18			A19		
	Measured	Absorption model	Dual model	Measured	Absorption model	Dual model	Measured	Absorption model	Dual model	Measured	Absorption model	Dual model
Acy	-1.70	-6.39	-5.91	-1.60	-6.33	-5.85	-1.92	-6.54	-6.06	-1.79	-6.32	-5.84

Ace	-2.09	-6.18	-5.72	-2.16	-6.12	-5.66	-2.42	-6.32	-5.86	-2.11	-6.10	-5.64
FI	-1.68	-5.73	-5.30	-1.74	-5.66	-5.23	-2.16	-5.87	-5.43	-1.96	-5.65	-5.21
Phe	-1.70	-4.82	-4.43	-1.99	-4.74	-4.35	-2.03	-4.95	-4.56	-1.74	-4.72	-4.34
Ant	-1.63	-4.78	-4.39	-2.04	-4.69	-4.31	-1.93	-4.90	-4.52	-1.78	-4.68	-4.30
Flu	-1.75	-3.57	-3.24	-1.76	-3.47	-3.14	-1.99	-3.68	-3.36	-1.62	-3.46	-3.13
Pyr	-1.78	-3.49	-3.24	-2.48	-3.39	-3.14	-2.26	-3.60	-3.35	-2.02	-3.38	-3.13
BaA	-0.80	-1.80	-1.72	-0.71	-1.68	-1.61	-0.98	-1.89	-1.82	-0.76	-1.67	-1.60
Chr	-1.39	-1.78	-1.53	-0.98	-1.66	-1.41	-1.45	-1.87	-1.63	-1.25	-1.65	-1.40
BbF	-0.39	-0.60	-0.49	-0.05	-0.46	-0.36	-0.64	-0.68	-0.58	-0.24	-0.46	-0.36
BaP	-1.00	-0.34	-0.25	-0.67	-0.20	-0.11	-0.71	-0.42	-0.33	-1.00	-0.20	-0.11
InP	-0.04	0.64	0.73	-0.28	0.80	0.87	-0.59	0.57	0.65	-0.48	0.80	0.88
DahP	0.05	0.82	0.90	0.25	0.98	1.05	-0.36	0.75	0.83	-0.04	0.98	1.06
BghiP	0.19	0.77	0.85	0.23	0.92	1.00	-0.32	0.70	0.78	-0.04	0.93	1.00

PAHs	A20			A21			A22			A23		
	Measured	Absorption model	Dual model	Measured	Absorption model	Dual model	Measured	Absorption model	Dual model	Measured	Absorption model	Dual model
Acy	-2.54	-6.24	-5.76	-1.66	-6.31	-5.82	-1.87	-6.30	-5.82	-2.07	-6.27	-5.78
Ace	-2.91	-6.03	-5.57	-2.15	-6.09	-5.63	-2.38	-6.08	-5.62	-2.23	-6.05	-5.59
FI	-2.21	-5.58	-5.14	-1.79	-5.64	-5.20	-2.07	-5.63	-5.19	-1.89	-5.60	-5.16
Phe	-2.26	-4.65	-4.26	-1.69	-4.71	-4.33	-1.76	-4.70	-4.32	-1.72	-4.67	-4.29
Ant	-2.07	-4.60	-4.22	-1.68	-4.66	-4.28	-1.77	-4.66	-4.28	-1.78	-4.62	-4.24
Flu	-2.35	-3.38	-3.05	-1.78	-3.44	-3.11	-1.70	-3.43	-3.11	-1.71	-3.40	-3.08
Pyr	-2.60	-3.30	-3.05	-1.81	-3.36	-3.11	-1.77	-3.35	-3.11	-2.14	-3.32	-3.07
BaA	-1.59	-1.59	-1.52	-0.57	-1.65	-1.58	-1.08	-1.64	-1.57	-1.51	-1.61	-1.54
Chr	-2.38	-1.57	-1.32	-0.70	-1.63	-1.38	-1.28	-1.62	-1.38	-1.63	-1.59	-1.34
BbF	-1.30	-0.37	-0.27	-0.21	-0.43	-0.33	-0.49	-0.43	-0.33	-0.49	-0.39	-0.29
BaP	-1.51	-0.12	-0.02	-0.54	-0.17	-0.08	-0.38	-0.17	-0.08	-0.83	-0.13	-0.04
InP	-1.49	0.88	0.96	-0.23	0.83	0.90	-0.26	0.83	0.91	-0.54	0.87	0.94
DahP	-0.84	1.07	1.14	0.65	1.01	1.08	-0.17	1.01	1.09	-0.50	1.05	1.12
BghiP	-1.77	1.01	1.09	0.03	0.96	1.03	0.03	0.96	1.03	-0.30	0.99	1.07

PAHs	A24			A25			A26			A27		
	Measured	Absorption model	Dual model	Measured	Absorption model	Dual model	Measured	Absorption model	Dual model	Measured	Absorption model	Dual model
Acy	-1.80	-6.21	-5.72	-2.26	-6.14	-5.66	-1.75	-6.26	-5.78	-1.91	-6.33	-5.85
Ace	-2.20	-5.99	-5.53	-2.23	-5.93	-5.46	-1.89	-6.05	-5.59	-2.01	-6.12	-5.66
FI	-1.83	-5.53	-5.09	-2.04	-5.47	-5.03	-1.72	-5.59	-5.16	-1.91	-5.67	-5.23
Phe	-1.80	-4.59	-4.21	-1.70	-4.54	-4.16	-1.55	-4.66	-4.28	-1.70	-4.75	-4.36
Ant	-1.71	-4.55	-4.17	-1.76	-4.50	-4.12	-1.56	-4.62	-4.24	-1.71	-4.71	-4.32
Flu	-1.82	-3.31	-2.99	-1.64	-3.27	-2.95	-1.57	-3.39	-3.07	-1.73	-3.49	-3.17
Pyr	-1.39	-3.23	-2.99	-2.10	-3.19	-2.95	-1.83	-3.31	-3.07	-1.99	-3.41	-3.16
BaA	-1.14	-1.50	-1.43	-0.95	-1.48	-1.41	-1.01	-1.60	-1.53	-1.23	-1.72	-1.64
Chr	-1.33	-1.48	-1.24	-1.25	-1.46	-1.21	-1.07	-1.58	-1.33	-1.78	-1.70	-1.45
BbF	-0.07	-0.27	-0.18	-0.60	-0.26	-0.17	-0.27	-0.38	-0.28	-1.42	-0.51	-0.41
BaP	-0.26	-0.01	0.08	-1.09	-0.01	0.09	-0.50	-0.12	-0.03	-1.87	-0.26	-0.16
InP	0.04	1.00	1.07	-0.85	0.99	1.07	-0.36	0.88	0.96	-1.54	0.74	0.82
DahP	0.19	1.18	1.25	-0.21	1.18	1.25	-0.13	1.06	1.14	-0.90	0.92	0.99
BghiP	0.40	1.12	1.20	-0.93	1.12	1.20	0.75	1.01	1.09	-1.36	0.86	0.94

PAHs	A28	A29	A30	A32

	Measured	Absorption model	Dual model	Measured	Absorption model	Dual model	Measured	Absorption model	Dual model	Measured	Absorption model	Dual model
Acy	-1.71	-6.29	-5.80	-1.82	-6.67	-6.18	-1.46	-6.80	-6.31	-2.54	-7.04	-6.55
Ace	-1.99	-6.08	-5.61	-1.93	-6.47	-6.00	-1.95	-6.61	-6.14	-2.77	-6.87	-6.39
FI	-1.76	-5.63	-5.19	-1.77	-6.04	-5.60	-1.55	-6.21	-5.76	-2.36	-6.49	-6.03
Phe	-1.58	-4.73	-4.34	-1.57	-5.17	-4.78	-1.75	-5.39	-4.99	-2.30	-5.71	-5.30
Ant	-1.60	-4.68	-4.30	-1.65	-5.13	-4.74	-1.71	-5.35	-4.95	-2.24	-5.67	-5.27
Flu	-1.58	-3.48	-3.16	-1.55	-3.98	-3.64	-1.75	-4.26	-3.92	-2.39	-4.64	-4.28
Pyr	-1.70	-3.41	-3.15	-1.86	-3.91	-3.64	-1.86	-4.20	-3.91	-2.50	-4.59	-4.27
BaA	-0.50	-1.73	-1.66	-0.81	-2.29	-2.20	-1.33	-2.67	-2.55	-1.79	-3.12	-2.97
Chr	-1.09	-1.71	-1.46	-1.51	-2.27	-2.01	-1.37	-2.65	-2.38	-2.42	-3.10	-2.82
BbF	-0.32	-0.54	-0.43	-0.65	-1.14	-1.02	-0.43	-1.58	-1.43	-1.27	-2.08	-1.90
BaP	-0.69	-0.29	-0.19	-0.73	-0.90	-0.78	-0.68	-1.34	-1.20	-1.39	-1.86	-1.68
InP	-0.30	0.69	0.78	-0.83	0.05	0.15	-0.59	-0.44	-0.32	-0.94	-0.99	-0.84
DahP	0.02	0.87	0.95	-0.41	0.22	0.32	-0.27	-0.28	-0.16	-0.34	-0.84	-0.69
BghiP	-0.02	0.82	0.90	-0.49	0.17	0.27	-0.80	-0.32	-0.20	-0.93	-0.87	-0.73

PAHs	A33			A34			A35			A36		
	Measured	Absorption model	Dual model	Measured	Absorption model	Dual model	Measured	Absorption model	Dual model	Measured	Absorption model	Dual model
Acy	-2.28	-7.33	-6.83	-3.40	-7.62	-7.13	-2.96	-7.62	-7.13	-3.00	-7.51	-7.02
Ace	-2.20	-7.16	-6.68	-3.04	-7.45	-6.97	-3.09	-7.45	-6.97	-3.23	-7.34	-6.87
FI	-1.72	-6.78	-6.32	-2.29	-7.08	-6.62	-2.69	-7.08	-6.62	-2.65	-6.96	-6.51
Phe	-2.13	-6.01	-5.60	-2.12	-6.31	-5.90	-2.86	-6.31	-5.90	-2.72	-6.19	-5.78
Ant	-2.09	-5.97	-5.57	-2.15	-6.28	-5.87	-2.66	-6.27	-5.86	-2.56	-6.15	-5.75
Flu	-2.12	-4.95	-4.59	-2.43	-5.26	-4.90	-2.39	-5.25	-4.89	-2.56	-5.12	-4.77
Pyr	-1.61	-4.90	-4.58	-2.18	-5.21	-4.89	-2.41	-5.20	-4.87	-2.54	-5.07	-4.75
BaA	-1.65	-3.44	-3.29	-1.68	-3.77	-3.61	-1.47	-3.75	-3.59	-1.57	-3.61	-3.46
Chr	-2.14	-3.43	-3.14	-2.77	-3.75	-3.46	-1.75	-3.73	-3.44	-1.89	-3.60	-3.31
BbF	-1.25	-2.41	-2.23	-1.66	-2.74	-2.56	-1.03	-2.71	-2.53	-1.63	-2.58	-2.40
BaP	-1.58	-2.19	-2.01	-1.43	-2.52	-2.34	-1.06	-2.49	-2.32	-1.57	-2.35	-2.18
InP	-0.82	-1.33	-1.18	-1.02	-1.67	-1.51	-0.87	-1.63	-1.48	-1.23	-1.49	-1.34
DahP	-0.22	-1.18	-1.03	-0.17	-1.52	-1.37	-0.35	-1.48	-1.34	-0.82	-1.34	-1.19
BghiP	-0.88	-1.21	-1.06	-0.82	-1.56	-1.40	-0.69	-1.52	-1.37	-1.05	-1.38	-1.23

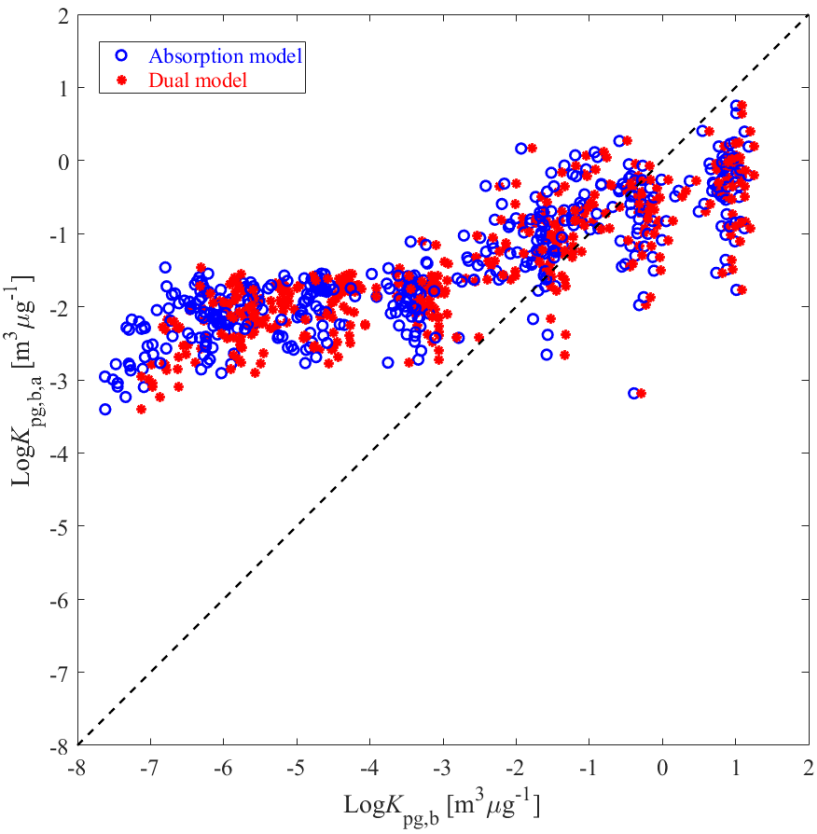

Fig. S4.6: Measured apparent gas/particle bulk distribution coefficients (Log$K_{pg,b,a}$) vs. equilibrium bulk gas/particle distribution coefficients (Log$K_{pg,b}$) based on absorption model (blue open circles) and dual model (red dots) for PAHs sampled in the marine atmosphere from the Western Pacific to the Southern Ocean (containing data of 32 locations as shown in Fig. 4.6a in the main text). The dashed black line denotes a 1:1 relationship.

References

Crank, J., 1975. The Mathematics of Diffusion. Second ed. Oxford University Press, London, pp. 69-88.

Lei, Y.D., Chankalal, R., Chan, A., Wania, F., 2002. Supercooled liquid vapor pressures of the polycyclic aromatic hydrocarbons. J. Chem. Eng. Data. 47, 801–806. https://doi.org/10.1021/je0155148.

Liu, B., Finkel, M., Grathwohl, P., 2022. First order approximation for coupled film and intraparticle pore diffusion to model sorption/desorption batch experiments. J. Hazard. Mater. 429, 128314. https://doi.org/10.1016/j.jhazmat.2022.128314.

Ma, W., Zhu, F., Hu, P., Qiao, L., Li, Y., 2020. Gas/particle partitioning of PAHs based on equilibrium-state model and steady-state model. Sci. Total Environ. 706, 136029.

https://doi.org/https://doi.org/10.1016/j.scitotenv.2019.136029.

Mu, L., Peng, L., Liu, X., Song, C., Bai, H., Zhang, J., Hu, D., He, Q., Li, F., 2014. Characteristics of polycyclic aromatic hydrocarbons and their gas/particle partitioning from fugitive emissions in coke plants. Atmos. Environ. 83, 202–210. https://doi.org/10.1016/j.atmosenv.2013.09.043.

Odabasi, M., Cetin, E., Sofuoglu, A., 2006. Determination of octanol-air partition coefficients and supercooled liquid vapor pressures of PAHs as a function of temperature: Application to gas-particle partitioning in an urban atmosphere. Atmos. Environ. 40, 6615–6625. https://doi.org/10.1016/j.atmosenv.2006.05.051.

Parnis, J.M., Taskovic, T., Celsie, A.K.D., Mackay, D., 2020. Indoor dust/air partitioning: Evidence for kinetic delay in equilibration for low-volatility SVOCs. Environ. Sci. Technol. 54, 6723–6729. https://doi.org/10.1021/acs.est.0c00632.

Sun, Y., Chen, J., Qin, W., Yu, Q., Xin, K., Ai, J., Huang, H., Liu, X., 2022. Gas-PM2.5 partitioning, health risks, and sources of atmospheric PAHs in a northern China city: Impact of domestic heating. Environ. Pollut. 313, 120156. https://doi.org/10.1016/j.envpol.2022.120156

Yin, F., He, Z., Song, Z., Zhang, W., Li, X., Qin, B., Zhang, L., Su, P., Zhang, J., Kitazawa, D., 2022. Gas-particle partitioning of polycyclic aromatic hydrocarbons from oil combustion involving condensate, diesel and heavy oil. Ecotoxicol. Environ. Saf. 242, 113866. https://doi.org/10.1016/j.ecoenv.2022.113866.

Zhang, X., Zhang, Z.F., Zhang, X., Zhu, F.J., Li, Y.F., Cai, M., Kallenborn, R., 2022. Polycyclic aromatic hydrocarbons in the marine atmosphere from the Western Pacific to the Southern Ocean: Spatial variability, gas/particle partitioning, and source apportionment. Environ. Sci. Technol. https://doi.org/10.1021/acs.est.1c08429.

Zhao, F., Riipinen, I., Macleod, M., 2021. Steady-state mass balance model for predicting particle-gas concentration ratios of PBDEs. Environ. Sci. Technol. 55, 9425–9433. https://doi.org/10.1021/acs.est.0c04368.

S5 Supplementary information for mass transfer principles in column percolation tests: Initial conditions and tailing in heterogeneous materials

S5.1 Empirical relationships for the estimation of Sherwood numbers

There are many studies available in the literature in which solid-liquid mass transfer in fluidized beds and flow through systems are investigated over a wide range of Reynolds numbers. Most of these correlations can be adequately described by the following equation:

$$Sh = A + BRe^{\theta}Sc^{\gamma} \tag{S5.1}$$

where Sh is the Sherwood number. A is a constant (theoretically = 2 for spherical particles in a stagnant infinite medium) and B is a constant to be determined by regression analysis of experimental data. Re and Sc denote the Reynolds and Schmidt number which are defined as:

$$Sc = \frac{\eta}{\rho_L D_{aq}} \qquad Re = \frac{\rho_L d\, v}{\eta} \tag{S5.2}$$

where η [M L^{-1} T^{-1}] denotes the dynamic viscosity of the fluid. ρ_L [M L^{-3}] is the density of the fluid and v [L T^{-1}] denotes the flow velocity.

The empirical exponents θ and γ in Eq. S5.1) may be determined experimentally or from theory. The Blasius (1908) solved the Navier-Stokes equation and continuity equation for laminar flow over a sharp leading edge and found that the ratio of fluid velocity boundary layer thickness to concentration boundary layer thickness is proportional to the Schmidt number with a power of 1/3 (= γ in Eq. S5.1) which is widely used in literatures (Blasius 1908; Calderbank et al., 1961; Levins et al., 1972; Ohashi et al., 1981; Kirwan et al., 1989; Arters et al., 1990; Mao et al., 1992). Liu et al. (2014) showed a higher empirical exponent γ of 1/2 based on penetration theory (Sherwood et al., 1975). θ values depend on the experimental setup and are generally adapted from experimental data. Most of the empirical relationships show that θ values lie in the range of 0.5–0.75 (Calderbank et al., 1961; Levins et al., 1972; Ohashi et al., 1981; Kirwan et al., 1989; Arters et al., 1990; Mao et al., 1992; Liu et al., 2014).

Liu et al. (2014) proposed an empirical relationship for mass transfer in packed beds only based on the Peclet number ($Pe = Re \times Sc$):

$$Sh = 2 + 0.1Pe^{1/2} \tag{S5.3}$$

Equation S5.3 is equivalent to Eq. S5.1 for $\theta = \gamma = 1/2$. This Sherwood number correlation was applied in the numerical models. Sh numbers obtained for the chosen column setup were close to 2 indicating slow mass transfer close to the theoretical limit (2).

S5.2 Film diffusion coupled to advective-dispersive transport

Equation 5.10 in the main text shows the governing equations of film diffusion coupled to advective-dispersive transport. These partial differential equations are solved numerically using the finite volume method (as illustrated in Fig. S5.1a).

Discretizing the transport operator in space while keeping the time derivative yields the following system of ordinary differential equations:

$$\begin{aligned}\frac{\partial C_{w,j}}{\partial \mathrm{t}} &= D_L \frac{(C_{w,j-1} - 2C_{w,j} + C_{w,j+1})}{\Delta x^2} - v\frac{(C_{w,j} - C_{w,j-1})}{\Delta x} \\ &\quad + \frac{D_{aq}}{\delta_{aq}}\frac{6(1-n)}{nd}\left(\frac{C_{s,j}}{K_d} - C_{w,j}\right) \\ \frac{\partial C_{s,j}}{\partial \mathrm{t}} &= -\frac{D_{aq}}{\delta_{aq}}\frac{6}{\rho_s\, d}\left(\frac{C_{s,j}}{K_d} - C_{w,j}\right)\end{aligned} \tag{S5.4}$$

where $C_{w,j}$ [M L^{-3}], $C_{w,j-1}$ [M L^{-3}] and $C_{w,j+1}$ [M L^{-3}] denote the solute concentration in the water phase in volume j, $j-1$ and $j+1$, respectively. $C_{s,j}$ [M M^{-1}] denotes the solute concentration in the solid phase in volume j.

The approximation of the time derivative of Eq. S5.4 can be expressed as the concentration difference between the new and the previous time, divided by the time interval Δt. A time weighting factor φ was used to navigate between implicit and explicit time integration. For $\varphi = 0.5$, the Crank-Nicholson-scheme is realized, whereas for $\varphi = 0$ and $\varphi = 1$, the fully implicit and explicit scheme is used, respectively.

$$\begin{aligned}&\frac{C_{w,j}^{k+1} - C_{w,j}^{k}}{\Delta t} = (1-\varphi)\left(D_L\frac{(C_{w,j-1}^{k+1} - 2C_{w,j}^{k+1} + C_{w,j+1}^{k+1})}{\Delta x^2} - v\frac{(C_{w,j}^{k+1} - C_{w,j-1}^{k+1})}{\Delta x} + \frac{D_{aq}}{\delta_{aq}}\frac{6(1-n)}{nd}\left(\frac{C_{s,j}^{k+1}}{K_d} - C_{w,j}^{k+1}\right)\right) + \varphi\left(D_L\frac{(C_{w,j-1}^{k} - 2C_{w,j}^{k} + C_{w,j+1}^{k})}{\Delta x^2} - v\frac{(C_{w,j}^{k} - C_{w,j-1}^{k})}{\Delta x} + \frac{D_{aq}}{\delta_{aq}}\frac{6(1-n)}{nd}\left(\frac{C_{s,j}^{k}}{K_d} - C_{w,j}^{k}\right)\right) \\ &\frac{C_{s,j}^{k+1} - C_{s,j}^{k}}{\Delta t} = -(1-\varphi)\left(\frac{D_{aq}}{\delta_{aq}}\frac{6}{\rho_s\, d}\left(\frac{C_{s,j}^{k+1}}{K_d} - C_{w,j}^{k+1}\right)\right) - \varphi\left(\frac{D_{aq}}{\delta_{aq}}\frac{6}{\rho_s\, d}\left(\frac{C_{s,j}^{k}}{K_d} - C_{w,j}^{k}\right)\right)\end{aligned} \tag{S5.5}$$

where the indices k and $k+1$ denote the corresponding concentration values at the

previous time step and at the new time step.

In order to solve this system of equations, we may merge the two concentration vectors into a single one ($C = [C_w; C_s]$; with the semicolon being a line delimiter):

$$C = \begin{bmatrix} C_{w,1} \\ C_{s,1} \\ \vdots \\ C_{w,j} \\ C_{s,j} \\ \vdots \\ C_{w,N} \\ C_{s,N} \end{bmatrix}_{2N\times 1} = \begin{bmatrix} C_1 \\ C_2 \\ \vdots \\ C_{2j-1} \\ C_{2j} \\ \vdots \\ C_{2N-1} \\ C_{2N} \end{bmatrix}_{2N\times 1} \tag{S5.6}$$

with $j\epsilon[1, 2, \ldots, N]$.

A standard method of solving non-linear ordinary equations is the Newton–Raphson scheme (Cirpka, 2020). It is based on linearizing the residual function $f(C^{k+1})$ at the current guess C_{guess}^{k+1} of C^{k+1}. The residual function $f(C^{k+1})$ is defined as:

$$\begin{aligned} f_{2j-1} = {} & \frac{C_{w,j}^{k+1} - C_{w,j}^{k}}{\Delta t} \\ & - (1-\varphi)\left(D_L \frac{\left(C_{w,j-1}^{k+1} - 2C_{w,j}^{k+1} + C_{w,j+1}^{k+1}\right)}{\Delta x^2} \right. \\ & \left. - v\frac{\left(C_{w,j}^{k+1} - C_{w,j-1}^{k+1}\right)}{\Delta x} + \frac{D_{aq}}{\delta_{aq}} \frac{6(1-n)}{nd}\left(\frac{C_{s,j}^{k+1}}{K_d} - C_{w,j}^{k+1}\right)\right) \\ & - \varphi\left(D_L \frac{\left(C_{w,j-1}^{k} - 2C_{w,j}^{k} + C_{w,j+1}^{k}\right)}{\Delta x^2} - v\frac{\left(C_{w,j}^{k} - C_{w,j-1}^{k}\right)}{\Delta x} \right. \\ & \left. + \frac{D_{aq}}{\delta_{aq}} \frac{6(1-n)}{nd}\left(\frac{C_{s,j}^{k}}{K_d} - C_{w,j}^{k}\right)\right) \end{aligned} \tag{S5.7}$$

$$\begin{aligned} f_{2j} = {} & \frac{C_{s,j}^{k+1} - C_{s,j}^{k}}{\Delta t} + (1-\varphi)\left(\frac{D_{aq}}{\delta_{aq}} \frac{6}{\rho_s\, d}\left(\frac{C_{s,j}^{k+1}}{K_d} - C_{w,j}^{k+1}\right)\right) \\ & + \varphi\left(\frac{D_{aq}}{\delta_{aq}} \frac{6}{\rho_s\, d}\left(\frac{C_{s,j}^{k}}{K_d} - C_{w,j}^{k}\right)\right) \end{aligned}$$

The residual function vector can be expressed as:

$$f(C^{k+1}) = \begin{bmatrix} f_1 \\ f_2 \\ \vdots \\ f_{2j-1} \\ f_{2j} \\ \vdots \\ f_{2N-1} \\ f_{2N} \end{bmatrix}_{2N\times 1} \tag{S5.8}$$

The residual function vector becomes a zero vector if C^{k+1} is chosen right and a single step of the Newton–Raphson method can be denoted as:

$$f(C^{k+1}) \approx f\left(C_{guess}^{k+1}\right) + \left(C^{k+1} - C_{guess}^{k+1}\right) \left.\frac{\partial f(C^{k+1})}{\partial C^{k+1}}\right|_{C^{k+1}=C_{guess}^{k+1}}$$

$$C^{k+1} = C_{guess}^{k+1} - \frac{f\left(C_{guess}^{k+1}\right)}{J} = C_{guess}^{k+1} - \frac{f\left(C_{guess}^{k+1}\right)}{\left.\frac{\partial f(C^{k+1})}{\partial C^{k+1}}\right|_{C^{k+1}=C_{guess}^{k+1}}} \quad \text{(S5.9)}$$

where J denotes the Jacobian matrix, which is the matrix of derivatives of all values of $f(C^{k+1})$ with respective to all values of C^{k+1}. The residual $f(C^{k+1})$ is reevaluated after updating C^{k+1}. If the resulting residual is not sufficiently close to zero, C_{guess}^{k+1} is set to the last solution of C^{k+1} and Eq. S5.9 is reapplied. In our case, the Jacobian matrix can be derived analytically:

$$J = \begin{bmatrix} \frac{\partial f_1}{\partial C_1} & \frac{\partial f_1}{\partial C_2} & \cdots & \frac{\partial f_1}{\partial C_{2N-1}} & \frac{\partial f_1}{\partial C_{2N}} \\ \frac{\partial f_2}{\partial C_1} & \frac{\partial f_2}{\partial C_2} & \cdots & \frac{\partial f_2}{\partial C_{2N-1}} & \frac{\partial f_2}{\partial C_{2N}} \\ \vdots & \vdots & \cdots & \vdots & \vdots \\ \frac{\partial f_{2N-1}}{\partial C_1} & \frac{\partial f_{2N-1}}{\partial C_2} & \cdots & \frac{\partial f_{2N-1}}{\partial C_{2N-1}} & \frac{\partial f_{2N-1}}{\partial C_{2N}} \\ \frac{\partial f_{2N}}{\partial C_1} & \frac{\partial f_{2N}}{\partial C_2} & \cdots & \frac{\partial f_{2N}}{\partial C_{2N-1}} & \frac{\partial f_{2N}}{\partial C_{2N}} \end{bmatrix}_{2N\times 2N} \quad \text{(S5.10)}$$

In order to ensure the accuracy of the model, error control was employed at each time step and an error vector (ΔC^{k+1}) was used to monitor the difference between the old and new guess values, which is defined as:

$$\Delta C^{k+1} = \begin{bmatrix} \left|C_{1,guess,new}^{k+1} - C_{1,guess,old}^{k+1}\right| \\ \left|C_{2,guess,new}^{k+1} - C_{2,guess,old}^{k+1}\right| \\ \vdots \\ \left|C_{2j-1,guess,new}^{k+1} - C_{2j-1,guess,old}^{k+1}\right| \\ \left|C_{2j,guess,new}^{k+1} - C_{2j,guess,old}^{k+1}\right| \\ \vdots \\ \left|C_{2N-1,guess,new}^{k+1} - C_{2N-1,guess,old}^{k+1}\right| \\ \left|C_{2N,guess,new}^{k+1} - C_{2N,guess,old}^{k+1}\right| \end{bmatrix}_{2N\times 1} \quad \text{(S5.11)}$$

The iteration process stops if the maximum value of error vector ΔC_{max}^{k+1} is smaller than the tolerable error e (e.g., $e = 10^{-15}$).

S5.3 Intraparticle pore diffusion coupled to advective-dispersive transport

Intraparticle pore diffusion is widely used to describe the sorptive uptake of pollutants in porous materials such as activated carbon, zeolites and many technical materials. Equations 5.11 and 5.17 describe intraparticle diffusion coupled to advective-dispersive transport. The intraparticle diffusion model approximates the solid grains as spherical particles. These spherical particles are discretized into a number of shells of equal volume. Mass transfer between solid and intra-granular water phases is assumed to be fast and local equilibrium is assumed. For sorption, the Freundlich isotherm model is employed for nonlinear and linear (exponent = 1) cases. Figure S5.1b shows the numerical grain model where the spherical grains are divided into L shells. For a specific shell p in volume j the corresponding difference-equations were used (Liedl et al., 2003):

$$\begin{aligned}&\frac{1}{\Delta t}\left(\varepsilon C_{p,j}^{k+1}+\rho_p K_{fr}\left(C_{p,j}^{k+1}\right)^{\frac{1}{n}}-\varepsilon C_{p,j}^{k}-\rho_p K_{fr}\left(C_{p,j}^{k}\right)^{\frac{1}{n}}\right)\\&=\frac{D_e}{r_p^2}\frac{1-\varphi}{r_{p+0.5}-r_{p-0.5}}\left(r_{p+0.5}^2\frac{C_{p+1,j}^{k+1}-C_{p,j}^{k+1}}{r_{p+1}-r_p}-r_{p-0.5}^2\frac{C_{p,j}^{k+1}-C_{p-1,j}^{k+1}}{r_p-r_{p-1}}\right)\\&+\frac{D_e}{r_p^2}\frac{\varphi}{r_{p+0.5}-r_{p-0.5}}\left(r_{p+0.5}^2\frac{C_{p+1,j}^{k}-C_{p,j}^{k}}{r_{p+1}-r_p}-r_{p-0.5}^2\frac{C_{p,j}^{k}-C_{p-1,j}^{k}}{r_p-r_{p-1}}\right)\end{aligned}\qquad\text{(S5.12)}$$

where the subscripts $p+0.5$ and $p-0.5$ represent the corresponding parameter value between shells (p and $p+1$) and (p and $p-1$), respectively. Subscript j denotes the corresponding parameter value in volume j. Subscripts k and $k+1$ denote the "old" and "new" time levels.

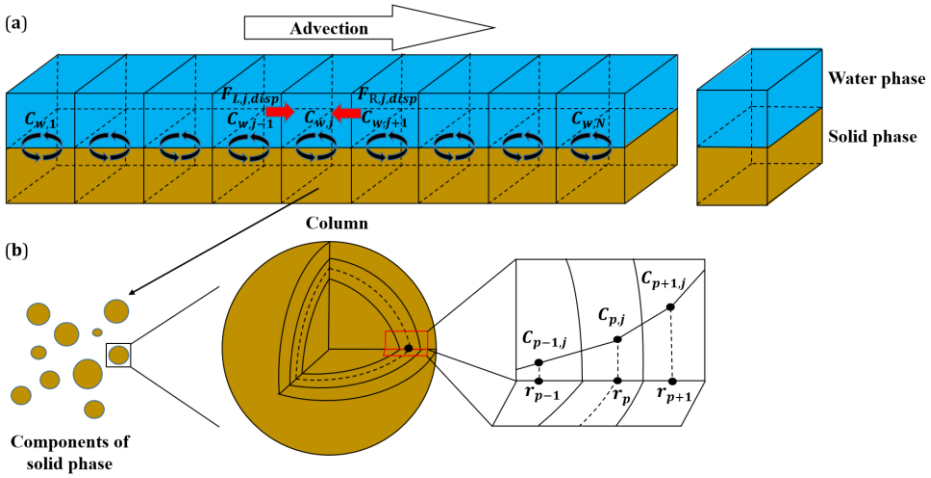

Fig. S5.1: Discretization of the column into N parts (**a**). Representation of the solid phase as a composition of grains having different sizes and properties, each discretized by a number

of L shells (**b**).

Based on the boundary conditions (Eqs. 5.12 and 5.13, main text), the innermost shell and the outermost shell are treated specially. The solute concentration in the intra-granular water phase at the new time step ($C_{p,j}^{k+1}$) can be expressed as:

$$\begin{aligned}
&\left[\varepsilon+\rho_p K_{fr}\left(C_{p,j}^{k+1}\right)^{\frac{1}{n}-1}+\frac{D_e\Delta t}{r_p^2}\frac{1-\varphi}{r_{p+0.5}-r_{p-0.5}}\left(\frac{r_{p+0.5}^2}{r_{p+1}-r_p}+\frac{r_{p-0.5}^2}{r_p-r_{p-1}}\right)\right]C_{p,j}^{k+1}\\
&=\left[\frac{D_e\Delta t}{r_p^2}\frac{1-\varphi}{r_{p+0.5}-r_{p-0.5}}\frac{r_{p+0.5}^2}{r_{p+1}-r_p}\right]C_{p+1,j}^{k+1}\\
&\qquad+\left[\frac{D_e\Delta t}{r_p^2}\frac{1-\varphi}{r_{p+0.5}-r_{p-0.5}}\frac{r_{p-0.5}^2}{r_p-r_{p-1}}\right]C_{p-1,j}^{k+1}\\
&+\left[\frac{D_e\Delta t}{r_p^2}\frac{\varphi}{r_{p+0.5}-r_{p-0.5}}\frac{r_{p+0.5}^2}{r_{p+1}-r_p}\right]C_{p+1,j}^{k}\\
&\qquad+\left[\frac{D_e\Delta t}{r_p^2}\frac{\varphi}{r_{p+0.5}-r_{p-0.5}}\frac{r_{p-0.5}^2}{r_p-r_{p-1}}\right]C_{p-1,j}^{k}\\
&+\left[\varepsilon+\rho_p K_{fr}\left(C_{p,j}^{k}\right)^{\frac{1}{n}-1}-\frac{D_e\Delta t}{r_p^2}\frac{\varphi}{r_{p+0.5}-r_{p-0.5}}\left(\frac{r_{p+0.5}^2}{r_{p+1}-r_p}+\frac{r_{p-0.5}^2}{r_p-r_{p-1}}\right)\right]C_{p,j}^{k}
\end{aligned}\tag{S5.13}$$

for shell $p=2$ to shell $p=L-1$ and

$$\begin{aligned}
&\frac{1}{\Delta t}\left(\varepsilon C_{1,j}^{k+1}+\rho_p K_{fr}\left(C_{1,j}^{k+1}\right)^{\frac{1}{n}}-\varepsilon C_{1,j}^{t}-\rho_p K_{fr}\left(C_{1,j}^{k}\right)^{\frac{1}{n}}\right)\\
&\quad=\frac{D_e}{r_1^2}\frac{1-\varphi}{r_{1+0.5}-r_{1-0.5}}\left(r_{1+0.5}^2\frac{C_{2,j}^{k+1}-C_{1,j}^{k+1}}{r_2-r_1}\right)\\
&\qquad\qquad+\frac{D_e}{r_1^2}\frac{\varphi}{r_{1+0.5}-r_{1-0.5}}\left(r_{1+0.5}^2\frac{C_{2,j}^{k}-C_{1,j}^{k}}{r_2-r_1}\right)
\end{aligned}$$

After transformation: (S5.14)

$$\begin{aligned}
&\left[\varepsilon+\rho_p K_{fr}\left(C_{1,j}^{k+1}\right)^{\frac{1}{n}-1}+\frac{D_e\Delta t}{r_1^2}\frac{1-\varphi}{r_{1+0.5}-r_{1-0.5}}\frac{r_{1+0.5}^2}{r_2-r_1}\right]C_{1,j}^{k+1}\\
&=\left[\frac{D_e\Delta t}{r_1^2}\frac{1-\varphi}{r_{1+0.5}-r_{1-0.5}}\frac{r_{1+0.5}^2}{r_2-r_1}\right]C_{2,j}^{k+1}+\left[\frac{D_e\Delta t}{r_1^2}\frac{\varphi}{r_{1+0.5}-r_{1-0.5}}\frac{r_{1+0.5}^2}{r_2-r_1}\right]C_{2,j}^{k}\\
&+\left[\varepsilon+\rho_p K_{fr}\left(C_{1,j}^{k}\right)^{\frac{1}{n}-1}-\frac{D_e\Delta t}{r_1^2}\frac{\varphi}{r_{1+0.5}-r_{1-0.5}}\frac{r_{1+0.5}^2}{r_2-r_1}\right]C_{1,j}^{k}
\end{aligned}$$

for shell 1 (or the innermost shell, $p=1$) and:

$$\frac{1}{\Delta t}\left(\varepsilon C_{L,j}^{k+1}+\rho_p K_{fr}\left(C_{L,j}^{k+1}\right)^{\frac{1}{n}}-\varepsilon C_{L,j}^{k}-\rho_p K_{fr}\left(C_{L,j}^{k}\right)^{\frac{1}{n}}\right)$$
$$=\frac{D_e}{r_L^2}\frac{1-\varphi}{a-r_{L-0.5}}\left(a^2\frac{C_{w,j}^{k+1}-C_{L,j}^{k+1}}{a-r_L}-r_{L-0.5}^2\frac{C_{L,j}^{k+1}-C_{L-1,j}^{k+1}}{r_L-r_{L-1}}\right)$$
$$+\frac{D_e}{r_L^2}\frac{\varphi}{a-r_{L-0.5}}\left(a^2\frac{C_{w,j}^{k}-C_{L,j}^{k}}{a-r_L}-r_{L-0.5}^2\frac{C_{L,j}^{k}-C_{L-1,j}^{k}}{r_L-r_{L-1}}\right)$$

After transformation:

$$\left[\varepsilon+\rho_p K_{fr}\left(C_{L,j}^{k+1}\right)^{\frac{1}{n}-1}+\frac{D_e\Delta t}{r_L^2}\frac{1-\varphi}{a-r_{L-0.5}}\left(\frac{a^2}{a-r_L}+\frac{r_{L-0.5}^2}{r_L-r_{L-1}}\right)\right]C_{L,j}^{k+1}$$
$$=\left[\frac{D_e\Delta t}{r_L^2}\frac{1-\varphi}{a-r_{L-0.5}}\frac{R^2}{R-r_L}\right]C_{w,j}^{k+1}+\left[\frac{D_e\Delta t}{r_L^2}\frac{1-\varphi}{a-r_{L-0.5}}\frac{r_{L-0.5}^2}{r_L-r_{L-1}}\right]C_{L-1,j}^{k+1}$$
$$+\left[\frac{D_e\Delta t}{r_L^2}\frac{\varphi}{a-r_{L-0.5}}\frac{a^2}{a-r_L}\right]C_{w,j}^{k}+\left[\frac{D_e\Delta t}{r_L^2}\frac{\varphi}{a-r_{L-0.5}}\frac{r_{L-0.5}^2}{r_L-r_{L-1}}\right]C_{L-1,j}^{k}$$
$$+\left[\varepsilon+\rho_p K_{fr}\left(C_{L,j}^{k}\right)^{\frac{1}{n}-1}-\frac{D_e\Delta t}{r_L^2}\frac{\varphi}{a-r_{L-0.5}}\left(\frac{a^2}{a-r_L}+\frac{r_{L-0.5}^2}{r_L-r_{L-1}}\right)\right]C_{L,j}^{k} \quad \text{(S5.15)}$$

for shell L (or the outermost shell, $p = L$).

Based on the mass balance, solute mass change in the external water phase (M_w) equals the solute mass change in the spherical particles; for better understanding, the simple case of particles with uniform size is shown:

$$\frac{\partial M_w}{\partial t}=V_w\frac{\partial C_w}{\partial t}=4\pi a^2 F N_p \quad \text{(S5.16)}$$

where F [M L^{-2} T^{-1}] denotes the solute flux density into the external water phase. a and N_p denote the radius and the total number of the spherical particles. The latter can be calculated by:

$$N_p=\frac{m_d}{\rho_p\left(\frac{4}{3}\pi a^3\right)} \quad \text{(S5.17)}$$

The solute flux density into the external water phase is given by:

$$F=D_e\frac{C_L-C_w}{a-r_L} \quad \text{(S5.18)}$$

Substituting F and N_p with Eq. S5.18 and Eq. S5.17 in Eq. S5.16 and taking advection and dispersion into account, the solute concentration in the external water phase at the new time step $C_{w,j}^{k+1}$ can be expressed by:

$$\frac{C_{w,j}^{k+1}-C_{w,j}^{k}}{\Delta t}=(1-\varphi)\left(D_L\frac{(C_{w,j-1}^{k+1}-2C_{w,j}^{k+1}+C_{w,j+1}^{k+1})}{\Delta x^2}-v\frac{(C_{w,j}^{k+1}-C_{w,j-1}^{k+1})}{\Delta x}+\frac{3D_e m_d}{\rho_p V_w a}\left(\frac{C_{L,j}^{k+1}-C_{w,j}^{k+1}}{a-r_L}\right)\right)+\varphi\left(D_L\frac{(C_{w,j-1}^{k}-2C_{w,j}^{k}+C_{w,j+1}^{k})}{\Delta x^2}-v\frac{(C_{w,j}^{k}-C_{w,j-1}^{k})}{\Delta x}+\frac{3D_e m_d}{\rho_p V_w a}\left(\frac{C_{L,j}^{k}-C_{w,j}^{k}}{a-r_L}\right)\right) \tag{S5.19}$$

After transformation:

$$\left[1+(1-\varphi)\left(\frac{3D_e m_d\Delta t}{\rho_p V_w a(a-r_L)}+\frac{2D_L\Delta t}{\Delta x^2}+\frac{v\Delta t}{\Delta x}\right)\right]C_{w,j}^{k+1}=\left[(1-\varphi)\left(\frac{D_L\Delta t}{\Delta x^2}+\frac{v\Delta t}{\Delta x}\right)\right]C_{w,j-1}^{k+1}+\left[\frac{(1-\varphi)D_L\Delta t}{\Delta x^2}\right]C_{w,j+1}^{k+1}+\left[\frac{(1-\varphi)3D_e m_d\Delta t}{\rho_p V_w a(a-r_L)}\right]C_{L,j}^{k+1}+\left[\varphi\left(\frac{D_L\Delta t}{\Delta x^2}+\frac{v\Delta t}{\Delta x}\right)\right]C_{w,j-1}^{k}+\left[\frac{\varphi D_L\Delta t}{\Delta x^2}\right]C_{w,j+1}^{k}+\left[\frac{\varphi 3D_e m_d\Delta t}{\rho_p V_w a(a-r_L)}\right]C_{L,j}^{k}+\left[1-\varphi\left(\frac{3D_e m_d\Delta t}{\rho_p V_w a(a-r_L)}+\frac{2D_L\Delta t}{\Delta x^2}+\frac{v\Delta t}{\Delta x}\right)\right]C_{w,j}^{k}$$

In order to solve this system of equations, we may merge the two concentration vectors to a single one ($C = [C_w; C_p]$; with the semicolon being a line delimiter):

$$C=\begin{bmatrix}C_{w,1}\\C_{1,1}\\\vdots\\C_{p,1}\\\vdots\\C_{L,1}\\\vdots\\C_{w,j}\\C_{1,j}\\\vdots\\C_{p,j}\\\vdots\\C_{L,j}\\\vdots\\C_{w,N}\\C_{1,N}\\\vdots\\C_{p,N}\\\vdots\\C_{L,N}\end{bmatrix}_{(L+1)*N\times 1}=\begin{bmatrix}C_1\\C_2\\\vdots\\C_{p+1}\\\vdots\\C_{L+1}\\\vdots\\C_{(L+1)*(j-1)+1}\\C_{(L+1)*(j-1)+2}\\\vdots\\C_{(L+1)*(j-1)+p+1}\\\vdots\\C_{(L+1)*j}\\\vdots\\C_{(L+1)*(N-1)+1}\\C_{(L+1)*(N-1)+2}\\\vdots\\C_{(L+1)*(N-1)+p+1}\\\vdots\\C_{(L+1)*N}\end{bmatrix}_{(L+1)*N\times 1} \tag{S5.20}$$

with $p\epsilon[1, 2, \ldots, L]$ and $j\epsilon[1, 2, \ldots, N]$.

Using the Newton–Raphson scheme, the following residual function $f(C^{k+1})$ is linearized at the current guess C_{guess}^{k+1} of C^{k+1} (Cirpka, 2020):

$$
\begin{aligned}
f_{(L+1)*(j-1)+1} = &\left[1+(1-\varphi)\left(\frac{3D_e m_d \Delta t}{\rho_p V_w a(a-r_L)}+\frac{2D_L\Delta t}{\Delta x^2}+\frac{v\Delta t}{\Delta x}\right)\right]C_{w,j}^{k+1}\\
&-\left[(1-\varphi)\left(\frac{D_L\Delta t}{\Delta x^2}+\frac{v\Delta t}{\Delta x}\right)\right]C_{w,j-1}^{k+1}+\left[\frac{(1-\varphi)D_L\Delta t}{\Delta x^2}\right]C_{w,j+1}^{k+1}\\
&-\left[\frac{(1-\varphi)3D_e m_d\Delta t}{\rho_p V_w a(a-r_L)}\right]C_{L,j}^{k+1}-\left[\varphi\left(\frac{D_L\Delta t}{\Delta x^2}+\frac{v\Delta t}{\Delta x}\right)\right]C_{w,j-1}^{k}\\
&-\left[\frac{\varphi D_L\Delta t}{\Delta x^2}\right]C_{w,j+1}^{k}-\left[\frac{\varphi 3D_e m_d\Delta t}{\rho_p V_w a(a-r_L)}\right]C_{L,j}^{k}\\
&-\left[1-\varphi\left(\frac{3D_e m_d\Delta t}{\rho_p V_w a(a-r_L)}+\frac{2D_L\Delta t}{\Delta x^2}+\frac{v\Delta t}{\Delta x}\right)\right]C_{w,j}^{k}
\end{aligned}
$$

$$
\begin{aligned}
f_{(L+1)*(j-1)+2} = &\left[\varepsilon+\rho_p K_{fr}\left(C_{1,j}^{k+1}\right)^{\frac{1}{n}-1}+\frac{D_e\Delta t}{r_1^2}\frac{1-\varphi}{r_{1+0.5}-r_{1-0.5}}\frac{r_{1+0.5}^2}{r_2-r_1}\right]C_{1,j}^{k+1}\\
&-\left[\frac{D_e\Delta t}{r_1^2}\frac{1-\varphi}{r_{1+0.5}-r_{1-0.5}}\frac{r_{1+0.5}^2}{r_2-r_1}\right]C_{2,j}^{k+1}-\left[\frac{D_e\Delta t}{r_1^2}\frac{\varphi}{r_{1+0.5}-r_{1-0.5}}\frac{r_{1+0.5}^2}{r_2-r_1}\right]C_{2,j}^{k}\\
&-\left[\varepsilon+\rho_p K_{fr}\left(C_{1,j}^{k}\right)^{\frac{1}{n}-1}-\frac{D_e\Delta t}{r_1^2}\frac{\varphi}{r_{1+0.5}-r_{1-0.5}}\frac{r_{1+0.5}^2}{r_2-r_1}\right]C_{1,j}^{k}
\end{aligned}
$$

$$
\begin{aligned}
f_{(L+1)*(j-1)+p+1} = &\left[\varepsilon+\rho_p K_{fr}\left(C_{p,j}^{k+1}\right)^{\frac{1}{n}-1}\right.\\
&\left.+\frac{D_e\Delta t}{r_p^2}\frac{1-\varphi}{r_{p+0.5}-r_{p-0.5}}\left(\frac{r_{p+0.5}^2}{r_{p+1}-r_p}+\frac{r_{p-0.5}^2}{r_p-r_{p-1}}\right)\right]C_{p,j}^{k+1}\\
&-\left[\frac{D_e\Delta t}{r_p^2}\frac{1-\varphi}{r_{p+0.5}-r_{p-0.5}}\frac{r_{p+0.5}^2}{r_{p+1}-r_p}\right]C_{p+1,j}^{k+1}-\left[\frac{D_e\Delta t}{r_p^2}\frac{1-\varphi}{r_{p+0.5}-r_{p-0.5}}\frac{r_{p-0.5}^2}{r_p-r_{p-1}}\right]C_{p-1,j}^{k+1}\\
&-\left[\frac{D_e\Delta t}{r_p^2}\frac{\varphi}{r_{p+0.5}-r_{p-0.5}}\frac{r_{p+0.5}^2}{r_{p+1}-r_p}\right]C_{p+1,j}^{k}-\left[\frac{D_e\Delta t}{r_p^2}\frac{\varphi}{r_{p+0.5}-r_{p-0.5}}\frac{r_{p-0.5}^2}{r_p-r_{p-1}}\right]C_{p-1,j}^{k}\\
&-\left[\varepsilon+\rho_b K_{fr}\left(C_{p,j}^{k}\right)^{\frac{1}{n}-1}-\frac{D_e\Delta t}{r_p^2}\frac{\varphi}{r_{p+0.5}-r_{p-0.5}}\left(\frac{r_{p+0.5}^2}{r_{p+1}-r_p}+\frac{r_{p-0.5}^2}{r_p-r_{p-1}}\right)\right]C_{p,j}^{k}
\end{aligned}
\tag{S5.21}
$$

$$
\begin{aligned}
f_{(L+1)*j} = &\left[\varepsilon+\rho_b K_{fr}\left(C_{L,j}^{k+1}\right)^{\frac{1}{n}-1}+\frac{D_e\Delta t}{r_L^2}\frac{1-\varphi}{a-r_{L-0.5}}\left(\frac{a^2}{a-r_L}+\frac{r_{L-0.5}^2}{r_L-r_{L-1}}\right)\right]C_{L,j}^{k+1}\\
&-\left[\frac{D_e\Delta t}{r_L^2}\frac{1-\varphi}{a-r_{L-0.5}}\frac{a^2}{a-r_L}\right]C_{w,j}^{k+1}-\left[\frac{D_e\Delta t}{r_L^2}\frac{1-\varphi}{a-r_{L-0.5}}\frac{r_{L-0.5}^2}{r_L-r_{L-1}}\right]C_{L-1,j}^{k+1}\\
&-\left[\frac{D_e\Delta t}{r_L^2}\frac{\varphi}{a-r_{L-0.5}}\frac{a^2}{a-r_L}\right]C_{w,j}^{k}-\left[\frac{D_e\Delta t}{r_L^2}\frac{\varphi}{a-r_{L-0.5}}\frac{r_{L-0.5}^2}{r_L-r_{L-1}}\right]C_{L-1,j}^{k}\\
&-\left[\varepsilon+\rho_p K_{fr}\left(C_{L,j}^{k}\right)^{\frac{1}{n}-1}-\frac{D_e\Delta t}{r_L^2}\frac{\varphi}{a-r_{L-0.5}}\left(\frac{R^2}{a-r_L}+\frac{r_{L-0.5}^2}{r_L-r_{L-1}}\right)\right]C_{L,j}^{k}
\end{aligned}
$$

The residual function vector can be organized as:

$$f(C^{k+1}) = \begin{bmatrix} f_1 \\ f_2 \\ \vdots \\ f_{p+1} \\ \vdots \\ f_{L+1} \\ \vdots \\ f_{(L+1)*(j-1)+1} \\ f_{(L+1)*(j-1)+2} \\ \vdots \\ f_{(L+1)*(j-1)+p+1} \\ \vdots \\ f_{(L+1)*j} \\ \vdots \\ f_{(L+1)*(N-1)+1} \\ f_{(L+1)*(N-1)+2} \\ \vdots \\ f_{(L+1)*(N-1)+p+1} \\ \vdots \\ f_{(L+1)*N} \end{bmatrix}_{(L+1)*N\times 1} \tag{S5.22}$$

Similar to the film diffusion case (see section S5.2), the C^{k+1} vector can be determined by Eq. S5.9 as well and the Jacobian matrix of intraparticle pore diffusion case can be expressed as:

$$J = \begin{bmatrix} \frac{\partial f_1}{\partial C_1} & \frac{\partial f_1}{\partial C_2} & \cdots & \frac{\partial f_1}{\partial C_{(L+1)*N-1}} & \frac{\partial f_1}{\partial C_{(L+1)*N}} \\ \frac{\partial f_2}{\partial C_1} & \frac{\partial f_2}{\partial C_2} & \cdots & \frac{\partial f_2}{\partial C_{(L+1)*N-1}} & \frac{\partial f_2}{\partial C_{(L+1)*N}} \\ \vdots & \vdots & \cdots & \vdots & \vdots \\ \frac{\partial f_{(L+1)*N-1}}{\partial C_1} & \frac{\partial f_{(L+1)*N-1}}{\partial C_2} & \cdots & \frac{\partial f_{(L+1)*N-1}}{\partial C_{(L+1)*N-1}} & \frac{\partial f_{(L+1)*N-1}}{\partial C_{(L+1)*N}} \\ \frac{\partial f_{(L+1)*N}}{\partial C_1} & \frac{\partial f_{(L+1)*N}}{\partial C_2} & \cdots & \frac{\partial f_{(L+1)*N}}{\partial C_{(L+1)*N-1}} & \frac{\partial f_{(L+1)*N}}{\partial C_{(L+1)*N}} \end{bmatrix}_{(L+1)*N\times(L+1)*N} \tag{S5.23}$$

In order to ensure the accuracy of the model, an error vector (ΔC^{k+1}) was used as described above for Eq. S5.11:

$$\Delta C^{k+1} = \begin{bmatrix} \left|C_{1,guess,new}^{k+1} - C_{1,guess,old}^{k+1}\right| \\ \left|C_{2,guess,new}^{k+1} - C_{2,guess,old}^{k+1}\right| \\ \vdots \\ \left|C_{p+1,guess,new}^{k+1} - C_{p+1,guess,old}^{k+1}\right| \\ \vdots \\ \left|C_{L+1,guess,new}^{k+1} - C_{L+1,guess,old}^{k+1}\right| \\ \vdots \\ \left|C_{(L+1)*(j-1)+1,guess,new}^{k+1} - C_{(L+1)*(j-1)+1,guess,old}^{k+1}\right| \\ \left|C_{(L+1)*(j-1)+2,guess,new}^{k+1} - C_{(L+1)*(j-1)+2,guess,old}^{k+1}\right| \\ \vdots \\ \left|C_{(L+1)*(j-1)+p+1,guess,new}^{k+1} - C_{(L+1)*(j-1)+p+1,guess,old}^{k+1}\right| \\ \vdots \\ \left|C_{(L+1)*j,guess,new}^{k+1} - C_{(L+1)*j,guess,old}^{k+1}\right| \\ \vdots \\ \left|C_{(L+1)*(N-1)+1,guess,new}^{k+1} - C_{(L+1)*(N-1)+1,guess,old}^{k+1}\right| \\ \left|C_{(L+1)*(N-1)+2,guess,new}^{k+1} - C_{(L+1)*(N-1)+2,guess,old}^{k+1}\right| \\ \vdots \\ \left|C_{(L+1)*(N-1)+p+1,guess,new}^{k+1} - C_{(L+1)*(N-1)+p+1,guess,old}^{k+1}\right| \\ \vdots \\ \left|C_{(L+1)*N,guess,new}^{k+1} - C_{(L+1)*N,guess,old}^{k+1}\right| \end{bmatrix}_{(L+1)*N\times 1} \quad \text{(S5.24)}$$

The iteration processes stop when the maximum value of the error vector ΔC_{max}^{k+1} is smaller than the tolerable error e (e.g., $e = 10^{-15}$).

S5.4 Length of the mass transfer zone (X_s) for the first order analytical solution

Analytical solutions can be derived for the case of the first flooding of the column which are used here for verification of the numerical codes.

S5.4.1 Analytical solution based on the film diffusion model

During the first flooding of the column, the front water flow is always contacting fresh contaminant material. Therefore, the solute concentration at the particle-water boundary is constant and in equilibrium with the solids:

$$C_{w,eq} = \frac{C_{s,ini}}{K_d} \quad \text{(S5.25)}$$

Inserting Eq. S5.25 into Eq. 5.7 gives:

$$\frac{\partial C_w}{\partial t} = k\frac{6(1-n)}{nd}(C_{w,eq} - C_w) \tag{S5.26}$$

which upon integration yields the following analytical solution for the initial condition $C_{w(t=0)} = 0$ (desorption):

$$\begin{aligned} &\int_0^{C_w} \frac{\partial C_w}{(C_{w,eq} - C_w)} = \int_0^t k\frac{6(1-n)}{nd}\partial t \\ &-\ln(C_{w,eq} - C_w) + \ln(C_{w,eq}) = -\ln\left(1 - \frac{C_w}{C_{w,eq}}\right) = k\frac{6(1-n)}{nd}t \\ &\frac{C_w}{C_{w,eq}} = 1 - \exp\left(-k\frac{6(1-n)}{nd}t\right) \end{aligned} \tag{S5.27}$$

The contact time in Eq. S5.27 can be substituted with the ratio of the travel distance (x) and the flow velocity (v). The length of the mass transfer zone is defined by setting the argument of the exponential function to -1, referring to the location x where the solute concentration in the groundwater reaches 63.2% of the equilibrium concentration.

$$X_{s,63.2\%} = \frac{v\,n\,d}{6\,k\,(1-n)} \tag{S5.28}$$

Equation S5.28 shows that the length of mass transfer zone depends on the flow velocity, inter-granular porosity as well as particle size, but is independent of the distribution coefficient.

If the length of the mass transfer zone is shorter than the column length (X_{col}), a concentration higher than 63.2% of the equilibrium concentration will be observed in the column effluent until the mass transfer zone arrives at the column outlet. The time needed to reach 63.2% equilibrium concentration at the column outlet equals:

$$\begin{aligned} t_{63.2\%} &= \frac{X_s}{v} + \frac{(X_{col} - X_s)}{v}R_d \\ &= \frac{X_{col}}{v}\left(1 + K_d\frac{\rho_b}{n}\left(1 - \frac{X_s}{X_{col}}\right)\right) \end{aligned} \tag{S5.29}$$

Considering fast kinetics ($X_s \to 0$), $t_{63.2\%}(\approx X_{col}/(v/R_d))$ is mainly dominated by the retarded seepage velocity (v/R_d).

S5.4.2 Analytical solution based on the intraparticle pore diffusion model

Expressing internal mass transfer resistance by means of intraparticle pore diffusion, with

mass transfer coefficient $k = D_e/\delta_p$, where D_e is the effective intraparticle diffusion coefficient ($D_e = D_{aq}\varepsilon/\tau \approx D_{aq}\varepsilon^2$) and the mean square displacement δ_p ($\delta_p = \sqrt{\pi D_a\, t_c}$) representing the diffusion distance, which grows with the square root of contact time between particles and water (t_c) at early times, leads to:

$$\frac{\partial C_w}{\partial t} = k\, A^o\left(C_{w,eq} - C_w\right) = \frac{D_e}{\sqrt{\pi D_a\, t_c}}\frac{6(1-n)}{nd}\left(C_{w,eq} - C_w\right) \tag{S5.30}$$

The contact time between water and dry particles can be estimated by the ratio of particle size and flow velocity ($t_c = d/v$).

For the initial condition $C_{w(t=0)} = 0$, integration of Eq. S5.30 yields the following analytical solution:

$$\begin{aligned}
&\int_0^{C_w} \frac{\partial C_w}{\left(C_{w,eq} - C_w\right)} = \int_0^{t} \frac{D_e}{\sqrt{\pi D_a\, t_c}}\frac{6(1-n)}{nd}\,\partial t \\
&-\ln\left(C_{w,eq} - C_w\right) + \ln\left(C_{w,eq}\right) = -\ln\left(1 - \frac{C_w}{C_{w,eq}}\right) = \frac{D_e}{\sqrt{\pi D_a \frac{d}{v}}}\frac{6(1-n)}{nd}\,t \\
&\frac{C_w}{C_{w,eq}} = 1 - \exp\left(-\frac{D_e}{\sqrt{\pi D_a \frac{d}{v}}}\frac{6(1-n)}{nd}\,t\right)
\end{aligned} \tag{S5.31}$$

The length of the mass transfer zone of intraparticle pore diffusion can be calculated by:

$$\begin{aligned}
X_{s,63.2\%} &= \frac{v\, n\, d}{6\frac{D_e}{\sqrt{\pi D_a \frac{d}{v}}}(1-n)} \\
&= \sqrt{\frac{\pi d^3 v}{D_e\left(\varepsilon + K_d \rho_p\right)}}\frac{n}{6(1-n)}
\end{aligned} \tag{S5.32}$$

$X_{s,63.2\%}$ based on intraparticle pore diffusion increases with particle size to the power of 3/2 ($d^{3/2}$) and decreases with the square root of the distribution coefficient ($\sqrt{K_d}$). The time required to observe the corresponding concentration of 63.2% of the equilibrium concentration at the column outlet can be determined with Eq. S5.29.

S5.4.3 Comparison of analytical and numerical solution and estimation of mass transfer zone length (X_s)

In Fig. S5.2, analytical solutions for the increase of the concentration in the first water parcel over distance (which here represents time: $t = x/v$) during the first flooding of the column are shown for FD (Eq. S5.28) and IPPD (Eq. S5.31). The numerical solutions are described in

sections S5.2 and S5.3.

A comparison reveals that the analytical solutions and the numerical solutions overlap almost perfectly for both FD and IPPD (see Fig. S5.2). This verifies the accuracy of the numerical model. The length of the mass transfer zone for FD is 0.35 cm and independent of K_d, and much shorter than for IPPD with X_s = 10 cm, 3.5 cm and 1.1 cm for K_d values of 0.1 L kg^{-1}, 1 L kg^{-1} and 10 L kg^{-1}, respectively. The deviations between FD and IPPD gradually vanish with increasing K_d values. If the initial concentration in the column leachate is close to equilibrium, it may be used for the determination of K_d ($K_d = C_{s,ini}/C_{w,peak}$); K_d is overestimated if the initial effluent concentration does not reach equilibrium ($C_{w,peak} < C_{w,eq}$). The length of the mass transfer zone (Eqs. S5.28 and S5.32) may be used to assess equilibrium at the beginning of the column test.

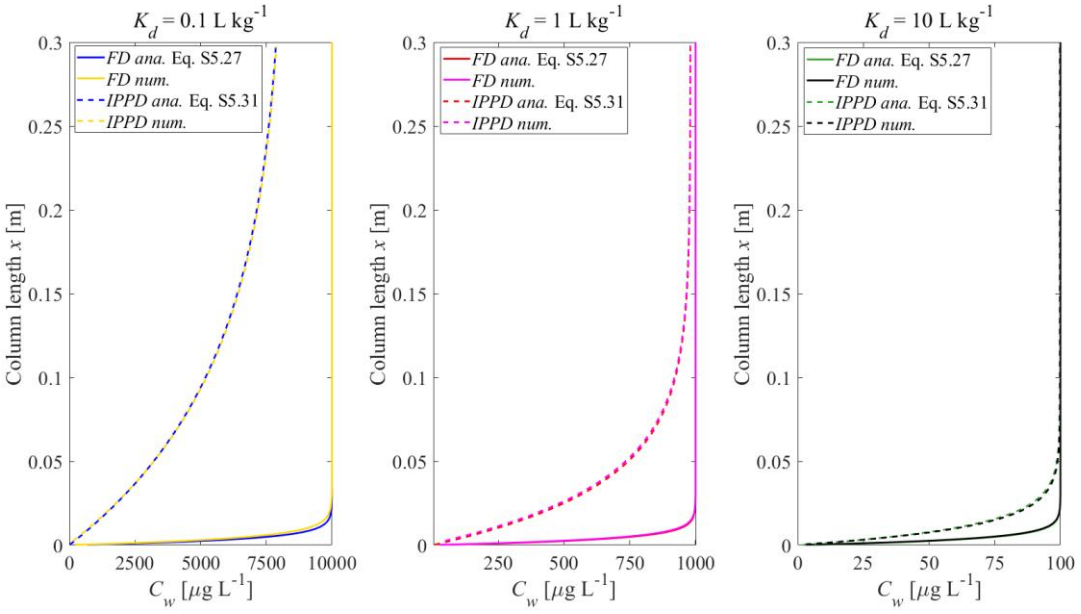

Fig. S5.2: Concentration increase in a water parcel ($C_{w,peak}$) in the column during the first flooding (up-flow); solid lines: film diffusion; dashed lines: intraparticle diffusion; comparison between analytical (ana.) and numerical (num.) solutions. n = 0.45, v = 1.67 × 10^{-5} m s^{-1}, α/x = 0 (no dispersion), $C_{s,ini}$ = 1000 µg kg^{-1}, t = 5 h, D_{aq} = 1 × 10^{-9} m^2 s^{-1}, ε = 0.05, $d_{p,coarse}$ = 2000 µm.

S5.5 Comparison of analytical and numerical solution (code verification)

In order to further confirm the accuracy of the numerical solution, the initial concentration

distribution in the column after first flooding, as well as leaching curves are compared with the analytical solution (Eq. 5.6). The analytical solution is only valid for equilibrium sorption conditions and to compare it with the numerical solution, fine particles ($d_{p,fine}$ = 63 µm) are used to get close to equilibrium (to fast FD kinetics). Figures S5.3 and S5.4 show the good agreement of both solutions. The slight deviations between analytical and numerical solutions, especially at low K_d values, are due to kinetics in the numerical solution. Deviations gradually vanish with the increase of K_d.

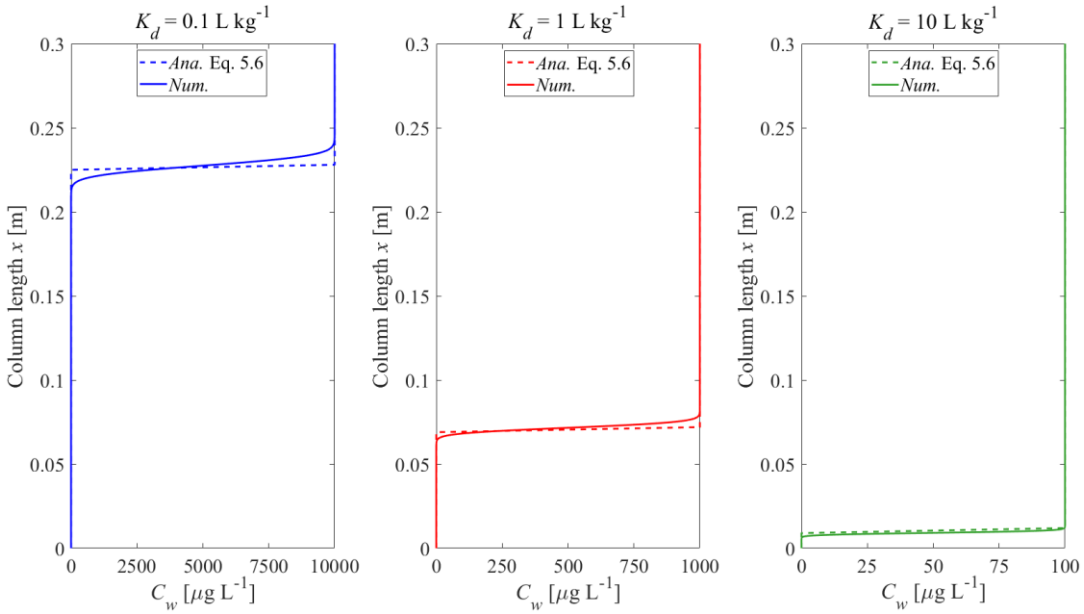

Fig. S5.3: Concentration vs. distance in the up-flow column test after the first flooding of the column (initial condition). Comparison of the analytical solution (Eq. 5.6, dashed lines) and numerical solution (solid lines); n = 0.45, v = 1.67 × 10^{-5} m s^{-1}, α = 0 (no dispersion), $C_{s,ini}$ = 1000 µg kg^{-1}, t_c = 5 h, $d_{p,fine}$ = 63 µm.

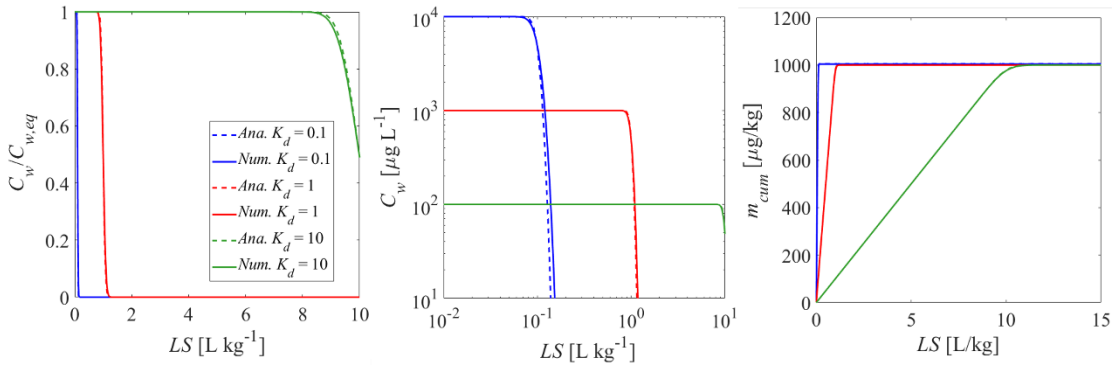

Fig. S5.4: Normalized and absolute concentration ($C_w/C_{w,eq}, C_w$) as well as cumulative concentration (m_{cum}) in the column effluent vs. time (expressed as liquid to solid ratio: LS)

for the initial conditions after the first flooding of the column (see Fig. S5.3); comparison of analytical solution (Ana. Eq. 5.6, dashed lines) and numerical solution (Num., solid lines).

S5.6 Impact of dispersion on leaching curves

The following figures (S5.5–S5.12) compare leaching scenarios without and with dispersion.

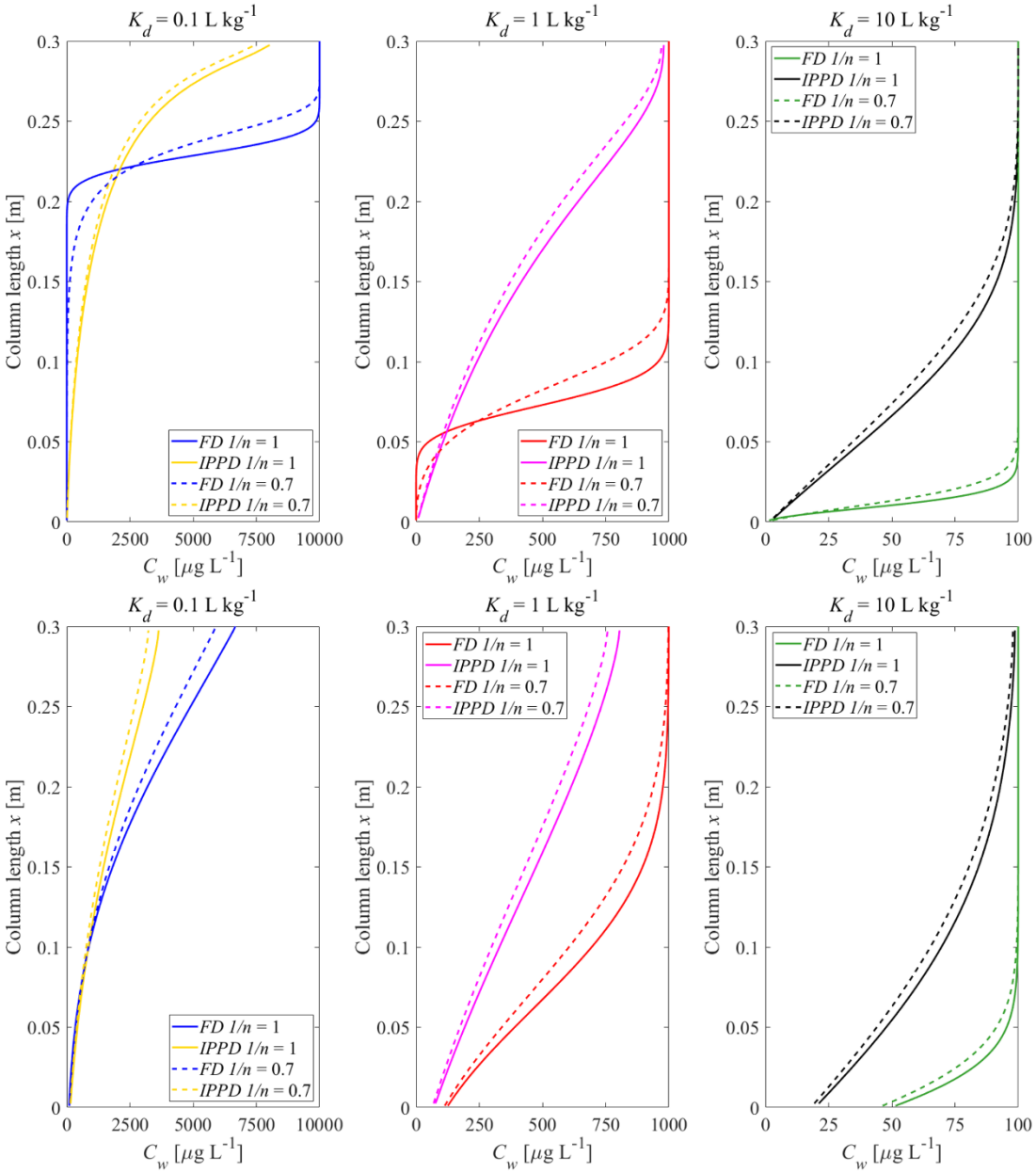

Fig. S5.5: Initial concentration profiles in the column after the first flooding (up-flow) without and with dispersion (top and bottom panel); solid lines: linear sorption; dashed lines: non-linear sorption cases (based on a Freundlich exponent $1/n$ = 0.7), n = 0.45, v = 1.67 × 10^{-5} m s^{-1}, α/x = 0 or 0.1, $C_{s,ini}$ = 1000 µg kg^{-1}, t_c = 5 h, D_{aq} = 1 × 10^{-9} m^2 s^{-1}, ε = 0.05,

$d_{p,coarse}$ = 2000 µm.

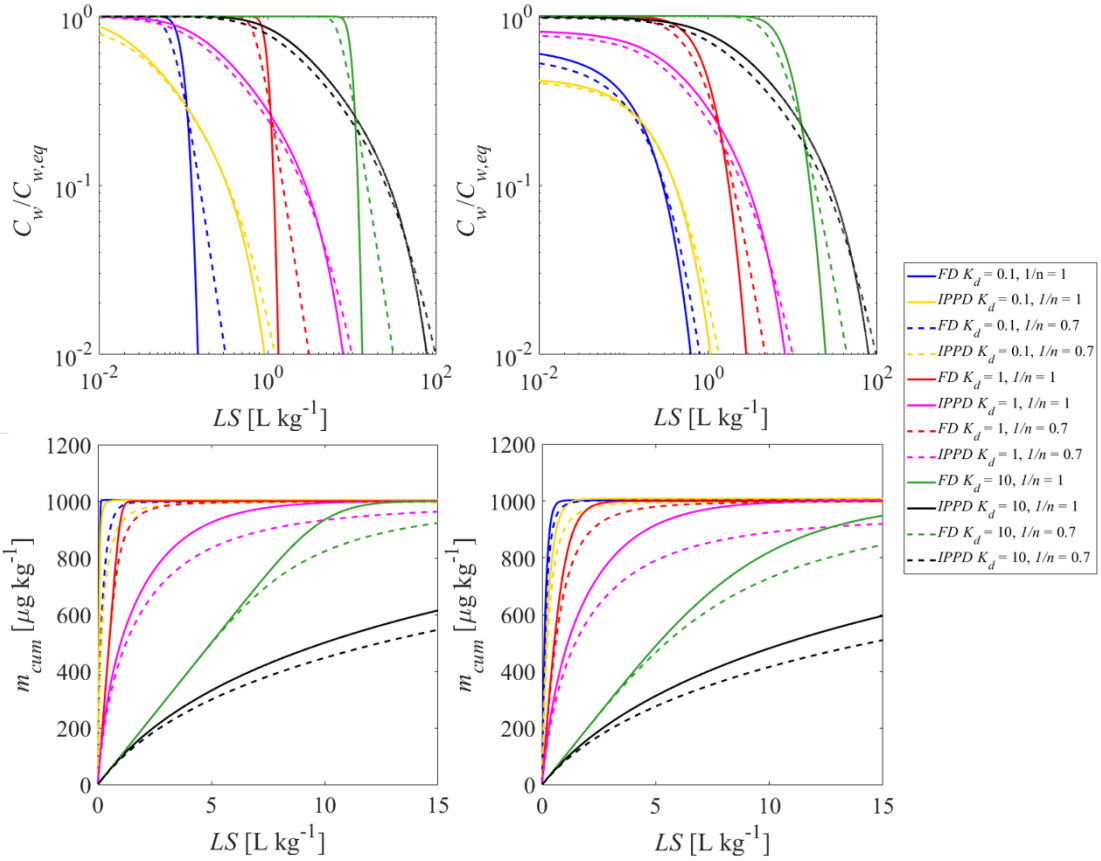

Fig. S5.6: Normalized concentrations ($C_w/C_{w,eq}$) as well as cumulative concentrations (m_{cum}) in the column effluent vs. time (expressed as liquid to solid ratio: LS) for different initial conditions depicted in Fig. S5.5; solid lines: linear sorption; dashed lines: nonlinear sorption. Left column: without dispersion; right column: with dispersion.

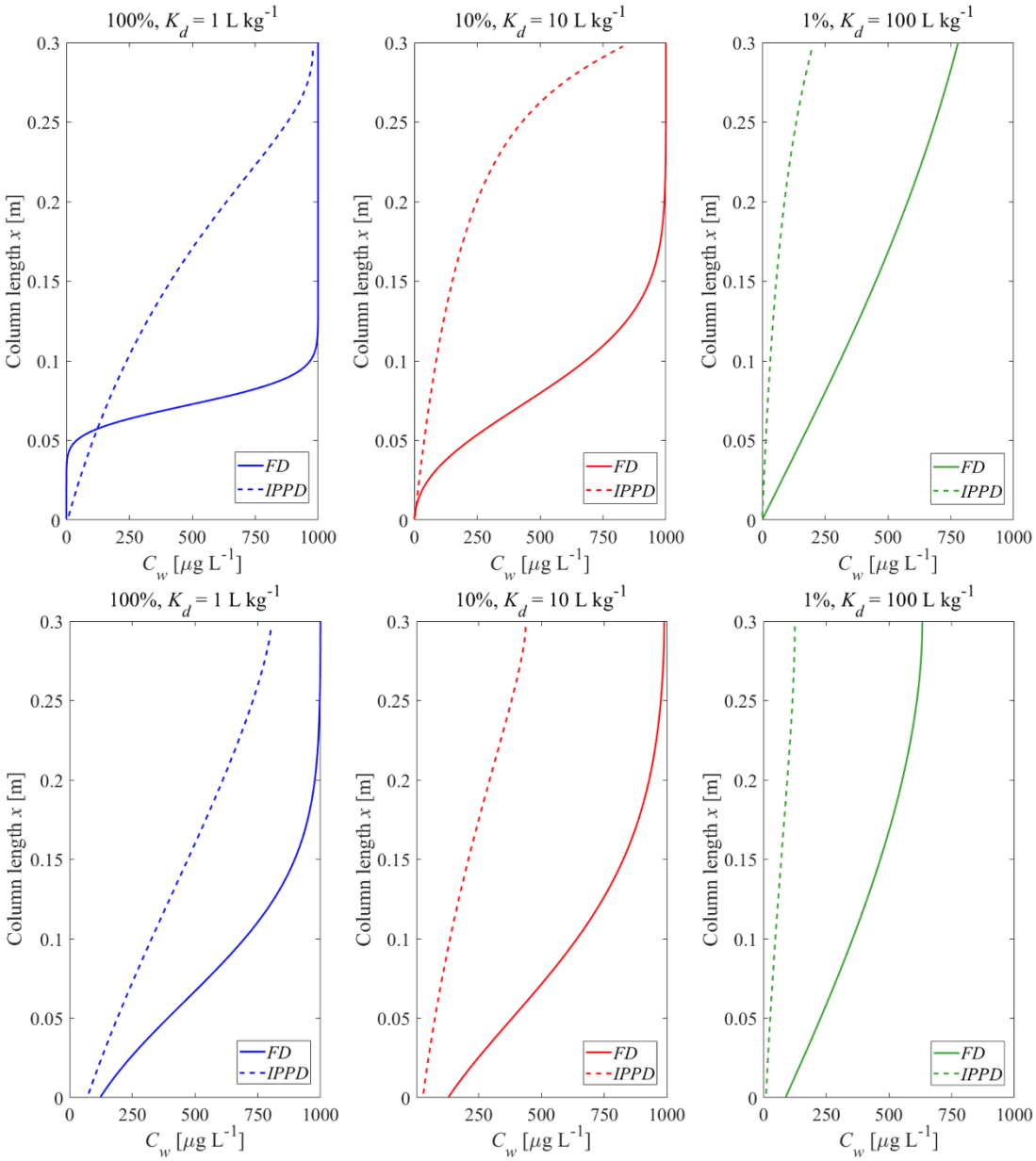

Fig. S5.7: Initial concentration distribution in the column after the first flooding (up-flow) for different bi-modal compositions of sorbing and non-sorbing particles; left column: homogeneous case with average K_d (= $K_{d,av}$ = 1 L kg^{-1}); mid column: only 10% of the particles carry the contaminant at K_d = 10 × $K_{d,av}$; right column: only 1% of the particles carry the contaminant at K_d = 100 × $K_{d,av}$; the average $K_{d,av}$ of the entire material is the same for all compositions; solid lines: film diffusion case, dashed lines: intraparticle diffusion case. Top panel: without dispersion; bottom panel: with dispersion; n = 0.45, v = 1.67 × 10^{-5} m s^{-1}, α/x = 0 or 0.1, $C_{s,ini}$ = 1000 µg kg^{-1}, t_c = 5 h, D_{aq} = 1 × 10^{-9} m^2 s^{-1}, ε = 0.05, $d_{p,coarse}$ = 2000 µm.

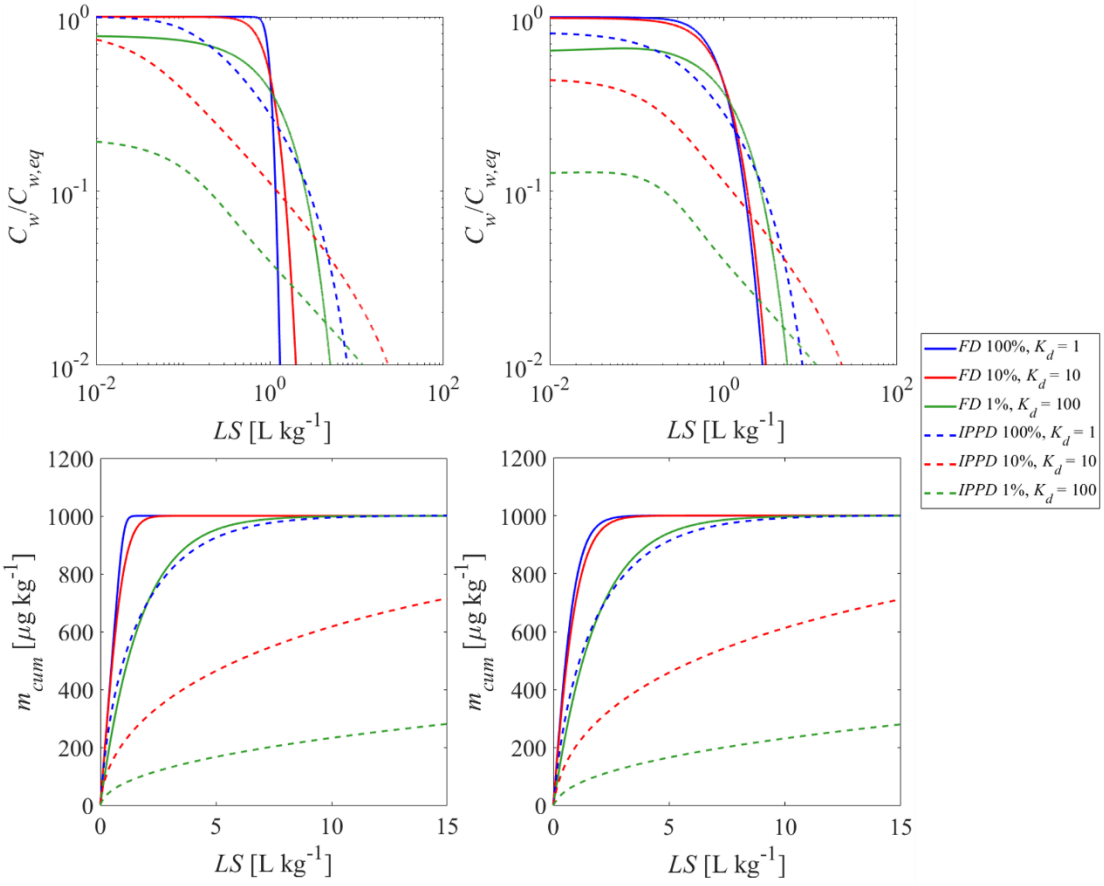

Fig. S5.8: Normalized concentrations ($C_w/C_{w,eq}$) as well as cumulative concentrations (m_{cum}) in the column effluent vs. time (expressed as liquid to solid ratio: *LS*) for different combinations of sorbing particles and distribution coefficients (initial conditions depicted in Fig. S5.7); left: without dispersion; right: with dispersion; solid lines: film diffusion cases, dashed lines: intraparticle diffusion cases.

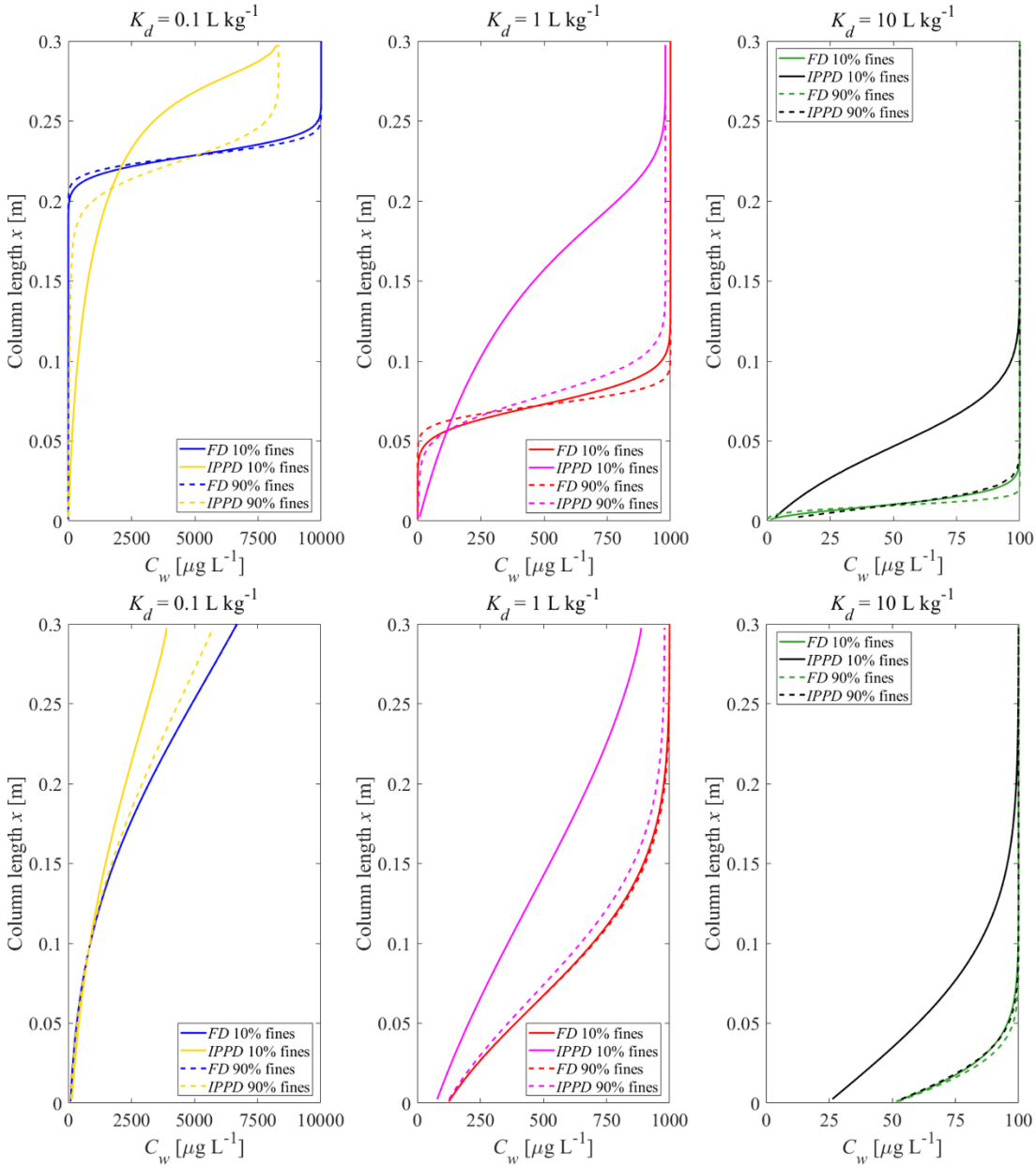

Fig. S5.9: Initial concentration distribution in the column after the first flooding (up-flow) for two different bi-modal grain size distributions of fine and coarse particles; solid lines: fine particle mass fraction 10%; dashed lines: fine particle mass fraction 90%. (n = 0.45, v = 1.67 × 10^{-5} m s^{-1}, α/x = 0 or 0.1, $C_{s,ini}$ = 1000 µg kg^{-1}, t_c = 5 h, D_{aq} = 1 × 10^{-9} m^2 s^{-1}, ε = 0.05, $d_{p,coarse}$ = 2000 µm, $d_{p,fine}$ = 63 µm); top panel: without dispersion; bottom panel: with dispersion.

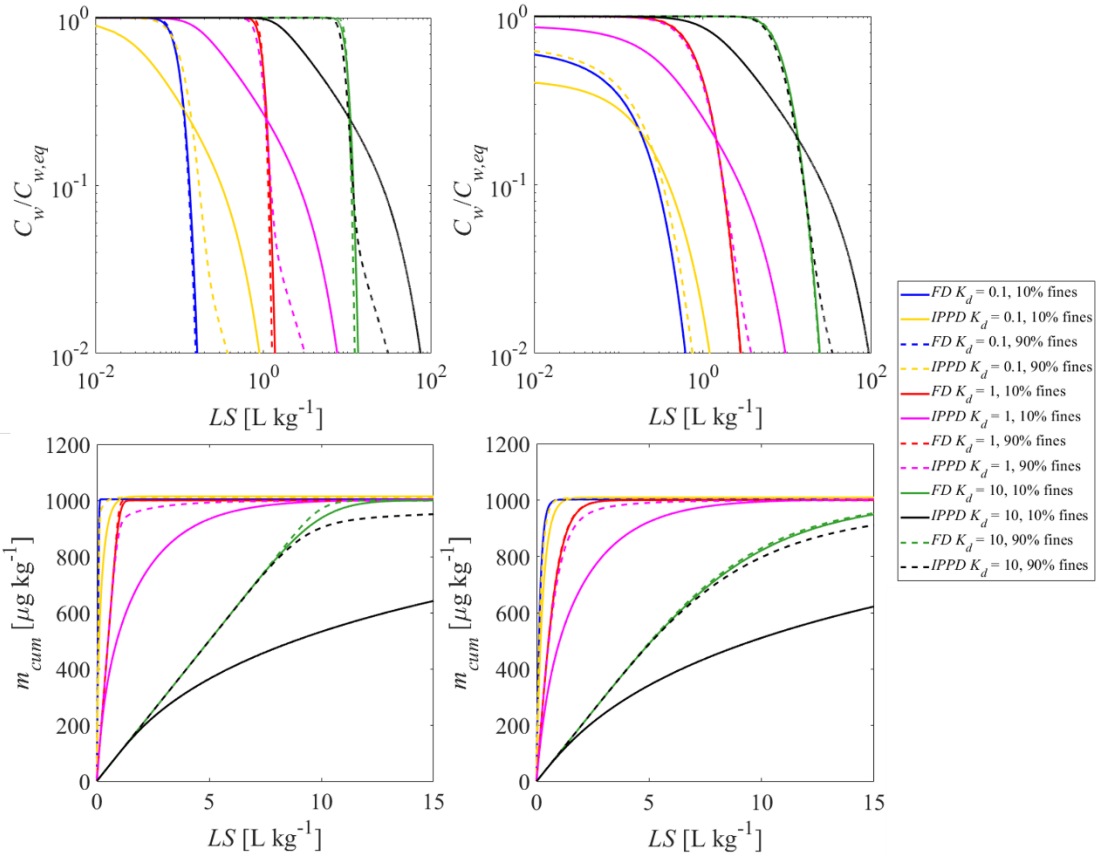

Fig. S5.10: Influence of different grain size fractions and distribution coefficients on normalized concentrations ($C_w/C_{w,eq}$) as well as cumulative concentrations (m_{cum}) in the column effluent vs. time (expressed as liquid to solid ratio LS); left: without dispersion; right: with dispersion; solid lines: fine particle mass fraction 10%; dashed lines: fine particle mass fraction 90%; kinetic parameters are the same as Fig. S5.9.

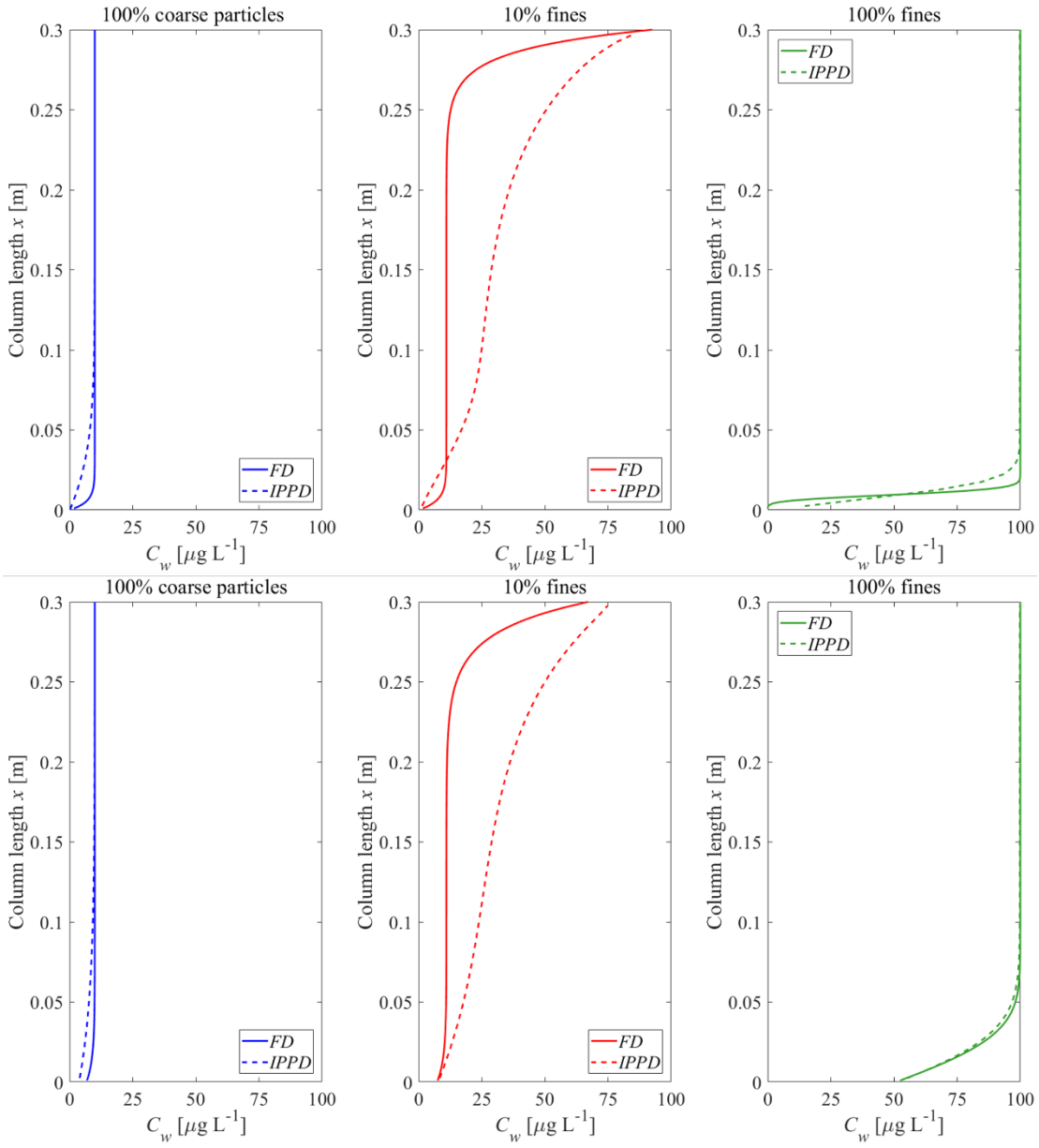

Fig. S5.11: Initial concentration distribution in the column after the first flooding (up-flow) for different bi-modal material compositions of fine particles with low sorption capacity (K_d = 10 L kg^{-1}) and coarse particles with high sorption capacity; left: 100% coarse particles (K_d = 100 L kg^{-1}); middle: mixed sample with 10% fine particles; right: 100% fine particles; solid lines: film diffusion (FD), dashed lines: intraparticle diffusion cases (IPPD); n = 0.45, v = 1.67 × 10^{-5} m s^{-1}, α/x = 0 or 0.1, $C_{s,ini}$ = 1000 µg kg^{-1}, t_c = 5 h, D_{aq} = 1 × 10^{-9} m^2 s^{-1}, ε = 0.05, $d_{p,coarse}$ = 2000 µm, $d_{p,fine}$ = 63 µm; top panel: without dispersion; bottom panel: with dispersion.

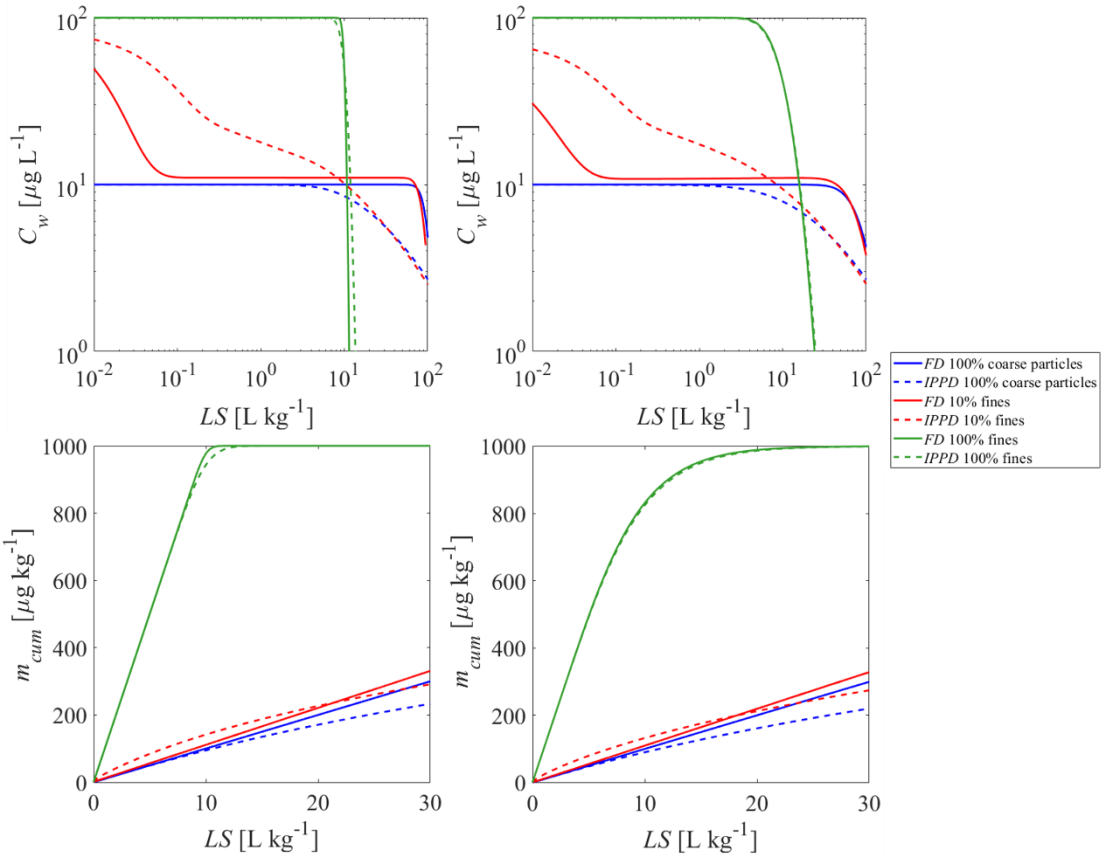

Fig. S5.12: Leachate concentrations (C_w) as well as cumulative concentrations (m_{cum}) in the column effluent vs. time (expressed as liquid to solid ratio: LS) for different combinations of fine particles with low sorption capacity ($K_d = 10$ L kg^{-1}) and coarse particles with high sorption capacity ($K_d = 100$ L kg^{-1}); left: without dispersion; right: with dispersion; solid lines: film diffusion cases, dashed lines: intraparticle diffusion cases; kinetic parameters are the same as Fig. S5.11.

References

Arters, D.C., Fan, L.S., 1990. Experimental methods and correlation of solid—liquid mass transfer in fluidized beds. Chem. Eng. Sci. 45, 965–975. https://doi.org/10.1016/0009-2509(90)85019-A.

Blasius, H., 1908. Grenzschichten in Flüssigkeiten mit kleiner Reibung (The boundary layers in fluids with little friction). In Zeitschrift für Angewandte Mathematik und Physik (Journal of Applied Mathematics and Physics), volume 56, pp. 1–37.

Calderbank, P.H., Moo-Young, M.B., 1961. The continuous phase heat and mass-transfer properties of dispersions. Chem. Eng. Sci. 16, 39–54. https://doi.org/10.1016/0009-2509(61)87005-X.

Cirpka, O.A., 2020. Solute and heat transport. In Lecture Notes “Environmental Modeling 2”; (unpublished, University of Tübingen).

Kirwan, J., Armenante, P.M., 1989. Mass transfer to microparticle systems. Chem. Eng. Sci. 44 (12), 2781–2796. https://doi.org/10.1016/0009-2509(89)85088-2.

Levins, D.M., Glastonbury, J.R., 1972. Application of Kolmogorov’s theory to particle—liquid mass transfer in agitated vessels. Chem. Eng. Sci. 27, 537–543. https://doi.org/10.1016/0009-2509(72)87009-X.

Liedl, R., Ptak, T., 2003. Modelling of diffusion-limited retardation of contaminants in hydraulically and lithologically nonuniform media. J. Contam. Hydrol. 66, 239–259. https://doi.org/10.1016/S0169-7722(03)00028-7.

Liu, Y., Illangasekare, T.H., Kitanidis, P.K., 2014. Long-term mass transfer and mixing-controlled reactions of a DNAPL plume from persistent residuals. J. Contam. Hydrol. 157, 11–24. https://doi.org/10.1016/j.jconhyd.2013.10.008.

Mao, H.H., Chisti, Y., Moo-Young, M., 1992. Multiphase hydrodynamics and solid-liquid mass transfer in an external-loop airlift reactor–a comparative study. Chem. Eng. Commun. 113, 1–13. https://doi.org/10.1080/00986449208936000.

Ohashi, H., Sugawara, T., Kikuchi, K.I., 1981. Correlation of liquid-side mass transfer coefficient for single particles and fixed beds. J. Chem. Eng. Japan. 14, 489–491. https://doi.org/10.1252/jcej.14.489.

Sherwood, T.K., Pigford, R.L., Wilke, R.L., 1975. “Mass Transfer”, McGraw-Hill: New York,

S6 Supplementary information for two mesh free methods for solving non-equilibrium advective-dispersive solute transport with coupled film-intraparticle diffusion

S6.1 Structure of deep neural networks

The universal approximation theorem has showed that neural networks possess a form of universality and there exists a network that can approximately approach the function with a high degree of accuracy regardless of the nature or complexation of the function (Hornik et al., 1989). This theorem remains valid no matter the quantity of inputs and outputs of the neural networks. Many types of neural networks have been developed and applied in computer vision, image processing, speech recognition, face recognition, complex classification, machine translation in the last decade, such as feed-forward neural networks, convolutional neural networks, recurrent neural networks, radial basis functional neural networks, etc. In this paper, we used the simplest neural networks (feed-forward neural networks), which has been widely used in solving most of PDE problems (Raissi, 2018; Raissi et al., 2019; McClenny et al., 2020; Lu et al., 2021; Cuomo et al., 2023). Define a network ($NN^L(\boldsymbol{x})$): $\mathbb{R}^{d_{in}} \rightarrow \mathbb{R}^{d_{out}}$ is a L-layers neural network with (L-1)-hidden layers. The ℓ-th layer contains N_ℓ neurons (input: $N_1 = d_{in}$; output: $N_{\mathrm{L}} = d_{out}$). The hyperparameters (θ) of network contains the weight matrix ($\mathbf{W}$) and bias vector ($\boldsymbol{b}$). In ℓ-th layer, the size of weight matrix and bias vector can be denoted as $\boldsymbol{W}^\ell \epsilon\, \mathbb{R}^{N_\ell \times N_{\ell-1}}$ and $\boldsymbol{b}^\ell \epsilon\, \mathbb{R}^{N_\ell}$, respectively. Activation functions (σ) are key components of neural network because they introduce non-linearity, allowing the neural network to learn complex relationships between input and output data. Various activation functions are used in neural networks and each of them has unique characteristics utilized for different scenarios. The most frequently used activation functions are logistic sigmoid ($1/(1+e^{-x})$), hyperbolic tangent (tanh) and rectified linear unit ($\mathrm{ReLU(x)} = \max(0, x)$). The logistic sigmoid function is used in our neural networks due to its better performance in training process of neural networks. In summary, a feed-forward neural network can be recursively defined as (see Lu et al., 2021):

$$\begin{aligned} &\text{Input layer: } NN^0(\boldsymbol{x}) = \boldsymbol{x} \epsilon\, \mathbb{R}^{d_{in}} \\ &\text{Hidden layers: } NN^\ell(\boldsymbol{x}) = \sigma\left(\mathbf{W}^\ell NN^{\ell-1}(\boldsymbol{x}) + \boldsymbol{b}^\ell\right) \epsilon\, \mathbb{R}^{N_\ell} \text{ for } 1 \le \ell \le L-1 \\ &\text{Output layer: } NN^L(\boldsymbol{x}) = \boldsymbol{W}^L NN^{\mathrm{L}-1}(\boldsymbol{x}) + \mathbf{b}^L \epsilon\, \mathbb{R}^{d_{out}} \end{aligned} \qquad \text{(S6.1)}$$

For solving one dimensional (1D) advective-dispersive transport coupled with intraparticle particle pore diffusion, two feed-forward neural networks are used ($NN_1^L(\boldsymbol{x_1})$ and $NN_2^L(\boldsymbol{x_2})$).

The inputs of the 1st network ($\boldsymbol{x_1}$) are dimensionless time (t^*) and space coordinate in transport direction (x^*) and the output is the dimensionless pollutant concentration in bulk water phase (C_w^*). The inputs of 2nd network ($\boldsymbol{x_2}$) not only includes the dimensionless time (t^*) and space coordinate (x^*) in transport direction, but also the dimensionless radial coordinate for pollutant transport in intraparticle pore space (r^*). The output is the dimensionless pollutant concentration in intraparticle pore water phase ($C_{w,p}^*$). Due to normalization of inputs and outputs of neural networks by their corresponding maximum values, all dimensionless variables range from 0 to 1.

S6.2 Automatic differentiation

In physical informed neural networks (PINNs), a crucial step is to compute the derivatives of the network outputs (C_w^* and $C_{w,p}^*$) with respective to the network inputs (t^*, x^* and r^*) for constructing the PDEs. Four methods are commonly used in computer programming: (1) manual differentiation; (2) numerical differentiation; (3) symbolic differentiation; (4) automatic differentiation (AD). Manual differentiation is both time-consuming and susceptible to errors. While numerical differentiation is easy to use, it would be inaccurate due to round-off and truncation errors (Jerrell, 1997). Symbolic differentiation is widely utilized in software program such as Mathematic, Maxima, Maple and Matlab, but it often results in complex and tedious expressions plagued with the problem of "expression swell" (Collobert et al., 2011). AD reinterprets a computer program by replacing variable domains with derivatives. It then redefines operator semantics to propagate derivatives using the chain rule of differential calculus (Güneş Baydin et al. (2018)). In the following, we present an example how to calculate the derivatives using backpropagation in Fig. S6.1, a typical technique of AD.

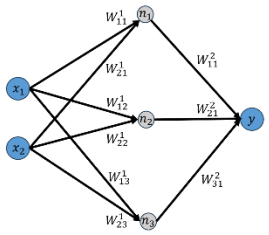

A simple neural network structure with 2 fully connect operations (1 input layer (x_1 and x_2) +1 hidden layers + 1 output layer (y)) with 3 hidden neurons (n_1, n_2 and n_3).

Calculation process:

$h_1 = (W_{11}^1 * x_1 + W_{21}^1 * x_2) + b_1^1$
$h_2 = (W_{12}^1 * x_1 + W_{22}^1 * x_2) + b_2^1$
$h_3 = (W_{13}^1 * x_1 + W_{23}^1 * x_2) + b_3^1$
$n_1 = \sigma(h_1)$
$n_2 = \sigma(h_2)$
$n_3 = \sigma(h_3)$
$y = (W_{11}^2 * n_1 + W_{21}^2 * n_2 + W_{31}^2 * n_3) + b_1^2$

Assumption of weights, bias and activation function (as an example):

$W_{11}^1 = W_{21}^1 = b_1^1 = 0.1$
$W_{12}^1 = W_{22}^1 = b_2^1 = 0.5$
$W_{13}^1 = W_{23}^1 = b_3^1 = 1$
$W_{11}^2 = W_{21}^2 = W_{31}^2 = b_1^2 = 1$
$\sigma(x) = \frac{1}{1+e^{-x}}$ (sigmoid function)
Note: $\frac{\partial \sigma(x)}{\partial x} = \sigma(x) * (1 - \sigma(x))$

Forward primal trace	Backward derivative trace
$x_1 = 1$ $x_2 = 2$	$\frac{\partial y}{\partial y} = 1$
$h_1 = (W_{11}^1 * x_1 + W_{21}^1 * x_2) + b_1^1$ $= (0.1 * 1 + 0.1 * 2) + 0.1 = 0.4$ $h_2 = (W_{12}^1 * x_1 + W_{22}^1 * x_2) + b_2^1$ $= (0.5 * 1 + 0.5 * 2) + 0.5 = 2$ $h_3 = (W_{13}^1 * x_1 + W_{23}^1 * x_2) + b_3^1$ $= (1 * 1 + 1 * 2) + 1 = 4$ $n_1 = \sigma(h_1) = \sigma(0.4) \approx 0.60$ $n_2 = \sigma(h_2) = \sigma(2) \approx 0.88$ $n_3 = \sigma(h_3) = \sigma(4) \approx 0.98$ $y = (W_{11}^2 * n_1 + W_{21}^2 * n_2 + W_{31}^2 * n_3) + b_1^2$ $= (1 * 0.60 + 1 * 0.88 + 1 * 0.98) + 1 = 3.46$	$\frac{\partial y}{\partial n_3} = W_{31}^2 = 1$ $\frac{\partial y}{\partial n_2} = W_{21}^2 = 1$ $\frac{\partial y}{\partial n_1} = W_{11}^2 = 1$ $\frac{\partial y}{\partial h_3} = \frac{\partial y}{\partial n_3}\frac{\partial n_3}{\partial h_3} = 1 * \sigma(h_3) * (1 - \sigma(h_3))$ $= 1 * 0.60 * (1 - 0.60) = 0.24$ $\frac{\partial y}{\partial h_2} = \frac{\partial y}{\partial n_2}\frac{\partial n_2}{\partial h_2} = 1 * \sigma(h_2) * (1 - \sigma(h_2))$ $= 1 * 0.88 * (1 - 0.88) \approx 0.11$ $\frac{\partial y}{\partial h_1} = \frac{\partial y}{\partial n_1}\frac{\partial n_1}{\partial h_1} = 1 * \sigma(h_1) * (1 - \sigma(h_1))$ $= 1 * 0.98 * (1 - 0.98) \approx 0.02$ $\frac{\partial y}{\partial x_2} = \frac{\partial y}{\partial h_3}\frac{\partial h_3}{\partial x_2} = 0.24 * W_{23}^1 = 0.24 * 1 = 0.24$ $\frac{\partial y}{\partial x_1} = \frac{\partial y}{\partial h_3}\frac{\partial h_3}{\partial x_1} = 0.24 * W_{13}^1 = 0.24 * 1 = 0.24$ $\frac{\partial y}{\partial x_2} = \frac{\partial y}{\partial x_2} + \frac{\partial y}{\partial h_2}\frac{\partial h_2}{\partial x_2} = 0.24 + 0.11 * W_{22}^1$ $= 0.24 + 0.11 * 0.5 = 0.35$ $\frac{\partial y}{\partial x_1} = \frac{\partial y}{\partial x_1} + \frac{\partial y}{\partial h_2}\frac{\partial h_2}{\partial x_1} = 0.24 + 0.11 * W_{12}^1$ $= 0.24 + 0.11 * 0.5 = 0.35$ $\frac{\partial y}{\partial x_2} = \frac{\partial y}{\partial x_2} + \frac{\partial y}{\partial h_1}\frac{\partial h_1}{\partial x_2} = 0.35 + 0.02 * W_{21}^1$ $= 0.35 + 0.02 * 0.1 = 0.352$ $\frac{\partial y}{\partial x_1} = \frac{\partial y}{\partial x_1} + \frac{\partial y}{\partial h_1}\frac{\partial h_1}{\partial x_1} = 0.35 + 0.02 * W_{11}^1$ $= 0.35 + 0.02 * 0.1 = 0.352$

Fig. S6.1: An example of automatic differentiation to calculate the partial derivatives of neural network output (y) respective to the inputs (x_1 and x_2).

S6.3 The half and one quarter of the full training data

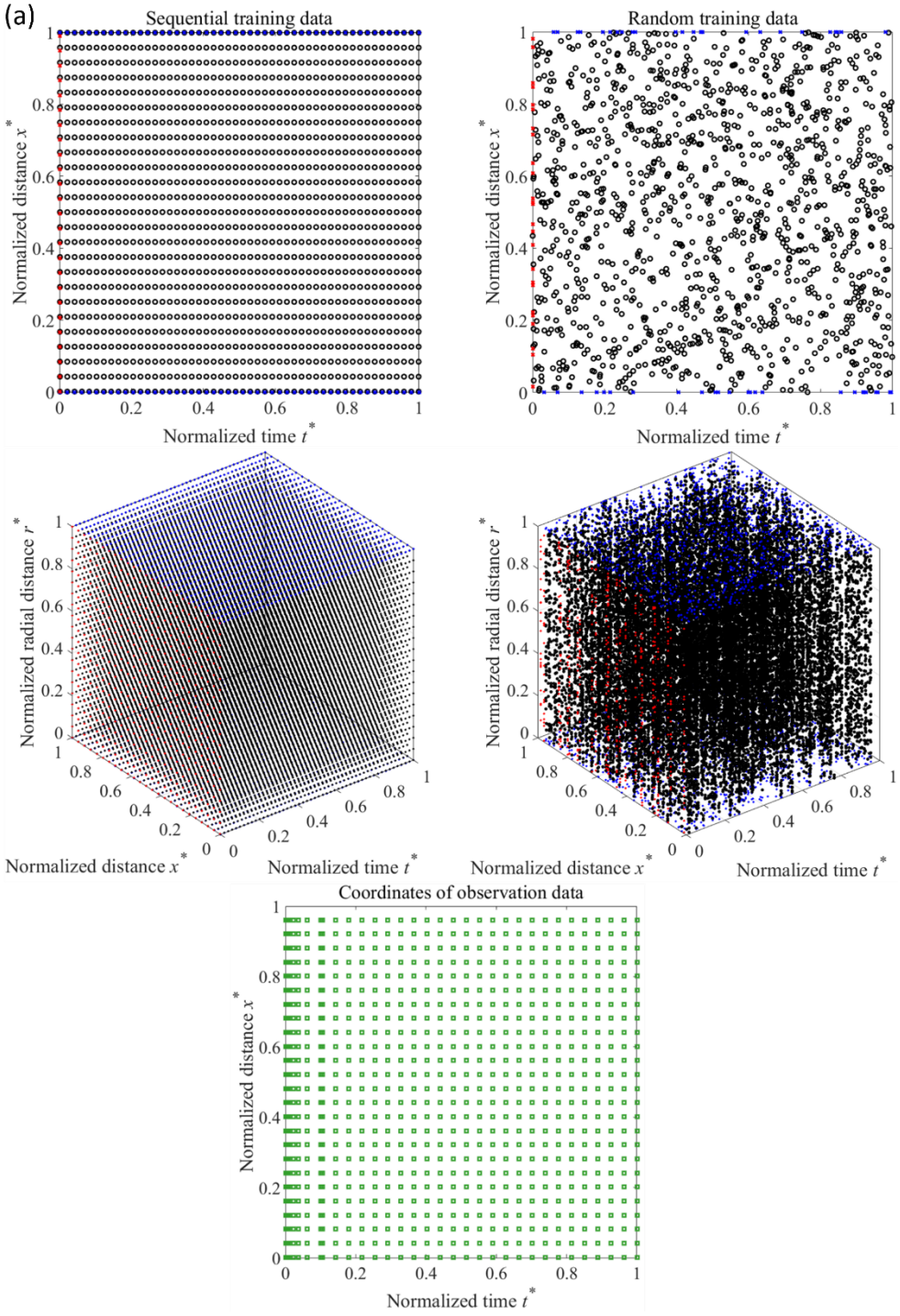

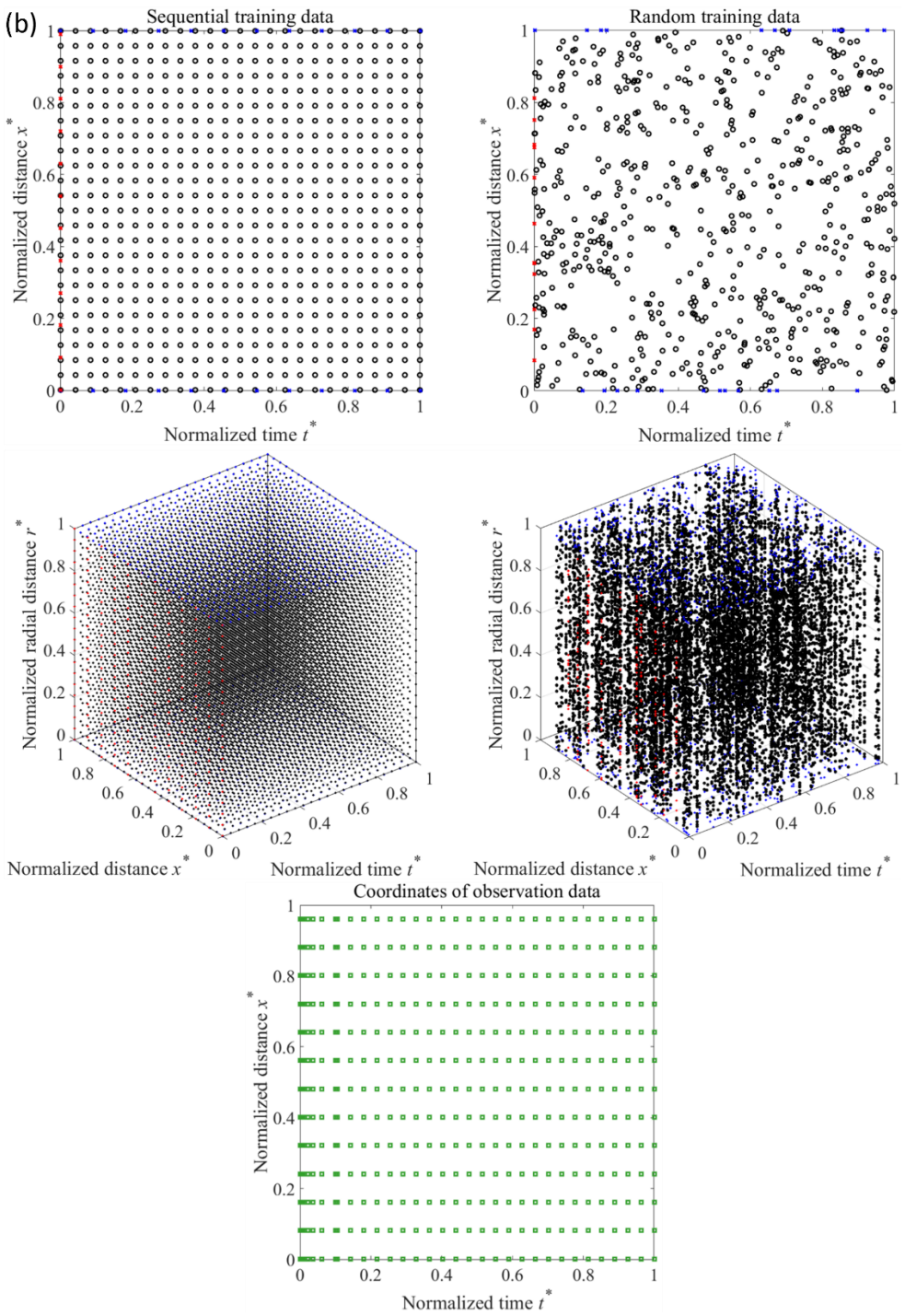

Fig. S6.2: Half of the full raining data (a) or one quarter of the full training data (b) of physical informed neural networks (PINNs). In each case, the first row and second row represent the training points of PDEs (black symbols), initial conditions (red symbols) and boundary conditions (blue symbols) of first (output of C_w^*) and second (output of $C_{w,p}^*$) neural network by using sequential (left column) or random (right column) training points, respectively. The third row shows the spatial temporal coordinates of observation data applied in semi-Laplace solution to generate virtual true concentrations (here only C_w^*) as training data of PINNs.

S6.4 Impacts of various factors on training PINNs

S6.4.1 Impact of amount of observation data (N_{data})

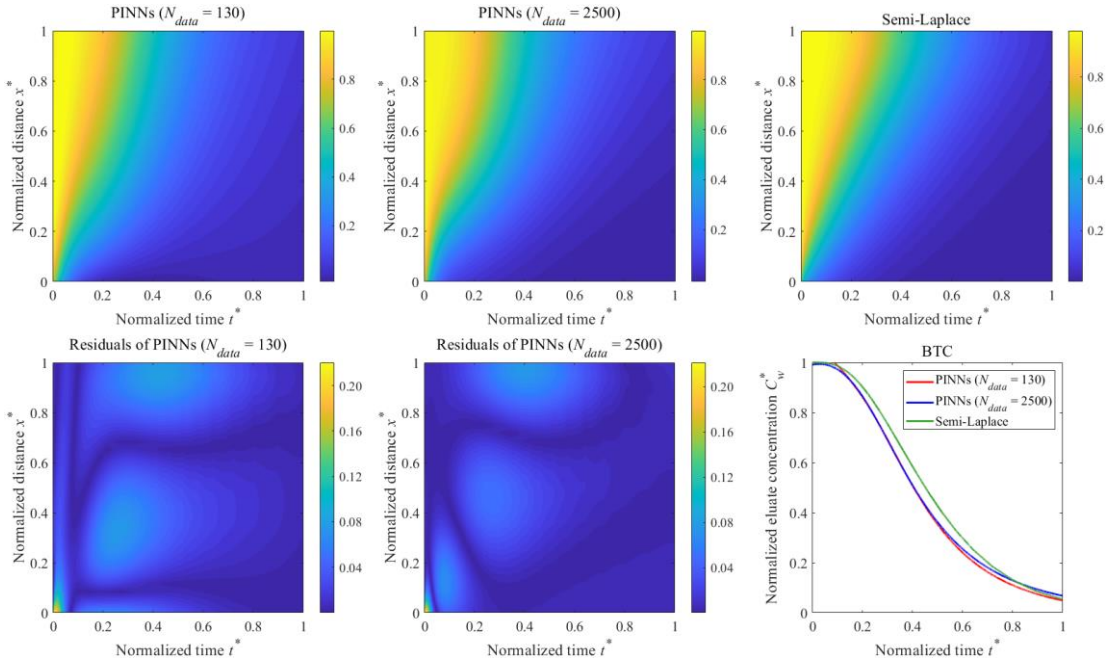

Fig. S6.3: Comparison of PINNs solutions by using different numbers of observation data in training (N_{data} =130, 2500) with semi-Laplace solution of advective-dispersive transport with coupled film intraparticle pore diffusion (ADE-FIPPD). In each case, spatial-temporal normalized solute aqueous concentrations (C_w^*) of PINNs solutions and semi-Laplace solution are presented in the top panel. The absolute errors of PINNs solutions ($|C_{w,PINNs}^* - C_{w,semi-Laplace}^*|$) as well as the breakthrough curves (BTCs) at the outlet ($x^* = 1$) of the transport are showed in the bottom panel. (Parameters used in model are described in section 6.2.4.1; here only case of K_d = 100 L kg^{-1} is displayed.)

S6.4.2 Impact of neuron numbers in each hidden layer of neural networks

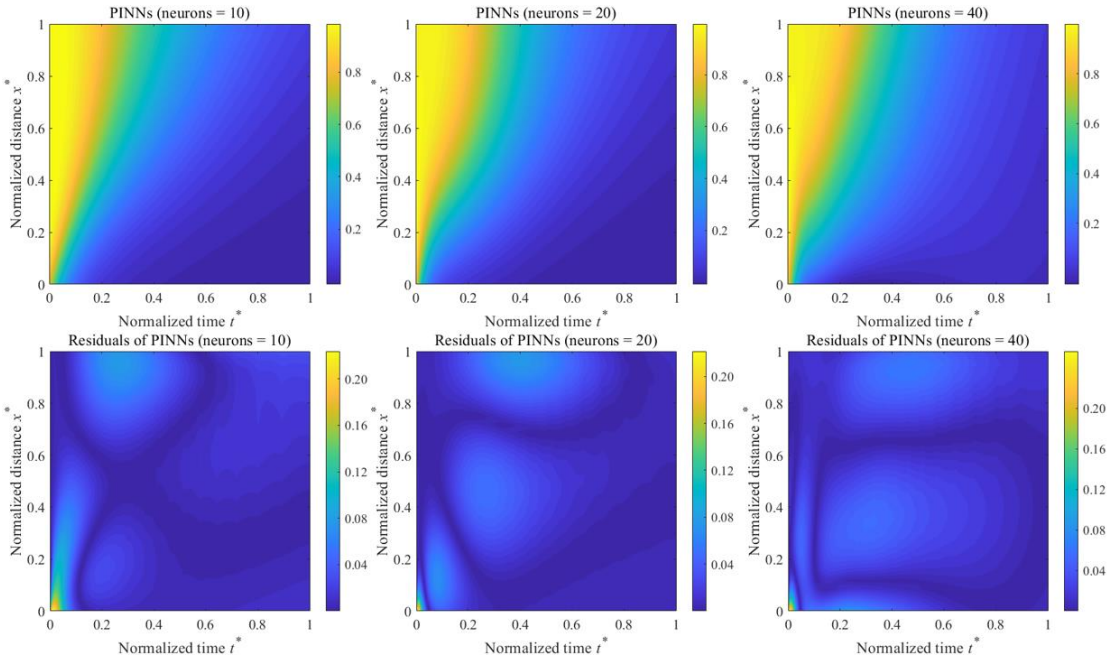

Fig. S6.4: Comparison of PINNs solutions by using different neurons in each hidden layer (neurons = 10, 20, 40) with semi-Laplace solution of advective-dispersive transport with coupled film intraparticle pore diffusion (ADE-FIPPD). In each case, spatial-temporal normalized solute aqueous concentrations (C_w^*) of PINNs solutions are presented in the top panel. The absolute errors of PINNs solutions ($|C_{w,PINNs}^* - C_{w,semi-Laplace}^*|$) and semi-Laplace solution as well as the breakthrough curves (BTCs) at the outlet ($x^* = 1$) of the transport are showed in the mid and bottom panel respectively. (Parameters used in model are described in section 6.2.4.1; here only case of $K_d = 100$ L kg^{-1} is displayed.)

S6.4.3 Impact of quantities of layers of neural networks

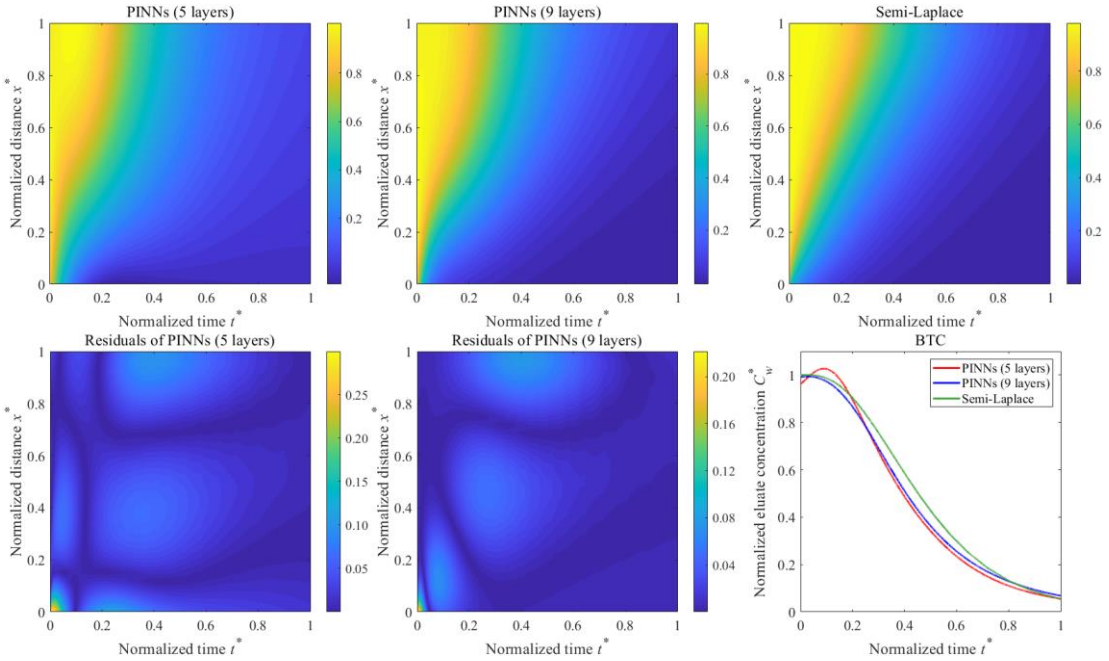

Fig. S6.5: Comparison of PINNs solutions by using different layers of neural networks in training (Layers = 5, 9) with semi-Laplace solution of advective-dispersive transport with coupled film intraparticle pore diffusion (ADE-FIPPD). In each case, spatial-temporal normalized solute aqueous concentrations (C_w^*) of PINNs solutions and semi-Laplace solution are presented in the top panel. The absolute errors of PINNs solutions ($|C_{w,PINNs}^* - C_{w,semi-Laplace}^*|$) as well as the breakthrough curves (BTCs) at the outlet ($x^* = 1$) of the transport are showed in the bottom panel. (Parameters used in model are described in section 6.2.4.1; here only case of $K_d = 100$ L kg^{-1} is displayed.)

S6.4.4 Impact of activation functions of neural networks

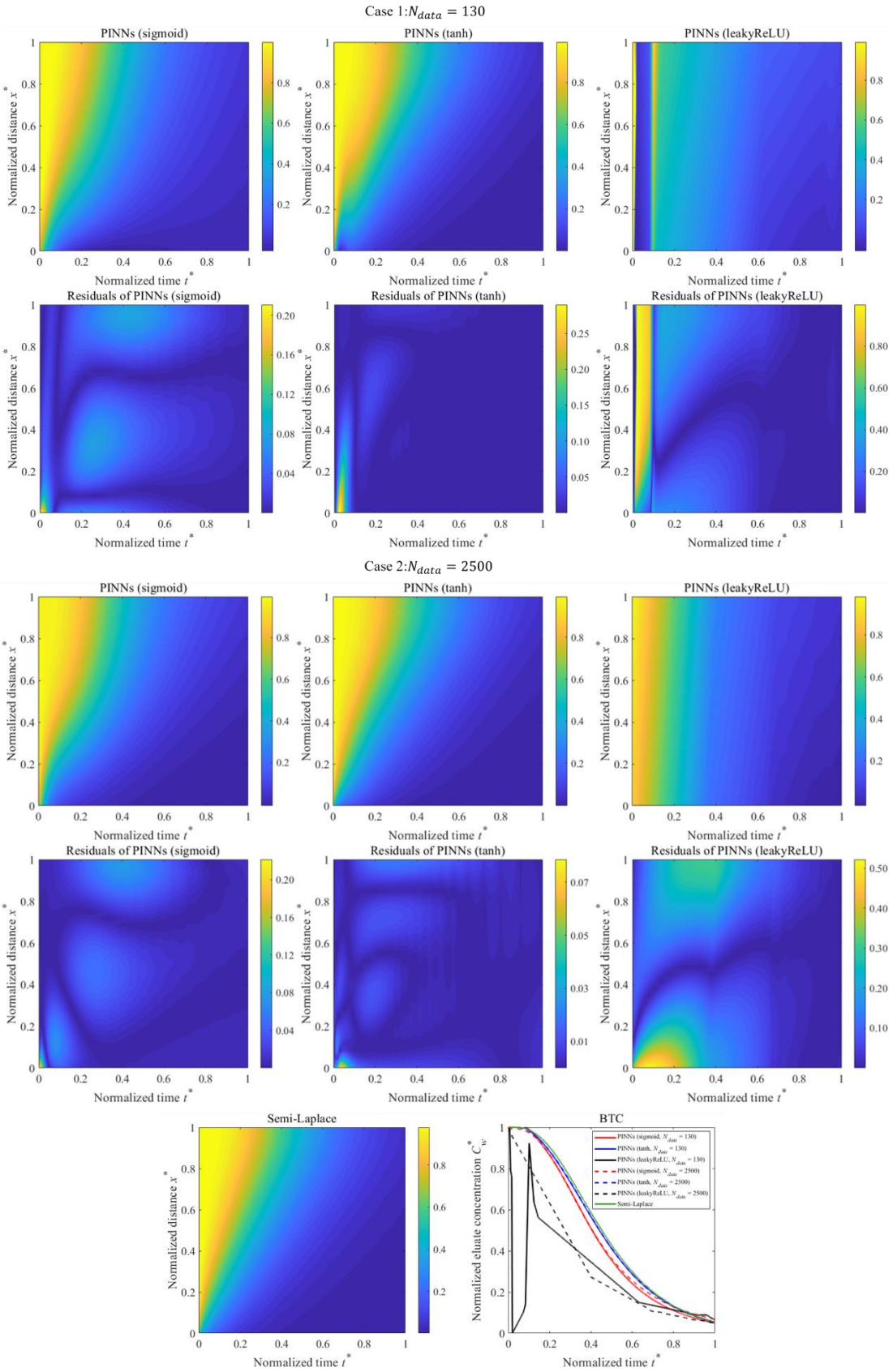

Fig. S6.6: Comparison of PINNs solutions by using different activation functions (sigmoid, tanh and leakyReLU) and different amount of observation training data (case 1:$N_{data} = 130$; case 2: $N_{data} = 2500$) with semi-Laplace solution of advective-dispersive transport with

coupled film intraparticle pore diffusion (ADE-FIPPD). In each case, spatial-temporal normalized solute aqueous concentrations (C_w^*) of PINNs solutions with different activation functions are presented in the top panel. The absolute errors of PINNs solutions ($|C_{w,PINNs}^* - C_{w,semi-Laplace}^*|$) and semi-Laplace solution are depicted in the bottom panel. The reference (semi-Laplace solution) and the breakthrough curves (BTCs) at the outlet ($x^* = 1$) of the transport of all scenarios are summarized in the last row. (Parameters used in model are described in section 6.2.4.1; here only case of $K_d = 100$ L kg^{-1} is displayed.)

S6.5 Loss components tracking in training PINNs

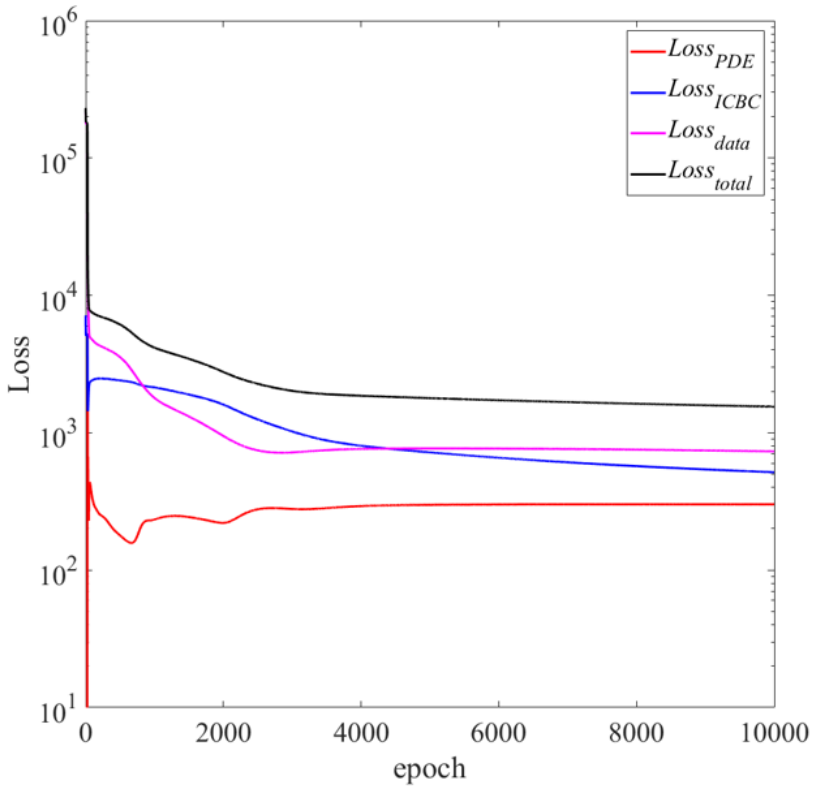

Fig. S6.7: The loss functions of training physical informed neural networks (PINNs) for solving 1-D advective dispersive transport with coupled film intraparticle diffusion (ADE-FIPPD). The loss components of PDEs ($Loss_{PDE}$), initial and boundary conditions ($Loss_{ICBC}$), observation data ($Loss_{data}$) as well as the total loss ($Loss_{total}$) are tracked in each epoch. (Parameters used in model are described in section 6.2.4.1; here only case of $K_d = 100$ L kg^{-1} is displayed.)

S6.6 Comparison of NN, PINNs and semi-Laplace solution

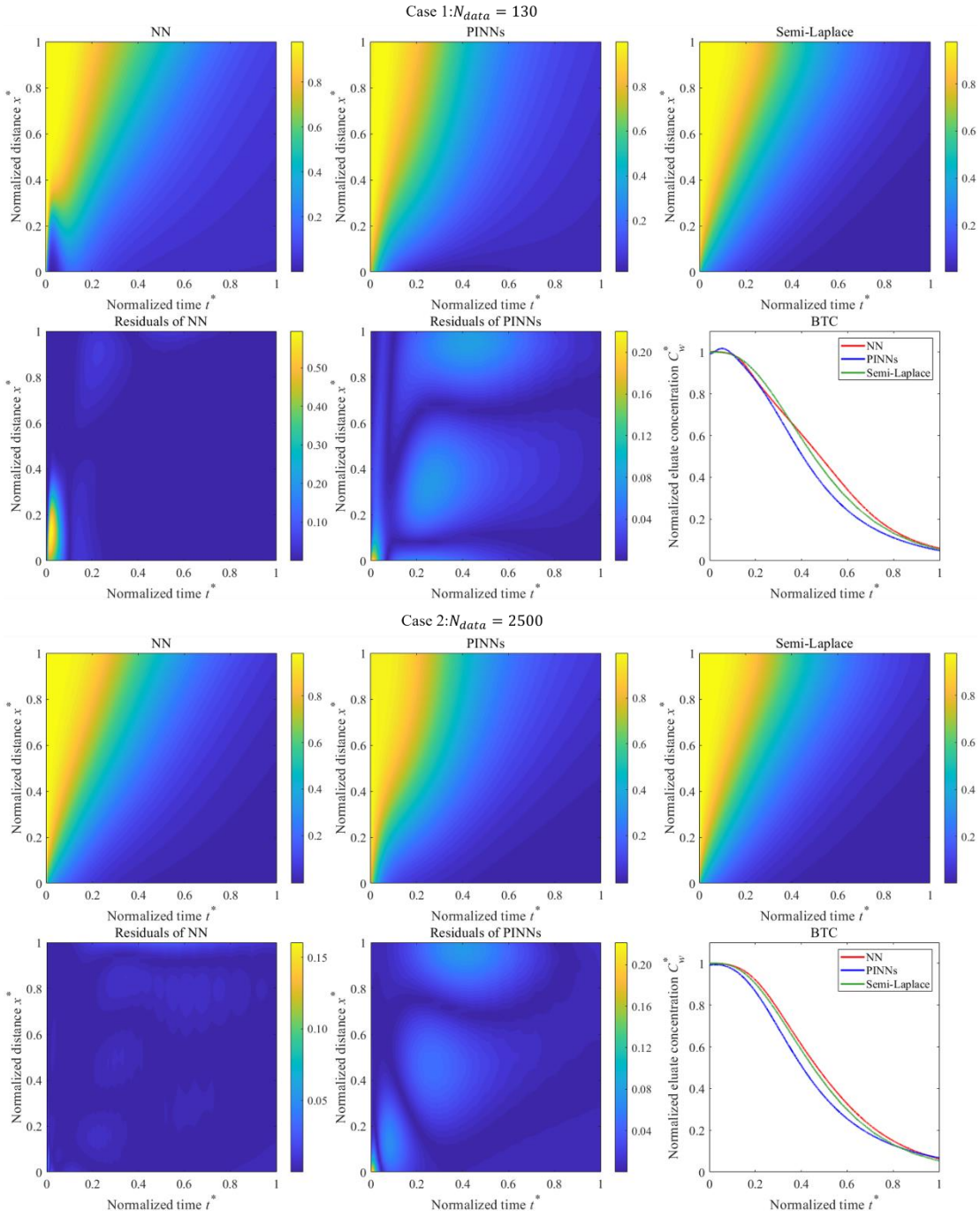

Fig. S6.8: Comparison of pure data driven model (neural network (NN)) and PINNs solution by using different numbers of observation data in training (N_{data} =130, 2500) with semi-Laplace solution of advective-dispersive transport with coupled film intraparticle pore diffusion (ADE-FIPPD). In each case, spatial-temporal normalized solute aqueous concentrations (C_w^*) of three methods are presented in the top panel. The absolute errors of NN ($|C_{w,NN}^* - C_{w,semi-Laplace}^*|$) and PINNs ($|C_{w,PINNs}^* - C_{w,semi-Laplace}^*|$) as well as breakthrough curves (BTCs) at the outlet ($x^* = 1$) of the transport are depicted in the

bottom panel. (NN uses the same layers and neurons as PINNs; parameters used in simulation are described in section 6.2.4.1.)

References

Collobert, R., Kavukcuoglu, K., Farabet, C., 2011. Torch7: A matlab-like environment for machine learning. BigLearn, NIPS Work. 1–6.

Cuomo, S., Rosa, M. De, Giampaolo, F., Izzo, S., Schiano, V., Cola, D., 2023. Solving groundwater flow equation using physics-informed neural networks. Comput. Math. with Appl. 145, 106–123. https://doi.org/10.1016/j.camwa.2023.05.036.

Güneş Baydin, A., Pearlmutter, B.A., Andreyevich Radul, A., Mark Siskind, J., 2018. Automatic differentiation in machine learning: A survey. J. Mach. Learn. Res. 18, 1–43.

Hornik, K., Stinchcombe, M., White, H., 1989. Multilayer feedforward networks are universal approximators. Neural Networks. 2, 359–366. https://doi.org/10.1016/0893-6080(89)90020-8.

Jerrell, M.E., 1997. Automatic Differentiation and Interval Arithmetic for Estimation of Disequilibrium Models. Comput. Econ. 10, 295–316. https://doi.org/10.1023/A:1008633613243.

Lu, L., Meng, X., Mao, Z., Karniadakis, G.E., 2021. DeepXDE: A deep learning library for solving differential equations. SIAM Rev. 63, 208–228. https://doi.org/10.1137/19M1274067.

McClenny, L.D., Braga-Neto, U.M., 2020. Self-Adaptive Physics-Informed Neural Networks using a Soft Attention Mechanism. arXiv, abs/2009.04544.

Raissi, M., 2018. Forward-backward stochastic neural networks: Deep learning of high-dimensional partial differential equations. arXiv preprint arXiv:1804.07010. https://doi.org/10.48550/arXiv.1804.07010

Raissi, M., Perdikaris, P., Karniadakis, G.E., 2019. Physics-informed neural networks: A deep learning framework for solving forward and inverse problems involving nonlinear partial differential equations. J. Comput. Phys. 378, 686–707. https://doi.org/https://doi.org/10.1016/j.jcp.2018.10.045.